

SECURITY CLASSIFICATION OF THIS PAGE (When Data Entered)

5

REPORT DOCUMENTATION PAGE		READ INSTRUCTIONS BEFORE COMPLETING FORM
1. REPORT NUMBER AFOSR-TR-82-0352	2. GOVT ACCESSION NO. AD-A114269	3. RECIPIENT'S CATALOG NUMBER
TITLE (and Subtitle) Solar Flare Studies		5. TYPE OF REPORT & PERIOD COVERED Final Scientific Report 1 July 1976-31 January 1982
AUTHOR(s) Richard C. Canfield		6. PERFORMING ORG. REPORT NUMBER UCSD-SP-82-17
PERFORMING ORGANIZATION NAME AND ADDRESS Center for Astrophysics & Space Sciences University of California, San Diego La Jolla, CA 92093		8. CONTRACT OR GRANT NUMBER(s) AFOSR 76-3071
CONTROLLING OFFICE NAME AND ADDRESS AFOSR/NP Building 410 Bolling AFB, DC 20332		10. PROGRAM ELEMENT, PROJECT, TASK AREA & WORK UNIT NUMBERS 61102F 2311/A1
MONITORING AGENCY NAME & ADDRESS (if different from Controlling Office)		12. REPORT DATE 20 March 1982
		13. NUMBER OF PAGES 548
		15. SECURITY CLASS. (of this report) <i>Unclass</i>
		15a. DECLASSIFICATION DOWNGRADING SCHEDULE

DISTRIBUTION STATEMENT (of this Report)

Approved for public release, distribution unlimited.

17. DISTRIBUTION STATEMENT (of the abstract entered in Block 20, if different from Report)

18. SUPPLEMENTARY NOTES

19. KEY WORDS (Continue on reverse side if necessary and identify by block number)

Solar Flares
Radiative Transfer
Quasars

20. ABSTRACT (Continue on reverse side if necessary and identify by block number)

See next page.

DTIC
ELECTE
MAY 07 1982

E

DD FORM 1 JAN 73 1473

SECURITY CLASSIFICATION OF THIS PAGE (When Data Entered)

DA 114269

DTIC FILE COPY

↓
ABSTRACT

The primary objective of the research described in this report was increased understanding of solar flares. In the course of the research, many tasks were carried out, which achieved not only the primary objective, but also secondary objectives in related areas. The research program started with active participation in the Skylab Solar Flare Workshop. New observations of solar flare spectra were obtained and interpreted in terms of basic solar flare mechanisms. It was shown that the basic process by which the X-ray radiation of flares is created is by heating the flare plasma to temperatures of about ten million degrees, through evaporation of the chromosphere. This process is driven both by beams of accelerated electrons and by thermal conduction. However, in the major flare for which data were interpreted, the principal energy release mechanism was found to be thermal in nature, implying that most of the flare energy is released in the form of heat, and not charged particles.

Theoretical modeling methods were developed for understanding the spectra of solar flares. These methods were applied to flare loop dynamics. The spectral signatures of both chromospheric evaporation and beams of accelerated electrons were established. Finally, a theoretical program of theoretical magnetohydrodynamic stability studies was begun.

↑



Accession For	
NTIS GRA&I	<input checked="" type="checkbox"/>
DTIC TAB	<input type="checkbox"/>
Unannounced	<input type="checkbox"/>
Justification	
By	
Distribution/	
Availability Codes	
Dist	Avail and/or Special
A	

CONTENTS

Page

I. Research Objectives	7
II. Research Accomplishments	9
a. Solar Flare Workshop	9
i. The Chromosphere and Transition Region	9
ii. Radiative Energy Output of the 5 September 1973 Flare	53
iii. Mass Ejections	75
b. Solar Flare Observations and Interpretation	147
i. ATM Evidence for a Low Nonthermal Proton/Electron Energy Flux Ratio in Solar Flares	147
ii. Observed L α Profiles for Two Solar Flares: 14:12 UT 15 June, 1973 and 23:16 UT 21 January, 1974	155
iii. Indirect Estimation of Energy Disposition by Non-thermal Electrons in Solar Flares	169

iv.	A Qualitative Interpretation of 7 August 1972	
	Impulsive Phase Flare H α Line Profiles	177
v.	Direct Evidence for Chromospheric Evaporation	
	in a Well-Observed Compact Flare	193
c.	Solar Flare Theory	253
i.	H α Profiles from Electron-Heated Solar Flares	254
ii.	Radiative Hydrodynamics of Flares: Preliminary	
	Results and Treatment of the Transition Region	265
iii.	The Dynamic Formation of Quasi-Static	
	Active Region Loops	271
iv.	A Probabilistic Approach to Radiative Energy	
	Loss Calculations for Optically Thick	
	Atmospheres: Hydrogen Lines and Continua	291
v.	Flare Loop Radiative Hydrodynamics.	
	I. Basic Methods	303
vi.	Flare Loop Radiative Hydrodynamics.	
	II. Radiative Stability of Empirical Models	367

vii.	The Effects on the MHD Stability of Field Line Tying to the End Faces of a Cylindrical Magnetic Loop	405
d.	Quiet Sun Studies	423
i.	Spatial Structure in Lines in the 3398-3526 Å Region at the Extreme Limb: Observation, Identification, and Interpretation	423
ii.	The Height Variation of Velocity and Temperature Fluctuations in the Solar Photosphere	441
e.	Quasar Theory	455
i.	The Implications of Hydrogen Emission Line Ratios in Quasi-Stellar Objects	455
ii.	Theoretical Quasar Emission Line Ratios. I. Transfer and Escape of Radiation	463
iii.	Theoretical Quasar Emission Line Ratios. II. Hydrogen $L\alpha$, Balmer, and Paschen Lines, and the Balmer Continuum	475

iv.	Theoretical Quasar Emission Line Ratios.	
	III. Flux Divergence and Photon Escape	491
v.	The Lyman α /H α Ratio in Solar Flares and Quasars	499
vi.	Theoretical Quasar Emission Line Ratios.	
	VI. A Probabilistic Radiative Transfer Equation for Finite Slab Atmospheres	509
	f. Summary	533
III.	Professional Personnel	535
IV.	Publications	537
V.	Spoken Papers	541
VI.	Consultative and Advisory Functions	545

I. RESEARCH OBJECTIVES

The primary objective of this research was the significant enhancement of scientific understanding of solar flares.

The secondary objective was to use the techniques developed for the primary objective to address other problems, when it was in the best interest of the primary objective.

The specific approach used was three-fold:

(1) Interpret available solar flare observations. When this grant started, there were already some spectroscopic observations available of the right general type. However, they were totally inadequate for a major advance in our understanding of flares. Our use of these observations quickly demonstrated their inadequacies.

(2) Make new improved solar flare observations. By combining the capabilities of several observing facilities in space and on the ground, we were able to make a major improvement in the observational data that was available.

(3) Develop new theoretical techniques. The theoretical techniques available at the start of the grant were obviously inadequate to interpret the data. This problem was rectified during the grant. The new theoretical techniques turned out to have very general applicability to problems dealing with radiating plasmas of all types.

II. RESEARCH ACCOMPLISHMENTS

a) Solar Flare Workshop

Relatively early in the report period, both Canfield and McClymont began participating in the Skylab Solar Flare Workshop. This Workshop was organized along team lines. One team, led by Canfield, focused its attention on the chromospheric and transition region parts of the flare, including the well-known $H\alpha$ flare phenomenon. Canfield also led another special study of the radiative output of a flare selected because it was particularly well observed by a wide variety of instruments. Among the quantities they measured was the radiative output in the ultraviolet and X-ray bands relative to that in $H\alpha$. This is of interest, of course, because of the terrestrial effects of the ultraviolet and X-ray flare radiation, as well as for the purpose of understanding flare physics. Another team, of which McClymont was an active member, studied flare mass ejections. Such mass ejections are of solar-terrestrial importance because they are associated with a variety of geomagnetic phenomena. They also provide considerable information on the magnetic field structure of the flare site, and hence the the flare energy supply. These papers review the state of knowledge of these aspects of solar flares as of about 1978, and form a suitable starting point for this report.

i) The Chromosphere and Transition Region

This paper, published as Chapter 6 of the monograph Solar Flares, edited

by P.A. Sturrock, had an important impact on our research program. On the theoretical side, it showed how poor the theoretical modelling of flares had been up to that time. It became obvious that such modelling could provide an effective means of determining from observations where the flare energy release was taking place and what its form was (i.e. is it primarily the acceleration of fast protons or electrons, or is it primarily heating? It led us to start a theoretical flare modelling program at UCSD, which is discussed below. Another Workshop contribution was to demonstrate the need for high temporal and spatial resolution observations of flare spectra, since the observations to date had neither. There were not even any spectral observations during the most critical phases of flares, i.e. just before and during the impulsive phase during which fast particles are accelerated. This led us to begin the observational program at Sacramento Peak Observatory, in conjunction with the Solar Maximum Mission, described below.

6. THE CHROMOSPHERE AND TRANSITION REGION

Richard C. Canfield; J.C. Brown, G.E. Brueckner, J.W. Cook, I.J.D. Craig, G.A. Doschek, A.G. Emslie, J.-C. Henoux, B.W. Lites, M.E. Machado, J.H. Underwood

6.1 INTRODUCTION

It is now generally believed that the site of the primary flare energy release is in the corona. If this viewpoint, which we call the *canonical* view, is correct, then the flare phenomena occurring lower in the atmosphere, in particular in the classic "chromospheric flare," must come about as a result of transfer of energy and momentum from the primary energy-release site in the corona. It is important to understand the basic physical processes that carry out this transfer, since it is probable that only through understanding these processes will the primary energy release mechanism be understood.

In this chapter we confine ourselves to studies of physical processes that involve the low-temperature part of the flare, principally the transition region and the chromosphere. The interaction of the corona with these lower layers will affect not only the low-temperature material, but will also have a profound effect on the development of the coronal plasma. The two cannot properly be treated separately from one another. However, since the corona and chromosphere differ considerably in some fundamental respects (e.g., the corona is optically thin, while the low-temperature regions are thick; the observational techniques are very different, etc.), the work of our group divided naturally into high- and low-temperature sections, and this chapter is arranged in the same manner.

The physical processes involved in the interaction between the coronal and chromospheric parts of the flare can effectively be studied through the comparison of theoretical models and the observational data. This is our basic approach in this chapter. The fundamental questions we address concern the role of conduction, radiation, fast particles, and mass motion in the chromospheric-coronal interaction. The data used in our approach to these problems are intensities of lines and continua in the EUV and XUV, broad-band soft X-ray and radio fluxes, spectral line profiles and Doppler shifts in the EUV and visible, and the variation of these quantities with space and time. Appendix A on the radiative energy output of the 5 September 1973 flare contains an important contribution to the data base for these studies.

There is inevitably some overlap of the material treated here with that covered in a much more general context in other chapters. We consider energetic particles, the impulsive phase, and the thermal X-ray plasma, but only insofar as they interact with the chromosphere and photosphere or play a role in model flare atmospheres. Also, we consider mass motions but restrict our attention to phenomena below the limit of present spatial resolution.

6.2 BACKGROUND

An important problem of solar-flare theory is to explain how the solar atmosphere is rapidly heated, and less rapidly cooled, during a flare. The flare models that describe this process must be internally consistent; also, they must agree with the compelling features of the data. As background for our work in this chapter, which is predominantly observational, we review the models that have had the greatest effect on our present understanding. We will not try to be encyclopedic in our discussion, since comprehensive reviews of flare models have been given by Švestka (1976) and Somov and Syrovatskii (1976). For convenience, we distinguish between static, dynamic, and hydrodynamic models. We note that all these models are one-dimensional and make the assumption that the magnetic pressure greatly exceeds the material pressure, an assumption we believe to be only marginally satisfied.

6.2.1. Static Models

The first attempts at theoretical flare modelling made the expedient *static* assumption, and concentrated on the high-temperature (coronal) flare in the cooling phase. Culhane *et al.* (1970) showed that the coronal flare cooled by radiation in optically-thin emissions and by heat conduction to the much cooler chromosphere. Strauss and Papagiannis (1971) showed that the energy input in energetic particles necessary to explain the evolution of the X-ray intensity of a single flare was compatible with total flare energy estimates. Without assuming a specific energy input mechanism, Shmeleva and Syrovatskii (1973) discussed the two limiting cases in which the static models are valid: (1) before mass motion can develop, the so-called *constant density limit*; and (2) after motions essentially cease, the so-called *constant pressure limit*. They found that in flares, like the quiet sun, a very thin coronal-chromospheric transition region occurs, which explains the similarity of flare images over a wide range of temperatures around 10^5 K. This also means that in *transition region* lines, the flare is thin—i.e., that it has a *shell* structure, in contrast to the thick flare, with filamentary structure, suggested by Švestka (1972) for the chromosphere. Finally, they showed that in the constant-pressure models the transition region must shift deeper into the atmosphere during flares, compared to the quiet sun. Antiochos and Sturrock (1976) showed that the magnetic field geometry has a significant effect on the heat flux into the chromosphere and the total conduction cooling of the high-temperature part of the flare.

Several papers have dealt with the lower-temperature flare, i.e., the chromospheric flare, in the constant-pressure limit. Brown (1973) calculated a grid of models assuming prolonged heating by fast electrons, i.e., free expansion was permitted to satisfy static energy balance between electron heating and radiative cooling. Canfield (1974a) solved the hydrogen equilibrium equations and radiative transfer equation for these models, and showed that H α equivalent widths, maximum electron densities, and integrated second-level populations were all typical of small- and medium-sized flares (cf. Švestka 1976). Large nonthermal velocities, of order tens of km s^{-1} , were required to make computed profiles agree with observation.

Somov (1975), Henoux and Nakagawa (1977), and Machado (1978) treat an effect neglected by all the above authors, viz., heating of the lower atmosphere

by soft X-ray flare radiation from the corona. Hénoux and Nakagawa construct model atmospheres assuming a steady state between X-ray heating and radiative cooling, using a modified optically-thin approximation. They showed that soft X-ray heating probably plays a significant, though not dominant, role in the chromospheric flare energy budget.

Machado and Linsky (1975) took an entirely different approach to model-building, the empirical approach. By trial and error they generated a grid of model atmospheres (i.e., temperature as a function of column mass) consistent with the radiative transfer and statistical equilibrium equations for model hydrogen and calcium atoms. These models reproduce the observed range of profiles of H α , the Lyman continuum, and the major Ca II lines reasonably well. They found: (1) with increasing flare importance, the upper chromosphere and transition region occur lower in the atmosphere; (2) there must be macrovelocities of order tens of km s⁻¹, increasing with height in the chromosphere; and (3) considerable heating is present in the lower atmosphere; for example, the temperature increase over active regions exceeds 10³ K at the level of the temperature minimum in the quiet sun.

Static calculations of the effects of nonthermal proton beams on the lower atmosphere have been made by Najita and Orrall (1970), Švestka (1970), Hudson (1973), Orrall and Zirker (1976), Lin and Hudson (1976), and Emslie (1978), with mixed conclusions regarding the role of protons. We refer the reader to Chapter 4 for a discussion of this problem. In view of the difficulty of modeling the thermal response of optically thick layers, the least ambiguous evidence of the presence of nonthermal protons in the low-energy range, $10 \leq E \leq 300$ keV, would probably be the asymmetry in the wings of L α predicted by Orrall and Zirker (1976). An observational attempt to detect this effect has been made by Canfield and Cook (1978) during this workshop and is discussed below.

6.2.2. Dynamic Models

In the past, some progress has been made by simultaneously solving not the full set of hydrodynamic equations, which we discuss separately below, but rather only part of the set. For example, Nakagawa *et al.* (1973) carried out a simple kinematic calculation that showed that downward-moving shocks caused by the impact of infalling material in the initial Mach number range $5 \leq M \leq 30$ could account for considerable heating of the chromosphere above the temperature minimum. However, the H α profiles computed by Canfield and Athay (1974) showed that the sense of the H α core asymmetry is opposite that which is observed. In the observations of major flares (see Švestka, 1976, p. 7), the red peak is brighter; in the calculations, the blue peak is brighter. This suggests that the observed core asymmetry is due to differential *expansion* of the chromosphere, not compression by infalling material.

Antiochos and Sturrock (1978) solved the energy and continuity equations and assumed that upward velocities are less than the sound speed. They showed that these motions (which have for some time now been called by the somewhat misleading term "evaporation") lead to reduced heat flux into the chromosphere and enhanced EUV flare emission, compared to their static model. A comparison of the predictions of the static and evaporative models was carried out during this workshop by Underwood *et al.*, and is discussed below.

6.2.3. Hydrodynamic Models

We now turn to what we call hydrodynamic models, i.e., models based on a simultaneous solution of the usual continuity, energy, and momentum equations of hydrodynamics. The calculations described below of course differ in boundary conditions, auxiliary equations, etc.

Craig and McClymont (1976) numerically solved the hydrodynamic equations for an infinitely long flux tube. They showed that the inclusion of mass motions has a major effect on the cooling of the coronal flare plasma. Their calculation is not a flare model per se, since an infinitely long flux tube without fixed, cool boundaries to represent the intersection of actual magnetic field lines with the photosphere is a realistic representation of only the first minute or two of flare-loop evolution. A related analytic solution of the special case of spatially constant pressure was carried out by Craig and McClymont (1978). They showed that only dynamic models can predict the initial rapid decrease of the temperature of flares accompanied by an *increase* in the amplitude of the emission measure, in the early cooling phase.

The first attempts to model the interaction of the chromosphere, transition region, and corona in a hydrodynamic framework were made by Kostyuk and Pikel'ner (1975) and Kostyuk (1976a). The former treats open field geometry, the latter closed loops. They modeled the effects of a beam of electrons of 100-second duration. Unfortunately, no density profiles are given, nor can they accurately be derived from the information given, as shown by McClymont and Craig (1977), described in Section 6.3.3 of this chapter. Somov and Syrovatskii (1976) have made an important point about the work of Kostyuk and Pikel'ner (1975) and Kostyuk (1976a)—in their numerical calculation they did not foresee the possibility that the characteristic times for the condensation thermal instability might be much shorter than the one-second time step they used. For this reason, Somov and Syrovatskii assert that the solutions Kostyuk and Pikel'ner (1975) and Kostyuk (1976a) obtained are not valid. With this qualification in mind, it is nonetheless instructive to consider the calculations made by Kostyuk (1976b), based on the possibly incorrect models, using the methods of Canfield and Athay (1974) to compute theoretical $H\alpha$ profiles. Several interesting results were obtained. As also found by Canfield and Athay (1974), Canfield (1974), and Machado and Linsky (1975) the profiles of $H\alpha$ were strongly self-absorbed and velocity inhomogeneities were required to produce weakly-reversed profiles as are observed. Secondly, the red asymmetry of $H\alpha$ was associated with chromospheric expansion, not infalling material, consistent with Canfield and Athay's (1974) result for the Nakagawa *et al.* (1973) infall models. The models produce strong $H\alpha$ profiles—rather stronger than usually observed—which appear to anticipate the workshop findings of Brown *et al.* (1978), discussed below. Finally, study of the source of continuous emission at two wavelengths shows that the observed white-light radiation occurs only for hard electron spectra and originates in the same region as the $H\alpha$ emission.

The recent hydrodynamic calculation of Somov, Spektor, and Syrovatskii (1977) has a somewhat different emphasis than the work of Kostyuk. The treatment of radiation from the chromosphere is not as complete, neglecting opacity effects. However, the electrons and ions are treated separately, and the effects of the thermal instability are taken into account. Sufficient information is given to

permit observational comparison. Differential emission-measure curves are given at several times; unfortunately, values for $T_e \lesssim 10^5$ K are unrealistic because of the optically-thin approximation.

The direction in which theoretical modeling should go in the future is clear. At present, the properties of the heating and cooling mechanisms have been modeled only crudely. There are no flare models based on a simultaneous solution of the hydrodynamic and radiative transfer equations. Effects of the radiative instability have not been fully explored. In short, no hydrodynamic treatment has yet convincingly handled the interaction between the high- and low-temperature regions. All models presently treat the magnetic field only to the extent that it defines the geometry of the flare. Finally, there remains the complication that real flares probably comprise many different coronal loops, and so cannot be identified with the evolution of a single flux tube. At present, therefore, we have at best only the basic components of a realistic flare model; the problem is to put them together.

6.3 THE CORONA AND TRANSITION REGION

During the Workshop, considerable interest centered around the interaction between the chromosphere and the corona during flares; specifically, how the high-temperature part of the flare ($T \gtrsim 10^6$ K) cooled by conducting heat to the chromosphere and how the chromosphere responded to this heating. In the background section (6.2), we reviewed pre-Workshop theoretical models. In contrast, during the Workshop we concentrated on observational tests. Underwood *et al.* (1978) studied Skylab UV, EUV, and X-ray data for the 9 August 1973 flare (Section 6.3.1) and compared their data with the predictions of the static and evaporative conductive-cooling models developed by Antiochos and Sturrock (1976, 1978), described in Sections 6.2.1 and 6.2.2. Doschek and Feldman (1978) studied mass motions in transition-zone lines (Section 6.3.2); they searched Skylab UV spectrograms for systematic relationships between temperature, density, and velocity in transition-region lines. Finally, McClymont and Craig (1977) have partially overcome the problems caused by Kostyuk and Pikel'ner (1975) and Kostyuk's (1976a) failure to provide density information for their models. They compute pressure, and coronal and transition-region emission measure for one of Kostyuk and Pikel'ner's (1975) models in Section 6.3.3.

6.3.1. Evolution of the Coronal and Transition-Zone Plasma

Underwood *et al.* (1978) have carried out a study of the thermal evolution of the coronal and transition-region plasma generated in a particular flare event—a particularly simple subflare that occurred at 1551 UT, 9 August 1973. They investigate in particular the flare decay or "cooling" phase, through a detailed study of its X-ray and EUV emissions and their time evolution. Observations of the 9 August event are interpreted and conclusions are drawn regarding the physical processes at work in the flare.

The models of Antiochos and Sturrock (1976, 1978), which were compared with observations, are based on their idealized cases of static and "evaporative" conductive cooling. These two models predict different forms of the differential

emission measure $\chi(T)$, where $\chi(T)$ is the usual emission measure $\xi(T)$ (cf. Craig and Brown, 1976) multiplied by T . For example, if T_0 is the temperature at the top of the loop, in the low-temperature regime ($T/T_0 \ll 1$), $\chi(T) \sim (T/T_0)^{1/2}$ in the evaporative case, but $\chi(T) \sim (T/T_0)^{3/2}$ in the static case.

The observational data that one must use to compare a flare with these two models must cover a range of values of temperature. This was done by using data from the S056 soft X-ray telescope and the X-ray event analyser (X-REA) (Underwood *et al.*, 1977), the S082 A EUV spectroheliograph (Tousey *et al.*, 1977), and the S082 B UV slit spectrograph (Bartoe *et al.*, 1977). The X-ray and XUV data were used to derive T_0 and $n_0^2 V$, which are the two free parameters of the Antiochos and Sturrock models. The EUV data consist of values of the power radiated by the whole flare by several tens of lines that span the temperature range $3.5 \times 10^4 \leq T_m \leq 1.6 \times 10^7$ K, where T_m is the value of T_c at which the line excitation function $G(T)$ is maximal. Data were obtained mainly during the early decay phase of the flare, in the period 1553–1557 UT.

The approach used was to compare the observed intensities with those predicted by the two models, static and evaporative. The predicted power radiated in all observed lines was computed using the forms of the differential emission measure $\chi(T)$ predicted in the static and evaporative models, the values of T_0 and $n_0^2 V$ from the X-ray and XUV data, and the excitation functions of the lines, $G(T)$. Underwood *et al.* chose to compare not the observed and predicted values of power, but rather the power divided by $0.7 G(T_m)$, which is approximately the differential emission measure in the line.

In Figure 6.1 the observed values of differential emission measure relative to Ca XVIII are plotted versus $\log T_m$, one point for each observed line, at 1554:01 UT, in the decay phase of the flare. They are compared with the values predicted by the evaporative model with $T_0 = 1.8 \times 10^7$ K, and the static model with $T_0 = 1.6 \times 10^7$ K. It may be seen that neither predicts even approximately the observed emission-measure distribution.

Data for later times (1555:01 UT and 1556:58 UT) were also examined. The inferred temperature gradient is less steep for later times, but, for 1556:58 UT, a comparison with the static model with $T_0 = 1.1 \times 10^7$ K shows that at that time the static conductive situation had not yet been reached. The evaporative model ($T_0 = 1.1 \times 10^6$) is still in gross disagreement with the observations. Finally, the density in the flaring plasma was estimated from line intensity ratios obtained from S082 B data. These values are in agreement with those inferred from the X-ray data above.

Underwood *et al.* (1978) conclude that it is inescapable that the flare of 9 August cooled radiatively. This conclusion is motivated by the fact that neither the static nor the evaporative conduction-cooling model predicts the observed temperature distribution of emission measure during the flare cooling phase.

The steep temperature gradients encountered at and immediately after the emission measure peak of the flare are interesting. Underwood *et al.* (1978) suggest that this temperature distribution, in which almost all of the material is at temperatures at or above 10^7 K, results from the heating of chromospheric material to coronal temperatures during the primary energy release of the flare. Because of the radiative instability below $T \approx 10^7$ K, the material will be driven rapidly to the higher temperatures, with a subsequent depletion of the 10^6 K material with respect to that at 10^7 K. This depletion appears as the minimum in the curves of Figure 6.1

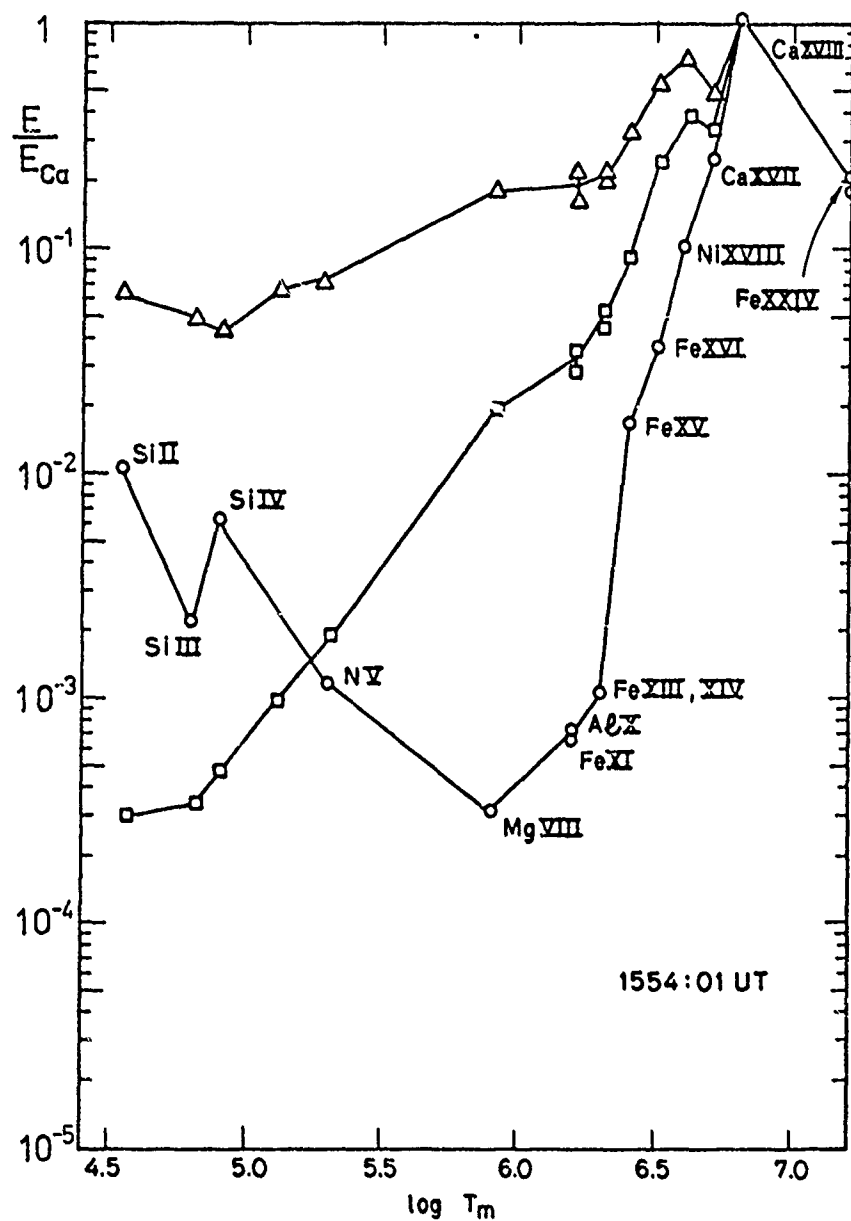


Fig. 6.1 Emission measure (normalized to Ca XVIII) versus temperature at 1554:01 UT. Points derived from the observations are plotted as circles. These are compared with the predictions of the static cooling model (squares) and the evaporative cooling model (triangles).

The decrease of the temperature gradient during the cooling phase is also consistent with a radiatively dominated model. Although the radiative instability will tend to perpetuate the minimum at 10^6 K, it will also tend to cause material to flow out of the coronal regions and the density to decrease (as is observed). As the density decreases, so will the relative importance of radiative losses, and the temperature distribution will approach that determined by conduction. Evidence for the flow of material out of the lower corona and transition region is provided by the profiles of transition-region lines, which show persistent redshifts during the cooling phase of this flare, becoming weaker with time. These observations are most readily understood in terms of a radiatively dominated model of flare cooling.

6.3.2. Empirical Transition-Zone Densities and Velocities

A hydrodynamic model of the temporal and spatial evolution of the flare atmosphere will predict, among other things, the relationships between temperature, density, and velocity of emitting material as a function of time. Doschek and Feldman (1978) have looked for empirical evidence for such relationships in the Skylab data from the NRL S082 B spectrograph. With this instrument one can determine densities at transition-zone temperatures, using approximately selected line ratios. Also, using line profiles, one can determine the velocities responsible for line shifts and broadening. Of course, ability to find such relationships depends critically upon instrumental parameters.

Two points are important to make. First, the data for this study have inevitably been greatly limited by undersampling in space and time, as well as their photographic nature—constraints that had to be accepted. Second, for electron-density estimates Doschek and Feldman (1978) used primarily the OIV technique explained in Feldman *et al.* (1977) and Feldman and Doschek (1978).

It is important to point out the criterion for selection of events to be studied—that the lines of strong resonance transitions, such as N V 1239 Å, Si IV 1402 Å, and C IV 1551 Å, be appreciably wider than in typical quiet regions. Because flares and flare-like eruptions in the transition zone are usually smaller than the S-082B spatial resolution ($2'' \times 60''$), a selection technique based on where the instrument was pointed in particular events would not be physically meaningful. The NRL Skylab plate collection was visually inspected for broad lines, and a list of plates exhibiting broad lines was prepared. From this list, a sample of plates was selected for detail study.

For each spectrum selected, profiles and intensities were obtained for the following lines: N V 1239 Å and 1243 Å, Si III 1300 Å, O IV 1401 Å, Si IV 1394 Å and 1403 Å, and Si III 1892 Å. Because of the transient nature of the events, it is necessary, unless we have data that show the lines are changing only slowly, to measure intensities and profiles of all the lines from the same spectrum, even when another spectrum may exist that was recorded only seconds earlier or later. The widths of the lines listed above are not significantly affected by opacity in the quiet sun, even above the solar limb. It is assumed that opacity has a negligible influence on the line widths in the transient events as well.

Doschek and Feldman (1978) selected five events for study, on the above basis. To identify the type of solar feature observed, they referred to Skylab H α images (Markey and Austin, 1977) and EUV spectroheliograms (Tousey *et al.*,

1977). They stress, however, that since their analysis implies that the volumes of the plasma they are observing are much smaller than the spatial resolution, the precise nature of the events as seen in H α is not critically important to their analysis. It is usually impossible to resolve the dynamical event observed. In some cases, however, the flare or surge plasma moves with sufficient speed along the line of sight to produce a large Doppler shift of the lines originating in the moving component (e.g., see Doschek et al., 1977). In these cases, emission from the event of interest and the solar background can be accurately resolved.

In order to measure line shifts and widths, Doschek and Feldman (1978) approximate the observed line profiles as the sum of two Gaussian components. In some cases it is obvious that a narrow, background component of the line is superposed on a broader component. They refer to the background component as the static component and the broad component as the dynamic component. After separation of the static and dynamic components, Doschek and Feldman (1978) still find very large values of the Doppler width for each component. Typically, the turbulent velocity in the static component is 10--50 km s⁻¹, and in the moving component it ranges from 30 to 190 km s⁻¹. Velocities over 80 km s⁻¹ are not uncommon, being observed in at least one transition-region line in all five events studied.

As an example, for the 2 December 1973 event (not reported as an H α flare, *Solar-Geophysical Data*, 1974), a much higher electron density is seen in a moving turbulent component, relative to a background static component. It is possible that a temperature versus mass-motion relationship exists. The dynamic component is blue-shifted relative to the static component for all lines. The shift is about 11 km s⁻¹ less for low-temperature allowed lines than for high-temperature allowed lines. However, this shift is quite small in terms of wavelength and may not be real. Electron densities for this event are high ($\geq 10^{12}$ cm⁻³), and volumes small ($< 10^{22}$ cm³).

A second example is the 13 January event. This event produced the widest transition-zone lines in the entire Skylab data collection. The event may have been a surge associated with a flare. For this event, the bulk motion of the dynamic component is rather large, about 80 km s⁻¹. Contrary to the 2 December event and the moving component of the 15 June 1973 flare (Feldman, Doschek, and Rosenberg, 1977), the density in the moving component of the 13 January event is comparatively low ($\approx 10^{11}$ cm⁻³), showing that the densities in surge-like events need not always be $\geq 10^{12}$ cm⁻³.

In summary, this work shows that interpretation of EUV transition-zone lines produced by flares or flare-like eruptions is a difficult problem with the Skylab data. The densities in dynamic events always seem to be higher than in the quiet sun, by at least an order of magnitude. No obvious correlation of mass motion with temperature is apparent, perhaps due to the small size of the sample. Frequently, the profiles of these lines indicate that several different plasma regions contribute to the total line intensity. The small volumes implied by the high densities indicate that resolving the fine structure of a dynamical event will require spatial resolution of ~ 0.1 arcsec, which is far better than the resolution of the best presently available instruments. The Skylab data simply do not have sufficient spatial and temporal resolution to provide a unique comparison of a single event with hydrodynamic calculations. The best tests will depend on statistical comparisons of amplitudes of observed velocities and densities at specific temperatures.

6.3.3. Implications of Kostyuk and Pikel'ner's Models

The models of Kostyuk and Pikel'ner (1975), in spite of their deficiencies (Section 6.2.3), are nevertheless one of the most complete treatments of the interaction of the chromosphere and corona during flares. However, the failure of Kostyuk and Pikel'ner to provide density or vertical displacement information for their models seemed to prevent us from making any observational tests, since we could not calculate emission measures, line profiles, etc., for their models without knowing density values.

McClymont and Craig (1977) have overcome this difficulty to some extent by using the velocity information presented in graphical form at several times. It is thus possible to estimate $\partial v / \partial t$ and then to obtain pressures by numerical integration of the momentum equation, assuming t and v do not change deep in the atmosphere.

Differential emission measures could not be obtained because it was not possible to estimate temperature gradients with accuracy from Kostyuk and Pikel'ner's results. However, McClymont and Craig were able to estimate total emission measures for the transition region ($10^5 < T < 10^6$ K) and the corona ($T > 10^6$ K). These total emission measures during the cooling phase of the $F_{20} = 10^9$ erg cm⁻² s⁻¹ model are shown in Figure 6.2. The peak transition-region emission measure is an order of magnitude higher than the peak coronal emission measure. This is just the opposite of what has been found earlier by Underwood *et al.* (1978), as can be seen in Figure 6.1, by comparing characteristic emission-measure values for $10^5 < T < 10^6$ K to $T > 10^6$ K. Also, the temporal behavior of the former is much different from the latter. The large relative values of the transition-region emission measure may be due to the open geometry of the model. Closed coronal loops, with their attendant larger density values, will give larger coronal emission measures. To check this, a comparison of the open- and closed-loop models would be worthwhile, using Kostyuk's (1976a) results.

6.4 THE CHROMOSPHERE AND PHOTOSPHERE

We now turn to that part of our research that is specifically directed toward flare physical processes that take place in the chromosphere and upper photosphere. From the canonical view of the flare phenomenon, it is easy to appreciate the importance and utility of such studies. These atmospheric layers serve as probes; they possess relatively well-documented physical properties in the steady state, and can be used as diagnostic tools. Their flare response measures the role of various possible flare phenomena such as fast particles, shocks, and radiation.

There are two different approaches to model-building that are used in this chapter. The first, the so-called *empirical* approach, determines what flare model atmosphere is necessary to give the observed radiation, consistent with the known physics of formation of the emergent radiation. This approach is often expedient because one need not presuppose how the model atmosphere gets to be the way the model says it is. In contrast, the *synthetic* approach does presuppose specific flare heating mechanisms, and evaluates their consequences, thereby deriving a model atmosphere.

In our studies of the chromosphere and photosphere, we made progress by using both approaches. Empirical models were constructed using Skylab and

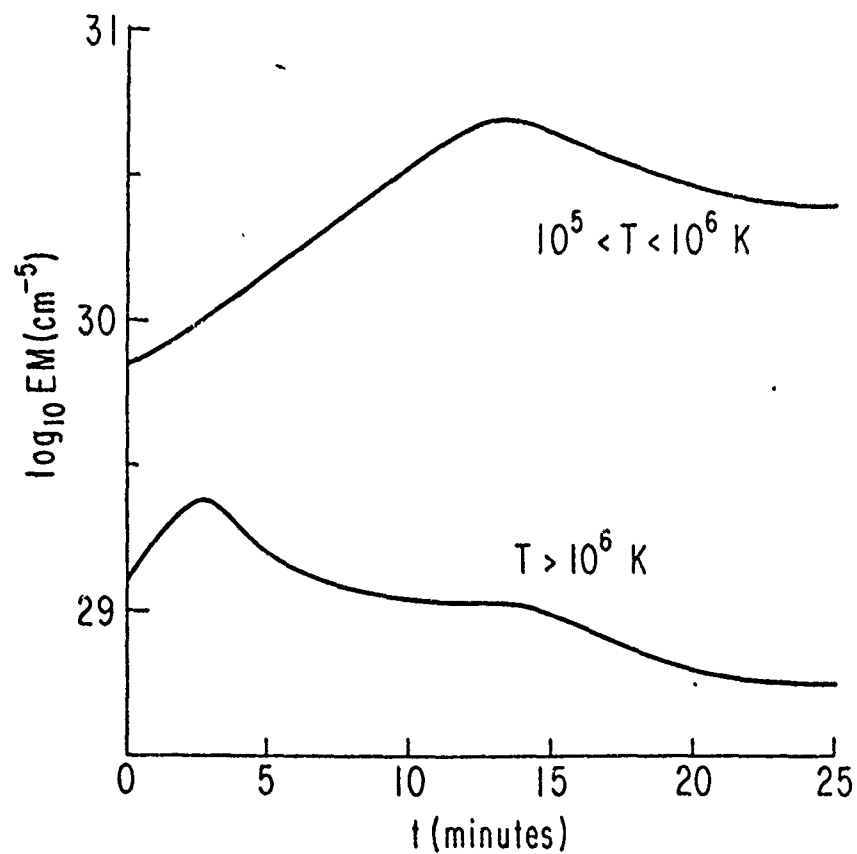


Fig. 6.2 Emission measures per cm^2 column as a function of time, during the cooling phase, for Kostyuk's (1975) $F_{20} = 4 \times 10^9 \text{ erg cm}^{-2} \text{ s}^{-1}$ model. Emission measure is divided into transition region ($10^5 < T < 10^6 \text{ K}$) and coronal ($T > 10^6 \text{ K}$) regimes.

ground-based observations of a variety of lines and continua to infer the temperature and density structure of the upper photosphere and chromosphere. Synthetic models of these same regions were constructed based on electron, proton, and soft X-ray heating. Putting them together, we were able to show what processes play a role during flares.

6.4.1. Observations for Empirical Models

Three observations have been used as the basis of empirical models. Cook and Brueckner (1979) observed the ultraviolet Si I 3P and 1D continua; Machado, *et al.* (1978) made Ca II K-line wing observations, and Lites and Cook (1979) observed the wings of $L\alpha$ and the blended C I 1D continuum. The level of origin of the observed radiation spans the temperature-minimum, extending from the upper photosphere well up into the chromosphere.

Cook and Brueckner (1979) studied the UV continuum from 1420–1960 Å in two flares that represent the two extremes: a compact, short-duration flare (9 August 1973) and a large, long-lived, double-ribbon flare (7 September 1973), using the NRL spectrograph (S082B). Active-region spectra were also obtained. After photographic photometry, smoothing, calibration, and field-of-view corrections, continuum intensities were determined, excluding obvious lines, and expressed as brightness temperature.

Figure 6.3 displays continuum brightness temperature versus wavelength for the earliest flare exposures from 9 August and 7 September, the plage exposures, and the Samain *et al.* (1975) quiet sun. The instrumental efficiency and declining intensity make it impossible to observe the continuum below 1400 Å with available exposure times. The observed brightness temperature minimum of the plages is approximately 310 K above the quiet sun, and the flare minima around 170–280 K (after correction of 9 August for field of view) above the plage. The location of the minimum also moves to progressively longer wavelengths from quiet sun to plage to flare, which is consistent (because of the wavelength dependence of the continuous absorption coefficient) with the temperature minimum occurring lower in the atmosphere, in qualitative agreement with flare atmospheres computed by Machado and Linsky (1975). There is good agreement with earlier quiet-sun and plage observations from 1750–2100 Å by Brueckner *et al.* (1976).

Machado *et al.* (1978) obtained new data on the Ca II K-line profiles in flares, specifically for the 1B flare of 19 February 1972, using the tower telescope of Sacramento Peak Observatory. The data are a significant improvement in spatial resolution over K-line data used previously for empirical model-building by Machado and Linsky (1975). It is immediately evident in the new data that there are many inhomogeneities. There are bright structures of the order of 1000–3000 km in size, in addition to an overall (average) structure. After the usual reduction of the photographic data, including correction for scattered light, Machado *et al.* (1978) selected spectra that were characteristic of the bright structures and the average. The resulting two observed K-line wing profiles are shown by the solid curves in Figure 6.4. Note that the point of minimum residual intensity in the bright structures is farther from line center than in the overall structure. Similarly, though not shown in the figure, this point is still farther from line center in both bright and average structures than in the quiet sun. Like the shift to longer wavelengths in the EUV continuum discussed above, this shift reflects heating of the temperature minimum and its displacement deeper into the atmosphere.

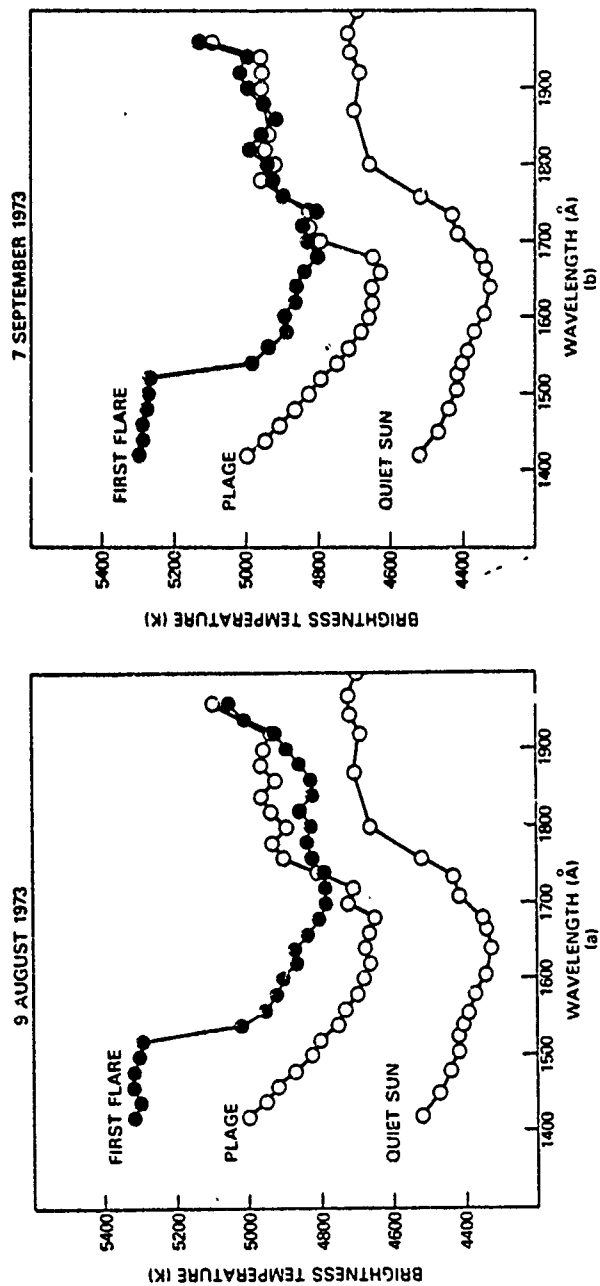


Fig. 6.3 Brightness temperature vs wavelength, for the 9 August and 7 September flares.

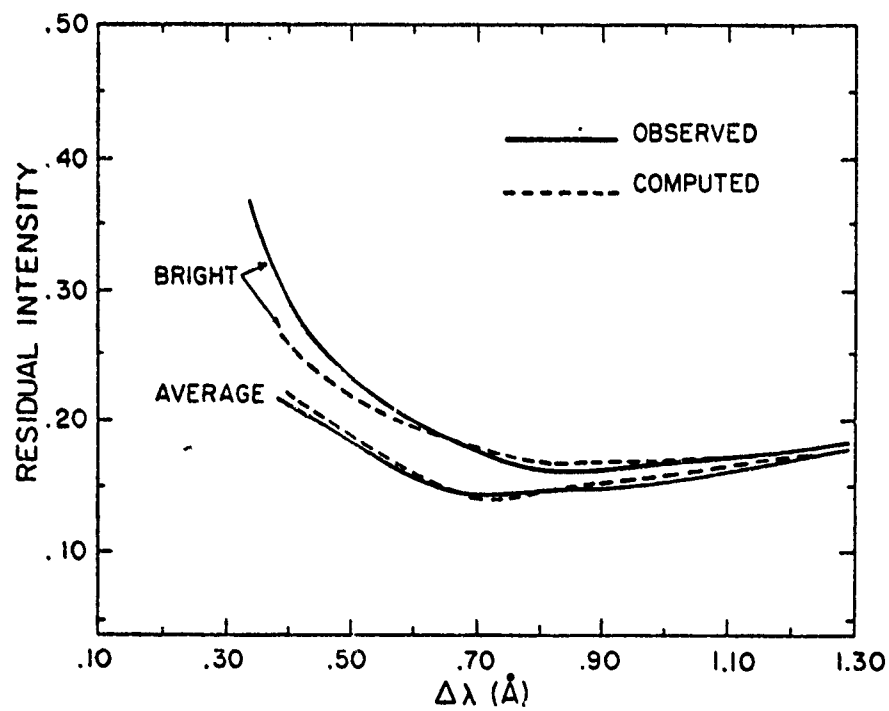


Fig. 6.4 Residual intensity as a function of wavelength from line center for the Ca II K-line wings. Observed and computed profiles are shown for both bright elements (upper curves) and overall structure (lower curves).

Lites and Cook (1979) have observed the wavelength range 1180–1250 Å with the NRL spectrograph (S082B), which includes the wings of $\text{L}\alpha$ and the continuum from $\text{C I } ^1\text{D}$, whose ionization limit appears at 1240 Å, blended with the $\text{L}\alpha$ wing. (The resonance continuum from the ^3P level is at 1100 Å, where the sensitivity of the NRL spectrograph is very low.) These data bear on the chromospheric region somewhat above the Si I and Ca II data discussed above. The spectrograms used are the same as those used for the Si I continua, as are the data reduction techniques. The resulting profiles, corrected for background effects, are shown by the dots and crosses in Figure 6.5, for the flares of 9 August and 7 September 1973. Note that at $\lambda > 1240$ Å and $\lambda < 1200$ Å the instrumental sensitivity is insufficient, even in flares at this relatively long exposure time, to give an accurate measurement of the continuum intensity. In the range $1230 < \lambda < 1240$ Å, the measured densities are only marginally above the background fog level. The indicated intensities are probably upper limits.

6.4.2. Empirical Models

On the basis of the Skylab and ground-based observations, we have constructed an empirical model of the upper photosphere and chromosphere for the 9 August 1973 flare.

A. Models from Si I and Ca II. Models that give synthetic spectra that match the observed UV continuum of Si I and the wings of the Ca II K line have been derived by Machado *et al.* (1978). In the lower atmosphere, where the K line determines the model, they get a first approximation to the final flare model atmospheres by the same procedure as Machado and Linsky (1975). Under the assumption that in the collisional-damping wings of the K line complete redistribution is valid and LTE conditions are met, one can derive a relation between hydrogen number density n_{H} , T_{e} , and $\Delta\lambda$ in the line from $I(\Delta\lambda)$ data alone. Then, assuming that the conditions for hydrostatic equilibrium are satisfied (a fairly good approximation at deep levels), one gets the pressure P and the mass column density $m = P/g$, where g is the solar gravity. In this manner, from the measured intensities in the line wings, $I(\Delta\lambda)$, one can immediately get a T_{e} versus m relation that determines a preliminary flare model.

Two-model flare atmospheres for the K-line wing-forming region were determined by trial-and-error adjustment of the $T(m)$ relationship to provide a satisfactory agreement between the observed and synthesized spectra of the K-line wings for both the bright and average structures. Machado *et al.* (1978) computed the synthetic profiles using a partial redistribution technique described by Linsky and Ayres (1978). The computed and observed profiles are compared in Figure 6.4. One can readily see that the model for the average structures reproduces the observations to ± 0.01 in residual intensity (R/I), or about 5–7% of the intensity itself, implying an uncertainty from this source of about 1–2% in temperature at the levels at which the radiation at $\Delta\lambda \gtrsim 0.4$ Å originates, which is $m \gtrsim 0.08 \text{ g cm}^{-2}$. The match for the bright model is equally satisfactory at $\Delta\lambda \gtrsim 0.5$ Å, while for $0.4 \leq \Delta\lambda \leq 0.5$ Å, the uncertainty is $0.02 \leq \Delta R/I \leq 0.03$, i.e., about 10% in intensity at $\Delta\lambda$, or 2–3% in temperature in the mass range $0.08 \leq m \leq 0.12 \text{ g cm}^{-2}$. The models are shown in Figure 6.6, the bright-region model by dashes, the average model by dots. These models are determined by the Ca II K-line profile synthesis in the mass range $\log m \gtrsim -1.0$.

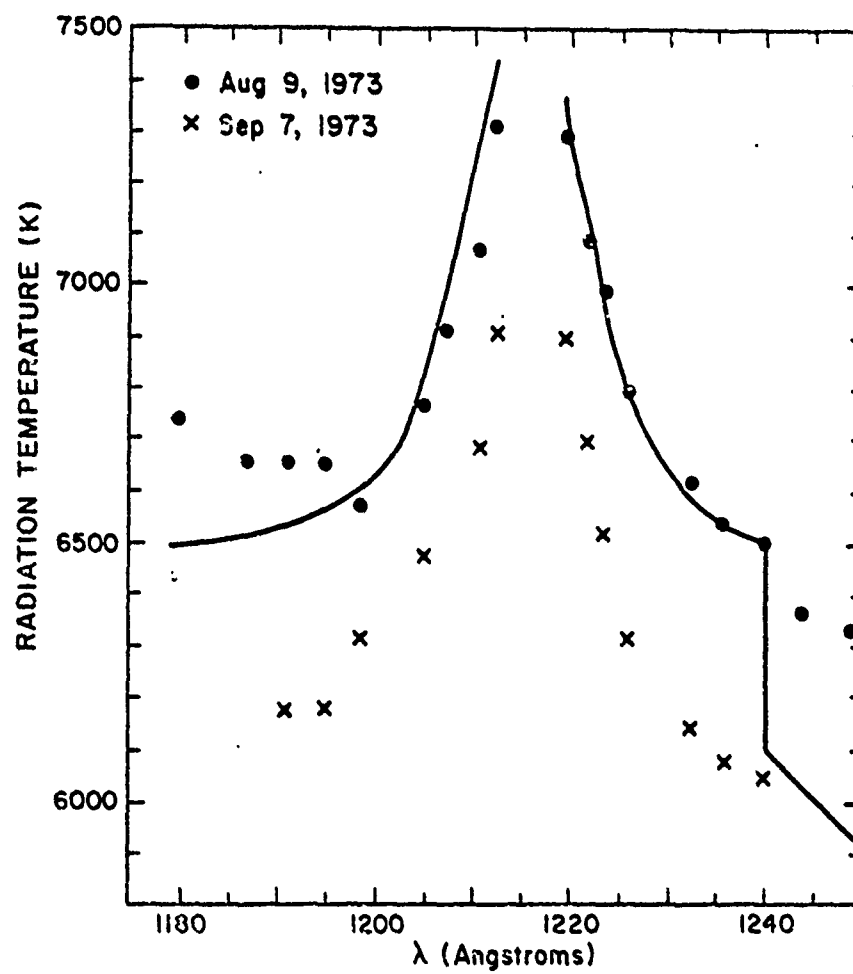


Fig. 6.5 Brightness temperature as a function of wavelength for the flares of 9 August and 7 September 1973, showing the wings of Lyman- α and the C I continuum. Solid curves are computed.

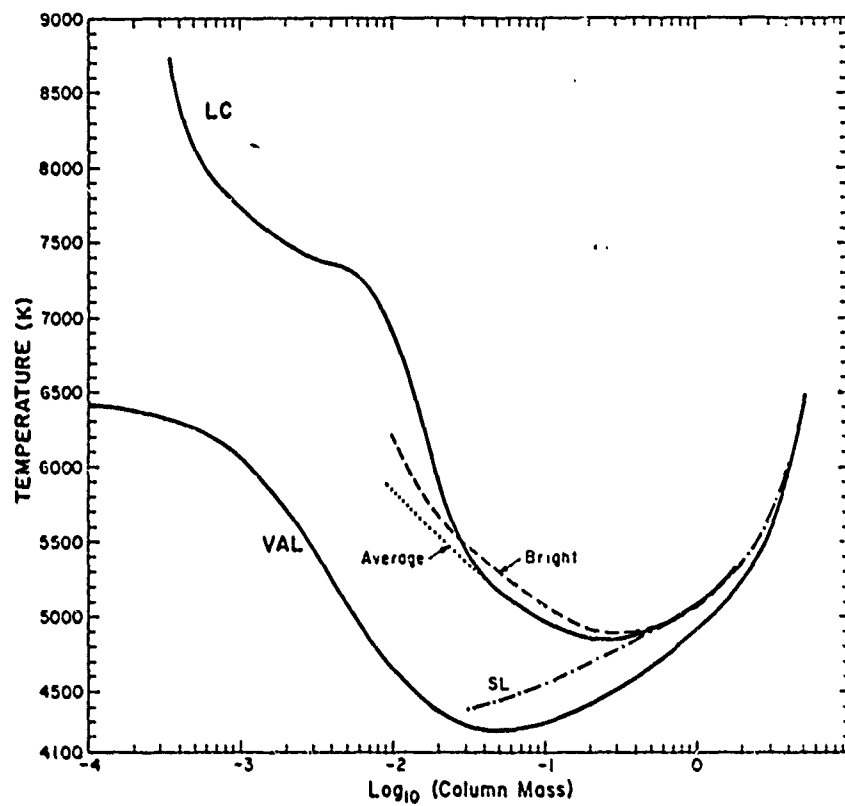


Fig. 6.6 The upper solid curve is an empirical one-dimensional model of the photosphere and chromosphere derived from observations of several small flares. For $\log_{10} m > -1.5$, the model is based on the Ca II K and Si I continuum analysis of Machado et al. (1978). For $\log_{10} m < -1.5$, the basis is La and the C I continuum from Lites and Cook (1979), labelled LC. Other curves shown are the quiet-sun model of Vernazza et al. (1976), labelled VAL, and the Shine and Linsky (1974) plage model, labelled SL.

The average flare and bright flare models are extended into the chromosphere to reproduce the Si I data of Cook and Brueckner (1979) in a very simplified way. Machado *et al.* (1978) assume LTE in the region of formation of the Si I continuum. They justify this on the basis of the calculations of Vernazza *et al.* (1973), which show that in the quiet sun the departures from LTE are less than a factor of two, and arguing that in the flares n_e is higher, therefore departures from LTE should be very small. They then identify the color temperature at the head of the Si I continuum with the electron temperature at the depth of formation. This identification is at least consistent with the expected values, since the observed values of T_c are in the range 5500–6300 K, and the calculated values are 5250–6300, when the empirical Machado and Linsky (1975) flare models are used. To determine where the Si I radiation comes from in the atmosphere, they also use these computations, which imply a height of formation in the range $580 \leq h \leq 700$ km ($0.02 \leq m \leq 0.05$ g cm⁻²). On this basis, they extend the $T(m)$ curves as shown in Figure 6.6, until $\log m \approx -1.5$. Two "plausible" models are so defined. The "bright" model is composed of the results for the Ca II K-line bright regions in the photosphere and the highest temperatures obtained from the Si I observations. The "average" model is defined by the overall K-line model and the average Si I temperatures. What the flare heating theories must explain is the temperature difference between the active-region model and the two flare models. Unfortunately, Machado *et al.* did not have observations of the preflare active region to match the two flare models, so they use the Shine and Linsky (1974) plage model for this purpose. The temperature difference between the two flare models and this model is given in Table 6.1. Interpretation will be deferred until Section 6.4.3.

TABLE 6.1
FLARE TEMPERATURE ENHANCEMENTS NEAR THE
TEMPERATURE MINIMUM

N (cm ⁻³)	m (g cm ⁻²)	Preflare T (K)	Flare (Average) ΔT (K)	Flare (Bright) ΔT (K)
1.28×10^{23}	0.03	4650	720	850
2.00×10^{23}	0.05	4600	590	720
2.56×10^{23}	0.06	4645	470	630
4.57×10^{23}	0.10	4680	280	430
8.54×10^{23}	0.20	4720	130	220
1.32×10^{24}	0.31	4855	-0-	43
1.96×10^{24}	0.46	4915	-0-	-0-

B. Models from C I and L α wings and the combined model. To obtain an empirical model that extends up still farther into the chromosphere than that based on the Si I continuum, Lites and Cook (1979) have used the observations of the L α wings and the C I ¹D continuum. As above, they make trial-and-error adjustments of the model atmosphere— $T(m)$ —to achieve sufficient agreement between synthesized and observed spectra. They thus find the run of hydrogen ionization that is

consistent with the radiative transfer equation, a steady-state solution of the atomic ionization- and excitation-rate equations, hydrostatic equilibrium, and the assumed $T(m)$.

The synthesis of the C I 1D continuum blended with the Lyman- α wing is complicated by the fact that the $L\alpha$ wing transfer is subject to significant partial frequency redistribution effects, while the C I continuum is not. Details of this aspect of the calculation are discussed by Lites and Cook (1979). They approximate the C I–C II ionization balance by specific computation of the radiative transfer for the resonance (3P) continuum (blended with the Lyman continuum) in addition to the 1D continuum, but they have ignored the effects of C I line transfer on the population of the ground state. They have included background continuous sources of opacity in LTE from Si I, Mg I, Al I, Fe I, and the Ca II 2D continuum at 1218 Å. Figure 6.5 shows the extent of agreement between the synthesized and observed spectra. In the range in which the data are significant, $1200 < \lambda < 1240$ Å, the synthesized spectra match the observed brightness temperature to ± 10 –20 K.

Figure 6.6 shows the combined empirical model for the 9 August flare. This model is a combination of the photosphere and low chromosphere "average" model from Machado *et al.* (1978), based on the Si I continuum and K-line wing, and the chromospheric model of Lites and Cook (1978), from the C I continuum and the $L\alpha$ wing. The C I and $L\alpha$ wing measurements define the flare model in the chromosphere from about 5800 K to about 9000 K. The observed rise in intensity of the $L\alpha$ wing for the 9 August 1973 flare suggests that the chromosphere in this flare was more pronounced than either of the Machado *et al.* (1978) models would indicate. The intensities of the $L\alpha$ wing between 1220 and 1230 Å are primarily responsible for the sharp rise in temperature at column mass 10^{-2} in the model.

Lites and Cook retain one characteristic of the Machado *et al.* (1978) model that is crucial to the results of the $L\alpha$ line profile synthesis. The coronal overburden, or the mass column density above the level of the Lyman continuum optical depth unity, is taken to be 3×10^{-4} g cm $^{-2}$ in these models. Machado and Noyes (1978) have studied the Lyman continuum intensities of several flares using the Harvard College Observatory S055 ultraviolet spectroheliometer aboard Skylab. These spectra indicate that the color temperature of the Lyman continuum is a measure of the electron temperature at optical depth unity, and that the brightness temperature at the head of the continuum gives a measure of the departures from LTE in the hydrogen ionization balance. The latter quantity is a measure of the pressure at optical depth unity and hence yields an estimation of the coronal overburden. The value of 3×10^{-4} g cm $^{-2}$ is about 75 times greater than the corresponding value for the quiet sun (Vernazza *et al.* 1973); hence, the pressures and densities in the flare chromosphere are correspondingly larger and the physical extent of the chromosphere is smaller. This compression is similar to the compression of plage models (Shine and Linsky, 1974) and earlier flare models (Machado and Linsky, 1975). However, observations of limb flares show that $H\alpha$ emission protrudes considerably above the surrounding chromosphere. This apparent contradiction is probably due to the invalidity of the hydrostatic equilibrium assumption in the models above. If this is the case, then what the semiempirical models imply is that the pressure is high in the regions that form the hydrogen spectrum, but not that the radiation originates low in the atmosphere. We already know that observations of transition-region and coronal lines

during flares also imply higher than normal pressures, so perhaps we should not be surprised that chromospheric lines do so, also. Another, alternate explanation of the H α emission above the limb, excitation by nonthermal particles, is discussed by Zirin (1978).

6.4.3. Interpretation Near the Temperature Minimum

We now turn to the problem of reconciling the empirical models with some heating mechanism. This has been done in the temperature-minimum (T_{\min}) region of the atmosphere by Machado *et al.* (1978). They assume steady-state energy balance between radiative cooling and flare heating, taking advantage of the fact that at T_{\min} levels the radiative terms are dominated by the H $^+$ ion, due to the relatively high electron pressures and low temperatures there. Thus the energy equation is simply:

$$E_{\text{em}}(\text{H}^+) = E_{\text{abs}}(\text{H}^+) + \nabla \cdot (F_{\text{ac}} + F_{\text{cond}} + F_{\text{flare}}), \quad (6.4.1)$$

where $E_{\text{em}}(\text{H}^+)$ and $E_{\text{abs}}(\text{H}^+)$ are the emitted and absorbed energies, respectively, of the H $^+$ ion, F_{ac} and F_{cond} are the acoustic and conductive fluxes respectively, in the T_{\min} region, and F_{flare} is due to the enhanced conditions in the flare.

Neglecting $\nabla \cdot F_{\text{cond}}$, due to the low temperatures present, and eliminating the absorption of acoustic and photospheric radiation field fluxes via the preflare temperature structure $T_0(m)$, it proves possible to solve equation (6.4.1) analytically for the flare temperature enhancements ($T/T_0 - 1$), for known $\nabla \cdot F_{\text{flare}}$. This was done by Machado *et al.* (1978) for three heating mechanisms—electron bombardment (c.f. Syrovatskii and Schmeleva, 1972; Brown, 1973; see also Sections 6.4.4 and 6.4.5), proton bombardment (Najita and Orrall, 1970; Švestka, 1970; Lin and Hudson, 1976), and soft X-ray irradiation (Somov, 1975; Hénoux and Nakagawa, 1977; Machado, 1978; see also Section 6.4.6).

The resulting temperature enhancements (over preflare temperature) are presented graphically in Figure 6.7, for three levels in the atmosphere—column number densities $N = 2 \times 10^{22} \text{ cm}^{-2}$, the preflare T_{\min} (dashed curves), $N = 8.5 \times 10^{22} \text{ cm}^{-2}$, deepest reliable ΔT observation (dot-dashed curves); $N = 1.2 \times 10^{23} \text{ cm}^{-2}$, flare T_{\min} (solid). For electron heating (upper figure), the parameters are $F_{20 \text{ keV}}$, the energy flux ($\text{erg cm}^{-2} \text{ s}^{-1}$) of electrons with energy above 20 keV, and δ , the differential spectral index of the assumed power-law energy spectra (c.f. Brown, 1973). Typically, observed hard X-ray spectral indices are in the range $3 \leq \gamma \leq 5$ (c.f. Hoyng *et al.*, 1976; Dattlowe *et al.*, 1974). For this reason, the calculations of heating by thick-target electrons (for which $\delta = \gamma + 1$) are carried out for $\delta = 4, 5$, and 6. Energy distributions with low values of δ are more efficient heaters at all depths shown, since only the high-energy tail can penetrate to those column number density values. The middle figure shows temperature enhancements for bombardment by protons with a power-law energy spectrum with index δ and boundary flux $F_{20 \text{ MeV}}$, the energy flux ($\text{erg cm}^{-2} \text{ s}^{-1}$) of protons with energy above 20 MeV. Here calculations have also been made only for $\delta = 4, 5$, and 6, although values as small as $\delta = 2$ have been found for major flares (c.f. Lin and Hudson, 1976). Note, however, that for a given $F_{20 \text{ MeV}}$, the harder spectra are less efficient heaters at the depths considered, since the protons that heat near the temperature minimum are those of $E \sim 10\text{--}20 \text{ MeV}$. The results given in the middle panel of Figure 6.7 show the most efficient heaters at the depths of interest. Results for other less-effective values of δ , as low as $\delta = 2$, can easily be

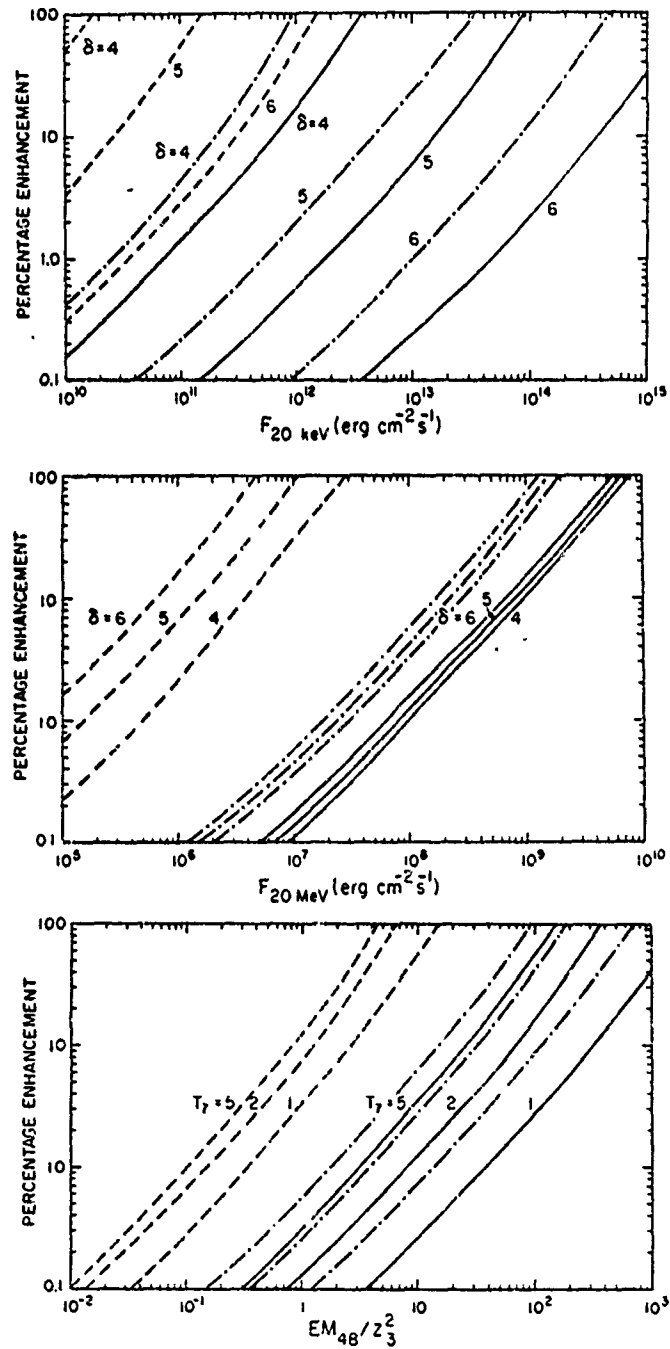


Fig. 6.7 Theoretical temperature enhancement relative to temperature at same depth in the preflare atmosphere for electron bombardment (top figure), proton bombardment (center), and X-ray irradiation. Enhancements are given at three atmospheric levels: the preflare T_{\min} (dashed curves); the greatest depth of reliable ΔT values in the observations (dot-dashed curves); and the flare T_{\min} (solid curves).

estimated from the results given. The lower figure shows enhancements for heating by a soft X-ray point source, with emission measure EM_{48} ($EM \times 10^{-48}$, cm^{-3}) and temperature T_7 ($T \times 10^{-7}$, K), situated at height z_3 ($z \times 10^{-3}$, km) above the heated column number density.

From the way in which the Machado *et al.* (1978) empirical models are calculated, it turns out that the most reliable $\Delta T(m)$ measurement is obtained at $m = 0.2 \text{ g cm}^{-2}$ ($N = 8.5 \times 10^{22} \text{ cm}^{-2}$); the enhancement at this level is (Table 6.1) $\approx 5\%$. Reference to Figure 6.7 shows that this implies, for each mechanism in turn, either $F_{20 \text{ keV}} \geq 10^{11} \text{ erg cm}^{-2} \text{ s}^{-1}$, $F_{20 \text{ MeV}} \approx 10^8 \text{ erg cm}^{-2} \text{ s}^{-1}$, or $EM_{48}/z_3^2 \approx 70$, respectively.

Considering, first, electron bombardment, such a high particle flux (especially some ten minutes after the maximum in microwave emission, when the Machado *et al.* observations were made) is incompatible not only with total flare energy requirements (the total energy needed is $\sim 3 \times 10^{33} \text{ erg}$), but also with the low electron fluxes inferred for other flares from the EUV observations of Emslie *et al.* (1978) and the H α profile studies of Brown *et al.* (1978) (see also Section 6.4.4).

Turning to proton bombardment, we again arrive at an unacceptably large energy requirement, approximately an order of magnitude greater than the inferred γ -ray fluxes of Ramaty *et al.* (1974) for large events. The requirement is even larger for the γ -ray events, since for them $\delta \approx 2$. However, since the threshold energy for γ -ray production is $\approx 30 \text{ MeV}$, it is conceivable to have a proton energy spectrum concentrated around 10–20 MeV. As stated above, these energies correspond to particles that deposit most of their energy in the vicinity of the T_{\min} levels (c.f. Emslie, 1978), and the reverse-current stability arguments, which discount such an energy spectrum in the case of electrons, do not hold for protons, due to the much larger growth times of such instabilities (c.f. Smith, 1970). Machado *et al.* find that such a mechanism is, in fact, marginally effective at producing the observed enhancements.

Third, using emission measures inferred from SOLRAD X-ray data, Machado *et al.* conclude that for X-rays to produce the observed enhancements, the source must be located at most 1000 km above the photosphere. The resulting very small source volume (from density plus emission measure considerations) and large temperature gradients near such a source make this model incompatible with currently favored models of chromospheric structure. Nevertheless, Machado *et al.* conclude that it would be marginally feasible to produce their "average" structures on the basis of such a heating process; however, reproducing the features of their "bright" model seems very unlikely.

Finally, Machado *et al.* offer three suggestions for mechanisms that might indeed be operating at T_{\min} levels. The first is the almost monoenergetic proton beams mentioned above. The second is heating by EUV radiation from transition-zone lines, to which the chromosphere is transparent but which are very effectively absorbed in the T_{\min} layers. Third, some form of local heating process is advocated, such as joule heating by steady currents.

6.4.4. Electron-Heated Models

Clearly, the chromosphere is the first place to look for the effects of heating by nonthermal electron bombardment. For the chromosphere, the first steady-state

model-building was done by Brown (1973), discussed in Section 6.2.1. There are two important areas in which Brown's (1973) calculations could be improved: (1) convection and conduction; and (2) radiative losses. Kostyuk and Pikel'ner (1975), Kostyuk (1975a), and Somov *et al.* (1977) did the former; during the Workshop, Brown *et al.* (1978) did the latter. They thus assumed that heating increases gradually enough to permit a steady-state radiative solution but still on a time scale shorter than that for arrival of heat flux conducted from the corona.

Brown *et al.* (1978) obtained quasi-steady-state solutions of the energy balance equation assuming heating by a flare electron spectrum of power-law form. If such electrons are injected downward into the chromosphere (thick-target model) the injection rate and spectral index are given from the hard X-ray observations by the expressions in Brown (1975). Parameters of the heating are $F_{20 \text{ keV}}$ and δ , as in Section 6.4.3.

This heating is balanced by radiative cooling. In the chromosphere, three radiative-loss contributions are important: heavy element lines and continua; H^- continuum; and the hydrogen Lyman and Balmer lines and continua. Heavy element lines and continua were crudely estimated by assuming them to be optically thin, using an extrapolation of McWhirter *et al.* (1975) to lower temperature. The H^- and optically-thick $\text{H}\alpha$ and $\text{L}\alpha$ losses were based on Canfield's (1974b) probabilistic radiative-loss technique. $\text{H}\alpha$ and $\text{L}\alpha$ were assumed to be the only hydrogen radiative-loss contributions. The validity of this approximation can only be checked by a more complete calculation. However, it is known that Canfield's (1974a) assertion that continuum losses were unimportant was incorrect, and is now known to be model-dependent (Labonte, 1979). Optical depth effects were incorporated by numerically solving a probabilistic form of the radiative transfer equation, whereas H^- was assumed to be optically thin. The energy balance equation was solved by an iterative scheme, adjusting T at each level in the model grid (at constant pressure) until a model converging on a steady state was obtained.

Brown *et al.* (1978) have calculated models for a single electron energy differential spectral index, $\delta = 4$, and four values of the energy input rate for electrons ($E > 20 \text{ keV}$), $F_{20 \text{ keV}} = 10^8, 10^9, 10^{10}$, and $10^{11} \text{ erg cm}^{-2} \text{ s}^{-1}$. The resulting model atmospheres are shown in Figure 6.8 in terms of, respectively, $T(z)$ and $N_{\text{H}}(z)$ (total hydrogen density) as functions of height z above the photosphere. In general, the results differ from Brown (1973) in deeper penetration of the heating (due to reduced radiative losses) and in local features on the $T(z)$ profiles due to the hydrogen-line losses. The plateau at $T = 10^4 \text{ K}$ is due to the manner in which the optically-thin radiative losses were cut off and so may be spurious. Particularly interesting in view of the ATM observations of EUV continua of neutral and singly-ionized elements is the heating between 500 and 1000 km (c.f. Section 6.4.2). It is cut off at the lower end by reduced penetration of heating and increased effectiveness of radiative cooling, primarily due to H^- . The models can be checked for self-consistency. The result is that they are only marginally self-consistent in that the radiative response time is only marginally less than typical beam durations, of order 100 s. They are fully self-consistent from the point of view of conduction; $\tau_{\text{cond}} \leq 10^5 \text{ s}$. However, the check neglects the possibility that, in reality, transient, steep conduction fronts may be present.

6.4.5. Tests of Electron-Heated Models

The obvious way to test the chromospheric electron-heating models is to establish

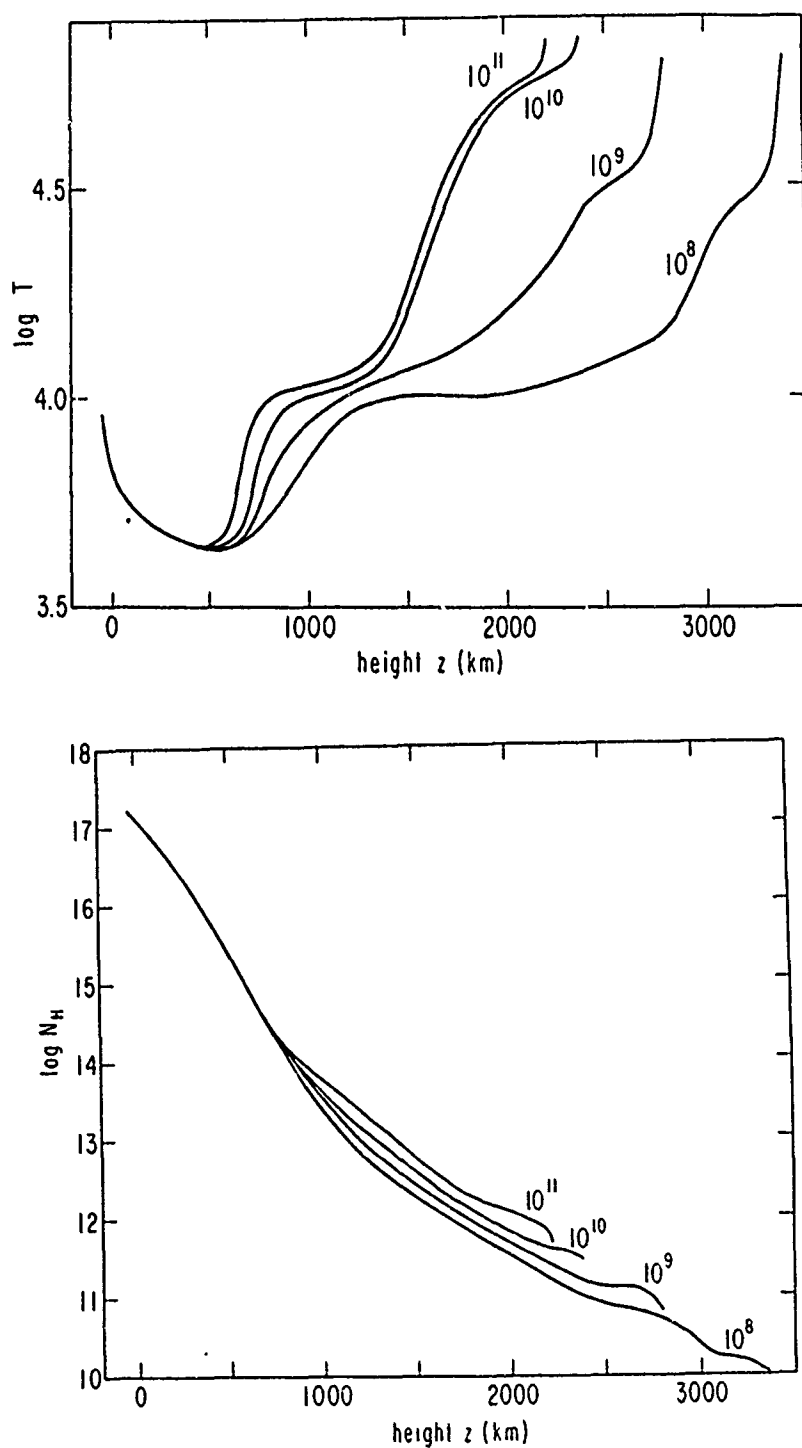


Fig. 6.8 Computed temperature (top) and hydrogen density (bottom) distributions of electron-heated models for $F_{20} = 10^8, 10^9, 10^{10}$, and $10^{11} \text{ erg cm}^{-2} \text{ s}^{-1}$.

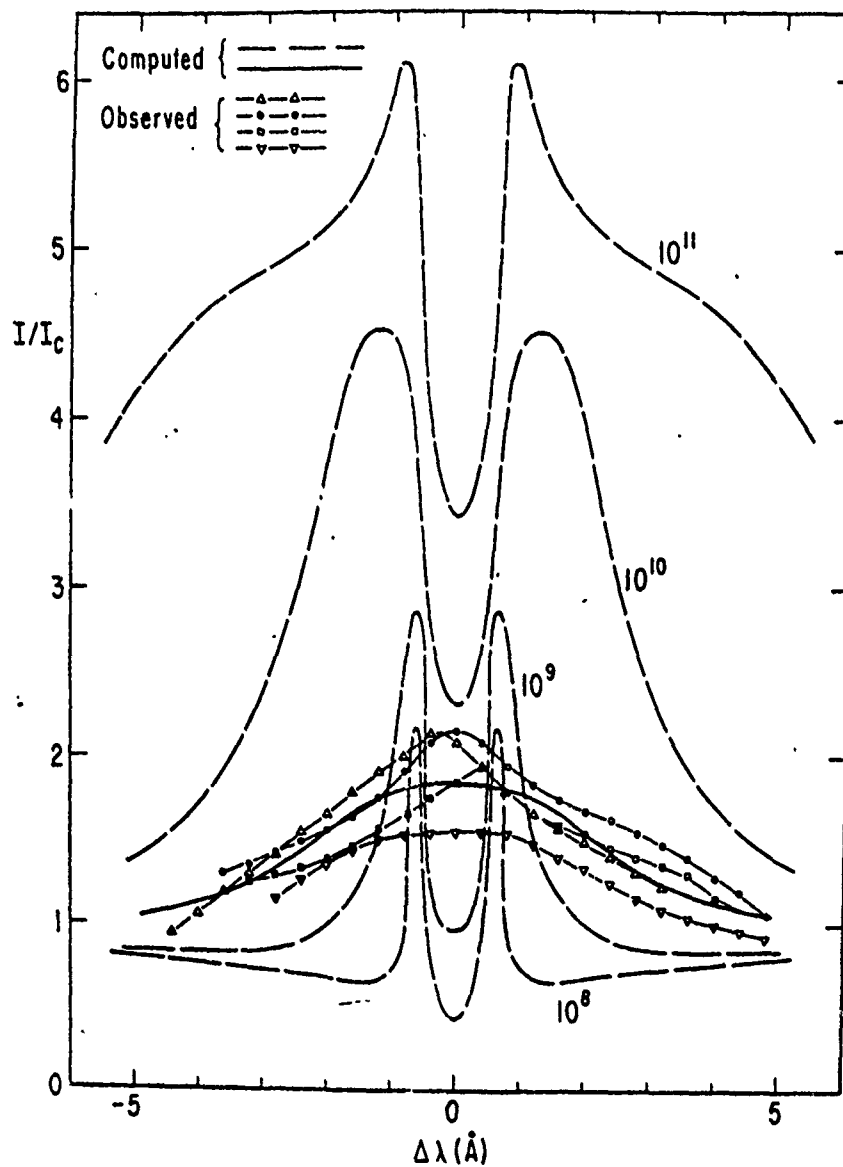


Fig. 6.9 Computed and observed H α line profiles for electron-heated models. Dashes: computed from the models for given F_{20} values. Dashes between various symbols: two observed 7 August 1972 flare kernels, each at 1518 and 1521 UT (Tanaka, 1977). Solid: combination of computed profiles with $F_{20} = 10^9$ and 10^{10} erg cm $^{-2}$ s $^{-1}$, after smoothing with 60 km/s random velocities.

the relationship between some chromospheric observable and the energy injection rate of electrons above 20 keV, via the models, and then to check whether this relationship is supported by the observational data.

Brown *et al.* (1978) have computed theoretical H α profiles following Canfield and Athay (1974). The computed H α profiles for the four models ($F_{20} = 10^8$, 10^9 , 10^{10} , and 10^{11} erg cm $^{-2}$ s $^{-1}$) are shown in Figure 6.9. Three facts immediately emerge from a comparison of the computed H α profiles in the figure and typical flare H α profiles (c.f. Švestka 1976, p. 7):

- (1) Large, unresolved variations of the radial velocity from point to point in the flare are implied, since the observed profiles do not show the strong central reversal found in the computed profiles. The characteristic velocity amplitudes must be of order several tens of km s $^{-1}$.
- (2) The observed total intensities of even major-flare H α profiles are less than those of the $F_{20 \text{ keV}} = 10^{10}$ or 10^{11} erg cm $^{-2}$ s $^{-1}$; most flares correspond to $F_{20 \text{ keV}} < 10^9$ erg cm $^{-2}$ s $^{-1}$.
- (3) The observed line widths of major flares give a similar picture, i.e., they fall between the calculated profile half-widths for $F_{20 \text{ keV}} = 10^9$ and $F_{20 \text{ keV}} = 10^{10}$ erg cm $^{-2}$ s $^{-1}$.

Brown *et al.* (1978) are able to make a strong test by using observations of the large flare of 7 August 1972, which was observed in both hard X-rays and H α . From the observed hard X-ray fluxes, Hoyng *et al.* (1976) infer a total energy input rate above 20 keV, or 3×10^{29} erg s $^{-1}$. Lin and Hudson (1976) obtain 2×10^{29} erg s $^{-1}$. If one assumes that the hard X-ray impact area is that of the broad, bright H α flare kernels observed by Zirin and Tanaka (1973), i.e., 6×10^{18} cm 2 , a value of $F_{20 \text{ keV}}$ of $3\text{--}4.5 \times 10^{11}$ erg cm $^{-2}$ s $^{-1}$ is implied. Brown *et al.* (1978) find that the best match between the observed and computed H α half-widths and total intensities implies a value of $F_{20 \text{ keV}}$, averaged over the kernel, of 3×10^9 erg cm $^{-2}$ s $^{-1}$, but concentrated in about 1/3 of the observed area. Four observed flash-phase H α profiles from Zirin and Tanaka's (1973) work were provided by Tanaka (1977). These are shown in Figure 6.9 (*dashes connecting various symbols*). Also shown is a theoretical profile (*solid curve*), a sum of the $F_{20 \text{ keV}} = 10^9$ and 10^{10} erg cm $^{-2}$ s $^{-1}$ profiles convolved with a Gaussian function of 60-km/s nonthermal Doppler width to mimic the spatial variation of the radial velocity, and scaled to match the central intensity of the observed profiles. The theoretical profile has a half-width that matches the observations within their observed scatter.

The result of the comparison of the observed and computed profiles is that the response of the chromosphere in H α seems to imply a nonthermal electron input that is 1–2 orders of magnitude less than that which would be inferred on the basis of purely thick-target bremsstrahlung X-ray emission. Since this result, if confirmed in general, would have important implication for the electron acceleration process in flares, Brown (1978) has attempted to extend this analysis to other flares. He has undertaken a search for suitable further candidates for tests among the ATM flares but has met with severely limited success. The chief difficulty in the problem lies in getting simultaneous *flash-phase* observations of hard X-ray and H α *kernel*

spectra. Problems with the hard X-rays lie in instrumental sensitivity and lack of continuous coverage. Problems with the H α observations result from the difficulty of covering a flare kernel with a spectrograph slit at the right time (even with a multislit spectrograph) and from the lengthy data reduction required if filtergrams are used. One would hope that the kind of difficulties that have been encountered will act as a stimulus to obtain good observational coverage and coordination in future missions such as SMM and to include rapid-scanning slit-spectrograph observations.

Of the ATM flares, only that of 21 January 1974 was covered in hard X-rays (by OSO-7), but there were no H α spectra for this event. For a number of flares, however, it was possible to use microwave data to get a rough estimate of the electron flux, using the method of Hudson *et al.* (1978), which is based on the empirical relationship between hard X-ray flux and microwave flux.

Brown (1978) has shown another approach, which is theoretical, rather than empirical. He uses the relationship given by Brown and Hoyng (1975) (for an electron spectral index $\delta \approx 3$, since for a thin target $\delta = \gamma - 1$ and typically $\gamma = 4$ in X-ray spectra, as discussed above) between the number of electrons $N(E \geq 20 \text{ keV})$ instantaneously in the microwave source and the microwave flux density ξ_ν ($10^{-22} \text{ W m}^{-2} \text{ Hz}^{-1}$) they produce at frequency ν (GHz); viz,

$$N \approx 10^{31} \xi_\nu / \nu (B/100)^{-2}, \quad (6.4.2)$$

where B is the source magnetic field in gauss. The thick-target power $P_{20 \text{ keV}}$ depends on the lifetime τ of electrons in the microwave source for precipitation into the chromosphere,

$$P_{20 \text{ keV}} \approx N \bar{E} / \tau \approx \frac{5 \times 10^{23}}{\tau} \frac{\xi_\nu}{\nu} \left(\frac{100}{B} \right)^2 \text{ erg s}^{-1}. \quad (6.4.3)$$

Comparison of Eq. (6.4.3) with Hudson *et al.* (1978) for $\nu \approx 10 \text{ GHz}$ ($\lambda = 3 \text{ cm}$) and $\delta = 3$ shows that the average value of τB^2 over many events is given by $\langle \tau (B/100)^2 \rangle \approx 2 \times 10^{-3}$. If the lifetime τ is interpreted as L/\bar{v}_e for a source size L , then the typical microwave source dimension should be $L \approx 100 \text{ km}$ for $B \approx 100$ gauss. Though this is not unreasonable, it will clearly vary from flare to flare, as will B , hence contributing to the scatter of about one order of magnitude in the observed correlations used by Hudson *et al.* (1978). Thus, one cannot expect to obtain $P_{20 \text{ keV}}$ for any individual event to better than an order of magnitude by this method. The actual thick-target energy flux ($\text{erg cm}^{-2} \text{ s}^{-1}$) is uncertain by a further factor in the impact area A , but this difficulty applies equally to use of hard X-ray data without spatial resolution.

David L. Croom has provided microwave data (mostly from AFCRL) for five ATM flares in the form of peak fluxes ξ_ν at a variety of frequencies ν , as listed in Table 6.2. Also listed are the values inferred for P_{20} following from Hudson *et al.* (1978) for an assumed spectral index of 4, applied to data in the 3–10 GHz range. One of these four flares, that of 5 September 1973, was also covered by the multislit H α spectrograph described by Martin (1974). Detailed versions of these H α results have been provided by Stephen A. Schoolman.

TABLE 6.2
ATM FLARE MICROWAVE DATA

Event	Microwave Peak (UT)	ν (GHz)	Peak Flux	$\xi_p (10^{-22} \text{ W m}^{-2} \text{ Hz}^{-1})$	$P_{30} \text{ keV (erg s}^{-1}\text{)}$
15 June 1973*	14:15	15.4 8.8 5.0		16.6 22.0 12.0	4×10^{37}
9 August 1973	15:50	15.4 8.8 5.0		31.6 30.8 20.4	6×10^{37}
5 September 1973	18:28	15.4 8.8 5.0		16.1 31.4 59.6	6×10^{37}
7 September 1973*	11:50	37.0 19.0 15.4 8.8 5.0		30.0 119. 121. 32.2 33.7	6×10^{37}
21 January 1974	23:37	0.208		120.	$\geq 2 \times 10^{39} \dagger$

† This value is questionable because the frequency involved is actually too low for validity of the Hudson *et al.* (1978) method.

* Time profiles available.

Examination of the H α spectra shows that the H α line width maximized about 4 minutes after the microwave peak. This delay does not necessarily arise from the properties of the flare itself, but may arise merely because none of the spectrograph slits drifted across any flare kernel until that time. The best one can do in these circumstances is to utilize the fact that as a matter of experience (Martin, 1977) the H α widths in the main phase of flares set a lower limit to those in the impulsive phase. Brown (1978) has therefore measured the half-width at half maximum at the time of maximum width, and full equivalent width of the flare H α profile in the brightest flare knot. After convolution with a 60 km s^{-1} Gaussian profile to remove the central reversal, the best-fit model profile from Brown *et al.* (1978) was found to be that for an average $F_{20 \text{ keV}} \cong P_{20 \text{ keV}}/A \cong 10^9 \text{ erg cm}^{-2} \text{ s}^{-1}$ over the flare kernel, concentrated in about 1/3 or less of the observed kernel area. For a kernel area of 10^{18} cm^2 , the total thick-target power required to heat the H α flares is thus $P_{20 \text{ keV}} \geq 10^{27} \text{ erg s}^{-1}$.

Reference to Table 6.2 shows that the value of $P_{20 \text{ keV}}$ obtained by use of the microwave data is approximately $6 \times 10^{27} \text{ erg s}^{-1}$, which is a factor of six higher than the lower limit needed for H α heating. Thus, this result for the 5 Sept. flare is not inconsistent with the discrepancy found by Brown *et al.* (1978), since it is in the same direction. However, it can in no way be regarded as serious support for the result, since the $P_{20 \text{ keV}}$ value for H α here is only a lower limit and the $P_{20 \text{ keV}}$ value from microwaves is uncertain by at least one order of magnitude, as discussed above.

6.4.6. Soft X-Ray Heated Models

In Section 6.2 we reviewed the pre-Workshop theoretical basis on which to expect measurable heating of the chromosphere due to photoionization by soft X-rays. Observationally, heating by short-wavelength radiation was first proposed by Jefferies (1957) and Švestka (1957) to explain some peculiarities in flare spectra in the visible. Thomas and Teske (1971) found a strong statistical correlation between H α X-ray flare emission for a large number of flares. Falciani *et al.* (1977) have recently found a close relationship between the temporal behavior of H α and soft X-rays within flares. There seems to be little doubt that soft X-ray heating accounts for *part*, though not all, of the flare response of the chromosphere.

Hénoux and Nakagawa (1978) have recently extended their theoretical work on soft X-ray heating by constructing dynamic models of the heating of the chromosphere by the 1–300 Å X-ray flux. The basic heating mechanism is generation of photoelectrons from helium and other abundant elements (C, N, O) through absorption of soft X-ray photons, followed by rapid thermalization of photoelectrons through elastic collisions with background electrons, as well as direct ionization and excitations of hydrogen by the photoelectrons.

They solve the basic hydrodynamic equations, and in addition incorporate the rate equations for excitation and ionization of hydrogen. The amount of energy deposited by soft X-rays is added as a source term in the energy equation. These are balanced by mass motions and radiation, which in their calculation is H γ , H α , and the Balmer continuum. Simultaneous solution of the radiative transfer equation is avoided by an approximate empirical approach. Work is currently in progress to improve on this approximation.

Numerical solutions are obtained assuming a constant soft X-ray flux after $t = 0$. The initial atmosphere is the HSRA, and extends over the column mass

range $-4.35 \leq \log m \leq 0.05$. The top point corresponds to $h \approx 1200$ km in the steady state; motions are forced to vanish at the bottom. At $t > 0$, the atmosphere moves to achieve a new equilibrium state. The extent of the atmosphere considered first increases from 1200 km at $m = 10^{-4.35}$ to 1500 km in the first 4 min, then decreases. The new equilibrium atmosphere extends to 1400 km. First, the motion starts as upward expansion with the maximum speed reaching 4 km s^{-1} after 100 s, while the velocity amplitude is always decreasing deep in the atmosphere. The temperature and velocity both then begin to oscillate, with a period of approximately 270 s. During the oscillation, the temperature increase coincides with downward motion. One would expect a real flare to be spatially and temporally inhomogeneous. If these inhomogeneities were below the limit of spatial resolution, the only effect would be a red asymmetry in chromospheric line profiles, as is observed.

The nearly-relaxed state of the atmosphere, after 30 min of X-ray irradiation, is shown in Figure 6.10, for a typical soft X-ray flare ($T = 10^7 \text{ K}$, $EM = 2 \times 10^{49} \text{ cm}^{-3}$, $A = 2 \times 10^{18} \text{ cm}^2$). Compared to the HSRA (Gingerich *et al.* 1971), one can see that the heated region extends down to about column mass $m \sim 10^{-1} \text{ gm cm}^{-2}$. Since the initial atmosphere was the HSRA, not an active-region atmosphere, the considerable disagreement with the empirical Machado-Linsky (1975) model at $m \geq 10^{-2} \text{ g cm}^{-2}$ is not surprising. Certainly there is good agreement for $m \leq 10^{-2}$. The implication of this figure is that one can account theoretically for at least some heating of the chromosphere during flares by soft X-rays.

6.4.7. Observational Evidence for Soft X-ray Heating

Machado (1978) has searched for quantitative observational evidence for soft X-ray heating in the upper chromosphere, as is predicted by the theoretical calculations (c.f. Section 6.4.6). He has used Skylab data from the Harvard College Observatory EUV spectroheliometer, specifically $L\alpha$ and Lyman continuum (Lc) intensities. These data are a useful estimate of the total chromospheric radiation, since hydrogen is a major contributor to the radiative output of flares (c.f. Appendix A, Radiative Output of the 5 September 1973 Flare). The basic approach taken is to identify theoretically the region from which the observed hydrogen radiation originates and to compare it with both the expected soft X-ray heating of the region and the observed hydrogen radiation of flares of known X-ray intensity.

First, Machado (1978) estimated the region of formation of the emergent $L\alpha$ and Lc radiation, in a two-level atom approximation, using the method of Athay (1972). He then used the same methods as Machado *et al.* (1978) to estimate the amount of soft X-ray radiation absorbed in these regions. Photons in the $30 \leq \lambda \leq 100 \text{ \AA}$ region are most important in heating the $L\alpha$ and Lc formation regions. One would then expect that if soft X-ray heating is playing a dominant role in heating some part of the chromosphere of a flare, the amount of $L\alpha$ and Lc radiation should not exceed energy absorbed from the soft X-rays known to be incident but should be approximately 10–30% of this value, (c.f. Appendix A) bearing in mind uncertainties in the observations and calculations.

The flare of 9 August 1973 gives the opportunity of testing these ideas. It is a compact flare, not so close to the limb to have serious projection-effect problems. One-dimensional scans of $L\alpha$ with 5 arc second resolution through the brightest kernel of the flare show a clear gradual decrease of the $L\alpha$ intensity with increasing distance from the kernel, as in Figure 6.11 (*dashed curves*). These data were obtained during the decay phase of the flare. The solid lines in Figure 6.11 are

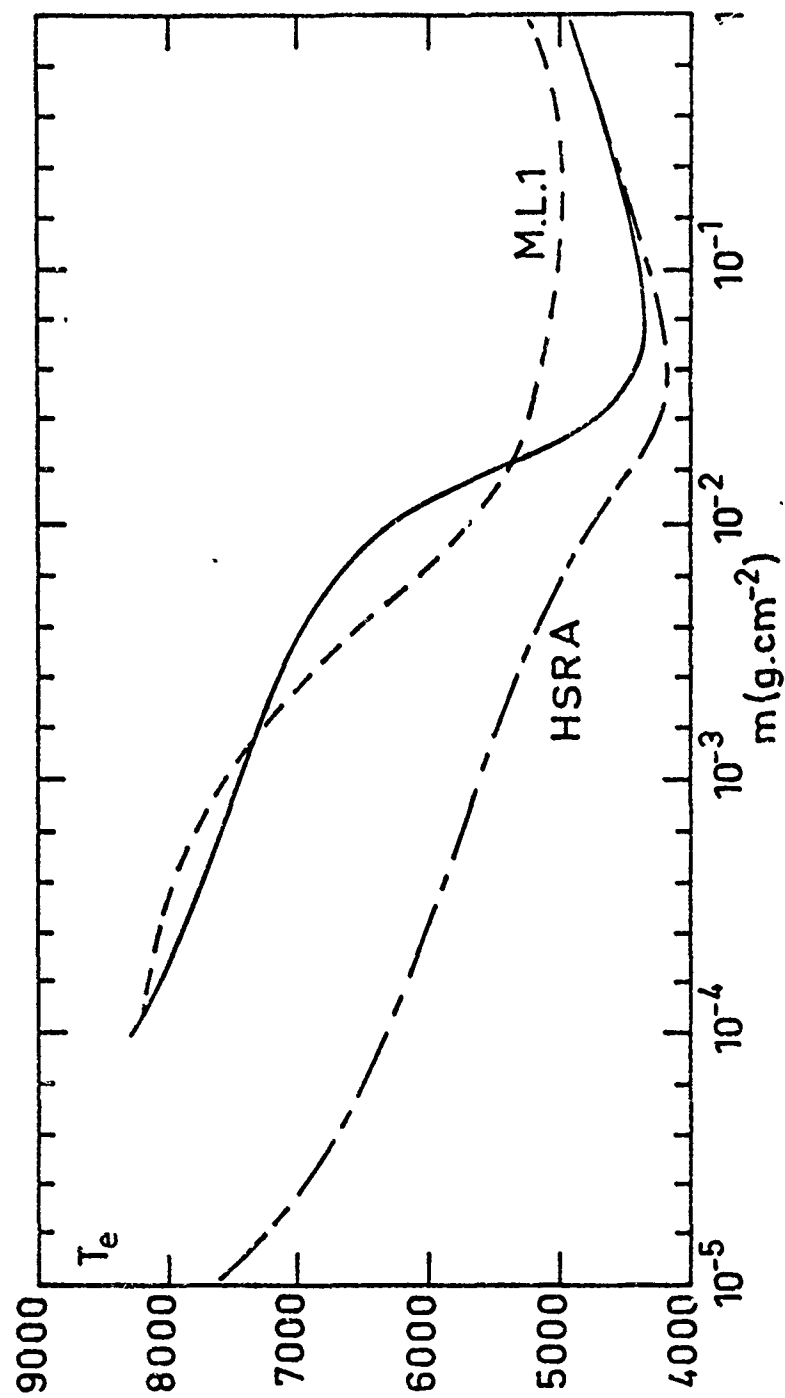


Fig. 6.10 The variation of electron temperature T_e with column mass m for X-ray heated models. Solid line: temperature distribution after 30 min of X-ray irradiation. Dashed line: Machado and Linsky flare-model 1. Dotted dashed line: HSRA model.

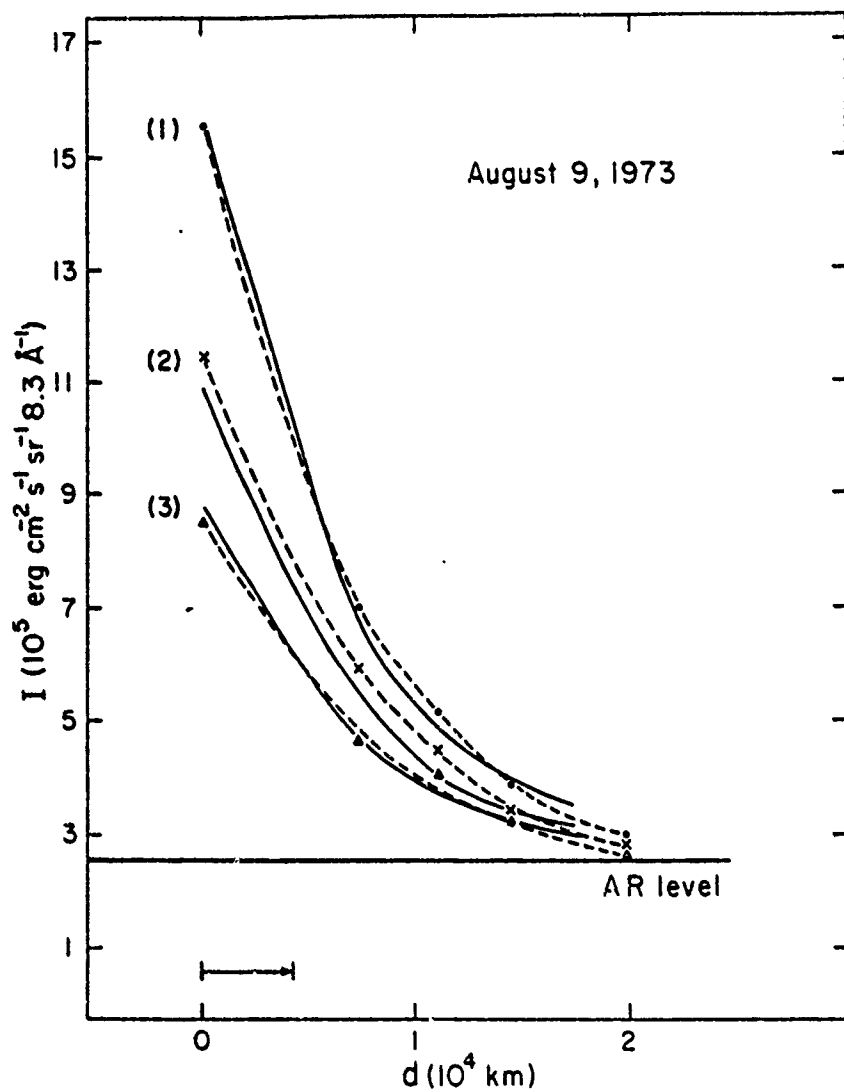


Fig. 6.11 Calculated (solid) and observed (dashed) $L\alpha$ intensities as a function of distance from the 9 August 1973 flare kernel, at three different times: (1) 1555 UT; (2) 1558 UT; and (3) 1601 UT. The arrow at the bottom shows the extent of the soft X-ray kernel region.

theoretical estimates of the energy deposited by soft X-rays in the region of origin of $L\alpha$, convolved with a 5 arc second resolution function. They have arbitrarily been scaled (by a factor of 1.5) to agree at the location of the observed bright X-ray kernel, assuming the source to be a point located 5000 km above the chromosphere with the observed temperature (1.4×10^7 K) and emission measure ($1.3 \times 10^{49} \text{ cm}^{-3}$) of the 9 August flare, using Solrad data. Bearing in mind the uncertainties of the observation and calculation, the model obviously agrees satisfactorily with the observations.

Machado (1978) also found other observational support for the belief that soft X-ray heating plays a role in the chromosphere from the flare of 7 September 1973, which is a large, double-ribbon flare, also observed in $L\alpha$ (and other lines). Features observed in $L\alpha$ include bright regions with sharp boundaries, thought to be footpoints of hot loops, with conductive, chromospheric heating, and a diffuse overall structure (see description of this event in Chapter 8). Measurements were obtained of the $L\alpha$ intensity in both types of structures. The energy deposited in the hydrogen-line forming region by soft X-rays from a source of height 15,000 km, between the bright ribbons, is estimated to be about $1.3 \times 10^6 \text{ erg s}^{-1}$, as compared with an observed $L\alpha + L\beta$ flux of $2.3 \times 10^6 \text{ erg s}^{-1}$. Here it does not appear so possible to account for the radiation solely by soft X-ray heating.

Studies carried out previously of $H\alpha$ filtergrams have not shown the soft X-ray halo predicted theoretically and reported in observations by Machado (1978). The only observations of apparent halos in $H\alpha$ indicate that they are flash-phase phenomena, and have a much more impulsive temporal behavior than soft X-rays (Martin, 1978). One would expect halos in $H\alpha$ if they are present in $L\alpha$. The observational evidence for soft X-ray heating of the chromosphere must therefore be considered to be very weak at this time.

6.4.8. Search for Chromospheric Flare Protons

Recently, Orrall and Zirker (1976) have suggested a method for detecting the existence of 10–300 keV nonthermal proton beams impinging on the chromosphere from above. Downward-injected fast nonthermal protons exchange electrons with ambient neutral hydrogen atoms, producing downward-moving nonthermal neutral hydrogen atoms. Some fraction of these atoms are excited, or become excited, and radiate $L\alpha$ photons. The effect on the flare $L\alpha$ profile, viewed from above, is a net red-shift of the emission due to the nonthermal proton beam. Orrall and Zirker (1976) go on to show that this effect should be observable even if nonthermal protons carry only 1 percent of the total flare energy.

Canfield and Cook (1978) carried out a search for this effect using $L\alpha$ data from the NRL UV spectrograph (Bartoe et al., 1977), S082B; these data were also used by Lites and Cook (1979), c.f. Section 6.4.1. Their initial examination of the data for the flares observed by S082B (Packer et al., 1977) revealed asymmetry, but it could always be ascribed to Doppler shifts, the CI 1240 Å ionization continuum, the decreasing sensitivity of the instrument toward shorter wavelengths, or the wavelength dependence of the Planck function. No other type of asymmetry, such as a flare-related broad excess intensity centered 5–10 Å redward of $L\alpha$ center, was apparent.

The 9 August 1973 flare was chosen for detailed study because it is the most likely flare of those observed to show impulsive-phase proton-induced asymmetries

in $L\alpha$. Preflare spectra were available near the location at which the flare occurred, which reduced uncertainties due to calibration and blends. The flare occurred close enough to disk center (latitude 8° N, longitude 49° W) to retain reasonably high Doppler sensitivity to downward motions. The on-board $H\alpha$ monitor and coalignment with S082 slit covered the point common to the two observed flare loops, the point most likely to show impact phenomena. The loop orientation made it unlikely that downward-injected protons spiraling along the field lines of the loop would have no significant line-of-sight component. Furthermore, a long-exposure (20 s) spectrogram was taken at 1554 UT, at which time solar microwave emission was detected at a variety of stations (*Solar-Geophysical Data*, 1974). Data from two observatories showed this radiation to be partially polarized, which is evidence for nonthermal electrons.

After the usual photometry and calibration, Canfield and Cook (1978) compared the red and blue wings of $L\alpha$ in the preflare active region to the flare. They found that the flare profile showed a slight red-wing excess relative to the preflare profile. In the inner-wing region, $5 < \Delta\lambda < 12 \text{ \AA}$, they obtain a flare excess $\Delta T_b = 37 \pm 17 \text{ K}$, where T_b is the brightness temperature. This value, since it is not statistically significant at the 3σ level, is viewed as an upper limit. The value applies to 1554 UT; later in the flare ΔT decreases further. This excess must be corrected for dilution with the active-region spectrum (the flare fills about one-fourth of the slit area of $2 \times 60 \text{ arcsec}$). The result is that the excess intensity in the red wing at $\Delta\lambda = 8 \text{ \AA}$ from the flare itself is $\Delta I \approx 2 \times 10^3 \text{ erg cm}^{-2} \text{ s}^{-1} \text{ sr}^{-1} \text{ \AA}^{-1}$.

The results of Orrall and Zirker (1976) were then used to compute the limits on the incident energy flux in protons. They calculate the nonthermal $L\alpha$ radiation to be expected at various $\Delta\lambda$ values for a power-law spectrum of protons, for three different exponents δ^p . Canfield and Cook (1978) used their results at $\Delta\lambda = 8 \text{ \AA}$ for $\delta^p = 3$ and $F_{10 \text{ keV}}^p = 10^7 \text{ erg cm}^{-2} \text{ s}^{-1}$, where $F_{10 \text{ keV}}^p$ is the incident energy flux of protons above 10 keV. They adopt $\delta^p = 3$, and assume that the calculated $L\alpha$ excess scales linearly with $F_{10 \text{ keV}}^p$. Also, for comparison with electron fluxes (see below) they convert this to $F_{10 \text{ keV}}^p$. The result is that the observed upper limit to the $L\alpha$ red-wing asymmetry corresponds to an input proton energy flux $F_{20 \text{ keV}}^p \lesssim 2 \times 10^7 \text{ erg cm}^{-2} \text{ s}^{-1}$.

Since the proton flux must be expected to vary considerably from flare to flare, the most interesting quantity is probably the nonthermal proton/electron energy flux ratio. Using the method of Hudson *et al.* (1978) it is possible to obtain the power in thick-target electrons from the observed 3–10 cm microwave flux density S_R . At 1554 UT, S_R was about 7 solar flux units and showed significant polarization (Alissandrakis and Kundu, 1975; Matzler, 1977). Since the spectral index of the electrons is unknown, a value typical of small flares ($\delta^e = 4$) is adopted. This leads to a power in injected electrons of $1.3 \times 10^{27} \text{ erg s}^{-1}$. An upper limit to the compact area is certainly the $H\alpha$ flare area, which to within a factor of two is $A = 1.2 \times 10^{18} \text{ cm}^2$. The implied value of $F_{20 \text{ keV}}^e = P_{20 \text{ keV}}^e/A \approx 10^9 \text{ erg cm}^{-2} \text{ s}^{-1}$. The electron impact area is probably much less than the entire $H\alpha$ area, so the value of $F_{20 \text{ keV}}^e$ is a conservative lower limit, i.e., $F_{20 \text{ keV}}^e \geq 10^9 \text{ erg cm}^{-2} \text{ s}^{-1}$.

The upper limit to the ratio $F_{20 \text{ keV}}^p/F_{20 \text{ keV}}^e$, by the above, is 2×10^{-2} , with an uncertainty of about an order of magnitude. This large uncertainty can be ascribed to several elements of the theory and observations. On the theoretical side, the calculations of Orrall and Zirker are highly simplified. Observationally,

uncertainty comes from: (1) only one flare has been observed by S082B at a time when there is a possibility of nonthermal electron injection into the chromosphere; (2) the spatial resolution of the ATM data is rather low, so the $L\alpha$ radiation comes from places in the loop other than just the footpoints, where the proton motions would be most parallel to the line of sight; (3) the electron flux is estimated by the method of Hudson *et al.* (1978), which has an uncertainty of about an order of magnitude. Of course, if the precipitation fraction of electrons were small, say 10^{-1} , as suggested above (see Section 6.4.5), then the upper limit to $F_{20 \text{ keV}}^p / F_{20 \text{ keV}}^e$ would increase by an order of magnitude. However, the very conservative value of the lower limit adopted for $F_{20 \text{ keV}}^e$ compensates for this partial precipitation, making it unlikely that $F_{20 \text{ keV}}^p / F_{20 \text{ keV}}^e$ was greater than 2×10^{-2} , with the uncertainty specified above.

6.5 CONCLUSIONS

At coronal and transition-zone temperatures, the ATM data have offered hard tests for some models and have been discouragingly inadequate to test others. We found by observing the amount of emission at $T \approx 10^5 \text{ K}$ compared to $T \geq 10^6 \text{ K}$ that the models of Antiochos and Sturrock (1976, 1978) did not pass the test for the small, compact flare of 9 August 1973. During the cooling phase of this flare, at any rate, the introduction of cool chromospheric material into the hot flare volume, and its subsequent effect on conductive cooling, evidently does not play an important role. The dominant energy-loss process at coronal temperatures in the cooling phase of this flare seems to be radiation, and the relative lack of transition-region radiation may well be an effect of radiative instability.

Our efforts to provide observational data with which to test the predictions of hydrodynamic models of the flare atmosphere have been partially frustrated by spatial and temporal resolution inadequate to resolve a unique event within the field of view of the instrument. However, this difficulty has been overcome to some extent by modeling the lower transition-zone data assuming two components within the field of view, one moving and one static. This has revealed tantalizing suggestions of temperature, density, and velocity interrelationships. The densities in dynamical events always appear to be at least an order of magnitude greater than in the quiet sun, suggesting shock phenomena. In all flares, the volumes implied by observed densities and emission measures are small, of order one second of arc along a side. Finally, in the events we have studied, which were chosen for their wide line profiles, the nonthermal broadening velocities often exceed 100 km s^{-1} , reaching almost 200 km s^{-1} in one extreme case. This is obvious evidence for either chaotic motions or waves whose amplitude is much in excess of what is normally found in active regions.

We have been able to demonstrate that the numerical hydrodynamic models of Kostyuk and Pikel'ner (1975) show rapidly decreasing temperature and increasing soft X-ray emission measure in the early cooling phase, which Craig and McClymont (1978) have shown to be a general characteristic of dynamic models. It is particularly interesting that these models also predict that the emission measure per column of unit cross-section should peak considerably later at transition-region temperatures ($10^5 < T < 10^6 \text{ K}$) than coronal temperatures ($T > 10^6 \text{ K}$). The rise in transition-region emission measure lags the coronal component by about eight

minutes in the model examined, and the fall is much slower. Finally, the transition-region emission measure is an order of magnitude greater than the coronal emission measure, which certainly is not what Underwood *et al.* (1978) found for the 9 August flare. These conclusions need to be strengthened, both observationally and theoretically.

In the chromosphere and upper photosphere we have made considerable progress on sorting out the mechanisms for the flare as manifested in the lower flare atmosphere. We have begun by using the observations to measure empirically the amount of flare heating as a function of depth in the atmosphere. Our ATM observations of ultraviolet continua and line wings in the visible confirm that during flares the chromosphere is heated more than the lower atmosphere, pushing the point of minimum temperature down deeper during flares. Considerable energy is radiated by these layers, as can also be seen in the 5 September 1973 flare study (Appendix A). Continuous heating of the temperature-minimum region is required during the cooling phase. We have constructed empirical heating models with temperature and density distributions that, when used to compute synthetic spectra, result in a satisfactory match to the observations. These models extend from the temperature minimum well into the chromosphere, up to about $T \sim 9000$ K.

The empirical models have been compared with theory primarily near the base of the chromosphere, at the temperature minimum. Our efforts to explain the empirical models in terms of the "canonical" model of heating—i.e., as a secondary effect of primary energy release elsewhere in the flare—suggest that this model may not be fully justified near the temperature minimum. Although it is hard for particles, conducted heat, shocks, or radiation to penetrate below the temperature minimum, it is also true that the heating at that depth is observed to be small—small enough, in fact, that the uncertainty of the measurements made to date is too great to rule out some heating sources. At about the flare temperature minimum, on the other hand, the heating is enough so that the observed enhancements are marginally significant; there, we find that we can completely rule out heating by nonthermal protons, except under very specialized assumptions of almost monoenergetic beams of deka-MeV protons. Electrons probably cannot account for more than a modest fraction of the observed heating in the lower chromosphere, although higher in the atmosphere (say the H α -forming region) they can do the job with energy to spare. We believe the most likely source for heating the temperature-minimum region is probably soft X-rays. They can account for much of the relatively homogeneous structure; on the other hand, spatially well-defined features are observed that are almost certainly caused by some other mechanism, perhaps UV or EUV radiation. Further observations at this level of the atmosphere are certainly needed, but they must include the preflare state at the flare site.

In the chromosphere, on the other hand, there is no doubt that the observed heating can be understood in terms of the canonical model. We have evidence that heating by nonthermal electrons is more than sufficient to produce observed H α flare kernel spectra. In fact, comparison of hard X-ray, H α , and EUV observations for the same flares implies that all the available electrons do not penetrate to the chromosphere—if they did so, the effect on the chromosphere would be larger than observed, even in kernels. We have been partially frustrated by the lack of hard X-ray instrumentation on ATM, for the determination of high-energy electron properties. We have managed to offset this in part by empirical and

theoretical methods using microwave data, but these are beset by an uncertainty of about an order of magnitude. Another result that has emerged both during the Workshop and before is the large flare mass motions implied by the large widths of strong lines from the chromosphere. The velocities implied are intermediate between the small values from weaker photospheric and lower-chromospheric lines and the larger values from the transition region. The fact that, in the visible, narrow metal lines are observed in flares must be due to their origin deeper in the atmosphere than lines like H α or Ca II K, where motions are apparently relatively small. Finally, it seems clear theoretically that some flare heating in the chromosphere must occur because of irradiation by soft X-rays. Our study of the Skylab data shows effects quantitatively consistent with the theoretical calculations, with regard to both amplitude and spatial dependence of the heating.

Our search for evidence of injection into the chromosphere of fast protons in the 10–100 keV range has yielded negative results. The data for the ATM flares showed none of the expected wing asymmetry in L α due to these protons. For the only flare studied quantitatively, an upper limit of about 2×10^{-2} , with an uncertainty of about one order of magnitude, could be placed on the proton-electron energy flux ratio, assuming a thick target and complete precipitation for both electrons and protons. Since we find that one would also not expect proton-heating effects at the temperature minimum, and since the identification of MeV protons with white-light flares is quite uncertain, the only evidence for the injection of nonthermal protons into the chromosphere during flares seems to be the γ -ray emission (see Chapter 4).

We would like to close by discussing a simplified model of the horizontal structure of a flare as seen in the chromosphere, which summarizes our view of the processes affecting the lower atmosphere during flares. This model is suggested by our Workshop results, building on previous knowledge. At risk of oversimplification, we represent in Figure 6.12 the phenomena that one might see along a line through a classical, large, two-ribbon flare, starting in a bright, chromospheric flare kernel. The abscissa represents the amount of flare heating; the ordinate is the horizontal distance from the kernel. *Region a* is the flare kernel. This is most probably the site of heating by electrons, and is, of course, connected by magnetic field lines to the site of particle acceleration. It is also part of a flare ribbon, so here normal ribbon-heating processes also obtain (see below). The temporal association of chromospheric flare kernels with microwave and hard X-rays supports the identification of nonthermal particles as the source of heating in kernels. Any models that invoke the presence of nonthermal particles therefore presumably apply only to kernels. White-light emission coincides spatially with kernels, but there is controversy about whether this is caused by protons or electrons. *Region b* lies between the flare ribbons, and apparently is heated in part by soft X-ray radiation from the overlying arcade of coronal loops. At this time, however, we believe that other sources of emission may exist, and the evidence for the soft X-ray heating is primarily theoretical. *Region c* is the flare ribbon, sharpest on the outer edge. The ribbons are known from the Workshop and before to be connected by bright X-ray loops. Hence, soft X-ray heating contributes here, but cannot be the dominant heating, since the outer edge is sharp. It would seem that thermal conduction is probably dominant here, but we know of no quantitative confirmation of this speculation. The theory of Kopp and Pneuman (1976) leads us to believe that the loops that connect to the outer edge of the ribbon are hottest,

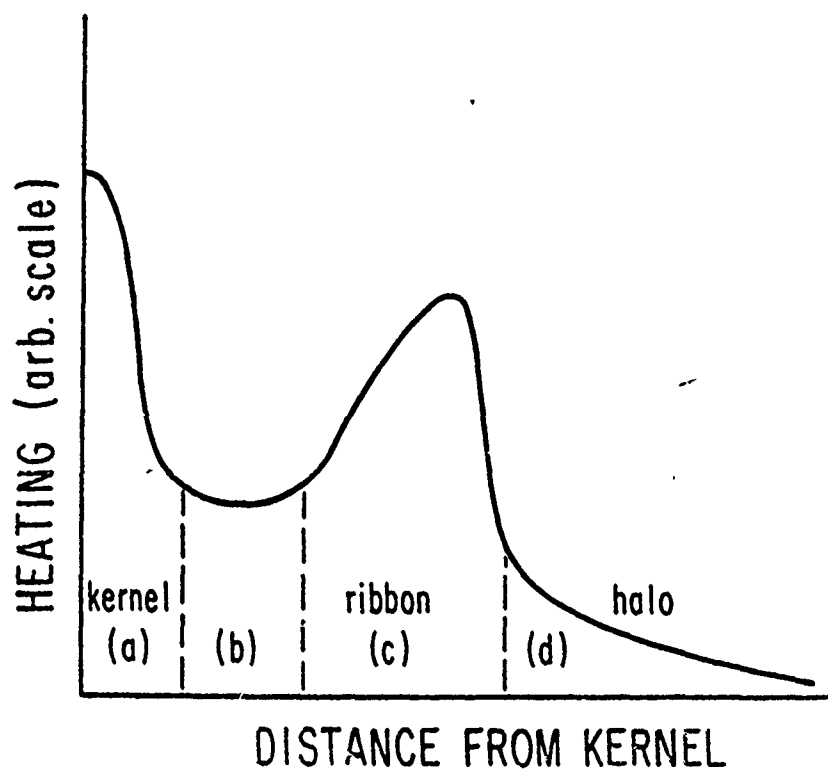


Fig. 6.12 Schematic representation of chromospheric flare features along a horizontal line through a flare, starting in a kernel.

which would imply greater conductive flux to the chromosphere, and account for the greater brightness at the outer edge. It is possible that shock heating plays a role at some point within the loops, since observational evidence for infalling material exists here. We have not considered either of the latter two topics in quantitative modeling during the Workshop; both are discussed by Švestka (1976) and in Chapter 8. Finally, *region d* is the soft X-ray halo, for which observational evidence is very sparse at present. Heating in the halo is due to soft X-rays, and is rather weak compared to heating in the kernel and ribbon. The heating falls off gradually with distance from the soft X-ray source, simply due to the decrease of the intensity of incident soft X-ray radiation.

- Alissandrakis, C. E. and Kundu, M. R.: 1975, *Solar Phys.* 41, 119.
- Antiochos, S. K. and Sturrock, P. A.: 1976, *Solar Phys.* 49, 359.
- Antiochos, S. K. and Sturrock, P. A.: 1978, *Astrophys. J.*, 220, 1137.
- Athay, R. G.: 1972, *Radiation Transport in Spectral Lines*, D. Reidel Publ. Co., Dordrecht, Holland.
- Bartoe, J.-D. F., Brueckner, G. E., Purcell, J. D. and Tousey, R.: 1977, *Applied Optics* 16, 879.
- Bloomberg, H. W., Davis, J., and Boris, J. P.: 1977, *J. Quant. Spectrosc. Radiat. Transfer* 18, 237.
- Brown, J. C.: 1971, *Solar Phys.* 18, 489.
- Brown, J. C.: 1973, *Solar Phys.* 31, 143.
- Brown, J. C.: 1975, in S. R. Kane (ed.), 'Solar γ -, x- and EUV Radiation', *IAU Symp.* 68.
- Brown, J. C.: 1978, unpublished.
- Brown, J. C., Canfield, R. C., and Robertson, M. N.: 1978, *Solar Phys.* 57, 399.
- Brown, J. C. and Hoyng, P.: 1975, *Astrophys. J.* 200, 734.
- Brown, J. C. and Melrose, D. B.: 1977, *Solar Phys.* 52, 117.
- Brueckner, G. E., Bartoe, J.-D. F., Kjeldseth Moe, O., and VanHoosier, M. E.: 1976, *Astrophys. J.* 209, 935.
- Canfield, R. C.: 1974a, *Solar Phys.* 34, 339.
- Canfield, R. C.: 1974b, *Astrophys. J.* 194, 483.
- Canfield, R. C. and Athay, R. G.: 1974, *Solar Phys.* 34, 193.
- Canfield, R. C. and Cook, J. W.: 1978, *Astrophys. J.* 225, 650.
- Cook, J. W. and Brueckner, G. E.: 1979, *Astrophys. J.* 227, 645.
- Craig, I. J. D. and Brown, J. C.: 1976, *Nature* 264, 340.
- Craig, I. J. D. and McClymont, A. N.: 1976, *Solar Phys.* 50, 133.
- Craig, I. J. D. and McClymont, A. N.: 1978, unpublished.
- Craig, I. J. D., McClymont, A. N., and Underwood, J. H.: 1978, *Astron. Astrophys.* 70, 1.
- Craddock, R., Paresce, F., Bowyer, S., and Hampton, M.: 1974, *Astrophys. J.* 187, 497.
- Culhane, J. L., Vesecky, J. F., and Phillips, K. J. H.: 1970, *Solar Phys.* 15, 394.
- Datlowe, D. W., Elcan, M. J. and Hudson, H. S.: 1974, *Solar Phys.* 39, 155.
- Donnelly, R. F. and Kane, S. R.: 1978, *Astrophys. J.* 222, 1043.
- Doschek, G. A. and Feldman, U.: 1978, *Astron. Astrophys.* 69, 11.
- Doschek, G. A., Feldman, U., and Rosenberg, F. D.: 1977, *Astrophys. J.* 215, 329.
- Emslie, A. G.: 1978, *Astrophys. J.* 224, 241.
- Emslie, A. G., Brown, J. C., and Donnelly, R. F.: 1978, *Solar Phys.* 57, 175.
- Falciani, R., Giordano, M., Rigutti, M., and Roberti, G.: 1977, *Solar Phys.* 54, 169.
- Feldman, U. and Doschek, G. A.: 1978, *Astron. Astrophys.* 65, 215.
- Feldman, U., Doschek, G. A., and Rosenberg, F. D.: 1977, *Astrophys. J.* 215, 652.
- Gingerich, O., Noyes, R. W., Kalkofen, W., and Cuny, Y.: 1971, *Solar Phys.* 18, 347.
- Hénoux, J. C. and Nakagawa, Y.: 1977, *Astron. Astrophys.* 57, 105.
- Hénoux, J. C. and Nakagawa, Y.: 1978, *Astron. Astrophys.* 66, 385.
- Hoyng, P., Brown, J. C., and van Beek, H. F.: 1976, *Solar Phys.* 48, 197.
- Hudson, H. S.: 1973, in R. Ramaty and R. G. Stone (eds.), *High Energy Phenomena on the Sun*, NASA, SP-342, 217.
- Hudson, H. S., Canfield, R. C., and Kane, S. R.: 1978, *Solar Phys.* 60, 137.
- Jefferies, J. T.: 1957, *Mon. Not. Roy. Astron. Soc.* 117, 493.
- Kane, S. R.: 1974, in G. A. Newkirk (ed.), 'Coronal Disturbances', *IAU Symp.* 54.
- Kopp, R. A. and Pneuman, G. W.: 1976, *Solar Phys.* 50, 85.
- Kostyuk, N. D.: 1976a, *Sov. Astron.* 19, 458.
- Kostyuk, N. D.: 1976b, *Sov. Astron.* 20, 206.
- Kostyuk, N. D. and Pikel'ner, S. R.: 1975, *Sov. Astron.* 18, 590.
- Labonte, B. J.: 1979, preprint.
- Lin, R. P. and Hudson, H. S.: 1976, *Solar Phys.* 50, 153.
- Linsky, J. L. and Ayres, T. R.: 1978, *Astrophys. J.* 220, 619.

- Lites, B. W. and Cook, J. W.: 1979, *Astrophys. J.* 228, 598.
- Machado, M. E.: 1978, *Solar Phys.* 60, 341.
- Machado, M. E., Emslie, A. G., and Brown, J. C.: 1978, *Solar Phys.* 58, 363.
- Machado, M. E. and Linsky, J. L.: 1975, *Solar Phys.* 42, 395.
- Machado, M. E. and Noyes, R. W.: 1978, *Solar Phys.* 59, 129.
- Markey, J. F. and Austin, R. R.: 1977, *Appl. Optics* 16, 917.
- Martin, S. F.: 1974, *Lockheed Solar Observatory Report (NAS 8-29608)*.
- Martin, S. F.: 1977, private communication.
- Martin, S. F.: 1978, private communication.
- Mätzler, C.: 1977, private communication.
- McClymont, A. N. and Craig, I. J. D.: 1977, unpublished.
- McWhirter, R. W. P., Thonemann, P. C., and Wilson, R.: 1975, *Astron. Astrophys.* 40, 63.
- Najita, K. and Orrall, F. Q.: 1970, *Solar Phys.* 15, 176.
- Nakagawa, Y., Wu, S. T., and Han, S. M.: 1973, *Solar Phys.* 30, 111.
- Orrall, F. Q. and Zirker, J. R.: 1976, *Astrophys. J.* 208, 618.
- Packer, I. G., Patterson, N. P., Mango, S. A., and Tousey, R.: 1977 *NRL Memorandum Report 3410* (Table 4.2 compiled by V. E. Scherrer).
- Ramaty, R., Kozlovsky, B. and Linfelfelter, R. E.: 1974, *GSFC Document X-660-74-360*.
- Reeves, E. M., Huber, M. C. E. and Timothy, J. G.: 1977, *Appl. Optics* 16, 837.
- Samain, D., Bonnet, R. M., Gayet, R. and Lizambert, C.: 1975, *Astron. Astrophys.* 39, 71.
- Shine, R. A. and Linsky, J. L.: 1974, *Solar Phys.* 37, 145.
- Shmeleva, O. P. and Syrovatskii, S. I.: 1973, *Solar Phys.* 33, 341.
- Smith, D. F.: 1970, *Solar Phys.* 15, 202.
- Solar-Geophysical Data*: 1974, Numbers 355, 358, 359 (Part II).
- Sonov, B. V.: 1975, *Solar Phys.* 47, 235.
- Sonov, B. V., Spektor, A. R., and Syrovatskii, S. I.: 1977, *Izv. Acad. Sci. USSR, Phys. Ser.* 41, 173.
- Sonov, B. V. and Syrovatskii, S. I.: 1976, *Sov. Phys. Usp.* 19, 813.
- Strass, F. M. and Papagiannis, M. D.: 1971, *Astrophys. J.* 164, 369.
- Švestka, Z.: 1957, *Publ. Astr. Inst. Prague*, No. 32.
- Švestka, Z.: 1970, *Solar Phys.* 13, 471.
- Švestka, Z.: 1972, *Ann. Rev. Astron. Astrophys.* 10, 1.
- Švestka, Z.: 1976, *Solar Flares*, D. Reidel Publ. Co., Dordrecht, Holland.
- Syrovatskii, S. I. and Shmeleva, O. P.: 1972, *Soviet Astr. A. J.* 16, 273.
- Tanaka, K.: 1977, private communication.
- Thomas, R. J. and Teske, R. G.: 1971, *Solar Phys.* 16, 431.
- Tousey, R., Bartoe, J.-D. F., Brueckner, G. E., and Purcell, J. D.: 1977, *Applied Optics* 16, 870.
- Underwood, J. H., Antiochos, S. K., Feldman, U., and Dere, K. P.: 1978, *Astrophys. J.* 224, 1017.
- Underwood, J. H., Milligan, J. E., de Loach, A. C. and Hoover, R. B.: 1977, *Applied Optics* 16, 858.
- Vernazza, J. E., Avrett, E. H., and Loeser, R.: 1973, *Astrophys. J.* 184, 605.
- Vernazza, J. E., Avrett, E. H., and Loeser, R.: 1976, *Astrophys. J. Suppl.* 30, 1.
- Zaumen, W. T. and Acton, L. W.: 1974, *Solar Phys.* 36, 139.
- Zirin, H.: 1978, *Solar Phys.* 58, 95.
- Zirin, H. and Tanaka, K.: 1973, *Solar Phys.* 32, 173.

ii) Radiative Energy Output of the 5 September 1973 Flare

This paper, published as Appendix A of the monograph Solar Flares, edited by P.A. Sturrock, is a benchmark reference paper; it is the only available measurement of the radiative energy output of any flare over such a wide range of the spectrum (X-rays to radio). In research work it has been useful often, to demonstrate that the kinetic energy that flares put into mass ejections is often one to two orders of magnitude more than their radiated energy. It has also been used as the observational data for theoretical studies; among other things, it demonstrates the role of thermal conduction in determining the structure of the flare plasma.

APPENDIX A RADIATIVE ENERGY OUTPUT OF THE 5 SEPTEMBER 1973 FLARE

Richard C. Canfield; C.-C. Cheng, K.P. Dere, G.A. Dulk, D.J. McLean,
R.D. Robinson, Jr., E.J. Schmahl, S.A. Schoolman

A.1 INTRODUCTION

In this appendix we present results of a unique study: for the first time, we have measured the radiative energy output of a single flare over a range of more than ten decades in wavelength, from below one Ångström to above one meter. Our data permit us to determine the absolute intensity of radiative energy output over this entire range at the time of flare maximum (1831 UT, 5 September 1973). Previous estimates of the distribution of radiation over a wide range in flare spectra have been made by Ellison (1963), Bruzek (1967), de Jager (1970), Lin (1974), Lin and Hudson (1976), and others. Our data represent an important improvement, since they apply to a single flare; the next step is to repeat what we have done, for a variety of flares.

This flare was chosen for analysis because it was well observed from *both* Skylab and Earth. We provide only limited morphological detail below; further information appears in Appendix B, in Chapter 2, and in *Solar-Geophysical Data* (1974). We have deliberately chosen to present these data in uninterpreted form; we expect that their utility will be amply demonstrated by their use in the future.

Throughout this appendix, we will assume that the specific intensity of the radiation emerging from the flare volume is isotropic. We also assume that radiation emitted back toward the sun is subsequently reemitted, so that the radiated power is obtained by multiplying the observed specific intensity by 2π steradians and the projected area of the flare.

A.2 SOFT X-RAYS (1-20 Å)

The X-ray flux at 1 AU in the band 0.5--20 Å was measured from SOLRAD-9. The instantaneous X-ray fluxes were determined once per minute in the bands 0.5-3 Å, 1-8 Å, and 8-16 Å. The values given by Dere *et al.* (1977) are shown in Figure A.1. This figure also shows the times of measurements at other wavelengths, reported later in this appendix. The apparent constancy of the 1-8 Å and 8-20 Å channels near flare maximum is due to coarse digitization of the ionization-chamber currents. The errors in these flux values due to detector uncertainties probably do not exceed 20%.

The flux values are derived from the ionization-chamber currents assuming a solar gray-body spectrum. The observed solar spectrum in this wavelength region is produced by optically thin thermal bremsstrahlung, radiative recombination, and line emission. If such a spectrum is used for the 5 September flare, the derived 0.5-3 Å flux values are increased by a factor 1.5 and the 1-8 Å flux is decreased by a factor of about 0.7 (see Dere *et al.*, 1974).

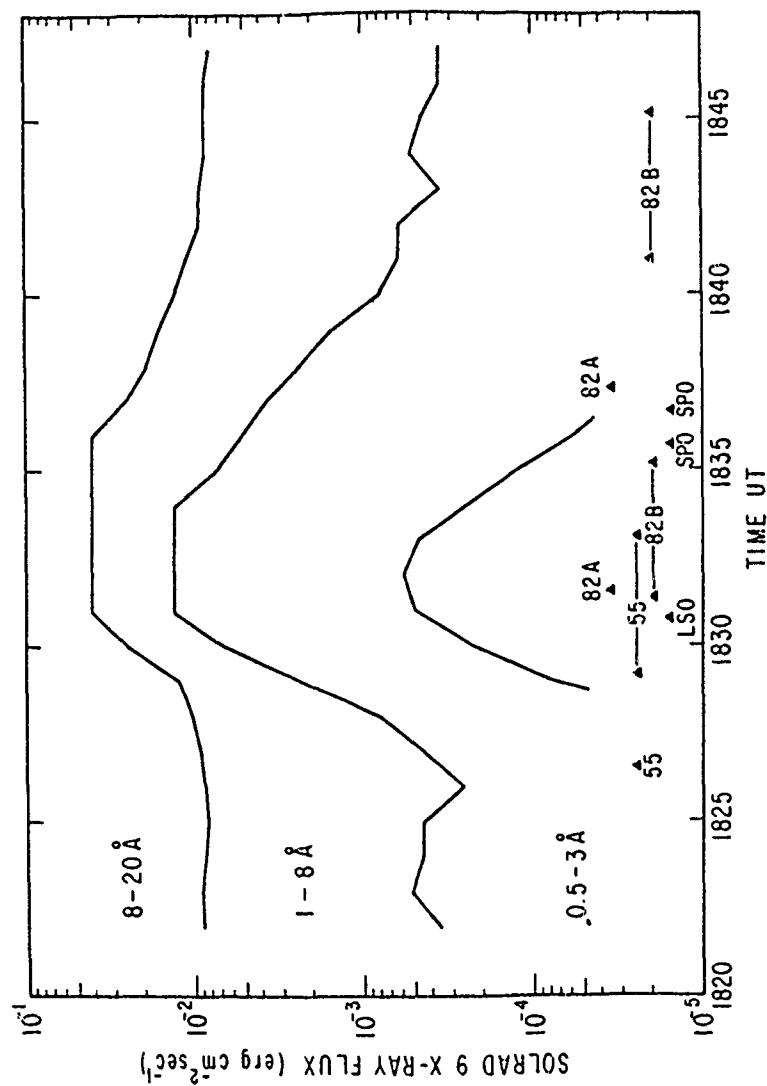


Fig. A.1 SOLRAD-9 X-ray flux as a function of universal time, for the 5 September 1973 flare. Times of other observations reported in this appendix are shown in the lower part of the figure. The abbreviations used are: 82A, the Naval Research Laboratory XUV spectroheliograph (see Sect. A.3); 55; the Harvard College Observatory EUV spectroheliometer (see Sect. A.4); 82B, the Naval Research Laboratory EUV spectrograph (see Sect. A.5); LSO, the Lockheed Solar Observatory H α multislit spectrograph (see Sect. A.6); SP0, The Sacramento Peak Observatory Universal Spectrograph (see Sect. A.7).

In Table A.1, columns 2 and 3, we give the SOLRAD-9 fluxes in the 1–8 Å and 8–20 Å bands. Powers of ten are enclosed in parentheses. In column 4 we have determined the radiative power output appropriate to the flare itself in the 1–20 Å range by first subtracting background flux values from both 1–8 Å and 8–20 Å channels, then computing the radiative power output P from the flux at 1 AU, F :

$$P = 2\pi (1 \text{ AU})^2 F \approx 1.41 \times 10^{27} F \text{ (cgs)}. \quad (\text{A.2.1})$$

A.3 XUV LINES (171–345 Å)

The Naval Research Laboratory's Skylab XUV spectroheliograph (S082A) obtained photographic flare images at 1831 UT and 1837 UT (see Fig. A.1). Both covered the wavelength region 171–345 Å, and were short exposures, so that spectroheliograms in only the most intense lines were recorded. Values of radiated power at these two times are given in Table A.2. These are based on the flux measurements of Dere *et al.* (1977) and Eq. (A.2.1), except for the He II lines, which have not been published previously, but are determined by the same method. The accuracy of the data is approximately a factor of two in absolute power, except for He II 304 Å, which is probably good to only an order of magnitude due to overexposure of its very intense image. Preflare background power values have not been subtracted, but they are negligible (within the accuracy of the data) for all lines except possibly He II 304 Å and He II 256 Å. Note that since the 304 Å line dominates the XUV lines, and is good only to order of magnitude, the total contribution of XUV lines in the table is also good only to order of magnitude. For 304 Å, the background contribution is certainly less than 20%, for 256 Å, the background contributes still less.

The time histories of these emissions are consistent with those observed in other flares, such as that of 9 August 1973 (Dere and Cook, 1979). There the flare ($T \sim 10^7$ K), lower transition-zone, and chromospheric lines monotonically fall during the decay phase, while the coronal and upper transition-zone lines exhibit a dramatic (as much as a factor of 10) rise and fall during this same period of time.

A.4 Mg X 625 Å, H I LYMAN- α AND C II 1335 Å

The Harvard College Observatory EUV spectropheliometer (S055) on Skylab (Reeves *et al.*, 1977) operated in two modes during this flare: one-dimensional "line scans" (5" \times 300" with 5 minute time resolution), and "raster scans" ($\leq 300'' \times 300''$ with ≤ 5.5 minute time resolution). In both modes, spatial resolution was 5" \times 5". Table A.3 summarizes the S055 observations; timing relative to other data is indicated in Figure A.1. It is important to note that, near flare maximum, the instrument was in the line-scan mode, so to infer the power radiated by the whole flare it is necessary to extrapolate from the line scan to the whole flare area. Four two-dimensional raster scans (Table A.3) are used for this purpose.

The reduction procedure consisted of the following steps. (1) Using the calibration of Reeves *et al.* (1977), determine the intensity as a function of position and time $I(x, t)$ along the line scan. (2) Form the differenced intensity

Table A.1			
SOFT X-RAYS (1-20 Å)			
Time (UT)	Flux at 1 AU (erg cm ⁻² s ⁻¹)		Power (erg s ⁻¹) 1-20 Å
	1-8 Å	8-20 Å	
1827	4.4(-4)	9.0(-3)	2.2(24)
1828	7.9(-4)	1.0(-2)	2.7(24)
1829	2.3(-3)	1.4(-2)	1.1(25)
1830	6.5(-3)	2.4(-2)	3.1(25)
1831	1.3(-2)	4.0(-2)	6.3(25)
1832	1.3(-2)	4.0(-2)	6.3(25)
1833	1.3(-2)	4.0(-2)	6.3(25)
1834	1.3(-2)	4.0(-2)	6.3(25)
1835	7.3(-3)	4.0(-2)	5.5(25)
1836	5.2(-3)	4.0(-2)	5.2(25)
1837	3.6(-3)	2.5(-2)	2.9(25)
1838	2.2(-3)	1.9(-2)	1.8(25)
1839	1.5(-3)	1.6(-2)	1.2(25)
1840	7.9(-4)	1.3(-2)	6.9(24)
1841	6.1(-4)	1.1(-2)	3.9(24)
1842	6.1(-4)	9.2(-3)	1.3(24)
1843	3.5(-4)	9.0(-3)	7.0(23)
1844	5.2(-4)	8.5(-3)	2.4(23)
1845	4.4(-4)	8.7(-3)	4.1(23)

TABLE A.2

BRIGHTEST XUV LINES (171--345 Å)

Ion	$\lambda(\text{\AA})$	Power (erg s^{-1})	
		1831 UT	1837 UT
He II	234	1.5(23)	—
	237	1.8(23)	5.5(22)
	243	3.4(23)	1.1(23)
	256	9.0(23)	1.7(23)
	304	1.0(25)	1.4(24)
Ca XVII	193	—	1.4(23)
Ca XVIII	345	—	5.6(22)
Fe XIII	204	—	8.9(22)
	252	—	3.5(22)
Fe XIV	211	—	8.9(22)
	219	—	1.4(23)
	252	—	4.5(22)
	265	2.8(23)	1.4(23)
	274	—	7.1(22)
Fe XV	234	—	1.1(23) b
	244	—	1.1(23)
	284	1.1(24)	1.1(24)
Fe XVI	251	—	1.4(23)
	263	2.2(23)	2.8(23)
	335	2.2(24)	2.8(24)
Fe XXIII	264	8.9(22)	—
Fe XXIV	192	5.6(23)	—
	255	2.8(23)	—
Ni XVII	249	—	1.8(23)
Ni XVIII	234	—	1.1(23) b
	321	—	1.8(23)
Total		1.6(25)	7.5(24)

Note: b - blended

TABLE A.3
SUMMARY OF EUV SPECTROHELIOMETER OBSERVATIONS

Start 5 September 1973	End	Scan Mode	Pointing	Data Quality							Remarks
				$\lambda 1335$	$\lambda 1216$	$\lambda 1032$	$\lambda 977$	$\lambda 896$	$\lambda 625$	$\lambda 554$	
1653:36	1659:06	Raster	McMath 510	a	a	a	a	e	a	a	Preflare
1824:58	1828:55	Raster	McMath 510	a	a	a	a	a	a	a	Flare Rise,
1829:05	1833:05	Line	Thru Flare	b	b	c	d	e	a	d	Flare Rise, Maximum, Fall
1838:45	1848:44	Line	20" W of Flare	a	a	c	c	e	a	d	Flare Fall
1850:18	1855:48	Raster	McMath 510	a	a	a	a	e	a	a	Flare Fall
1903:57	1909:30	Raster	McMath 510	a	a	a	a	x	a	a	Post-Flare

Notes: a—good data; b—1 or 2-bit overflows (recoverable); c—3 or more bit overflows (irrecoverable); d—high-voltage tripouts during flare peak; e—small amount of data; x—no data.

$I(x, t) = J(x, t) - J(x, 1826 \text{ UT})$. (3) Obtain the flare power in the line scan $P'(t)$ by integrating $I(x, t)$ along the line scan and multiplying by 2π . (4) Multiply this power by an extrapolation factor to obtain the total radiated flare power $P(t)$ for the three spectral lines scanned throughout the flare.

The extrapolation factor in step (4) is $P(t)/P'(t)$. Flare-rise and flare-fall values of this factor were determined for each line from the differenced intensity rasters, Figure A.2. This figure shows the two-dimensional distribution of differenced intensity on a simple five-level scale based on I_c , the cutoff value of I that defines a differenced intensity slightly above the "noise" level of intensity changes that are not specifically related to the flare. Some areas in the raster darken between the preflare and flare-rise rasters, which accounts for areas for which $I < 0$. The flare-rise and flare-fall values of the extrapolation factor were determined for each line from the differenced intensity rasters shown in Figure A.2. Flare-rise ($t \sim 1829 \text{ UT}$) values of the extrapolation factor were 2.2, 1.3, and 2.1 for $\lambda 1216$, $\lambda 1335$ and $\lambda 625$, respectively. Corresponding flare-fall ($t \sim 1833 \text{ UT}$) values were 12, 16, and 16. We were forced by lack of alternatives to adopt a linear time-dependence of these $P(t)/P'(t)$ values to interpolate between 1829 UT and 1833 UT. This technique does not strictly give a unique result because of the limited field of view and possible subflares between the flare-rise and flare-fall spectroheliograms. Nevertheless, various trials with subsets of the spectroheliograms suggest that the extrapolation factor is accurate to within about a factor of 2. The absolute intensities, on the other hand, are better determined, with an estimated uncertainty of 35%.

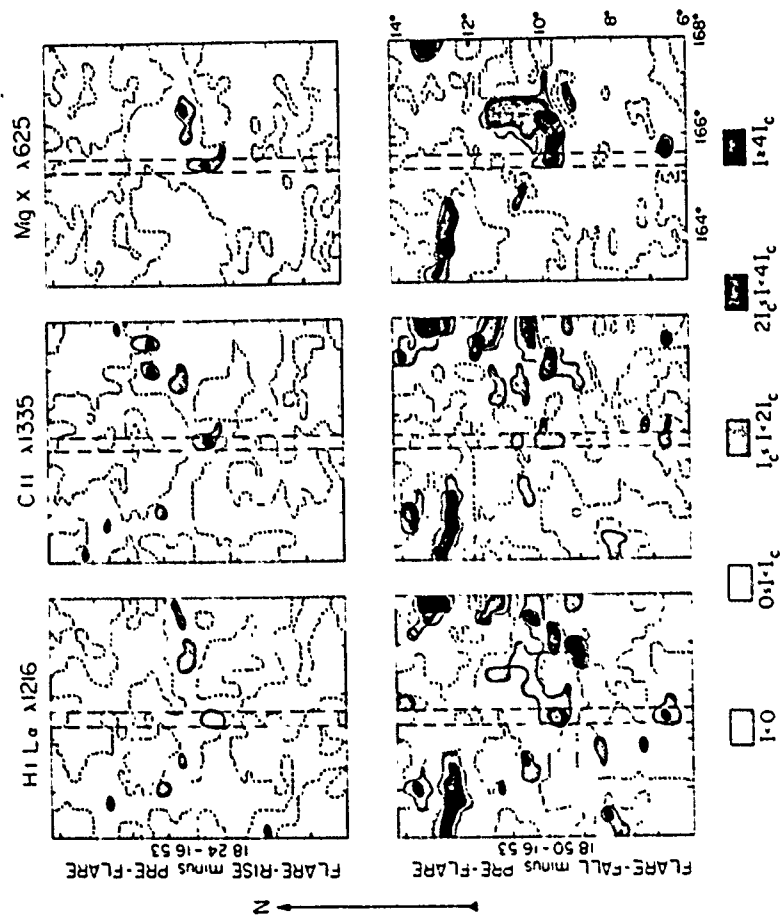


Fig. A.2 Spatial distributions of differenced intensities I from the EUV spectroheliometer, at flare rise (upper row) and flare fall (lower row). I_c is a cutoff value of I chosen to define the flare-related brightenings. Solar latitude and longitude is given at the lower right.

Table A.4 lists the observed radiated power in the line scan $P'(t)$ and the extrapolated total radiated power $P(t)$, using the adopted flux-extrapolation factors.

TABLE A.4						
LYMAN- α , C II 1335 Å, Mg X 625 Å						
Time UT	Line Scan Power P' (erg s ⁻¹)			Total Flare Power P (erg s ⁻¹)		
	1216 Å	1335 Å	625 Å	1216 Å	1335 Å	625 Å
1826:26	5.2(23)	2.8(22)	6.8(20)	1.1(24)	1.2(23)	1.5(21)
1829:05	5.6(24)	6.4(23)	2.0(22)	1.2(25)	3.6(24)	7.2(22)
1829:35	6.4(24)	6.8(23)	2.8(22)	2.2(25)	4.0(24)	1.1(23)
1830:05	6.6(24)	8.0(23)	2.8(22)	2.4(25)	4.8(24)	1.2(23)
1830:35	6.0(24)	8.6(23)	1.7(21)	2.2(25)	5.4(24)	7.6(22)
1831:05	5.6(24)	5.6(23)	1.4(22)	2.2(25)	3.6(24)	6.6(22)
1831:35	4.8(24)	6.2(23)	1.2(22)	2.0(25)	4.2(24)	6.2(22)
1832:05	4.2(24)	5.4(23)	1.1(22)	1.8(25)	3.8(24)	5.8(22)
1832:35	3.8(24)	6.0(23)	1.1(22)	1.7(25)	4.4(24)	6.2(22)
1833:05	3.6(24)	4.8(23)	1.4(22)	1.7(25)	3.6(24)	8.0(22)
1851:52	7.0(23)	3.4(22)	7.0(20)	8.2(24)	5.4(23)	1.1(22)

A.5 EUV LINES (1175–1863 Å) AND CONTINUA (1400–1960 Å)

Two sequences of photographic exposures (2.5, 10, 40, 160s) were obtained with the Naval Research Laboratory's EUV slit spectrograph on ATM (S082B) (Bartoe *et al.*, 1977), starting at 1831 and 1841 UT, respectively, as shown in Figure A.1. The S082B slit subtends 2" X 60", some of which covered nearby nonflaring active region. Figure A.3 indicates the slit position (centered on the cross-hairs), relative to the H α flare at 1831 UT, from the on-board H α camera (Markey and Austin, 1977). This picture has been used to estimate both the fraction of the slit filled by the flare and the total area of the flare, on the assumption that the H α flare and EUV flare horizontal dimensions are the same to within the factor-of-two accuracy desired for this project.

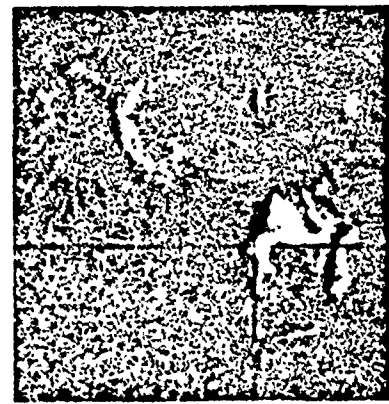
The optical densities were converted into absolute intensities by employing absolute calibrations from exposures obtained with a calibration rocket flown on 4 September 1974. The calibration is estimated to give measured absolute intensities an accuracy of $\pm 35\%$ (rms). Detailed descriptions of the calibrations of the NRL spectrograph have been given by Brueckner *et al.* (1976) and by Kjeldseth Moe and Nicolas (1977).

Fe XXIV 255 He II 256 Å

18 31

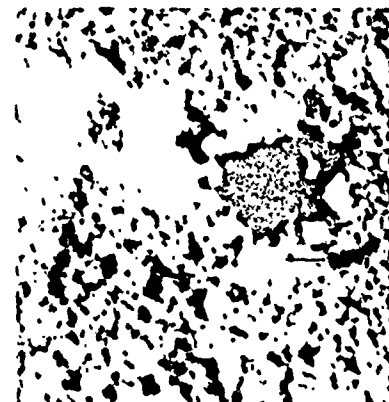
H α

18 31 UT



Fe XVI 335

18 37



KITT PEAK MAGNETOGRAM

16 24

UT

60"
SLIT

Fig. A.3 The slit position of the NRL spectrograph (S082B). The slit is pointed at one of the ribbons, as shown in the picture taken by the H α telescope on Skylab. The XUV spectroheliograms were taken by the NRL slitless spectrograph (S082A) on Skylab. The arrow on the magnetogram shows the position of the S082B slit.

To determine the intensity of the flare itself from the observed intensities, one assumes the observed intensity I_0 is the weighted sum of flare and background active-region intensities, I_f and I_{ar} respectively:

$$I_0 = \alpha I_f + (1 - \alpha) I_{ar} , \quad (\text{A.5.1})$$

or

$$I_f = I_0 \alpha^{-1} - (\alpha^{-1} - 1) I_{ar} , \quad (\text{A.5.2})$$

where α is the fraction of the slit filled by the flare. From the H α pictures (Fig. A.3), $\alpha = 0.27$ at 1831 UT and $\alpha = 0.13$ at 1841 UT. For the background, a previous exposure of the same active region was used, corrected to the same value of $\cos \theta$ as the flare, using the 1400–2000 Å limb darkening functions from Samain *et al.* (1975).

In Table A.5, we estimate the power radiated in the continuum between 1400 and 1960 Å. These values are based on the continuum intensities I of Cheng and Kjeldseth Moe (1978), which have been corrected using Eq. (A.5.2) and the specified values of α . The power values have been computed from the intensities by

$$P = 2\pi \overline{\Delta I} A \Delta\lambda , \quad (\text{A.5.3})$$

where $\overline{\Delta I}$ is the observed average intensity difference (flare minus background) in the interval $\Delta\lambda$, and A is the estimated flare area.

The flare area A was estimated from the H α observations. Three independent estimates gave the following H α areas: on-board ATM camera, $2.7 \times 10^{18} \text{ cm}^2$ at 1831; Sacramento Peak Observatory, $3.3 \times 10^{18} \text{ cm}^2$ at 1835; Lockheed Solar Observatory, $4.2 \times 10^{18} \text{ cm}^2$ at 1831. Since the last value is thought to be an overestimate due to atmospheric deterioration of spatial resolution, we adopt $A = 3 \times 10^{18} \text{ cm}^2$, with an uncertainty of $\pm 40\%$.

Power radiated in *lines* in the range 1175–1863 Å, by the whole flare, at 1831 UT, is given in Table A.6. These values are the result of the same reduction procedure as for the continuum, except that the preflare active-region values have not been subtracted. They are based on the same observations as Cheng (1978), using a slightly different calibration (specified above). The strong lines are nearly saturated, so the power values given may be affected, and should not be used for line-ratio density diagnostics, etc. For Lyman α , the value given is a lower limit. However, evidence that the strongest lines are reasonably good is provided by comparing the S055 and S082B data for H I 1216 Å (L α) and C II 1335 Å. For L α at 1831 UT we find: S055, $P = 2.2 \times 10^{25} \text{ erg s}^{-1}$; S082B, $P = 7.5 \times 10^{24} \text{ erg s}^{-1}$. Since we know that the L α value from S082B is a lower limit, we adopt the S055 value. For C II 1335 Å at 1831 UT: S055, $P = 3.6 \times 10^{24} \text{ erg s}^{-1}$; S082B, $P = 4.7 \times 10^{23} \text{ erg s}^{-1}$.

A.6 H I BALMER α (H α)

Photographic observations of H α throughout the flare were obtained with the Lockheed Solar Observatory's H α multislit spectrograph (Martin *et al.*, 1974).

TABLE A.5		
EUV CONTINUUM (1400--1960 Å)		
Wavelength Interval (Å)	Flare Power (erg s ⁻¹)	
	1831 UT	1841 UT
1400--1420	1.25(24)	2.03(23)
1420--1440	1.52(24)	1.92(23)
1440--1460	1.79(24)	2.30(23)
1460--1480	2.03(24)	2.88(23)
1480--1500	2.25(24)	3.62(23)
1500--1520	2.49(24)	4.17(23)
1520--1540	2.12(24)	3.62(23)
1540--1560	1.61(24)	3.03(23)
1560--1580	1.57(24)	2.87(23)
1580--1600	1.52(24)	3.11(23)
1600--1620	1.45(24)	3.03(23)
1620--1640	1.43(24)	2.59(23)
1640--1660	1.44(24)	2.55(23)
1660--1680	1.45(24)	1.89(23)
1680--1700	1.85(24)	5.17(23)
1700--1720	2.57(24)	1.01(24)
1720--1740	3.40(24)	1.40(24)
1740--1760	4.66(24)	2.11(24)
1760--1780	5.84(24)	2.90(24)
1780--1800	6.39(24)	3.87(24)
1800--1820	6.51(24)	4.78(24)
1820--1840	6.63(24)	5.52(24)
1840--1860	6.64(24)	5.85(24)
1860--1880	6.68(24)	5.59(24)
1880--1900	7.07(24)	5.04(24)
1900--1920	7.52(24)	5.40(24)
1920--1940	7.88(24)	6.94(24)
1940--1960	8.14(24)	8.78(24)
TOTAL.		
1400--1960	1.06(26)	6.4 (25)

TABLE A.6

EUV EMISSION LINES (1175–1863 Å)

Ion	Wavelength (Å)	Power (1831 UT) (erg s ⁻¹)
H I	1215.7	7.5(24) a
He II	1640.4	1.9(23)
C I	1656.3	6.0(23)
	1656.9	
	1657.0	
	1657.4	
	1657.9	
	1658.1	
C II	1335.7	4.7(24) a
C III	1174.9	1.2(24)
	1175.3	
	1175.6	
	1175.7	
	1176.0	
C IV	1176.4	1.9(24)
	1548.2	
N V	1550.8	4.7(24)
	1238.8	3.0(23)
O I	1242.8	1.9(23)
	1301.2	1.9(23)
	1304.8	1.9(23)
	1306.0	1.9(23)
A III	1670.8	1.9(23) b
	1854.7	6.0(22)
	1862.8	6.0(22)
Si II	1260.4	7.5(22)
	1264.7	9.4(22)
	1309.3	9.4(22)
	1526.7	2.4(23)
	1533.4	2.4(23)
	1808.0	6.0(22)
	1816.9	6.0(22)
	1817.5	
Si III	1206.5	1.9(24)
	1294.5	1.5(23)
	1296.7	1.2(23)
	1298.9	3.0(23)
	1301.1	9.4(22)
	1303.3	1.2(23)
Si IV	1393.8	1.9(24)
	1402.8	1.9(21)
Total		3.0(25)

Note: a—also measured by S055, see section A.1; b—blended.

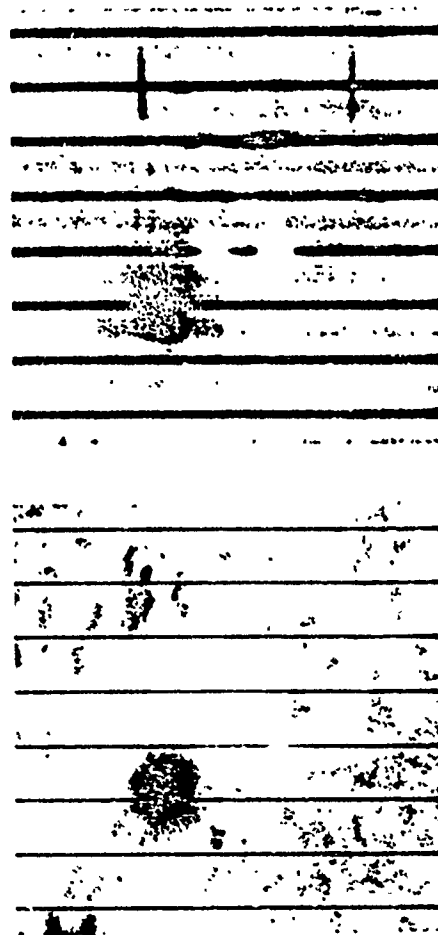


Fig. A.4 Slit-jaw $H\alpha$ filtergrams ($\frac{1}{2}$ λ birefringent $H\alpha$ filter), on the left, and multiple $H\alpha$ spectra, on the right, of the 5 September 1973 flare at 1830:45 UT, from Lockheed Solar Observatory.

The instrument was operating in a patrol mode, taking a H α spectrogram and a H α slit-jaw filtergram every 15 s. Data have been reduced only at flare maximum.

Figure A.4 shows both the filtergram (*left*) and the spectrogram (*right*) obtained at 1830:45 UT, the time of brightest H α emission. The vertical dark lines in the filtergram are the multiple spectrograph slits. The slit to the right of the sunspot passes through the center of an intense flare knot (the lowest bright flare feature), and crosses a bright flare ribbon near the edge of the penumbra. The spectrogram in which the dark vertical lines are the cores of the H α lines correspond to the multiple spectrograph slits. It can be seen that the H α profile from the slit to the right of the spot shows the brightest and widest H α profile at the lower bright knot, with fainter emission from the upper ribbon: the spatial resolution was no better than 3-4 arcsec, due to poor atmospheric conditions.

Data reduction consisted of relative photographic photometry and elimination of wavelength-dependent instrumental transmission effects and scattered light by fitting the quiet-sun profiles to photoelectric H α profiles of White (1964). This was carried out for the spectra at 1830:45 UT, along the slit that passed through the flare. The quiet-sun spectra were then subtracted at each point along the slit to determine the excess flare (and, to a small extent, active-region) emission along the slit. At the center of the bright spot this differenced H α intensity was $\Delta I \approx 5.5 \times 10^6 \text{ erg cm}^{-2} \text{ s}^{-1} \text{ sr}^{-1}$. The differenced intensity averaged over the flare as a whole was approximately $2.4 \times 10^6 \text{ erg cm}^{-2} \text{ s}^{-1} \text{ sr}^{-1}$, observed over a (seeing-broadened) area of $4.2 \times 10^{18} \text{ cm}^2$. Since the differenced intensity and the area are affected in compensating directions by seeing, their product should be valid. Thus, the flare power radiated in H α at 1830:45 UT is about $2\pi(\Delta I)A = 6.3 \times 10^{25} \text{ erg s}^{-1}$. The active region probably contributes less than 10% of this value. An independent value of the power radiated in H α appears in the following section.

A.7 VISIBLE LINES AND CONTINUA (3700-8700 Å)

Observations of the visible spectrum covering the range 3700-8700 Å were obtained at 1835:40 (time 1) and 1836:50 UT (time 2), with the universal slit spectrograph at Sacramento Peak Observatory, with accompanying H α slit-jaw and flare-patrol images to determine the H α area of the flare. The slit intersected two flare kernels (called k1 and k2 here) at time 1 and the brighter kernel (k1) at time 2.

The original data are photographic. Relative intensities were determined using a step wedge. Absolute calibration was accomplished by fitting selected quiet-sun continuum windows to the data of Labs and Neckel (1970), with limb darkening data from Pierce and Waddell (1961). By this means, calibrated spectra were obtained at many locations along the slit, ranging from the flare kernels to the quiet sun. At each position along the slit, a differenced spectrum was computed by subtracting a reference scan, which was the average of several quiet scans, thereby obtaining the radiative excess (due to the flare and active region) for all points along the slit. The power in all lines that showed a significant flare enhancement is given in Table A.7, at the two times indicated. Columns 3, 4, and 5 give the differenced intensity in each line, at the center of the observed kernels. Columns 6 and 7 are estimates of the radiative power output of the entire flare. These were

TABLE A.7
VISIBLE LINES (3700–8700 Å)

Wavelength (Å)	Intensity at Kernel Center ($\text{erg cm}^{-2} \text{s}^{-1} \text{Å}^{-1}$)		Flare Power (erg s^{-1})	
	k_1 1835:40	k_2 1835:40	k_1 1835:50	k_2 1836:50 UT
Ca II 3706.0	8.9(4)	8.0(4)	9.5(4)	8.8(23)
Fe I 3719.9	1.7(5)	1.3(5)	1.3(5)	1.2(24)
Fe I 3733.3	2.1(5)	1.4(5)	1.9(5)	1.8(24)
Ca II 3736.9	1.8(5)	1.1(5)	1.4(5)	1.3(24)
Fe I 3757.2	1.1(5)	8.9(4)	1.5(5)	1.4(24)
Fe I 3745.6	2.6(5)	1.9(5)	3.0(5)	2.8(24)
Fe I 3745.9	9.9(4)	1.1(5)	1.3(5)	1.2(24)
Fe I 3750.0	1.4(5)	7.0(4)	1.4(5)	1.3(24)
Fe I 3770.6	5.7(4)	6.0(4)	4.5(4)	4.2(23)
Mg I 3832.3	1.8(5)	1.8(5)	1.0(5)	9.4(23)
Fe I 3835.9	6.4(4)	6.4(4)	7.0(4)	6.6(23)
Mg I 3838.3	8.3(4)	7.0(4)	8.6(4)	8.1(23)
Fe I 3859.9	2.1(5)	1.6(5)	1.9(5)	1.8(24)
Fe I 3889.1	6.7(4)	6.7(4)	6.4(4)	7.9(23)
Si I 3905.5	1.0(6)	8.3(5)	6.4(5)	6.0(23)
Ca II 3933.7	9.2(5)	1.1(6)	8.9(5)	8.4(24)
Ca II 3968.5	3.5(5)	2.9(5)	2.2(5)	2.1(24)
Fe I 3970.1	1.9(5)	1.9(5)	9.5(4)	8.9(23)
Fe I 4101.7	1.9(5)	3.2(5)	1.3(5)	1.2(24)
Fe I 4346.7	5.4(5)	4.1(5)	5.7(5)	5.4(24)
Fe I 4861.3	9.5(5)	8.0(5)	7.0(5)	6.6(24) a
Fe I 6562.8	2.2(5)	1.9(5)	1.6(5)	1.5(24)
Ca II 8498.1	2.9(5)	2.5(5)	2.5(5)	2.4(24)
Ca II 8542.1	3.2(5)	3.2(5)	2.9(5)	2.7(24)
Ca II 8662.2	6.9(6)	6.2(6)	5.8(6)	5.5(25)
Total				

Note: a—also measured at Lockheed Solar Observatory; see Section 6 of this appendix.

obtained using the observed kernel-center difference intensities I_{k1} and I_{k2} :

$$P = 2\pi \overline{\Delta I} A \quad (\text{A.7.1})$$

where $A = 3 \times 10^{18} \text{ cm}^2$, as above, and $\overline{\Delta I} = 0.63(\Delta I_{k1} + \Delta I_{k2})/2$ at time 1 and $\Delta I = 0.50 \Delta I_{k2}$ at time 2. The values 0.63 and 0.50 (at times 1 and 2, respectively) express the ratio between the observed kernel-center intensities and the observed average intensity for the kernels and intermediate-intensity flare areas.

Calibrated H α -line center filtergrams at one-minute intervals have been used to estimate the ratio of power at 1831 UT and that at times 1 and 2. A twenty-level linear brightness scale was established, with level 20 assigned to the maximum intensity (film saturation) and level 10, the average intensity for the whole frame. In practice, pixels at and above level 15 best defined the flare area. The flare measurements of H α flare power P (flare minus preflare) from points at intensity level 15 and higher imply that the ratio $P(1831 \text{ UT})/P(\text{time 1})$ is 2.1 and $P(1831 \text{ UT})/P(\text{time 2})$ is 2.6. If the cutoff is at level 20 instead of level 15, the ratios are 1.5 and 1.8, respectively. The former is thought to be a better value, but the uncertainty must be regarded as at least 50%. We note that this value is also a lower limit to the true power ratio, due to insensitivity of the extrapolation method to very broad line profiles that extend beyond the bandwidth of the filter.

We now combine these Sacramento Peak Observatory results with the H α measurements at 1831 UT from Lockheed Solar Observatory. From Sacramento Peak, $P_{\text{H}\alpha}(1831) \approx (2.1)(1.0 \times 10^{25}) = 2.1 \times 10^{25} \text{ erg s}^{-1}$. From Lockheed Solar Observatory, $P_{\text{H}\alpha}(1831) \approx 6.3 \times 10^{25} \text{ erg s}^{-1}$. We therefore adopt the average value of $4 \times 10^{25} \text{ erg s}^{-1}$ with a probable error of $\pm 2 \times 10^{25} \text{ erg s}^{-1}$, as the H α output at flare maximum, 1831 UT. To obtain the output in the other lines in Table A.7 at 1831 UT one should therefore multiply the power at 1835:40 by a factor of 4, or the power at 1836:50 by a factor of 6.

In addition to the flare enhancements in visible lines, it is well known that, on occasion, flares show continuum radiations. This flare appears to be such a "white-light" flare. It is evident that in the region below 3900 Å there are continuum enhancements near the center of the kernels. The enhancements are only 2–3% on the average, and vary appreciably with wavelength, apparently disappearing entirely at some wavelengths and reaching 5% at others. Since the average enhancement is on the order of the accuracy of the process of photographic photometry, we cannot be sure what the energy output should be on a level of accuracy comparable with the estimates of line radiation in Table A.7. We can only estimate the possible order of magnitude of the contribution. The observed intensity of the mean solar disk (Allen, 1973) at 3900 Å is about $1.5 \times 10^{10} \text{ erg sr}^{-1} \text{ cm}^{-2} \mu^{-1} \text{ s}^{-1}$. If the flare intensity excess I_f is 2% of this, then $I_f = 3 \times 10^8 \text{ erg sr}^{-1} \text{ cm}^{-2} \mu^{-1} \text{ s}^{-1}$. Since we have no clear spectroscopic evidence on what the radiation mechanism might be, we can only guess the spectral variation of I_f . If this radiation extends uniformly over the visible band (say over a band $\Delta\lambda = 0.3 \mu$ in width), and the emitting area A is 10% of that of the observed H α kernels, i.e., $A = 3 \times 10^{17} \text{ cm}^2$, then the power from the whole flare in this continuum would be $P \sim 2\pi I_f \Delta\lambda A \sim 2 \times 10^{26} \text{ erg s}^{-1}$. Clearly, the possible importance of this radiation cannot be overstated, since this power is quite comparable to that of all lines in this wavelength region combined, and also of the same order as the total observed radiative power output at flare maximum (see below).

A.8 RADIO EMISSION (CENTIMETER-METER WAVELENGTHS)

Observations at radio wavelengths are available from the dynamic spectrographs of Harvard and the University of Colorado and fixed-frequency radiometers at centimeter and decimeter wavelengths as compiled in *Solar-Geophysical Data* (1974). At centimeter wavelengths the radio emission was quite weak, only about 10 sfu. It started at about 1828 UT, lasted only about 5 to 10 minutes, and was classified mostly as a simple burst. At meter and decimeter wavelengths, the emission consisted of a strong, complex group of Type III bursts from about 1828 UT to 1840 UT and a strong Type II burst from about 1833 UT to 1900 UT.

The power output of the flare at centimeter wavelengths can be estimated from the published flux density S at Earth at flare maximum and the frequency band covered Δf :

$$P = 2\pi(1 \text{ AU})^2 S \Delta f \quad (\text{A.8.1})$$

From the published data we find $S \approx 3 \times 10^{-21} \text{ W m}^{-2} \text{ Hz}^{-1}$ and $\Delta f \approx 10^4 \text{ MHz}$ (1000 to 15400 MHz, with the largest flux density at about 5000 MHz). Thus, the power output at the peak of the centimetric burst (duration $\tau \approx 500 \text{ s}$) was $P_{\text{cm}} \approx 4.2 \times 10^{19} \text{ erg s}^{-1}$. The uncertainty in this estimate is about a factor of 3. The duration of the burst was about 500 s.

At meter wavelengths, the radiative energy output from the flare can be estimated in a similar fashion. The Type III bursts were reported as intensity 3, which gives $S \approx 10^{-19} \text{ W m}^{-2} \text{ Hz}^{-1}$, and covered a band of about 100 MHz. Thus $P_{\text{III}} \approx 1.4 \times 10^{19} \text{ erg s}^{-1}$. The uncertainty in this estimate is larger, about a factor of 10, because the flux calibration of spectrographs is poorer than radiometers. The group of bursts lasted about 400 s.

For the Type II burst, which occurred between about 5 and 30 minutes after flare maximum, $S \approx 10^{-19} \text{ W m}^{-2} \text{ Hz}^{-1}$ and $\Delta f \approx 10 \text{ MHz}$. Thus $P_{\text{II}} \approx 1.4 \times 10^{18} \text{ erg s}^{-1}$. Again, the uncertainty in this estimate is about a factor of 10.

A.9 SUMMARY

The best-determined observational quantities for this flare are the estimates of the power output at flare maximum, approximately 1831 UT. We summarize these in Table A.8. The total power in observed wavelength regions is probably uncertain by at least half an order of magnitude, and perhaps even more, for a simple reason: the dominant contributors, the EUV and visible radiation, are uncertain by that amount. There are several reasons for this large uncertainty. First, in both these wavelength regions we were able to measure the flare output along only a single line through the flare. The methods available for extrapolating from power radiated along this line to power radiated by the whole flare are uncertain by at least a factor of two or three. Second, and possibly of greatest importance, the photographic nature of the visible observations has made it impossible to accurately measure the amplitude and spatial distribution of the continuum enhancements. In Section A.7 we estimate that this radiation may carry away as much energy as all visible lines, but this is only an order-of-magnitude estimate, and not a measurement. Third, the accuracy of our estimates would have been much higher had coordination between facilities covering different wavelength regions been carried out in advance. A glance at Figure A.1 shows how poor and haphazard the time

TABLE A.8	
OBSERVED RADIATIVE POWER OUTPUT AT FLARE MAXIMUM	
Wavelength Region	Power (erg s^{-1})
X-Rays, 1--20 Å	6.3×10^{25}
XUV Lines, 174--345 Å	1.6×10^{25}
EUV Continuum, 1400--1960 Å	1.1×10^{26}
Lyman α ($\text{Ly}\alpha$)	2.2×10^{25}
Other EUV Lines, 1175--1863 Å	2.3×10^{25}
Balmer α ($\text{H}\alpha$)	4.0×10^{25}
Other Visible Lines, 3700--8700 Å	2.7×10^{26}
Radio Continuum, cm--m Wavelengths	5.6×10^{19}
Total in Observed Wavelength Regions:	5.4×10^{26}

coverage is. A factor that does not seem to be a serious source of error in our present work is absolute calibration--this potential problem has been kept under control better than those discussed above. The three sources of uncertainty discussed above are those that we would identify as the areas needing greatest attention in future observations.

Another factor to be borne in mind is that we have observed only parts of the spectrum. Most important in the total radiative-energy budget is probably the unobserved range 1960--3700 Å, where the most important lines and continua are due to atoms and ions abundant at chromospheric and photospheric temperatures. Next most important is the region 345--1175 Å, dominated by the Lyman continuum and chromospheric and transition-region lines. The omission of measurements at and above X-ray energies is diagnostically important, but has little consequence in the total radiated-power estimate. At best we can only estimate that these missing regions contribute roughly as much as the observed regions, bringing the total power at flare maximum to $P_{\text{max}} \sim 1 \times 10^{27} \text{ erg s}^{-1}$.

For estimation of the total amount of energy radiated during the full duration of the flare, one must know the time history of at least the most important emissions. Unfortunately, the data are not sufficient for this purpose. At this time, the best that we can do is use the characteristic time that one would infer from the best currently-reduced data, i.e., the soft X-ray data. If we define τ to be the time between rise and fall through the SOLRAD-9 half-maximum power levels in Figure A.1, then $\tau(1-8 \text{ Å}) \approx 320 \text{ s}$ and $\tau(8-20 \text{ Å}) \approx 480 \text{ s}$, so we adopt $\tau = 400 \text{ s}$. The total energy radiated by the flare, W_f , is given approximately by the product $P_{\text{max}} \tau$. From our estimates, we obtain $W_f \sim 4 \times 10^{29} \text{ erg}$.

REFERENCES

- A'len, C. W.: 1973, *Astrophysical Quantities*, 3rd ed., Athlone Press, London.
- Bartoe, J.-D. F., Brueckner, G. E., Purcell, J. D., and Tousey, R.: 1977, *Appl. Optics*, **16**, 875.
- Brueckner, G. E., Bartoe, J.-D. F., Kjeldseth Moe, O., and Van Hoosier, M. E.: 1976, *Astrophys. J.* **209**, 935.
- Bruzek, A.: 1967, in J. Xanthakis (ed.), *Solar Physics*, Interscience, New York, p. 414.
- Cheng, C.-C.: 1978, *Solar Phys.* **56**, 205.
- Cheng, C.-C. and Kjeldseth Moe, O.: 1978, *Solar Physics* **59**, 361.
- Dere, K. P. and Cook, J. W.: 1979, *Astrophys. J.*, **229**, 772.
- Dere, K. P., Horan, D. M., and Kreplin, R. W.: 1974, *J. Atm. Terr. Phys.* **36**, 989.
- Dere, K. P., Horan, D. M., and Kreplin, R. W.: 1977, *Astrophys. J.* **217**, 976.
- Ellison, M. A.: 1963, *Publ. Roy. Obs. Edinburgh*, **4**, 62.
- Jager, C. de: 1970, in E. R. Dyer (ed.), *Solar-Terrestrial Physics*, Part I, D. Reidel, Dordrecht, Holland, p. 1.
- Kjeldseth Moe, O. and Nicolas, K. R.: 1977, *Astrophys. J.* **211**, 579.
- Labs, D. and Neckel, H.: 1970, *Solar Phys.* **15**, 79.
- Lin, R. P.: 1974, *Space Sci. Rev.* **16**, 189.
- Lin, R. P. and Hudson, H. S.: 1976, *Solar Phys.* **50**, 153.
- Markey, J. F. and Austin, R. R.: 1977, *Appl. Optics* **16**, 917.
- Martin, S. F., Ramsey, H. E., Carroll, G. A., and Martin, D. C.: 1974, *Solar Phys.* **37**, 343.
- Pierce, A. K. and Waddell, J. H.: 1961, *Mon. Not. Roy. Astron. Soc.* **68**, 89.
- Reeves, E. M., Huber, M. C. E., and Timothy, J. G.: 1977, *Appl. Optics* **16**, 837.
- Samain, D., Bonnet, R. M., Gajet, R., and Lizarbert, G.: 1975, *Astr. Astrophys.* **39**, 71.
- Solar-Geophysical Data*: 1974, No. 355 Part II.
- White, O. R.: 1964, *Astrophys. J.* **139**, 1340.

iii) Mass Ejections

This paper is published as Chapter 7 of the monograph Solar Flares, edited by P.A. Sturrock. One of the main results of this team's work was to show that some flare-associated mass ejections, including so-called "sprays", take place because the entire magnetic field structure overlying the flare is torn apart, whereas other mass ejections, such as "surges", follow existing magnetic field structures. Parts of the paper to which McClymont contributed include numerical modelling of shocks, which showed that observations of flare-associated shocks far from their source will be of little value in ascertaining the nature of the energy release that gave rise to the shock. McClymont also studied the acceleration of solar surges by release of energy in the chromosphere; he showed that this mechanism can eject mass in a manner that matches the surge observations. Because of the realization that much useful information about flares could be deduced from comparison of the results of numerical models with observations, we started a much more sophisticated program of numerical modelling at UCSD. This program is discussed in a later section.

7. MASS EJECTIONS

David M. Rust and Ernest Hildner; M. Dryer, R.T. Hansen, A.N. McClymont, S.M.P. McKenna Lawlor, D.J. McLean, E.J. Schmahl, R.S. Steinolfson, E. Tandberg-Hanssen, R. Tousey, D.F. Webb, S.T. Wu

7.1 INTRODUCTION

7.1.1. *Purposes of the Study*

The purpose of our study was to discover what role mass ejections play in the flare phenomenon. We sought to determine the energy and mass of the ejecta and to discover the forces that propel matter from the flare site and constrain it as it moves. We tried to determine the physical conditions in the ejecta and in the disturbed atmosphere. Although the study of ejecta may not bear directly on the energy-release process in flares, it provides insight into the origins of the flare plasma, the height and duration of energy release, and the large-scale magnetic field configuration before and after flare onset.

7.1.2. *Definitions*

We shall define mass ejections as those transient phenomena in which large-scale (cross-section ≥ 500 km) motion away from the sun takes place; that is, where the Doppler effect has been detected, or is detectable, at least in principle. Coronal ejecta are usually detected by their continuum emission, but there is little doubt that if a spectrograph could be made with sufficient sensitivity, the Doppler shift in faint coronal lines could be detected. Note that material need not escape the sun to be termed an ejection. The terms usually used to describe the various manifestations of mass ejection are: eruptive prominence, spray, surge, and coronal transient. A brief discussion of each follows. For a more detailed description, see Tandberg-Hanssen (1977).

A. Sprays. Sprays are fast ejections always associated with flares, their velocities frequently exceeding the velocity of escape. The ejection is extremely violent, and, contrasting with surges, in narrow-band observations matter appears not to be contained by the magnetic field, but to fly out in fragments (Warwick, 1957; Zirin, 1966; Smith, 1968). More recent, broadband observations, however, indicate that most of the material is in fact entrained on expanding loops. The spray material reaches its high velocity in a few minutes. A spray is shown in Figure 7.1.

B. Eruptive prominences (filaments). An eruptive prominence has a preflare existence, either as an active-region prominence or as a quiescent prominence, often located far from active regions with sunspots. During a "disparition brusque"

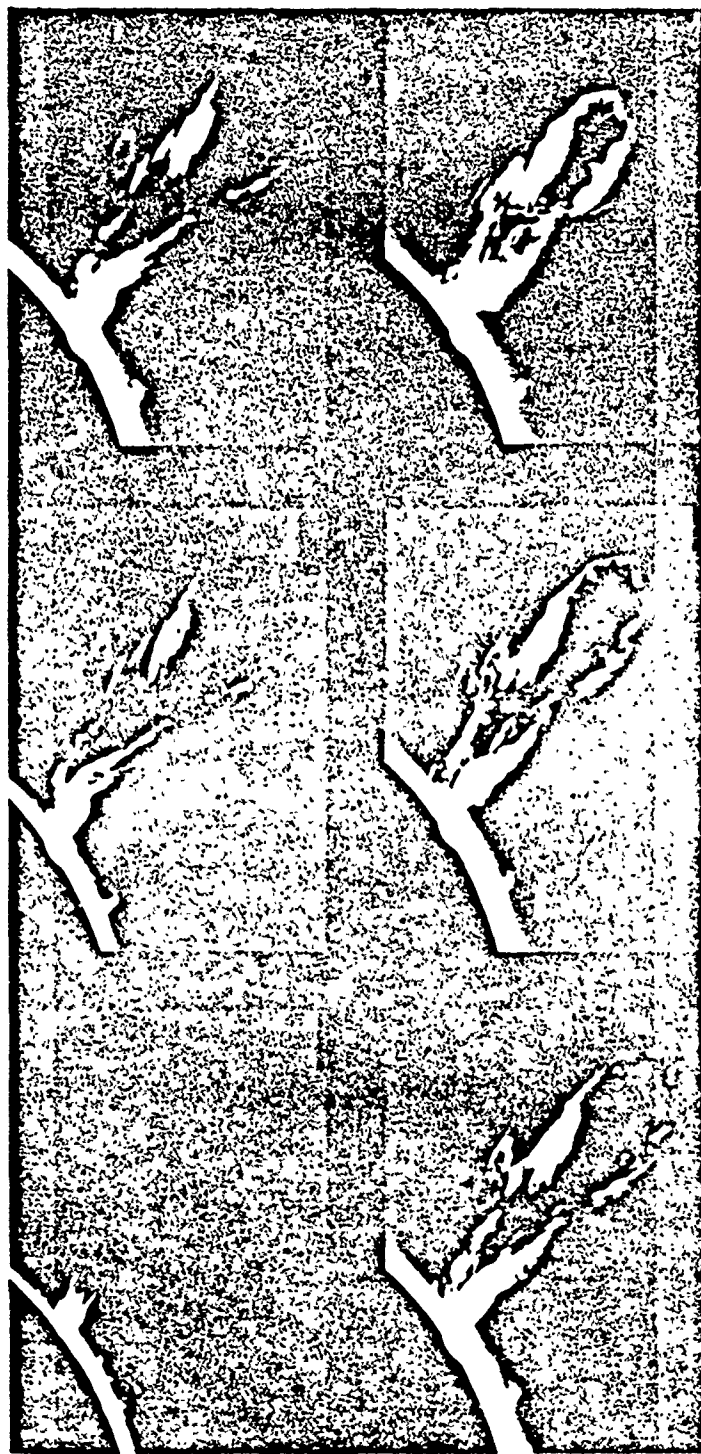


Fig. 7.1 The photographs of the floor spray of 12 August 1972.

(sudden disappearance) the prominence erupts and ascends, slowly at first, then at increasing velocity. The eruptive prominence of 19 December 1973 is shown in Figure 7.2. The term "filament" is used for prominences on the solar disk. There is no physical distinction between prominences and filaments, so the two terms will be used interchangeably except in describing specific observations.

C. Surges. These ejections of chromospheric material originate near sunspot penumbrae (Giovanelli and McCabe, 1958) or polarity reversals associated with satellite sunspots (Rust, 1968). Velocities are about $100\text{--}200\text{ km s}^{-1}$. In most cases, a small flare or chromospheric brightening is observed at the base. Surges follow long, straight, or curved columnar paths upward and return along the same trajectories. These probably outline magnetic flux tubes. The initial acceleration of the surge may be due to Lorentz forces or to heating at the base, as assumed in several models described in the present report. A major surge is illustrated in Figure B.2 of Appendix B.

D. Coronal transient. Changes in coronal brightness patterns on time scales of tens of minutes, indicating outward mass motions at ~ 100 to 1000 km s^{-1} , are called coronal transients. One is illustrated in Figure 7.3. These mass ejections are most spectacular in white light, although their manifestations are also seen in X-rays and in the Fe XIV green line. In white-light observations, the main, dense part of a transient is surrounded by a region of enhanced density called a fore-runner, which contains ~ 20 percent of the total excess mass thrown into the corona above $2R_{\odot}$. Coronal mass ejections are often associated with ejections of low-temperature material in flares and radio bursts. Large flares are almost always accompanied by coronal transients, though the causal, physical mechanisms linking the two are not well understood. Indeed, the forces driving transients outward are the subject of debate. Coronal transients appear to represent a major energy-loss mechanism in flares.

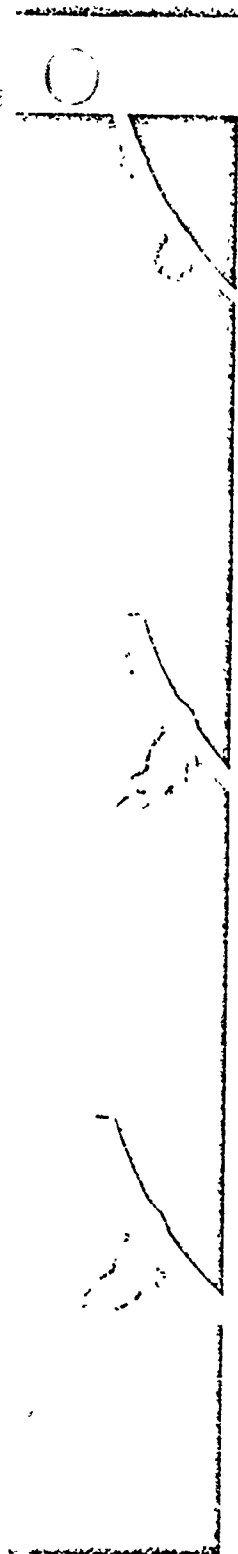
Not usually included in lists of flare mass motions are the flare, or Moreton, waves described by Smith and Harvey (1971). Many large flares generate a wave front that moves across the chromosphere at $\sim 1000\text{ km s}^{-1}$ in a wide arc outward from the flare center. These waves have been recorded to distances of $\sim 1 R_{\odot}$ from the flaring active region, and, according to Uchida *et al.* (1973), they are shock waves. However, in the course of our study, we have found reason to assert that some flare waves are due to fast-moving ejecta rather than shocks.

7.1.3. Approach to the Problem

The approach of the Team to the problem of mass ejections has been to study Skylab and other observations of each kind of phenomenon separately and to simulate all but the flare waves with various models. No attempt was made to study the magnetic field instabilities that might propel filaments and/or coronal loop transients, but several models of expanding magnetic loops were developed during the Flare Workshop by nonmembers of the Team, and these are mentioned in this chapter. Magnetic field instabilities are discussed in Chapter 2 with preflare phenomena.

Skylab observations obtained near solar minimum were the focal point of our work. New data on mass motions were obtained principally with the HAO white-light

Fig. 7.1 $H\alpha$ photographs of the flare spray of 12 August 1972.



He II $\lambda 304$



←SC

06:32

Fig. 7.2 The eruptive prominence of 19 December 1973. Sun center, at the edge of the photograph, is indicated by an arrow. (Courtesy of the Naval Research Laboratory).



of the photo-

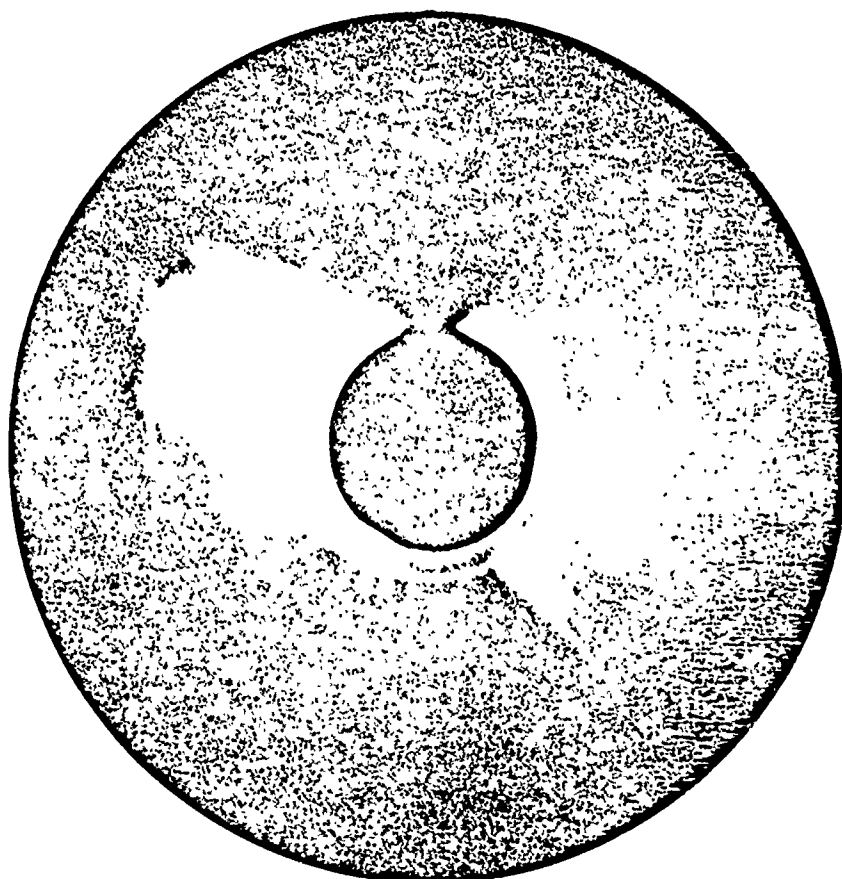


Fig. 7.3 The coronal transient of 10 June 1973. The support for the coronagraph occulting disk casts a shadow at solar north; the crescent opposite the support shadow is an artifact. The field of view is $12 R_{\odot}$ diameter (Hildner et al., 1975b).

TABLE 7.1
PHYSICAL CHARACTERISTICS OF MASS EJECTA

Phenomenon	$\Delta p/p$	$T(K)$	$B(G)$	Scale (cm)	$V(\text{cm s}^{-1})$	Mass (g)	Kinetic Energy (erg)
Eruptive Prominences	2	10^4	10 at 1.1 ϵ_0	5×10^8	2×10^7	10^{15}	2×10^{29}
Sprays	10	$10^4 - 10^5$	100 at 1.02 ϵ_0	5×10^8	6×10^7	10^{15}	2×10^{30}
Surges	5	8×10^3	30 at 1.02 ϵ_0	10^9	1×10^7	$10^{14} - 10^{15}$	$5 \times 10^{27} - 5 \times 10^{29}$
Coronal Transients	$10 - 10^2$	10^4	2 at 2.0 ϵ_0	3×10^{10}	4×10^7	$10^{15} - 10^{16}$	$10^{29} - 10^{30}$

p = gas pressure, T = temperature, B = magnetic field strength, V = characteristic velocity, Δ = change from surroundings

coronagraph, the AS&E the Harvard photoelectric violet. The NRL objective striking images of ejecta the disk. Throughout the on the interplanetary m: Shea *et al.* (1977) for a rec

Following the separat coronal transients, we sol tant differences. Table 7. have collected existing a etc., on flare-associated e portion of a flare's energ of the entire corona ove thermal, and magnetic ene

Exciting new results o follows, but equally imp causality; that is, do the after? Are the ejecta en and cause the flare, or a the flare? Can mass mo release process by showir of the plasma and heating:

7.2 SPR

7.2.1. Introduction

Over the years, several scl the parameters used in th has played an important interest in prominences ar of prime importance for t There is a bewildering div and become associated wit

Recent space observat are associated with transi radio bursts, and X-ray er prominences is well unde stages of their developm well documented. In the ejected material comes fro

One difficulty, already patrols with narrow wav sight velocities greater th are "blobs" of material ti resulting in the familiar "c

The study of sprays Mass Ejections because a

coronagraph, the AS&E and the Marshall/Aerospace soft X-ray telescopes, and the Harvard photoelectric spectroheliograph, which operated in the extreme ultraviolet. The NRL objective grating telescope and the NRL spectrograph yielded striking images of ejecta at the solar limb and spectra of erupting filaments on the disk. Throughout the study, the focus was on the *solar* phenomena and not on the interplanetary manifestations of mass ejections. We refer the reader to Shea *et al.* (1977) for a recent review of travelling interplanetary phenomena.

Following the separate studies of surges, sprays, eruptive prominences, and coronal transients, we sought to identify their common characteristics and important differences. Table 7.1 is a very rough summary of some of the results. We have collected existing and new knowledge about the mass, energy, size range, etc., on flare-associated ejecta. As the table makes clear, ejecta carry off a major portion of a flare's energy. And, an amount of material equivalent to evacuation of the entire corona over the flare appears to leave the sun, delivering kinetic, thermal, and magnetic energy to the interplanetary medium.

Exciting new results on many aspects of mass ejections are reported in what follows, but equally important and unanswered by our work is the question of causality; that is, do the great ejections start just before the flare emission or just after? Are the ejecta entrained in opening magnetic fields, which then collapse and cause the flare, or are the ejecta driven by forces or shocks that originate in the flare? Can mass motions tell us something fundamental about the energy-release process by showing how energy is partitioned between bulk acceleration of the plasma and heating?

7.2 SPRAYS AND ERUPTIVE PROMINENCES

7.2.1. Introduction

Over the years, several schemes have been devised to classify prominences. Among the parameters used in these classifications, the motion of the prominence plasma has played an important role. With the advent of space observations, renewed interest in prominences and in prominence-corona interactions has developed, and of prime importance for these interactions is the motion of ascending prominences. There is a bewildering diversity in the way prominences rise in the solar atmosphere and become associated with coronal response.

Recent space observations show that both sprays and eruptive prominences are associated with transient coronal phenomena (white-light change, Type II/IV radio bursts and X-ray emission). While the physics of neither sprays nor eruptive prominences is well understood, the latter are more easily observed in the early stages of their development, and the relationship to preexisting prominences is well documented. In the case of sprays, it is very difficult to ascertain where the ejected material comes from.

One difficulty, already pointed out by Bruzek (1969), is that routine flare patrols with narrow wavelength-band filters inevitably miss ejecta with line of sight velocities greater than about 100 km s^{-1} . Furthermore, what is observed are "blobs" of material that happen to have slightly lower line of sight velocities, resulting in the familiar "clumpiness" reported for spray prominences.

The study of sprays was a prime objective of the Flare Workshop Team on Mass Ejections because all sprays originate in flares and probably all major flares

p = gas pressure, T = temperature, B = magnetic field strength, V = characteristic velocity, Δ = change from surroundings

are accompanied by sprays. We found, however, that the distinction between eruptive prominences and sprays is probably not fundamental, and it results more from the limitations of earlier observing techniques than from physical differences. The observations of Rust and Webb (1977) suggest that the X-ray signatures of the two phenomena are similar. During the Workshop, Tandberg-Hanssen, Martin, and Hansen showed that no sharp distinction between eruptive prominences and sprays may be drawn from H α observations.

However, sprays are frequently associated with flare waves, which have been described by Smith and Harvey (1971) and Martin (1978), who thought the emission fronts, of which most flare waves consist, are mass ejecta seen in projection against the disk. Alternatively, flare waves have been interpreted by Uchida *et al.* (1973) as evidence for the skirts of MHD shocks on the chromosphere. The X-ray observations from Skylab have provided yet another interpretation: that spray ejecta successively fall into and excite the chromosphere after traversing progressively longer magnetic loops which have one footpoint near the flare site (Section 7.2.7).

7.2.2. Observations of Sprays

Our view of flare sprays (or "spray prominences") has changed considerably in the last several years. This is due to the introduction of powerful new instruments and observing techniques, including: high-resolution cinematography; tunable and broadband filters; multislit spectroscopy; extended field-of-view coronagraphs; and soft X-ray telescopes. During the Workshop, Tandberg-Hanssen, Martin, and Hansen consulted data obtained with the first four techniques, relying in particular on observations from the Mauna Loa Observatory. Jackson, Hildner, Rust, and Webb studied the Skylab soft X-ray and coronagraph data.

7.2.3. Acceleration Profiles

A list (Smith, 1968) of sprays studied over the period 1937–1966 was augmented by Tandberg-Hanssen, Martin, and Hansen with additional flare sprays documented during solar cycle No. 20 (see Table 7.2). Several of the events listed in Table 7.2 were recorded in sufficient detail to allow determination of the height of the accelerated material above the solar surface versus time. From these events, whose height vs time curves are shown in Figure 7.4, Tandberg-Hanssen, Martin, and Hansen found that:

a. The height versus time curves for most spray prominences indicate constant velocity for the ejected material above 200 Mm, although acceleration is quite evident below that height.

b. The velocities of sprays cover a wide range, and the concept that the motion of the ejecta may be represented by one or two particular curves (Valnicsek, 1964) is misleading.

7.2.4. Morphology of Sprays

Observations of flare sprays projected above the solar limbs show that the overall shape of the envelope containing spray elements may be described as "loop-shaped," and one can nearly always distinguish two legs of a loop tying the spray to the

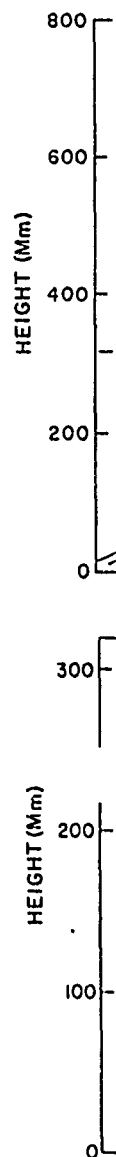


Fig. 7.4 Height vs time for flare sprays photographed from Hawaii. Because some or all time for all events is taken by USAF Air Weather Service, the curves taken by USAF Air Weather Service are quite different from the curves taken on the disk in 1973. Curves give the tangential or both radial and tangential velocities of several events are quite different from Figure 7.4a.

at the distinction between
amental, and it results more
in from physical differences.
at the X-ray signatures of the
ndberg-Hanssen, Martin, and
ative prominences and sprays

are waves, which have been
i (1978), who thought the
re mass ejecta seen in pro-
been interpreted by Uchida
s on the chromosphere. The
another interpretation: that
romosphere after traversing
footpoint near the flare site

changed considerably in the
f powerful new instruments
inematography; tunable and
field-of-view coronagraphs;
ndberg-Hanssen, Martin, and
hiques, relying in particular
'ac', Hildner, Rust, and
ata.

1937-1966 was augmented
onal flare sprays documented
the events listed in Table 7.2
tion of the height of the
e. From these events, whose
ndberg-Hanssen, Martin, and

rominences indicate constant
though acceleration is quite

the concept that the motion
cular curves (Mal'nicsek, 1964)

limbs show that the overall
is described as "loop-shaped,"
a loop tying the spray to the

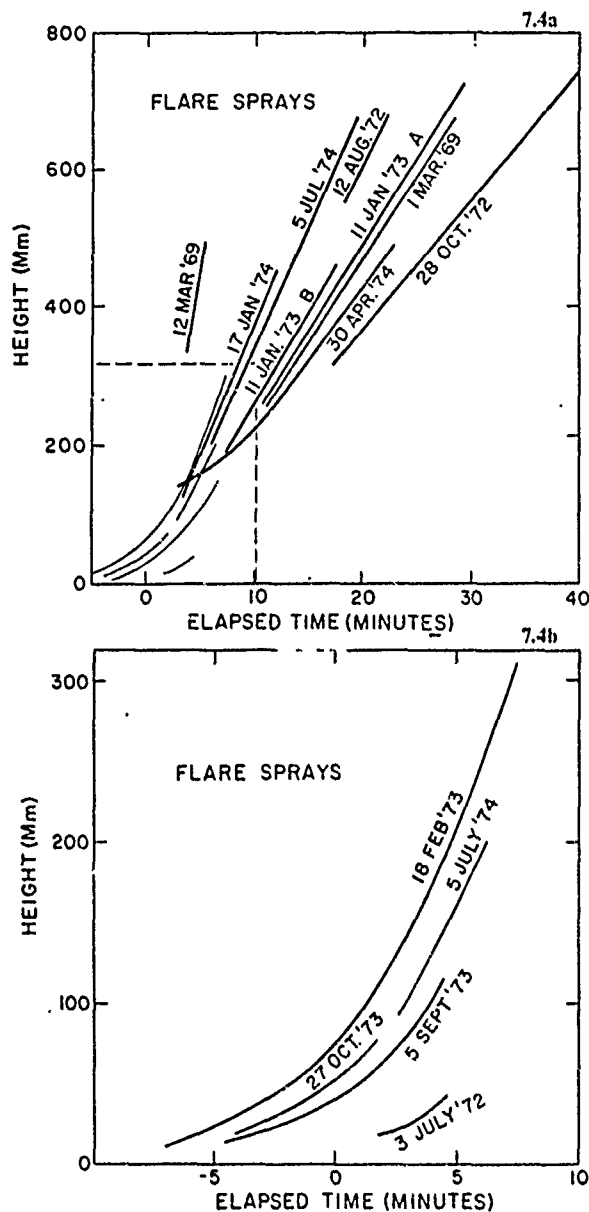


Fig. 7.4 Height vs time for flare sprays observed from 1969 through 1974. Heavy lines are for flare sprays photographed above the limb by the High Altitude Observatory at Mauna Loa, Hawaii. Because some originated behind the limb and flare starting times are unknown, zero time for all events is taken to be the projection to zero height of the straight-line part of the velocity curve. The curve for 27 October 1973 is the tangential velocity from 11a-disk movies taken by USAF Air Weather Service at Ramey Air Force Base. Lighter lines are for sprays photographed on the disk with Lockheed's multispectrograph. The 3 July 1972 and 18 February 1973 curves give the tangential velocity derived from motion across the disk. The resultant of both radial and tangential velocities is shown for the 5 July event. The early accelerations of several events are quite evident in Figure 7.4b, an expansion of the low-altitude, low-speed portion of Figure 7.4a.

No	Date	Associated Flare Time (UT) Position	Observed Spray Time (UT)	Speed (km s ⁻¹)	Radio Responses Type II and/or Type IV	Transient Observed from Satellite*	Comments	References
1	1 Mar 69	2149-2203 N10-W89	2143-2237	396	II 2142-2149	No	2	McCabe & Fisher, 1970 Riddle, 1970
2	12 Mar 69	1739-1808 N12-W80	1745-1824	980	IV 1741-1748 II 1742-1800	No	1,5	McCabe, 1971 Kundu <i>et al.</i> , 1970
3	12 Aug 72	(2042)	2055-2103	510	IV 2042-2240	No	4,7	Gergely & Kundu, 1974 Riddle <i>et al.</i> , 1974
4	28 Oct 72	1752-1911 S09-E67	1800-1905	309	II 1807-1812 II 1808-1837 II 1810-1819	No	3,5,7	McCabe <i>et al.</i> , 1974
5	11 Jan 73	0035-0127 N13-W80	0036-0112	414	II 0047-0102 IV 0037-0107	OSO-7	3,7	Stewart <i>et al.</i> , 1974b
6	11 Jan 73	(1807) N15-W90	1802-1828	480	II 1807-1826 IV 1815-1902	OSO-7	3,7	Stewart <i>et al.</i> , 1974a
7	29 Jul 73	1312-1600 N14-E45	?	?	II 1321-1348 IV 1321-1400	Skylab	1,6	
8	21 Aug 73	1344-1433 N12-E90	?	200	IV 1442-1734	Skylab	2	Poland & Munro, 1976 Smith <i>et al.</i> , 1977
9	7 Sep 73	1139-1345 S17-W46	2223-2350	?	II 1200-1207, 1226 IV 1155-1200, 1404	Skylab	1,6	Gosling <i>et al.</i> , 1975

10	27 Oct 73	1547-1746 N18-E54	1547-1635	?	II 1321-1348 IV 1321-1400	Skylab	1,6	
11	17 Jan 74	1925-2020	1934-1949	650	II 1931-1948 II 1937-1952	Skylab	4	Tousey, 1975 Webb & Jackson, 1979
12	30 Apr 74	?	1804-1832	1300 375 1310	?	No	4	Wagner, 1975 Wu <i>et al.</i> , 1975 Sawyer, 1976

6	11 Jan 73	(1807) N15 W90	1802-1828	480	II 1807-1826 IV 5-1902	OSO-7	3,7	Stewart et al., 1974a
7	29 Jul 73	1312 1600 N14 E45	?	?	II 1321-1348 IV 1321-1400	Skylab	1,6	
8	21 Aug 73	1344-1433 N12-E90	?	200	IV 1442-1734	Skylab	2	Poland & Munro, 1976 Smith et al., 1977
9	7 Sep 73	1139 1345 S17 W46	2223-2350	?	II 1200-1207, 1226 IV 1155-1200, 1404	Skylab	1,6	Gosling et al., 1975

10	27 Oct 73	1547-1746 N18-E54	1547-1635	?	II 1321-1348 IV 1321-1400	Skylab	1,6	
11	17 Jan 74	1925-2020	1934-1949	650	II 1931-1948 II 1937-1952	Skylab	4	Tousey, 1975 Webb & Jackson, 1979
12	30 Apr 74	?	1804-1832	1300 375 1300	?	No	4	Wagner, 1975 Wu et al., 1975 Sawyer, 1976
13	5 Jul 74	2120-2326 S15-W26?	2136-2214	583	IV 2137-2153 II 2148-2156	No	1	Tanaka, 1976

Comments for Table 7.2

1.	Flare spray observed to originate from pre-existing filament on the disk.	6.	No coronagraph observations of H α prominence above limb; observed only as filament; disruption on solar disk.
2.	Flare spray observed to originate from pre-existing prominence above the limb.	7.	Velocity determination from leading edge of overall envelope of spray-loop; generally this is greater than that of individual knots or blobs.
3.	Flare observed on the visible disk, but no conclusive observation made of pre-existing filament.		
4.	Flare spray presumably originated from invisible disk, observed only above limb.		
5.	Coronagraph observations of the prominence did not begin until after event was already in progress.	*	Observations made from OSO-7 or Skylab spacecraft of an associated white-light coronal transient.

chromosphere as the envelope expands. The broadband observations have drastically reduced the "clumpiness" of the ejected material, referred to by earlier observers, and most of the matter appears to be entrained in expanding loops. Some material drains down along one or both loop legs into the chromosphere, while material in the upper part of the loop rapidly moves outward. In a few cases, the outermost extremity of the loop seems to become detached, forming a separate "bubble."

Exceptionally fine, high-resolution filtergrams taken at the Sacramento Peak Observatory on 21 August 1973 show quite clearly the movement of prominence knots up one side of the loop and downward on the other. With less certainty, such motions have been inferred for the 12 August 1972 spray (Riddle *et al.*, 1974) and for the 17 January 1974 event, by comparison of Mauna Loa H α films with Naval Research Laboratory photographs of the same prominence in He II 304 Å. In addition to this up or down motion, there is sometimes observed a spiralling of the falling material. It is likely that this helical motion is responsible in part for the clumpy "bits-and-pieces" appearance when viewed with narrow band-pass filters.

In the several instances for which concomitant coronal observations were available (12 August 1972, 11 January 1973, 21 August 1973, 17 January 1974), major disruptions in the overlying corona were observed either as "depletions" of the lower corona (Hansen *et al.*, 1974) or as rapidly rising white-light plasma clouds associated with flare sprays (Howard *et al.*, 1976; MacQueen *et al.*, 1976). Consequently, it seems that the flare-spray phenomenon is only one facet of a very widespread disturbance affecting a large part of the solar atmosphere.

Because sprays are accelerated to velocities of 500-1000 km s⁻¹ in a few minutes, observations of them on the disk are among the most difficult to obtain. Nevertheless, in the last several years there has been convincing evidence that sprays are just fast filament eruptions. From disk observations of the start of several spray prominences, Tandberg-Hanssen, Martin, and Hansen concluded that sprays consist of material ejected from a previously extant active-region prominence. Figure 7.5 is a generalization from the events studied and depends on interpretation of observations of the many flares studied at the Lockheed Solar Observatory during solar cycles Nos. 19 and 20 (Martin and Ramsay, 1972). An essentially identical picture could be drawn for disparition brusques, except that in the latter case, there may be no H α flare.

In addition to the new inference that sprays typically originate in filaments, Figure 7.4 shows that sprays gradually accelerate from rest, as do eruptive prominences. Perhaps due to the stronger magnetic field and field gradients at their origins, sprays tend to accelerate to higher speeds than eruptive prominences and to achieve constant speeds at lower heights. These differences seem less important than the similarities; we will regard sprays as fast eruptive prominences in what follows and treat both together by the term eruptive prominence.

7.2.5. MHD Interpretation of Eruptive Prominences

A most interesting comparison of theory and observation has been published by T. Sakurai (1976). Sakurai assumed that prominence material is an infinitely conducting, nonviscous fluid that outlines magnetic flux tubes with sharp boundaries. Also, he assumed that these tubes expand into a perfectly conducting, unmagnetized fluid of negligible density. He treats the eruption of prominences as



ervations have drastically
d to by earlier observers,
ling loops. Some material
sphere, while material in
few cases, the outermost
ng a separate "bubble."
at the Sacramento Peak
ovement of prominence
her. With less certainty,
72 spray (Riddle *et al.*,
of Mauna Loa Ha films
ne prominence in Ha II
sometimes observed a
cal motion is responsible
hen viewed with narrow

onal observations were
1973, 17 January 1974),
d either as "depletions"
rising white-light plasma
MacQueen *et al.*, 1976).
only one facet of a very
mo: ie.

-1. km s^{-1} in a few
most difficult to obtain.
cing evidence that sprays
s of the start of several
n concluded that sprays
itive-region prominence.
depends on interpretation
heed Solar Observatory
y, 1972). An essentially
except that in the latter

y originate in filaments,
m rest, as do eruptive
d field gradients at their
ruptive prominences and
nces seem less important
ve prominences in what
nence.

n has been published by
material is an infinitely
flux tubes with sharp
a perfectly conducting,
ption of prominences as

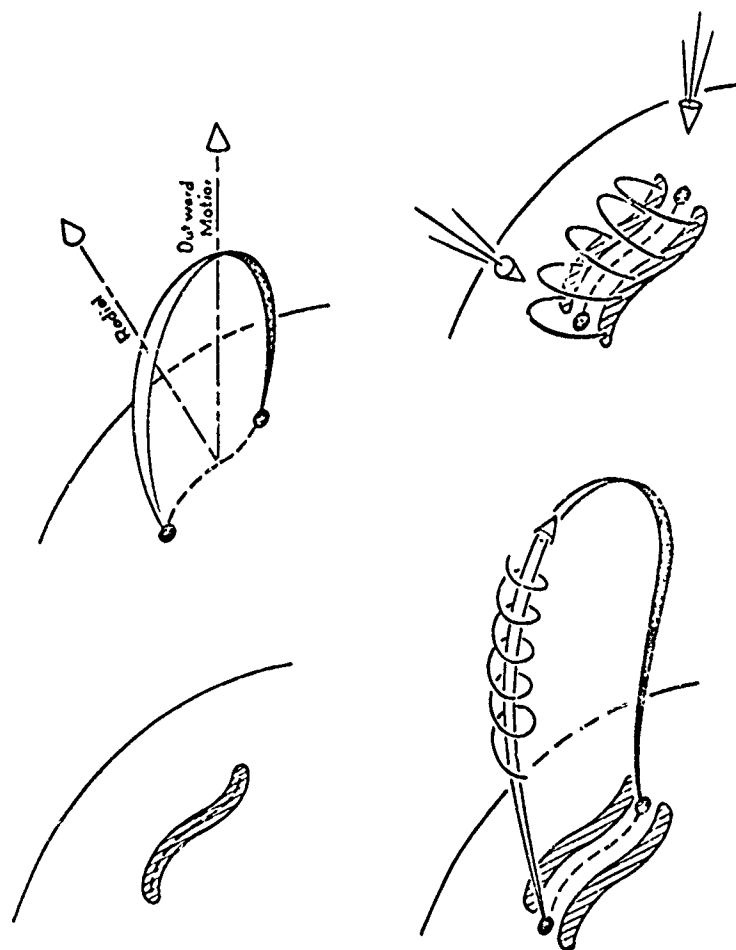


Fig. 7.5 Schematic description of a flare spray or a prominence eruption suggested by Tandberg-Hanssen, Martin, and Hansen (1978). Eruption starts with darkening (top left) of a filament (prominence seen on the solar disk). Then, the whole structure expands radially (top right) with the internal structure taking on a helical shape (bottom left). In many such eruptions, a two-ribbon flare appears at the site formerly occupied by the filament and the two ribbons are linked by bright post-flare loops (bottom right). At the same time, material from the eruptive may still be falling to the surface.

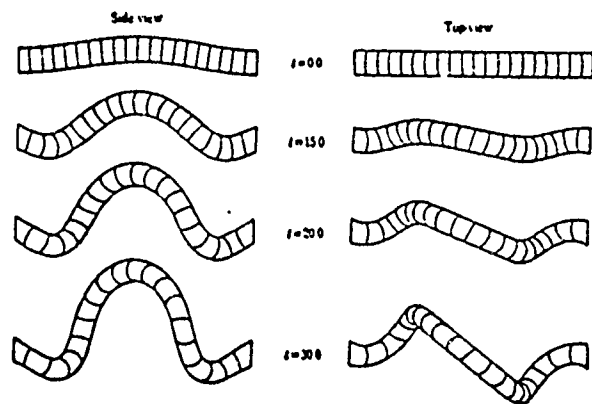


Fig. 7.6 Computed motion of a magnetic flux tube. A uniform pinch of radius R , length L , pitch P , and Alfvén speed V_A is modeled, with gravitational force neglected and external pressure assumed constant. The unit of time is R/V_A ; $P/R = 1/4$ and $L/R = 20$, in the case illustrated (Sakurai, 1976).

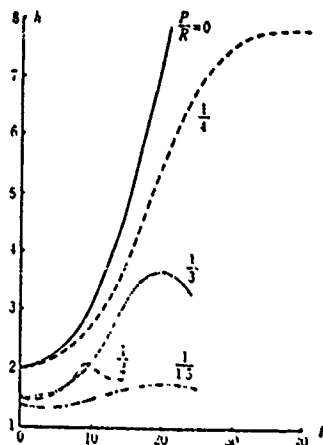


Fig. 7.7 Computed rising motion for several model flux tubes. The units of height h and time t are R and R/V_A , respectively. According to this figure, only the more strongly twisted flux tubes will rise indefinitely (Sakurai, 1976).

evidence for a magnetohydrodynamic slow-rise phase frequently observed in solar prominence instability. A more rapid type of motion that Sakurai refers to as 'slow rise' we refer the reader to Ch. 8. As is apparent from Figure 7.4, the trajectory depends upon the degree of twist of the prominence. Sakurai (1974) plotted by Figure 7.4 the trajectory of a prominence (Figure 7.4) plotted by Sakurai (1974). Note that the pinch time t_p depends on the degree of twist of the prominence. This would seem to imply that the trajectory of a prominence field, which is determined by the tension in the axial field, would add to the deceleration.

7.2.6. Physical Conditions

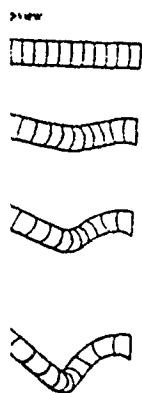
The trajectory, temperature, and density of the 19 December 1973 loop-shaped coronal prominence that passed through the outer corona on 19 December 1973, other, less well-observed prominences.

On 18 December 1973, the temperature of the prominence was close to the average value of the EUV (Orrall and Sakurai, 1974) and the prominence was of 2×10^{15} g, it was not observed.

At about 0449 UT the prominence started to rise, although it was tightly wound and at 0632 UT the coils were visible in white light at the edge of the solar disk.

When the prominence was visible in white light at the edge of the solar disk, it was seen with other instruments. Figure 7.8. The prominence was essentially unchanged in height and temperature for about 3 hours as the prominence rose. The most prominent temperature was 10×10^6 to 8×10^6 K, and the height in the prominence decreased with time.

The warming and rise of the prominence was surprisingly slight, considering the distance travelled ($\sim 2 \times 10^6$ km) and the fact that the rapid dispersal of the edge rose above 3.0 Ω , and its hot coronal surface



Pinch of radius R , length L ,
force neglected and external
field H and $L/R = 20$, in the case

The units of height h and
width w are the more strongly twisted

evidence for a magnetohydrodynamic instability in a twisted magnetic field. The slow-rise phase frequently seen in eruptives is identified with the onset of the instability. A more rapid rise-phase follows. Figures 7.6 and 7.7 illustrate the types of motion that Sakurai modeled. (For a general discussion of instabilities, we refer the reader to Chapter 2 dealing with preflare phenomena.)

As is apparent from Figure 7.6 and 7.7, the rate of rise of the prominence depends upon the degree of twist and the length of the field lines, i.e., the length of the prominence. Some of the curves in Figure 7.7 are suggestive of the curves (Figure 7.4) plotted by Tandberg-Hanssen, Martin, and Hansen from observation. Note that the pinch that rises without deceleration has no axial magnetic field. This would seem to be in disagreement with observations of active-region prominence fields, which have strong axial components (Tandberg-Hanssen, 1967, 1974). Sakurai finds that deceleration of his model pinches (prominences) is due to the tension in the axial magnetic field. Gravity, if included in the model, would add to the deceleration.

7.2.6. Physical Conditions of the Eruptive Prominence of 19 December 1973

The trajectory, temperature, and density of the classic helical eruptive prominence of 19 December 1973 were studied by Schmahl and Hildner (1977). A large, loop-shaped coronal transient preceded the previously quiescent prominence through the outer corona. Since this event can be considered as an archetype for other, less well-observed transients, it will be discussed here in some detail.

On 18 December the prominence showed helical structure, and the electron temperature of the material within the preeruptive prominence was 8000 ± 600 K, close to the average electron temperature of nine other prominences observed in the EUV (Orrall and Schmahl, 1976; Schmahl et al., 1974). The preeruptive prominence was of great extent, stretching $\sim 44^\circ$ in position angle, but, at 2×10^{15} g, it was not exceptionally massive (Tandberg-Hanssen, 1974).

At about 0449 UT on 19 December, the central portions of the prominence started to rise, although the northern and southern footpoints remained fixed, and the tightly wound spirals within the preeruptive prominence uncoiled. By 0632 UT the coils were nearly unwound (as Figure 7.1 shows).

When the prominence reached $\sim 1.6 R_\odot$ from sun center, bright knots became visible in white light at the same positions as the H α and He II prominence material seen with other instruments. The heights of these knots are plotted vs time in Figure 7.8. The prominence reached $1.3 R_\odot$ with its temperature, mass, and density essentially unchanged from the preeruptive values. However, the mass of cool material observed above $1.6 R_\odot$ decreased monotonically by ~ 25 percent over 3 hours as the prominence rose from 2.2 to $3.0 R_\odot$. During this time, the outermost prominence temperature rose from 16,000 to 20,000 K as its density fell (30×10^6 to 8×10^8 cm $^{-3}$). Temperature increased and density decreased with height in the prominence; also, at each height temperature increased and density decreased with time.

The warming and rarefaction experienced by the prominence material were surprisingly slight, considering the time lag (up to 7 hours after eruption) and the distance travelled ($\sim 2 R_\odot$) through the corona. Schmahl and Hildner speculate that the rapid dispersion and dimming of the prominence material after the leading edge rose above $3.0 R_\odot$ indicates that thermal insulation between the prominence and its hot coronal surroundings abruptly broke down.

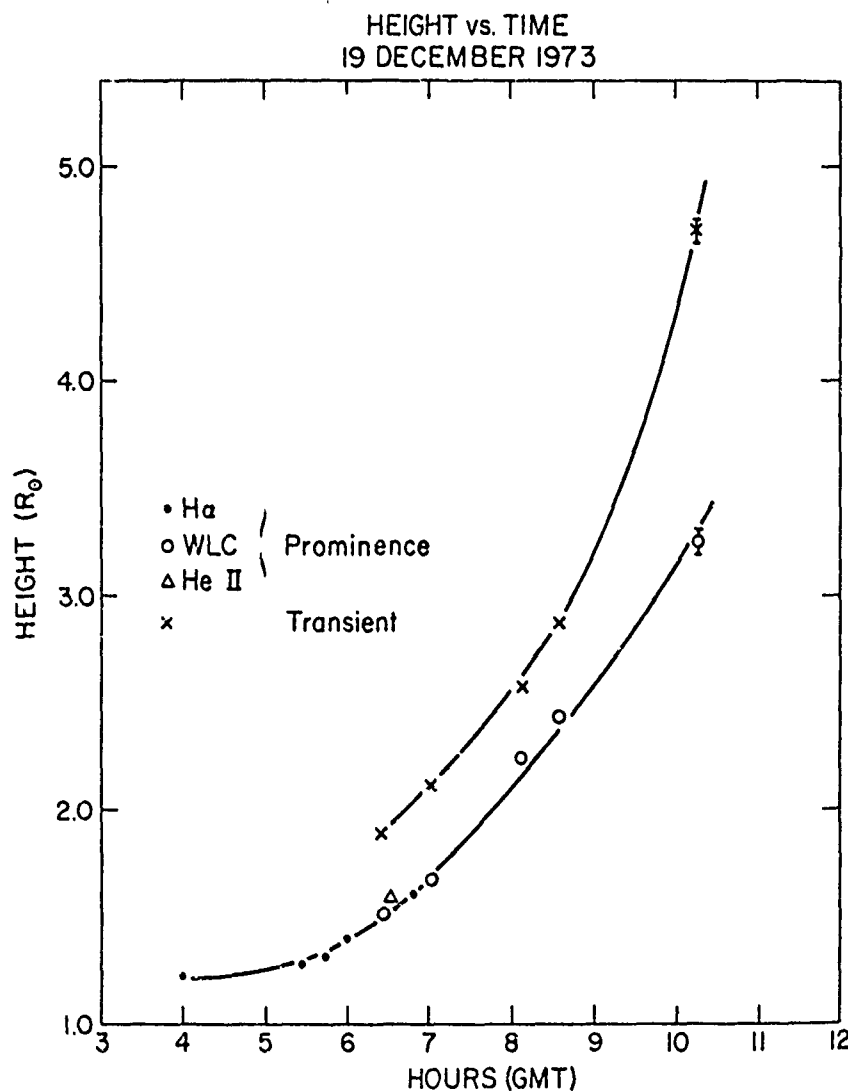


Fig. 7.8 Height versus time for expelled material (Schmuhl and Hildner, 1977).

About one-half hour material appeared in E as much as 1 percent (2 into the chromosphere in percent) of the preeruptive material; and (2) the amount with time.

This event is an example of prominence material. The early ascent, and its height ($< 10''$), cool, unresolved (1974; Dulk *et al.*, 1976) 19 December 1973 prominence.

This work and, for (1974b), Dulk *et al.* (1978) showed that nine were associated with coronal atmosphere become unstable to suggest that a prominence field which becomes unstable carries outward the variation.

7.2.7. Mass Motion

Rust and Webb (1977) elements observed in active regions. One hundred fifty-six active regions appeared in form of H α filament active eruptive nature. Sixty-nine associated with reported 63 occurred in conjunction with filaments; only 6 flares occurred.

Dark H α material, which along trajectories parallel to dark material's path was too faint or too diffuse for movies, and Rust and Webb indicate the progress of exposure at 1013 UT, along with some faint X-ray loops in X-rays at about 1430 at 1755 UT, a series of 30 were 6–10 times brighter they appeared somewhat faded and resembled preceded the H α brighten-

About one-half hour after the eruption's start, fine vertical threads of falling material appeared in EUV emission below the still-rising prominence. Perhaps as much as 1 percent (2×10^{13} g) of the mass of the preeruptive prominence fell into the chromosphere in these threads. Evidently: (1) only a small fraction (~ 10 percent) of the preeruptive prominence rose into the corona above $1.6 R_{\odot}$ as cool material; and (2) the amount of cool prominence material above $1.6 R_{\odot}$ decreased with time.

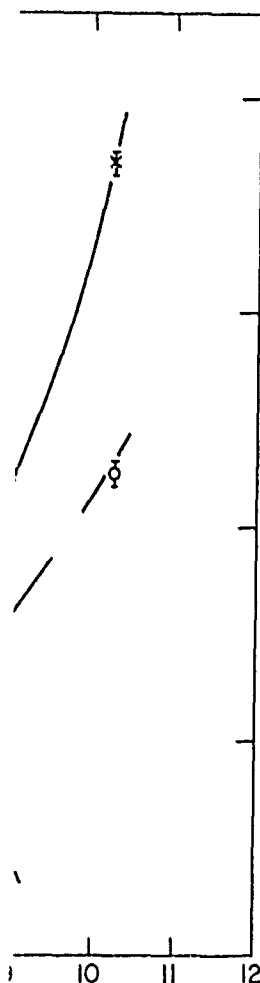
This event is an example of the heating and rarefaction of cool, rising prominence material. The unity of the prominence material was maintained during its early ascent, and it appears that the material was still concentrated into small ($< 10''$), cool, unresolved structures at $3 R_{\odot}$. As in other events (Gosling *et al.*, 1974; Dulk *et al.*, 1976; Hildner *et al.*, 1975b) a coronal loop transient above the 19 December 1973 prominence eruption carried off the bulk of the ejected mass.

This work and, for other mass ejection events, the work of Stewart *et al.* (1974b), Dulk *et al.* (1976), and Wu *et al.* (1975) has made clear the positional and temporal unity of prominence eruptions and coronal transients. Munro *et al.* (1978) showed that nine of ten flares with ejections of chromospheric material were associated with coronal transients, indicating that great volumes of solar atmosphere become unstable at times of ejections. Schmahel and Hildner were led to suggest that a prominence and the corona around it are permeated by a magnetic field which becomes unstable everywhere nearly simultaneously. As the field rises, it carries outward the various highly-conductive features strung upon it.

7.2.7. Mass Motions in Coronal Loops Associated with Sprays; X-ray Observations

Rust and Webb (1977) examined all large-scale ($> 60,000$ km) soft X-ray enhancements observed in active regions during the Skylab mission to determine their morphological characteristics and the number associated with mass ejections. One hundred fifty-six enlargements and loop-like extensions of well-established active regions appeared on the X-ray pictures. Of these, 126 accompanied some form of H α filament activity. Of these, 94 were associated with activity of a clearly eruptive nature. Sixty-nine of the 156 X-ray events were definitely or probably associated with reported H α flares, as listed by Hirman *et al.* (1975). Of these, 63 occurred in conjunction with at least one of the categories of eruptive or active filaments; only 6 flares occurred in the absence of other H α activity.

Dark H α material, where observed, was ejected from the flaring active regions along trajectories paralleling the X-ray loops, but it is impossible to say that the dark material's path was within the observed loops. In general, the H α ejecta were too faint or too diffuse to be identified on single prints from the flare-patrol movies, and Rust and Webb relied upon chains of chromospheric brightenings to indicate the progress of H α excitation. An example is shown in Figure 7.9. The exposure at 1013 UT, about 4 hours before the events, shows McMath 12387 with some faint X-ray loops surrounding it. A 2B flare began at 1419 and peaked in X-rays at about 1430. When the first post-event X-ray images were obtained at 1755 UT, a series of 360,000-km-long loops arched toward the southwest. They were 6–10 times brighter than the loops in the same region before the flare, and they appeared somewhat less twisted. In the 24 hours after the flare, the loops faded and resemblance to the preflare morphology increased. The flare clearly preceded the H α brightenings at the remote ends of the interconnecting X-ray



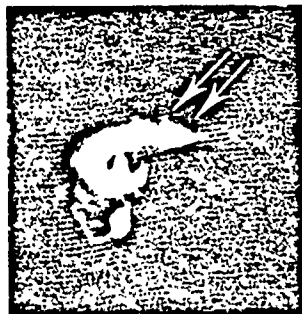
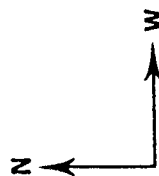
and Hildner, 1977).

JUNE 16, 1973



1013 UT

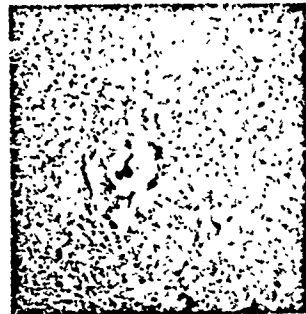
5 arc min.



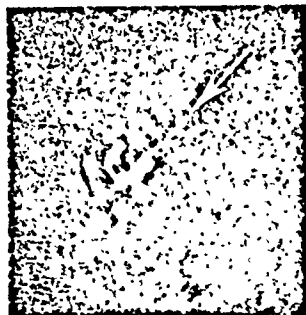
1758 UT



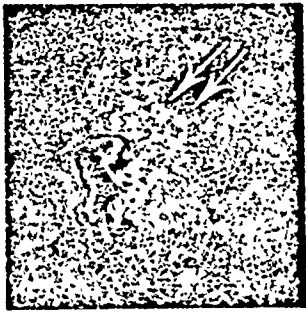
1411 UT



1423 UT



1424 UT



1803 UT

Fig. 7.9 Soft X-ray and H α observations of a 2B flare on 16 June 1973. At flare onset, the narrow, dark filament (1411 UT image) sprays I northward into the base of the X-ray enhanced loop. Arrows indicate the apparent intersections of the loop with the chromosphere (Rust and Webb, 1977).

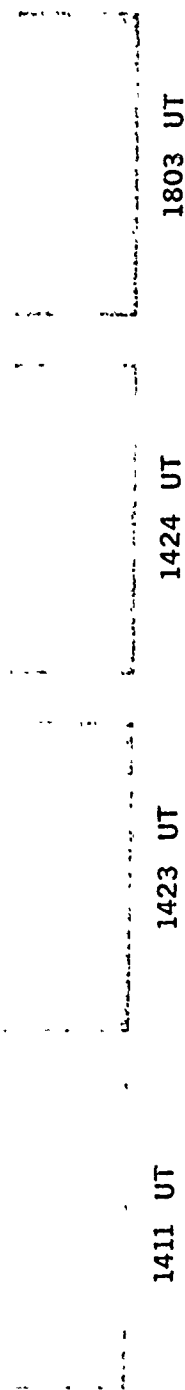


Fig. 7.9 Soft X-ray and H α observations of a 2B flare on 16 June 1973. At flare onset, the narrow, dark filament (1411 UT image) sprayed northward into the base of the X-ray enhanced loop. Arrows indicate the apparent intersections of the loop with the chromosphere (Rust and Webb, 1977).

loops, which, Rust and Webb suggest, guided material or a shock from the flare site. The *excitation velocity*, deduced from the 5-minute interval between flare onset and the 1424 UT brightening at the nearest H α patch (*indicated by an arrow*), was $1200 \pm 300 \text{ km s}^{-1}$. The loops in Figure 7.9 were attached to the active region at the base of an H α spray.

Rust found evidence for a "knot" of high-temperature material associated with a spray on 6 September 1973. In this event, a number of loops were excited, apparently by the passage of material from the active region. Magnetograms indicated that almost all the H α brightenings at one end of the loops in the active region overlay positive fields, while the bright H α archipelago traced by the opposite ends of the loops followed a chain of negative field patches. The inferred propagation velocity of material moving along the loops from the flare site was $400\text{--}1000 \text{ km s}^{-1}$. It appeared that the enhanced loops lay just below the spray trajectory and that the excitation velocity in the loops was comparable to the spray velocity. The sequential brightening of H α patches along a chain stretching from the active region resembled the phenomenon usually called a "flare wave" (Smith and Harvey, 1971). Rust concluded that some, perhaps many, flare waves may be due to the sequential excitation of loop footpoints outside active regions with mass ejections, although at least Dryer, Steinolfson, and Wu felt that a shock such as that proposed by Uchida *et al.* (1973) could also be responsible.

A photograph that shows directly the moving, X-ray-emitting ejecta appears in Figure 7.10. In the event illustrated, both hot (X-ray-emitting) and cooler (H α -emitting) ejecta were escaping from the sun. This event was associated with a major disturbance of the white-light, outer corona and a Type II radio burst, which started as the X-ray ejecta rose above the limb (Webb and Jackson, 1979). The mass ejection was likely associated with a flare over the limb (Tousey, 1975).

In this 17 January 1974 event, an X-ray-emitting, expanding arch rose through the lower corona at $\sim 400 \text{ km s}^{-1}$. Webb and Jackson concluded that the tops of the X-ray and H α arches were coincident and that the X-ray arch coincided with that side of the H α arch which was rising and most rapidly detaching from the solar surface. Webb and Jackson interpret these observations as evidence for the rapid heating of cool prominence material to coronal temperatures. Heating of erupting material has been implied in observations of other events (Roy and Tang, 1975; Rust and Webb, 1977; Zirin *et al.*, 1969). Schmahl and Hildner (1977) also inferred ongoing heating of cool material to coronal temperatures from observation of a slow ($\sim 75 \text{ km s}^{-1}$) prominence eruption.

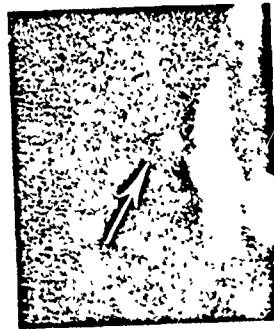
From photometric analysis of the X-ray films, Webb and Jackson concluded that the corona was *depleted* behind the rising arch of prominence material newly heated to coronal temperatures. In addition, a *knot containing preexisting hot coronal material* was ejected. This does not mean that the knot contained only preexisting coronal material, since an admixture of cool prominence and hot coronal material may have coexisted in the knot to great heights.

X-ray observations of transients in the inner corona led us to a picture of loop-shaped features, probably one or more magnetic flux tubes, expanding above eruptive prominences and carrying $10^{14}\text{--}10^{15} \text{ g}$ of coronal material into interplanetary space. As in the 17 January event, a knot of X-ray-emitting material may be ejected at the same time as overlying loops expand.

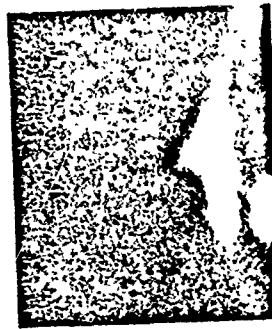
17 JANUARY 1974



1933:27



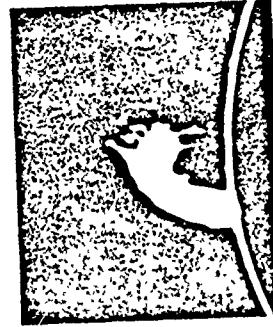
1930:38



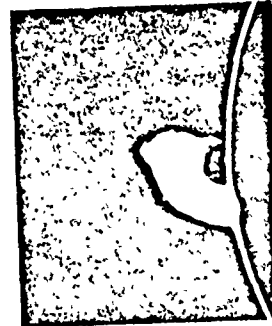
1927:49



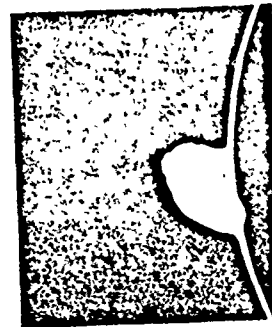
1925:00



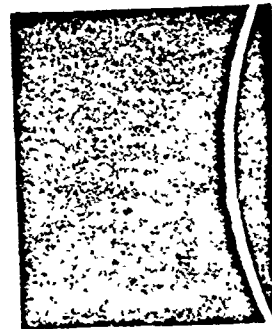
1932:7



1931



1930



1925

Fig. 7.10 Soft X-ray (top) and Ha images (bottom) of the limb spray of 17 January 1974. The arrow points to spray-associated ejecta at coronal temperatures (Rust and Webb, 1977).

7. D of th X ki in er o si (ci ti (te th c fi A o n u o t p f s c u i s c c i t

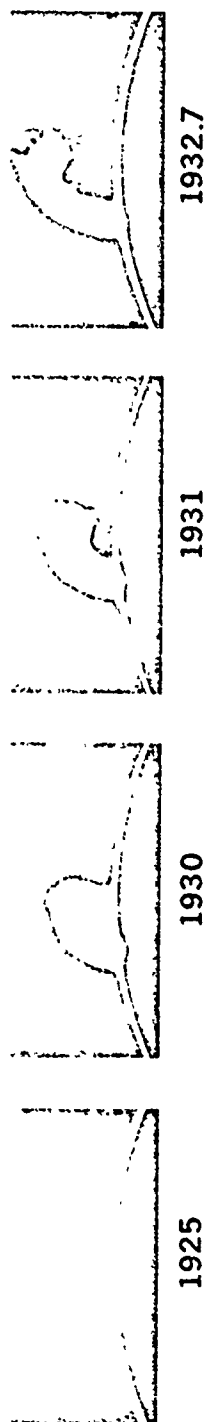


Fig. 7.10 Soft X-ray (top) and *Ifo* images (bottom) of the limb spray of 17 January 1974. The arrow points to spray-associated ejecta at coronal temperatures (Rust and Webb, 1977).

7.2.8. Mass Motion in Coronal Loops Associated with Sprays; A Model

During the course of the Workshop, McClymont continued his work with Craig on mass motions confined to magnetic flux tubes. In the following, we describe their model, and we suggest that it will explain the principle features of the fast X-ray loop brightenings observed by Rust and Webb, may have relevance to the knots of X-ray-emitting material ejected from active regions, and may have important implications for the flare energy-release process itself.

In earlier work, Craig and McClymont (1976) found that the injection of energy into the upper part of a high-density coronal loop leads to the formation of shock fronts that propagate down to the chromosphere, thus carrying off a sizeable fraction of the flare energy. In a new model, McClymont and Craig (1978) assume that heating takes place at one end of a horizontal tube of uniform cross-section in which the magnetic pressure dominates the gas pressure. The flux tube can then be regarded as rigid. The initial density and temperature (1.6×10^6 K) are taken to be uniform, and gravity is neglected.

To simplify the model, the response of the chromosphere at the end of the tube to energy deposition in the tube is ignored by imposing the boundary condition that no mass flows from the energy injection site. The energy input function comprises a half sine wave in both space and time, of half-width λ in space and full-width τ in time.

Variations in the initial formation of shocks for a range of energy inputs are shown in Figure 7.11. For each case, the ambient density is 10^{10} cm^{-3} ; the size of the energy injection region, $3 \times 10^9 \text{ cm}$; and the energy injection period, 1 minute. The same size and heating duration apply to all the results given here unless λ and τ are otherwise specified. Each curve is labelled by the relevant value of $\chi = \log_{10} (Q/n)$, where Q is the total energy injected into unit cross-section at the base of the flux tube (erg cm^{-2}). Thus χ is a measure of the injected energy per particle. The full line indicates the Mach number M_2 determined from the Rankine-Hugoniot conditions applied across the wavefront, while the broken line shows the Mach number M_1 corresponding to the propagation speed of the disturbance. Strictly speaking, the initial disturbance is not a fully developed shock until the two curves join ($M_1 = M_2$) at $t \approx 2$ min, although the wavefront may, for most purposes, be regarded as a shock at times as early as ~ 1 min.

In Figure 7.12, the initial development of shocks in plasmas of different ambient densities is compared. The three curves in Figure 7.12 are labelled by $\log_{10} n$; in each case $\chi = 1/2$. From Figures 7.11 and 7.12, it can be inferred that: (1) a shock's final Mach number depends strongly on input energy, but only weakly on ambient density, and (2) the time to achieve a fully formed shock at fixed energy per particle depends upon ambient density. This latter effect may, in part, be due to the increased ratio of the thermal conduction time scale to the dynamical time scale at lower densities.

The effect of different energy-injection length scales and time scales were investigated and shown to be minor. The characteristics of the fully developed shock depend principally on the amount of energy injected. The initial evolution was computed for the case $n = 10^{10} \text{ cm}^{-3}$, $\chi = 1/2$. Energy injection lengths of $\lambda = 3 \times 10^8 \text{ cm}$ and $3 \times 10^9 \text{ cm}$ were used with injection durations $\tau = 15, 30$, and 60 s. As expected, rapid heating (smaller τ) produces a faster risetime and a higher peak speed of the wavefront. However, by the time the shocks are fully

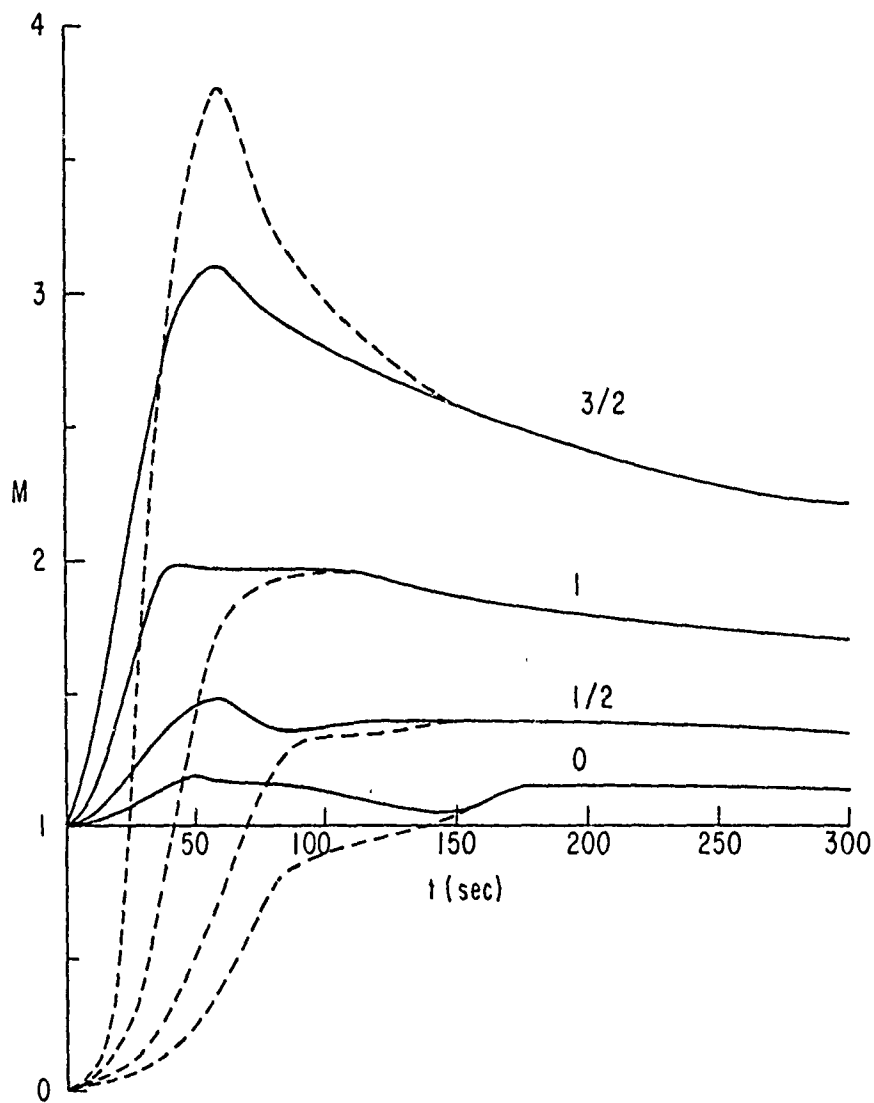


Fig. 7.11 Initial evolution of shock Mach number M_1 (----) and M_2 (—) at a density of 10^{10} cm^{-3} for different total energy inputs, denoted by χ values marked on the curves. $\lambda = 3 \times 10^9 \text{ cm}$ and $\tau = 60 \text{ s}$. M_1 , M_2 , χ , λ , and τ are defined in the text. (McClymont and Craig, 1978).

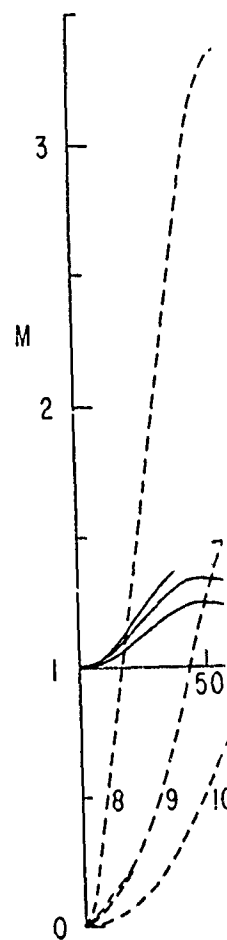
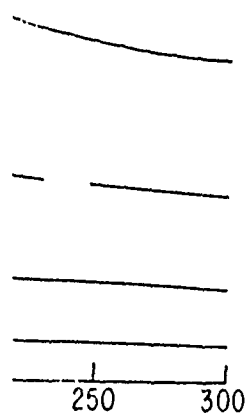


Fig. 7.12 Initial evolution of shock Mach number M versus time t for different total energy inputs, such that $\chi = 1$, $\lambda = 3 \times 10^9 \text{ cm}$ and $\tau = 60 \text{ s}$. (McClymont and Craig, 1978).



M_2 (—) at a density
values marked on the curves.
the text (McClymont and

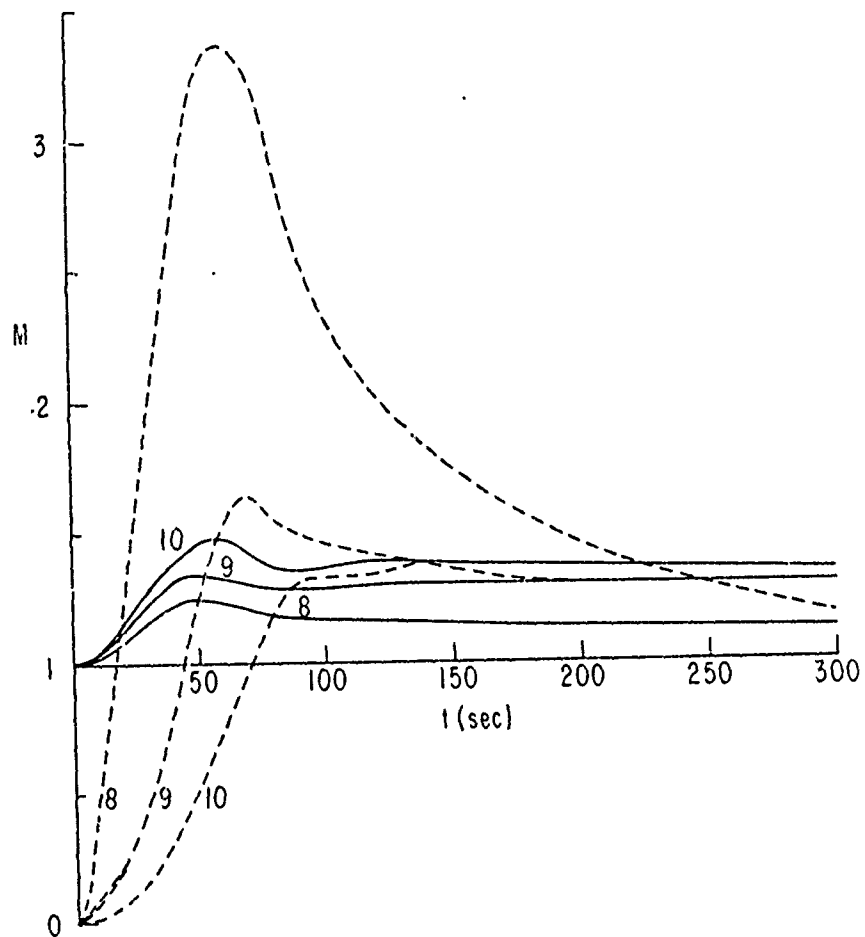


Fig. 7.12 Initial evolution of shock Mach number M_1 (---) and M_2 (—) for energy inputs, such that $\chi = 1/2$, with different densities ($\log_{10} n$ is marked against each curve). $\lambda = 3 \times 10^9$ cm and $\tau = 60$ s. See text for definitions of M_1 , M_2 , χ , λ , and τ . (McClymont and Craig, 1978).

developed, the time scale of heating has ceased to have an effect on the Mach number. After 3 minutes the shock fronts arrive at the same position, regardless of the extent λ of the heated region.

Since the plasma in the flux tube is still approximately at constant density when shocks form, the pressure gradients which drive the shocks arise mainly from temperature gradients. Therefore, a strong correlation between the peak shock speed and the maximum temperature reached in the heated region is expected. McClymont and Craig show that for models spanning ranges of density ($10^8 \leq n \leq 10^{11} \text{ cm}^{-3}$), energy input ($-1/2 \leq \chi \leq 3/2$), heating times ($15 \leq \tau \leq 60 \text{ s}$), and length scales ($3 \times 10^8 \leq \lambda \leq 3 \times 10^9 \text{ cm}$), the shock speed increases logarithmically with maximum temperature.

Having established that the propagation of shocks does not depend sensitively on details of the energy injection, Craig and McClymont examined the decay of shocks as a function of ambient density and energy input. It is difficult to discuss the decay rate of shocks in a simple but quantitative manner since the behavior depends on the evolution of the entire region behind the shock; but the evolution of shocks in plasmas of ambient density $n = 10^8, 10^9$, and 10^{10} cm^{-3} was followed to 1000 s for values of the energy input parameter $\chi = 0, 1/2, 1$, and $3/2$. Shocks previously found to form more slowly in a lower density plasma also take longer to develop as the energy per particle (χ) increases. As expected, the rate of shock decay increases with increasing Mach number. Results are relatively insensitive to the ambient density; at a given Mach number, the decay rate increases slowly with increasing density.

In Figure 7.13, the distribution of temperature and pressure in the flux tube after 1000 seconds is shown for $n = 10^9 \text{ cm}^{-3}$ and $\chi = 0, 1/2$, and 1 . These distributions were also computed for a density 10^{10} cm^{-3} . Although the temperature distribution is different in this case, the pressure distribution is found to be almost identical when scaled according to the ratio of ambient densities.

Finally, the average velocity of shock propagation over the interval $t = 0$ to 1000 s was studied as a function of energy input χ for $n = 10^8, 10^9$, and 10^{10} cm^{-3} . The velocity increases from $\sim 250 \text{ km s}^{-1}$ at $\chi = 0$ to $\sim 500 \text{ km s}^{-1}$ at $\chi = 1.5$. Velocity decreases slightly with increasing ambient density.

The general characteristics of the shocked atmospheres in the theoretical flux tubes are similar to those observed in the X-ray corona. The X-ray enhancements studied by Rust and Webb propagate with velocities between 400 and 1200 km s^{-1} . The degree of enhancement over the prespray emission level is consistent with the temperature increases predicted by McClymont and Craig.

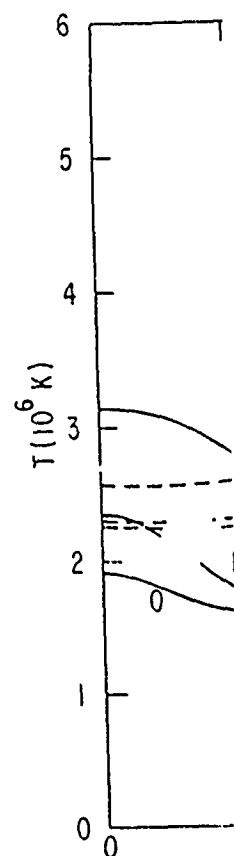


Fig. 7.13 Distribution of temperature and pressure. Curves are labelled by the energy input parameter χ .

7.3 SURGES

7.3.1. Introduction

In this section we discuss new observational studies of surges and two new approaches to modeling them. Before launching into the new observations, we summarize the characteristics of surges that we believe are especially important for understanding their physical mechanisms.

- (i) Surges have a continuous distribution in size. Very small surges accompanying small, impulsive, chromospheric brightening are much more common

an effect on the Mach
same position, regardless

it constant density when
ocks arise mainly from
etween the peak shock
ated region is expected.
ing ranges of density
eating times ($15 \leq \tau \leq$
e shock speed increases

s not depend sensitively
examined the decay of
. It is difficult to discuss
anner since the behavior
shock; but the evolution
 10^{10} cm^{-3} was followed
1/2, 1, and 3/2. Shocks
plasma also take longer
ected, the rate of shock
relatively insensitive to
ate increases slowly with

pressure in the flux tube
1/2 and 1. These distri-
tho... the temperature
on is found to be almost
sities.

ver the interval $t = 0$ to
 0^6 , 10^9 , and 10^{10} cm^{-3} .
 $\sim 500 \text{ km s}^{-1}$ at $\chi = 1.5$.

s in the theoretical flux
The X-ray enhancements
en 400 and 1200 km s^{-1} .
el is consistent with the

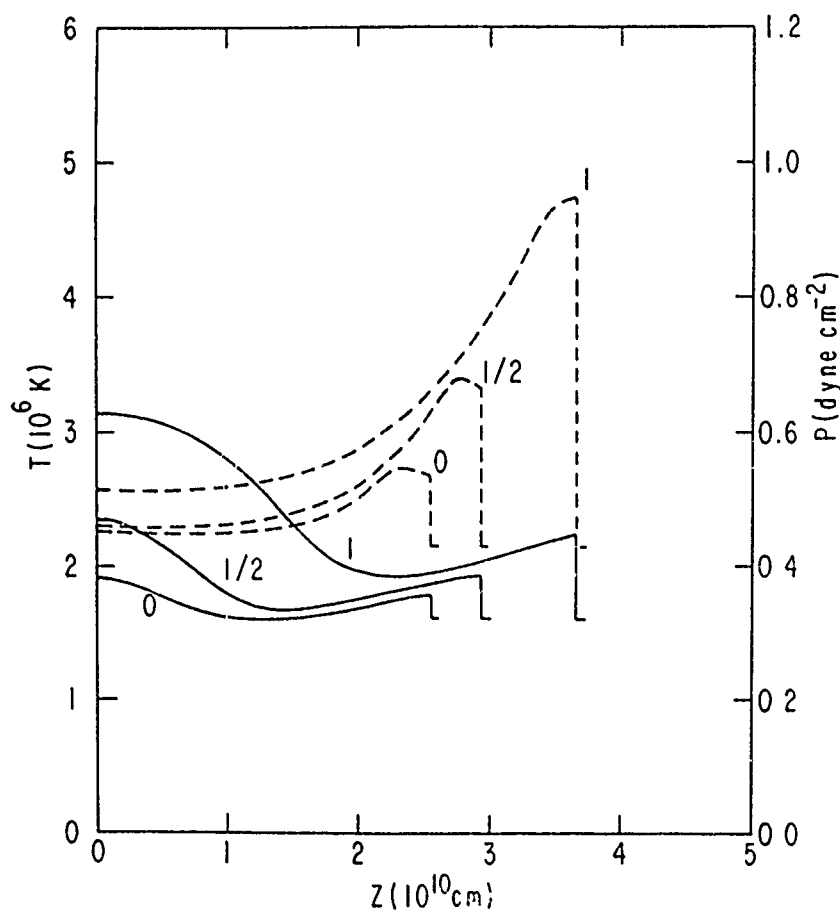


Fig. 7.13 Distribution of temperature and pressure in a flux tube at $\tau = 1000 \text{ s}$ for $n = 10^9 \text{ cm}^{-3}$. Curves are labelled by the value of the energy input χ . (McClymont and Craig, 1978).

of surges and two new
ie new observations, we
especially important for

small surges accompany-
re much more common

than large surges associated with major flares (Vorpahl and Pope, 1972; Roy and Leparskas, 1973).

- (ii) Chromospheric brightenings ("bombs," Ellerman, 1917) from which all non-flare-associated surges appear to originate (Roy, 1973a) are found at magnetic polarity reversals (satellite sunspots; Rust, 1968). Many bombs are associated with satellite spots too small to be apparent.
- (iii) These bombs lie deep in the chromosphere, around the temperature minimum, and require a continuous input of energy (Bruzek, 1972). They appear as a rapid brightening (time scale of a few minutes), after which the brightness remains roughly constant for ~ 10 –40 minutes, followed by a rapid decay (Bruzek, 1972; Roy and Leparskas, 1973). They appear to be closely connected with photospheric facular granules (Bruzek, 1972).
- (iv) Surges on the disk frequently appear bright in H α initially, but darken rapidly after leaving the chromosphere (Bruzek, 1969).
- (v) During their acceleration phase, which normally lasts several minutes, the mean (upward) acceleration is ~ 1 –5 times the solar gravitational acceleration (Roy, 1973b; Platov, 1973). During this time, the H α line width indicates macroscopic velocities of ~ 20 –50 km s $^{-1}$, or kinetic temperatures of $\geq 10^5$ K. The line width drops sharply at the end of the acceleration phase (Platov, 1973).
- (vi) Magnetic field measurements indicate that the field strength in surges is higher than would be expected if the field is due only to photospheric sources. The field strength decreases with height (Tandberg-Hanssen and Malville, 1974).
- (vii) Once the surge begins to decelerate, its velocity decreases more rapidly than can be accounted for by gravity alone. During its return to the surface, the surge velocity is less than the freefall velocity (Roy, 1973b; Platov, 1973).
- (viii) Soft X-ray measurements indicate that no appreciable heating of coronal material at $T \geq 10^6$ K takes place (see Sections 7.3.2 and 7.3.3, below).
- (ix) Type III radio bursts are often associated with surges. Usually the radio burst appears considerably later (~ 10 min) than the surge (Westin, 1969).
- (x) Pressure gradients along the surge trajectory may be sufficient to drive it (Schmahl, 1978).
- (xi) Surges have a strong tendency to recur; a series of surges at a rate ≥ 1 per hour may erupt from a given location (e.g., Tandberg-Hanssen, 1967).

7.3.2. Observations in the EUV

Throughout the Skylab mission, nearly continuous solar observations were made in the EUV ($300 \leq \lambda \leq 1350 \text{ \AA}$) by the Harvard College Observatory spectroheliometer (Reeves *et al.*, 1977). Partial or complete observations of more than 250 flares were obtained. From these data, Schmahl chose a subset of 21 well-observed

events for which simultaneous EUV flares without reported flares were obtained from flares was reported, small

Twelve of the 24 flares no surge was observed in quality of patrol films, the H α surge, the flare period was very short, or

The EUV data suggest, however, flares lead to surges seem to follow flares

In the typical event, of loops) visible in high 1975). The flaring region $\lambda 625$ or Si XII $\lambda 521$) second stage begins near end, brightens in trans end of the loop. Almost coronal lines are not seen. Observations of Rust *et al.*, 1975, of coronal heating in surges either falls back to

In only a few of the features fall back toward surges. Another interesting observation (Hyder, 1967a, b) at the

The emission from the transition region between the H α -absorbing layers (Reeves *et al.*, 1971). Surges appear in the EUV between 5×10^4 and 7×10^4 K. Ne VII $\lambda 465$, and Ne V $\lambda 444$ and the Lyman continuum are formed at temperatures

Schmahl's observations on the physical mechanism

1. The pressure gradient of two above the preflare appears sufficient to drive the surge. After the surge is ejected

2. The e-folding time is the same in all layers of the surge. The pressure gradient along the surge

3. Coronal lines are formed after separation of the surge from the

(Vorpahl and Pope, 1972;

ian, 1917) from which all
(Roy, 1973a) are found at
Rust, 1968). Many bombs
are apparent.

, around the temperature
of energy (Bruzek, 1972).
of a few minutes), at
int for ~ 10 –40 minutes,
oy and Leparskas, 1973).
photospheric facular granules

1 H α initially, but darken
1969).

ally lasts several minutes,
es the solar gravitational
ng this time, the H α line
20–50 km s $^{-1}$, or kinetic
ps sharply at the end of

field strength in surges is
due only to photospheric
at Jberg-Hanssen and

y decreases more rapidly
During its return to the
all velocity (Roy, 1973b;

ceivable heating of coronal
7.3.2 and 7.3.3, below).

surges. Usually the radio
the surge (Westin, 1969).
ay be sufficient to drive

s of surges at a rate ≥ 1
and Jberg-Hanssen, 1967).

observations were made
Observatory spectroheli-
ations of more than 250
ubset of 21 well-observed

events for which simultaneous H α flare observations were available. Three more EUV flares without reported H α flares were found. H α images of each of the 24 flares were obtained from the NOAA flare-patrol films. In the three cases where no flare was reported, small, unreported flares were found.

Twelve of the 24 flares had reported, associated H α surging. In the events where no surge was observed in H α , the lack of an event report was likely due to the poor quality of patrol films, and in two cases where no EUV surge was associated with the H α surge, the flare loops were very compact and the post-flare observation period was very short, or the flare event was close to the edge of the field.

The EUV data suggest that surges may be associated with all flares. In H α , however, flares lead to surges only about 20 percent of the time, although all surges seem to follow flares or puffs (Giovannelli and McCabe, 1958).

In the typical event, a flare appears first, near or on a preexisting loop (or set of loops) visible in highest contrast in spectral lines formed near 10^5 K (see Foukal, 1975). The flaring region (defined by isophotes of a coronal line such as Mg X $\lambda 625$ or Si XII $\lambda 521$) is frequently elongated along the axis of the loop. The second stage begins near flare maximum, when a preexisting loop, flaring near one end, brightens in transition-zone lines further along its length toward the other end of the loop. Almost simultaneously and co-spatially, a dark, H α surge advances. Coronal lines are not strongly enhanced in the surge loop, confirming the observations of Rust et al., 1977 (and Section 7.3.3), who give evidence for the absence of coronal heating in surges. The third stage is the flare decline, during which the surge either falls back along the loop or fades out during its advance along the loop.

In only a few of the flare/surge events studied by Schmahl did the EUV emission features fall back towards their source, though such behavior is common in H α surges. Another interesting result is the absence of any infall-impact phenomena (Hyder, 1967a, b) at the end of the EUV surge loop opposite the flaring end.

The emission from transition-region lines arises from the surge-corona interface between the H α -absorbing material and the ambient corona (Kirschner and Noyes, 1971). Surges appear in highest contrast (~ 10) in lines formed at temperatures between 5×10^4 and 7×10^5 K (C II $\lambda 1335$, O II $\lambda 834$, C III $\lambda 977$, O IV $\lambda 1032$, Ne VII $\lambda 465$, and Ne VIII $\lambda 780$), and in low contrast (~ 1.3) in H I Lyman-alpha and the Lyman continuum. No enhancement of a surge loop is observed in lines formed at temperatures above 1×10^6 K (Mg X $\lambda 635$, Si XII $\lambda 521$, Fe XVI $\lambda 361$).

Schmahl's observations of surges yielded several important new results bearing on the physical mechanism of surge acceleration.

1. The pressure gradient from flares into surge loops increases about a factor of two above the preflare state. The logarithmic pressure gradient along the loop appears sufficient to drive material outward at the observed rates and distances. After the surge is ejected, the pressure gradient relaxes to preflare conditions.

2. The e-folding length of intensity along a given surge is approximately the same in all layers of the surge-corona transition region, so that the logarithmic pressure gradient along the surge can be inferred.

3. Coronal lines are at most very slightly enhanced in the moving emission feature after separation from the flare.

4. Little or no heating occurs. The temperature layers, 3×10^4 to 3×10^5 K, of the surge-corona transition zone are more enhanced over presurge values than others, and the intensity vs temperature profile of the loop is the same five minutes after the passage of the surge as before. A simple explanation for this selective enhancement of the transition zone is that the ejected cool material within the zone compresses the warmer layers momentarily. Even with an adiabatic compression, the transition zone will radiate more, since increasing the pressure while conserving mass increases the emission measure.

7.3.3. Lack of Coronal Effects Due to Surges

It has been reported that brief X-ray bursts, as recorded by full-sun detectors, accompany surges (Teske, 1971). Does the passage of a surge through the corona lead to heating either of the surge material itself or of the coronal material in its path? Schmahl's EUV results imply it does not. However, the flare volume, as defined by the Mg X extent, does increase dramatically, indicating some heating behind the surge volume. To pursue the matter further, Rust *et al.* (1977) searched for surge-associated X-ray emission on high-resolution images obtained with the AS & E soft-X-ray telescope (Vaiana *et al.*, 1977) between 28 May and 27 November 1973. During that period, several hundred "dark H α surges on the disk" were reported, and to study their effects upon the corona, Rust *et al.* selected events for which X-ray observations obtained not more than 8 h before and not more than 4 h after surge onset were available. In only 6 of 54 selected cases was there a noticeable change in the brightness or size of any X-ray-emitting region with a surge. Enlargements of active regions of less than $15''$ in one dimension or brightenings in loops of less than $15''$ cross-section were not noted. These cases appeared to be related to rapid active-region evolution and not necessarily to surge activity alone. Nine of the events were inconclusive because of obscuration from bright flares and/or emission associated with active filaments. This left 39 of the 54 events with no apparent change in X-ray emission at all. Rust *et al.* concluded from the lack of detectable brightness change that $< 6 \times 10^8$ electrons cm^{-3} were added to the corona at 2×10^6 K, or, alternatively, that the temperature did not increase from 2 to 2.4×10^6 K, for example. The minimum detectable density enhancement was less than 5 percent of the density of most surges.

Rust *et al.* concluded that surges pass through the corona without significant heating, that is, without leaving a noticeable X-ray brightness increase. This conclusion is compatible with the slight enhancement seen by Schmahl in Mg X loops during the course of surges. It is also qualitatively consistent with Steinolfson and Schmahl's computational results (Section 7.3.7) which show weak shocks propagating ahead of surge ejecta and slight, transient coronal heating. We interpret the present results as confirmation of the customary view of surges as cool ejections following preexisting field lines. Thus, surges are to be contrasted with sprays and filament eruptions, which appear to distort the magnetic fields and certainly leave heated loops in the corona.

7.3.4. Mass Ejections Accompanying the Flare of 5 September 1973

In a large flare, many forms of ejecta may be observed, and it is important to learn how they interact with each other. The flare with the most complete complement of observations occurred at 1826 UT on 5 September 1973. There is an

extensive discussion and a discussion of in Appendices A and B.

On 5 September 1973, a soft X-ray emission from a ground-based limit-of-visibility spectacular filament showed excellent coverage of the release sequence and the energies involved in the description of the of such events discussed.

In the 5 September 1973 flare of the surge. The erupting filament have "passed through the surge differed from close to the base of the flare, i.e., the filament. (2) maximum line-of-sight velocity of 1838 UT, when the surge, unlike the surge slowed, stopped, while the bulk motion of the surge at the base. (3) occurred at the solely of outward sphere. (6) Except for X-ray enhancement which began with brightening the solar equator coincided closely with the trajectory.

7.3.5. Models and

Except for the various simulations of the mass ejections have been reported (e.g., Rust *et al.*, 1978b). Theoretical descriptions of convective or of the flare plasma stand but difficult rather than an equilibrium thin regime ($T \gg T_c$) formalism, but it

re layers, 3×10^4 to 3×10^5 K,anced over presurge values than the loop is the same five minutes e explanation for this selective ejected cool material within the . Even with an adiabatic com- ce increasing the pressure while

recorded by full-sun detectors, : of a surge through the corona or of the coronal material in its

However, the flare volume, as tically, indicating some heating ther, Rust *et al.* (1977) searched tion images obtained with the 7) between 28 May and 27 "dark H α surges on the disk" corona, Rust *et al.* selected more than 8 h before and not only 6 of 54 selected cases was any X-ray-emitting region with han 15" in one dimension or n not noted. These cases ion, a not necessarily to surge e because of obscuration from laments. This left 39 of the 54 n at all. Rust *et al.* concluded hat $< 6 \times 10^8$ electrons cm^{-3} natively, that the temperature ple. The minimum detectable nsity of most surges.

the corona with out significant ray brightness increase. This ent seen by Schmahl in Mg X ly consistent with Steinolfson .7) which show weak shocks ient coronal heating. We inter- tomary view of surges as cool rges are to be contrasted with istort the magnetic fields and

September 1973

served, and it is important to ith the most complete comple- September 1973. There is an

extensive discussion of the flare's morphology in Chapter 2 and Appendix B, and a discussion of the 5 September flare's radiative and mechanical energy budgets in Appendices A and B, respectively.

On 5 September, the Skylab instruments recorded a preflare enhancement of soft X-ray emission from an activated filament. Many instruments, including ground-based limited-field and full-disk H α patrols, recorded the flare onset and the spectacular filament eruption, flare wave, and surge that followed. Because of the excellent coverage of this flare, McKenna-Lawlor (1977) was able to determine the release sequence of the ejecta, measure their trajectories, and estimate the energies involved. This work is discussed in Appendix B. Here we present a brief description of the surge which occurred during the flare and was perhaps the largest of such events during the Skylab mission.

In the 5 September flare, a dark filament erupted ~ 5 minutes before the onset of the surge. Then, at 1833 UT, blue-shifted surge material became visible behind the erupting filament. By 1834 UT the developing surge appeared in projection to have "passed through" the eruptive and to be moving slightly ahead of it. The surge differed from the filament eruption in the following respects. (1) It began close to the base of a leg of the filament which had exhibited downflow prior to the flare, i.e., the surge was not spatially coincident with the ejected portion of the filament. (2) The surge travelled more slowly than the erupting filament. The maximum line-of-sight velocity in the surge was $150 \pm 20 \text{ km s}^{-1}$, occurring at 1838 UT, when the total velocity of the surge was $\sim 195 \pm 20 \text{ km s}^{-1}$. (3) The surge, unlike the erupting filament, followed a sharply curved trajectory. (4) The surge slowed, stopped, and fell back into the sun nearly along its original trajectory, while the bulk of the ejected filament continued to ascend. (5) The outward motion of the surge lasted ~ 90 min, indicating sustained energy and mass input at the base. (See Figure B.8 in Appendix B.) On the other hand, mass input occurred at the base of the ascending filament; the filament eruption consisted solely of outward streaming of material previously suspended above the chromosphere. (6) Except for a flare-like brightening at the base of the surge, no coronal X-ray enhancement was observed. This is in contrast to the filament eruption, which began with X-ray brightening over the whole length of the filament and with brightening in a coronal loop that extended from the site of the flare across the solar equator to another active region (see Figure 7.14). The bright loop coincided closely with the eruptive filament trajectory, and not with the surge trajectory.

7.3.5. Models and Simulations

Except for the work by Altschuler *et al.* (1968), little attention has been paid to simulating the hydrodynamic aspects of surges, although other sorts of mass ejections have been simulated (Nakagawa *et al.*, 1975; Wu *et al.*, 1978; Steinolfson *et al.*, 1978b). There are severe practical difficulties in achieving a complete theoretical description that includes heating, conduction, and radiation, as well as convective or turbulent processes. Heating, for example, of coronal loops and of the flare plasma is of unknown origin (Emslie, 1977). Conduction is well understood but difficult to simulate because the computation requires an implicit, rather than an explicit, numerical differencing scheme. Radiation in the optically thin regime ($\tau < 10^4$ K) may be approximated by the Cox and Tucker (1969) formalism, but for the optically thick regime it requires treatment by various

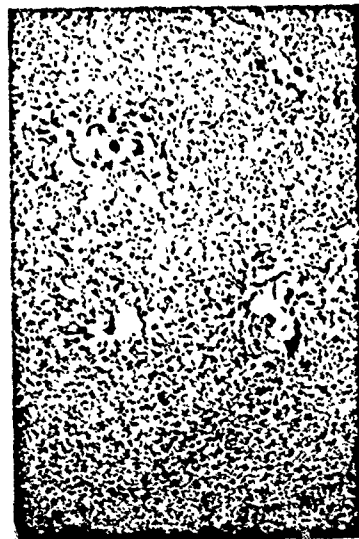
SEPTEMBER 5, 1973



1650 UT



1920 UT



1702 UT



1900 UT

Fig. 7.14 (top) X-rays ($2-32 \pm 44-54 \text{ \AA}$) show brightening of a loop that crossed the solar equator. The loop appeared after the H α flare spray and surge event (bottom) that started at 1828 UT on 5 September 1973. The X-ray loop coincided more closely with the spray trajectory than with the surge, shown in the red wing of H α (bottom left). (X-ray images: American Science and Engineering, Inc., Cambridge; H α images: Space Environment Laboratory, Boulder).

approximate formulas for opacity effects (Brown, 1973). In view of these difficulties and uncertainties, we restricted our theoretical analyses of surges to simpler, gas-dynamic modeling. McClymont developed a new nonmagnetic surge model in which radiation is treated in an approximate manner, and Steinolfson and Schmahl attempted a hydrodynamic simulation of a surge and its effects in the corona. Specifically, the modelers set out to answer the following questions:

- (i) Can a thermal gradient provide a sufficient pressure gradient to account for the surge acceleration?
- (ii) Is it possible to introduce the required heating in such a way that the surge material remains cool? If the surge is heated appreciably, will it cool rapidly enough for compatibility with observation?

McClymont considered a very simple, but illustrative, model in which the surge material is ejected en masse by the adiabatic expansion of an impulsively heated layer of the chromosphere beneath the surge base. The lower boundary of the "explosion site" is regarded as fixed, and the gravitational potential energy of the heated material is neglected.

For simplicity a vertically emerging surge above a high-pressure region of vertical extent x (initial extent x_0) was considered. Thus $x(t)$ measures the height of the trailing edge of the surge above the lower boundary of the heated region.

In the adiabatically expanding hot region, the pressure and density are given by

$$P \sim \rho^\gamma, \text{ and } \rho \sim 1/x. \quad (7.3.1)$$

The equation of motion is then

$$\sigma \dot{v} = P - \sigma g, \quad (7.3.2)$$

or

$$\dot{v}/g = (1 + \xi) (x/x_0)^{-\gamma} - 1, \quad (7.3.3)$$

where σ is the column density of the surge above the heated region, $v = \dot{x}$, P_0 and P are the gas pressures in the heated region initially and during the surge, respectively. In Equations 7.3.2 and 7.3.3, g is solar gravity, $\gamma = 5/3$ is the ratio of specific heats for a fully ionized gas, and

$$\xi = \frac{\Delta P_0}{P_{00}} = \frac{\Delta P_0}{\sigma g} = \frac{P_0}{\sigma g} - 1. \quad (7.3.4)$$

Note that ξ is the initial acceleration in units of g .

For various initial accelerations and a fixed maximum height of 3×10^4 km, the thickness of the heated region (λ_0), the height above the initial position at which deceleration begins ($x_1 - x_0$), and the maximum velocity v_{\max} attained at this point, are shown in Table 7.3. The case $\xi \rightarrow \infty$ corresponds to impulsive ejection of the surge, which then follows a ballistic trajectory. From Table 7.3 we can rule out values of $\xi \lesssim 10$, since the required thickness of the heated region

1920 UT

1900 UT

a loop that crossed the solar event (bottom) that started more closely with the spray (bottom left). (X-ray images: images: Space Environment

TABLE 7.3			
PARAMETERS DEPENDING ON ξ FOR SURGE HEIGHT 3×10^4 km			
$\log_{10} \xi$	x_0 (km)	$x_1 - x_0$ (km)	v_{\max} (km s $^{-1}$)
0.5	7190	9795	73.3
1.0	2180	7170	91.5
1.5	665	4695	104
2.0	205	3060	113
2.5	64	1965	118
3.0	20.1	1250	122
∞	0	0	129

is then larger than the depth of the chromosphere. Although the thickness of the heated layer (660 km) is reasonable for $\xi = 30$, the mass of the heated region is then large compared to the surge mass.

The time to reach maximum height is only weakly dependent on ξ . For acceptable values of ξ (as defined above) this is reasonable, since the velocity profile is not too different from the ballistic ($\xi \rightarrow \infty$) case. A vertically moving surge takes 9.3 minutes to reach a maximum height of 3×10^4 km for $\xi = 10$, while for $\xi \rightarrow \infty$ it takes 7.8 minutes.

McClymont also considered conditions in the heated region driving the surge. He found that we might expect to see a brief (1–20 s) burst of EUV emission at the surge base. He also found that the gas expands so rapidly that, in practice, heating cannot be regarded as impulsive.

The total energy input required to drive the surge can be estimated by calculating the energy to maintain the expanding hot region in its assumed adiabatic state. This is given by

$$\epsilon = \int_0^{t_0} A x(t) n_e(t)^2 f(r(t)) dt, \quad (7.3.5)$$

where t_0 is the time to reach maximum height, $f(t)$ is the radiative loss function (Tucker and Koren, 1971), and A is the surge area. The energy required to offset radiative losses as a surge of mass 10^{14} g ascends to a height of 3×10^4 km, according to (7.3.5), is shown in Table 7.4. These values may be compared to the mechanical energy requirements of $\sim 8 \times 10^{27}$ erg (see Table 7.1)

TABLE 7.4			
RADIATIVE ENERGY LOSSES			
σ (g cm $^{-2}$) =	10^{-4}	10^{-3}	10^{-2}
$\log_{10} \xi$:	ϵ (erg)		
1.5	2.7×10^{30}	4.1×10^{31}	9.0×10^{32}
2.0	4.9×10^{28}	7.1×10^{29}	1.4×10^{31}
2.5	9.3×10^{26}	1.4×10^{28}	2.7×10^{29}
3.0	2.0×10^{25}	2.7×10^{26}	5.2×10^{27}

Except for large values of ξ , the release, while for ξ in the flare. For a less massive surge, the radiative losses are comparable with the radiated energy.

McClymont showed that the large radiative losses are not too different from the ballistic ($\xi \rightarrow \infty$) case. The more accurate estimates are given in Table 7.5.

Next, McClymont calculated the conditions in the surge material (optically thin). The optical depth $\tau \leq 300$. The equilibrium radiation from the hot region is balanced by the losses from the surge. Table 7.5, are compatible with the above.

$\log_{10} \xi$	σ
1.5	
2.0	
2.5	
3.0	

Unfortunately, McClymont's calculations, $\xi \approx 30$, for the mass of the surge; radiative losses for the assumed impulsive chromospheric "bomb" input used here drops below observed surge times. An energy input with a duration of 10 s could well satisfy observations.

An alternative model for the flare sites that lie near the base of the surge, or, in some cases, from the base of a hydrostatic surge (where subscript 0 refers to the base of the surge) (Švestka, 1976; Pallares, 1976) mass-ejections much

HEIGHT

 v_{\max} (km s⁻¹)

73.3
91.5
104
113
118
122
129

ough the thickness of the
ass of the heated region is

ependent on ξ . For accept-
ance the velocity profile is
ritically moving surge takes
km for $\xi = 10$, while for

d region driving the surge.
burst of EUV emission at
rapidly that, in practice,

can be estimated by calcula-
in its assumed adiabatic

(7.3.5)

the radiative loss function
energy required to offset
at of 3×10^4 km, accord-
compared to the mechan-

 10^{-2}

9.0 $\times 10^{32}$
1.4 $\times 10^{31}$
2.7 $\times 10^{29}$
5.2 $\times 10^{27}$

Except for large values of ξ , the bulk of the injected energy is lost to radiation. If ξ is as small as 30, the total energy required is comparable to a large flare energy release, while for ξ in the range 100–300 the energy requirement is that of a small flare. For a less massive surge (smaller base area) the case $\xi \approx 300$ is also comparable with the radiated energy of an Ellerman bomb.

McClymont showed that the hot region becomes optically thick for $\xi \leq 100$, so that the large radiated energies found in Table 7.4 for $\xi \sim 30$ are in fact overestimates. The more acceptable values for $\xi \geq 100$ are realistic.

Next, McClymont calculated the temperature T_{eq} at which radiative heating of the surge material is balanced by radiative losses from the surge (assumed optically thin). The opacity of the surge in its initial state was found to be high for $\xi \leq 300$. The equilibrium temperature was calculated taking into account the radiation from the hot region (Table 7.4), the surge opacity, and the radiative losses from the surge. The calculated equilibrium temperatures, summarized in Table 7.5, are compatible with observation.

TABLE 7.5

RADIATIVE HEATING OF SURGE

σ (g cm ⁻²) =		10 ⁻⁴	10 ⁻³	10 ⁻²
log ₁₀ ξ	T_{RAD} (K)	T_{eq} (K)		
1.5	10 ³	Hot region optically thick, amount of radiation escaping to heat surge unknown.		
2.0	5 $\times 10^3$	6.5 $\times 10^4$	7.5 $\times 10^4$	9 $\times 10^4$
2.5	10 ⁴	10 ⁴	1.5 $\times 10^4$	2 $\times 10^4$
3.0	5 $\times 10^4$	Little effect on surge		

Unfortunately, McClymont's analysis breaks down for the most promising accelerations, $\xi \approx 30$, because the mass of the heated region is comparable to the mass of the surge; radiation is important; and the dynamic time scale is too short for the assumed impulsive heating to be realistic. The constant brightness of chromospheric "bombs" implies a continuous energy input, whereas the energy input used here drops rapidly as surge expansion begins. The model cannot reproduce observed surge trajectories under the impulsive-heating hypothesis, although an energy input with a rise time of ~ 2 min, the rise time of bomb brightenings, could well satisfy observed trajectories.

An alternative model for the hydrodynamic simulation of a surge was investigated by Steinolfson *et al.* (1978a). Since flare-associated surges emanate from flare sites that lie near the footpoints of preexisting coronal loops (Schmahl, 1977) or, in some cases, from flare-puffs (Giovannelli and McCabe, 1958). Steinolfson *et al.* modeled the flare source by an impulsive increase in the pressure p at the base of a hydrostatic atmosphere. Large flares show pressure enhancements p/p_0 (where subscript 0 represents the initial base value) on the order of $p/p_0 \sim 100$ (Švestka, 1976; Pallavicini *et al.*, 1977). Many such flares were associated with mass-ejections much more energetic than surges; smaller flares and subflares

presumably have smaller pressure enhancements and are associated with the less energetic surge ejections. Hence the impulses used in the computations by Steinolfson *et al.* (1978a) to simulate small flares fall in the range $p/p_0 = 5$ to 30. Further, observations indicate that the material motion in surges is parallel to inferred, long-lived magnetic structures emanating from sunspot umbras (Tandberg-Hanssen, 1974). This flow is constrained by the field, so it is essentially hydrodynamic and nearly one-dimensional. Therefore, Steinolfson *et al.*'s computations were one-dimensional and neglected curvature. The computations were carried out in spherical coordinates with spherical symmetry. Comparison to observed surges was obtained by considering only a small section ($\sim 10^{-4}$ sr).

The one-dimensional hydrodynamic equations used are (assuming spherically symmetric and polytropic flows):

$$\frac{\partial p}{\partial t} + \frac{\partial}{\partial r}(\rho v) + \frac{2\rho v}{r} = 0, \quad (7.3.6)$$

$$\frac{\partial v}{\partial t} + v \frac{\partial v}{\partial r} + \frac{1}{\rho} \frac{\partial p}{\partial r} + \frac{GM_\odot}{r^2} = 0, \quad (7.3.7)$$

$$\frac{\partial p}{\partial t} + \gamma p \frac{\partial v}{\partial r} + v \frac{\partial p}{\partial r} + \frac{2\gamma p v}{r} = 0, \quad (7.3.8)$$

where ρ is the density, v the velocity, p the pressure, γ the polytropic index, G the gravitational constant, and M_\odot the solar mass.

The initial conditions were specified to satisfy the hydrostatic equilibrium equation with temperature increasing from a plateau (the chromosphere), at 10^4 K through the transition region, with constant conductive flux ($T^{5/2} dT/dr = \text{constant}$), to the corona at 1.2×10^6 K. The conductive flux thereafter was not computed, and its neglect will be discussed later. The initial density at the top of the chromosphere (considered as the base in the following discussion) was taken to be 10^{11} cm^{-3} . A polytropic index of 5/3 was used.

The hydrodynamic response of the atmosphere to a 5-min pressure pulse of strength $p/p_0 = 10$ is shown in Figures 7.15, 7.16, and 7.17. The dashed curves in Figures 7.15 and 7.16 illustrate the initial temperature and density profiles.

A shock forms ahead of the disturbance and is shown on the $t = 3$ min curves. At later times it has propagated beyond the region shown in the figures. The shock travels at approximately 240 km s^{-1} , so its Mach number is 1.34, and the increase in the thermodynamic variables across the shock is small. The amplitude of the post-shock temperature (density) enhancement is about 1.3 (1.5) \times ambient. The degree of enhancement remains almost constant as the shock propagates through the corona. The material accelerated to the highest velocities by the shock is the hottest and least dense material in the event.

Following far behind the leading shock is the contact surface (labelled by the solid vertical tick marks) defined by the fluid particles ejected from the base at $t = 0$. The contact surface (the leading edge of the ejected material) lies near the minimum of the temperature profile at all times throughout the pulse. The temperature at the contact surface decreases with time until infall occurs after the pulse is removed. Since the pressure pulse is doing work on the gas and since thermal and radiative losses are not included, the first law of thermodynamics

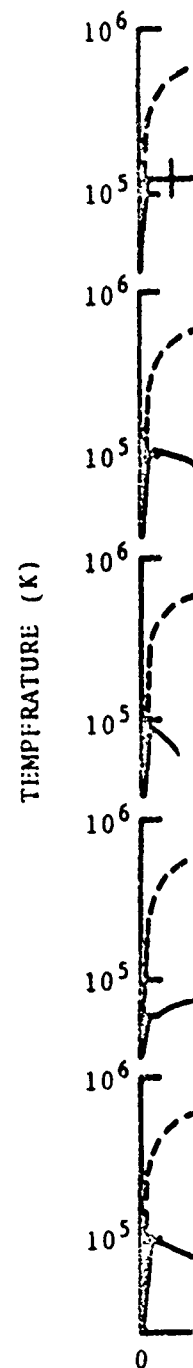


Fig. 7.15 Temperature

are associated with the less
 l in the computations by
 n the range $p/p_0 = 5$ to 30.
 ion in surges is parallel to
 sunspot umbras (Tandberg-
 , so it is essentially hydro-
 olfson *et al.*'s computations
 nputations were carried out
 nparison to observed surges
 'sr).

d are (assuming spherically

(7.3.6)

(7.3.7)

(7.3.8)

, γ the polytropic index, G

be static equilibrium
 e chromosphere), at 10^4 K
 luctive flux ($7^{5.2} dT/dr =$
 ive flux thereafter was not
 nitial density at the top of
 ing discussion) was taken to

a 5-min pressure pulse of
 7.17. The dashed curves in
 nd density profiles.

n on the $t = 3$ min curves.
 vn in the figures. The shock
 er is 1.34, and the increase
 all. The amplitude of the
 t 1.3 (1.5) \times ambient. The
 : shock propagates through
 locities by the shock is the

act surface (labelled by the
 < ejected from the base at
 cted material) lies near the
 hroughout the pulse. The
 until infall occurs after the
 work on the gas and since
 st law of thermodynamics

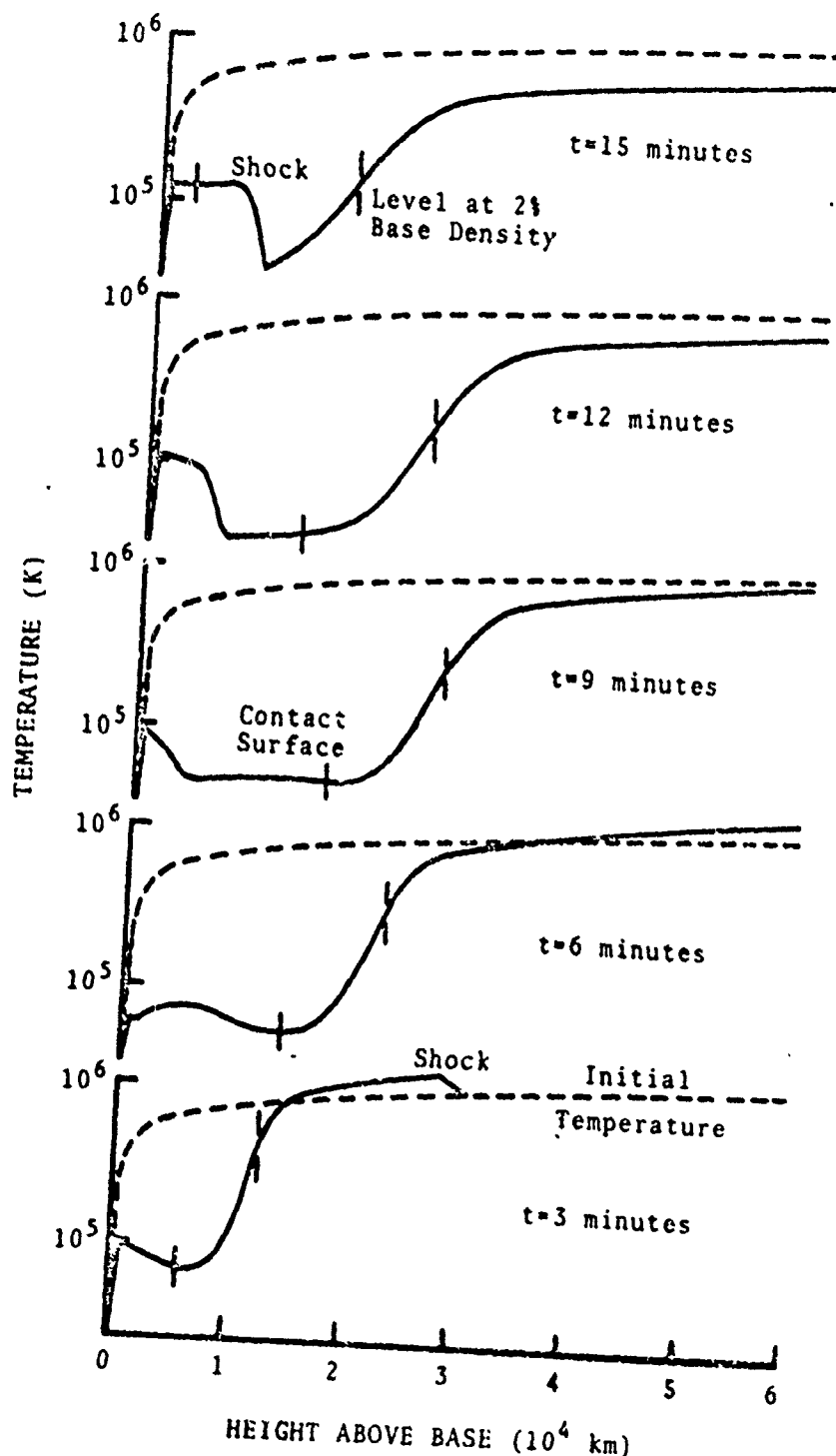


Fig. 7.15 Temperature profiles of a simulated surge; $p/p_0 \approx 10$ (Steinolfson *et al.*, 1978a).

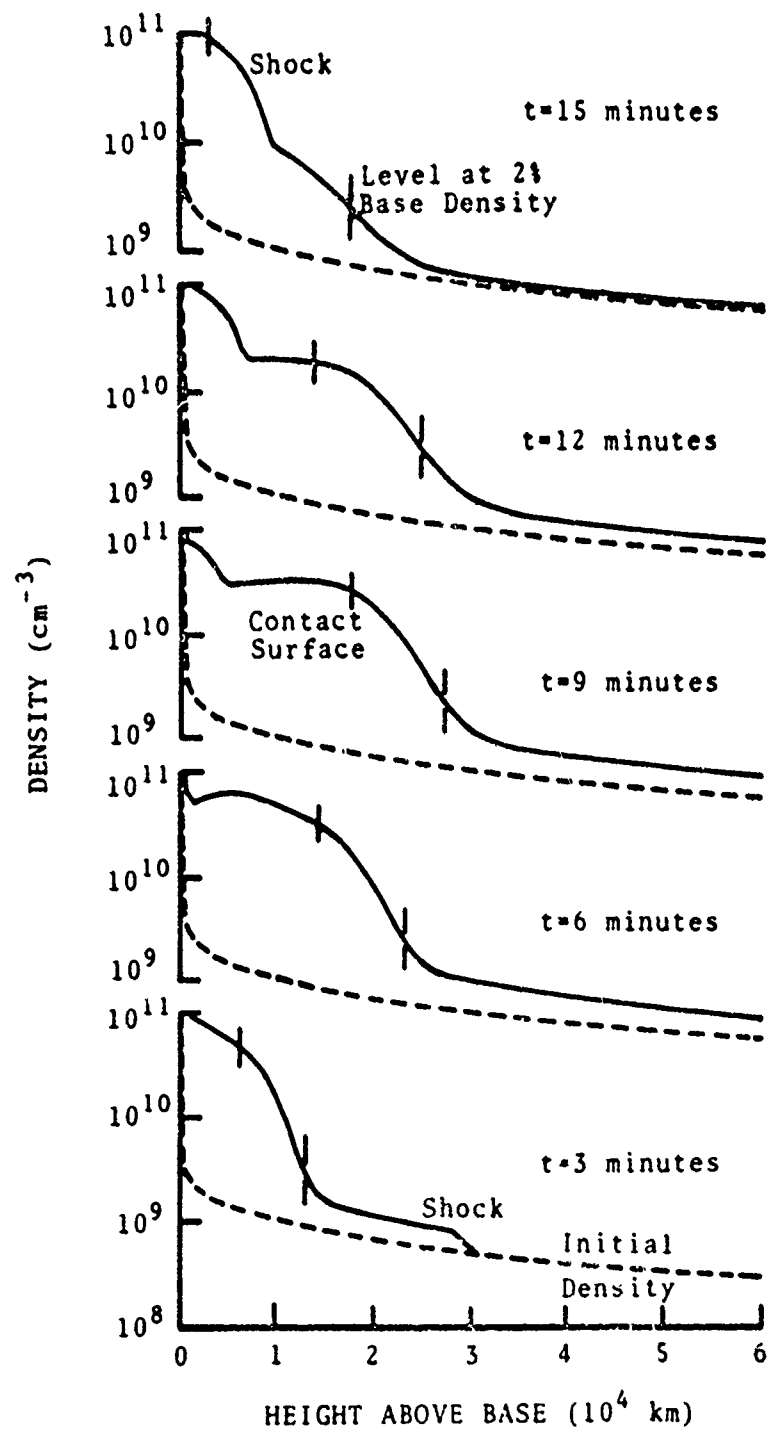


Fig. 7.16 Density profiles of a simulated surge, as in Figure 7.16 (Steinolfson et al., 1978a).

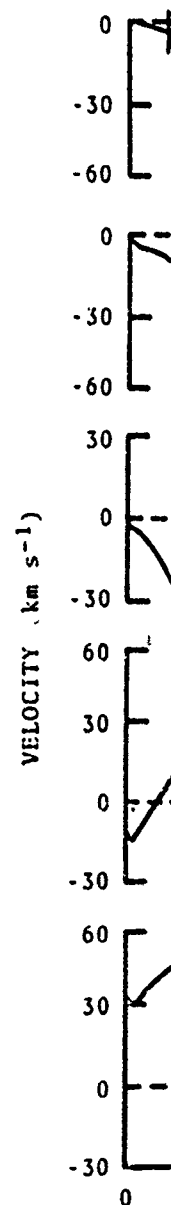


Fig. 7.17 Velocity

15 minutes

2 minutes

9 minutes

6 minutes

3 minutes

Initial

density

5 6

10^4 km)

(Steinolfson et al., 1978a).

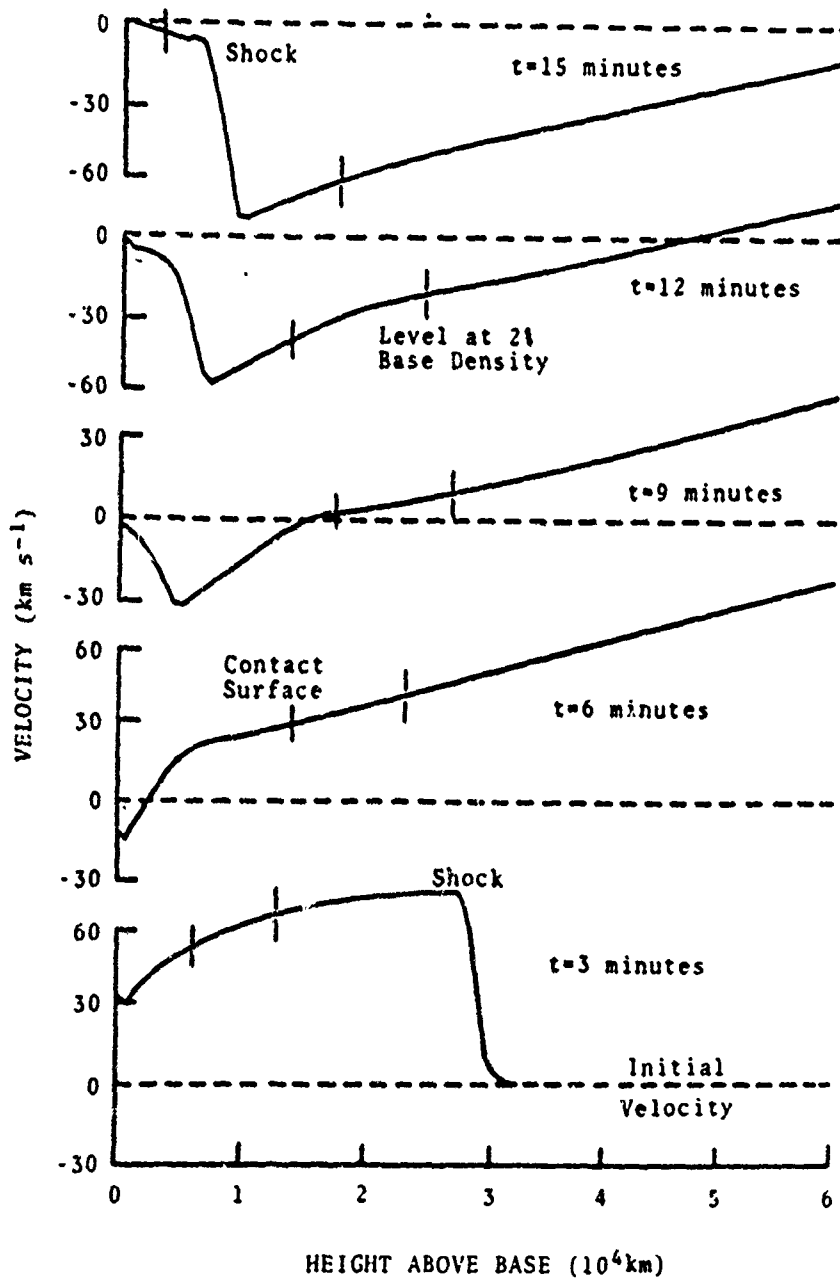


Fig. 7.17 Velocity profiles of a simulated surge, as in Figure 7.16 (Steinolfson et al., 1978a).

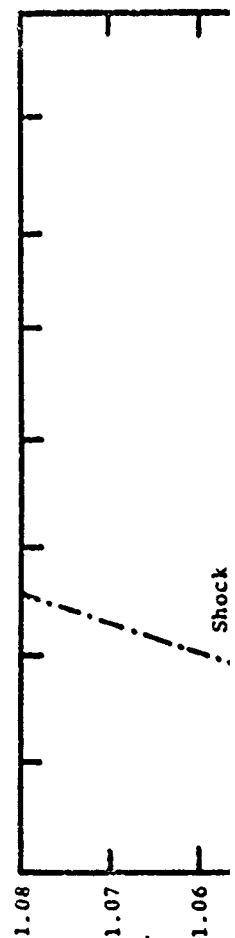
$p d(1/\rho) + c_v dT = 0$, c_v the specific heat at constant volume, requires that the temperature increase ahead of the contact surface as the density decreases. These steep temperature and density gradients ahead of the contact surface may correspond to the surge-corona interface observed in the EUV, and the relatively cool, dense material behind the gradients may correspond to the surge material. After the pulse is removed, some of the material starts falling downward, due to gravitational forces, as shown by the negative velocities in Figure 7.17.

The vertical dashed line on the curves indicates the height at which the density drops to 2 percent of the base density, or $2 \times 10^9 \text{ cm}^{-3}$. This value was (arbitrarily) selected as being representative of the leading edge of the cool, dense region created by the pressure pulse. It is clear that the contact surface is not a good indicator of this quantity since it is embedded within the cool, dense material. The trajectories of the 2% base density level, contact surface, and the shock are summarized in Figure 7.18 for this case. As shown in the figure, the 2% base density indicator mimics the vertical motion of the contact surface in that it first moves upward and then (after $\sim 10 \text{ min}$) falls back down as the material below it heats up and becomes less dense—ultimately acquiring characteristics not representative of surge material.

Intuitively, one expects that more intense pulses will eject more material to greater heights, and that sufficiently intense pulses will eject material from gravitational confinement. To compare with such expectations, Steinolfson *et al.* (1978a) computed the effect of pulses of various strengths ($p/p_0 = 5$ to 30) and two kinds (thermal and adiabatic). The results are shown in Table 7.6 where $r_{\text{max}}^{\text{cs}}$ is the maximum height achieved for the contact surface, $r_{\text{max}}^{2\%}$ is the maximum height reached by the level at which the density falls to 2% of the base value, $t(r_{\text{max}}^{2\%})$ is the time at which the 2% density level reaches the maximum height, and $v_{\text{max}}^{2\%}$ is the maximum velocity of the 2% density level. The shock velocities are given for $t = 5 \text{ min}$. The results confirm our qualitative expectations: larger pressure pulses generate higher and faster surge ejections.

Finally, we find that "thermal" pulses—corresponding to rapid heating of the chromosphere—can account for the gross features of surges. "Adiabatic" pulses were less satisfactory. As Table 7.6 shows, adiabatic pulses produce significantly smaller ejection heights and velocities than do thermal pulses of equivalent p/p_0 . This results because the additional mass ejected in an adiabatic pulse is more retarded by gravitation. The adiabatic pulses produce more compression and lower temperatures at the contact surface than do thermal pulses.

The predicted surge acceleration is not in good agreement with Roy's (1973b) and Platov's (1973) observations, which show a steady acceleration of $\sim 1-5 \times g_\odot$. Hydrodynamic effects were not found to produce the rapid deceleration near the top of the surge trajectory found by Roy (1973b); Figure 7.17 shows that the deceleration is less than g_\odot at both the contact surface and the base density level. Acceleration during downward motion is less than freefall, in agreement with Roy's observation. The one event studied by Roy (1973b) that decelerated gravitationally was a limb event; those that decelerated more rapidly were disk events. The possibility that the apparent rapid deceleration is due to the leading edge of the surge becoming optically thin (suggested but discounted by Roy) should be carefully investigated. Finally, on the question of dynamics, it is interesting to note that Figure 7.17 shows that the velocity of the model surge



volume, requires that the density decreases. These contact surface may correspond, and the relatively cool, the surge material. After falling downward, due to Figure 7.17.

right at which the density this value was (arbitrarily) cool, dense region created is not a good indicator of material. The trajectories shock are summarized in this base density indicator at it first moves upward and below it heats up and is not representative of

It eject more material to will eject material from stations, Steinolfson *et al.* this ($\rho/\rho_0 = 5$ to 30) and own Table 7.6 where at r_{\max}^{25} is the y falls to 2% of the base el reaches the maximum density level. The shock qualitative expectations: ons.

to rapid heating of the rges. "Adiabatic" pulses ses produce significantly al pulses of equivalent in adiabatic pulse is more e compression and lower

ment with Roy's (1973b) celeration of $\sim 1.5 \times g_0$. id deceleration near the re 7.17 shows that the el the base density level. fall, in agreement with 973b) that decelerated more rapidly were disk on is due to the leading ut discounted by Roy) ion of dynamics, it is ility of the model surge

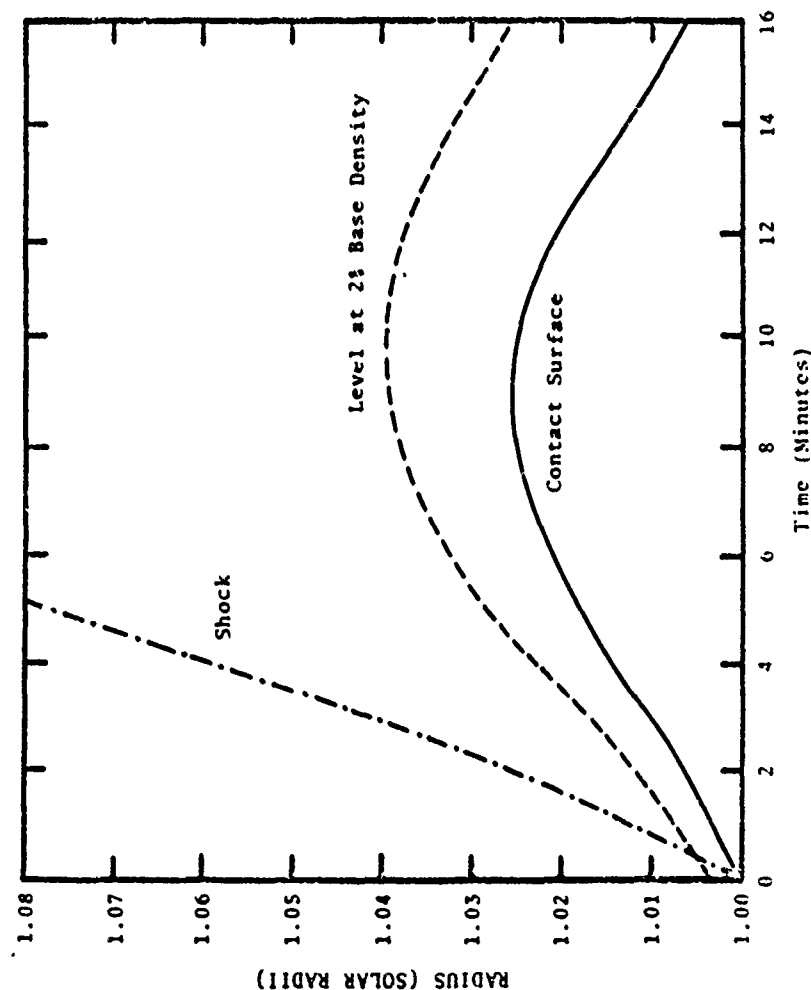


Fig. 7.18 Height vs time for the contact surface, the fluid level at which the density equals 2 percent of the initial base density and of the shock (Steinolfson *et al.*, 1978a).

TABLE 7.6
PHYSICAL PARAMETERS OF SIMULATED SURGES

Kind of Pulse	Physical Quantity*	Pulse Strength ρ/ρ_0 (pulse duration = 5 min)					
		5	10	15	20	30	
Thermal $\rho/\rho_0 = 1$	r_{\max}^{CS} ($\times 10^4$ km)	0.52	1.7	4.6	6.9	12.9	
	$\rho(t, r_{\max}^{CS})/\rho(0, r_{\max}^{CS})$	33	30	28	27	26.3	
	$T(t, r_{\max}^{CS})/T(0, r_{\max}^{CS})$	0.057	0.056	0.054	0.053	0.052	
	$r_{\max}^{2\%}$ ($\times 10^4$ km)	1.1	2.7	5.6	8.2	15.8	
	$t(r_{\max}^{2\%})$ (min)	6	9	12	16.5	22.5	
	$v_{\max}^{2\%}$ (km s^{-1})	29	61	128	140	191	
	v_{shock} (km s^{-1})	195	244	315	326	380	
Adiabatic $\frac{p}{p_0} = \left(\frac{\rho}{\rho_0}\right)^{1/\gamma}$	r_{\max}^{CS} ($\times 10^4$ km)		0.42	0.69	0.98		
	$\rho(t, r_{\max}^{CS})/\rho(0, r_{\max}^{CS})$		70	70	70		
	$T(t, r_{\max}^{CS})/T(0, r_{\max}^{CS})$		0.025	0.025	0.025		
	$r_{\max}^{2\%}$ ($\times 10^4$ km)		1.1	1.5	1.7		
	$t(r_{\max}^{2\%})$ (min)		5.1	6.1	6.7		
	$v_{\max}^{2\%}$ (km s^{-1})		30	41	46		
	v_{shock} (km s^{-1})		214	215	215		

* The superscript CS refers to the contact surface, and the superscript 2% refers to the level at which the density falls to 2% of the base density at $t = 0$; the density and temperature at the contact surface are given relative to the ambient values at that height; t is measured from the start of the pulse; and shock velocities are listed for $t = 5$ min.

reverses first near upper material.

Where they compare *et al.*'s surge model surge of height *et al.*'s model in 7 maximum heights that the one-dimensional is a spherically other differences results is only for

7.4.1. Introduction

Coronal transient Such mass ejection at least three events MacQueen, 1977, than one hundred white-light coronal

Coronal transients and 21. At least were imaged during early 1974 (Munro). Other classes are (12 events). The than 8 examples of

From the profile can be drawn. For Skylab transients low-latitude phenomena angles as they produce shocks.

Some quite rapid polarization with consistent with was a planar local plane.

7.4.2. Physical Processes

During the World transients are seen. The mass excess of the excess mass associated one-dimensional same speed as

reverses first near the solar surface; lower material starts draining back before the upper material.

Where they can be compared, the results of McClymont's and Steinolfson *et al.*'s surge models are qualitatively quite similar. Table 7.3 for McClymont's model surge of height 3×10^4 km and $\log \xi = 1.0$ can be compared to Steinolfson *et al.*'s model in Table 7.6 with initial thermal pulses $p/p_0 = 10$ and 15. Speeds and maximum heights are in good agreement between the two models, despite the fact that the one-dimensional flow in McClymont's model is confined to a tube where it is a spherically expanding shell in the model of Steinolfson *et al.* This and the other differences between the models may mean that the agreement between their results is only fortuitous.

7.4 CORONAL TRANSIENTS

7.4.1. Introduction

Coronal transients are mass ejections seen in the outer corona (see Figure 7.3). Such mass ejections were seen but their true nature went unrecognized during at least three eclipses between 1860 and 1941 (Shklovskii, 1965; Eddy, 1974; MacQueen, 1977). More recently, satellite-borne coronagraphs have imaged more than one hundred rapid changes in the appearance of the Thomson-scattering white-light corona.

Coronal transients were frequent near the minimum between solar cycles 20 and 21. At least 115 transient brightenings, including 77 definite mass ejections, were imaged during the Skylab coronagraph's 227 observing days in 1973 and early 1974 (Munro *et al.*, 1979). Some 20 of the ejections had a loop appearance. Other classes are amorphous clouds (13 events) and material injected into streamers (12 events). The remaining 32 events can be put into classes containing no more than 8 examples each; 14 events defy classification (Munro, 1977, 1978).

From the projected appearance of transients some inferences about their sizes can be drawn. Hildner (1977) indicates that, as seen from sun center, very few Skylab transients were larger than 65° in apparent extent, and they were relatively low-latitude phenomena. Transients appeared to subtend smaller and smaller solid angles as they progressed from 2 to $6 R_\odot$ contrary to what one might expect for shocks.

Some quite narrow transients are seen in the Skylab data. The variation of polarization with height for one of these, the event of 10 January 1974, is consistent with a nearly planar loop seen edge-on (Munro, 1978). If this event was a planar loop seen edge on, it was $\sim 0.8 R_\odot$ thick perpendicular to the loop's plane.

7.4.2. Physical Parameters

During the Workshop, Jackson and Hildner (1978) discovered and reported that transients are surrounded by broad regions of slightly enhanced coronal density. The mass excess over the pre-event background in a forerunner is typically 20% of the excess mass of its associated transient. These surrounding regions were associated one-to-one with transients and moved outward at approximately the same speed as their underlying transients. These regions, called forerunners by

Adiabatic $\frac{p}{p_0} = \left(\frac{\rho}{\rho_0}\right)^{1/\gamma}$	$r(t, r_{\max}^{2\%}) / (r_0, r_{\max}^{2\%})$ ($\times 10^4$ km)	$t(r_{\max}^{2\%})$ (min)	$u_{\max}^{2\%}$ (km s ⁻¹)	u_{shock} (km s ⁻¹)
	0.025	0.025	0.025	
	1.1	1.5	1.7	215
	5.1	6.1	6.7	215
	30	41	46	214

* The superscript 2% refers to the contact surface, and the superscript 2% refers to the level at which the density falls to 2% of the base density at $t = 0$; the density and temperature at the contact surface are given relative to the ambient values at that height; t is measured from the start of the pulse; and shock velocities are listed for $t = 5$ min.

Date	Mass (1) (10^{15} g)	Speed(2) (km s ⁻¹)	[B] (G)	Associations			GRG(4)	AR(2)	Energy(10^{30} erg)		Total
				H α (2)	Radio(2)	LDE(3)			Potential	Kinetic(5)	
Column 1	2	3	4	5	6	7	8	9	10	11	12
11 Jan 73 (A)(6)	17(6)	620(6)		FLA(6)	II;IVm; IVs(6)	—	—	—		8.2	10(6)
11 Jan (B)(7)	8(7)	750(7)		FLA(7)	II;IVm(7)	—	—	—		5.6	
10 Jun (8)	3.8	450		EPL II		Y	Y	Y	7.0(8)	1.0	8.0
24 Jun	2.5	135		EPL?			N			0.06	
9 Aug	>1.0	155		EPL	N	N	N	Y		> 0.03	
10 Aug(A)	0.9	50(1)					N			0.003	
10 Aug(B)(9)	4.2	400		EPL	N	N	N	Y	1.9(9)	0.8	2.7
13 Aug(A)	3.0	700		EPL	II	N	N	N		1.8	
13 Aug(B)(10)	2.2	250		EPL	N	Y	Y	N		0.2	3.4(18)
21 Aug(11)	5.0	525	2-4.5(12)	EPL	IV	Y	Y	Y		1.7	14.3(18)
26 Aug(13)	1.0(13)	150		EPL	N	N	Y(13)	N	2(13)	0.03	2.0
7 Sep(A)(14)	24(14)	>1000		FLA (DSD)	II,IV	Y	Y	Y	31(14)	>30	>61
7 Sep(B)	4.8	350		EPL	N	N	N	N		0.7	
10 Sep	3.2	400		EPL	N	N	N	Y		0.6	
15 Sep(15)	2.3	675	1.7(15)	FLA?	IV	N	N	Y?	3.4(15)	1.3	4.7
27 Oct	5.1	620		DB/FLA II;IV		Y	N			2.4	
3 Nov	>7.9	>1220		FLA II;IV		Y	Y	Y		14.7	
14 Dec	0.8	550		EPL	N	N	N	Y		0.3	
16 Dec	3.2	365		FLA	N	N	N	N		0.5	

19 Dec 73(16)	2.2	190		EPL	N	N	N	N	2.6(16)	0.1	2.7
10 Jan 74	1.6	400		FLA?	N	N	N	Y		0.3	1.6(18)
12 Jan	1.7	350		FLA		N	N			0.3	5.4(18)
17 Jan(17)	2.8	1000		EPL (FLA?)	II	N	Y	Y		3.5	12.8(18)

Event Date	Time (hr)	Latitude	Class	FLA (DSD)	II, IV	Y	Y	31(14)	>30	>61
7 Sep(B)	4.8	350	EPL	N	N	N	N		0.7	
10 Sep	3.2	400	EPL	N	N	N	N		0.6	
15 Sep(15)	2.3	675	1.7(15) FLA?	IV	N	N	Y?	3.4(15)	1.3	4.7
27 Oct	5.1	620	DB/FLA II;IV	Y	N	N			2.4	
3 Nov	>7.9	>1220	FLA II;IV	Y	Y	Y	Y		14.7	
14 Dec	0.8	550	EPL	N	N	N	Y		0.3	
16 Dec	3.2	365	FLA	N	N	N	N		0.5	

19 Dec 73(16)	2.2	190	EPL	N	N	N	N	2.6(16)	0.1	2.7
10 Jan 74	1.6	400	FLA?	N	N	N	Y		0.3	1.6(18)
12 Jan	1.7	350	FLA		N	N			0.3	5.4(18)
17 Jan(17)	2.8	1000	EPL (FLA?)	II	N	Y	Y		3.5	12.8(18)
21 Jan	3.6	60(11)							0.02	

FLA	8.2[8]	672[8]						17.2[2]	7.6[8]	16.5[5]
EPL	3.0[14]	420[14]						3.4[4]	0.9[14]	6.3[7]
A11	4.7[24]	474[24]						8.0[6]	3.1[24]	10.6[12]

NOTES

- Ito Associations: FLA = flare; EPL = eruptive prominence on the limb; DSD = dark surge on the disk; DB/FLA = disparition brusque followed by a flare (considered as an EPL event for the summaries at the bottom of the table).
- Radio Associations: II and IV refer to metric wave bursts reported in NOAA Solar-Geophysical Data: N means no reported burst.
- LDE Associations: Y implies the event is listed in Kahler's (1977) table of long-decay soft X-ray events, whereas N implies that event is unlisted.
- GRF Associations: Y implies the event is listed in Sheeley et al.'s (1975) table of gradual rise and fall events, whereas N implies the event is unlisted. The 26 Aug. event has a very weak GRF not listed by Sheeley et al. (1975).
- AR Association: Y implies the event can be associated with an active region; N implies the event was not associated with an active region.
- Numbers in parentheses refer to the papers listed below. Additional information about some events can be found in the papers indicated after the event dates.

1) Jackson and Hildner (1978)	6) Stewart et al. (1974b)	13) Hildner et al. (1975a)
2) Except as noted, these values are from Munro et al. (1978)	7) Stewart et al. (1974a)	14) Gosling et al. (1975)
3) Kahler (1977)	8) Hildner et al. (1975b)	15) Dulk et al. (1976)
4) Sheeley et al. (1975)	9) Gosling et al. (1974)	16) Schmahl and Hildner (1977)
5) Obtained assuming all the tabulated mass moves at half the tabulated speed	10) Rust and Hildner (1976)	17) Tousey (1975); Webb and Jackson (1979)
	11) Poland and Munro (1974)	18) Hildner (1977)
	12) Gergely et al. (1979)	

Jackson and Hildner, certainly arrive earlier at a given point in the corona than their associated transients. Jackson (1979) has inferred that a forerunner is in motion prior to the onset of its associated H α surface activity. This work is discussed in more detail in Chapter 2.

Table 7.7 lists 24 mass ejections for which some analysis has been carried out. The tabulated mass, in most cases taken from Jackson and Hildner (1978), is the excess mass in the field of view of the coronagraph as determined by the method described by Hildner *et al.* (1975b) and therefore includes the excess mass of the forerunner. For two reasons the listed values are lower-limit estimates for the mass lifted into the corona during the transient event. First, the lower corona is occulted, so that only mass above a certain height ($2 R_{\odot}$ in the case of the Skylab instrument and $3 R_{\odot}$ in the case of the OSO-7 instrument) is measurable. Second, the masses are determined assuming that the excess material was at the limb, where a minimum amount of material would give the observed brightness change. The mass expelled from the lower corona during mass ejections appears to escape to the interplanetary medium, and no obvious down draining of material has been observed in the outer corona.

The speeds of the transients' leading edges, taken primarily from Munro *et al.* (1978), are given in the third column of Table 7.7 and are determined by visual inspection of images of each event. Speeds for several of the events are quite poorly determined (\pm several hundred km s^{-1}) due to a paucity of observations, but a more typical uncertainty is $\pm 100 \text{ km s}^{-1}$. For those events which accelerate, an average speed is entered in the table.

Gosling *et al.* (1976) and Jackson (see Hildner, 1977) have shown that no events show strong decelerations. Figure 7.19, taken from Hildner (1977), shows speed versus height for 10 events. It is apparent from the figure that a strong initial acceleration is required to boost the mass from rest near the solar surface to its observed speed at $\sim 3 R_{\odot}$. For example, the leading edge of the 10 August event shows an average acceleration of 0.9 m s^{-2} from $\sim 460 \text{ km s}^{-1}$ at $3.5 R_{\odot}$ to $\sim 510 \text{ km s}^{-1}$ at $5.5 R_{\odot}$, while an average acceleration of 72 m s^{-2} is required for the leading edge to start from zero speed at $1 R_{\odot}$ and reach $\sim 450 \text{ km s}^{-1}$ at $3 R_{\odot}$.

Column 4 of Table 7.7 gives the magnetic field strengths which have been inferred from radio measurements of two transients. Unfortunately, the direction of the magnetic fields is not known. The magnetic field strengths indicate that the material within a transient is a low- β plasma ($\beta \equiv 2n_e kT / (B^2 / 8\pi)$); that is, the magnetic energy density dominates the thermal energy density in the plasma. For the 15 September event, Dulk *et al.* (1976) estimate $\beta \approx 0.007$ and suggest that the magnetic energy density exceeds the kinetic energy density as well.

Potential, kinetic, and total energy estimates for the transients are listed in columns 10, 11, and 12 of Table 7.7. The potential energy or work required to lift additional mass from the solar surface to achieve the observed excess mass distribution is determined by integration over the transient. Because the mass values are lower-limit estimates, the potential energy estimates obtained in this fashion represent lower limits. The listed kinetic energies assume that all the mass moves outward at half the speed of the leading edge. The potential and kinetic energy of material out of sight below the occulting disk are not included. Note that one-half of the work expended to lift material from the solar surface to infinity is expended to raise the material to $2 R_{\odot}$. In Table 7.7, neither the thermal

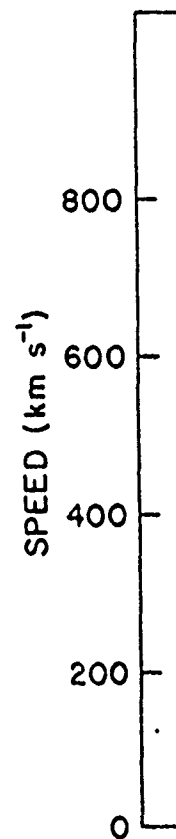


Fig. 7.19 Speeds is plotted at the connected to gu after the date in respectively. (Al)

point in the corona than that a forerunner is in activity. This work is dis-

sis has been carried out. and Hildner (1978), is the terminated by the method is the excess mass of the -limit estimates for the first, the lower corona is in the case of the Skylab) is measurable. Second, aterial was at the limb, erved brightness change. ctions appears to escape ing of material has been

arily from Munro *et al.* are determined by visual of the events are quite auctuity of observations, events which accelerate,

7) ¹ shown that no a H. er (1977), shows he figure that a strong t near the solar surface e of the 10 August km s^{-1} at $3.5 R_{\odot}$ to 72 m s^{-2} is required for $h \sim 450 \text{ km s}^{-1}$ at $3 R_{\odot}$. ngths which have been rtunately, the direction strengths indicate that $\Gamma(B^2/8\pi)$; that is, the sity in the plasma. For 07 and suggest that the is well.

transients are listed in gy or work required to b observed excess mass ent. Because the mass mates obtained in this ssume that all the mass b potential and kinetic are not included. Note n the solar surface to 7, neither the thermal

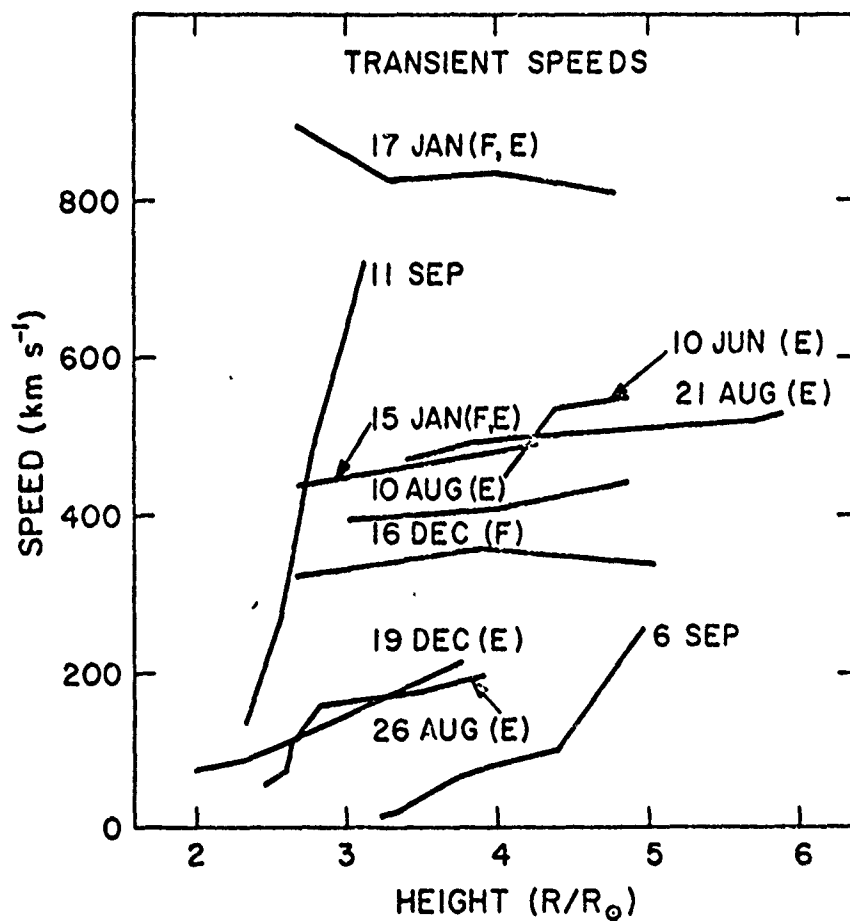


Fig. 7.19 Speeds of loop transients' leading edges versus distance from sun center. Each point is plotted at the mid-height of the interval used to determine it. The points for each event are connected to guide the eye. All but the January (1974) events occurred in 1973. An F or E after the date indicates that the ejection was associated with a flare or eruptive prominence, respectively. (After Gosling *et al.*, 1976, as revised by Jackson, 1977.)

energy supplied to or given up by the transient material, nor the magnetic energy contained within the volume, is listed. The thermal and magnetic energies delivered to the interplanetary medium by the flare of 5 September 1973, for example, are estimated by Dulk and McLean (1978a) as a few times 10^{30} erg and $>10^{31}$ erg, respectively, in Appendix B. The simulation of a transient described in Section 7.4.4 implies much larger thermal energies. Note that much of the thermal and magnetic energy of the expelled material resided in the material prior to the ejection and is convected, rather than created, by the event which caused the ejection.

The amount of energy liberated by a coronal transient in the form of radio bursts is negligible in comparison with kinetic, potential, and magnetic energies (Dulk and McLean, 1978b). The energy released by transients in the form of energetic particles is probably small but is unknown at the present time; an association between energetic particles and coronal transients will be mentioned below.

Because of their large energies and frequent association with flares, it is apparent that coronal transients play an important role in the flare process. The sizes and trajectories of flare-associated transients indicate that large volumes of the corona above the flare site are affected by a transient's passage. As indicated in Table 7.7, a great deal of energy, often comparable to the energy liberated in other manifestations of a flare, is necessary for production of a coronal transient.

The association between coronal transients and other forms of solar activity is traced by Munro *et al.* (1979) for transients observed from Skylab. For the 34 Skylab transients that can be definitely or probably associated with H α surface activity, only 8 were associated with phenomena far from an active region. That is, approximately 3/4 of all transients with associated H α activity apparently originated in or near active regions, though not all of the transients associated with active regions were accompanied by reported flares. In two cases, one originating in a spotless active region, the other adjacent to an active region, a prominence erupted followed by a flare in the same location. Even though these two transients were associated with flares, the timing implies that the flares were an effect of the eruption and coronal disturbance, not a cause.

There is a strong correlation between transients and H α activity such as brightening or movement. Considering those Skylab events that can be associated with H α phenomena, some half of the transients were associated with eruptive prominences or filament disappearances in the absence of flares, as shown by the value in Table 7.8. The other values in Table 7.8 give the fraction of transients in the presence or absence of events (shown by the row and column headings). Clearly, transients are more closely associated with eruptions than with flares.

The association between soft X-ray activity in the low corona and white-light, outer coronal transients is not yet clear. Kahler (1977) and Sheeley *et al.* (1975) found a close correspondence between coronal transients and soft X-ray brightenings of the low corona that had a long decay. Why the eruptions of coronal transients lead to long-lasting, soft X-ray enhancements in the lower corona (or conversely) is obscure, although Dryer, Steinolfson, Wu, and colleagues have presented simulations which require long-duration heating at the base of the corona. Little has been done to analyze individual soft X-ray events in conjunction with individual white-light coronal transients, though Rust and Hildner (1976) and Webb and Jackson (1979) have associated outward-moving, X-ray-emitting

for the magnetic energy
magnetic energies delivered
1973, for example, are
 10^{30} erg and $> 10^{31}$ erg,
not described in Section
each of the thermal and
material prior to the
event which caused the

it in the form of radio
and magnetic energies
transients in the form of
at the present time; an
events will be mentioned

with flares, it is apparent
process. The sizes and
volumes of the corona
indicated in Table 7.7,
generated in other mani-
transient.

forms of solar activity
on Skylab. For the 34
related with H α surface
active region. That
flare activity apparently
transients associated
s. In two cases, one
to an active region, a
on. Even though these
es that the flares were

tivity such as brighten-
be associated with H α
eruptive prominences
own by the value in
n of transients in the
nn headings). Clearly,
flares.

corona and white-light,
Sheeley *et al.* (1975)
d soft X-ray brighten-
eruptions of coronal
the lower corona (or
and colleagues have
at the base of the
events in conjunction
and Hildner (1976)
oving, X-ray-emitting

TABLE 7.8
ASSOCIATION BETWEEN TRANSIENTS, FLARES, AND ERUPTIVE PROMINENCES

	In the Absence of Flares	In the Absence of Eruptive Prominences	Regardless of Other Activity
Fraction of Transients Associated with: Eruptive Prominences or Flares	0.5	—0— 0.2	0.7 0.4

material with coronal transients seen later in white light in the outer corona. Sheridan *et al.* (1978) report that the very slow ($\sim 60 \text{ km s}^{-1}$) coronal transient of 21 January 1974 was detectable in the 80 MHz quiet-sun radiation formed at about $2 R_{\odot}$ as an enlargement of the emission region at the limb of the sun. Comparison of the remarkably similar properties of green-line events (De Mastus *et al.*, 1973) and transients lead Wagner and De Mastus (1977) to suggest that white-light mass ejections and the subset of green-line disturbances not associated with surges are but different observational manifestations of the same parent phenomenon (though practical difficulties have so far precluded observation of both manifestations of any particular event).

7.4.3. Origin of the Ejected Mass

The material ejected in a coronal transient appears to come from the low corona. With at least 5 transients, those of 16 June 1972 (Koomen *et al.*, 1974), 11 January 1973 (Stewart *et al.*, 1974a, b), 13 August 1973 (Rust and Hildner, 1976), and 17 January 1974 (Webb and Jackson, 1979), the lower corona changed markedly. The K-coronameter polarization X brightness (pB) signal, almost solely due to Thomson scattering of photospheric light from free electrons, showed enhancements, particularly at the positions of the legs of the loop transients, or depletions in the height range 1.1 to $1.8 R_{\odot}$ for all five events.

Using coronal models such as that of Saito, 1970 (or Saito *et al.*, 1977), it is possible to show that the corona typically has an abundant supply of material at heights below $1.3 R_{\odot}$, more than adequate to provide the excess material seen in coronal transients. Further, it has been shown that the eruptive prominence often associated with a coronal transient does not supply the majority of the mass in the coronal transient (Schmahl and Hildner, 1977; Poland and Munro, 1974; and Hildner *et al.*, 1975a).

7.4.4. Numerical Simulation of a Coronal Transient

During the Workshop, concurrently with the analysis of observations, numerical simulations of coronal transients were developed. These simulations have progressed from one-dimensional hydrodynamic codes to two-dimensional magneto-hydrodynamic models with adjustable initial temperature and density perturbations and almost arbitrarily selectable initial conditions. After the perturbation is introduced, the reaction of the corona is followed in time and space; then, the modeled configuration is compared with observations. It should be kept in mind that numerical solutions of all MHD models are nonunique. That is, the results depend upon a number of parameters: (i) initial equilibrium atmosphere, (ii) magnetic topology, and (iii) magnitude and duration of the pulse that drives the transient response. Effects of various magnetic topologies are illustrated in Figure 7.20.

Ad hoc pulses have been used heretofore (e.g., Wu *et al.*, 1978, and Steinolfson *et al.*, 1978b), but recently, Smith *et al.* (1977) provided a quantitative analysis (see Figure 7.21) of the soft (8–20 Å) X-ray emission from an intensely bright, coronal condensation associated with an eruptive prominence on 21 August 1973. The condensation remained at enhanced densities and temperatures for more than three hours. Values of T and n_e estimated by Smith *et al.* were used by Dryer, Nakagawa, Steinolfson, and Wu ("Dryer *et al.*") as a pressure pulse for simulating

Fig. 7.20 The enhancement $t = 10 \text{ min.}$ (b) with $\beta = 0.7$ (lines and for magnetic conf for $t = 0$ (dash

light in the outer corona. (km s^{-1}) coronal transient at-sun radiation formed at the limb of the sun. sun-line events (De Mastus us (1977) to suggest that disturbances not associated tions of the same parent precluded observation of

ime from the low corona. (et al., 1974), 11 January and Hildner, 1976), and corona changed markedly. tial, almost solely due to tions, showed enhance- tients, or depletions

n Saito et al., 1977), it is tant supply of material at ne excess material seen in rimp prominence often majority of the mass in the l and Munro, 1974; and

f observations, numerical se simulation have pro- wo-dimensional magneto- and density perturbations the perturbation is intro- space; then, the modeled d be kept in mind that hat is, the results depend tmosphere, (ii) magnetic that drives the transient ustrated in Figure 7.20. al., 1978, and Steinolfson ed a quantitative analysis from an intensely bright, ence on 21 August 1973. peratures for more than al., were used by Dryer, sure pulse for simulating

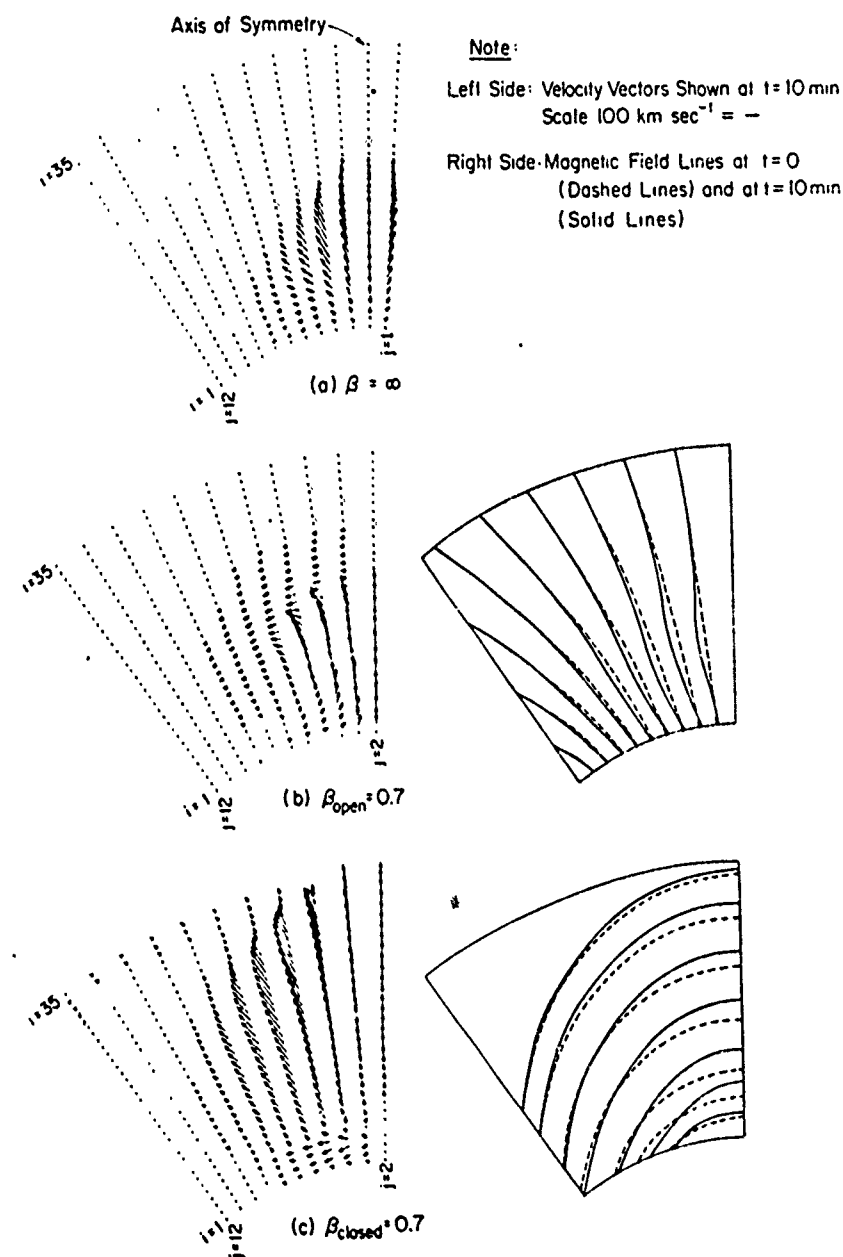


Fig. 7.20 The velocity and magnetic field changes resulting from an impulsive temperature enhancement ($T = 10 T_0$) of 5 s duration. (a) Velocity vectors in a nonmagnetic flow at $t = 10 \text{ min}$. (b) Velocity vectors and magnetic field lines in an open magnetic configuration with $\beta = 0.7$ (computed at $i = 1$, $j = 2$). Magnetic field lines are plotted for $t = 0$ (dashed) lines and for $t = 10 \text{ min}$ (solid) lines. (c) Velocity vectors and magnetic field lines in a closed magnetic configuration with $\beta = 0.7$ (computed at $i = 1$, $j = 2$). Magnetic field lines are plotted for $t = 0$ (dashed) lines and for $t = 10 \text{ min}$ (solid) lines (Wu et al., 1978).

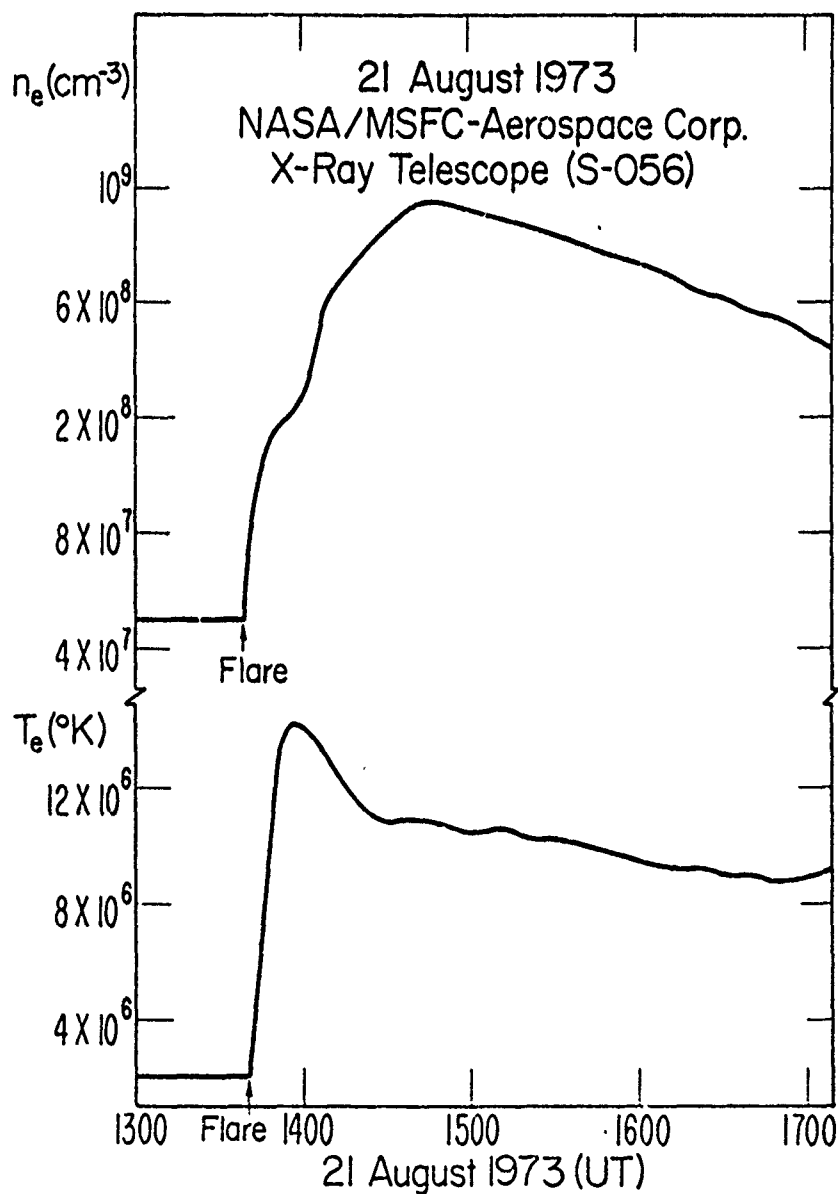


Fig. 7.21 Electron temperature and density vs time for the eruptive prominence event on 21 August 1973 as derived from the NASA/Marshall Aerospace Corporation X-ray experiment (Dryer et al., 1979).

the 21 August coronal event of Smith *et al.* (1977) velocity in the simulation.

The H α part of the eruptive prominence on the 21 August event commenced at 1.42 R_{\odot} and the photographs in H α were obtained at the total event was much leading edge of the wave extent of the moving radial extent than the Poland and Munro to

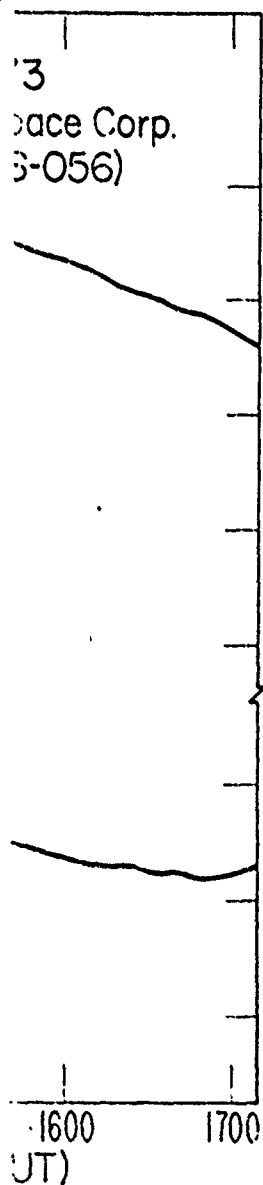
Temperature and density are shown in Figure 7.21. The temperature continues to rise (by Smith *et al.*, the temperature addition for a period of 10 minutes).

The simulation was that the energy and density were considered as low. Figure 7.21 shows long after the simulation radiative heating and (Smith *et al.*, 1978b), resistivity, and

The full set of electron wave phenomena (simulation procedures for their (1978), and Steinolfus. Instead, we briefly assumed, with the for 1 R_{\odot} : electron (or ion) density is lower than minimum density (Smith *et al.*, 1978b).

The assumed per cent centered at the equator portion of a six-lobed actual events is open match the properties of the event.

Two values of the ratio of gas pressure base and on the axis $\beta = 1.0$ case and $\beta = 0.1$ case. β increases rapidly with $\beta(1.0 R_{\odot}) = 0.1$, $\beta(1.0 R_{\odot})$ diminishes rapidly with values may be compared transient studied



sive prominence event on 21
orporation X-ray experiment

the 21 August coronal transient (Poland and Munro, 1976). The earlier simulation of Smith *et al.* (1977) used an input pressure pulse iteratively adjusted until the velocity in the simulation matched the observed velocity of the eruptive prominence.

The H α part of the 21 August event began with the eruption of a quiescent prominence on the northeast limb (Smith *et al.*, 1977) at ~ 1300 UT. X-ray emission commenced at ~ 1340 UT. At 1410 UT, the rising prominence was visible at $1.42 R_{\odot}$ and the observed velocity exceeded 200 km s^{-1} . The prominence was photographed in He II emission at 1441 UT. The first white-light observations were obtained at the same time, and, as Poland and Munro (1976) said: "... the total event was much larger than the H α and He II eruptive prominence. The leading edge of the white-light event was more than a solar radius above the farthest extent of the moving prominence material ... and was also much larger in latitudinal extent than the prominence." The thickness of the transient was estimated by Poland and Munro to be approximately $0.2 R_{\odot}$.

Temperature and density in the X-ray emitting region, as found by Smith *et al.*, are shown in Figure 7.21. The temperature peaks within 20 min, while the density continues to rise (by more than a factor of ten) for ~ 1 h after onset. According to Smith *et al.*, the temperature remained above 10^7 K for ~ 3 h. Energy and mass addition for a period of hours is strongly suggested.

The simulation was carried out only for the period 1340–1555 UT. This means that the energy and mass added to the model corona during the simulation must be considered as lower bounds to the amounts added to the real corona, since Figure 7.21 shows that the pressure at the base of the corona remained elevated long after the simulation ended. All macroscopic physical processes, except for radiative heating and losses (which are negligible as noted by Steinolfson *et al.*, 1978b), resistivity, and thermal conduction were considered.

The full set of equations, a description of the physics of MHD fast and slow wave phenomena (such as their steepening into shock waves), and the numerical procedures for their solution are discussed by Nakagawa *et al.* (1978), Wu *et al.* (1978), and Steinolfson *et al.* (1978b) and, therefore, are not repeated here. Instead, we briefly note that a polytropic (index = 1.08) solar atmosphere was assumed, with the following unperturbed conditions at the coronal base (taken as $1 R_{\odot}$): electron (or proton) density, $n = 5 \times 10^7 \text{ cm}^{-3}$; $T = 2 \times 10^6$ K. The model density is lower than the value usually given ($\sim 3 \times 10^8 \text{ cm}^{-3}$) for the equatorial minimum density (Saito 1970; Saito *et al.*, 1977).

The assumed perturbation is sinusoidal in space over a 10° latitudinal range centered at the equatorial plane and on the axis of a so-called "open" magnetic portion of a six-lobed hexapole. It is not clear whether the preeruption field in actual events is open or closed, and since simulations with closed fields cannot match the properties of transients, an open field was chosen.

Two values of the initial magnetic field strength, B , were chosen such that the ratio of gas pressure to magnetic energy density ($\beta \equiv 16 \pi n_e k T / B^2$) at the coronal base and on the axis of symmetry, was either 1.0 or 0.1. Thus, $B = 0.834$ G for the $\beta = 1.0$ case and $B = 2.64$ G for $\beta = 0.1$. In the initial (hexapole) field configuration, β increases rapidly with height. For the $\beta(1.0 R_{\odot}) = 1.0$ case, $\beta(1.8 R_{\odot}) = 5$; for $\beta(1.0 R_{\odot}) = 0.1$, $\beta(1.8 R_{\odot}) = 0.7$. The relative importance of the magnetic field diminishes rapidly with height in this initial configuration. The model values may be compared with an inferred $\beta(R > 1.8 R_{\odot}) = 0.035$ in a transient studied by Dulk *et al.* (1976). These authors also suggest

that $0.04 < \beta < 0.11$ is appropriate for the ambient medium ahead of the shock front for that event. Alternatively, Dulk and McLean (1978) point out that the value of β is not well known for the pre-event corona, and Kuijpers (1975) has suggested values of β ranging between 0.5 and 12.6 and of B ranging between 0.36 and 36 G. In view of the uncertainty in magnetic field strengths, the rather high β used in the simulations may possibly be within the range indicated by observations.

In Figure 7.22 the effect of the magnetic field is clearly seen: the plasma behind the shock moves several tenths of a solar radius farther in the weaker fields (hence, smaller induced Lorentz forces) for $\beta = 1.0$ than does the corresponding plasma in the stronger fields of the $\beta = 0.1$ case. The material motion behind the $\beta = 0.1$ shock is more constrained laterally by the larger $\mathbf{J} \times \mathbf{B}$ forces. In general, however, the shape of the peak density surface (particularly that for the $\beta = 0.1$ case) resembles the white-light coronal transient observed at 1441 UT by Poland and Munro (1976, Figure 1b).

The simulated shock and contact-surface (or piston) trajectories and velocities are compared to observations in Figure 7.23, drawn for the axis of symmetry. Note that the shock velocity responds very sensitively to the temporal variations in the input temperature and density at the coronal base (reference Figure 7.21), while the contact surface responds more gradually. According to the simulation, the plasma moved radially into the interplanetary medium and laterally in the corona close to the base.

Computer-generated plots of the local density ratio n/n_0 , instantaneous plasma velocity vectors \mathbf{V} , local temperature ratio T/T_0 , and excess-density $n - n_0$ contours are presented for the case $\beta = 0.1$ in Figure 7.24 for $t = 60$ min (i.e., 1440 UT). The subscript 0 refers to the local undisturbed state. Results for the $\beta = 1.0$ case are generally similar. In Figure 7.24, the density enhancement takes the shape of an expanding loop. This shape, and the maximum densification ratios of 5.9 and 4.9 for $\beta = 1.0$ and 0.1, respectively, are consistent with the observations of white-light transients (Hildner, 1977). The simulation's latitudinal extent, however, is much larger than observed.

Figure 7.24 also shows the local plasma velocity. The shock and contact surface (CS) velocities (along the axis) are listed for reference. The high velocities shown are due to the continued energy input at the coronal base. Note that most of the motion is radially outward, with some lateral movement along the base.

The region of elevated (up to 6.7 times the ambient value) temperature extends from the source of energy and mass addition up to the contact surface, as shown in Figure 7.24. The temperature is anticorrelated with the density. The shock increases the temperature only by a factor of ~ 2 , as indicated in the key for the half-tone graphical presentation.

The excess mass distribution along radial scans through the simulated excess-density distributions are shown in Figure 7.25 for the $\beta = 1.0$ case at $1410 \text{ UT} \leq t \leq 1455 \text{ UT}$ at the latitudes of $\pm 40^\circ$. The distribution shown is relevant to the plane of the sky in a two-dimensional model. Incorporating variation in the longitudinal dimension, i.e., a three-dimensional model, might change the plotted values appreciably.

Poland and Munro proposed an upper limit of $0.2 R_\odot$ on the thickness of the transient in the line of sight, and this value is used to compare observation and simulation of the 21 August 1973 event. Multiplication of the vertical scale of

21 Aug

Shock —

Max. Density —

Shock —

Max. Density —



Compu
"Field

Fig. 7.22 Simulation
 $\beta = 0.1$ (Dryer et al.)

dium ahead of the shock (1978) point out that the and Kuijpers (1975) has of β ranging between 0.36 strengths, the rather high indicated by observations. y seen: the plasma behind the weaker fields (hence, the corresponding plasma in motion behind the $\beta = 0.1$ forces. In general, however, hat for the $\beta = 0.1$ case) 1441 UT by Poland and

trajectories and velocities he axis of symmetry. Note temporal variations in the (see Figure 7.21), while to the simulation, the and laterally in the corona

n_0 , instantaneous plasma excess-density $n - n_0$ contours = 60 min (i.e., 1440 UT), esu for the $\beta = 1.0$ case tem... takes the shape of ification ratios of 5.9 and the observations of white- idinal extent, however, is

shock and contact surface The high velocities shown se. Note that most of the along the base. (value) temperature extends contact surface, as shown the density. The shock dicated in the key for the

ough the simulated excess- for the $\beta = 1.0$ case at he distribution shown is nal model. Incorporating limensional model, might

β_0 on the thickness of the compare observations and n of the vertical scale of

21 August 1973, 1440 UT

Shock ————— } $\beta = 1.0$
Max. Density Ratio - - - - }
Shock ————— } $\beta = 0.1$
Max. Density Ratio - - - - }

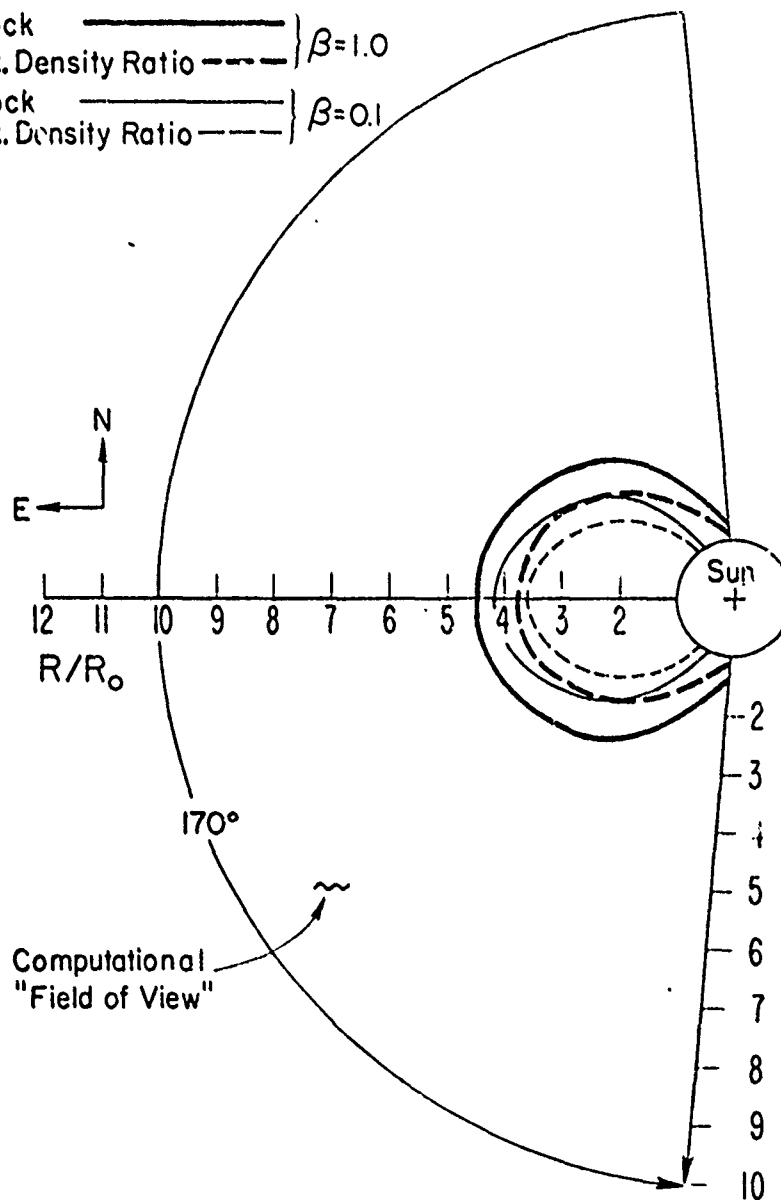


Fig. 7.22 Simulated shock and contact-surface positions at $t = 1440$ UT, for $\beta = 1.0$ and $\beta = 0.1$ (Dryer et al., 1979).

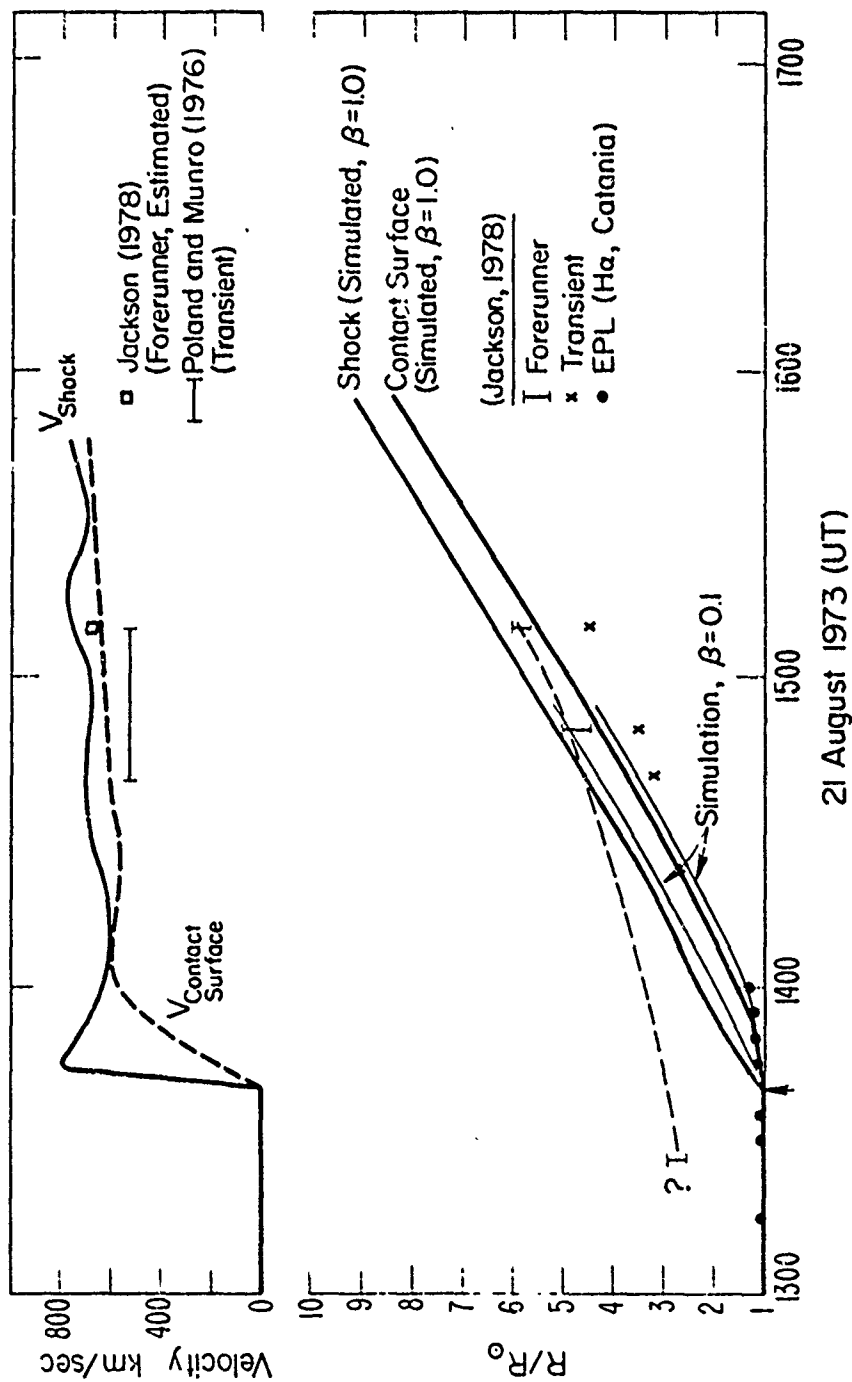


Fig. 7.23 Comparison (along the axis of symmetry) of the simulated shock and contact-surface trajectories and velocities with the observed Ha emission prominence and central white-light transient and forerunner (Dwyer et al., 1979).

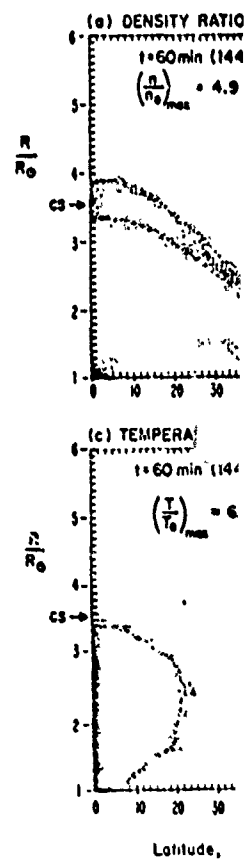


Fig. 7.24 Cross-section plasma properties for 11

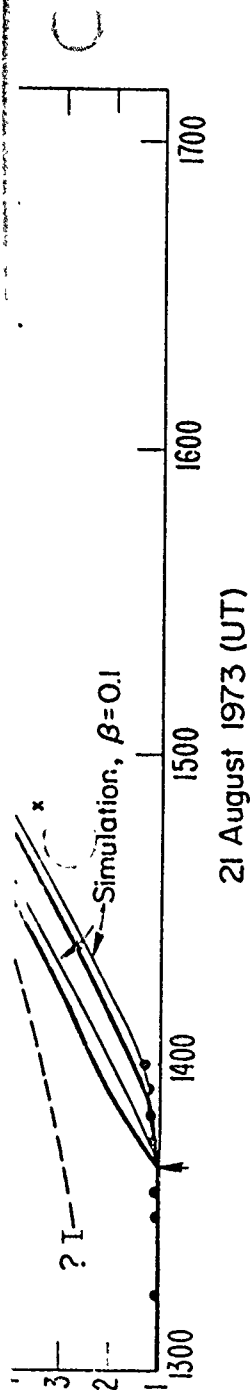


Fig. 7.23 Comparison (along the axis of symmetry) of the simulated shock and contact-surface trajectories and velocities with the observed flux eruptive prominence and coronal white light transient and forerunner (Dryer et al., 1979).

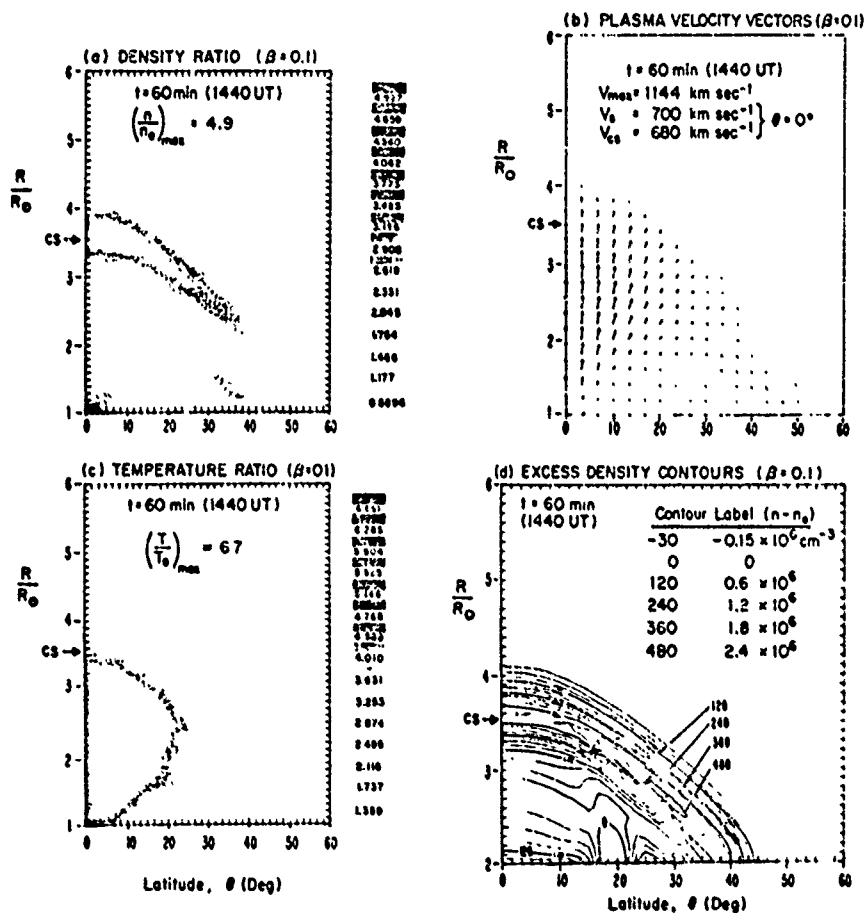


Fig. 7.24 Cross-sectional views (through one-half of the simulated "field of view") of various plasma properties for the case $\beta = 0.1$ (Dryer et al., 1979).

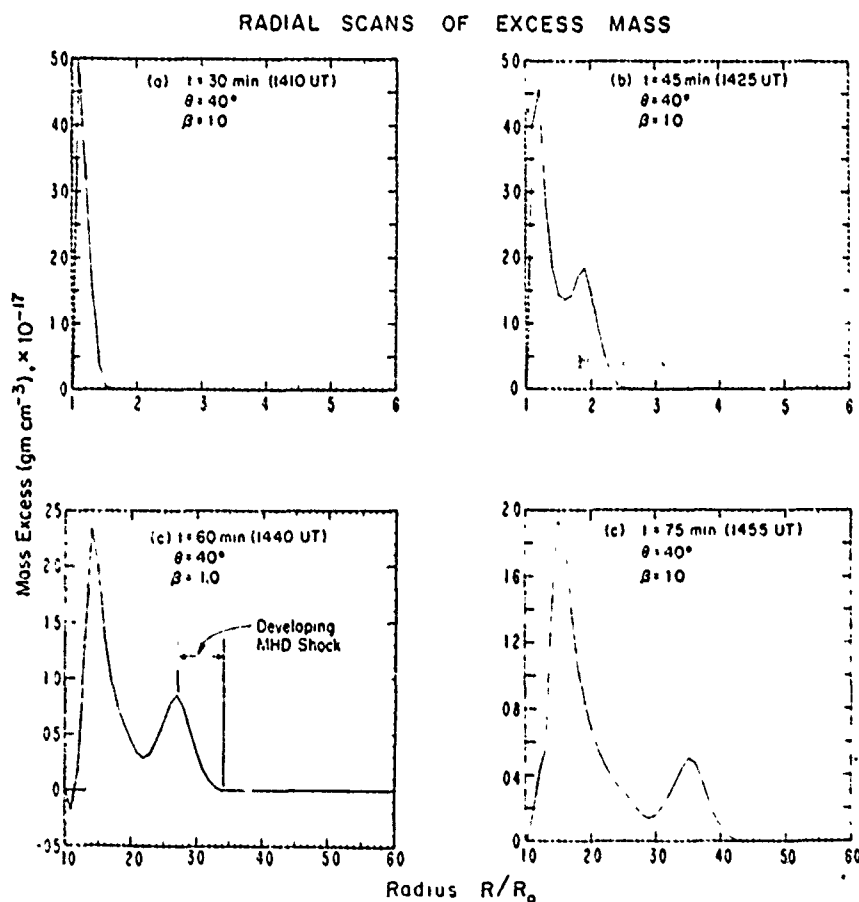


Fig. 7.25 Simulated excess-density scans at $\theta = +40^\circ$ (or -40°) at 15 min intervals for the case $\beta = 1.0$ (Dryer et al., 1979).

Figure 7.25 by 1.4×10^5 compared directly with the observed values are 9×10^6 electron transient's centerline.

The energies and can be quantitatively vations. The net mas line of sight at $\sim 15^\circ$ ness of 1.4×10^5 k 1 to $6 R_\odot$ and ± 85 the additional mass 2 to $6 R_\odot$ coronagraph.

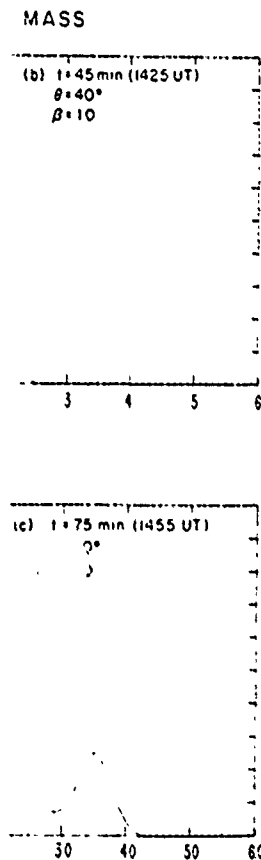
The various energy lation are shown ve distributed to the sol for the entire transie

Comparison of si the fields of view 1 (2 to $6 R_\odot$). Further within the actual tr. Tables 7.7 and 7.9 the energy modes: the energy and ex estimates for the d and observed mass e transient is much considering the diffe

7.4.5. Magnetic Loop

In contrast to the p in Section 7.4.4, an forces raise materia instability rather t necessary forces. Th observation (Dulk e at least semiquantit and Anzer (1978). l induced by emergi Steinolfson, Dryer, forcing studies have

At least three v outward have been the loop of the 15 inward (radial) gra around the transier near-constancy of 1 the loop the short the loop is a helix



at 15 min intervals for the

Figure 7.25 by $1.4 \times 10^{10} \text{ cm}$ results in simulated column densities, which can be compared directly with observational scans. For example, at $t = 1425 \text{ UT}$, there are $9 \times 10^6 \text{ electrons cm}^{-3}$ ($1.8 \times 10^{-17} \text{ g cm}^{-3}$) at $1.9 R_\odot$, 40° from the simulated transient's centerline.

The energies and mass added to the solar atmosphere by the simulated transient can be quantitatively compared to those inferred from Skylab coronagraph observations. The net mass addition over the whole transient per unit thickness along the line of sight at $\sim 1510 \text{ UT}$ is $1.7 \times 10^{11} \text{ g km}^{-1}$ for the $\beta = 1.0$ case. Using a thickness of $1.4 \times 10^5 \text{ km}$ ($0.2 R_\odot$), the total additional mass is $2.3 \times 10^{16} \text{ g}$ in the 1 to $6 R_\odot$ and $\pm 85^\circ$ computational field of view; this compares favorably with the additional mass of $5 \times 10^{15} \text{ g}$ given by Jackson and Hildner (1978) for the 2 to $6 R_\odot$ coronagraph field of view.

The various energies (magnetic, gravitational, thermal, and kinetic) in the simulation are shown versus time in Figure 7.26. The total excess energy which is distributed to the solar wind by $\sim 1510 \text{ UT}$ is $1.4 \times 10^{27} \text{ erg km}^{-1}$ or $3.9 \times 10^{32} \text{ erg}$ for the entire transient of thickness $0.2 R_\odot$.

Comparison of simulated with observed values is qualified by the differences in the fields of view between the computation (1 to $6 R_\odot$) and the coronagraph (2 to $6 R_\odot$). Further, neither the temperature nor the magnetic field distributions within the actual transient could be measured. Thus, the observed total energy in Tables 7.7 and 7.9 is the sum of kinetic and potential energies only, whereas all the energy modes are known for the simulation. Table 7.9 shows (at 1510 UT) the energy and excess mass densities and their totals for the simulation; it includes estimates for the observed kinetic plus potential energy (Hildner, 1977). Simulated and observed mass estimates are in fair agreement, but the energy of the simulated transient is much greater than that inferred from observations, even after considering the differing fields of view.

7.4.5. Magnetic Loop Models of Coronal Transients

In contrast to the pressure pulses which drive the numerical simulations described in Section 7.4.4, an alternative explanation of coronal transients is that magnetic forces raise material from the lower into the outer corona. That is, a magnetic instability rather than a thermodynamic (pressure) perturbation provides the necessary forces. This idea is in keeping with the low values of β inferred from observation (Dulk et al., 1976; Gergely et al., 1979), and has been put forward at least semiquantitatively by Dulk et al. (1976), Mouschovias and Poland (1978), and Anzer (1978). Numerical modeling of the coronal response to magnetic forces induced by emerging magnetic flux at the solar surface is being started by Steinolfson, Dryer, and Wu, but results are not yet available. The other magnetic-forcing studies have been analytic in nature.

At least three variations on the theme of magnetic forces driving transients outward have been put forward. Dulk et al. (1976) suggest that the mass within the loop of the 15 September 1973 event was ejected because there existed an inward (radial) gradient of axial (along the loop) magnetic field strength in and around the transient. To contain the material in the loop and account for the near-constancy of the width of the loop, they invoke a circumferential (around the loop the short way) magnetic field component. Thus, the resultant field within the loop is a helix; this field has a strength of approximately 1.7 G and a pitch

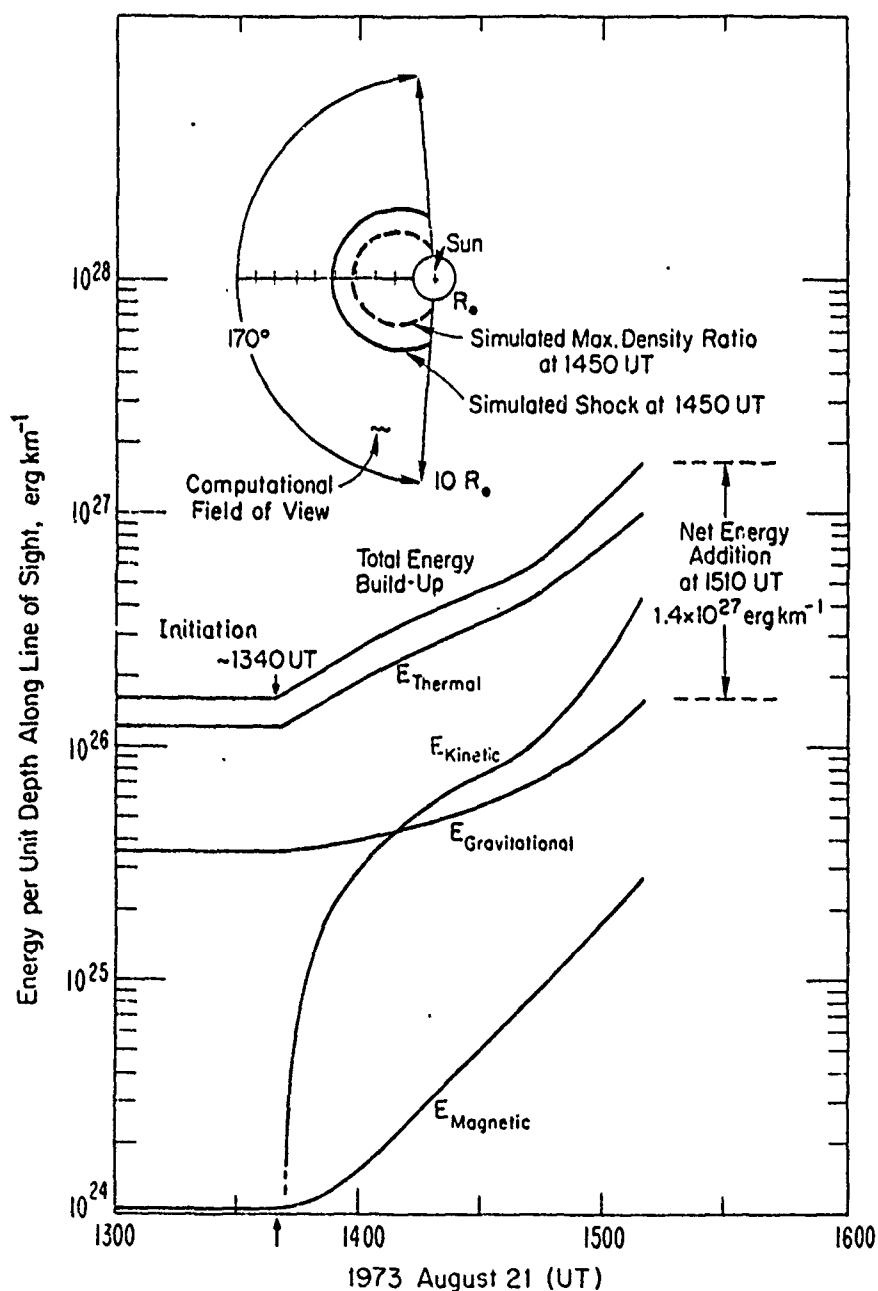


Fig. 7.26 Simulated temporal energy addition to the corona and solar wind. As this energy is transmitted to the solar wind (outside of the field of view), this value would of course, decrease to the final equilibrium state, which need not be the same as that existing at < 1340 UT (Dryer et al., 1979).

Comparison of Observed
Medium

Energy
Mode
(or Mass)

Magnetic

Thermal

Potential

Kinetic

Total

Total (assuming $0.2 R_{\odot}$
accounting for symmetry)

Kinetic plus
Potential only

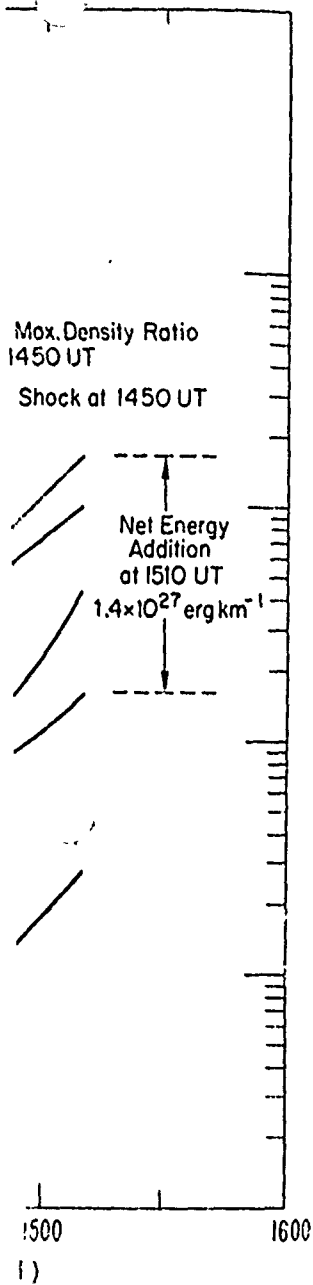
Same as above, assuming
depth and accounting for

Mass

Same as above, assuming
depth and accounting for

^aSimulated field-of-view:

^bObserved field-of-view:
(Poland and Munro, 1979)



and solar wind. As this energy
, this value would of course,
the same as that existing at

TABLE 7.9

Comparison of Observed and Simulated Energy and Mass Ejected into the Interplanetary Medium (per unit depth in km unless noted otherwise).

Energy Mode (or Mass)	Partial Values at $6R_{\odot}$ (1510 UT)	
	Simulated ^a	Observed ^b
Magnetic	2.7×10^{31}	—
Thermal	8.4×10^{30}	—
Potential	1.3×10^{30}	—
Kinetic	4.3×10^{30}	—
Total	1.4×10^{31}	—
Total (assuming $0.2 R_{\odot}$ depth and accounting for symmetry)	$3.9 \times 10^{33} \text{ erg}$	—
Kinetic plus Potential only	5.6×10^{30}	—
Same as above, assuming $0.2 R_{\odot}$ depth and accounting for symmetry	$1.6 \times 10^{33} \text{ erg}$	$1.43 \times 10^{31} \text{ erg}$
Mass	$8.4 \times 10^{10} \text{ g km}^{-1}$	—
Same as above, assuming $0.2 R_{\odot}$ depth and accounting for symmetry	$2.3 \times 10^{14} \text{ g}$	$5-8 \times 10^{13} \text{ g}$
^a Simulated field-of-view: $1-6 R_{\odot}; -85^{\circ} < \theta < +85^{\circ}$.		
^b Observed field-of-view: $2-6 R_{\odot}; -180^{\circ} < \theta < +180^{\circ}$ (Poland and Munro, 1976; Hildner, 1977; and Jackson and Hildner, 1978).		

angle of 30° when the top of the loop is at $3.1 R_\odot$. The ratio of thermal to magnetic energy within the loop at that height is approximately $\beta = 0.007$, indicating that the magnetic energy density dominates the thermal energy density.

The proposal of Mouschovias and Poland (1978) is somewhat different. Like Dulk *et al.* (1976), they suppose that a loop-shaped transient has within it a helical field, but they assume that the outward force arises from the circumferential rather than the axial field of the loop. The loop's curvature ensures that the circumferential field is stronger on the underside of the loop than at the top, and this magnetic field gradient tends to drive the transient outward. In the Mouschovias and Poland model, the ambient field around the loop is considered unimportant. For one transient (10 August 1973) observed rising from 2.2 to $5 R_\odot$ this model successfully reproduces the observations of the broadening and the change in the radius of curvature of the transient loop with time. For this event, they found that a helical field of strength ~ 1 G with pitch angle 50° is appropriate when the top of the loop is at $2 R_\odot$. At that height their model field strength and the observed density indicate that the ratio of thermal to magnetic energy density is $\beta \approx 0.2$. In agreement with Dulk *et al.* (1976), they conclude that a reasonable magnetic field configuration provides adequate forces to drive mass ejections outward, and, if transients are magnetically driven, the gas pressure is unimportant.

Anzer (1978) investigates a similar physical mechanism but uses the concept of a ring current carried by the loop of the transient. After several simplifying assumptions, Anzer finds that an average field strength of ~ 0.5 G is sufficient to drive the average transient outward as observed. Whereas Mouschovias and Poland assume a constant outward transient speed above $2 R_\odot$, Anzer obtains curves of velocity as a function of height. These curves show rapid initial acceleration followed by nearly constant velocity, successfully matching the observed speed vs height curves of Figure 7.20.

None of these three approaches addresses the question of the origin of the motion of coronal transients. Each of these three analytic treatments considers a coronal transient already in existence at the time the analysis and modeling begins, ignoring the coronal evolution leading to a transient.

7.5 SUMMARY AND CONCLUSIONS

7.5.1. Introduction

The objective of our study of mass ejecta was to discover what *forces* accelerate and channel bulk motion before and after flares. We also wished to know whether ejecta are incidental to flares or whether they reveal something fundamental about the energy-release process. We believe that good progress has been made toward realization of these goals.

7.5.2. Effects of Magnetic Forces

From our study of *sprays*, it appears that no purely hydrodynamic model will explain the motion. The classical picture of sprays is that of violently heated material tearing free of the magnetic fields. *Eruptive prominences*, on the other hand, have always been supposed to illustrate $\mathbf{J} \times \mathbf{B}$ forces. New observations by Tandberg-Hanssen, Martin, and Hansen removed the supposedly fundamental

distinction between *sprays* and *prominences*. Material originates in the corona, is confined within streamer envelopes. Part of the material is ejected in loops. Limb observations of which sprays seem to be those often noticed and eruptive prominences are those often noticed. Magnetic forces in the corona are important. If this picture is correct, the loops often are driven by unstable pinches (Mouschovias, 1978) and this has not been taken into account.

Work performed by Anzer indicates that at least some of the material is undergoing very little acceleration. This is evidence enough to insulate the material from the weakening during expansion.

Confirming earlier work, we find that *sprays* and *prominences* in that streamer lines, while eruptive prominences are driven by magnetic fields.

Dulk and McPherson find that the energy expelled from a coronal transient is at least as large as the kinetic energy of the transient. This suggests that coronal transients are magnetically driven.

Magnetic loop models suggest that the material is driven along a flux tube to the surface. The properties of coronal transients are important. However, neither a purely hydrodynamic model is completely adequate nor does it occur in a magnetic field in planetary space, but, it is clear that the magnetic field is important.

Current models of coronal transients are through which the material is driven and into the chromosphere.

Forerunners, the coronal transients, are driven by magnetic forces (Jackson and Hildner, 1979). That coronal mass is ejected from the surface, H α manifestations of coronal transients, 1979, and Chapter 2 of the total ejected mass and the gasdynamic forces.

R_0 . The ratio of thermal to approximately $\beta = 0.007$, indicating the thermal energy density is somewhat different. Like a transient has within it a helical structure from the circumferential curvature ensures that the circle loop than at the top, and outward. In the Mouschovias model is considered unimportant. from 2.2 to $5 R_0$, this model widening and the change in β . For this event, they found 50° is appropriate when the model field strength and the magnetic energy density is to include that a reasonable β to drive mass ejections gas pressure is unimportant. anism but uses the concept it. After several simplifying β of ~ 0.5 G is sufficient to eas Mouschovias and Poland R_0 . Anzer obtains curves of β with initial acceleration rate the observed speed

question of the origin of the analytic treatments considers the analysis and modeling agent.

NS

over what forces accelerate so wished to know whether something fundamental about mass has been made toward

hydrodynamic model will is that of violently heated prominences, on the other sides. New observations by supposedly fundamental

distinction between sprays and eruptive prominence. We conclude that (i) spray material originates in preexisting active-region filaments, and that (ii) spray material is confined within steadily expanding, loop-shaped (i.e., magnetically controlled) envelopes. Part of the material drains back down along one or both legs of the loops. Limb observations through very wide-band filters reveal that the clumps, of which sprays seem to be composed, are really linked in helical strands similar to those often noticed in eruptive prominences. The helical loop-shape of sprays and eruptive prominences leads us to conclude that these ejecta are confined by magnetic forces in large flux tubes as these tubes expand away from the solar surface. If this picture is more or less correct, the details remain uncertain because the loops often are difficult to observe in their full extent, and current models of unstable pinches (magnetic loops) (Sakurai, 1976; Anzer, 1978; Poland and Mouschovias, 1978) are rudimentary since the response of the solar atmosphere has not been taken into account.

Work performed by Schmahl and Hildner (1977) during the Workshop showed that at least some eruptive prominences endure to approximately $3 R_0$ while undergoing very little change in temperature or fine structure. We take this observation to be evidence for magnetic fields in the prominence which are strong enough to insulate the cool material from the surroundings even after considerable weakening during expansion into the outer corona.

Confirming earlier studies, we found that *surges* differ from eruptive prominences and sprays in that surges appear to follow *unmoving*, preexisting magnetic field lines, while eruptive prominences and sprays appear entrained in moving magnetic fields.

Dulk and McLean (1978a; Appendix B this volume) estimated that the magnetic energy expelled from the sun and deposited in the interplanetary medium by a coronal transient is about 10^{31} erg. They estimated the thermal energy at 10^{30} erg and the kinetic energy at 3×10^{30} erg. These results indicate that coronal transients are magnetically driven.

Magnetic loop models of coronal transients that invoke a helical magnetic field along a flux tube to drive the tube out were successful in matching some observed properties of coronal transients (Mouschovias and Poland, 1978; Anzer, 1978). However, neither a pressure-pulse model (see below) nor the helical-field-in-a-tube model is completely realistic. The pressure-pulse model presumes that transients occur in a magnetic configuration where the fields are weak and open to interplanetary space, but, in fact, transients occur above neutral lines where one can infer that the magnetic fields are closed and that $\beta(16\pi nkT/B^2) \ll 1$.

Current models of moving flux tubes ignore any possible effects of the ambient corona through which the loops rise. Too, the current flowing along a flux tube and into the chromosphere to sustain the helical field must evolve in a specified way.

Forerunners, the regions of enhanced density surrounding the main bodies of coronal transients, were discovered in the Skylab data during the Workshop (Jackson and Hildner, 1978). The existence and locations of forerunners indicate that coronal mass is moving outward well above and perhaps prior to the near-surface. Its manifestations of solar activity associated with transients (Jackson, 1979, and Chapter 2 this volume). Forerunners comprise approximately 20 percent of the total ejected mass. It is not clear whether they are driven by magnetic or gasdynamic forces.

7.5.3. Effects of Gasdynamic Forces

Sprays and eruptive prominences are correlated with coronal heating and with coronal transients. Therefore, we thought it reasonable to simulate the effects of a pressure pulse at the bottom of the corona. Theoretically, the sudden injection of heated material into the corona should cause a substantial disturbance, and coronal transients might be the manifestation of this disturbance.

Models of the effects of a sudden pressure pulse upon the corona were constructed, and many aspects of coronal transients were simulated. A two-dimensional, self-consistent, planar MHD model was used to simulate some features of the coronal disturbance associated with the eruptive prominence of 21 August 1973. We used experimentally determined values of density and temperature increases at the base of the disturbance as an extended thermodynamic pulse. The trajectory and the amount of mass and energy added to the corona resembled the values inferred from observations. However, increasing the magnetic field strength to the values indicated by observation, and placing the perturbation in a region of closed (rather than open) field greatly reduced the agreement between simulated and observed trajectories. With the (weaker than observed) simulated magnetic field reacting so as to slow plasma flow, the 21 August 1973 mass ejection was reproduced only at the expense of injections of possibly unrealistic levels of thermal energy. Perhaps this type of simulation describes those transients accompanying very large flares better than it describes the far more common transients accompanying eruptive prominences and small flares. In fact, the survey of coronal transients made during the Workshop (see Table 7.7) shows that, on average, coronal transients associated with flares are more massive, faster, and more energetic than those associated with eruptive prominences.

Observations in soft X-rays by Rust and Webb (1977) showed that the response of the X-ray emitting corona is similar for sprays and eruptive prominences. In the low corona, some of the material from the filament is heated to several million degrees and may appear as a *faint*, rapidly moving knot, but the major portion of the coronal heating does not begin until after the eruption is well on its way. This means that coronal transients associated with such events can hardly be started by the coronal heating, although it seems likely that mass flow within long-lived transients may be sustained by it.

Work by Martin, McKenna-Lawlor, Webb, and Rust indicated that some flare waves, or "Moreton" waves, may not be the purely MHD wave phenomena modeled by Uchida *et al.* (1973). Some kinds of flare waves (i.e., chains of successively illuminated points in the chromosphere) were associated with hot and cold ejecta originating in the flare center and travelling along field lines. Rust and Webb (1978) suggested that material was ejected from the flare site into magnetic flux tubes of various lengths. As the material traverses the tubes, the ejecta in the shorter flux tubes reach the surface at the far end of the tubes before material in the longer flux tubes. The appearance of the brightenings at the impact points at the far ends of the tubes is that of an excitation front moving across the solar disk from the flare site.

Numerical modeling by McClymont and Craig (1978) showed that a flare at one end of a rigid flux tube produces a shock whose speed depends almost entirely on the total energy input from the flare. The shock speed does not depend so strongly

on the density within or upon the duration deposition is sufficient from their sources with deposition which produced by a pressure pulse. Conversely, these result from its source to across the shock.

Extreme ultraviolet that the e-folding length surge-corona transition logarithmic gradient of This longitudinal, logarithmic the surge material out magnetic forces) if the temperature minimum the pressure there prior

The extreme ultraviolet surges do not heat the enhancement of the coronal heating with soft X-ray-emitting corona limits on temperature is increased by less than

During the Workshop techniques (McClymont employed impulsive modeling efforts are the chromosphere characteristics as seen in observations.

7.5.4. Concluding Remarks

As the Workshop progresses that understanding mass ejections. Even base, as for surges and constrains the nature perhaps, coronal trajectories forces.

The numerical MHD they can be until the the numerical MHD outward movement field is actually forced modeled.

with coronal heating and with
ble to simulate the effects of a
tically, the sudden injection of
antial disturbance, and coronal
nce.

Upon the corona were con-
simulated. A two-dimensional,
mulate some features of the
ominence of 21 August 1973.
ity and temperature increases
dynamic pulse. The trajectory
corona resembled the values
magnetic field strength to the
urbation in a region of closed
ment between simulated and
ed) simulated magnetic field
1973 mass ejection was repro-
unrealistic levels of thermal
ose transients accompanying
r more common transients
In fact, the survey of coronal
1977) shows that, on average,
n. re, faster, and more
ices.

77) showed that the response
eruptive prominences. In the
is heated to several million
t, but the major portion of
uption is well on its way.
such events can hardly be
likely that mass flow within

ist indicated that some flare
D wave phenomena modeled
(i.e., chains of successively
ted with hot and cold ejecta
lines. Rust and Webb (1978)
into magnetic flux tubes of
he ejecta in the shorter flux
before material in the longer
impact points at the far ends
ross the solar disk from the

S) showed that a flare at one
l depends almost entirely on
does not depend so strongly

on the density within the flux tube, on the size of the energy deposition region, or upon the duration of the energy deposition so long as the rate of energy deposition is sufficiently fast. This result allows one to model shocks at a distance from their sources without worrying too much about the details of the energy deposition which produced the shock. That is, one need not care if the shock was produced by a pressure pulse, a pure density pulse, a pure thermal pulse, etc. Conversely, these results imply that it is futile to use observations of a shock far from its source to ascertain the details of the energy deposition which produced the shock.

Extreme ultraviolet observations of *surges* during the Skylab mission showed that the e-folding length of intensity along the surge is the same in all layers of the surge-corona transition region (Schmahl, 1978). From these observations, the logarithmic gradient of pressure along the surge can be inferred for each layer. This longitudinal, logarithmic, pressure gradient is found to be sufficient to drive the surge material outward without invoking any other type of force (e.g., diamagnetic forces) if the heating extends deep into the chromosphere, almost to the temperature minimum. The pressure at the base of the surge is approximately twice the pressure there prior to the occurrence of the surge.

The extreme ultraviolet observations analyzed by Schmahl also indicate that surges do not heat the corona significantly. That is, there is only a slight, brief enhancement of the EUV corona at the time of a surge. This lack of significant coronal heating with surges is confirmed by Rust *et al.* (1977), who show that the X-ray-emitting corona above and around surges is enhanced so little that the upper limits on temperature and density changes are 0.4 MK above 2 MK or the density is increased by less than 5 percent.

During the Workshop, surges were numerically modeled with two quite different techniques (McClymont and Craig, 1978; Steinolfson *et al.*, 1978a), both of which employed impulsive heating low in the chromosphere. The results of the two modeling efforts are surprisingly similar and show that impulsive heating low in the chromosphere can yield ejections which have the same observational characteristics as surges. The validity of the models could be tested by specific observations.

7.5.4. Concluding Remarks

As the Workshop progressed, it became increasingly clear to the Team members that understanding the magnetic field is crucially important to understanding mass ejections. Even though an ejection might be driven by a pressure pulse at its base, as for surges and, perhaps, coronal transients, the magnetic field guides and constrains the motion. Ejections such as eruptive prominences, sprays, and, perhaps, coronal transients, appear to be both driven and guided by magnetic forces.

The numerical MHD simulations of transients have been carried about as far as they can be until the magnetic field is incorporated as an active agent. Until now, the numerical MHD models' magnetic field has tended to retard or delay the outward movement of the ejected material. Alternatively, perhaps the magnetic field is actually forcing the motion of the ejecta in ways that have not yet been modeled.

One area which frustrated the mass ejections Team is the general question of timing. For instance, is there a hard X-ray burst coincident with the beginning of a surge, in agreement with the predictions of the thermal-pulse models of surge initiation? As other examples: Are Type III metric radio bursts associated with surges? Do coronal transients' forerunners begin before their associated H α manifestation at the surface of the sun? Each of these timing questions requires new observations, but, when answered, will yield clues to the physical mechanisms at work in mass ejections.

Our present understanding of the relation between mass ejections and solar magnetic fields seems analogous to our understanding of solar flares and the magnetic field. In both cases it is apparent that the magnetic field must be the ultimate source of the energy which drives the observed phenomena. In both cases the magnetic field's three-dimensional configuration and temporal evolution are extremely difficult, if not impossible, to observe or deduce. In our view, the key to understanding mass ejections lies in the better understanding of solar magnetic fields.

- Altschuler, M. D., Lillie
Anzer, U.: 1978, *Solar*
Brown, J. D.: 1973, *So*
Bruzek, A.: 1969, in
North-Holland, Am
Bruzek, A.: 1972, *Sola*
Cox, D. P. and Tucker,
Craig, I. J. D. and McCl
De Mastus, H. L., Wagn
Dryer, M., Wu, S. T.,
Dulk, G. A. and McLea
Dulk, G. A. and McLea
Dulk, G. A., Smerd, S.
K. V., Robinson, R.
Eddy, J. A.: 1974, *Ast*
Ehlerman, F.: 1917, *As*
Emslie, G.: 1977, *Repr*
Foukal, P. V.: 1975, *S*
Gergely, T. E. and K
Gergely, T. E., Kuc
Giovannelli, R. and McC
Gosling, J. T., Hildner,
J. Geophys. Res. 75
Gosling, J. T., Hildner,
Solar Phys. 40, 439
Gosling, J. T., Hildner,
Solar Phys. 48, 389
Hansen, R. T., Garcia,
500.
Hildner, E.: 1977, in
Symp., Tel Aviv, Ju
Hildner, E., Gosling, J.
Hildner, E., Gosling,
1975b, *Solar Phys.*
Hildner, E., Gosling,
1976, *Solar Phys.* 4
Hirman, J., Losey, R.
Skylab Mission, Spa
Howard, R. A., Koon
Seal, R. T., Whitne
1976, NOAA World
Hyder, C. L.: 1967a, *So*
Hyder, C. L.: 1967b, *So*
Jackson, B. V.: 1977, *B*
Jackson, B. V.: 1978, p
Jackson, B. V.: 1979, p
Jackson, B. V. and Hild
Kahler, S.: 1977, *Astro*
Kahler, S. W., Hildner,
Kirshner, R. P. and Nov
Koomen, M. J., He
Kuipers, J.: 1975, 5

is the general question of
ident with the beginning of
small-pulse models of surge
radio bursts associated with
the their associated H α mani-
fying questions requires new
to the physical mechanisms

in mass ejections and solar
ing of solar flares and the
magnetic field must be the
phenomena. In both cases
of temporal evolution are
free. In our view, the key to
fing of solar magnetic fields.

REFERENCES

- Altschuler, M. D., Lilliequist, C. G., and Nakagawa, Y.: 1968, *Solar Phys.* 5, 366.
Anzer, U.: 1978, *Solar Phys.* 57, 111.
Brown, J. D.: 1973, *Solar Phys.* 29, 421.
Bruzek, A.: 1969, in de Jager, C. and Švestka, Z. (eds.) *Solar Flares and Space Research*, North-Holland, Amsterdam, p. 61.
Bruzek, A.: 1972, *Solar Phys.* 26, 94.
Cox, D. P. and Tucker, W. H.: 1969, *Astrophys. J.* 157, 1157.
Craig, I. J. D. and McClymont, A. N.: 1976, *Solar Phys.* 50, 133.
De Mastus, H. L., Wagner, W. J., and Robinson, R. D.: 1973, *Solar Phys.* 31, 449.
Dryer, M., Wu, S. T., Steinolfson, R. S., and Wilson, R. M.: 1978, *Astrophys. J.* 227, 1059.
Dulk, G. A. and McLean, D. J.: 1978a, Report to Skylab Solar Flare Workshop.
Dulk, G. A. and McLean, D. J.: 1978b, *Solar Phys.* 57, 279.
Dulk, G. A., Smerd, S. F., MacQueen, R. M., Gosling, J. T., Magun, A., Stewart, R. T., Sheridan, K. V., Robinson, R. D., and Jacques, S.: 1976, *Solar Phys.* 49, 369.
Eddy, J. A.: 1974, *Astron. and Astrophys.* 34, 235.
Ellerman, F.: 1917, *Astrophys. J.* 45, 298.
Emslie, G.: 1977, Report to Skylab Solar Flare Workshop.
Foukal, P. V.: 1975, *Solar Phys.* 43, 27.
Gergely, T. E. and Kundu, M. R.: 1974, *Solar Phys.* 34, 433.
Gergely, T. E., Kundu, M. R., Munro, R. H., Poland, A. I.: 1979, *Astrophys. J.* 230, 575.
Giovannelli, R. and McCabe, M.: 1958, *Australian J. Phys.* 11, 130.
Gosling, J. T., Hildner, E., MacQueen, R. M., Munro, R. H., Poland, A. I., and Ross, C. L.: 1974, *J. Geophys. Res.* 79, 4581.
Gosling, J. T., Hildner, E., MacQueen, R. M., Munro, R. H., Poland, A. I., and Ross, C. L.: 1975, *Solar Phys.* 40, 439.
Gosling, J. T., Hildner, E., MacQueen, R. M., Munro, R. H., Poland, A. I., and Ross, C. L.: 1976, *Solar Phys.* 48, 389.
Hansen, R. T., Garcia, C. J., Hansen, S. F., Yasukawa, E.: 1974, *Publ. Astron. Soc. Pacific* 86, 500.
Hildner, E.: 1977, in M. A. Shea et al. (eds.), *Proceedings of the L. D. de Feiter Memorial Symp.*, Tel Aviv, June, D. Reidel, *Astrophys. and Space Sci. Library* 71.
Hildner, E., Gosling, J. T., Hansen, R. T., and Bohlin, J. D.: 1975a, *Solar Phys.* 45, 363.
Hildner, E., Gosling, J. T., MacQueen, R. M., Munro, R. H., Poland, A. I., and Ross, C. L.: 1975b, *Solar Phys.* 42, 163.
Hildner, E., Gosling, J. T., MacQueen, R. M., Munro, R. H., Poland, A. I., and Ross, C. L.: 1976, *Solar Phys.* 48, 127.
Hirman, J., Losey, R., and Heckman, G.: 1975, *Prelim. Comp. of Flares Rep. During the Skylab Mission*, Space Environ. Lab., Boulder, CO.
Howard, R. A., Koomen, J. J., Michels, D. J., Tousey, R., Detwiler, C. R., Roberts, D. E., Seal, R. T., Whitney, J. D., Hansen, R. T., Hansen, S. F., Garcia, C. J., and Yasukawa, E.: 1976, NOAA World Data Center A for Solar-Terrestrial Phys. Rep. UAG-18A.
Hyder, C. L.: 1967a, *Solar Phys.* 2, 49.
Hyder, C. L.: 1967b, *Solar Phys.* 2, 267.
Jackson, B. V.: 1977, *Bull. Amer. Astron. Soc.* 9, 368.
Jackson, B. V.: 1978, personal communication.
Jackson, B. V.: 1979, in preparation.
Jackson, B. V. and Hildner, E.: 1978, *Solar Phys.* 60, 155.
Kahler, S.: 1977, *Astrophys. J.* 214, 891.
Kahler, S. W., Hildner, E., and van Hollebeke, M. A. I.: 1978, *Solar Phys.* 57, 429.
Kirshner, R. P. and Noyes, R. W.: 1971, *Solar Phys.* 20, 428.
Koomen, M. J., Howard, R. A., Hansen, R. T., and Hansen, S. F.: 1974, *Solar Phys.* 34, 447.
Kuipers, J.: 1975, *Solar Phys.* 44, 173.

- Kundu, M. R., Erickson, W. C., and Jackson, P. D.: 1970, *Solar Phys.* 14, 394.
- MacQueen, R. M.: 1977, personal communication.
- MacQueen, R. M., Gosling, J. T., Hildner, E., Munro, R. H., Poland, A. I., and Ross, C. L.: 1976, *Phil. Trans. Roy. Soc. London* 281, 405.
- Martin, S. F.: 1978, *Bull. Amer. Astron. Soc.* 10, 462.
- Martin, S. F. and Ramsey, H. E.: 1972, in P. S. McIntosh and M. Dryer (eds.), 'Solar Activity, Observations, and Predictions', *Progress in Astronautics and Aeronautics* 30, 370.
- McCabe, M.: 1971, *Solar Phys.* 19, 451.
- McCabe, M. and Fisher, R. R.: 1970, *Solar Phys.* 14, 212.
- McCabe, M. K., Riddle, A. C., and Hansen, R. T.: 1974, *Bull. Amer. Astron. Soc.* 6, 291.
- McClymont, A. N. and Craig, I. J. D.: 1978, Report to the Skylab Solar Flare Workshop.
- McKenna-Lawlor, S. M. P.: 1977, Report to the Skylab Solar Flare Workshop.
- Mouschovias, T. Ch. and Poland, A. I.: 1978, *Astrophys. J.* 220, 675.
- Munro, R. H.: 1977, *Bull. Amer. Astron. Soc.* 9, 271.
- Munro, R. H.: 1978, personal communication.
- Munro, R. H., Gosling, J. T., Hildner, E., MacQueen, R. M., Poland, A. I., and Ross, C. L.: 1979, *Solar Phys.* 61, 201.
- Nakagawa, Y., Wu, S. T., and Han, S. M.: 1978, *Astrophys. J.* 219, 314.
- Nakagawa, Y., Wu, S. T., and Tandberg-Hanssen, E.: 1975, *Astrophys. J.* 41, 387.
- Orrall, F. Q. and Schmahl, E. J.: 1976, *Solar Phys.* 50, 365.
- Pallavicini, R., Serio, S., and Vaiana, G. S.: 1977, *Astrophys. J.* 216, 108.
- Platov, Yu. V.: 1973, *Solar Phys.* 28, 477.
- Poland, A. I. and Munro, R. H.: 1974, *Astrophys. J.* 187, L85.
- Poland, A. I. and Munro, R. H.: 1976, *Astrophys. J.* 209, 927.
- Reeves, E. M., Huber, M. C. E., and Timothy, J. G.: 1977, *Applied Optics* 16, 837.
- Riddle, A. C.: 1970, *Solar Phys.* 13, 448.
- Riddle, A. C., Tandberg-Hanssen, E., and Hansen, R. T.: 1974, *Solar Phys.* 35, 171.
- Roy, J.-R.: 1973a, *Solar Phys.* 28, 95.
- Roy, J.-R.: 1973b, *Solar Phys.* 32, 139.
- Roy, J.-R. and Leparskas, H.: 1975, *Solar Phys.* 30, 449.
- Roy, J.-R. and Tang, F.: 1975, *Solar Phys.* 42, 425.
- Rust, D. M.: 1968, in Kiepenheuer, K. O. (ed.), 'Structure and Development of Active Regions', *IAU Symp.* 35, 77.
- Rust, D. M. and Hildner, E.: 1976, *Solar Phys.* 48, 381.
- Rust, D. M. and Webb, D. F.: 1977, *Solar Phys.* 54, 403.
- Rust, D. M., Webb, D. F., and MacCombie, W.: 1977, *Solar Phys.* 54, 53.
- Saito, K.: 1970, *Ann. Tokyo Astron. Obs.*, 2nd Series XII, 53.
- Saito, K., Poland, A. I., and Munro, R. H.: 1977, *Solar Phys.* 55, 121.
- Sakurai, T.: 1976, *Pub. Astron. Soc. Japan* 28, 177.
- Sawyer, C.: 1976, *Royal Astron. Soc. Canada J.* 70, 228.
- Schmahl, E. J.: 1977, Report to Skylab Solar Flare Workshop.
- Schmahl, E. J.: 1978, *Solar Phys.* (to be submitted).
- Schmahl, E. J., Foukal, P. V., Huber, M. C. E., Noyes, R. W., Reeves, E. M., Timothy, J. G., Vernazza, J. E., and Withbroe, G. L.: 1974, *Solar Phys.* 19, 337.
- Schmahl, E. and Hildner, E.: 1977, *Solar Phys.* 55, 473.
- Schmahl, E. J. and Hildner, E.: 1977, *Solar Phys.* 55, 473.
- Shea, M. A., Smart, E. F., and Wu, S. T. (eds.): 1977, Proceedings of the L. D. de Feiter Memorial Symp., Tel Aviv, June, D. Reidel, *Astrophys. and Space Sci. Library* 71.
- Sheeley, N. R., Jr., Bohlin, J. D., Brueckner, G. E., Purcell, J. D., Scherrer, V. E., Tousey, R., Smith, J. B., Jr., Speich, D. M., Tandberg-Hanssen, E., Wilson, R. M., De Loach, A. C., Hoover, R. B., and McGuire, J. P.: 1975, *Solar Phys.* 45, 377.
- Sheridan, K. V., Jackson, B. V., McLean, D. J., and Sulk, G. A.: 1978, *Proc. Astron. Soc. Australia* (in press).
- Shklovskii, I. S.: 1965, *Physics of the Solar Corona*, Addison-Wesley Publ. Co., Reading, Mass. (Figure 5, showing 1941 eclipse), p. 12.

- Smith, E. van P.: 1968.
- Smith, J. B., Jr., Spe.
- Solar Phys.* 52, 37.
- Smith, S. F. and Harv
- Steinolfson, R. S., Sch
- Steinolfson, R. S., W
- 225, 259.
- Stewart, R. T., Howa
- Phys.* 36, 219.
- Stewart, R. T., McCat
- Phys.* 36, 203.
- Švestka, Z.: 1976, *Sol*
- Tanaka, K.: 1976, *Sol*
- Tandberg-Hanssen, E.
- Tandberg-Hanssen, E.
- Tandberg-Hanssen, E.
- Solar and Solar-Fer*
- Tandberg-Hanssen, E.
- Tandberg-Hanssen, E.
- Teske, R. G.: 1971, *Sol*
- Tousey, R.: 1975, *Ast*
- Tucker, W. H. and K
- 621).
- Uchida, Y., Altschuler
- Vaiana, G. S., Van Sp
- 1977, *Space Sci. In*
- Valniček, B.: 1964, *Bu*
- Vorpahl, J. and Pope,
- Wagner, W.: 1975, per
- Wagner, W. J. and De N
- Warwick, J. W.: 1957,
- Webb, D. F.: 1978, Re
- Webb, D. F. and Jacks
- Westin, H.: 1969, *Solar*
- Wu, S. T., Dryer, M., M
- Wu, S. T., Dryer, M., N
- Zirin, H.: 1966, *The Sc*
- Zirin, H., Ingham, W., I

- Phys. 14, 394.
- Poland, A. I., and Ross, C. L.:
M. Dryer (eds.), 'Solar Activity,
'Aeronautics 30, 370.
- mer. Astron. Soc. 6, 291.
ab Solar Flare Workshop.
lare Workshop.
, 675.
- Poland, A. I., and Ross, C. L.:
9, 314.
ophys. J. 41, 387.
216, 108.
- ed Optics 16, 837.
- Solar Phys. 35, 171.
- Development of Active Regions',
54, 53.
, 121.
- Reeves, E. M., Timothy, J. G.,
337.
- eedings of the L. D. de Feiter
space Sci. Library 71.
D., Scherrer, V. E., Tousey, R.,
Wilson, R. M., De Loach, A. C.,
A.: 1978, Proc. Astron. Soc.
Wesley Publ. Co., Reading, Mass.
- Smith, E. van P.: 1968, *Nobel Symp. No. 9*, p. 137.
Smith, J. B., Jr., Spelch, D. M., Wilson, R. M., Tandberg-Hanssen, E., and Wu, S. T.: 1977, *Solar Phys.* 52, 379.
Smith, S. F. and Harvey, K. L.: 1971, in J. Macris, (ed.), *Physics of the Solar Corona*, p. 156.
Steinolfson, R. S., Schmahl, E. J., and Wu, S. T.: 1978a, *Solar Phys.* (submitted).
Steinolfson, R. S., Wu, S. T., Dryer, M., and Tandberg-Hanssen, E.: 1978b, *Astrophys. J.* 225, 259.
Stewart, R. T., Howard, R. A., Hansen, S. F., Gergely, T. E., and Kundu, M.: 1974a, *Solar Phys.* 36, 219.
Stewart, R. T., McCabe, M. K., Koomen, M. J., Hansen, R. T., and Dulk, G. A.: 1974b, *Solar Phys.* 36, 203.
Švestka, Z.: 1976, *Solar Flares*, D. Reidel, Dordrecht, Holland.
Tanaka, K.: 1976, *Solar Phys.* 47, 247.
Tandberg-Hanssen, E.: 1967, *Solar Activity*, Blaisdell, Waltham, Mass.
Tandberg-Hanssen, E.: 1974, *Solar Prominences*, Reidel, Dordrecht, Holland.
Tandberg-Hanssen, E.: 1977, in A. Bruzek and D. Durrant (eds.), *Illustrated Glossary for Solar and Solar-Terrestrial Physics*, D. Reidel, Dordrecht, Holland, p. 97.
Tandberg-Hanssen, E. and Malville, J. M.: 1974, *Solar Phys.* 39, 107.
Tandberg-Hanssen, E., Martin, S. F., and Hansen, R. T.: 1978, *Solar Phys.* (submitted).
Teske, R. G.: 1971, *Solar Phys.* 21, 146.
Tousey, R.: 1975, *Astrophys. and Space Sci.* 38, 327.
Tucker, W. H. and Koren, M.: 1971, *Astrophys. J.* 168, 283 (Erratum: *Astrophys. J.* 170, 621).
Uchida, Y., Altschuler, M. D., and Newkirk, G.: 1973, *Solar Phys.* 28, 495.
Valana, G. S., Van Speybroeck, L., Zombeck, M. V., Krieger, A. S., Silk, J. K., and Timothy, A.: 1977, *Space Sci. Inst.* 3, 19.
Valniček, B.: 1964, *Bull. Ast. Inst. Czech.* 15, 207.
Vorpahl, J. and Pope, T.: 1972, *Solar Phys.* 25, 347.
Wagner, W.: 1975, personal communication and *Solar Phys.* 45, 274.
Wagner, W. J. and De Mastus, H.: 1977, *Bull. Amer. Astron. Soc.* 9, 369.
Warwick, J. W.: 1957, *Astrophys. J.* 125, 811.
Webb, D. F.: 1978, Report to the Skylab Solar Flare Workshop.
Webb, D. F. and Jackson, B. V.: 1979, in preparation.
Westin, H.: 1969, *Solar Phys.* 7, 393.
Wu, S. T., Dryer, M., McIntosh, P. S., and Reichmann, E. J.: 1975, *Solar Phys.* 44, 117.
Wu, S. T., Dryer, M., Nakagawa, Y., and Han, S. M.: 1978, *Astrophys. J.* 219, 324.
Zirin, H.: 1966, *The Solar Atmosphere*, Blaisdell-Ginn, Waltham, Mass.
Zirin, H., Ingham, W., Hudson, H., and McKenzie, D.: 1969, *Solar Phys.* 9, 269.

b) Solar Flare Observations and Interpretation

Observational and interpretive studies have been a significant part of the research program. The first four papers are based on observations obtained by other people; in all cases, the low spatial and temporal resolution leaves much to be desired. The fifth paper is based on our new observations from Sacramento Peak Observatory (SPO); the conclusions from this paper are much more compelling, owing to their superior spatial and temporal resolution, as well as their coordination with the Solar Maximum Mission (SMM), the Air Force Solar Observing Optical Network (SOON), and other facilities.

The objective of this research is to determine the nature of the physical processes that heat the chromosphere during flares. The main results of these papers are:

1. At the peak of a small flare, much less energy was present in the form of accelerated protons than electrons.
2. During the major flare of 7 August 1972 the chromosphere was heated by a purely thermal process.
3. During a compact flare observed well from the SMM and SPO, proof was obtained that the hot flare plasma originated in the chromosphere.

i) ATM Evidence for a Low Nonthermal Proton/Electron

Energy Flux Ratio in Solar Flares

This paper, and the following one, are part of a program to infer the

properties of flares from their spectrum in the hydrogen Lyman- α line. In this flare we were able to establish an upper limit to the amount of energy in accelerated protons. The limit was interesting, because its value was much smaller than the energy in accelerated electrons. However, the result is only suggestive, since it is based on only a single good flare observation, and it is always possible that it is compromised by poor temporal and spatial coverage. Our attempts to do the problem better from SMM were rebuffed, and the observation was not made at all during the nine months of normal SMM operation, before its pointing system failed in late 1980. Whether or not it is possible to follow up with better observations in the near future is unknown at this time.

ATM EVIDENCE FOR A LOW NONTHERMAL PROTON/ELECTRON ENERGY FLUX RATIO IN SOLAR FLARES

RICHARD C. CANFIELD*

Department of Physics, University of California, San Diego

AND

J. W. COOK†

E. O. Hulburt Center for Space Research, Naval Research Laboratory

Received 1978 February 3; accepted 1978 April 18

ABSTRACT

We have carried out an observational search for asymmetry in the wings of $L\alpha$ during flares, produced by beams of nonthermal protons injected into the chromosphere from the corona as suggested by Orrall and Zirker. The data base is the ATM/Skylab EUV spectrograms from the NRL S082B spectrograph. We first discuss the asymmetries we would expect to be present in the normal thermal profile. We consider in detail the 1551 UT 1973 August 9 flare, observed during the nonthermal phase. In this flare only very small $L\alpha$ asymmetries are observed, not large enough to be statistically significant. We show that this result, combined with microwave radio data for information on nonthermal electrons, implies that the energy flux of nonthermal protons injected into the chromosphere at energies above 20 keV is less than approximately 2×10^{-2} that of electrons of the same energy range in the observed events.

Subject headings: Sun: chromosphere — Sun: flares — Sun: spectra — ultraviolet: spectra

I. INTRODUCTION

In a recent paper in this *Journal* Orrall and Zirker (1976) suggested that $L\alpha$ profiles from solar flares should show detectable asymmetry due to effects of nonthermal proton beams impinging on the solar chromosphere from above. They draw the following picture by analogy with that of the generation of hard X-rays by thick-target bremsstrahlung from downward-injected beams of nonthermal electrons (Brown 1971): Downward-injected fast nonthermal protons exchange electrons with ambient neutral hydrogen atoms, producing downward-moving nonthermal neutral hydrogen atoms. Some fraction of these atoms are excited or become excited and radiate $L\alpha$ photons. The effect on the flare $L\alpha$ profile, viewed from above, is a net redshift of the emission due to the nonthermal proton beam. Orrall and Zirker (1976) go on to show that this effect should be observable even if nonthermal protons carry only 1% of the total flare energy.

In this paper we present and interpret the results of our search for this proton-induced asymmetry, using data from the Naval Research Laboratory's S082B EUV slit spectrograph on ATM/Skylab.

* Supported by the Air Force Office of Scientific Research, Air Force Systems Command, USAF, under grant AFOSR-76-3071.

† Skylab Solar Workshop Postdoctoral Appointee, 1976-1977. The Skylab Solar Workshops are sponsored by NASA and NSF and are managed by the High Altitude Observatory, National Center for Atmospheric Research.

II. OBSERVATIONS

a) General

We began by making a visual inspection of $L\alpha$ on the original spectrograms. We considered those flares listed in the summary of NRL flare observations compiled by V. E. Scherrer (Packer *et al.* 1977). We visually inspected the data for those flares thought most likely to show the predicted asymmetry, i.e., those with proper exposure (20 s or more) obtained early in the flare, never later than 1 minute after the peak time of soft X-rays. This defines a group of 13 flares, none of which is associated with one of the 13 major proton ($E > 20$ MeV) events detected during ATM by the Goddard Space Flight Center cosmic ray experiments on IMP 7 and 8 (Lin 1977).

The visual inspection revealed only two types of asymmetry, neither of which bore an obvious resemblance to an impulsive-phase proton-induced effect. First, the core region of $L\alpha$, the central 1-2 Å, was often seen to be redshifted relative to the geocoronal feature, by an amount corresponding to Doppler velocities in the range $5 \text{ km s}^{-1} \lesssim v_D \lesssim 40 \text{ km s}^{-1}$. Second, the C I continuum with an edge near 1240 Å (discussed below) always appeared, both in flare and in active region spectra, if the exposure was sufficiently long. This feature, combined with the decreasing sensitivity of the instrument toward the blue, often created an apparent red-enhanced asymmetry, both in flares and in active regions. Since no flare showed visible effects of the type expected from the work of Orrall and Zirker (1976), we decided to select for

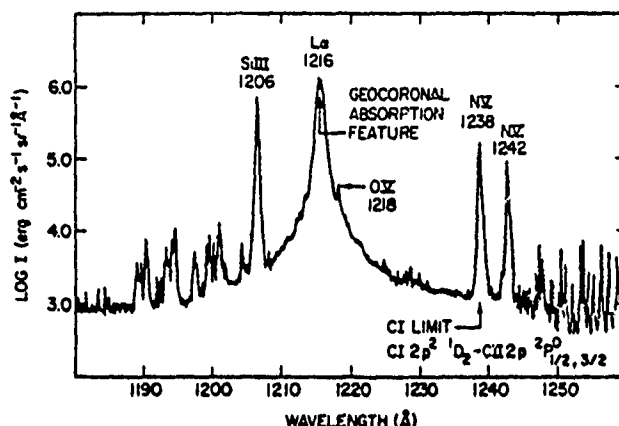


FIG. 1.—S082B spectra near $L\alpha$ of the 1973 September 2 flare. Exposure times of 2.5, 10, 40, and 160 s have been used to make this composite spectrum.

careful photometry a single flare that might provide the strictest upper limits on protons. This flare, that of 1551 UT 1976 August 9, is discussed in § IIc. We first discuss sources of asymmetry not related to the proton effect.

b) Other Asymmetry Sources

Figure 1 shows a composite spectrum for the flare observations of 1973 September 2 1904 UT. The center of $L\alpha$, associated with the geocoronal absorption feature, is indicated in order to make the asymmetry particularly evident. The asymmetry is due in part to the wavelength dependence of the source function. For this reason we measure the intensity of the spectrum in terms of the brightness temperature (see below).

An important source of asymmetry, intrinsic to $L\alpha$ itself, is due to Stark broadening. Recent experimental work by Fussmann (1975) shows a wavelength-dependent asymmetry of the wing absorption coefficient in the range of interest here. From 2 to 20 Å from line center the absorption coefficient has a red-excess asymmetry of from 8% to 14%. There is reasonably good agreement between these experimental results and theoretical work by Bacon (1977).

Shortward of 1240 Å is the ionization continuum of C I, whose limit corresponds to the transition $C\text{ I } 2p^2\ ^1D_2 - C\text{ II } 2p\ ^2P_{1/2, 3/2}$. This identification seems well established from the work of Feldman *et al.* (1976). We are aware of no experimental measurements of the value of the ionization cross section for this transition. Theoretical calculations by Henry (1970) indicate that it increases very slowly with decreasing wavelength below 1240 Å, reaching a broad maximum at $\lambda \approx 1160$ Å. Here its value exceeds its threshold value by only 1%, so it is nearly constant over $L\alpha$.

There are several other possible blends (excluding lines) that should be mentioned, though they could make only a small contribution. These include doubly excited H^- and ionization continua of Ca II and Ne II. The total continuous absorption for transitions to

doubly excited states of H^- has been calculated by Jacobs, Bhatia, and Temkin (1975). Two broad peaks are present in their calculations but are not present in a long exposure of an active region spectrum from S082B, furnished by Feldman (1977).

Ionization limits of continua of Ne II, suggested by Zirker (1977), correspond to the transitions Ne II $3p\ ^4D_{3/2, 5/2, 7/2} - Ne\text{ III } 2p\ ^4P_{0, 1, 2}$ and fall in the range 1200–1230 Å. Their actual importance is ruled out by the absence of the strongest Ne II lines in the 1600–2000 Å region in the S082B flare spectra furnished by Doschek (1977).

Ionization limits of continua of Ca II, suggested by Sandlin (1977), correspond to the transitions Ca II $3d\ ^2D_{3/2, 5/2} - Ca\text{ III } 3p\ ^4S_0$ and fall at 1218 Å. Using a 7 minute active region exposure which we scanned over the $L\alpha$ region during this project, we have observed weak Ca II lines from the series Ca II $3d\ ^2D_{3/2, 5/2} - H\text{ I } ^2F_{5/2, 7/2}$ up to $n = 19$, using line identifications from Sandlin (1977), and C I lines from the series C I $2p^2\ ^1D_2 - 2pnd\ ^1F_0$, up to $n = 29$ and C I $2p^2\ ^1D_2 - 2pnd\ ^3F_0$, up to $n = 22$, using line identifications from Feldman *et al.* (1976). We conclude from comparison of intensities of unblended Ca II and C I lines of equal n -value that the Ca II continua below 1218 Å contribute negligibly (less than $\frac{1}{4}$ the C I continuum intensity at 1239 Å) to the observed intensity of $L\alpha$.

c) The Flare of 1551 UT 1973 August 9

This flare was chosen for detailed study because it is the most likely flare of those observed by ATM to show impulsive-phase proton-induced asymmetries in $L\alpha$. Preflare spectra are available near the location at which the flare occurred, which reduces uncertainties due to calibration and blends. The flare occurred close enough to disk center (N8W49) to retain reasonably high Doppler sensitivity to downward motions. From the on-board $H\alpha$ monitor and from coalignment with S082A spectroheliograms, it appears that the S082B slit covered the point common to the two observed flare loops, the point most likely to show impact

phenomena. The loop orientation makes it unlikely that downward-injected protons spiraling along the field lines of the loop will have no significant line-of-sight component. Furthermore, a long-exposure (20 s) spectrogram was taken at 1554 UT, at which time solar microwave emission was detected at a variety of stations (*Solar-Geophysical Data* 1974). Data from two observatories (discussed below) show this radiation to be partially polarized, which is evidence for nonthermal electrons.

Information on pointing comes from the on-board H α monitor and from the NRL S082A slitless XUV spectroheliograph (Packer *et al.* 1977). Both H α and XUV images indicate that about $\frac{1}{2}$ of the $2'' \times 60''$ slit of the S082 spectrograph was filled by flare emission at 1554 UT.

Photographic photometry was carried out using the NRL Grant microdensitometer. We used the absolute calibration of Kjeldseth Moe and Nicolas (1977), which at L α is probably uncertain to a factor of 2 and is based on a calibration rocket flight (Nicolas 1977).

Figure 2 shows values of the measured brightness temperature of the red and blue wings of L α , with the blue wing reflected about line center. The upper part of the figure shows the flare spectrum; the lower shows the spectrum of the preflare active region. The axis, $\Delta\lambda$, is the distance from the center of L α , measured by the geocoronal absorption feature. The red wing is indicated by crosses, the blue wing by circles. The values of T_b in the blue wing for $\Delta\lambda > 15 \text{ \AA}$ should be ignored because of low photographic density on the original spectrograms.

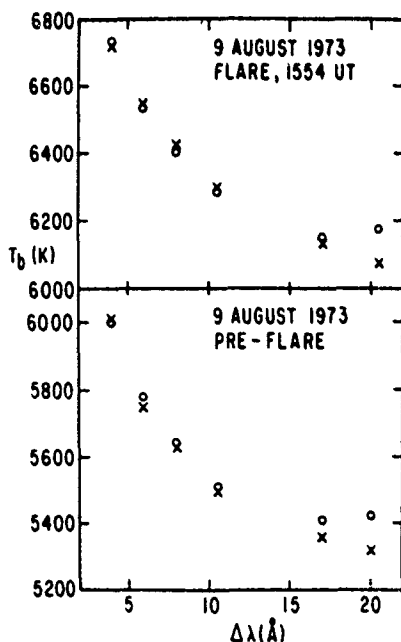


FIG. 2.—Observed brightness temperatures of the red wing (crosses) and blue wing (circles) of the L α line. The upper figure was obtained during the impulsive phase of the flare; the lower is the nonflaring active region.

The important feature of Figure 2 is that the flare profile shows a slight red-wing excess relative to the preflare profile, in the region $\lambda < 15 \text{ \AA}$, where the data are photometrically reliable. A useful measure of the change is the average value of $T_{\text{red}} - T_{\text{blue}}$ for the three points in the range $5 \text{ \AA} < \Delta\lambda < 12 \text{ \AA}$, which we call $\langle \delta T \rangle$ (we do not use the point at $\Delta\lambda = 4 \text{ \AA}$, since it primarily measures the Doppler shift of the core region). Before the flare $\langle \delta T \rangle = -17 \pm 12 \text{ K}$; during the flare $\langle \delta T \rangle = +20 \pm 5 \text{ K}$. Hence the flare red excess ΔT , defined by $\Delta T \equiv \langle \delta T \rangle_{\text{flare}} - \langle \delta T \rangle_{\text{preflare}}$, has the value $\Delta T = 37 \pm 17 \text{ K}$. Clearly, this value is not significant at the 3σ level. Four other profiles were obtained in the interval 1554–1556 UT, during which time the flare L α intensity decreases by a factor of 3. These profiles also do not show statistically significant ΔT values. For our calculations below, we characterize our observations by an upper-limit temperature excess $\Delta T = 35 \text{ K}$ at $\Delta\lambda = 8 \text{ \AA}$ in the red wing. At this value of $\Delta\lambda$, the observed flare brightness temperature, uncorrected for dilution with the active region, is 6425 K at 1554 UT.

III. INTERPRETATION

a) Protons

We now interpret quantitatively the observed (upper-limit) excess L α red-wing intensity, using Orrall and Zirker's (1976) calculations. We neglect factor-of-2 effects such as might exist because of deviations of the beam direction from the line of sight. The observed ΔT and T values correspond to an intensity enhancement $\Delta I \approx 5 \times 10^2 \text{ ergs cm}^{-2} \text{ s}^{-1} \text{ sr}^{-1} \text{ \AA}^{-1}$. Corrections must be made to obtain the enhancement to the flare itself, since the observed value is a mixture of both the flare and the neighboring active region. The slit was about $\frac{1}{2}$ filled by flare (see above); the rest was active region. The latter is so much fainter than the flare that it is negligible to an accuracy of a few percent. To obtain the flare enhancement itself, the correction for this dilution is thus simply a factor of 4. The excess red-wing radiation at $\Delta\lambda = 8 \text{ \AA}$ in the flare itself must be $\Delta I_{\text{flare}} \approx 2 \times 10^3 \text{ ergs cm}^{-2} \text{ s}^{-1} \text{ sr}^{-1} \text{ \AA}^{-1}$.

Orrall and Zirker (1976) calculate the excess red-wing radiation due to a specific incident energy flux. We measure the incident energy flux by \mathcal{F}_i^p , the energy of all injected nonthermal particles of species i above a specific energy η , per unit area and time. Orrall and Zirker (1976) assume a total incident energy flux of protons above 10 keV $\mathcal{F}_{10}^p = 10^7 \text{ ergs cm}^{-2} \text{ s}^{-1}$ and calculate the effect of various values of the exponent of the power-law proton-number distribution δ^p , specifically, $\delta^p = 2.5, 3.0$, and 4.0 . We adopt $\delta^p = 3$ as representative. For comparison with the electron results, for which a minimum energy of 20 keV rather than 10 keV is usually chosen, we want to know how much proton energy lies above 20 keV. Since $\mathcal{F}^p \propto \eta^{-\delta^p+2}$, Orrall and Zirker's (1976) calculation corresponds to $\mathcal{F}_{20}^p = \mathcal{F}_{10}^p/2 = 5 \times 10^6 \text{ ergs cm}^{-2} \text{ s}^{-1}$, for which they find that the excess red-wing photon flux Φ at $\Delta\lambda = 8 \text{ \AA}$ is $4 \times 10^2 \text{ ergs cm}^{-2} \text{ s}^{-2} \text{ sr}^{-1} \text{ \AA}^{-1}$. We now assume that the photon intensity scales

linearly as the proton energy flux. This leads to the result that the observed red-wing excess at $\Delta\lambda = 8 \text{ \AA}$ in $L\alpha$ corresponds to an input proton energy flux $\mathcal{F}_{20}^p \approx 2 \times 10^7 \text{ ergs cm}^{-2} \text{ s}^{-1}$.

b) Electrons

We now use the limited data available to infer the rate of energy deposition by nonthermal electrons. We are aware of no hard X-ray data for this flare, so we must use indirect means. Microwave radio data on this flare were obtained by many stations (*Solar-Geophysical Data* 1974). It is particularly important to look for evidence that the emission is nonthermal. Such evidence is provided by the polarization observed at 3.7 and 11.1 cm at the National Radio Astronomy Observatory (Alissandrakis and Kundu 1975) and at 2.9, 3.4, and 3.6 cm at the University of Bern (Mätzler 1977). The former data show polarization of several tens of percent when observations started, at 1555 UT. The latter show about 10% polarization from 1553:30 to 1556 UT. The differences in level of polarization are probably due to the higher spatial resolution of the former data.

Hudson, Canfield, and Kane (1978) show how observed correlations between microwave emission and X-ray emission (Kane 1974) can be used to infer the energy flux of thick-target nonthermal electrons (we note that this correlation has a scatter of about an order of magnitude). The electron spectral index γ^e is not known. There seems to be no reason to require $\gamma^e = \gamma^p$, so we adopt a typical observed X-ray spectral index $\gamma^e = 4$ (Datlowe, Elcan, and Hudson 1974). For this value of γ^e , Hudson, Canfield, and Kane (1978) give $P_{20}^e/S_R = 1.9 \times 10^{26}$, where P_{20}^e is the total power of injected electrons (ergs s^{-1}) and S_R is the observed impulsive 3–10 cm microwave flux density in solar flux units (sfu). For the August 9 flare at 1554 UT, the 3–10 cm flux density S_R was about 7 sfu (decreasing to 1 sfu by 1556 UT), so $P_{20}^e \approx 1.3 \times 10^{27} \text{ ergs s}^{-1}$ is implied. The area observed to brighten in $H\alpha$, to within a factor of 2, is $A = 1.2 \times 10^{18} \text{ cm}^2$. We assume that this is the electron impact area and that all electrons are precipitated into the chromosphere. The implied value of $\mathcal{F}_{20}^e = P_{20}^e/A \approx 10^9 \text{ ergs cm}^{-2} \text{ s}^{-1}$.

This value is probably uncertain by an order of magnitude. On one hand, the electron impact area is almost certainly less than the chromospheric $H\alpha$ area, perhaps by an order of magnitude. On the other hand, recent evidence from Brown, Canfield, and Robertson (1978), Emslie, Brown, and Donnelly (1978), and Donnelly and Kane (1978) indicates that only a small

percentage, perhaps 10%, of the electrons precipitate into the chromosphere. These two effects work in opposite directions.

c) Proton/Electron Energy Flux Ratio

From the results of §§ IIIa and IIIb, we see that the best value we can obtain from the ATM data for the ratio $\mathcal{F}_{20}^p/\mathcal{F}_{20}^e$ is an upper limit of 2×10^{-2} . Both \mathcal{F}_{20}^p and \mathcal{F}_{20}^e are good to only an order of magnitude, for the theoretical and observational reasons discussed above. In particular, one must bear in mind that our proton result is a null result. It may be true that neither protons nor electrons in the keV range are precipitating efficiently into the chromosphere during flares. We cannot exclude this alternative interpretation on the basis of our data.

IV. DISCUSSION

Our initial visual search of the ATM data does not reveal an effect with the properties expected for the impulsive-phase proton-induced $L\alpha$ asymmetry. Our careful quantitative study of the flare thought most likely to display the effect also shows no statistically significant result. When combined with data on electrons of comparable energy ($E > 20 \text{ keV}$), the results imply $\mathcal{F}_{20}^p/\mathcal{F}_{20}^e \lesssim 2 \times 10^{-2}$ for the latter flare. The upper limit is probably uncertain by an order of magnitude.

We have several suggestions for observational improvements in future studies. Particularly important are (1) improved data on the injection of electrons into the chromosphere, especially simultaneous $L\alpha$ wing data (including polarization) and hard X-ray images; (2) preflare and impulsive-phase coverage, to sort out alternative asymmetry sources; (3) obviously, comparison of the $L\alpha$ effect discussed here due to keV protons to the γ -ray effects due to MeV protons, with time dependence, threshold effects, first- and second-stage acceleration mechanisms, etc., kept in mind.

We are grateful to G. A. Doschek, U. Feldman, H. S. Hudson, M. R. Kundu, R. P. Lin, B. W. Lites, D. Neidig, G. Sandlin, and J. B. Zirker for help and advice. We thank Dr. A. Magun of the University of Bern for unpublished data, the existence of which was called to our attention by C. Mätzler. We appreciate M. Machado's comments on the manuscript. In carrying out this research, the authors have benefited considerably from their participation in the Skylab Solar Workshop Series on Solar Flares. The workshops are sponsored by NASA and NSF and are managed by the High Altitude Observatory.

REFERENCES

- Alissandrakis, C. E., and Kundu, M. R. 1975, *Solar Phys.*, **41**, 119.
 Bacon, M. E. 1977, *J. Quant. Spectrosc. Rad. Transf.*, **17**, 501.
 Brown, J. C. 1971, *Solar Phys.*, **18**, 489.
 Brown, J. C., Canfield, R. C., and Robertson, M. N. 1978, *Solar Phys.*, in press.
 Datlowe, D. W., Elcan, M. J., and Hudson, H. S. 1974, *Solar Phys.*, **39**, 155.
 Donnelly, R. F., and Kane, S. R. 1978, *Ap. J.*, **222**, 1043.
 Doschek, G. A. 1977, private communication.
 Emslie, A. G., Brown, J. C., and Donnelly, R. F. 1978, *Solar Phys.*, in press.
 Feldman, U. 1977, private communication.
 Feldman, U., Brown, C. M., Doschek, G. A., Moore, C. E., and Rosenberg, F. D. 1976, *J. Opt. Soc. Am.*, **66**, 853.
 Fussmann, G. 1975, *J. Quant. Spectrosc. Rad. Transf.*, **15**, 791.

- Henry, R. J. W. 1970, *Ap. J.*, **161**, 1133.
Hudson, H. S., Canfield, R. C., and Kane, S. R. 1978, in preparation.
Jacobs, V. L., Bhatia, A. K., and Temkin, A. 1975, *Ap. J.*, **200**, 239.
Kane, S. R. 1974, in *Coronal Disturbances*, ed. G. Newkirk (Dordrecht: Reidel), p. 105.
Kjeldseth Moe, O., and Nicolas, K. R. 1977, private communication.
Lin, R. P. 1977, private communication.
Mätzler, C. 1977, private communication.
Nicolas, K. R. 1977, Ph.D. thesis, University of Maryland.
Orrall, F. Q., and Zirker, J. B. 1976, *Ap. J.*, **208**, 618.
Packer, I. G., Patterson, N. P., Mango, S. A., and Tousey, R. 1977, *NRL Memorandum Rept.*, No. 3410 (Table 4.2 compiled by V. E. Scherrer).
Sandlin, G. D. 1977, private communication.
Solar-Geophysical Data: 1974, No. 354, Part 2 (February) (Boulder, CO: U.S. Department of Commerce), p. 17.
Zirker, J. B. 1977, private communication.

RICHARD C. CANFIELD: Department of Physics C-011, University of California, San Diego, La Jolla, CA 92093

JOHN W. COOK: Code 7163, Naval Research Laboratory, Washington, DC 20375

ii) Observed $L\alpha$ Profiles for Two Solar Flares:

14:12 UT 15 June, 1973 and 23:16 UT 21 January, 1974

This paper has as its objective to provide observed Lyman- α profiles for other studies. We will use these data at a later time, if no better data become available. The unique feature of these data is that they cover a wider band around the Lyman- α line than others, such as those that might have been obtained from SMM. This means that they are uniquely suited for determining the heating mechanism of the deep chromosphere during these flares, and are of good photometric quality. The main superficial result is that the profiles do not show any strong velocity fields, such as would be present if shocks or infalling material played a strong role in the chromospheric flare phenomenon. It has also been valuable to have the measurement of the amount of energy radiated in the Lyman- α line, since it shows that it is comparable to that in $H\alpha$. The latter will be a useful test of flare theories in the future, since the two lines come from much different depths in the chromosphere. Their ratio will probably be a sensitive test of the role of heating by accelerated particles. It has also provided a useful datum for our comparative studies of the spectra of flares and quasars (see below).

**OBSERVED $L\alpha$ PROFILES FOR TWO SOLAR FLARES:
14:12 UT 15 JUNE, 1973 AND 23:16 UT 21 JANUARY,
1974**

RICHARD C. CANFIELD

*Center for Astrophysics and Space Sciences, C-011, University of California, San Diego, La Jolla, Calif.
92093, U.S.A.*

and

M. E. VAN HOOSIER

E. O. Hulbert Center for Space Research, Naval Research Laboratory, Washington, D.C. 20375, U.S.A.

(Received 31 December, 1979)

Abstract. Photographic observations of the time development of the profile of the $L\alpha$ line of hydrogen during flares were obtained with the NRL spectrograph on ATM. The profiles for the 15 June, 1973 and 21 January, 1974 flares reported here cover both core and wings of the line. The time sequences begin before flare maximum, and continue well into the decay phase. Careful attention has been given to photometry and absolute calibration. In the case of the 15 June, 1973 flare, data are presented both first-order corrected and uncorrected for incomplete filling of the spectrograph slit by flaring material. Correction of the 21 January, 1974 flare was not possible. We discuss core symmetry and shift, and show that our observations imply integrated flare $L\alpha/H\alpha$ intensity ratios within a factor of two of unity for these two flares.

1. Introduction

Observations of the $H\text{ I } L\alpha$ line during solar flares are of two-fold importance. First, it is observed to be a major contributor to the radiative output of flares in the $T \sim 10^4$ K range (Canfield *et al.*, 1979). Second, its profile is a useful diagnostic for the determination of temperatures, densities and velocities in the chromosphere during flares. The only published work of this latter type is that of Lites and Cook (1979), who used observations of the $L\alpha$ wings from the NRL spectrograph on ATM, S082B, to construct a semi-empirical model of the chromosphere during the flare of 9 August, 1973. On the other hand, the $L\alpha$ profile of the quiet Sun and non-flaring active regions is fairly well observed. The best data on these profiles have been published by Bonnett *et al.* (1978), Lemaire *et al.* (1978), and Artzner (1978) from OSO-8 observations, and Basri *et al.* (1979) from HRTS rocket spectra. Semi-empirical models based on these data have been constructed by Gouttebroze *et al.* (1978) and Basri *et al.* (1979). In addition to the construction of semi-empirical flare chromospheres, observations of $L\alpha$ profiles during flares can also be used to test theoretical models by comparing the profiles predicted by these models to the observations. This approach has been applied to only $H\alpha$ to date, by Canfield and Athay (1974), Canfield (1974), Kostyuk (1976), and Brown *et al.* (1978).

The purpose of this paper is to provide observations of the core and inner wing regions of $L\alpha$ during two flares, for the applications discussed above. These data

include the $L\alpha$ rise, maximum, fall and post-flare phases. These are the first such data; the only previously published flare $L\alpha$ data, the ATM S082B data of Lites and Cook (1979), did not include the line core and did not begin until one minute after soft X-ray maximum. In the present paper we have chosen to examine flares for which the overexposure in the line core was not prohibitively severe, and we have used a reduction procedure designed to circumvent systematic errors due to a high level of exposure.

2. Observations

Our observations were made with the Naval Research Laboratory's S082B slit spectrograph flown on Skylab, described in detail by Bartoe *et al.* (1977). This instrument, which was not stigmatic, photographically recorded the spectrum of all radiation that entered the $2'' \times 60''$ slit. The spectral resolution, full width at half-maximum, was approximately 0.07 \AA at $L\alpha$, including instrumental, film and microdensitometer effects.

The flares of 14:12 UT 15 June, 1973 and 23:16 UT 21 January, 1974 have been discussed in many places, including the bibliography of McGuire (1976) and the proceedings of the Skylab Solar Flare Workshop (Sturrock, 1980).

The 15 June flare was a large event, and $H\alpha$, soft X-rays, ionospheric effects and radio bursts are well documented in *Solar Geophysical Data* (1973, 1974). The $H\alpha$ flare, which many observatories reported, took place in McMath 12379 at central meridian distance $r/r_{\odot} \sim 0.58$. It started about 14:04 UT, peaked at about 14:12 UT, and ended about 15:00 UT. $H\alpha$ classifications ranged from 1N to 2B. The Solrad-9 soft X-ray time history was very similar, with the peak flux at 14:13 UT.

Our flare observations began during the soft X-ray rise phase, at 14:11:37 UT, and continued until 14:30:03 UT. Table I summarizes the spectra we used for our 15 June flare profiles. For each exposure we list the time and duration. The time is the universal time at the middle of the exposure. The strip numbers identify the individual spectrum in the NRL data file, and are useful for relating our results to those of other authors on other aspects of the same flare. The spectra are grouped in sets, identified by a letter code. Each set consists of a series of four or five exposures, each differing from the next by a factor of four in exposure duration. This permits us to cover the wide dynamic range of intensity over the core and inner wings of $L\alpha$. Set A was obtained before $H\alpha$ flare maximum. Sets B and C coincide approximately with the $H\alpha$ and soft X-ray maximum. The post-flare spectra are those of set H.

The spacecraft pointing relative to the flare, which was maintained throughout sets A through G, can be determined by $H\alpha$ slit jaw monitor pictures. The orientation of the spectrograph slit, which has been shown by Brueckner (1975, 1976), was such that much of the slit was located *between* the two brightest parts of the flare. Only one end of the slit crossed part of a ribbon, which was of only moderate brightness in $H\alpha$. For purposes of estimation of the absolute intensity of the flare ribbon region, we assume below that only one-third of the slit was filled by flaring material. This

TABLE I
Details of the exposures of the 15 June, 1973 flare

Set	Time (UT)	Duration (s)	Strip
A	14:11:37	0.31	1B164-3
	14:11:37	1.25	1B164-4
	14:11:41	5.0	1B164-5
	14:11:54	20.0	1B164-6
B	14:12:04	0.31	1B164-7
	14:12:05	1.25	1B164-8
	14:12:10	5.0	1B165-1
	14:12:23	20.0	1B165-2
C	14:12:49	0.31	1B165-7
	14:12:50	1.25	1B165-8
	14:12:50	5.0	1B166-1
	14:13:08	20.0	1B166-2
D	14:13:19	0.31	1B166-3
	14:13:20	1.25	1B166-4
	14:13:23	5.0	1B166-5
	14:13:35	20.0	1B166-6
E	14:18:08	1.25	1B168-3
	14:18:11	5.0	1B168-4
	14:18:24	20.0	1B168-5
	14:19:14	80.0	1B168-6
F	14:22:11	1.25	1B169-3
	14:22:14	5.0	1B169-4
	14:22:27	20.0	1B169-5
	14:23:16	80.0	1B169-6
G	14:26:46	0.31	1B171-7
	14:26:47	1.25	1B171-8
	14:28:21	5.0	1B173-4
	14:28:34	20.0	1B173-5
	14:29:24	80.0	1B173-6
H	15:21:57	2.5	1B176-4
	15:22:08	10.0	1B176-6
	15:22:42	40.0	1B176-8
	15:25:01	160.0	1B177-2

estimation is clearly subjective to some extent, since a continuous distribution of intensities is actually present.

The 21 January flare was small, though some modest amount of documentation appears in *Solar Geophysical Data* (1974). A single observatory reported the $H\alpha$ flare: start time 23:07 UT, maximum at 23:20 UT and end at 23:51 UT in McMath 19325. Solrad-9 missed the start of the flare, but observed the soft X-ray maximum at 23:21 UT. A brief hard X-ray burst was observed by the UCSD spectrometer aboard OSO-7, at 23:15 UT (see Brueckner, 1976); a pre-flare rise in soft X-rays was observed in progress at 23:11 UT, but data gaps precluded identification of

either soft X-ray start or maximum with this instrument. An SID was observed to start at 23:15 UT, with maximum at 23:23 UT, ending at 00:26 UT.

Our observations began at 23:13:44 UT and continued until 23:45:13 UT. Table II summarizes the spectra we used for our 21 January flare profiles. The data used for the flare profiles are all from the flare rise and flare maximum period (Set *F* is approximately coincident with $H\alpha$ maximum); set *G* was originally intended to be used for the post-flare spectrum, though the $H\alpha$ data show that the flare was not yet over.

No slit-location information of the type available for the 15 June flare is available for this flare, though we have reconstructed the pointing from the spacecraft coordinates. This procedure implies a slit filling factor of $\frac{1}{4}$ – $\frac{1}{3}$, though it is very uncertain. Support for the value of $\frac{1}{4}$ comes from the astronaut's comments in the NRL science log; visually, the flare filled about $\frac{1}{4}$ of the spectrograph slit, which was visible with the $H\alpha$ slit jaw monitor.

3. Data Reduction

The reduction of the data to the final digitized absolute intensities given below in this paper was done in a manner dictated by the orders-of-magnitude range of intensity present over the $L\alpha$ profile. The film was scanned with the NRL digitizing microphotometer with a slit of width 3 μm and length 160 μm . The width is much less than the full-width at half-maximum of the spectrograph point-spread function. The sampling interval was 1 μm . Digitized data were recorded on magnetic tape. Scans were carefully aligned parallel to the dispersion, and kept short enough to maintain this alignment to high accuracy.

Relative photographic photometry was carried out with a characteristic curve that was established in an iterative manner. An initial approximation was derived by assuming reciprocity, by measuring density at various wavelengths on exposures of various known durations within sets *A* and *H* for the 15 June flare and sets *F* and *G* for the 21 January flare. Using the characteristic curve, relative intensity profiles were calculated from density profiles. These intensity profiles were then filtered with a numerical filter (Brault and White, 1971) with sufficient width in frequency space that even the narrowest observed feature, the geocoronal $L\alpha$ line, was not distorted. All exposures in each set were then used to construct a single combined profile for each set. Trial-and-error changes were then made in the characteristic curve, and the above process iterated until all the profiles of all the sets of each flare could satisfactorily be overlaid within the noise level of the data, in all regions in which the overlay test was not compromised by: (1) extremely low exposure, for which the density was very close to the background fog level; (2) extremely high exposure, showing solarization effects; and (3) apparently real time variations in the intrinsic solar profile. The latter were evident primarily in set *A* of the 15 June flare (though not in $L\alpha$, but in $\text{Si III } \lambda 1206.510$), which was early in the flare, at which time rapid time variations could be expected. The result of this process was an optimal

TABLE II
Details of the exposures of the 21 January, 1974 flare

Set	Time (UT)	Duration (s)	Strip
A	23:13:44	2.50	3B187-2
	23:13:54	10.0	3B187-3
	23:14:23	40.0	3B187-4
B	23:16:05	2.50	3B187-5
	23:16:15	10.0	3B187-6
	23:16:44	40.0	3B187-7
C	23:17:45	0.31	3B187-8
	23:17:48	1.25	3B188-1
	23:17:50	5.0	3B188-2
	23:18:04	20.0	3B188-3
D	23:18:14	0.31	3B188-4
	23:18:15	1.25	3B188-5
	23:18:18	5.0	3B188-6
	23:18:31	20.0	3B188-7
E	23:19:01	0.31	3B189-4
	23:19:01	1.25	3B189-5
	23:19:05	5.0	3B189-6
	23:19:18	20.0	3B189-7
F	23:19:28	0.31	3B189-8
	23:19:31	1.25	3B190-1
	23:19:33	5.0	3B190-2
	23:19:47	20.0	3B190-3
G	23:36:08	2.50	3B193-4
	23:36:18	10.0	3B193-5
	23:36:46	40.0	3B193-6

characteristic curve which we call the iterated characteristic curve for each of the two flares. In principle, our iterated characteristic curve should be free of the effects of reciprocity failure. We compared our curve for the 15 June flare with that of Doschek *et al.* (1976). The latter was based on known line intensity ratios of optically thin lines, and should also be free of reciprocity-failure effects. The two curves were found to be identical to 10^{-2} in $\log I_\lambda$ in the range $0.01 \leq D \leq 0.61$, where D is the density, measured relative to the background fog level. The Doschek *et al.* curve was not defined above $D = 0.7$, so we have to rely on the success of our overlay procedure for these large densities. At the emission peaks of $L\alpha$ we had to use some exposures which reached $D = 0.95$ for the 15 June flare. At these high densities our overlay procedure implies uncertainties that may reach 0.3 in $\log I_\lambda$. For the 21 January flare peak intensity values are very much more certain, since observed densities did not exceed 0.6 in the data we used. The profiles for various exposure times in each set of the 21 January flare overlay very well. We can place an upper limit of 0.1 on the uncertainty of the relative intensity over the entire $L\alpha$ profile, on this basis of the

quality of the overlays. In fact, we expect the uncertainty of the characteristic curve is actually much less, probably of order 10^{-2} as for the 15 June flare, since we did not have to use any exposures with $D > 0.6$ for the 21 January flare.

A $L\alpha$ profile was determined for each set by using the appropriate iterated characteristic curve, filtering the data as described above, rejecting data based on either too-low or too-high densities, and averaging the remaining data. Relative intensity profiles formed in this way are shown in Figure 1, for the 15 June flare. Note that the ordinate is the logarithm of the relative intensity, in arbitrary units. The profiles are shifted in log relative intensity, and the tick marks are at intervals of one order of magnitude. No attempt was made to accurately render the profile of the weak $O\ v$ feature in the red wing of $L\alpha$.

The reduction from relative intensity to absolute intensity was done by two methods, the ATM calibration rocket flights (CALROC) as discussed by Kjeldseth Moe *et al.* (1978), and the SOLMIN flight results. For each flare the calibration factor

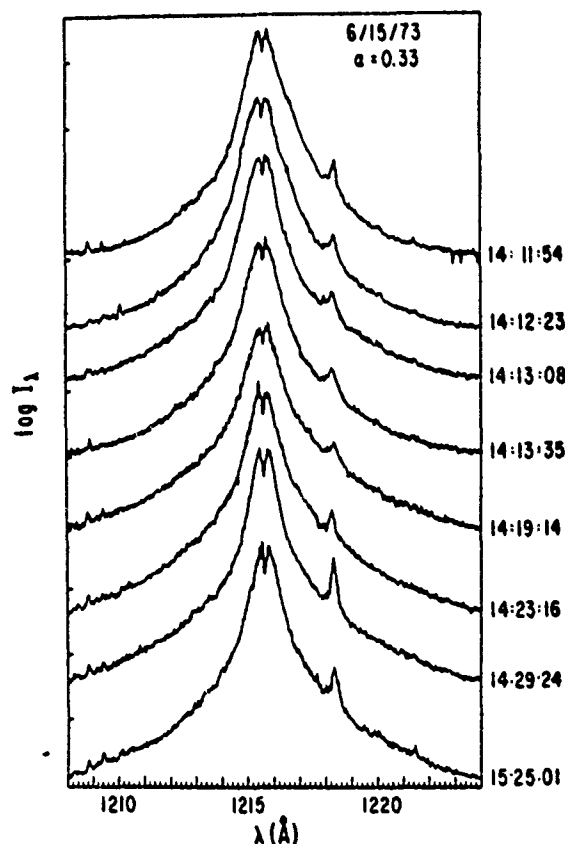


Fig. 1. Observed profiles of the $L\alpha$ line during and after the 14:12 UT 15 June, 1973 flare. The $\log I_\lambda$ scale is in arbitrary units, and profiles at different times have been shifted in $\log I_\lambda$ to avoid overlap. Tick marks are at one order of magnitude intervals. A slit-filling factor of $\alpha = \frac{1}{3}$ was used here; the same data are given in absolute intensity units, in digital form, in Table IV.

was determined that would give the CALROC and SOLMIN absolute intensities from the ATM slew scan films, reduced using our relative intensity scale. Individual calibration factors were determined for the Si III λ 1206, O V λ 1218, and N V λ 1239 lines, in ATM slew-scan exposures of 10, 40, and 160 s. Insufficient data were available to determine the wavelength dependence of the calibration factor. The wavelength-independent calibration factor so determined has an uncertainty of about 30%, based on the scatter of the results for the individual lines and exposure times given above. This is approximately the same accuracy as that of the absolute calibrations from the CALROC itself (c.f. Kjeldseth Moe *et al.*, 1978). The differences between the values of the calibration factor determined relative to the ATM CALROC atlas and the SOLMIN data turned out to differ by less than one estimated standard deviation, so we used as our final calibration factor for each flare the average of the CALROC and SOLMIN calibrations.

One final factor related to the absolute intensity of $L\alpha$ during flares is the slit filling factor, i.e. the fraction α of the area of the $2'' \times 60''$ spectrograph entrance aperture filled by flaring material. It must be realized that the estimates given above ($\alpha = \frac{1}{3}$ for 15 June, $\alpha = \frac{1}{4}$ for 21 January) are very rough, and introduce an uncertainty that we estimate to be approximately a factor of two, independent of wavelength. We assumed that the observed intensity was composed of two contributions, the non-flaring active region and the flare itself, i.e. that I_λ (observed) = αI_λ (flare) + $(1 - \alpha) I_\lambda$ (active region).

4. Observed $L\alpha$ Profiles

In Tables III through V we give, in digital form, $L\alpha$ line profiles for the two flares. For wavelengths between 1208 and 1225 Å we give the logarithm of the specific intensity at the Sun, in units of $\text{erg cm}^{-2} \text{s}^{-1} \text{sr}^{-1} \text{Å}^{-1}$. Each column corresponds to one lettered set of exposures in Tables I and II. The sets are identified by the time of the longest exposure in the set. At the bottom we give the wavelength and log intensity of three points, the blue peak, the central (geocoronal) absorption and the red peak. In addition to the uncertainties that arise in the reduction procedure, which we have discussed above, there is a digitization uncertainty of several units in the last figure in all tabulated values of $\log I$ and λ .

Profiles for the 15 June flare are given in Table III, with no correction for partial filling of the slit. In Table IV, we make that correction, using $\alpha = \frac{1}{3}$ (these are the data that are shown on an arbitrary relative scale in Figure 1). Nearly the only effect of this correction is to raise the overall intensity level of the profiles, with minor effects on the shape of the line profile, because the active region profile (set H) is quite a bit fainter than the observed (uncorrected) flare profiles. The correction, however, is the dominant source of uncertainty in the absolute intensity (except perhaps near maximum intensity, where photometric errors may be comparable) because of the assumption of a single flare profile and a single active region profile within the field of view of the spectrograph. We estimate that our correction factor of $\frac{1}{3}$ is conservative:

TABLE III
 $L\alpha$ profiles for 15 June, 1973 flare, $\alpha = 1$
 $\log I_{\lambda}$ (erg cm⁻¹ s⁻¹ sr⁻¹ Å⁻¹)

λ (Å)	14:11:54	14:12:23	14:13:08	14:13:35	14:19:14	14:23:16	14:29:24	15:25:01
1208.0	2.61	2.54	2.81	2.73	2.61	2.41	2.41	2.01
10.0	2.73	2.72	3.01	2.91	2.89	2.72	2.66	2.26
12.0	3.07	3.15	3.45	3.31	3.29	3.18	3.11	2.71
13.0	3.41	3.48	3.73	3.62	3.59	3.51	3.33	3.10
14.0	3.93	4.06	4.23	4.16	4.04	4.04	3.85	3.56
14.2	4.09	4.26	4.46	4.31	4.19	4.20	4.03	3.75
14.4	4.29	4.46	4.54	4.49	4.34	4.33	4.21	3.90
14.6	4.56	4.81	4.91	4.74	4.51	4.53	4.40	4.08
14.8	4.90	4.98	5.21	5.01	4.77	4.84	4.51	4.33
15.0	5.12	5.43	5.52	5.30	5.05	5.00	4.96	4.61
15.1	5.34	5.56	5.74	5.39	5.20	5.18	5.20	4.83
15.2	5.49	5.72	5.84	5.51	5.35	5.35	5.37	4.95
15.3	5.65	5.80	5.98	5.66	5.49	5.54	5.62	5.15
15.4	5.82	5.96	6.10	5.80	5.64	5.66	5.77	5.29
15.5	5.95	5.95	6.14	5.93	5.69	5.78	5.83	5.43
15.6	5.78	5.67	6.00	5.80	5.53	5.61	5.72	5.35
15.7	5.74	5.91	6.19	5.75	5.60	5.63	5.70	5.24
15.8	5.91	5.98	6.14	5.87	5.73	5.76	5.91	5.53
15.9	5.83	5.93	6.05	5.81	5.58	5.67	5.81	5.37
16.0	5.70	5.72	5.91	5.69	5.42	5.45	5.63	5.21
16.1	5.52	5.49	5.66	5.52	5.26	5.24	5.40	5.05
16.2	5.38	5.36	5.38	5.37	5.11	5.05	5.13	4.88
16.3	5.25	5.19	5.27	5.16	5.02	4.84	4.99	4.70
16.4	5.15	5.10	5.06	5.02	4.88	4.76	4.83	4.45
16.6	4.96	4.81	4.73	4.86	4.56	4.43	4.43	4.15
16.8	4.67	4.57	4.51	4.46	4.38	4.27	4.29	3.93
17.0	4.45	4.36	4.32	4.27	4.23	4.14	4.13	3.80
18.0	3.63	3.64	3.82	3.73	3.72	3.62	3.55	3.21
19.0	3.24	3.25	3.51	3.41	3.41	3.29	3.22	2.81
21.0	2.75	2.75	3.10	2.98	2.99	2.81	2.81	2.39
23.0	2.61	2.53	2.84	2.76	2.72	2.53	2.50	2.09
25.0	2.51	2.46	2.79	2.69	2.41	2.38	2.36	1.91
λ_b	1215.50	1215.47	1215.50	1215.50	1215.50	1215.50	1215.47	1215.54
$\log I_{\lambda_b}$	5.95	6.01	6.14	5.93	5.69	5.78	5.96	5.54
λ_0	1215.65	1215.60	1215.62	1215.65	1215.65	1215.63	1215.65	1215.63
$\log I_{\lambda_0}$	5.64	5.67	5.85	5.62	5.40	5.40	5.47	5.05
λ_r	1215.83	1215.80	1215.70	1215.75	1215.80	1215.80	1215.80	1215.80
$\log I_{\lambda_r}$	5.97	5.98	6.19	5.93	5.73	5.76	5.91	5.53

however, further attention to this point is meaningless in view of the existence of intensity variations within the flaring area itself.

Profiles for the 21 January flare are given in Table V, with $\alpha = 1$. No correction for filling factor is possible for this flare, since no post-flare active region spectrum was obtained (the H α flare had not yet ended at the time of the last exposure).

TABLE IV
 $L\alpha$ profiles for 15 June, 1973 flare, $\alpha = \frac{1}{3}$
 $\log I_{\lambda}$ ($\text{erg cm}^{-2} \text{s}^{-1} \text{\AA}^{-1}$)

$\lambda(\text{\AA})$	14:11:54	14:12:23	14:13:08	14:13:35	14:19:14	14.23.16	14:29:24
1208.0	3.01	2.91	3.23	3.16	3.01	2.74	2.75
10.0	3.10	3.10	3.41	3.31	3.29	3.06	3.02
12.0	3.41	3.51	3.83	3.71	3.71	3.51	3.48
13.0	3.73	3.84	4.13	4.03	3.96	3.83	3.77
14.0	4.24	4.51	4.62	4.51	4.42	4.36	4.20
14.2	4.43	4.71	4.83	4.67	4.61	4.50	4.31
14.4	4.63	4.95	5.16	4.85	4.77	4.60	4.52
14.6	4.97	5.30	5.51	5.16	4.91	4.81	4.72
14.8	5.31	5.51	5.71	5.41	5.12	5.08	4.92
15.0	5.66	5.88	5.91	5.71	5.37	5.38	5.23
15.1	5.81	6.02	6.16	5.84	5.55	5.46	5.50
15.2	5.92	6.15	6.28	5.94	5.68	5.64	5.82
15.3	6.10	6.22	6.41	6.07	5.76	5.83	6.00
15.4	6.33	6.38	6.52	6.21	5.89	5.99	6.22
15.5	6.29	6.36	6.57	6.25	5.88	6.14	6.35
15.6	6.01	5.99	6.40	6.02	5.74	5.65	5.98
15.7	6.22	6.29	6.63	6.23	5.94	6.09	6.03
15.8	6.29	6.35	6.55	6.23	6.03	6.01	6.31
15.9	6.15	6.34	6.43	6.16	5.81	5.93	6.25
16.0	6.02	6.09	6.31	6.03	5.64	5.72	5.99
16.1	5.86	5.87	6.07	5.77	5.53	5.44	5.65
16.2	5.76	5.76	5.78	5.61	5.41	5.37	5.42
16.3	5.66	5.60	5.49	5.49	5.32	5.25	5.09
16.4	5.55	5.48	5.36	5.32	5.17	5.14	4.97
16.6	5.31	5.16	5.11	5.10	4.91	4.86	4.72
16.8	5.06	4.94	4.87	4.90	4.72	4.64	4.54
17.0	4.81	4.70	4.67	4.69	4.61	4.54	4.42
18.0	4.04	4.05	4.21	4.14	4.12	4.01	3.89
19.0	3.61	3.63	3.92	3.81	3.81	3.67	3.61
21.0	3.11	3.14	3.50	3.36	3.37	3.15	3.14
23.0	2.99	2.93	3.25	3.19	3.11	2.84	2.86
25.0	2.94	2.84	3.18	3.11	2.93	2.69	2.71
<hr/>							
λ_b	1215.40	1215.44	1215.50	1215.50	1215.42	1215.50	1215.50
$\log I_{\lambda_b}$	6.33	6.41	6.57	6.29	5.98	6.14	6.35
λ_0	1215.60	1215.60	1215.62	1215.65	1215.58	1215.60	1215.65
$\log I_{\lambda_0}$	6.01	5.99	6.31	6.02	5.55	5.65	5.83
λ_r	1215.76	1215.75	1215.70	1215.75	1215.80	1215.70	1215.80
$\log I_{\lambda_r}$	6.36	6.41	6.63	6.41	6.03	6.09	6.31

5. Discussion

The two flares studied here are very different in $L\alpha$, as they are in other spectral features. Our observations of the 15 June flare reach a maximum integrated intensity (at about 14:13 UT) of $4.1 \times 10^6 \text{ erg cm}^{-2} \text{s}^{-1} \text{sr}^{-1}$, after correction for the filling factor assuming $\alpha = \frac{1}{3}$. We measure the intensity of the post-flare active region to be $3.0 \times 10^5 \text{ erg cm}^{-2} \text{s}^{-1} \text{sr}^{-1}$. In comparison, Basri *et al.* (1979) obtain $3.3 \times$

TABLE V
 $L\alpha$ profiles for 21 January, 1974 flare, $\alpha = 1$
 $\log I_{\lambda}$ ($\text{erg cm}^{-2} \text{s}^{-1} \text{sr}^{-1} \text{\AA}^{-1}$)

$\lambda(\text{\AA})$	23:14:23	23:16:44	12:18:04	23:18:31	23:19:18	23:19:47	23:36:46
1208.0	3.16	3.24	3.29	3.28	3.28	3.25	3.08
1210.0	3.33	3.43	3.45	3.45	3.43	3.40	3.26
1212.0	3.68	3.78	3.72	3.72	3.76	3.72	3.58
1213.0	3.93	4.06	3.98	4.00	3.99	3.98	3.81
1214.0	4.38	4.43	4.30	4.33	4.32	4.38	4.13
1214.2	4.48	4.51	4.41	4.45	4.46	4.48	4.23
1214.4	4.65	4.63	4.57	4.48	4.57	4.61	4.38
1214.6	4.80	4.78	4.73	4.68	4.73	4.78	4.54
1214.8	5.09	5.08	4.94	4.93	4.88	4.93	4.78
1215.0	5.32	5.28	5.23	5.19	5.19	5.23	5.09
1215.1	5.38	5.37	5.28	5.29	5.34	5.33	5.18
1215.2	5.54	5.47	5.43	5.46	5.46	5.47	5.42
1215.3	5.76	5.71	5.65	5.60	5.61	5.67	5.59
1215.4	6.10	5.95	5.80	5.78	5.84	5.77	5.79
1215.5	5.99	6.13	5.80	5.78	5.80	5.86	5.99
1215.6	5.81	5.81	5.73	5.62	5.67	5.63	5.69
1215.7	5.80	5.83	5.68	5.67	5.61	5.72	5.68
1215.8	6.03	6.11	5.92	5.88	5.80	5.82	5.81
1215.9	6.09	6.10	5.80	5.79	5.80	5.79	6.05
1216.0	5.80	5.68	5.72	5.68	5.71	5.64	5.79
1216.1	5.49	5.55	5.56	5.52	5.54	5.51	5.61
1216.2	5.45	5.46	5.40	5.37	5.41	5.38	5.34
1216.3	5.35	5.36	5.25	5.19	5.26	5.26	5.17
1216.4	5.18	5.18	5.13	5.06	5.17	5.16	4.88
1216.6	4.89	4.93	4.88	4.83	4.86	4.83	4.55
1216.8	4.68	4.73	4.68	4.61	4.60	4.64	4.40
1217.0	4.51	4.58	4.51	4.48	4.48	4.49	4.29
1218.0	4.07	4.21	4.13	4.09	4.14	4.11	3.92
1219.0	3.80	3.95	3.88	3.88	3.87	3.88	3.72
1221.0	3.46	3.58	3.58	3.58	3.53	3.56	3.39
1223.0	3.26	3.36	3.38	3.39	3.39	3.38	3.23
1225.0	3.13	3.23	3.28	3.31	3.28	3.28	3.11
λ_b	1215.40	1215.46	1215.44	1215.45	1215.40	1215.48	1215.50
$\log I_{\lambda_b}$	6.10	6.14	5.89	5.81	5.84	5.93	5.99
λ_0	1215.65	1215.65	1215.65	1215.65	1215.65	1215.64	1215.66
$\log I_{\lambda_0}$	5.59	5.48	5.41	5.46	5.47	5.50	5.50
λ_r	1215.87	1215.87	1215.80	1215.84	1215.84	1215.80	1215.90
$\log I_{\lambda_r}$	6.13	6.24	5.92	5.88	5.86	5.82	6.05

$10^5 \text{ erg cm}^{-2} \text{s}^{-1} \text{sr}^{-1}$ for a typical active region and $7.1 \times 10^4 \text{ erg cm}^{-2} \text{s}^{-1} \text{sr}^{-1}$ for the quiet Sun. In contrast, the flare of 21 January was weaker in $L\alpha$. At its maximum integrated intensity (at about 23:16 UT, just after the hard X-ray burst), it reached about $2.3 \times 10^6 \text{ erg cm}^{-2} \text{s}^{-1} \text{sr}^{-1}$, after correction for the filling factor of $\alpha = \frac{1}{4}$, using the late-phase data of set G for the post-flare active region. It would not be surprising to find $L\alpha$ integrated intensities a factor of two or more above these values, even at

modest spatial resolution like ours. Our observations of the 15 June flare are probably atypically faint since the slit did not cover the brightest part of the flare. Unpublished data on the $L\alpha$ wings (Cook, 1978) show some flares that may be as much as 2.5 times brighter than our 15 June data.

During the 15 June flare the departures from symmetry of the line core seem to show systematic variation. First, the asymmetry is never very strong. Our data are too noisy to tell anything about the relative amplitude of the red and blue peaks. If we consider the outer regions of the core ($0.5 \leq \Delta\lambda \leq 1.0 \text{ \AA}$) where our data are better, the intensity is greater on the red side before $L\alpha$ maximum, and slightly brighter on the blue side at and after flare maximum. The post-flare profile is symmetric. The quantitative extent of the asymmetry is dependent on the distance from the core, and its description is best left to detailed digital data in Tables III to V. Measurements of shift of the centroid of the line at the half-power point, relative to the geocoronal absorption feature, give a crude estimate of the velocity of the emitting material in the chromosphere. In the post-flare observations, this shift is zero. It is also zero in set A, the pre-maximum profile. In sets B, C, and D, around flare maximum, there is a shift of $0.03 \text{ \AA} \pm 0.01 \text{ \AA}$ to the blue, corresponding to a bulk chromospheric motion of about $7 \pm 2 \text{ km s}^{-1}$. After flare maximum, the shift reverts to zero for the rest of the flare. The full-width at half maximum intensity before maximum (set A) is essentially that of the post-flare profile, i.e. $\Delta\lambda_{1/2} = 0.76 \text{ \AA}$. Near $L\alpha$ maximum $\Delta\lambda_{1/2}$ peaks at $0.85\text{--}0.88 \text{ \AA}$, and then decreases to the post-flare value within ten minutes (by set F).

For the 21 January flare the data at the red and blue emission peaks are not quite as noisy as for the 15 June flare, and one can make some statements regarding their asymmetry. In set A, the peak appears slightly brighter on the red side. Immediately following the hard X-ray burst (set B), the profile is most strongly asymmetric, with the red peak appearing 30–40% brighter. As time passes the asymmetry weakens, but the red peak remains stronger. Within six minutes of the hard X-ray burst, the asymmetry is lost in the noise (i.e. well below 10%). The late-phase spectrum, set G, also shows no peak asymmetry. At no time during this event is there a measureable shift (to $\pm 0.01 \text{ \AA}$) of the centroid of the Doppler core (at the half-power point) relative to the geocoronal absorption. The full-width at half-maximum (maximum being defined by the average of the red and blue peaks) also shows quite systematic behavior. Before and immediately after the hard X-ray burst $\Delta\lambda_{1/2} = 0.71 \pm 0.02 \text{ \AA}$. Within two minutes of the hard X-ray burst the half-width has increased rather abruptly to $\Delta\lambda_{1/2} = 0.82 \text{ \AA} \pm 0.02 \text{ \AA}$, and it increases further to $\Delta\lambda_{1/2} = 0.89 \pm 0.02 \text{ \AA}$ by sets E and F, 5–6 min after the hard X-ray burst.

Finally, we wish to close with a brief comment on the radiative output in $L\alpha$ relative to $B\alpha$, at flare maximum. For the 5 September, 1973 flare, Canfield *et al.* (1979) measured the Lyman/Balmer intensity ratio to be approximately $\frac{1}{2}$. In the flares of 15 June and 21 January we measure the $L\alpha$ intensity to be 4.1×10^6 and $2.3 \times 10^6 \text{ erg cm}^{-2} \text{ s}^{-1} \text{ sr}^{-1}$. Švestka (1976) gives typical Balmer- α flare profiles which imply $B\alpha$ intensities from 2.2×10^6 to $6.6 \times 10^6 \text{ erg cm}^{-2} \text{ s}^{-1} \text{ sr}^{-1}$ for average and bright flares respectively. It would then be reasonable to say that our observed

$L\alpha$ intensities are compatible with the hypothesis that the $L\alpha/B\alpha$ intensity ratio in flares is typically unity, within a factor of two.

Acknowledgements

We wish to thank those who contributed to the data reduction: Marc Allen and Dennis Ruff at Sacramento Peak Observatory, Ken Nicolas at NRL and Dean Jacobs at UCSD. This research was sponsored by the Air Force Office of Scientific Research, Air Force Systems Command, USAF, under Grant No. AFOSR-76-3071.

References

- Artzner, G.: 1978, *Astron. Astrophys.* **70**, L11.
 Bartoe, J.-D. F., Brueckner, G. E., Purcell, J. D., and Tousey, R.: 1977, *Applied Opt.* **16**, 879.
 Basri, G. S., Linsky, J. L., Bartoe, J.-D. F., Brueckner, G. E., and VanHoosier, M. E.: 1979, *Astrophys. J.* **230**, 924.
 Bonnet, R. M., Lemaire, P., Vial, J. C., Artzner, G., Gouttebroze, P., Jouchoux, A., Liebacher, J. W., Skumanich, A., and Vidal-Madjar, A.: 1978, *Astrophys. J.* **221**, 1032.
 Brault, J. W. and White, O. R.: 1971, *Astron. Astrophys.* **13**, 169.
 Brown, J. C., Canfield, R. C., and Robertson, M. N.: 1978, *Solar Phys.* **57**, 399.
 Brueckner, G. E.: 1975, in S. R. Kane (ed.), 'Solar Gamma-, X-, and EUV Radiation', *IAU Symp.* **60**, 105.
 Brueckner, G. E.: 1976, *Phil. Trans. Roy. Soc. London* **A281**, 443.
 Canfield, R. C.: 1974, *Solar Phys.* **34**, 339.
 Canfield, R. C. and Athay, R. G.: 1974, *Solar Phys.* **34**, 193.
 Canfield, R. C., Cheng, C.-C., Dere, K. P., Dulk, G. A., McLean, D. J., Robinson, R. D., Schmahl, E. J., and Schoolman, S. A.: 1980, in P. A. Sturrock (ed.), *Solar Flares*, Boulder, University of Colorado Press.
 Cook, J. W.: 1978, private communication.
 Doschek, G. A., Feldman, U., VanHoosier, M. E., and Bartoe, J.-D. F.: 1976, *Astrophys. J., Supp. Ser.* **31**, 417.
 Gouttebroze, P., Lemaire, P., Vial, J. C., and Artzner, G.: 1978, *Astrophys. J.* **225**, 655.
 Kjeldseth Moe, O., VanHoosier, M. E., Bartoe, J.-D. F., and Brueckner, G. E.: 1978, NRL Report 8056 or 8057.
 Kostyuk, N. D.: 1976, *Sov. Astron.* **20**, 206.
 Lemaire, P., Charra, J., Jouchoux, A., Vidal-Madjar, A., Artzner, G. E., Vial, J. C., Bonnet, R. M., and Skumanich, A.: 1978, *Astrophys. J.* **223**, L55.
 Lites, B. W. and Cook, J. W.: 1979, *Astrophys. J.* **228**, 598.
 McGuire, J. P.: 1976, NASA TM X-73312, Marshall Space Flight Center, Alabama.
Solar-Geophysical Data: No. 347, Part I, pp. 17, 19, July 1973; No. 348, Part I, pp. 94, 99, 113, August 1973; No. 352, Part II, pp. 6, 21, 22, 43; December 1973; No. 353, Part II, pp. 44, 47, January 1974; No. 355, Part I, pp. 95, 96, March 1974; No. 359, Part II, pp. 7, 16, 28, July 1974; No. 360, Part II, p. 27, August 1974. U. S. Department of Commerce, Boulder, Colorado.
 Švestka, Z.: 1976, *Solar Flares*, D. Reidel Publ. Co., Dordrecht, Holland, p. 7.

iii) Indirect Estimation of Energy Disposition by
Non-thermal Electrons in Solar Flares

This paper presents a method useful for inferring the number of electrons accelerated by flares, based on their microwave spectrum. This method was used to establish the flux of accelerated electrons in the proton/electron energy flux ratio study above.

INDIRECT ESTIMATION OF ENERGY DISPOSITION BY NON-THERMAL ELECTRONS IN SOLAR FLARES

H. S. HUDSON and R. C. CANFIELD

Physics Department, C-011, University of California, San Diego, La Jolla, Calif. 92093, U.S.A.

and

S. R. KANE

Space Sciences Laboratory, University of California, Berkeley, Calif. 94720, U.S.A.

(Received 12 March; in revised form 4 August, 1978)

Abstract. The broad-band EUV and microwave fluxes correlate strongly with hard X-ray fluxes in the impulsive phase of a solar flare. This note presents numerical aids for the estimation of the non-thermal electron fluxes from these correlations, using the SFD (sudden frequency deviation) ionospheric data to measure the EUV flux.

1. Introduction

In the absence of hard solar X-ray data, as for example during the Skylab mission, we sometimes must use indirect means for finding the number of non-thermal electrons. For a thick-target model, this permits us to estimate the collisional energy deposition by these electrons in the solar atmosphere. This note provides numerical methods for estimating this energy deposition from observations of impulsive microwave bursts (based on the results of Kane, 1974), or of impulsive EUV bursts (Kane and Donnelly, 1971; Donnelly and Kane, 1978). In addition, we give graphical means for estimating the numbers of electrons responsible for the observed hard X-ray bremsstrahlung in both thick-target and thin-target models.

2. Numerical Relationships for Bremsstrahlung

We use the Bethe-Heitler cross-section (e.g. Jackson, 1962) for bremsstrahlung of electrons on protons:

$$\frac{d\sigma}{d(h\nu)} = 1.58 \times 10^{-24} \frac{1}{Eh\nu} \ln \left[\left(\frac{E}{h\nu} \right)^{1/2} + \left(\frac{E}{h\nu} - 1 \right)^{1/2} \right] \text{ cm}^2 \text{ keV}^{-1} \quad (1)$$

with electron energy E and photon energy $h\nu$ in keV. For a power-law fit to the photon spectrum at Earth,

$$\phi_{h\nu} = A(h\nu)^{-\gamma} \text{ ph}(\text{cm}^2 \text{ s keV})^{-1}, \quad (2)$$

we find

$$\frac{d^2 N_e}{dE dt} = 3.28 \times 10^{33} b(\gamma) A E^{-\delta} \text{ electrons } (\text{keV s})^{-1} \quad (3)$$

$$\delta = \gamma + 1$$

in a thick target (Brown, 1971; Lin and Hudson, 1976). This allows a factor 1.8 to account for heavy elements, but assumes isotropic emission in a fully-ionized target. Here $b(\gamma) = \gamma^2(\gamma-1)^2 B(\gamma-\frac{1}{2}, \frac{3}{2})$, with $B(x, y)$ the beta function. The energy deposited by electrons of energy ≥ 20 keV, P_{20} , and the ≥ 20 keV electron loss rate or injection rate, dN_{20}/dt , are

$$P_{20} = 1.6 \times 10^{-9} \int_{20 \text{ keV}}^{\infty} E \frac{d^2 N_e}{dE dt} dE \text{ erg s}^{-1},$$

$$\frac{dN_{20}}{dt} = \int_{20 \text{ keV}}^{\infty} \frac{d^2 N_e}{dE dt} dE \text{ electrons s}^{-1}.$$
(4)

We can now derive relationships between Φ_{20} , the X-ray spectral flux [$\text{ph}(\text{cm}^2 \text{s keV})^{-1}$] at 20 keV as derived from observations, and these two quantities:

$$P_{20}/\Phi_{20} = 1.05 \times 10^{26} \frac{b(\gamma)}{(\gamma-1)},$$

$$\frac{dn_{20}/dt}{\Phi_{20}} = 3.28 \times 10^{33} \frac{b(\gamma)}{\gamma}.$$
(5)

Table I lists the quantities $b(\gamma)/(\gamma-1)$ and $b(\gamma)/\gamma$ needed to calculate these relationships.

Generally, as a thin target, the X-ray flux determines the instantaneous number of radiating electrons. We define N_{20} as the integral number of electrons above 20 keV, and W_{20} as the instantaneous integral energy stored in these electrons:

$$N_{20} = \int_{20 \text{ keV}}^{\infty} \frac{dN_e}{dE} dE;$$

$$W_{20} = 1.6 \times 10^{-7} \int_{20 \text{ keV}}^{\infty} E \frac{dN_e}{dE} dE \text{ erg}.$$
(6)

TABLE I
Numerical quantities

γ	$\frac{b(\gamma)}{\gamma}$	$\frac{b(\gamma)}{\gamma-1}$	$\frac{C(\gamma)}{\gamma-\frac{1}{2}}$	$\frac{C(\gamma)}{\gamma-\frac{3}{2}}$
2	0.786	1.57	1.00	-
2.5	1.50	2.50	0.955	-
3	2.35	3.53	1.00	3.00
3.5	3.33	4.66	1.06	2.12
4	4.43	5.90	1.13	1.88
4.5	5.60	7.20	1.19	1.78
5	6.87	8.59	1.25	1.75
5.5	8.23	10.1	1.31	1.75
6	9.66	11.6	1.37	1.76

From the bremsstrahlung cross-section we compute

$$\frac{dN_e}{dE} = 1.05 \times 10^{42} C(\gamma) A E^{-\delta} / n_i \text{ electrons keV}^{-1}, \quad (7)$$

$$\delta = \gamma - \frac{1}{2}$$

with n_i the target density (cm^{-3}), so that

$$N_{20} n_i / \Phi_{20} = 9.4 \times 10^{43} \frac{C(\gamma)}{(\gamma - \frac{1}{2})}, \quad (8)$$

$$W_{20} n_i / \Phi_{20} = 3.01 \times 10^{36} \frac{C(\gamma)}{(\gamma - \frac{1}{2})},$$

where

$$C(\gamma) = (\gamma - 1) / B(\gamma - 1, \frac{1}{2}). \quad (9)$$

Table I also gives the quantities $C(\gamma)/(\gamma - \frac{1}{2})$ and $C(\gamma)/(\gamma - \frac{3}{2})$ that occur in Equation (8).

3. Inferred Thick-Target Energy Deposition

We relate microwave and EUV fluxes to P_{20} by using the observed correlations. Kane (1974) showed that the peak X-ray energy flux $\xi_x (\geq 20 \text{ keV})$ is approximately proportional to the peak 3–10 cm microwave flux density ξ_R . This correlation is given by

$$\xi_x \approx 10^{-7} \xi_R, \quad (10)$$

where ξ_x is expressed in $\text{erg} (\text{cm}^2 \text{ s})^{-1}$ and ξ_R in $10^{-22} \text{ W} (\text{m}^2 \text{ Hz})^{-1}$. This leads to

$$P_{20} / \xi_R = 1.6 \times 10^{25} b(\gamma) \frac{(\gamma - 2)}{(\gamma - 1)}, \quad (11)$$

as shown in Figure 1.

Finally, for the EUV relationship, Kane (1974) shows that there is a correlation between the X-ray energy flux in the 10–50 keV band,

$$\xi'_x = 1.6 \times 10^{-9} \int_{10 \text{ keV}}^{50 \text{ keV}} h\nu \Phi_{h\nu} d(h\nu) \text{ erg} (\text{cm}^2 \text{ s})^{-1}, \quad (12)$$

and the energy flux $\xi_{\text{EUV}} (\text{erg cm}^{-2} \text{ s}^{-1})$ in the broad EUV band (10–1030 Å) inferred from SFD's (sudden frequency deviations) (Kane and Donnelly, 1971; Donnelly and Kane, 1978):

$$\frac{\xi'_x}{\xi_{\text{EUV}}} = 2 \times 10^{-5}. \quad (13)$$

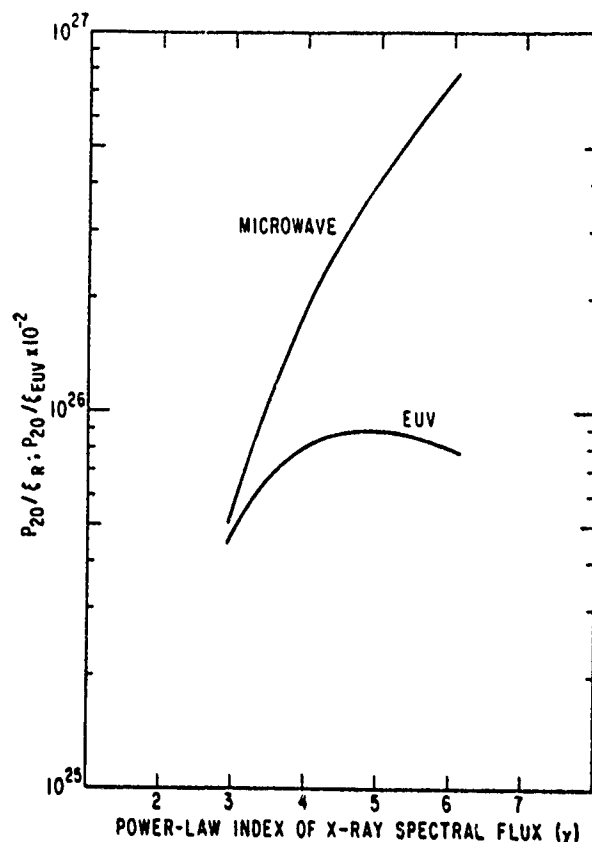


Fig. 1. Approximate thick-target energy deposition rates per unit 3–10 cm microwave flux density ξ_R , $10^{-22} \text{ W (m}^2 \text{ Hz)}^{-1}$, and 10–1030 Å energy flux ξ_{EUV} , $\text{erg (cm}^2 \text{ s)}^{-1}$. These curves give indirect approximations for estimating collisional energy losses by non-thermal electrons during the impulsive phase of a solar flare. The plotted curve for P_{20}/ξ_{EUV} refers to flares on the central meridian; the EUV directivity (Donnelly and Kane, 1978) is such that the values read from the curve must be increased for flares at finite central-meridian distance (CMD). For $0 < \text{CMD} < 80^\circ$, $\xi_{\text{EUV}}(\text{CMD})/\xi_{\text{EUV}}(0) = 1 - 0.01 \text{ CMD}$.

This correlation refers to events occurring on the solar central meridian. As a result, we find (designating by $\xi_{\text{EUV}}(0)$ the EUV flux on central meridian)

$$P_{20}/\xi_{\text{EUV}}(0) = 1.1 \times 10^{28} \times 2^{-\gamma} b(\gamma) \frac{(\gamma - 2)}{(\gamma - 1)}, \quad (14)$$

as shown in Figure 1. A strong dependence upon central meridian distance (CMD) exists (Donnelly and Kane, 1978) for which we can approximately correct in the following manner:

$$\xi_{\text{EUV}}(\text{CMD})/\xi_{\text{EUV}}(0) = 1 - 0.01 \times \text{CMD}, \quad 0 \leq \text{CMD} < 80^\circ. \quad (15)$$

For $\text{CMD} > 80^\circ$ the uncertainty becomes too large to permit a reliable guide.

Table II tabulates all of these results for a nominal value of $\gamma = 4$, which falls near the median value (Datlowe *et al.*, 1974). These numbers can be used for order-of-magnitude estimations.

TABLE II
Thick-target power for $\gamma = 4$

P_{20}/Φ_{20}	6.2×10^{26}	$\text{erg s}^{-1} (>20 \text{ keV}) \text{ per } (\text{ph/cm}^2 \text{ s keV})^{-1} \text{ at } 20 \text{ keV}$
P_{20}/ξ_R	1.9×10^{26}	$\text{erg s}^{-1} (>20 \text{ keV}) \text{ per solar flux unit, } 3\text{--}10 \text{ cm}$
$P_{20}/\xi_{\text{EUV}}(0)$	8.1×10^{27}	$\text{erg s}^{-1} (>20 \text{ keV}) \text{ per erg } (\text{cm}^2 \text{ s})^{-1} 10\text{--}1030 \text{ \AA}$

4. Cautionary Notes

The correlations hardly constitute exact relationships; there is appreciable scatter in Kane's comparisons between OGO ion chamber data for hard X-rays and the radio and SFD parameters. Presumably part of this is measurement error, but much of it must be true variability induced by variation in magnetic-field strength or geometry. In microwaves it is also fairly clear that at least two separately-generated components must occur (e.g. Kundu, 1965); the impulsive burst and the microwave type IV emission. These components might correlate differently. We would therefore like to emphasize that the results given here apply only to the peak of the impulsive burst.

The simple relationships described in this note are expressed in terms of power-law fits to the X-ray spectra. These are convenient for numerical work but may not adequately represent the spectral distribution over the entire X-ray energy range (Kane and Anderson, 1970; Elcan, 1978). Any refinement however will not affect the value of our order-of-magnitude results. Korchak (1976) has described the uncertainties involved in energetic considerations based upon the bremsstrahlung models.

Acknowledgements

The authors have benefitted from their participation in the Skylab Solar Workshop series on solar flares. The workshops are sponsored by NASA and NSF and managed by the High Altitude Observatory. Hudson also acknowledges support from the NSF under AST-76-01280. Canfield acknowledges support by the Air Force of Scientific Research, Air Force Systems Command, USAF, under Grant No. AFOSR-76-3071. We would especially like to thank Peter Hoyng for a careful reading of the manuscript and for useful comments.

References

- Brown, J. C.: 1971, *Solar Phys.* **18**, 489.
Dallowe, D. W., Elcan, M. J., and Hudson, H. S.: 1974, *Solar Phys.* **39**, 155.
Donnelly, R. F. and Kane, S. R.: 1978, *Astrophys. J.* **222**, 1043.
Elcan, M. J.: 1978, Ph.D. Thesis (UCSD).
Jackson, J. D.: 1962, *Classical Electrodynamics*, Wiley, New York.
Kane, S. R.: 1974, in G. Newkirk, Jr. (ed.), 'Coronal Disturbances', *IAU Symp.* **57**, 105.
Kane, S. R. and Donnelly, R. F.: 1971, *Astrophys. J.* **164**, 151.
Korchak, A. A.: 1976, *Soviet Astron.* **20**, 211.
Kundu, M. R.: 1965, *Solar Radio Astronomy*, Interscience, New York.
Lin, R. P. and Hudson, H. S.: 1976, *Solar Phys.* **50**, 153.

iv) A Qualitative Interpretation of 7 August 1972

Impulsive Phase Flare H α Line Profiles

This paper served two purposes. First, it showed, somewhat surprisingly, that the H α spectra of the brightest part of this major flare did not show the effects expected of a beam of accelerated electrons. This supports the idea that the hard X-ray spectrum does not come from the acceleration of electrons into the chromosphere, and that the hard X-ray spectrum arises primarily from thermal electrons confined to the corona. Other observations obtained during SMM seem to contradict this idea, but they are no more compelling than the results of this paper. The answer to the question of whether a major fraction of the energy of flares goes into accelerated electrons is still an open question, faced with contradictory and incomplete evidence.

The second purpose of this paper was to develop qualitative criteria for inferring the nature of chromospheric heating, using H α line profiles. It provided guidelines that were useful in the subsequent paper, for distinguishing between parts of the flare that show evidence for accelerated electrons, and those that do not.

A QUALITATIVE INTERPRETATION OF 7 AUGUST 1972 IMPULSIVE PHASE FLARE $H\alpha$ LINE PROFILES

RICHARD C. CANFIELD

Center for Astrophysics and Space Sciences, C-011, University of California,
San Diego, La Jolla, 92093, U.S.A.

(Received 18 April; in revised form 18 September, 1980)

Abstract. Tanaka's (1977) unique $H\alpha$ profiles of the kernels of the 7 August 1972 flare were quantitatively interpreted by Brown *et al.* (1978; henceforth BCR) in terms of a thick target electron beam model. They found that this interpretation required beam inhomogeneity and/or partial precipitation and large ($60\text{--}100\text{ km s}^{-1}$) macroturbulence. The latter requirement is somewhat suspect, since the only independent evidence also comes from efforts to understand the profiles of optically thick chromospheric lines. Relationships between model atmosphere parameters and line profile parameters calculated by Dinh (1980) show that these requirements could be considerably reduced, if not totally eliminated, if the actual chromospheric flare heating mechanism were simultaneously capable of pushing the flare transition region to greater column density and causing less heating of the residual chromosphere than the BCR models. This then implies that the chromosphere is heated primarily by a mechanism through which the heating effects do not penetrate as far below the flare transition region as is the case for a power-law spectrum of non-thermal electrons whose parameters are chosen appropriate to the non-thermal thick target interpretation of hard X-rays. Thermal conduction and optically thick radiation are examples of such a mechanism.

1. Introduction

A particularly interesting recent observational result from hard X-ray spectroscopy of solar flares is that for many flares the form of their spectra in the 10–100 keV range is better fit by functions of thermal form than power-law form (Crannell *et al.*, 1978; Elcan, 1978). This result has led various authors to consider models in which most of the hard X-rays are generated by bremsstrahlung from thermal electrons in regions with temperatures in the range 10–100 keV. Recent studies of the confinement of plasma in such hot regions by Brown *et al.* (1979), Smith and Lilliequist (1979), Smith and Auer (1980), and Smith and Brown (1980) have led to the conclusion that ion-sound turbulence generated by the reverse current required to electrically neutralize the fast electrons moving away from the hot region confines all electrons of velocity less than about two times the mean electron velocity behind a steep temperature front that propagates at approximately the ion-sound speed. This is a much different physical model than the basic 'thick target' model envisioned early on by Korchak (1971), Hudson (1972, 1973), and Brown (1973), in which most of the 10–100 keV radiation was thought to come from the chromosphere as a result of a beam of fast electrons of power-law energy distribution.

The purpose of this paper is to show that existing models of the formation of the $H\alpha$ line during flares appear to provide clear qualitative evidence that heating of the $H\alpha$ -forming regions of the flare chromosphere in the bright $H\alpha$ kernels

Solar Physics 75 (1982) 263–275. 0038-0938/82/0752-0263 \$01.95.

Copyright © 1982 by D. Reidel Publishing Co., Dordrecht, Holland, and Boston, U.S.A.

PRECEDING PAGE BLANK-NOT FIL

observed during the impulsive phase of solar flares is not due primarily to heating by Coulomb collisions of a power-law distribution of 10–100 keV electrons with chromospheric material; instead some shorter-range process, perhaps conduction or optically thick radiative transfer, seems to be favored. This is clearly relevant to the collisionless confinement modelling. Unfortunately, much work remains to be done on them before there will be a basis for quantitatively testing the consistency of this picture with chromospheric diagnostics.

Among the many aspects that must be studied are the effects to be expected when the thermal front reaches the transition from coronal to chromospheric temperatures and densities; in fact, the only quantitative work done so far, the numerical simulations of Smith and Lilliequist (1979) and Smith and Auer (1980) covers only the first few seconds after the creation of the hot flare material. During these few seconds the thermal front is passing through material that was initially at coronal temperatures and densities; the question of what must be expected when the thermal front encounters the region of the pre-flare transition region is currently under study. The few seconds about which we know at least a little regarding the energy transport from the work discussed above unfortunately represent only a small fraction of the duration of typical hard X-ray bursts (40–50 s, Datlowe *et al.*, 1974) and is certainly well below the present limits of our ability to observe line profiles throughout a flare.

We know very little from the present work on the collisionless confinement models about what to expect to be the dominant transport mechanisms in the chromosphere during most of the flare event, even during the impulsive phase. For this reason, it seems quite appropriate to consider a rather broad range of possibilities in a most straightforward and uncomplicated way. There already exist models for this purpose. Kane *et al.* (1980) have clearly defined a set of idealized models that form a classification in terms of which it is easy to discuss chromospheric flare effects. These models are the thin target, thick target, partial precipitation and thermal models. In this paper we will use these clearly defined names, in an effort to prevent the confusion associated with calling models such as the collisionless confinement models with the name 'thermal', which is appropriate from the perspective of only one aspect of the flare, namely the hard X-ray radiation. In all four models, the energetic electrons are supposed to be accelerated above the chromosphere. Only one dimension is considered, viz. distance (or alternatively column density or mass) along a magnetic field line. In the thin target model, none of the non-thermal electrons that are responsible for hard X-rays penetrate into the chromosphere. Chromospheric transport must thus take place by radiation, conduction or mass motion. In the thick target model, many of the hard X-ray producing electrons penetrate into the chromosphere. Hence Coulomb collisions between these incident electrons and ambient electrons causes significant heating. Partial precipitation models are those in which only part of the fast electrons precipitate into the chromosphere as envisioned in the thick target model. Finally, thermal models, like thin target models, generate none of their hard X-rays in the

chromosphere, and hence chromospheric heating due to electron precipitation also does not take place.

At the present level of development of the collisionless confinement models it appears that they combine properties of both the thermal and partial precipitation models.

2. Observations of Impulsive Phase $H\alpha$ Profiles

Observations of the $H\alpha$ profile during flares are a valuable indicator of the thermodynamic structure of the flare chromosphere for two reasons. First, because the $H\alpha$ line is strong and optically thick, the profile (i.e., central reversal, emission peaks, wing slope, and amplitude etc.) contains information on the depth dependence of thermodynamic variables. Whereas in the quiet Sun $H\alpha$ is formed largely in a low-density region and is quite insensitive to chromospheric temperature and density (Gebbie and Steinitz, 1974), in flares it is formed at much higher densities (Canfield and Athay, 1974; Švestka 1976), and is quite sensitive.

The second reason why $H\alpha$ spectroscopy is valuable is the significant role played by $H\alpha$ as a chromospheric radiative cooling mechanism. The observations of the radiative output of the 5 September 1973 flare (Canfield *et al.*, 1980b) show empirically that $H\alpha$ is one of several predominant chromospheric cooling lines, any one of which could be used to identify regions of enhanced chromospheric energy output, hence enhanced chromospheric heating. Under solar flare conditions, one can equate enhanced $H\alpha$ output to enhanced chromospheric heating.

In contrast to the omnipresence of $H\alpha$ filtergrams of flares, $H\alpha$ profiles are poorly observed with even modest temporal or spatial resolution, as a consequence of the difficulty of simultaneously observing temporal, spatial and spectral characteristics. There exists only one published observation of an $H\alpha$ profile that can compellingly be identified with a flare kernel at the hard X-ray maximum of a flare, with accompanying simultaneous measures of the hard X-ray output, *viz.* that of Tanaka (1977). He observed two kernels of the August 7, 1972 flare, while Lin and Hudson (1976) and Hoyng *et al.* (1976) obtained hard X-ray spectra. Tanaka's profiles include two different kernels at two different times, both during intense hard X-ray bursts. The critical aspect of these impulsive-phase spectra for the present discussion is that while they are very strong, they show no central reversals, which develop only later in the flare.

3. Chromospheric Flare Heating Models

Theoretical modelling that describes the chromospheric effects of flare energy transport by non-thermal particles, radiation, thermal conduction and mass motion has been reviewed recently by several authors, including Brown and Smith (1980), Brown *et al.* (1980), and Canfield *et al.* (1980). Such modelling postulates specific transport mechanisms, and computes atmospheres based on a representation of

these mechanisms. Of course numerical complexity in all cases precludes a completely realistic simulation of an actual flare, and in fact realism is not the immediate objective of much worthwhile modelling. Such energy transport modelling is valuable both to the extent that one actually produces model atmospheres that quantitatively reproduce important features of observations and to the extent that one finds trends and relationships between model parameters, model atmospheres and observables. Two theoretical calculations have been carried out recently that I wish to single out for discussion below, those of BCR and Sermulina *et al.* (1980).

3.1. THE MODELS OF BROWN *et al.* (1978)

BCR calculated several quasi-steady model flare chromospheres in which thick target heating by Coulomb collisions of a simple beam of fast electrons is balanced by radiative cooling by $H\alpha$ and $L\alpha$ (in which radiative transfer effects were treated), negative hydrogen and optically thin heavier elements. The electron beam spectrum was characterized by two parameters, the flux F_{20} in electrons above 20 keV incident on the top of the chromosphere and the spectral index of the assumed power-law energy spectrum. Four model atmospheres were generated for four different values of F_{20} . BCR found that for the values of F_{20} and spectral index most compatible with hard X-ray observations of the 7 August 1972 flare, the model produced an $H\alpha$ profile that was much too bright and had the wrong profile shape. They chose to explain the excess brightness by invoking spatial inhomogeneity and/or partial precipitation of the electron beam. They explained the difference between observed and calculated profile shapes by invoking a random non-thermal velocity of 60 km s^{-1} amplitude. Both these explanations have no specific independent observational justification in solar flares, so they must be approached with some skepticism. Below we point out that semi-empirical modelling implies an alternative explanation of the discrepancy between the computed BCR profiles and those observed during the 7 August flare.

The need to postulate a random non-thermal macroscopic velocity (macroturbulence) on the order of many tens of kilometers per second for the purpose of broadening line profiles and smearing relatively sharp spectral features has arisen not only in the course of the BCR work, but also elsewhere. Canfield and Athay (1974) showed that the kinematic flare-shock atmospheres of Nakagawa *et al.* (1973) could not be made to produce $H\alpha$ profiles that agreed with observations unless $40\text{--}70 \text{ km s}^{-1}$ macroturbulence was hypothesized. Motions of only somewhat lesser amplitude were required for the same purpose in Brown's (1973) electron-beam heated atmospheres (Canfield, 1974). Even some semi-empirical models, for which the model atmospheres are not constrained by credible physics of energy transport, have required velocities of 30 km s^{-1} to explain Ca II K line profiles in even small flares (Machado and Linsky, 1975). It may be significant that although there exists considerable evidence for velocities on the order of 100 km s^{-1} at temperatures around 10^5 K (Doschek and Feldman, 1978), Švestka (1976) cites no unambiguous evidence for such large random velocities in the chromosphere.

As suggested above, it therefore seems appropriate to retain considerable skepticism about the existence of macroturbulent motions in the flare chromosphere with amplitudes as great as several tens of kilometers per second, until independent confirmation is obtained, preferably with optically thin chromospheric lines.

On the other hand, there seems to be little specific reason to object to the hypotheses of spatial inhomogeneity and partial precipitation. The Earth's aurora offers useful examples of these phenomena (Akasofu, 1979). First, considerable inhomogeneity is present. Second, electrical potential drops parallel to the magnetic field have been observed to be present, which one would expect to be associated with both trapping and acceleration.

3.2. THE MODELS OF SERMULINA *et al.* (1980)

The models of Sermulina *et al.* (1980) are the most recent results of the Soviet group that has produced the most physically and mathematically complete numerical simulations of chromospheric flare energy transport that are presently available (Somov *et al.*, 1977, 1979). Bearing in mind the two different interpretations for the hard X-ray output of flares, thermal and thick-target, Sermulina *et al.* made two different calculations that serve to illustrate differences that would be expected on first principles. Both calculations were based on a two-temperature hydrodynamic treatment of flare plasma in a strong vertical magnetic field with a coronal pressure at the movable upper boundary, and a fixed lower boundary located deep in the chromosphere. They adopted an isothermal hydrostatic atmosphere as the initial condition, which though not realistic, is adequate for the present discussion.

Figure 1 shows the results of Sermulina *et al.*, which serve to illustrate the different chromospheric heating effects that one would expect in two rather idealized thermal and non-thermal cases. The electron temperature T_e is plotted as a function of column density ξ , the number of atoms and ions in a column of one cm^2 cross-section above the point in question. The initial chromospheric temperature is constant ($T_e = 6700$ K), and is indicated by a short-dashed line. The atmosphere is initially in hydrostatic equilibrium. The temperatures in a non-thermal, thick-target case (solid line) and a thermal case (long-dashed line) are shown, five seconds after the start of the event. In the non-thermal model, an electron beam with maximum energy flux $F_0 = 10^{11} \text{ erg cm}^{-2} \text{ s}^{-1}$ above a low-energy cutoff of 10 keV and slope $\gamma = 3$ is applied with a time dependence of the hard X-ray flux given by a symmetric function of half-width 5 s. No collective effects are included in the physics of the electron beam; heating is by Coulomb collisions. In the thermal model the upper boundary temperature follows the temperature required to give the same dependence of the hard X-ray intensity. The effective heat conduction coefficient they have used replaces the classical value by forms approximately appropriate to the limiting and anomalous forms of the heat flux (Brown *et al.*, 1979; Smith and Auer, 1980).

The important understanding to be gleaned from a comparison of the two different model atmospheres shown in Figure 1 is that certain qualitative differences exist

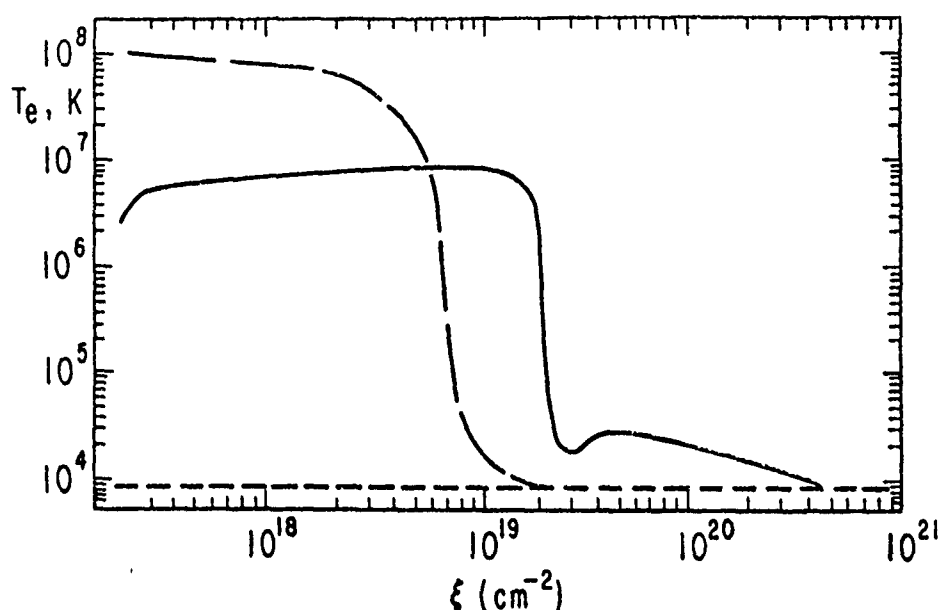


Fig. 1. Comparison of theoretical temperature distributions in a hydrodynamic flare simulation, 5 s after flare start (from Sermulina *et al.*, 1979). Results are shown for a thermal case (long-dashed curve) and a thick-target non-thermal case (solid curve). The short-dashed line indicates the assumed pre-flare temperature. The flare chromosphere shows much more heating in the thick-target non-thermal case than in the thermal case.

that would be expected on the basis of first principles. The most important is this: whereas the electron-heated model (the solid line) shows significant heating that penetrates to values of the column density much above that of the transition region, the model heated only by classical and anomalous thermal conduction (the dashed line) shows very little such penetration. This is to be expected on the basis of very simple physics; whereas there is heating spread over a wide range of column densities through the stopping of fast electrons with a wide spectrum of energies in the non-thermal model, thermal conduction is a comparatively short-range process due to the exponential dropoff of the electron distribution function toward high energies in a thermal population. In the thermal conduction model one expects heating of the material initially at chromospheric temperatures only closer to the top of the flare chromosphere, near the transition region. Note that if the energy in the electron beam were to be increased, the transition region would be displaced toward greater column density; however, it would remain true that there would still be considerable heating of the chromosphere at yet greater column densities. In any case, the column density of the transition region should not be an issue, since from first principles it is clear that it is due to the radiative instability (Field, 1965) and thermal conduction, and is highly insensitive to the heating mechanism. Its location in the model atmospheres at the instant shown depends primarily on

the amplitude of the heating and cooling functions included. The amplitudes of these functions are not realistic for various reasons, including the lack of inclusion of radiative transfer effects.

Before proceeding, it is necessary to comment on certain aspects of the modelling by Sermulina *et al.* The thermal model is not a partial precipitation model, as should be the case if a non-thermal tail of fast electrons are able to penetrate the conduction front, as suggested by Brown *et al.* (1979). The non-thermal model does not take into account instabilities thought to arise in such electron beams (cf. Brown and Smith, 1980). Instead, the two simulations illustrated are quite comparable to the idealized models of Kane *et al.* (1980) discussed in the introduction. These facts make them unsuitable for direct comparison to observations, but to not alter their utility for work such as this that attempts to gain understanding of the implications of observations before undertaking simulations that in fact may be more directly comparable to reality.

4. Semi-Empirical Interpretation of $H\alpha$ Profiles

A common technique for understanding solar and stellar spectra is the construction of semi-empirical models. These models describe the relationship between thermodynamic variables such as electron temperature T_e , electron density n_e , and non-thermal velocity ζ , all as functions of a vertical coordinate such as height, depth, column mass or column density. The models suppose no particular heating or cooling mechanism, but use certain assumptions (e.g. plane-parallel stratification, stationarity) to solve the radiative transfer equation based on assumed atomic cross-sections and processes. Such techniques have been applied to solar flare $H\alpha$ profiles only very recently, by Machado *et al.* (1980), henceforth called MAVN, and Dinh (1980). On the other hand, the technique has been applied to a variety of other lines in the past, by Machado and Linsky (1975), Machado *et al.* (1978), and Lites and Cook (1979).

A semi-empirical model atmosphere can be used to draw meaningful conclusions only if the profiles computed from it quantitatively match observations. The profiles computed by Dinh and MAVN do not quantitatively match the observed impulsive-phase $H\alpha$ profiles of Tanaka (1977). However, as Dinh shows, his models are successful in the sense that they agree with certain basic parameters of observed profiles during the decay phase. Specifically, his models reproduce the half-widths and equivalent widths of the observed profiles. He finds that to do so he has to postulate the existence of 25 km s^{-1} random macroscopic velocities, which has the effect of making the computed profiles smoother than the observed profiles. This is evidence that his postulated velocity is unrealistically large; we return to this point below. Tanaka's observed profiles have half-widths and equivalent widths that are factors of 2–4 times larger than the decay-phase profiles with which Dinh compared his models. The profiles shown by MAVN have not been shown to quantitatively resemble any observed flare profiles; in fact, the authors only claimed

that they cover the range of equivalent widths observed in flares of an unspecified range of importance! These authors made no comparison with specific observations of $H\alpha$ profiles. Hence although MAVN make several assertions about the physical processes they believe to be operating during flares, these conclusions are not supported by a model that correctly reproduces the observed half-width, equivalent width and line profile of $H\alpha$ in either a well-documented 'typical' flare of some type or in any individual observed flare.

One must recognize that there is more to be learned from semi-empirical modeling than what is represented in the specific model that is finally produced. In particular, it is very valuable to establish the relationship between parameters of model atmospheres and parameters of line profiles computed from them. Dinh's work is especially valuable in this sense because it includes a systematic study of the relationships between the $H\alpha$ profile and various parameters of the model atmosphere. Of the several relationships he points out, two are particularly relevant to the $H\alpha$ observations discussed above. First, *narrower transition regions* produce both *lower central intensity* and *lesser central reversal*. Second, *higher transition region pressure* (i.e., a transition region closer to the photosphere) produces *lesser central reversal*. The latter effect has also been pointed out explicitly by Baliunas *et al.* (1979) regarding the profiles of the Ca II and Mg II resonance lines in active chromosphere stars, by MAVN in solar flares, and several others. The work of MAVN includes no systematic study comparable to that of Dinh.

Another relationship exists in Dinh's results between the *total intensity* of the $H\alpha$ line (i.e. the intensity integrated over the line profile) and the *effective chromospheric temperature*. The meaning of the relationship is best illustrated by means of Dinh's (1980) results, some of which are shown in Figure 2. In Figure 2a three model flare chromosphere temperature distributions are shown, indicated by I, II, and III. All three have very steep temperature gradients in the transition region, i.e. it is thin. As a result, the transition region contributes negligibly to the $H\alpha$ opacity, except at the very top of the chromosphere. In all three models (I, II, and III) the temperatures at the base of the transition region are the same. On the other hand, since Dinh's models are in hydrostatic equilibrium under the solar gravity, with a depth-independent turbulent pressure, the density (or pressure) at the top of the chromosphere is lower for model I than for II, and lower for II than III. As a result, opacity in $H\alpha$ builds up more rapidly with geometric distance into the chromosphere in model II than model I. At any given value of $\tau_{H\alpha}$, $T_e(\tau_{H\alpha})$ is greater in model II than model I. This means that the source term $\epsilon^*B/(1 + \epsilon^*)$ in the $H\alpha$ line source function (see Athay, 1972), which is proportional to the intensity of radiation *created* per unit optical depth, is greater at a given $\tau_{H\alpha}$ in model II than in model I. Since the probability of escape of the radiation, once created, is proportional only to $\tau_{H\alpha}$, and the $H\alpha$ radiation from the upper part of the chromosphere dominates (the region near and below 500 km height contributes a negligible amount to the excess flare emission), the total amount of flare $H\alpha$ emission created in model II is greater than in model I. Model II has a higher *effective chromospheric*

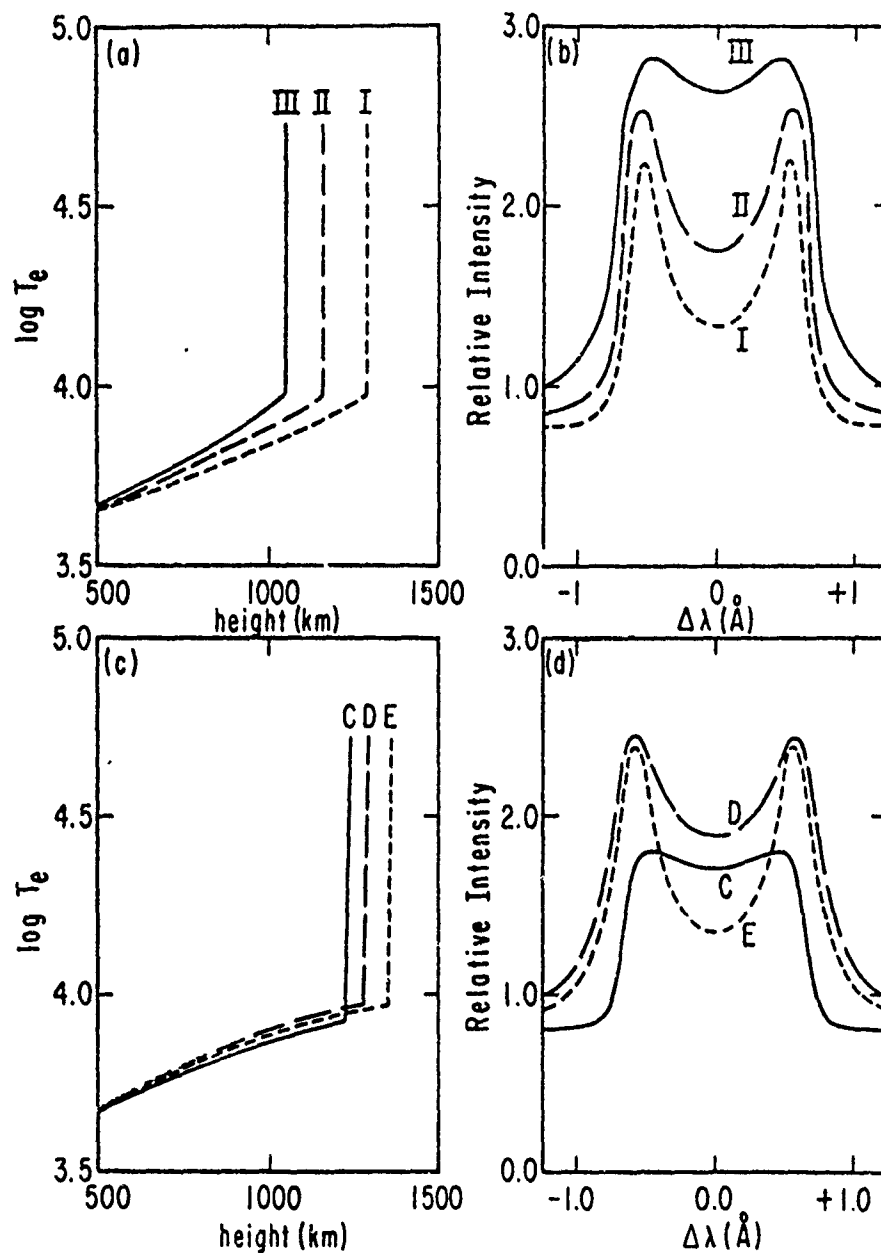


Fig. 2. Calculated $H\alpha$ profiles (frames (b) and (d)) for several semi-empirical chromospheric flare temperature distributions (frames (a) and (c)), from Dinh (1980). These results demonstrate the sensitivity of the profile of $H\alpha$ (particularly the total intensity and amplitude of central reversal) to the effective chromospheric temperature and the location of the flare chromosphere-corona transition region. Model C, with a chromosphere of low effective temperature and a low-lying (high-pressure) chromosphere-corona transition region, has an $H\alpha$ profile with the desirable properties of low total $H\alpha$ intensity and weak central reversal.

temperature than model I. The relationship that one would expect from the physical argument given above is clearly evident in Dinh's (1980) calculations. Model II has a greater total $H\alpha$ intensity than model I (Figure 2b). Similarly, model III has a higher effective temperature and total $H\alpha$ intensity than either model II or model I.

The interplay of two of the relationships discussed above is illustrated in Dinh's (1980) models C, D, and E and their $H\alpha$ profiles, shown in Figures 2c and 2d. Both transition region pressure and effective chromospheric temperature play a role. Model D has a higher transition region pressure than model E, hence a weaker central reversal. Also, D has a higher effective temperature than E, hence a greater total intensity. Model C has a still higher transition region pressure, hence a still weaker central reversal. On the other hand, model C has much lower effective chromospheric temperature than D, and hence a much lower total intensity. As we discuss below, the combination of a weak reversal and low total intensity is very important.

5. Discussion

The previous sections have summarized the evidence that supports the following statements:

(1) The only presently available observations of $H\alpha$ line profiles in flare kernels during the impulsive phase (Tanaka, 1977) do not show central reversals.

(2) $H\alpha$ profiles computed from the electron-beam heated atmospheres of BCR have two difficulties: first, they show strong central reversals; second, they are too bright compared to the observations.

(3) Although BCR explained these difficulties by hypothesizing spatial inhomogeneity and/or partial precipitation and macroturbulent velocities on the order of tens of kilometers per second, there exists no compelling independent evidence for substantiation of these requirements, particularly that of the large macroturbulent velocity.

(4) Semi-empirical modelling by Dinh (1980) shows that the need for these two hypotheses can be reduced if the chromosphere in the flare kernel simultaneously has two desirable properties relative to the models of BCR: first, less material at $H\alpha$ emitting temperatures ($T \sim 10^4$ K); second, a transition region located at greater column density.

(5) No model in which the predominant mechanism for chromospheric flare heating is Coulomb collisions of a power-law spectrum of fast electrons with the ambient chromosphere, as simulated by BCR, can combine these two desirable properties.

The principal conclusion of this paper is that the best theoretical modelling of chromospheric flare energy balance presently available implies that the flare chromosphere is not heated primarily by a power-law spectrum of electrons in the 10–100 keV energy range as has been inferred from the observed hard X-ray

spectra of flares and the thick-target interpretation. In fact, this work points to a mechanism that is capable of pushing the transition region to a much greater value of the column density than the value at which it is found in the pre-flare atmosphere, while simultaneously producing considerably less heating of the remaining flare chromosphere than the power-law thick-target model. Of the four idealized models of the hard X-ray flare defined by Kane *et al.* (1980), only a thermal-type model is compatible with these properties.

Although some of the semi-empirical model chromospheres of flares such as the models F1 and F2 of MAVN bear the desired qualitative relationship to the BCR model chromospheres that are most relevant to the 7 August 1972 flare, it is necessary to point out that they do not produce computed $H\alpha$ line profiles that are in quantitative agreement with observed $H\alpha$ line profiles, despite the fact that semi-empirical models have many degrees of freedom and are quite free of any specific laws of flare energy transport. These model atmospheres succeed only in reproducing the observed $H\alpha$ equivalent widths. Many models can, of course, achieve the observed $H\alpha$ equivalent widths. It remains true that to reconcile the profiles from the MAVN models with observations it is necessary to introduce an *ad hoc* amount of macroturbulence. Second, MAVN do not explore the effect of variation of the parameters of their semi-empirical model atmospheres on the ability of their models to reproduce the complete $H\alpha$ line profile. Hence one has no idea of the uniqueness of the MAVN models, nor of how much better one might be able to reproduce the full observed profiles if the MAVN model atmospheres were subjected to independent variation of the parameters that control effective chromospheric temperature in $H\alpha$ and column density of the transition region. It appears that probably the macroturbulence requirements could be reduced, or even eliminated, by exploring other model atmospheres, bearing in mind the relationships discussed above and by Dinh (1980).

The principal conclusion of this paper is relevant to collisionless confinement of hot flare plasma. The work of Brown *et al.* (1979), Smith and Auer (1980), and Smith and Brown (1980) leads one to expect that the high temperature ($T_e \sim 10^8$ K) thermal X-ray source region is confined by a collisionless conduction front that moves through the relatively cool ($T < 10^7$ K) material of the corona at velocities of order 100 km s^{-1} . Fast electrons with velocity greater than approximately two times the mean thermal velocity in the high temperature region will escape with diminished energy through the conduction front. Assuming that the high temperature region is initially created in a limited space at the top of a flare loop, for a short period of time (probably 1–10 s) whose length depends on loop geometry and physical conditions the conduction front will not yet have arrived at the top of the pre-flare chromosphere. This interval is sufficiently short that present observations of flare $H\alpha$ profiles are not relevant to it; Tanaka's (1977) observations of nonreversed profiles span a period of several minutes.

The phase of the chromospheric flare event that is relevant to the observations of flare $H\alpha$ profiles is after the thermal front has reached the chromosphere. During

this phase, the conclusion of this paper is that apparently so few 10–100 keV electrons (relative to the number required in the power-law thick-target hypothesis) penetrate through the thermal front that they do not dominate the heating of the $H\alpha$ -emitting chromosphere, and do not lead to a major portion of the $H\alpha$ emission. Those electrons that do penetrate into the chromosphere must be primarily very short-range and dominate the heating only in the immediate vicinity of the transition between the high temperature region and the remaining chromosphere, which shows relatively little flare heating. It may be entirely reasonable, of course, that the electrons that penetrate the thermal front do indeed have the required spectrum. A determination of the spectrum of the electrons that pass through the front would be directly testable through modelling of their effect on the chromosphere.

One final note of caution needs to be expressed regarding the fact that I base my arguments above on the BCR calculations. Their results depend on their representation of the important contributors to radiative loss in the chromosphere. It is clear from the observations themselves and from calculations such as those of MAVN that there are several other spectral features that radiate chromospheric flare energy just as effectively as $H\alpha$ and $L\alpha$, which were the only features for which BCR specifically treated radiative transfer. In order to reach the conclusions above in a fully satisfactory way a theoretical energy balance calculation should be done that incorporates radiative transfer in more spectral features, as well as time dependence and thermal conduction.

Acknowledgements

I wish to thank A. N. McClymont for calling my attention to the Sermulina *et al.* (1980) paper, Q.-V. Dinh for permission to cite his results in advance of publication, and K. Tanaka for his unpublished $H\alpha$ flare profiles. I wish to thank A. N. McClymont, H. S. Hudson, and M. J. Elcan for stimulating discussions and comments.

This research has been supported by the Air Force Office of Scientific Research, Air Force Systems Command, USAF, under grant AFOSR-76-3071, and by the National Aeronautics and Space Administration, under grant NSG-7406.

References

- Akasofu, S. I.: 1979, *Solar Phys.* **64**, 333.
- Athay, R. G.: 1972, *Radiation Transport in Spectral Lines*, D. Reidel Publ. Co., Dordrecht, Holland.
- Baliunas, S. L., Avrett, E. H., Hartmann, L., and Dupree, A. K.: 1979, *Astrophys. J. Letters* **233**, L129.
- Brown, J. C.: 1973, *Solar Phys.* **31**, 133.
- Brown, J. C. and Smith, D. F.: 1980, *Rep. Prog. Phys.* **43**, 125.
- Brown, J. C., Canfield, R. C. and Robertson, M. H.: 1978, *Solar Phys.* **57**, 399.
- Brown, J. C., Melrose, D. B., and Spicer, D. S.: 1979, *Astrophys. J.* **228**, 592.
- Brown, J. C., Smith, D. F., and Spicer, D. J.: 1980, in *The Sun as a Star*, NASA/CNRS, in press.
- Canfield, R. C.: 1974, *Solar Phys.* **34**, 339.
- Canfield, R. C. and Athay, R. G.: 1974, *Solar Phys.* **34**, 163.

- Canfield, R. C. and Ricchiazzi, P. J.: 1980, *Astrophys. J.* **239**, 1036.
- Canfield, R. C., Brown, J. C., Brueckner, G. E., Cook, J. W., Craig, I. J. D., Doschek, G. A., Emslie, A. G., Hénoux, J.-C., Lites, B. W., Machado, M. E., and Underwood, J. H.: 1980a, in P. A. Sturrock (ed.), *Solar Flares*, A Monograph from Skylab Solar Workshop II, University of Colorado Press, Boulder, p. 231.
- Canfield, R. C., Cheng, C.-C., Dere, K. P., Dulk, G. A., McLean, D. J., Robinson, R. D., Schmahl, E. J., and Schoolman, S. A.: 1980b, in P. A. Sturrock (ed.), *Solar Flares*, A Monograph from Skylab Solar Workshop II, University of Colorado Press, Boulder, p. 451.
- Crannell, C. J., Frost, K. J., Mätzler, C., Ohki, K., and Saba, J. L.: 1978, *Astrophys. J.* **223**, 620.
- Datlowe, D. W., Elson, M. J., and Hudson, H. S.: 1974, *Solar Phys.* **39**, 155.
- Dinh, Q.-V.: 1980, *Publ. Astron. Soc. Japan* **32**, 515.
- Doschek, G. A. and Feldman, U.: 1978, *Astron. Astrophys.* **69**, 11.
- Elcan, M. J.: 1978, *Astrophys. J. Letters* **226**, L99.
- Field, G. B.: 1965, *Astrophys. J.* **142**, 531.
- Gebbie, K. B. and Steinitz, R.: 1974, *Astrophys. J.* **188**, 399.
- Hoyng, P., Brown, J. C., and van Beek, H. F.: 1976, *Solar Phys.* **48**, 197.
- Hudson, H. S.: 1972, *Solar Phys.* **24**, 414.
- Hudson, H. S.: 1973, in R. Ramaty and R. G. Stone (eds.), *Symposium on High Energy Phenomena on the Sun*, NASA GSFC X-693-73-193, p. 207.
- Kane, S. R., Crannell, C. J., Datlowe, D., Feldman, Y., Gabriel, A., Hudson, H. S., Kundu, M. R., Mätzler, C., Neidig, D., Putrosian, V., and Sheeley, N. R., Jr.: 1980, in P. A. Sturrock (ed.), *Solar Flares*, A Monograph from Skylab Solar Workshop II, University of Colorado Press, Boulder, p. 215.
- Korchak, A. A.: 1971, *Solar Phys.* **18**, 284.
- Lin, R. P. and Hudson, H. S.: 1976, *Solar Phys.* **50**, 153.
- Lite, B. W. and Cook, J. W.: 1979, *Astrophys. J.* **228**, 598.
- Machado, M. E. and Linsky, J.: 1975, *Solar Phys.* **42**, 395.
- Machado, M. E., Emslie, A. G., and Brown, J. C.: (1978), *Solar Phys.* **58**, 363.
- Machado, M. E., Avrett, E. H., Vernazza, J. E., and Noyes, R. W.: 1980, *Astrophys. J.* **242**, 336.
- Nakagawa, Y., Wu, S. T., and Han, S. M.: 1973, *Solar Phys.* **30**, 111.
- Schoolman, S. A. and Ganz, E. D.: 1981, *Solar Phys.* **70**, 363.
- Serulina, B. J., Somov, B. V., Spektor, A. R., and Syrovatskii, S. I.: 1980, in M. Dryer and E. Tandberg-Hanssen (eds.), 'Solar and Interplanetary Dynamics', *IAU Symp.* **91**, 491.
- Somov, B. V., Spektor, A. R., and Syrovatskii, S. I.: 1977, *Bull. Acad. Sci. USSR, Phys. Series* **41**, 32.
- Somov, B. V., Spektor, A. R., and Syrovatskii, S. I.: 1979, *Proc. Lebedev Phys. Inst.* **110**, 73.
- Smith, D. F. and Auer, L. H.: 1980, *Astrophys. J.* **238**, 1126.
- Smith, D. F. and Brown, J. C.: 1980, *Astrophys. J.* **242**, 799.
- Smith, D. F. and Lilliequist, C. G.: *Astrophys. J.* **232**, 582.
- Švestka, Z.: 1976, *Solar Flares*, D. Reidel Publ. Co., Dordrecht, Holland, p. 7.
- Tanaka, K.: 1977, in Brown *et al.*, *Solar Phys.* **57**, 399, Figure 3.
- Zirin, H. and Tanaka, K.: 1973, *Solar Phys.* **32**, 173.

v) Direct Evidence for Chromospheric Evaporation
in a Well-Observed Compact Flare

This paper reports our most important observational result. This paper proved that the chromosphere was the source of the hot flare plasma that emitted the observed flare X-rays. This paper was the first result of our effort to improve the quality of solar flare spectroscopic observations. We anticipate many more important results to come out of other applications of this same observational technique. These observations were a dramatic improvement over previous results, primarily in temporal resolution, temporal coverage (including the pre-flare and impulsive phases), and spatial coverage (the whole flare). The main reason we were able to do so much better than previous observers was improved technology; we used a charge-coupled device detector, rather than photographic film. Various interesting possibilities for future work were uncovered in this research, which will be followed up in the future. Among them is the possibility of using H α profiles for prompt evidence for accelerated flare electrons. Another possibility is quantitative diagnosis of the nature of the accelerated particles themselves, perhaps both electrons and protons.

DIRECT EVIDENCE FOR CHROMOSPHERIC EVAPORATION
IN A WELL-OBSERVED COMPACT FLARE

Loren W. Acton¹, Richard C. Canfield²,
Todd A. Gunkler², Hugh S. Hudson²,
Alan L. Kiplinger³, John W. Leibacher¹.

Submitted _____

- 1 Lockheed Palo Alto Research Laboratory,
Lockheed Missiles and Space Co., Inc.
- 2 Center for Astrophysics and Space Sciences,
University of California, San Diego.
- 3 Applied Research Corporation, Landover, Maryland, and
Goddard Space Flight Center, NASA.

ABSTRACT

We have observed the flare of 1980 May 7 1456 UT with several Solar Maximum Mission instruments, in coordination with the Sacramento Peak Observatory Vacuum Tower Telescope. From the X-ray data we are able to determine the total emission measure of all material at $T > 2 \times 10^6$ K, commonly attributed to chromospheric evaporation. Volume estimates from the X-ray and H α images lead to an estimate of the number of electrons in the soft X-ray plasma.

Comparison of theoretical calculations of the H α signature of an evaporated state of the chromosphere to H α line profile observations provides direct evidence that chromospheric evaporation indeed has taken place concurrently with the appearance of the X-ray plasma. We have determined the amount of material that has been evaporated from the chromosphere, relative to the pre-flare state. This leads us to the conclusion that more than enough material has been evaporated from the chromosphere to account for the material in the X-ray plasma.

Taken together, the H α , soft and hard X-ray images suggest that chromospheric evaporation is driven by two mechanisms. During the impulsive phase, there is evidence that chromospheric evaporation is due to flare accelerated electrons. During the thermal phase, it appears to be driven by thermal conduction from the hot coronal plasma created earlier in the flare.

I. INTRODUCTION

Various flare-associated phenomena demonstrate that during solar flares, an enhanced amount of material is found at high temperatures, $T \gg 10^6$ K. These phenomena include flare soft x-ray emission (reviewed by Culhane and Acton, 1974), post-burst increases at radio wavelengths (see, e.g., Kundu, 1965) and sporadic coronal condensations in visible coronal emission lines (see, e.g., Evans, 1963). The existence of these phenomena suggests the heating of previously cool material, most probably from the chromosphere, to high temperatures. The heating mechanism is of basic interest for the theory of solar and stellar flares, interplanetary disturbances, and the theory of stellar mass loss in general. Several recent monographs review related aspects of this problem (Sturrock, 1980; Priest, 1981; Jordan, 1981).

Neupert (1968) initially suggested that nearly simultaneously with, and perhaps as a result of, the energy losses of fast electrons (implied by microwave impulsive bursts), the chromosphere becomes heated to temperatures on the order of 2×10^7 K. This produces the characteristic soft x-ray emission of a flare. He inferred that this soft x-ray plasma not only accounted for the enhancement of interplanetary material that ultimately leads to geomagnetic storms, but also reappeared at visible wavelengths as loop prominence systems and "coronal rain" as it cooled. Hudson and Ohki (1972) pointed out that the increase of the soft x-ray emission measure during flares might be accounted for in

two different ways, either by "coronal condensation", i.e. reduction of the volume occupied by the soft x-ray emitting material, starting from material at typical coronal temperatures and densities previous to the flare, or by what they termed "chromospheric rarefaction", now more commonly called chromospheric evaporation. They ruled out coronal condensation on the basis of straightforward coronal mass content arguments, and concluded that the chromosphere is the only plausible source of material not previously observed in soft x-rays or microwaves. Hudson (1973) then extended Neupert's (1968) conclusions to postulate that the main direct effect of the flare energy release is the production of 10-100 keV electrons, which impinge on the dense chromosphere to give hard x-rays. The energy deposited by the non-thermal electrons could then heat and expand the chromospheric material, accounting for the increase of the soft x-ray emission measure. H α and the rest of the main phase would then be due to heat conduction from the soft X-ray source (see also Lin and Hudson, 1971; 1976).

Sturrock (1973) summarized this evolving picture and coined the term *chromospheric evaporation*, which has remained in use until the present time. Although the phenomenon envisioned is clearly not literally evaporation, it does suggest the physically relevant distinction between two phases, the cool chromospheric phase and the hot coronal phase. (A few authors have used the term *ablation* recently, in analogy to the burning away of rocket nose cones on

reentry. However, its medical use to indicate the surgical removal of organs and abnormal growths somewhat reduces its appeal!) The mechanisms that drive the change from the cool to the hot phase are not known with certainty, though the phase change itself upon both heating and cooling appears to be a consequence of thermal instability (Field, 1965; Goldsmith, 1971). In this paper we will use the term chromospheric evaporation to denote the change from the cool phase to the hot phase.

The first semi-quantitative model of the phenomenon of chromospheric evaporation from the point of view of the cool (chromospheric) part of the flare, as opposed to the high-temperature (coronal) part, is due to Hirayama (1974). He showed that it was reasonable to expect chromospheric evaporation to take place as a consequence of both direct bombardment by electrons and by thermal conduction. He made a basic argument based on pressure balance across the chromosphere-corona transition region. This argument is reasonable even for an entire flare loop, in view of the short hydrodynamic scale time of material at characteristic flare soft X-ray temperatures (2×10^7 K), compared to the duration of flares. Pressure balance requires that the top of the chromosphere be lowered by roughly 1000 km during flares; it is not sufficient to simply compress the chromosphere, since this fails to account for the increase of soft x-ray emission measure. It is interesting that typically observed soft X-ray pressures match the range of pressures at the top of the empirical chromospheric flare models of Machado and Linsky (1975), which are

determined by chromospheric line profiles, independent of soft X-rays.

On the basis of microwave and soft x-ray data, Ohki (1975) showed that the continued rise of the soft x-ray emission measure after the cessation of the impulsive microwave phase of the flare implies that evaporation is driven primarily by thermal conduction, not by fast electrons. Support for this argument was provided by Datlowe (1975). He found that both timing and energetics indicate that the creation of the soft x-ray plasma cannot be due entirely to the dissipation of the energy of fast electrons. Counter-arguments, indicating the importance of electrons injected into the chromosphere, leading to explosive heating of chromospheric material to soft x-ray temperatures, were advanced by Lin and Hudson (1976), who also suggested the possible importance of heating by soft x-ray irradiation of the chromosphere lying underneath the source.

Evaporation as a phenomenon that operates during the thermal phase of flares has been discussed by Antiochos and Sturrock (1978). They argue that evaporation is the inevitable consequence of the heat flux deposited at the top of the chromosphere due to the overlying soft x-ray plasma, since the material at ordinary chromospheric temperatures and densities cannot radiate energy away fast enough. Assuming that conductive losses dominate the cooling of the soft x-ray plasma, and evaporative velocities are subsonic, they show that such evaporation would reduce the heat

flux conducted into the underlying chromosphere. An observational requirement for such a process was found by Krieger (1977), in order to account for what appeared to be inadequate chromospheric $H\alpha$ radiative output compared to that from the flare corona. However, this argument was considerably weakened, if not destroyed, by subsequent actual measurement of the much smaller than supposed contribution of H alpha to the total radiative output of a flare (Canfield *et al.*, 1980). The strongest argument against the picture of cooling-phase evaporation as drawn by Antiochos and Sturrock (1978), at least in one compact flare, seems to be the disagreement between the predicted and observed spectrum, as shown by Underwood *et al.* (1978).

In their Skylab Solar Flare Workshop summary of the importance of chromospheric evaporation, Moore *et al.* (1980) concluded that it appears highly probable that the bulk of the mass of the soft x-ray emitting plasma is supplied during the rise phase by chromospheric evaporation from the feet of the soft x-ray loops. They perceived very little need to supply mass by explosively heating and evaporating the chromosphere by the precipitation of nonthermal high-energy electrons in the flash phase.

On the other hand, Cheng, Feldman and Doschek (1981), argued that *chromospheric evaporation is not important* as a source of soft X-ray plasma for three reasons: (1) upward velocities are not observed; (2) the Antiochos and Sturrock evaporative model disagrees with observations, as shown by Underwood *et al.* (1978); (3) Dere and Cook

(1979) found coronal pressures to exceed chromospheric pressures by one to two orders of magnitude during a compact flare. Cheng, Feldman and Doschek (1981) advocated a compression model, in which the compression is a magnetohydrodynamic effect of flare currents. However, in disagreement with (1), large upward motions in transition region lines have been reported by Hiei and Widing (1979) and in the rise phase of soft X-rays by Feldman *et al.* (1980) from P78-1 observations, Antonucci *et al.* (1981) from SMM, and Tanaka (1981) from Astro-A.

Both Underwood *et al.* and Dere and Cook treat the decay phase of the same small flare (1973 August 9 at 1550 UT). Underwood *et al.* first concluded that radiative cooling dominates for this flare. They then compared the differential emission measure distribution of this flare to that predicted by the Antiochos and Sturrock (1978) evaporative flare cooling model and found poor agreement. This is not surprising, as this model explicitly excludes radiative cooling.

Dere and Cook's estimate of flare densities extends from Fe XXII at 10^7 K to Si III at 3.5×10^4 K. Straightforward interpretation of their results indeed shows an overpressure in the high temperature part of the flare as compared with the transition region regime. However, the flare studied by these workers has much in common with the event we report here in which direct chromospheric observation contradict Cheng, Feldman and Doschek's conclusion about the unimportance of chromospheric

evaporation during flare decay.

Although there has been a great deal of discussion of the phenomenon of chromospheric evaporation during the last decade, there has been no direct evidence that it indeed is a real phenomenon of the chromosphere. Chromospheric evaporation has always been an inference, without compelling, positive evidence. In this paper, we present observations that we believe constitute such evidence; they show *chromospheric evaporation in progress* - the appearance of soft x-ray emitting plasma accompanied by the disappearance of chromospheric material. In Section II of this paper we discuss the Solar Maximum Mission (SMM) and Sacramento Peak Observatory (SPO) observations that substantiate this assertion, for the flare of 1980 May 7 1456 UT. In Section III we analyze and interpret these observations, showing how they demonstrate the existence of evaporation and reveal the physical nature of the chromospheric heating mechanisms that cause it.

II. OBSERVATIONS

a) Introduction

The important manifestations of this flare were over in five or six minutes, but were unusually well observed as part of a Solar Maximum Mission coordinated observing sequence. The flare was associated with an isolated area of leading magnetic polarity in the following portion of NOAA active region 2418, at S23 W12. The flare commenced at 1455 UT on 1980 May 7. It was assigned

importance SB in *Solar Geophysical Data*, classed as C7 in soft X-rays, and produced decimetric Type IV and dekametric Type III radio bursts.

b) Hard X-Ray Spectra

The SMM Hard X-Ray Burst Spectrometer (HXRBS), described by Orwig, Frost and Dennis (1980), is a large-area scintillation counter sensitive in the energy range 28 - 470 keV. Its data clearly delineate the impulsive phase of this flare, with an instrumental time resolution of 128 ms. An initial gradual increase of hard X-radiation beginning at approximately 145515 UT culminated in an impulsive burst with a relatively hard spectrum (observable at energies up to 260 keV) from 145603 to 145612, followed by a multiple impulsive burst with a softer spectrum extending from 145624 to 145647, ending in a fairly smooth decay into background at about 1459. The impulsive emission thus extended over 44 seconds and was characterized by numerous rapid fluctuations of hard X-ray flux. Figures 1 and 4 compare the hard X-ray light curves with other optical and X-ray radiation from this flare.

According to power-law fits to the HXRBS data, the initial component approached a spectral index of about 3.8, whereas the remainder of the impulsive emission had a spectral index of approximately 4.8. The spectra obtained from HXRBS may be characterized either with a non-thermal (power law) model, as

described above, or an isothermal bremsstrahlung (free-free) model. The distinction is not important for the purposes of the present paper, since either model requires the presence of 10 - 50 keV electrons in comparable numbers, and (see the HXIS data below) these electrons have a separate distribution from the thermal source seen in soft x-rays.

c) Hard X-Ray Imaging Spectra

The SMM Hard X-Ray Imaging Spectrometer (HXIS) (van Beek *et al.*, 1980) provides simultaneous spectral and imaging information in pixels 8 arc sec square, in six energy bands ranging from 3.5 to 30 keV. The time resolution during this flare was 4.5 sec, but in the higher-energy bands the effective time resolution is governed more strongly by the length of time needed to accumulate sufficient photon counts. This leads us to consider the impulsive phase as a whole, without trying to resolve it temporally.

The time profile of the highest-energy band (22-30 keV) of HXIS matches that of HCRBS shown in Figure 1, confirming that HXIS response in this channel is due to the impulsive emission. In the first (harder) period, the 16-22 keV channel is also clearly dominated by impulsive emission, so we have summed the higher two channels to characterize this component in the images shown in Figure 2. The soft channel, 3.5-8.0 keV, is the sum of the lowest two HXIS bands and matches the time profile of the BCS light curve in Figure 1. Coalignment of the images from the different

instruments is illustrated in Figure 5.

The EXIS images in Figure 2 are broken down to show pre-burst, burst, and post-burst information in the two broad spectral regions. The pre-burst data show the soft source to be centered between EXIS pixels 5 (the north pixel) and 8 (the south pixel). The pre-burst hard source probably was located mainly in the south pixel, although insufficient counts were detected for certainty about this. The soft X-ray source in the burst (impulsive) phase peaked in the north pixel; the hard X-ray source peaked in the south pixel. Finally, the post-burst soft X-ray source peaked in the north pixel and could not be measured in the highest-energy EXIS band.

d) Soft X-Ray Spectra

The Bent Crystal Spectrometer (BCS) observations of this flare include coverage of the Ca XIX and Fe XXV line groups and their satellites, with an instrumental time resolution of 1 s. Gabriel and Mason (1981) review the use of such data for the determination of plasma temperature and ionization state. The BCS is sensitive to emission within a 6 x 6 arc-minute field of view. Details of the instrument operation may be found in Acton *et al.* (1980), and Culhane *et al.* (1981) present some preliminary results. Figure 1 shows the flux in the Fe XXV resonance line, which increases nearly simultaneously with the onset of the hard X-ray burst.

This event was relatively weak in soft X-ray emission, and we have integrated for 20 seconds to improve the statistical significance of the line spectra. The data do not permit a statistically significant line shift determination. Nonetheless, an increased line width coincident with the initial hard X-ray increase is evident. These observations are consistent with an observational model which has emerged from the examination of many other events: the soft X-ray emitting plasma initially appears with large upward velocity (up to 500 km/sec) and non-thermal broadening (150-200 km/s), both of which last for only a short time, comparable with the duration of the hard X-ray burst, during which time the 10^7 K emission measure has risen to only a few tenths of its maximum value (Feldman, *et al.*, 1980; Antonucci, *et al.*, 1981; Tanaka, 1981).

e) Polychromatic Soft X-Ray Images

The SMM Flat Crystal Spectrometer (FCS) was being operated in its polychromatic raster mode (Acton *et al.*, 1980) to provide images of the flaring region in the resonance lines of O VIII, Ne IX, Mg XI, Si XIII, S XV and Fe XXV, sensitive to electron temperatures in the range $2 \times 10^6 \leq T_e \leq 5 \times 10^7$ K. Each FCS pixel subtended $15'' \times 15''$. The image repetition rate was 152 s. This small flare was confined to a single FCS pixel, which was observed at the times indicated by arrows in Figure 1. Fortunately, the flare was observed by the FCS within a few

seconds of the peak of emission in the highest temperature emission lines observed by the BCS, at 145710. This was well into the smooth decay of the hard x-ray burst, but earlier than the peak emission in the three lowest-temperature FCS channels (O VIII, Ne IX, and Mg XI), which was recorded in the subsequent FCS sample at 145944. The combined BCS and FCS observations show that the Fe XXV emission decayed to 10% of peak intensity in 2 minutes, while Ca XIX, Mg XI and O VIII took about 4, 11 and 20 minutes respectively. This temperature-dependent flare decay is characteristic of the thermal X-ray plasma of flares in general (c.f. Neupert *et al.*, 1968), and establishes that this flare, while more impulsive than most small flares observed by SMM, was not peculiar in its soft X-ray temporal evolution.

1) H α Line Profiles

H α line profiles were obtained at the Sacramento Peak Observatory (SPO) Vacuum Tower Telescope, using the methods described in detail in the appendix. We observed an area 100" x 267", consisting of 50 x 100 pixels, each 2" x 2.67" in size. The 50 pixels aligned along the 100" spectrograph slit were obtained simultaneously; the slit was scanned across the solar image with a repetition period of 25.6 s. All parts of the flare were within the area scanned. The spectrum of each pixel is the average of two simultaneous 50-point spectra, obtained 1/8 s apart in time. The spacing between spectral points was 204 mÅ, and the

spectrum was approximately centered on $H\alpha$. Data were obtained from 142415 to 151227 UT.

Figure 1 includes $H\alpha$ light curves for the entire flare, as well as for the two brightest kernels. What we call the $H\alpha$ power is the excess flare radiation of the whole flare over a 10 Å wide band of the spectrum centered on $H\alpha$. The power excess for each spatial pixel is computed by subtracting the average profile for a reference time period from the profile during the flare, and summing over all spectral pixels. The reference period contains 17 consecutive scans, and extends from 1426 to 1450 UT. The conversion from fractions of the quiet solar continuum to absolute cgs units is made by adopting Allen's (1973) absolute continuum intensity value of $2.84 \times 10^6 \text{ erg (cm}^2 \text{ s Å ster)}^{-1}$ at $H\alpha$; we assume energy is radiated isotropically into 2π ster. The values of time at which all $H\alpha$ data are plotted are those at which the spectrograph slit crosses the north kernel; since we have an $H\alpha$ measurement at any given pixel only every 25.6 s, the fact that the slit crosses the south kernel 2 s before the north kernel is of little consequence.

It is clear from Figure 1 that the total $H\alpha$ light curve is different from both of the x-ray light curves. $H\alpha$ peaks during the hard x-ray burst, and has fallen significantly before Fe XXV peaks. $H\alpha$ rises above the measured pre-flare variations ($2 - 3 \times 10^{24} \text{ erg s}^{-1}$) before the first hard x-ray burst at 145603, though both show some indications of increases starting at

about 145530. There is considerable increase of the H α power in association with both hard X-ray bursts; the H α peak occurs during the second burst. The characteristic rise time in H α is about 70 s; the characteristic decay time is 2 - 3 m. The relationship between hard x-ray and H α start times is well known (cf. Zirin, 1978), though the fact that H α leads Fe XX' by about 30 s disagrees with Zirin's finding that the H α peak lasts until the 5-6 keV peak. We have checked that this disagreement is not due to Zirin's 1/4 Å pass-band width. In fact, the power in the band 1/4 Å wide centered on H α peaks at the same time as the that in the full 10 Å band; the only differences occur during the decay phase, during which the power in the wider band falls considerably faster.

We use the term kernel to denote a well defined exceptionally bright area as measured in total H α power. We define the kernel area by including all pixels brighter than half the brightness of the brightest pixel at flare maximum. The south kernel is twice as big as the north one; its brightest pixel is 50% brighter than that of the north kernel. The light curve of the south kernel is somewhat more impulsive, in that it falls more rapidly ($\tau \approx 120$ s, as opposed to 180 s) immediately after the hard x-ray burst period. Finally, some preflare brightening (before 1455) is observed at the south kernel, but not at the north. However, the amplitude of the preflare brightening is not unusual, in the sense that the same kernel showed other similar brightenings during the 30 m before the flare.

Figure 3 shows corrected H α line profiles for various pixels of interest, two in the south kernel and three in and near the north kernel. Each column of the figure shows the temporal behavior of a single image pixel. The pixels are identified by their spectroheliogram (row,column) index (see Figure 5). In comparing the profiles, it is important to note the intensity of each, relative to the quiet sun continuum level. The latter is indicated by a tick mark to the right of each profile, connected to the profile by a diagonal line. We begin showing profiles at 145408 UT, before any significant flare-associated enhancement began. Between 145459 and 145824 we show every profile. After that time we show every fourth profile, at somewhat over 100 s intervals. The first period of impulsive hard x-ray bursts lasted from 145603 to 145612. H α profiles are shown at 145616, just a few seconds after this first period ended. H α profiles were also obtained at 145642, toward the end of the second period of (softer) impulsive hard x-ray emission. The time labels for these two H α profile samples are underlined.

There are both similarities and important differences between the spectra of the north and south kernels. Similarities include: (1) The widths of the line profiles are greatest during the impulsive phase, and decrease rapidly thereafter, in agreement with Schoolman and Ganz (1981), called SG below. This great width during the impulsive phase is associated with substantial emission even at 15 Å, which means that our H α power measurements are lower

limits. (2) In the vicinity of both kernels, we see spectral changes associated with the well-known spreading of the $H\alpha$ kernels away from the neutral line as the flare develops. The point (40,43) near the north kernel shows an example of such behavior. After an insignificant impulsive phase brightening, it finally goes into emission during the last phase of the flare. Also, the profile is never particularly wide at such points.

Differences in the nature of the $H\alpha$ profiles in the vicinity of the two kernels include: (1) Unreversed profiles are almost exclusively confined to the north kernel. In the south kernel, for example at (36,45), when the profiles are unreversed, they remain so for only about one minute during and immediately after the impulsive phase. Unreversed $H\alpha$ profiles have been reported previously, most recently by SG and Zirin and Tanaka (1973). (2) During the impulsive phase, the full width at half maximum of the profiles in the south kernel is much greater than in the north kernel. The maximum width in the south kernel is about 4 Å, while it is less than 3 Å in the north kernel. Possible reasons for these differences, in terms of physical processes in the chromosphere, will be discussed in Section III d).

One of the major advantages of measuring the full line profile is that it is possible to infer velocities from the position of the center of reversed lines. It has been shown that simple wing difference or bisector methods can be completely misleading for optically thick lines, including $H\alpha$ (Athay, 1970).

We have determined velocities at the top of the H α -forming region of the chromosphere by measuring the shift of the central absorption feature. Although there are not yet theoretical treatments of flare dynamics that are realistic in the chromosphere, the velocity observations themselves are of interest for use later, when such treatments become available.

Before the impulsive phase, the flare region shows a mixture of upward and downward velocities in the range $\pm 5 \text{ km s}^{-1}$. At the time of the first H α observation after the start of the first hard X-ray burst (at 145616 UT, about 10 s after the peak of the first burst), upward motions are observed at all south kernel points. Velocities of $10 - 20 \text{ km s}^{-1}$ persist at all these points for several minutes. At the north kernel, where no hard x-rays are observed, no such consistent pattern of motions is observed. After the impulsive phase, one of the two pixels shows downflows of 10 km s^{-1} , and the other shows upflows of $10 - 20 \text{ km s}^{-1}$. Non-kernel points show mostly weak blue shifts. The lack of a consistent pattern over the flare as a whole or in the north kernel, as well as the consistency of blue shifts in the south kernel, argues against mechanisms that invoke or result in compression or downward moving shocks in kernels or the overall structure of the flare, unless the expected interval of downward motions can be less than the interval between our profile observations.

g) Combined Morphology

Achieving a common spatial scale and rigorous co-alignment of images from different experiments is always a challenge. In this case we benefitted from good photospheric sunspot images from Sacramento Peak Observatory, Big Bear Solar Observatory, Marshall Space Flight Center, and the Flat Crystal Spectrometer. Furthermore, the flare was compact and was covered from start to finish by SPO, BBSO, and FCS. Seeing was variable, in the few arc second range, at the two ground-based sites.

The SPO spectroheliograms were processed to produce "continuum" images at $\Delta\lambda = \pm 5 \text{ \AA}$ from line center in the far wings of $H\alpha$, to show the sunspots. We also produced line center $H\alpha$ spectroheliograms roughly comparable to the BBSO $H\alpha$ filtergrams. The SPO data established that the brightest northern flare kernel remained in the same $2'' \times 2.7''$ pixel throughout the flare. This fact was used to determine the relative positions of the BBSO images in Figure 4. The SPO $H\alpha$ kernels have been taken for our spatial reference for analysis of the SMM X-ray data, as illustrated in Figure 5.

The FCS X-ray collimator incorporates an optical sensor that builds up a low-resolution white-light image as the instrument is rastered to acquire polychromatic X-ray images. The alignment of this device with respect to the X-ray boresight has been determined in orbit to approximately $\pm 5''$. The alignment of the FCS images with respect to the $H\alpha$ images was accomplished by overlaying the

FCS sunspot images and the SPO sunspot images. By comparing counting rates in adjacent FCS pixels it was possible to determine that the soft X-ray flare was well centered in a single pixel at the location shown in the center panel of Figure 5. As illustrated in Figure 2, the HXIS soft X-ray source was well centered in HXIS pixel 5, and the superposition of this on the FCS source location determined the co-alignment of the HXIS pixel array shown in the leftmost sketch of Figure 5. Although the HXIS and FCS pixels are relatively large, 8" x 8" and 15" x 15" respectively, the strong signal from this compact flare permits a relative co-alignment for the X-ray images of about $\pm 3''$. However, the limited resolution of the FCS sunspot image and the FCS internal alignment uncertainty permit an alignment error of the X-ray images with respect to the sunspots and H α of $\pm 5''$. This uncertainty is of little consequence for the present study. In fact, this flare has been of considerable importance in the ongoing co-alignment analysis of the SMM instruments.

To summarize the morphology of this flare, spatial extent, fast rise time and decay phase, and lack of any substantial mass ejections place it in the class commonly referred to as compact flares (Pallavicini, Serio and Vaiana 1977, Moore *et al.*, 1980). However, it is a two ribbon flare in the sense of having two well defined H α kernels, which are presumably the footpoints of one or more magnetic arches which appear as an intense soft X-ray source following the impulsive phase. The SMM and SPO observations show

the flare was not simply a single symmetric loop. The most intense impulsive phase radiation and impulsive chromospheric evaporation were associated with the south kernel, while the north kernel displayed an evaporation time profile more closely related to the thermal or gradual phase of the flare.

III. ANALYSIS AND INTERPRETATION

a) Amount of Material Evaporated from the Chromosphere

The $H\alpha$ signature of chromospheric evaporation can be inferred from a grid of semi-empirical model flare chromospheres recently developed by Dinh (1980). He has solved the steady-state equations of radiative transfer and atomic populations for a model hydrogen atom consisting of three bound levels and the continuum state, assuming hydrostatic equilibrium. He addresses the question of uniqueness, which is a matter of concern in all semi-empirical modelling, by carrying out a systematic study of the effects of the major atmospheric parameters on the profiles. His work shows that there are four key atmospheric parameters: the transition region thickness, the pressure at the top of the chromosphere, the temperature distribution within the chromosphere itself, and nonthermal velocities. Since nonthermal velocities significantly in excess of the thermal velocity of hydrogen would broaden the $H\alpha$ emission peaks more than is shown by the observations, we assume they play no role (cf. Canfield, 1982). Of the other three parameters, only the increase in the pressure at the top of the

chromosphere due to the displacement of the transition region deeper into the preflare chromosphere (i.e. chromospheric evaporation) can affect the key property of the profiles from the point of view of this paper, i.e. the central reversal, without distorting the other profile parameters and characteristics of other emission (e.g. the strength of the Lyman continuum) outside the range of observationally acceptable values.

The most relevant parameter of Dinh's models from the point of view of chromospheric evaporation is the pressure of the overlying corona, which Dinh expresses in terms of the mass (m_{top}) of an overlying vertical column that gives the corresponding hydrostatic pressure at the top of the chromosphere. In this paper we use the column number (N_{top}), rather than the column mass. Changes in the value of N_{top} can be used to measure chromospheric evaporation, assuming that the material evaporated from the chromosphere during the flare contributes to N_{top} . The number of evaporated atoms at any given time is simply the difference between N_{top} implied by the flare spectrum and the value implied by the pre-flare spectrum.

Active region models and models of bright elements of the quiet sun have been developed by various authors (e.g. Basri et al., 1979, Vernazza, Avrett and Loeser, 1981), and are all characterized by values of N_{top} that are in the range $4 \times 10^{18} < N_{\text{top}} < 4 \times 10^{19} \text{ cm}^{-2}$. Those of Dinh's model flare chromospheres that produce profiles with central intensities and

reversals similar to those we observe in the kernels of this flare (e.g. his Model 2) all are characterized by values of N_{top} of about $4 \times 10^{20} \text{ cm}^{-2}$. The pre-flare mass is thus unimportant to the mass balance of the kernels during the most interesting times of the flare.

We begin by estimating the amount of evaporated chromospheric material through comparison of the observed profiles with Dinh's profiles for his models S, 1, 2 and 3. The parts of the models that represent the chromosphere and lower transition region are shown in Figure 6, along with Dinh's computed $H\alpha$ profiles. The values of N_{top} for these models are 1.3, 2.2, 4.3 and $8.7 \times 10^{20} \text{ cm}^{-2}$ respectively. To each of the pixels that shows any perceptible departure from its preflare state, we assign a value of N_{top} at each time of measurement, based on the amplitude of the central reversal and the central intensity of the observed $H\alpha$ profile, compared to Dinh's calculated profiles. We then sum the assigned values of N_{top} over the whole flare, taking into account the area per pixel. Thus we obtain the estimated number of evaporated atoms as a function of time, for the entire flare, or for any sub-area of interest.

Our estimate of the amount of material that has been evaporated from the chromosphere (i.e. its state of evaporation) as a function of time is shown in Figure 7. The thick curve gives the result for the whole flare; the broken curve, the region around the south kernel; the thin curve, the region around the north kernel.

The south region, where the hard X-ray emission originates, contributes the spike seen at about 1457 UT, during the impulsive phase. The north region, on the other hand, gives a much more gradual evaporation signature, which peaks after the time of the Fe XXV intensity peak. During the period 1446 - 1500 UT, $0.7 - 1.2 \times 10^{38}$ atoms had been evaporated from the chromosphere. We take 0.7×10^{38} atoms as a characteristic value for this period, which is chosen because it corresponds with the period of maximum soft X-ray emission measure, ignoring the somewhat uncertain spike of impulsive evaporation in the south kernel.

There are various qualifications that must be made regarding the procedures we have used in this section. First, though Dinh has provided the best grid of models presently available for use of H α profiles as a measure of the state of evaporation of the chromosphere, we expect that future models may imply amounts of evaporated material that differ from the present estimates by factors like two to four, while still satisfying other important observational constraints. Most notably, the south region, and particularly the south kernel, shows profiles whose wings are much different from those computed by Dinh. Thus we cannot be as confident of the actual numbers of evaporated atoms assigned to the south kernel as for the north kernel, where the resemblance between the widths, central intensities, and central reversals of Dinh's profiles is quite strong. Further uncertainty is introduced because evaporation takes place during the impulsive phase; one

must expect that at least for 10 - 100 s, the sound propagation time across dimensions of the same order as the observed flare, the quantitative estimate of the state of evaporation will be affected substantially by departures from hydrostatic equilibrium. Moreover, hydrostatic pressure may not be the sole contributor to the pressure at the top of the chromosphere; there may be a contribution from the confinement of the soft X-ray plasma by a sufficiently strong magnetic field. Third, the actual observations show H α asymmetries due to line of sight velocity gradients, which are not incorporated in Dinh's models. We assume that these asymmetries are not sufficiently large to mask the central reversal. Finally, we note that as Dinh shows, his profiles are not free of a systematic effect which will lead us to underestimate of the amount of evaporated material. Because he uses a model hydrogen atom with only three bound levels, which has the effect of incorrectly reducing the central intensity and strengthening the relative amplitude of the central reversal, our method of estimation will give a value of N_{top} that is too low, for a given observed profile. Judging from Dinh's calculations, the estimates made here are probably low by a factor less than or about two, for this reason.

b) Amount of Material in the Soft X-Ray Plasma

Calibrated measurements of the X-ray emission line intensities provide direct information on the line's emission

measure, $\int n_e^2 dV$, where n_e is the electron number density and V is the volume. Intensity measurements of a series of X-ray lines produced by plasmas over a range of temperatures can help reduce the temperature ambiguity of an emission measure determination from a single line, and help to determine the distribution of emission measure with temperature.

The emission measure distribution has been determined from the lines observed by the FCS according to the analysis technique of Sylwester, Schrijver and Mewe (1980). The ionization tables of Jacobs *et al.* (1977a,b,c, 1980) were used with the following values of atomic abundance relative to hydrogen: O (2.8×10^{-4}), Ne (4.5×10^{-5}), Mg (4.5×10^{-5}), Si (4.7×10^{-5}), S (1.6×10^{-5}), Ca (3.2×10^{-6}), and Fe (4.5×10^{-5}). These are based primarily on the work of Veck and Parkinson (private communication). For the purposes of this paper the total emission measure of the soft X-ray plasma is required. This was accomplished by computing the distribution of emission measure with temperature, and then integrating over temperature. Calculation of such differential emission measures from X-ray line fluxes is fraught with pitfalls, but the integral value tends to be relatively more stable in the presence of calibration and abundance uncertainties. This proved to be the case here, as a number of determinations encompassing the extrema of allowable parameters yielded a maximum total emission measure variation of only a factor of two.

Figure 8 shows the total X-ray emission measure (all material at $T > 2 \times 10^6 \text{ K}$) for this flare, as well as that within two higher temperature intervals. These values have been corrected for the approximate size and location of the X-ray source in the FCS collimator transmission pattern. The BCS yields characteristic temperatures by the satellite-to-resonance-line technique in the line-forming region of Ca XIX and Fe XXV (Culhane *et al.*, 1981). These determinations yield temperatures and emission measures that agree well with the FCS results for Fe XXV, the only line both instruments observed. For Ca XIX, the mean temperature of line formation is measured by the BCS to be lower than the FCS predictions, but the difference is not significant for this study.

For the samples at the two times of greatest interest, 145712 and 145944 UT, the FCS emission measure solution for this flare is bimodal, with peaks at $4 \times 10^6 \text{ K}$ and $19 \times 10^6 \text{ K}$ in the first case and $4 \times 10^6 \text{ K}$ and $15 \times 10^6 \text{ K}$ in the second case. Average temperatures of the entire source are 10^7 K and $6 \times 10^6 \text{ K}$ respectively, for the two times. The FCS is not sensitive to plasma below $2 \times 10^6 \text{ K}$ but, as shown by Dere and Cook (1979) and others, the amount of emission measure at lower temperatures is relatively small around and shortly following the peak of the soft X-ray light curve.

The total number of atoms involved in the X-ray plasma is approximated by $(V n_e^2 V)^{1/2}$. In this case the volume is the most poorly determined parameter. From the HXIS image we have derived a source size of about $8'' \times 9''$. The assumption that the source is

also 8" deep yields a volume of about $2 \times 10^{26} \text{ cm}^3$. Alternatively, if we assume that the H α flare kernels are each about 12 square arc seconds in area and are separated by 10", and are connected by a soft X-ray emitting semicircular tube of uniform cross-section, we get a source volume of about $7 \times 10^{25} \text{ cm}^3$. Thus we choose a source volume estimate of 10^{26} cm^3 and estimate a factor of two uncertainty.

From Figure 8 we conclude that the soft X-ray emission measure around the peak of the thermal flare is 10^{49} cm^{-3} , with an uncertainty conservatively estimated as a factor of three. The resulting uncertainty in the amount of soft X-ray emitting material is slightly less than a factor of two, which is quite adequate for our purposes. For the above values of $n_e^2 V$ and V , the total number of atoms in the soft X-ray source is 3×10^{37} .

c) Comparison of H α and X-Ray Evaporation Estimates

We are now able to compare the evaporative process from the H α and X-ray points of view. Table 1 summarizes the quantities of interest.

The H α profiles imply that for the flare as a whole, during the gradual phase (when the evaporation estimate is most reliable), the number of atoms evaporated from the chromosphere is 7×10^{37} . The soft X-ray emission measure of $1 \times 10^{49} \text{ cm}^{-3}$, coupled with the flare volume estimate of 10^{26} cm^3 , implies that there are 3×10^{37} electrons in the soft X-ray plasma with $T > 2 \times 10^6 \text{ K}$.

The H α and soft X-ray values agree within their observational uncertainty. We therefore conclude that enough material is evaporated from the chromosphere to account for the soft X-ray emitting plasma of this flare.

d) The Chromospheric Evaporation Mechanism

It is apparent that two different evaporation mechanisms are operating in two different spatial regions of this flare. The first is cospatial with strong hard X-ray radiation; the second is not.

The type of chromospheric evaporation originally hypothesized by Neupert (1968) appears to be observed at the south kernel. The H α observations indicate that during the hard X-ray burst, the chromosphere at the south kernel, from which hard X-rays are observed to originate, was the site of substantial short-lived evaporation, as well as some longer-lived evaporation. Here we apparently see chromospheric evaporation that is at least initially a result of heating by the hard X-ray emitting electrons. For most of the observed hard X-ray burst, a power-law spectrum provides a satisfactory representation of the spectrum. The appropriate coefficients for the observed spectrum of photons of energy $h\nu$, $dJ/d(h\nu) = A (h\nu)^{-\gamma}$, are $A = 2.6 \times 10^6$ and 7.1×10^7 photons $(\text{cm}^2 \text{ s keV})^{-1}$ and $\gamma = 3.8$ and 4.8 , for the first and second bursts respectively ($h\nu$ measured in keV). Following Lin and Hudson (1976), we calculate the column number N_c to which the atmosphere is explosively heated by a nonthermal power-law electron spectrum. We find N_c to have been 1.4×10^{20} and

$1.5 \times 10^{20} \text{ cm}^{-2}$ for the first and second bursts respectively. We have assumed that the fast electrons are injected into the the south kernel seen in $H\alpha$, which has an area of $1.1 \times 10^{17} \text{ cm}^{-2}$. This assumption is supported by the impulsiveness and strength of both the $H\alpha$ light curve and the evaporation signature at the south kernel. It is also supported by the broad nature of the $H\alpha$ profiles in the south kernel, which can plausibly be associated with the heating effects of the hard X-ray producing energetic electrons (see below). These broad profiles are confined to the south kernel. The hard X-ray producing electrons may not carry quite enough energy to evaporate the chromosphere explosively to the depth that is implied by the observed south kernel $H\alpha$ profiles (see Table 1), though we cannot be sure until the broad $H\alpha$ kernel profiles are better understood theoretically. Finally, a very brief period of blue-shifted and broadened X-ray emission lines is associated with the impulsive phase; such expansion of the X-ray plasma is consistent with impulsive evaporation.

The candidate mechanisms for chromospheric evaporation are the same as those for chromospheric flare heating in general. Those most commonly considered include fast electrons, soft X-ray irradiation, and thermal conduction (accompanied by irradiation in chromospheric lines like $L\alpha$). The preceding quantitative analysis of the effects of fast electrons on the chromosphere at the south kernel leads naturally to the conclusion that any weak hard X-ray emission that may be coming from the vicinity of the north kernel

does not imply a sufficient flux of fast electrons to cause the evaporation observed there in $H\alpha$. More importantly, almost no hard X-ray radiation is observed to come from the north kernel. Hence, only two of the three most likely mechanisms for chromospheric evaporation at this kernel remain, i.e. thermal conduction and soft X-ray irradiation. It is logically inconsistent to argue that the latter might play a primary role; if the creation of the soft X-ray plasma depends on chromospheric evaporation, it cannot be that the soft X-ray radiation itself is the primary driver of chromospheric evaporation. Hence, we conclude that one must attribute the considerable evaporation at the north to thermal conduction from the overlying hot coronal plasma, as suggested by Hirayama (1974) and Antiochos and Sturrock (1978). The continued increase of the amount of material evaporated from the north kernel until well after the impulsive phase is over is the type of behavior that one would expect from the modelling of Antiochos and Sturrock.

The $H\alpha$ profiles provide further evidence that conduction is the primary mechanism at the north kernel, whereas heating by nonthermal electrons is important in the south kernel. As shown by Canfield (1982), $H\alpha$ emission profiles like those observed at the north kernel during the period of maximum soft X-ray emission measure (which are not centrally reversed, yet not of unusually great total intensity), are not compatible with electron beam heating; such profiles indicate heating that does not penetrate deep into the flare chromosphere, beneath the flare transition

region, yet causes the transition region to be located far below its preflare location. Thermal conduction is the prime candidate for such a mechanism. On the other hand, Brown, Canfield and Robertson (1978) showed that H α profiles from nonthermal-electron heated flare chromospheres are intense and strongly centrally reversed, as is observed, for example, in pixel (37, 44) of the south kernel (Fig. 3). We would then speculate that the greater width of the profiles from this kernel is a consequence of heating quite deep in the flare chromosphere by the nonthermal electrons whose existence is evidenced by the hard X-ray emission from the south kernel.

e) Pressure Balance

There remains one puzzling inconsistency in the picture drawn here. Hirayama (1974) originally postulated conductively driven evaporation primarily on the basis of pressure balance arguments, i.e. that the pressure at the top of the flare chromosphere should be that same as the of the soft X-ray flare plasma. In this flare we do not find such pressure balance, even many hydrodynamic scale times after the impulsive phase. The pressures from the H α analysis never exceed about 50 dyne cm^{-2} , whereas the pressure in the soft X-ray plasma is about 400 dyne cm^{-2} at 1457 UT and 250 dyne cm^{-2} at 1500 UT. The HXIS and FCS observations do not permit the soft X-ray flare volume to be as large as 10^{28} cm^3 , i.e. a characteristic linear volume to be as large as 10^{28} cm^3 , i.e. a characteristic linear dimension of $30''$,

which would be required for balance at the pressure indicated by the H α analysis. A similar pressure difference was found by Dere and Cook (1979), in another compact flare. The possibility remains that there is more fine structure (i.e. a smaller filling factor) in the chromosphere than in the corona, and that our observed SFO H α profiles from a single 2" x 2.7" pixel are a combination of highly perturbed regions with a pressure at the top of the chromosphere that corresponds to the observed X-ray pressure, and relatively unperturbed regions that are thermally isolated from the soft X-ray plasma. At this time we can only speculate that part of the problem may arise from the use of Dinh's profiles, which assume hydrostatic equilibrium.

IV. CONCLUSIONS

In this paper we have demonstrated for the first time from direct *chromospheric* observations that the chromospheric evaporation postulated for more than a decade to be an important mass and energy balance mechanism in solar flares does in fact occur. Comparison with flare X-ray observations indicates that during the impulsive phase, evaporation is driven primarily by flare accelerated electrons. During the thermal phase of the flare chromospheric evaporation appears to be driven by thermal conduction downward from the hot coronal plasma created earlier in the flare. The amount of material evaporated from the chromosphere, from the H α observations, is adequate to supply the

material observed in the soft X-ray source at the peak of the X-ray flare. Thus, the two types of chromospheric evaporation originally suggested by Neupert (1968) and Hirayama (1974) both seem to exist and be important in this flare.

Detailed study of the temporal evolution of the relationship between chromospheric and coronal material and the dynamics and energetics of the evaporation process are among the many topics that remain for future work. Published $H\alpha$ profiles are inadequate to deal with the extremely broad and asymmetric profiles appearing in the energetic-electron-driven evaporative region, and must be prepared before quantitative studies of impulsive evaporation are meaningful. The apparent bimodal temperature distribution of the soft X-ray source needs to be investigated, as does the order-of-magnitude discrepancy between the gas pressure in the X-ray source and its value at the top of the chromosphere in the $H\alpha$ flare kernels.

The authors wish to thank the many individuals who have contributed time and data to this research. Drs. Harold Zirin and Ronald Moore provided BBSO $H\alpha$ filtergrams. Dr. Mona Hagyard provided MSFC magnetograms, and Dr. David Rust both helped coordinate the data acquisition and provided $H\alpha$ filtergrams from the USAF SOON system. Dr. Marcos Machado helped with the early analysis of the EXIS data and contributed valuable comments on an

early draft of the manuscript. Dr. Keith Strong and Mr. Michael Levay assisted in the analysis of the X-ray emission measure and source size, respectively. Invaluable help with the SPO observations was provided by Mr. Horst Mauter, Mr. Gary Phyllis and Mr. Philip Wiborg.

The Lockheed work has been supported by NASA Goddard Space Flight Center under contract NAS 5-23758 and the Lockheed Independent Research Program. The UCSD work has been supported by the Air Force Office of Scientific Research, Air Force Systems Command, under grant 76-3071, and by NASA, under grant NSG-7161. The Sacramento Peak Observatory is supported by the National Science Foundation.

The SMM-XRP experiment has been developed jointly by the UCL Mullard Space Science Laboratory (Dr. J.L. Culhane), Lockheed Palo Alto Research Laboratory (LWA) and the SERC Rutherford and Appleton Laboratory (Dr. A.H. Gabriel).

APPENDIX

H α LINE PROFILE OBSERVING SETUP

H α line profiles were obtained using the Echelle Spectrograph of the SPO Vacuum Tower Telescope (Dunn 1969, 1970). Using image reduction optics to achieve a 20-fold reduction in the size of the solar spectrum, a Fairchild 202 charge coupled device (CCD) was placed at the site of the reimaged H α spectrum within the Echelle Spectrograph. A 79 line/mm grating was used in the 32nd order, with H α centered on the 50 x 100 pixel area used on the CCD. The 3 x 4 mm face of the CCD consists of 100 3 mm-long columns, each 40 μ m wide. Each of these consists of a column of 100 image sensing elements (photosites) and a column shift register. The photosites are 18 μ m wide; the remaining 22 μ m are occupied by the column shift register. The CCD was read out every 0.25 s; only every other full CCD readout was written to magnetic tape, since the tape writing time was the limiting factor on the data acquisition rate. The Fairchild 202 operates by reading the full CCD face in two steps, first the odd columns, then the even columns. Since we illuminated the CCD at all times, this means that what we wrote on our tapes was two images, which are the result of 0.25 s integrations. The two images are not quite simultaneous, but are 0.125 s out of phase. As a result, at each slit position on the image, we have two partially independent 50-pixel spectra. There are perceptible differences between the even and odd column images

(which we refer to as the even and odd fields), especially during the flare. These differences are due, in part, to artifacts of the CCD. However, the greatest effects are due to image changes, and do not repeat from one CCD readout to the next. Whether these are due to real flare-associated temporal variations or simply steep gradients associated with flare elements of size much less than one pixel aliased into temporal changes by image motion cannot be determined from our data.

This digital approach offers many advantages over photographic methods. These are large dynamic range, linearity, freedom from saturation, and high speed. The analog signal from each photosite is digitized in 16-bit form, and the analog gain is chosen so that even during the brightest flare, the signal remains in the linear portion of the CCD response curve at all points in the spectrum. Since we use the high speed of the CCD to observe the full $H\alpha$ profile, not just a narrow band centered on $H\alpha$, it is straightforward to determine unambiguously such parameters as total $H\alpha$ emission, actual line-center shift, and line profile asymmetries (to minimize the ambiguity of velocity interpretations). The last two advantages cannot be overstated; it would be very easy to infer a wrong value of the velocity (even a wrong sign) from the difference of two wing spectroheliograms or filtergrams, due to the complex structure of $H\alpha$ flare profiles.

The CCD was oriented such that its 4 mm side was parallel to the slit, and its 3 mm side parallel to the spectral dispersion.

The resultant scale was 2.67" per pixel parallel to the slit and 102 mÅ per pixel parallel to the dispersion. The $18 \times 30 \mu\text{m}$ photosensitive area of each pixel hence corresponds to $1.20'' \times 102 \text{ mÅ}$. Small differences between the directions of the slit and a normal to the dispersion were corrected in the data reduction. A spectrograph slit width corresponding to 2.0" (101 mÅ) was chosen. Spectroheliograms were built up by scanning the solar image in 2.0" steps, two steps per second of time. This image scanning rate gave sufficient time to write the signal from all 10^4 pixels of the CCD on magnetic tape, filling a 2400 foot tape in approximately 8 minutes! A full scan consisted of 50 slit positions, from which a spectroheliogram consisting of 50×100 pixels could be generated, covering an area $100'' \times 267''$, with a repetition rate for any single feature of 25.6 s. Spectroheliograms were always made by scanning in only a single direction. After completion of each spectroheliogram, the image was rapidly slewed back to the original starting position in less than one second. Data were written continuously on magnetic tape, but were saved only if a flare occurred.

The data may, of course, be displayed either as spectroheliograms or as spectra. For each spatial position, we have the two 50-point spectra (from the odd and even fields), each with an interval of 204 mÅ between pixels. This interval is somewhat smaller than the 283 mÅ thermal Doppler width of H α at 10^4 K, and the more than 1 Å full width at half maximum of the core

of the observed quiet sun H α profile. We simply average the two independent spectra for this paper.

We have corrected the H α spectra for vignetting in the spectrograph and the image reduction optics, as well as scattered light in the spectrograph. We have not found it necessary for this paper to correct the profiles for the finite resolution of the combined spectrograph and detector system or for the small gain variations of single pixels.

REFERENCES

Allen, C.W. 1973, *Astrophysical Quantities*, Athlone Press, London.

Antiochos, S.K., and Sturrock, P.A. 1978, *Ap.J.* 220, 1137.

Antonucci, E., Gabriel, A.H., Acton, L.W., Culhane, J.L., Doyle, J.G., Leibacher, J.W., Machado, M.E., Orwig, L.E., and Rapley, C.G. 1981, *Solar Phys.* (in press).

Athay, R.G. 1970, *Solar Phys.* 12, 175.

Basri, G.S., Linsky, J.L., Bartoe, J.-D.P., Brueckner, G.E. and Van Hoosier, M.E. 1979, *Ap.J.* 230, 924.

van Beek, H.F., Hoyng, P., Lafleur, B., and Simnett, G.M. 1980, *Solar Phys.* 65, 39-52.

Brown, J.C., Canfield, R.C., and Robertson, M.H. 1978, *Solar Phys.* 57, 399.

Canfield, R.C. 1982, *Solar Phys.*, in press.

Canfield, R.C., Cheng, C.-C., Dere, K.P., Dulk, G.A., McLean, D.J., Robinson, R.D., Schmahl, E.J., and Schoolman, S.A. 1980, in P.A. Sturrock (ed.), *Solar Flares, A Monograph from Skylab Solar Workshop II*, University of Colorado Press, Boulder.

Cheng, C.-C., Feldman, U., and Doschek, G.A. 1981, *Astr.Ap.* 97, 210.

Culhane, J.L., and Acton, L.W. 1974, *Ann.Rev.Astr.Ap.* 12, 359.

Culhane, J.L., Gabriel, A.H., Acton, L.W., Rapley, C., Phillips, K.J., Wolfson, C.J., Antonucci, E., Bentley, R.D., Catura, R.C., Jordan, C., Kayat, M.A., Kent, B.J., Leibacher, J.W., Parmar, A.N. Sherman, J.C., Springer, L.A., Strong, K.T., and Veck, N.J. 1981, *Ap.J. (Letters)* 244, L141.

Datlowe, D.W. 1975, in S.R. Kane (ed.), *Solar Gamma, X- and EUV Radiation*, D. Reidel Publ. Co., Dordrecht, p 191.

Dere, K.P., and Cook, J.W. 1979, *Ap.J.* 229, 772.

Dinh, Q.-V. 1980, *Publ.Astr.Soc. Japan* 32, 515.

Dunn, R.B. 1969, *Sky and Tel.* 38, 1.

Dunn, R.B. 1971, *The Menzel Symposium on Solar Physics, Atomic Spectra, and Gaseous Nebulae*, ed. K.B. Gebbie (NBS Spec.Pub. 35, Washington, U.S. Book Printing Office), p 71.

Evans, J.W. (ed.) 1963, *The Solar Corona* (New York: Academic Press.

Feldman, U., Doschek, G.A., Kreplin, R.W., and Mariska, J.T. 1980, *Ap.J.* 241, 1175.

Field, G.W. 1965, *Ap.J.* 142, 531.

Gabriel, A.H., and Mason, H.E. 1980, in *Applied Atomic Collision Physics, I., Atmospheric Physics and Astrophysics*, H.S.W. Massey and D.R. Bates

(eds.), in press.

Goldsmith, D.W. 1971, *Solar Phys.* 19, 81.

Hiei, E., and Widing, K. 1979, *Solar Phys.* 61, 407.

Hirayama, T. 1974, *Solar Phys.* 34, 323.

Hudson, H.S. 1973, in R. Ramaty and R.G. Stone (eds.), *Symp. High Energy Phenomena on the Sun*, Goddard Space Flight Center X-693-73-193, p 207.

Hudson, H.S., and Ohki, K. 1972, *Solar Phys.* 23, 155.

Jacobs, V.L., Davis, J., Kepple, P.C., and Blaha, M. 1976, *Astrophys. J.* 211, 605.

Jacobs, V.L., Davis, J., Kepple, P.C., and Blaha, M. 1977b, *Astrophys. J.* 215, 690.

Jacobs, V.L., Davis, J., Rogerson, J.E., and Blaha, M. 1977c, *NRC Mem. Report 3572*.

Jacobs, V.L., Davis, J., Rogerson, J.E., Blaha, M., Cain, J., and Davis, M., 1980, *Ap.J.* 239, 1119.

Jordan, S. 1981, *The Sun as a Star*, NASA SP-450.

Krieger, A.S. 1977, *Solar Phys.* 56, 107.

Kundu, M.R. 1965, *Solar Radio Astronomy*, Interscience, New York.

Lin, R.P., and Hudson, H.S. 1971, *Solar Phys.* 17, 412.

Lin, R.P., and Hudson, H.S. 1976, *Solar Phys.* 50, 153.

Machado, M.E., and Linsky, J. 1975, *Solar Phys.* 42, 395.

Moore, R., McKenzie, D.L., Svestka, Z., Widing, K.G., Antiochos, S.K., Dere, K.P., Dodson-Prince, H.W., Hiei, E., Krall, K.R., Krieger, A.S., Mason, H.E., Petrasso, R.D., Pneuman, G.W., Silk, J.K., Vorpahl, J.A., and Withbroe, G.L. 1980, in P.A. Sturrock (ed.), *Solar Flares*, Colorado Assoc. University Press, Boulder.

Neupert, W.M. 1968, *Ap.J. (Letters)* 153, L59.

Neupert, W.M., Gates, W., Swartz, M., and Young, R. 1968, *Ap.J.* 149, L79.

Ohki, K. 1975, *Solar Phys.* 45, 435.

Orwig, L.E., Frost, K.J., and Dennis, B.R. 1980, *Solar Phys.* 65, 25.

Pallavicini, R., Serio, S., and Vaiana, G.S. 1977, *Ap.J.* 216, 108.

Priest, E. (ed.) 1981, *Solar Flare Magnetohydrodynamics* (Gordon and Breach, New York).

Schoolman, S.A., and Ganz, E.D. 1981, *Solar Phys.* 70, 363.

Sturrock, P.A. 1973, in Ramaty and Stone (ed.), *Symp. High Energy Phenomena in the Sun*, Goddard Space Flight Center, X-693-73-193, p 3.

Sturrock, P.A. 1980, in P.A. Sturrock (ed.), *Solar Flares*, Colorado Assoc. Univ. Press, p 411.

Sylvester, J., Schrijver, J. and Mewe, R. 1980, *Solar Phys.* 67, 285.

Tanaka, K. 1981, *Symposium on Flaring Astrophysical Plasmas*, Utrecht, Holland, November 2-3.

Underwood, J.H., Antiochos, S.K., Feldman, U., and Dere, K.P. 1978, *Ap.J.* 224, 1017.

Vernazza, J.E., Avrett, E.H., and Loeser, R. 1981, *Ap.J. (Supplement)* 45, 619.

Zirin, H. 1978, *Solar Phys.* 58, 95.

Zirin, H. and Tanaka, K. 1973, *Solar Phys.* 32, 173.

TABLE 1

CHROMOSPHERIC EVAPORATION, FLARE OF 1456 UT, 7 MAY 1980

 Number of evaporated chromospheric atoms

 implied by H α profiles 7×10^{37}

 Number of soft X-ray emitting electrons 3×10^{37}

Column depth of evaporation implied

 by H α profiles, $N_{H\alpha}$ $4 \times 10^{20} \text{ cm}^{-2}$

Column depth of explosive heating

 implied by hard X-rays, N_c $1.5 \times 10^{20} \text{ cm}^{-2}$

FIGURE CAPTIONS

Fig. 1. Temporal development of the 1980 May 7 flare. Emission from the thermal plasma, characterized by the Fe XXV line intensity, shows little of the impulsive structure of the hard X-ray burst. The H α output of the flare is shown by the thick line in the lower panel, and the scale on the left. It shows both impulsive and gradual character. The percentage contributions of the south kernel (thin curve) and north kernel (broken curve) are given by the right-hand scale, in terms of the total H α output at the peak of the flare. The open circles on the H α curves indicate the times of measurement; the 25.6 s interval between measurements is much longer than the 0.25 s sampling time. The times of the FCS measurements are indicated by the double-headed arrows below the top panel.

Figure 2. Each rectangle displays the percentage of counts collected in the indicated time interval and energy band that appeared in each of the EXIS pixels of interest. The counts contributing to each image are shown below the rectangles. The quoted errors represent one-standard-deviation counting statistics. The insets show the orientation of the image and relate the pixels to Figure 5. Some of the spread in source extent apparent in the right-hand images may reflect a partial transparency of the

HXIS collimator at the highest energies.

Fig. 3. Time sequences of H α spectra for five image pixels. Relative intensity and wavelength scales are shown for the (40,43) spectrum at 145459. Note the line segment to the right of each spectrum linking it to the $I/I_c = 1.0$ point for the appropriate time. The 145616 and 145642 spectra were obtained between the first and second hard X-ray burst periods and during the second burst period, respectively.

Fig. 4. Appearance of the 1980 May 7 flare in H α throughout the course of the hard X-ray burst. The time of each filtergram is given and referenced to the timeline of the 28-260 keV X-ray burst, as recorded by the HXRBS. The first (H $\alpha \pm 0.5 \text{ \AA}$) and last (H α) images are courtesy of the Solar Optical Observing Network of the U.S. Air Weather Service. The remainder of the H α images are courtesy of Big Bear Solar Observatory, California Institute of Technology. The negative prints in the upper row have been prepared with the same photographic negatives as the conventional prints in the lower row, but have been processed individually to display only the most intense kernels of emission. Therefore, relative intensities from frame to frame are meaningless in the negative prints. Image scale and heliographic orientation are indicated to the right of the upper row of images.

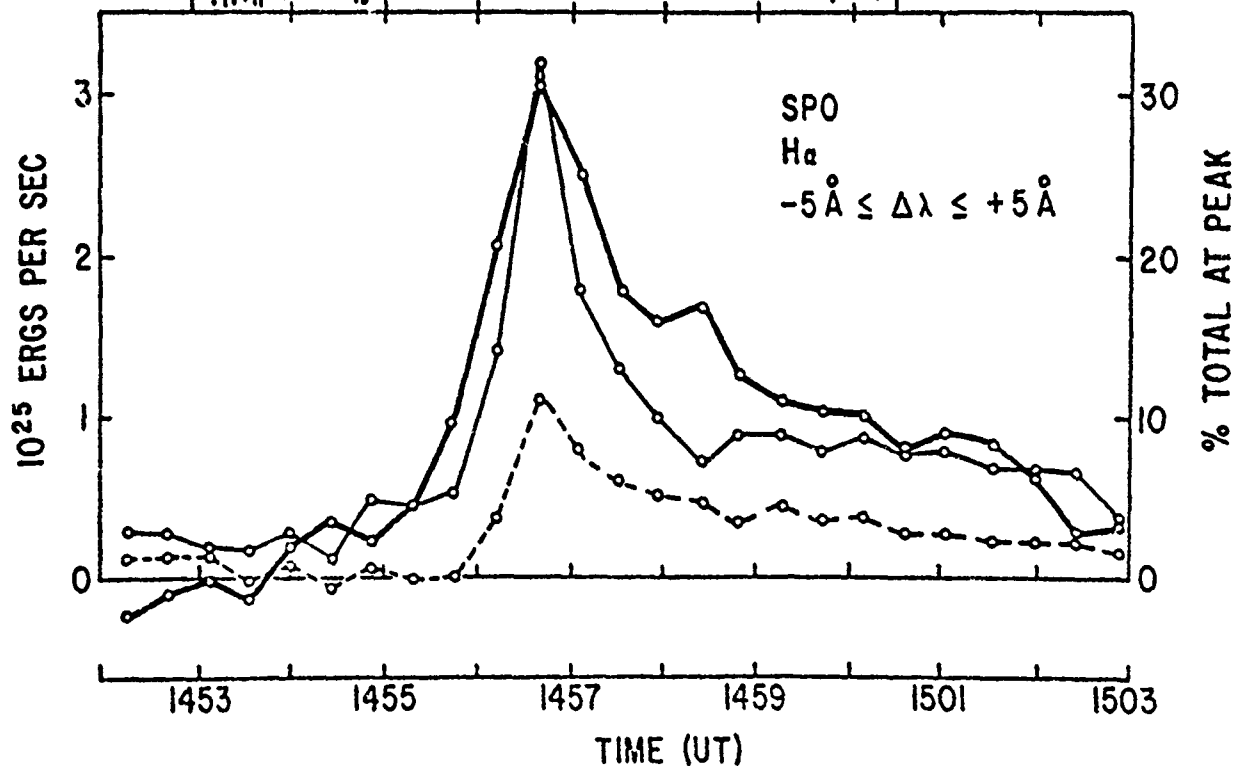
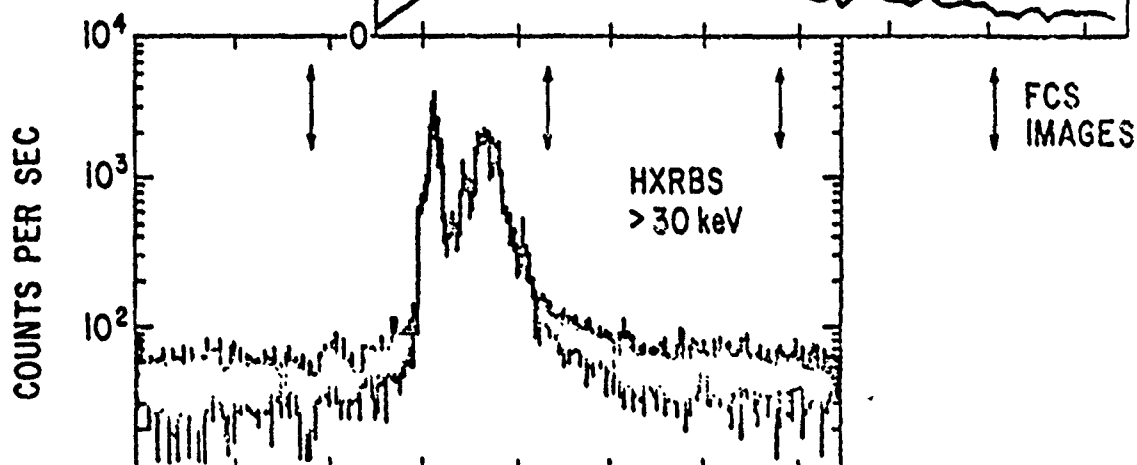
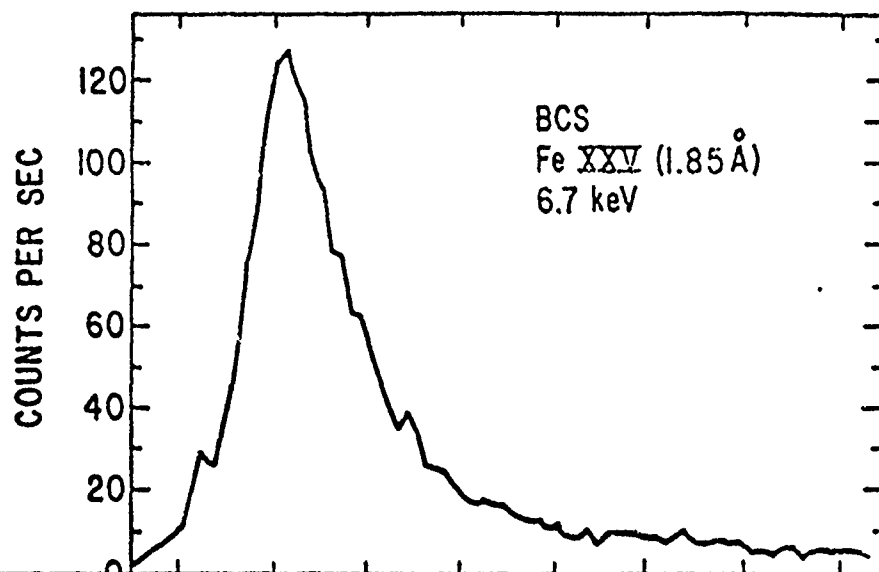
Fig. 5. The most intense SPO H α kernels serve as convenient spatial references relating the various observations contributing to this study. The SPO spectroheliogram row, column (i,j) indices are given in the rightmost sketch, and the six pixels producing an H α power greater than half that of the brightest pixel, at H α flare maximum, are indicated by the crosshatch. The leftmost sketch identifies the location of the twelve HXIS pixels of Figure 2. The center panel shows a rectangle of dimensions 8" x 9", the size of the soft X-ray flare source derived from the HXIS and FCS images, centered at the location derived from the FCS. The uncertainty in location of the rectangle is roughly equal to its size.

Fig. 6. Semi-empirical temperature distributions and computed H α profiles of the quiet sun and the grid of flare models of Dinh (1980), used to estimate the amount of chromospheric evaporation.

Fig. 7 Number of atoms evaporated from the chromosphere during the flare, as implied by the H α profiles. The curve labelled *total* applies to the whole flare. *North* and *south* refer to the north and south kernels and their respective vicinities.

Fig. 8. Soft X-ray emission measures, $\int n_e^2 dv$, in three temperature ranges.

7 MAY
1980



PRE - BURST
14:55:39
-14:56:02 UT

ALL BANDS

3 ± 1	2 ± 1	2 ± 1
6 ± 1	33 ± 3	4 ± 1
9 ± 2	32 ± 3	5 ± 1
2 ± 1	2 ± 1	0

316 COUNTS



BURST
14:56:02
-14:56:47

3.5 - 8 keV

2	11	2
6	47 ± 1	6
4	19 ± 1	2
0	1	0

6006 COUNTS

16 - 30 keV

4 ± 1	6 ± 2	1 ± 1
8 ± 2	15 ± 2	6 ± 2
8 ± 2	38 ± 3	6 ± 2
3 ± 1	3 ± 1	2 ± 1

216 COUNTS

POST - BURST
14:56:47
-14:57:10

1	10	2
6	49 ± 1	9
3	15	2
0	1	0

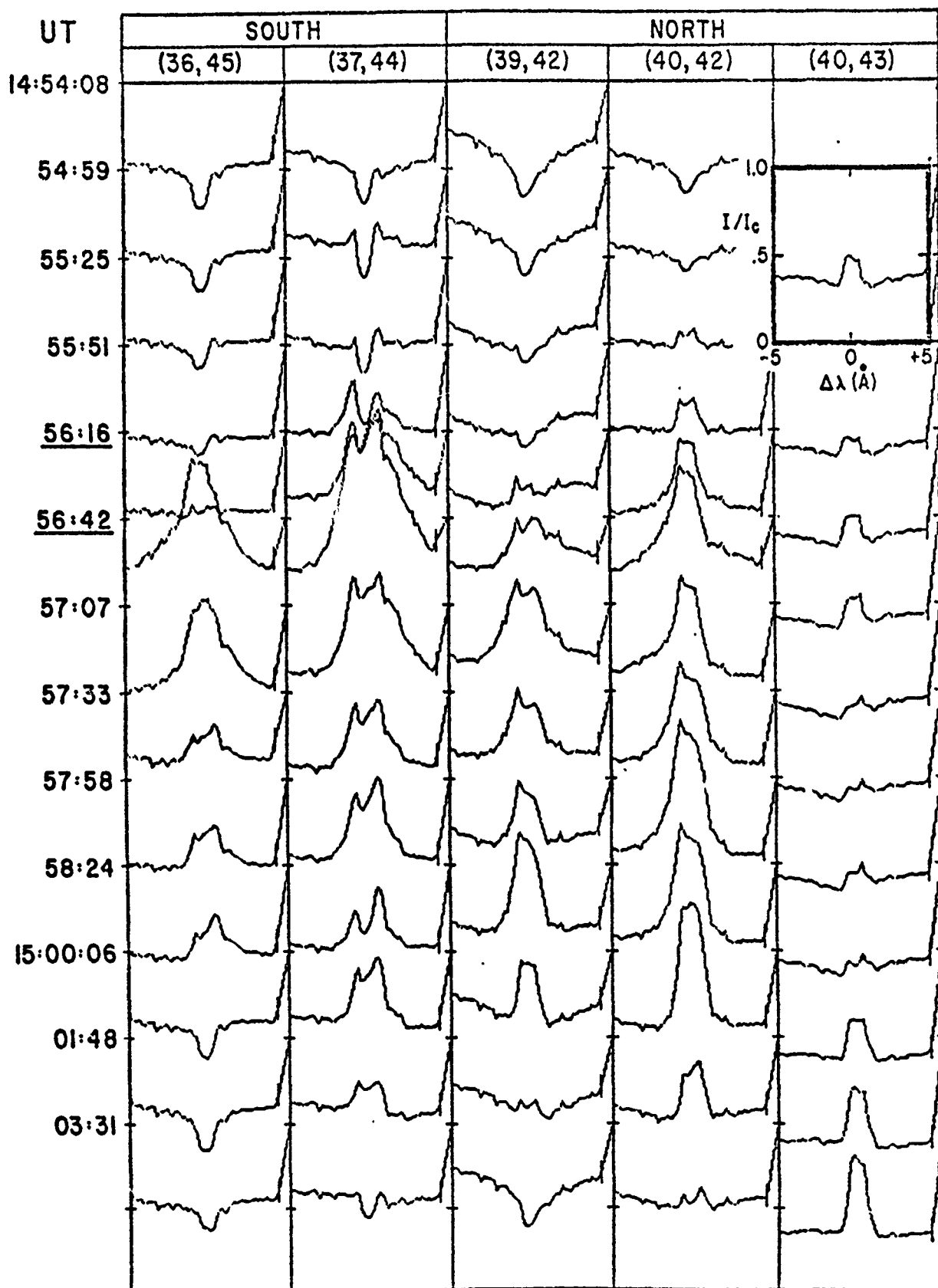
6868 COUNTS

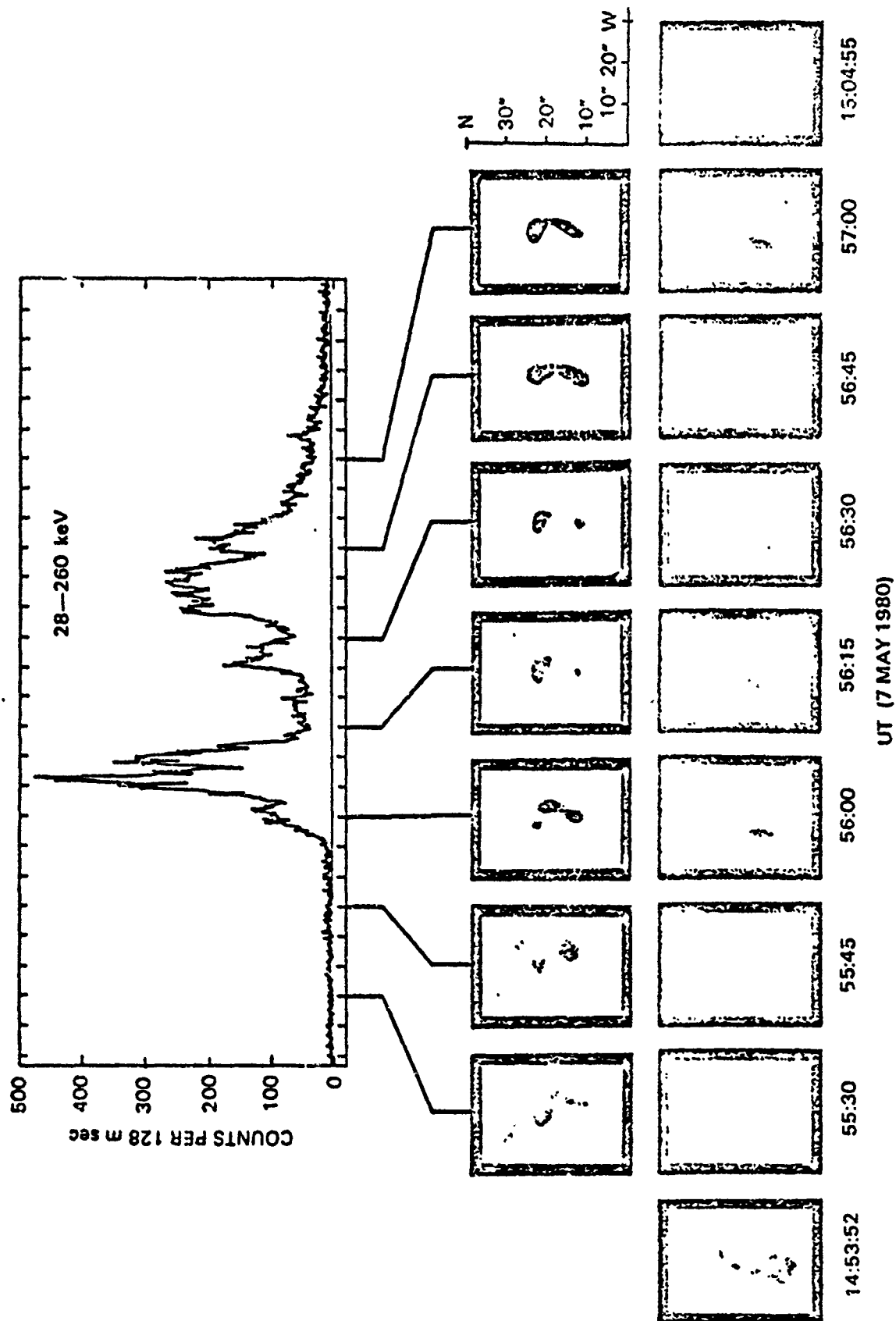
3 ± 2	13 ± 4	6 ± 3
15 ± 4	25 ± 5	10 ± 3
3 ± 2	17 ± 4	1 ± 1
1 ± 1	6 ± 3	1 ± 1

72 COUNTS

7 MAY
1980

H α PROFILES

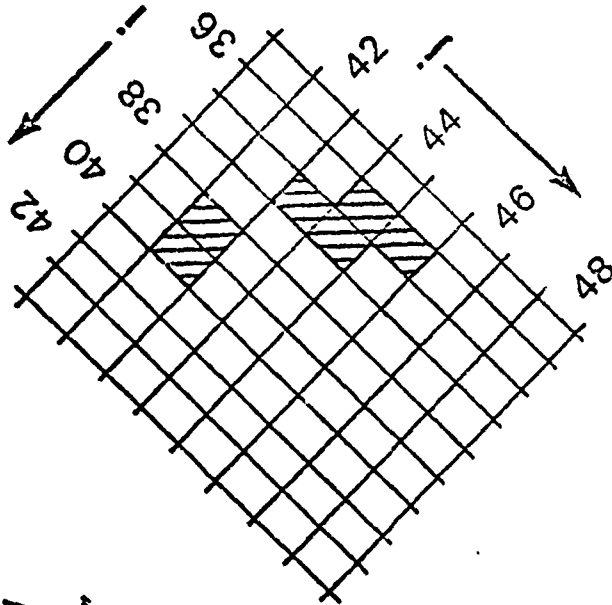
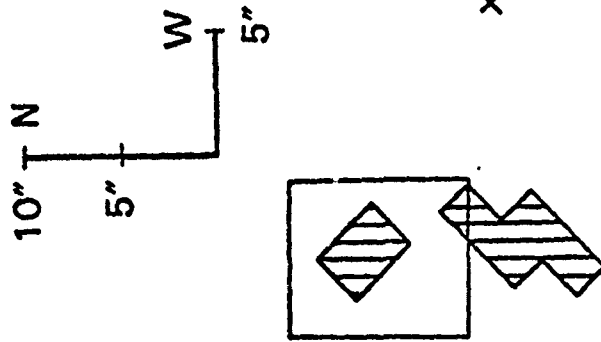




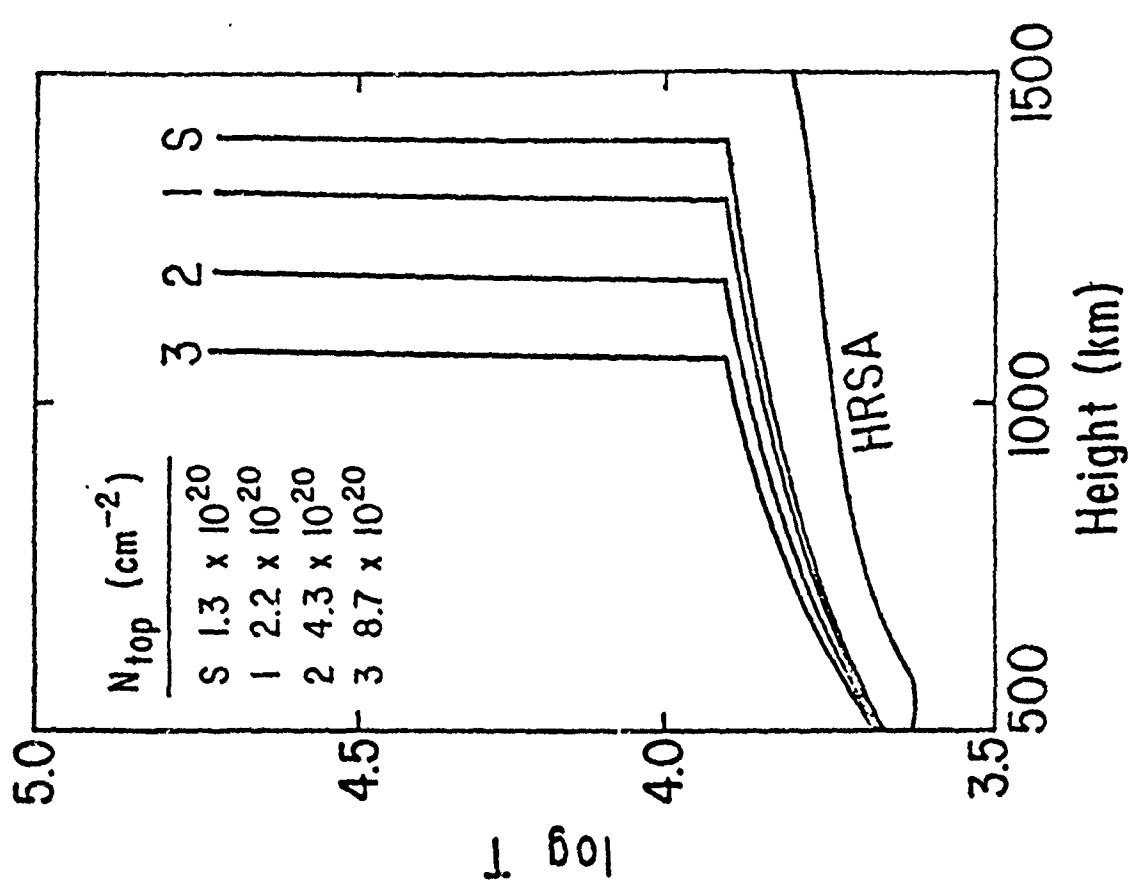
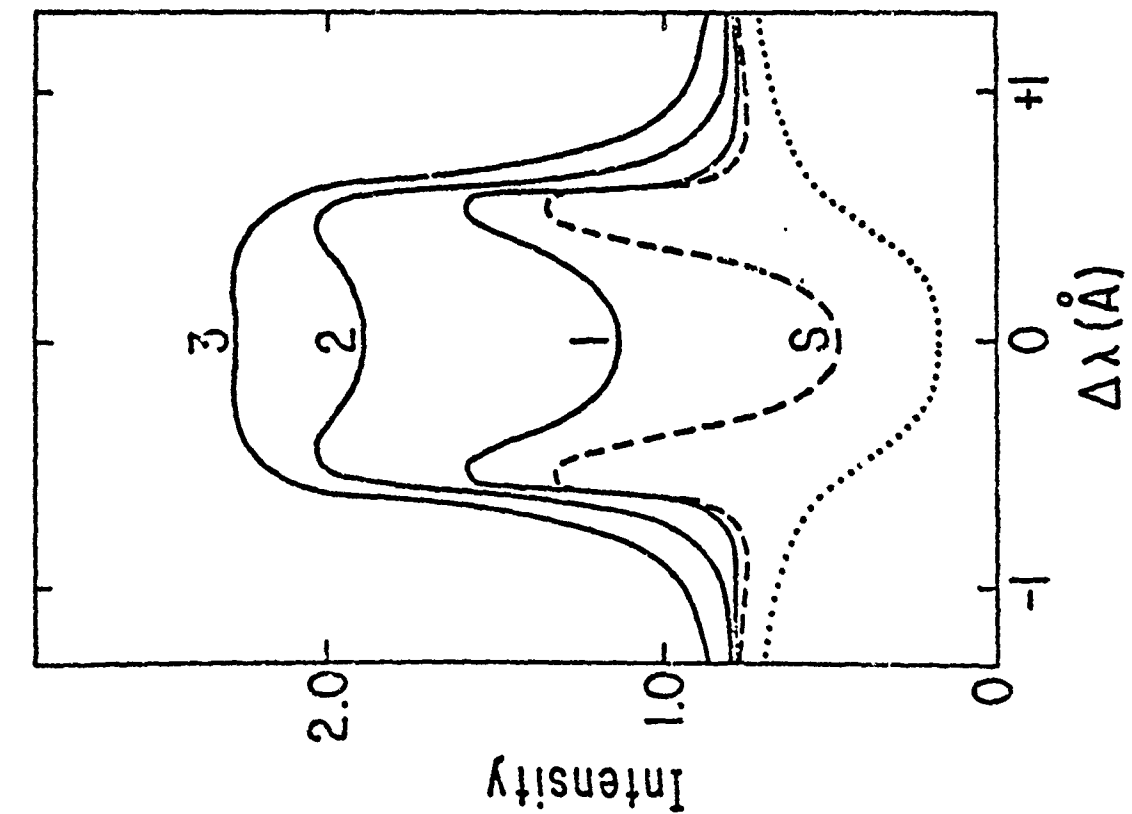
1	2	3
4	5	6
7	8	9
10	11	12

HXIS

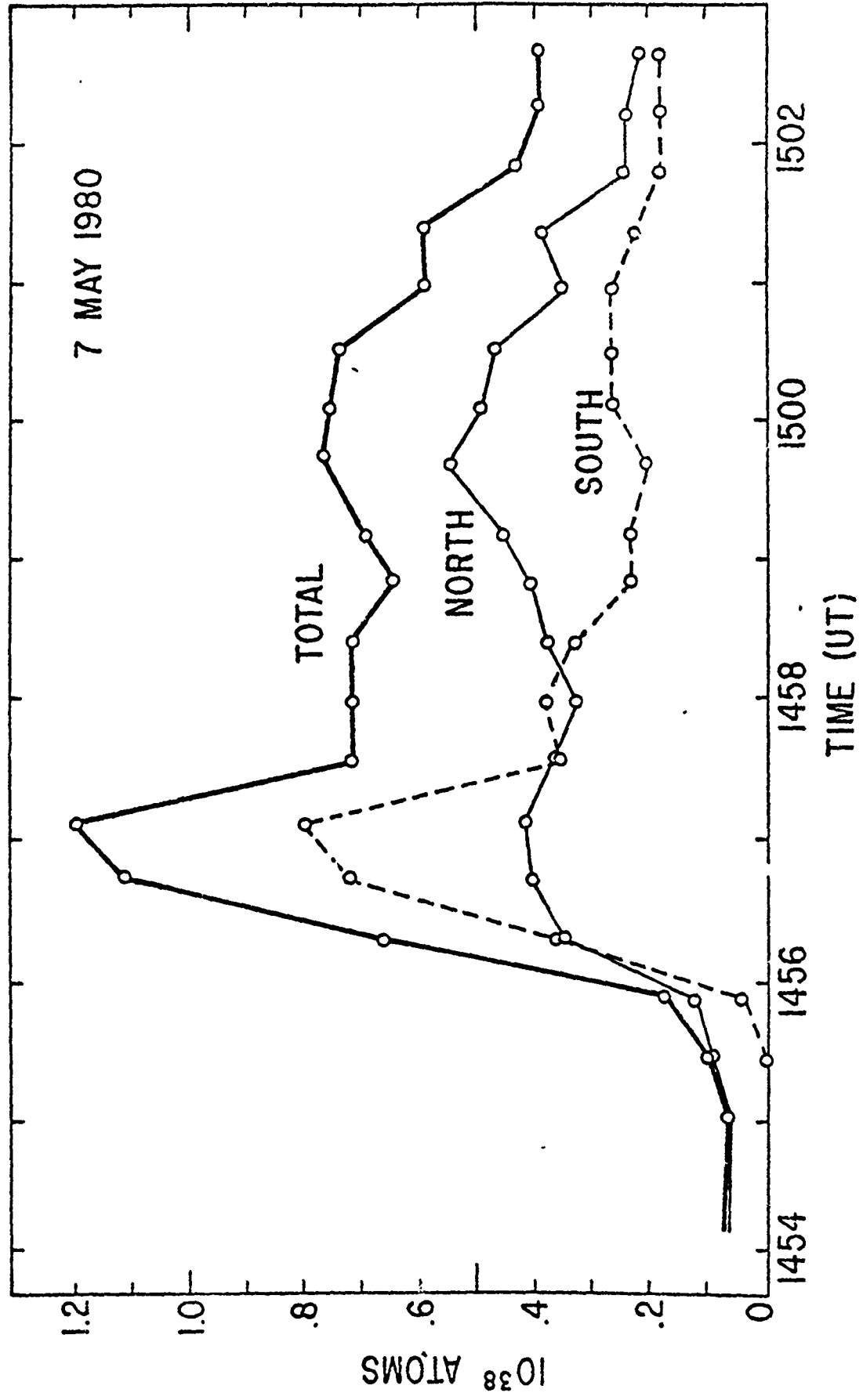
FCS



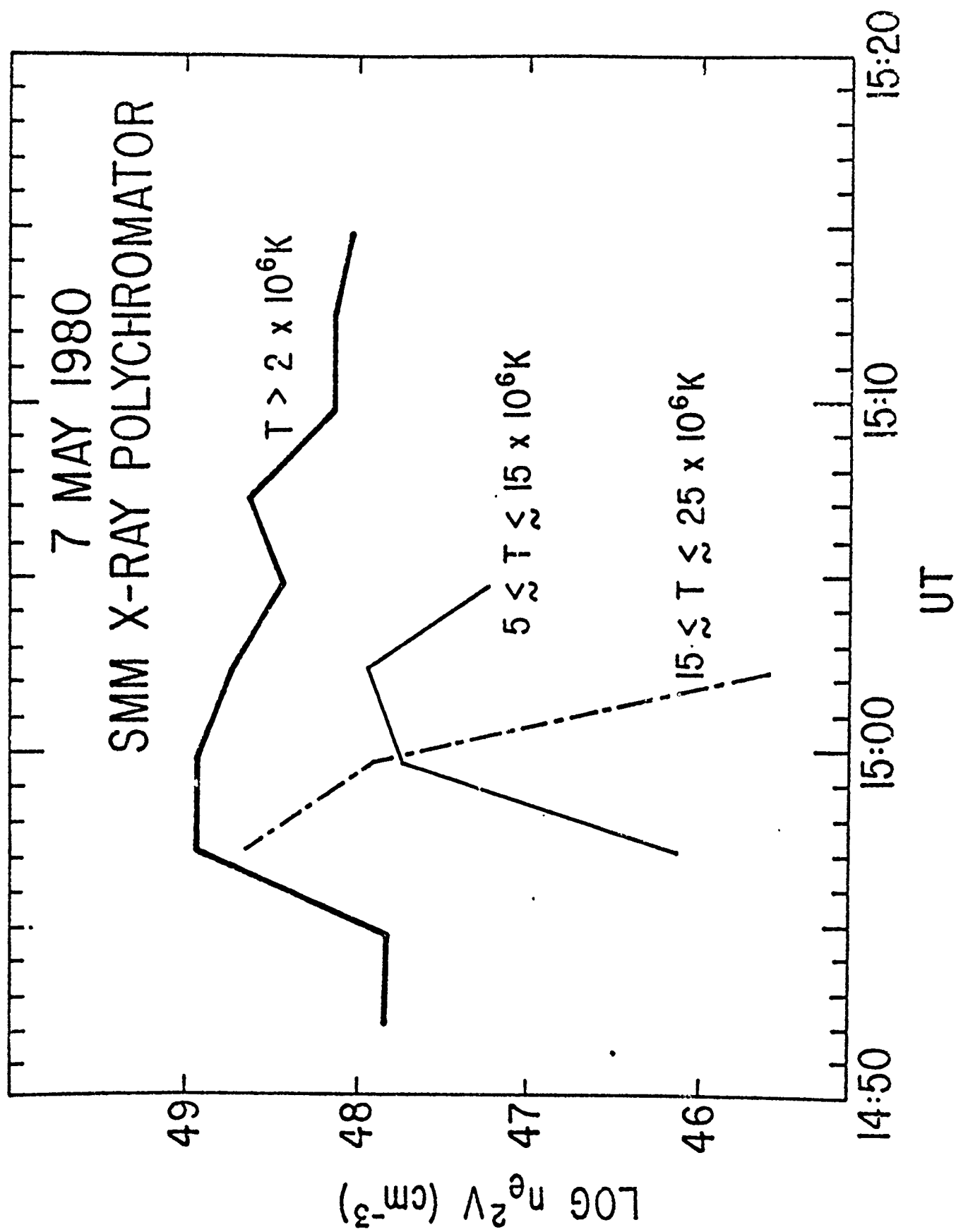
SPO



NUMBER OF EVAPORATED ATOMS IMPLIED BY H α PROFILES



7 MAY 1980
SMM X-RAY POLYCHROMATOR



AUTHORS' ADDRESSES

Loren W. Acton and John W. Leibacher
Org. 52-12, Bldg. 255,
Lockheed Palo Alto Research Laboratory
3251 Hanover St.
Palo Alto, CA 94304.

Richard C. Canfield, Todd A. Gunkler, Hugh S. Hudson
Center for Astrophysics and Space Sciences, C-011
University of California, San Diego
La Jolla, CA 92093

Alan L. Kiplinger
SMM Project, Code 684
Goddard Space Flight Center
Greenbelt. MD 20771

c) Solar Flare Theory

It is often the case in science that in order to understand the implications of data on a complex physical phenomenon, a simple phenomenological approach is inadequate. This is especially true in solar flare studies, which have progressed to the point where in many cases observations in a single spectral region, such as $H\alpha$ or X-rays, can contribute little to our understanding without supporting data from other regions. As mentioned in the introduction, at the inception of this grant the theoretical modelling of flare dynamics was in a very preliminary state, inadequate to the task of helping to interpret observations of $H\alpha$ spectra. For this reason, we embarked on a program of numerical modelling of chromospheric processes during flares.

An important aspect of all our theoretical work was treatment of the manner in which flares radiate. This was important for two reasons. First, the only means we have to sample what is happening at the sun is by remote sensing, which depends on knowing what the relationship is between physical conditions in the flare and the observable characteristics of the flare radiation. Second, the rate at which the flare plasma radiates is one major aspect of its hydrodynamics; if you have no theory for the radiation, you can understand only a small fraction of what you can observe.

The objective of this theoretical program was to be able to understand what the spectroscopic signature of various flare processes is. The first success of this program was the clear picture of the theoretical $H\alpha$ signature of

chromospheric evaporation, and the qualitative distinction between the signatures of thermal and nonthermal chromospheric heating processes. There is every reason to expect that further theoretical work will result in a comparably clear picture of the signature of beams of accelerated electrons in the chromosphere.

1) $H\alpha$ Profiles from Electron-Heated Solar Flares

In this paper we studied the effect of a beam of accelerated flare electrons on the chromosphere. It was done several years ago, but it remains the best work on the topic, because it attempts to include the effect of radiative cooling in the energy balance, in a way that includes the effects that make it relatively difficult for an optically thick plasma to cool. It is presently the definitive paper on the $H\alpha$ signature of accelerated electrons in the chromosphere. Much of the later work in this theoretical section is devoted to the development of theoretical techniques to improve on this paper. These include the ability to model not only radiative transfer, but also thermal conduction and mass motion (flows).

H α PROFILES FROM ELECTRON-HEATED SOLAR FLARES

JOHN C. BROWN

Dept. of Astronomy, University of Glasgow, Glasgow, G12 8QQ, Scotland

RICHARD C. CANFIELD

Dept. of Physics, University of California, San Diego, La Jolla, Calif. 92093, U.S.A.

and

MATTHEW N. ROBERTSON

Dept. of Astronomy, University of Glasgow, Glasgow, G12 8QQ, Scotland

(Received 29 September, 1977; in revised form 4 January, 1978)

Abstract. We briefly review the status of models of optical flare heating by electron bombardment. We recompute Brown's (1973a) flare model atmospheres using considerably revised radiative loss rates, based on Canfield's (1974b) method applied to H α , L α , and H γ . Profiles of H α are computed and compared with observation. The computed profiles agree satisfactorily with those observed during the large 1972 August 7 flare, if spatial and velocity inhomogeneities are assumed. The electron injection rate inferred from H α is one order of magnitude less than that inferred from hard X-rays, for this event. This may be due to either (1) the neglect of a mechanism that reduces the thick-target electron injection rate or (2) failure to incorporate important radiative loss terms.

1. Previous Work

Over the last decade or so there has been considerable enthusiasm for the idea that energetic electrons (in the 10–100 keV range) may be a primary product of the energy release in many solar flares, their collisional degradation in the atmosphere resulting in the various flash phase thermal phenomena (optical, UV and soft X-ray emission and the onset of mass motions) as secondary products. The evidence for this suggestion in terms of the total energy of the electrons and the synchronism between the various thermal and non-thermal emissions has been reviewed by several authors (e.g. Brown, 1973a, 1975, 1976; Hudson, 1973; Kane, 1974; Lin, 1975). Detailed theoretical models have been developed (see these reviews for references) to predict the structure of various regimes in the solar atmosphere where the electron input appears in the energy equation together with thermal conduction and radiative losses. In the high temperature regime conduction is dominant and Shmeleva and Syrovatskii (1973) have obtained a steady state description of its temperature structure, and also of that in the UV flare where radiation becomes important. Recently some quantitative work has begun (Craig and McClymont, 1976; Kostyuk and Pikel'ner, 1975; Kostyuk, 1975, 1976) on the role of mass motions.

In the low temperature (chromospheric) flare mass motions undoubtedly still play an important role. However, optical depth effects also become significant

there, adding to the complexity of numerical modeling. Brown (1973a) calculated steady state chromospheric models with a simplified Lyman-continuum radiative-loss method. There are two areas in which Brown's (1973a) calculations obviously could be improved: (1) convection and conduction; (2) radiative losses. Kostyuk and Pikel'ner (1975) and Kostyuk (1975) did only the former; here, we do only the latter.

In this paper we amend Brown's (1973a) models, maintaining the steady-state, constant-pressure electron-input, radiative-output approximation for the optical flare, but taking into account Canfield's (1974a) criticisms of Brown's radiative losses. We are thus assuming that heating increases gradually enough to permit a steady state radiative solution but still on a time scale shorter than that for arrival of heat flux conducted from the corona, cf. next section. Canfield (1974a) computed the $H\alpha$ profiles expected from Brown's (1973a) models and found major discrepancies with observations. Pursuing this, Canfield (1974a) then found that Brown had overestimated the hydrogen radiative losses by up to two orders of magnitude. Brown omitted the radiative input of the Balmer continuum from the photosphere in his energy equation, though including it in his ionization equation, thus overestimating the radiative loss rate. The Lyman continuum radiative output was obtained by reducing the optically thin output by $\exp(-\tau_{Ly-c})$, which we now view as overly simplified. Methods were then developed by Canfield (1974b, c) to allow a relatively simple method for radiative losses in lines. Subsequent work (in progress) has shown that the situation is more complex than originally stated by Canfield (1974a). Due to a numerical error, Canfield (1974a) found that hydrogen continuum radiative losses were much less than hydrogen line losses. In fact, these subsequent calculations show hydrogen continuum cooling to be sometimes comparable to line cooling, and sometimes greater. Interestingly, they also show regions dominated by continuum heating. Because of these findings, we view the present models as an evolutionary improvement upon previous work, but consider it likely that further improvements will result from still more complete treatments of radiative aspects of the problem.

2. Solution of the Energy Equation

Hard X-ray burst observations are consistent with a flare electron spectrum of approximately power-law form above about 20 keV. If such electrons are injected downward into the chromosphere (thick target model) the injection rate F (electrons s^{-1}) and spectral index are given from the hard X-ray observations by the expressions in Brown (1975). When the electron energy flux above 20 keV is \mathcal{F}_{20} the rate of collisional energy deposition at a total hydrogen (atoms plus ions) column depth N cm^{-2} into the atmosphere is (cf. Brown, 1973a)

$$Q(N) = 1.7 \times 10^3 \mathcal{F}_{20} B_x(\delta/2, \frac{1}{3}) \left(\frac{6 \times 10^{19}}{N} \right)^{8/2} \text{ erg g}^{-1} \text{ s}^{-1}, \quad (1)$$

where δ is the electron injection spectral index and

$$\begin{aligned} x = 1 & \quad N \geq 1.5 \times 10^{17} E_c^2 \\ & = \frac{N}{1.5 \times 10^{17} E_c^2} \quad N < 1.5 \times 10^{17} E_c^2. \end{aligned} \quad (2)$$

E_c (keV) is the low energy cutoff (if any) in the electron spectrum and B_x is the partial beta function (total if $x = 1$). Equation (1) corrects some algebraic errors in Brown's (1973a) expression (cf. Lin and Hudson, 1976).

As many authors have pointed out, the flare atmosphere is divided into a high and a low temperature region by the radiative instability of cosmic plasma above $T \approx 5 \times 10^4$ K (at constant pressure), cf. Cox and Tucker (1969). Material above this transition zone rapidly becomes too hot to participate in forming the optical flare spectrum so we only consider the atmospheric structure below $T = 5 \times 10^4$ K. In this region three radiative loss contributions are important: heavy element lines and continua; H-negative continuum; and the hydrogen Lyman and Balmer lines and continua.

Heavy element lines and continua are assumed to be optically thin. They are somewhat problematic in that their loss contribution has only been computed down to around 2×10^4 K. Below this temperature their behavior becomes model dependent because of the effect of decreasing hydrogen ionization on the collisional ionization equilibrium and because some of the important lines may become optically thick. The best that seems possible at present is an empirical fit to the solar radiative loss curve (McWhirter *et al.*, 1975) extrapolated to lower temperatures (similar to Brown, 1973a).

The H-negative and H α and L α losses here have been based on Canfield's (1974b, c) probabilistic radiative loss technique. This complicates the practical handling of the problem considerably over Brown's (1973a) original treatment.

For a quasi-steady state throughout the heated region, the energy balance equation can still be written as

$$Q(N) = R \quad (3)$$

at all N but R is no longer just a local function of N (through n , T) as in Brown's (1973a) treatment. Instead R depends on the entire structure of the atmosphere model, $T(N')$, $n(N')$ for all N' , through radiative transport effects. Consequently (3) had to be solved by an iterative scheme using some starting model flare atmosphere and adjusting T at each level N' in the model grid (at constant pressure) until a model converging on condition (3) was obtained. In this iteration scheme we used Canfield's (1974c) program to approximate the radiative losses but confirmed previous estimates of the accuracy of the method by comparison with a detailed calculation for the converged model (see below). We have neglected any effect of direct non-thermal ionization or excitation by beam collisions, the

importance of which is still disputed (cf. Hudson, 1972; Brown, 1973b; Lin and Hudson, 1976).

In this approach it was found that the deeper layers were very slow (iteratively) to approach a steady state. This is because the radiative response time to the small input is long (due to radiative transport effects) so that in practice a steady state would only be reached slowly in real time also – in fact in a time long compared to typical beam durations (10–100 s). We therefore refined our procedure somewhat by estimating the real elapsed time up to any iterated stage in the model – i.e. we performed the iteration in quasi-real time steps. (The elapsed time was approximated by $(kT/m_H)/(Q-R)$.) The final model adopted was that reached after an estimated real elapsed time equal to a beam input duration τ_B as parameter. (Here we use only $\tau_B \approx 60$ s.) The deepest layers of the atmosphere were thus not yet in a steady state when heating was terminated. Note that this procedure does *not* incorporate time dependent radiative transfer but is a first approximation in avoiding the overestimate of the temperatures of deep layers incurred by assuming a steady state throughout.

It is appropriate at this point to consider the various time scales involved (cf. Brown, 1973a, b, 1974). First, the radiative response time τ_R is of order $(kT/m_H)/Q$ which rises rapidly with depth due to the N dependence in (3). Thus a fair approximation is

$$\tau_R \sim \left(\frac{10^9}{\mathcal{F}_{20}}\right) \left(\frac{N}{6 \times 10^{19}}\right)^2 \approx \left(\frac{10^9}{\mathcal{F}_{20}}\right) \left(\frac{n}{10^{12}}\right)^2 \quad (4)$$

and we see that for the \mathcal{F}_{20} values we require (Section 4) $\tau_R \leq \tau_B$ except in the deepest layers (as noted above) so that a quasi-steady radiative treatment is not unreasonable, though not perfect either. The importance of conduction is harder to estimate since it may differ drastically according to whether transient steep conduction fronts are involved, or the atmosphere is quasi-steady. We can at least check the self-consistency of our model atmosphere using the simple estimate

$$\tau_{\text{cond}} \approx nkT/[\kappa(T)T/L^2] \quad (5)$$

for the conduction time. Using $n \geq 10^{13} \text{ cm}^{-3}$, $T \approx 10^4 \text{ K}$ in the $\text{H}\alpha$ region, Coulomb conductivity $\kappa(T)$ and adopting the shortest possible temperature scale length L from our Figure 1 in this region we find $\tau_{\text{cond}} \geq 10^5 \text{ s}$. (The chief uncertainty in this estimate rests on the possibility that our temperature structure at $T \approx 10^4 \text{ K}$ could be substantially modified when linked conductively to the hot region above $5 \times 10^4 \text{ K}$ which we ignore.) Our calculation is thus at least self-consistent.

3. Model Atmospheres

Here we present only results for the typical parameters $\delta = 4$, $E_c = 10 \text{ keV}$, $\tau_B = 60 \text{ s}$ for flux values, $\mathcal{F}_{20} = 10^8, 10^9, 10^{10}$, and $10^{11} \text{ erg cm}^{-2} \text{ s}^{-1}$. The resulting model atmospheres are shown in Figures 1 and 2 in terms of respectively $T(z)$ and $n(z)$

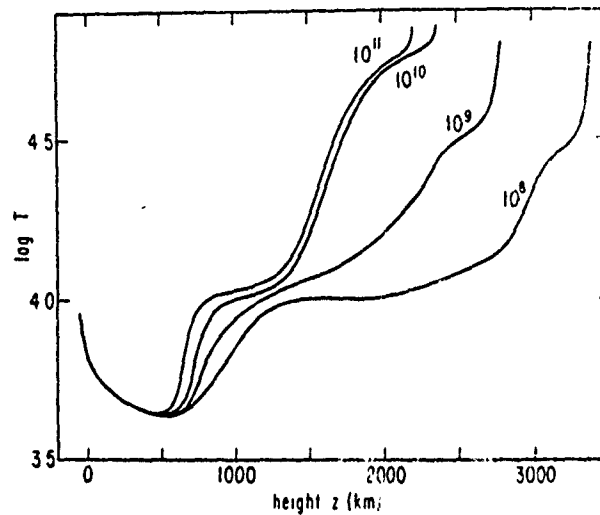


Fig. 1. The computed temperature distributions for $\mathcal{F}_{70} = 10^8, 10^9, 10^{10}$, and 10^{11} $\text{erg cm}^{-2} \text{s}^{-1}$.

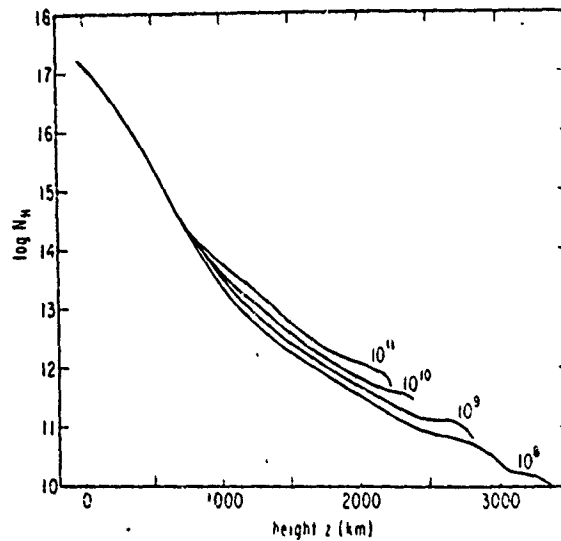


Fig. 2. The computed hydrogen (atoms and ions) number density distributions for $\mathcal{F}_{20} = 10^8, 10^9, 10^{10}$, and 10^{11} $\text{erg cm}^{-2} \text{s}^{-1}$.

(total hydrogen density) as functions of height z above the photosphere. In general the results differ from Brown (1973a) in deeper penetration of the heating (due to reduced radiative losses) and in local features on the $T(z)$ profiles due to the hydrogen line losses. The plateau at $T = 10^4$ K is due to the manner in which the optically-thin radiative losses were cut off and so may be spurious. Particularly

interesting in view of the ATM observations of EUV continua of neutral and singly-ionized elements is the heating between 500 and 1000 km. It is cut off at the lower end by reduced penetration of heating and increased effectiveness of radiative cooling, primarily due to H^- .

4. Computed and Observed $H\alpha$ Profiles

Although the present models are based on very limiting assumptions concerning the dynamical and radiative effects, a preliminary comparison with the observations is nevertheless interesting. $H\alpha$ line profiles were computed as before (Canfield, 1974a). Figure 3 shows the computed $H\alpha$ profiles (dashed lines) for the four atmospheres, together with observed profiles (dash-dot lines) of the 1972, August 7 flare (Zirin and Tanaka, 1973; Tanaka, 1977). We will compare our computations with these data because we also have hard X-ray data (Hoyng *et al.*, 1976; Lin and Hudson, 1976) for the August 7 flare.

When we compare computed ($\mathcal{F}_{20} = 10^9$ and 10^{10} erg cm $^{-2}$ s $^{-1}$) and observed profiles in Figure 3, three features are striking:

(i) The theoretical degree of central reversal is much higher than observed. The lack of such reversals in the observed profiles can be attributed to the fact that even in the $H\alpha$ kernels, considerable fine-scale line-of-sight variation is probably present, but not incorporated in the calculations. During flares, motions at chromospheric levels almost certainly reach several tens of km s $^{-1}$ and also cannot be expected to be the same throughout the field of view of the spectrograph.

(ii) The observed total intensities (emission equivalent widths) fall between those of the computed profiles for $\mathcal{F}_{20} = 10^9$ and 10^{10} erg cm $^{-2}$ s $^{-1}$. These computed total intensities are much greater than Brown's (1973a) models gave (Canfield, 1974a). This is due to the greater depth of penetration of heating, i.e. to the reduced radiative losses.

(iii) The observed line widths fall between those of the computed profiles for \mathcal{F}_{20} between 10^9 and 10^{10} erg cm $^{-2}$ s $^{-1}$. The computed line widths are much greater than those for Brown's (1973a) models, in better agreement with the observations. This is a combination of the effects of greater optical thickness of the $H\alpha$ -forming region and Stark broadening due to higher values of n_e for a given value of \mathcal{F}_{20} . The major difference between these profiles and those from the earlier models is a measure of the importance of the method used for computing radiative losses.

An elaborate comparison of computed and observed profiles is premature at this point. Briefly speaking, we find that the half-widths and equivalent widths of the computed profiles and the observed profiles can be made to agree within the observational uncertainty by incorporating effects of spatial inhomogeneity in \mathcal{F}_{20} and in radial velocity.

We represent the radial velocity inhomogeneities by convoluting the computed profiles with a gaussian profile of $\frac{1}{2}$ width of 60 km s $^{-1}$ (macro-turbulence), comparable to velocities observed in the 1973, June 15 flare by Doschek *et al.* (1977). This

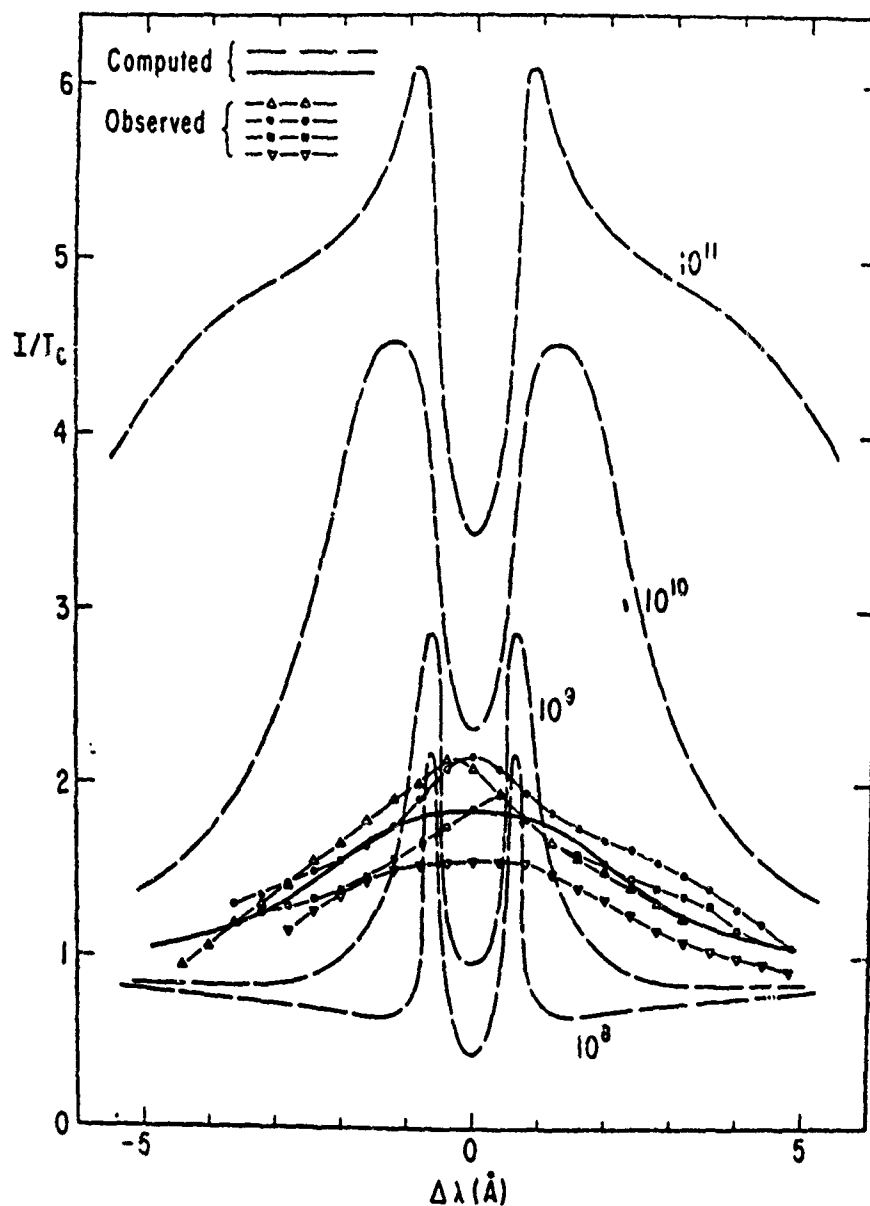


Fig. 3. Computed and observed H α line profiles. *Dashed*: computed from the models for given \mathcal{F}_{20} values. *Dot-dashed*: two observed 1972, August 7 flare kernels each at 15:18 and 15:21 UT (Tanaka, 1977). *Solid*: combination of computed profiles with $\mathcal{F}_{20} = 10^9$ and 10^{10} , after smoothing with 60 km s^{-1} random velocities.

is just sufficient to remove the central reversal from the model profile. Once this has been done we find that although the observed half widths and equivalent widths both fall in the range of theoretical profiles for $\mathcal{F}_{20} = 10^9 - 10^{10}$, the ratios of the two

widths still do not fall anywhere along the theoretical curve for this ratio. However they may be made to do so by assuming that the heated region (electron impact area) occupies only a fraction α of the observed kernel area. The appropriate model H α profiles are then a combination of α times the electron heated model profile for any chosen electron flux plus $(1-\alpha)$ times the quiet Sun (or preflare) profile, α being the 'filling factor'. We find that the best match to the data obtains for $\alpha = \frac{1}{3}$ and that for this value the best fit value of \mathcal{F}_{20} , *averaged over the whole kernel area*, is about $3 \times 10^9 \text{ erg cm}^{-2} \text{ s}^{-1}$, implying local values $\approx 10^{10} \text{ erg cm}^{-2} \text{ s}^{-1}$ on the impact areas. Had we adopted a macroturbulent velocity as high as 100 km s^{-1} we could obtain a fit to the data with rather less horizontal beam inhomogeneity in the kernels but then the necessary \mathcal{F}_{20} would also have been less, and merely emphasized our conclusions in the following discussion.

Since we have profiles and models only for discrete \mathcal{F}_{20} values, some idea of how the combined profile discussed above would compare with the observations is shown by the solid curve in Figure 3. This profile is an arbitrarily scaled average of the $\mathcal{F}_{20} = 10^9$ and 10^{10} profiles, after convolution with a gaussian (Doppler) profile of width 60 km s^{-1} .

From the observed hard X-ray fluxes for this same August 7 event Hoyng *et al.* (1976) infer an energy input rate in electrons of $E > 20 \text{ keV}$ of $3 \times 10^{29} \text{ erg s}^{-1}$, while Lin and Hudson (1976) obtain $2 \times 10^{29} \text{ erg s}^{-1}$. If, as with the H α profiles, we adopt an impact area $\frac{1}{3}$ of $6 \times 10^{18} \text{ cm}^2$, the H α kernel area given by Zirin and Tanaka (1973), a value of $\mathcal{F}_{20} \approx 1-1.5 \times 10^{11} \text{ erg cm}^{-2} \text{ s}^{-1}$ is thus implied by the hard X-rays. This is approximately one order of magnitude greater than the injection rate inferred from the H α profiles computed from the models. This discrepancy cannot be reduced, but rather is increased, by supposing that the bulk of the thick target electrons impact not in the kernels alone, but over the area of the entire H α flare. According to Zirin and Tanaka (1973), this latter area is $2.5 \times 10^{19} \text{ cm}^2$, which corresponds to an injection of all the thick target electrons with a flux of $\mathcal{F}_{20} \approx 1 \times 10^{10} \text{ erg cm}^{-2} \text{ s}^{-1}$. For this value of \mathcal{F}_{20} we compute an emission equivalent width of about 25 \AA , if the flux is homogeneous over the entire flare area. The observed value of the equivalent width given by Zirin and Tanaka (1973) for the flare outside the kernels is about 1 \AA . This large discrepancy also cannot be explained by inhomogeneities in the energy flux. Only imaging of the hard X-ray emission will enable us to incorporate inhomogeneities properly and provide a more stringent constraint on the electron heating model. Roy (1976) has argued that hard X-ray spikes (in the flare of 1972, August 2, - c.f. Hoyng *et al.*, 1976) are not in fact coincident with optical (3835 \AA) flashes (Zirin and Tanaka, 1973). However Zirin (1978) has found an exact correspondence and pointed out that Roy (1976) used incomplete optical data.

The discrepancy between fluxes inferred from H α profiles versus hard X-rays may be attributed to the following:

(i) The electron injection rate into the chromosphere is considerably less than inferred above for a purely thick target model. For instance the thick target may be

fed by collisional precipitation from a trapped source, in which case \mathcal{F}_{10} would take $\frac{1}{3}$ of the above value (Melrose and Brown, 1976). Further reduction may be involved if electrons are confined by turbulent scattering or if the hard X-rays are significantly thermal.

(ii) Important sources of radiative cooling may have been omitted, e.g. bound-free hydrogen emission. As mentioned above, our preliminary calculations show this to be a complex, model-dependent radiative heating and cooling mechanism whose effects will be the subject of later work.

Support for the former explanation comes from the low EUV output of flares found by Emslie *et al.* (1978).

There are also a few factors that must be mentioned that would *increase* the discrepancy: (1) use of an active region model instead of a quiet-Sun model as the unperturbed atmosphere; (2) added heating terms such as heat conduction and soft X-ray heating; and (3) any additional line broadening mechanism such as Stark effect from plasma waves (Spicer and Davis, 1975). The only effects which could reduce the discrepancy are thus radiative losses higher than our estimates or a net conductive loss from the H α region. Such improvements are appropriate for further work.

Acknowledgements

We thank K. Tanaka for permission to use his H α profiles and M. Machado for useful discussions and comments on the manuscript.

The contribution of R. C. Canfield to this research has been sponsored by the Air Force Office of Scientific Research, Air Force Systems Command, USAF, under Grant No. AFOSR 76-3076, and by the Air Force Geophysics Laboratory, Air Force Systems Command, under Contract No. F19628-77-C-0165. M. N. Robertson has been supported by a U.K. Science Research Council Studentship. Two of us (J.C.B. and R.C.C.) have benefited considerably, in carrying out this research, from our participation in the Skylab Solar Workshop Series on Solar Flares. The workshops are sponsored by National Aeronautics and Space Administration and The National Science Foundation and managed by the High Altitude Observatory. Computing support was provided by the National Center for Atmospheric Research, which is supported by the National Science Foundation.

References

- Brown, J. C.: 1973a, *Solar Phys.* **31**, 143.
- Brown, J. C.: 1973b, *Solar Phys.* **29**, 421.
- Brown, J. C.: 1974, *Solar Phys.* **36**, 371.
- Brown, J. C.: 1975, in S. R. Kane (ed.), 'Solar Gamma-, X-, and EUV Radiation', *IAU Symp.* **68**, 245.
- Brown, J. C.: 1976, *Phil. Trans. Roy. Soc. London* **281**, 473.
- Canfield, R. C.: 1974a, *Solar Phys.* **34**, 339.
- Canfield, R. C.: 1974b, *Astrophys. J.* **194**, 483.
- Canfield, R. C.: 1974c, AFCRL-TR-74-0158, Environmental Research Papers, No 471

- Cox, R. P. and Tucker, W. W.: 1969, *Astrophys. J.* **157**, 1157.
Craig, I. J. D. and McClymont, A. N.: 1976, *Solar Phys.* **50**, 133.
Duschek, G. A., Feldman, U., and Rosenberg, F. D.: 1977, *Astrophys. J.* **215**, 329.
Emslie, A. G., Brown, J. C., and Donnelly, R. F.: 1978, *Solar Phys.* **57**, 175.
Hovng, P., Brown, J. C., and van Beek, H. F.: 1976, *Solar Phys.* **48**, 197.
Hudson, H. S.: 1972, *Solar Phys.* **24**, 414.
Hudson, H. S.: 1973, in R. Ramaty and R. G. Stone (eds.), *High Energy Phenomena on the Sun*, NASA-X-693-73-193.
Kane, S. R.: 1974, in G. A. Newkirk (ed.), 'Coronal Disturbances', *IAU Symp.* **57**, 105.
Kostyuk, N. D.: 1975, *Soviet Astron. AJ* **19**, 458.
Kostyuk, N. D.: 1976, *Soviet Astron. AJ* **20**, 206.
Kostyuk, N. D. and Pikel'ner, S. B.: 1975, *Soviet Astron. AJ* **18**, 590.
Lin, R. P.: 1975, *Space Sci. Rev.* **16**, 184.
Lin, R. P. and Hudson, J. S.: 1976, *Solar Phys.* **50**, 153.
McWhirter, R. W. P., Thonemann, P. C., and Wilson, R.: 1975, *Astron. Astrophys.* **40**, 63.
Melrose, D. B. and Brown, J. C.: 1976, *Monthly Notices Roy. Astron. Soc.* **176**, 15.
Nakagawa, Y., Wu, S. T., and Han, S. M.: 1973, *Solar Phys.* **30**, 111.
Roy, J.-R.: 1976, *Solar Phys.* **48**, 265.
Shmeleva, O. P. and Syrovatskii, S. I.: 1973, *Solar Phys.* **33**, 341.
Tanaka, K.: 1977, personal communication.
Spicer, D. S. and Davis, J.: 1975, *Solar Phys.* **43**, 107.
Zirin, H.: 1978, preprint.
Zirin, H. and Tanaka, K.: 1973, *Solar Phys.* **32**, 173.

ii) Radiative Hydrodynamics of Flares: Preliminary

Results and Treatment of the Transition Region

This paper, as the title suggests, is a preliminary report of early progress on the development of numerical techniques for simulating the dynamics of the flare plasma. It is published in Solar and Interplanetary Dynamics, edited by M. Dryer and E. Tandberg-Hansen. Its primary contribution is to suggest various ways of treating the steep temperature gradient at the top of the chromosphere in numerical schemes. It also describes our work on accelerating surge material, following up on what was done during the Solar Flare Workshop, in the Mass Ejections Team.

RADIATIVE HYDRODYNAMICS OF FLARES: PRELIMINARY RESULTS AND NUMERICAL
TREATMENT OF THE TRANSITION REGION

A.N. McClymont and R.C. Canfield
Department of Physics, C-011
University of California, San Diego
La Jolla, California 92093 U.S.A.

We report on a comprehensive numerical simulation of flare dynamics, encompassing the corona, transition region and chromosphere. A coronal loop geometry, whose magnetic pressure dominates gas pressure, is assumed. These preliminary results assume optically thin radiation; we are currently incorporating optically thick radiative transfer in the chromosphere. We discuss difficulties in modelling the transition region under flare conditions, and suggest tentative solutions.

The hydrodynamic equations, incorporating the effects of thermal conduction, viscosity and radiation, are described by Craig and McClymont (1976) while the probabilistic method for radiative transfer is discussed by Canfield and Ricchiazzi (1979). We write the continuity, momentum and energy equations in Lagrangian form using column mass as the independent variable and consider the atomic rate equations for the fractional populations rather than absolute number densities. Thus we eliminate all convective terms. The equations are then written in fully implicit finite difference form and are solved by simultaneous iteration at each timestep.

We have carried out preliminary calculations neglecting radiative transfer effects. The simple model atmosphere used is not claimed to be a faithful replica of a loop in the solar atmosphere, rather it is intended to illustrate global features. Figure 1 shows the velocity response of a loop to the impulsive injection of energy at its apex, raising the coronal temperature from $1.6 \times 10^6 \text{K}$ to $5 \times 10^6 \text{K}$. Coronal material is driven down the legs of the loop and collides with the dense transition region after 1 minute. The chromosphere is then compressed downwards while coronal material is reflected upwards again. Thereafter the atmosphere undergoes oscillations, heavily damped by conduction and radiation, of period ~ 4 minutes. Global oscillations of this type (and of greater amplitude for stronger flare heating) appear in all our calculations but, as far as we know, have not been reported observationally. Figure 2 shows the results of injecting the same amount of energy at a height of 1000 km in the chromosphere; in this case a surge-like ejection

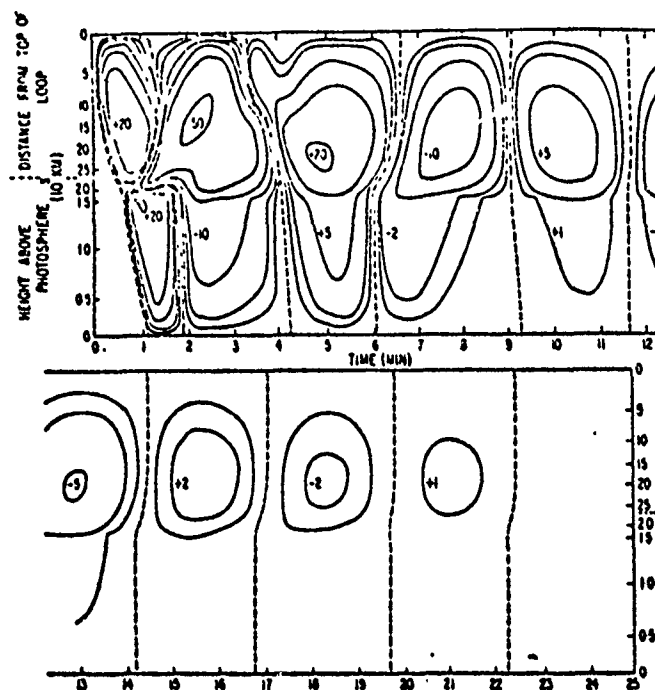


Fig. 1. Velocity as a function of height and time following the injection of impulse of energy at the top of the loop. Contours are labelled in units of km s^{-1} (positive velocities downward). Note that the vertical axis is a Lagrangian coordinate, heights and distances correspond to the initial position of gas elements. The scale is distorted non-linearly to show both the corona and chromosphere, which extends to a height of ~ 2000 km.

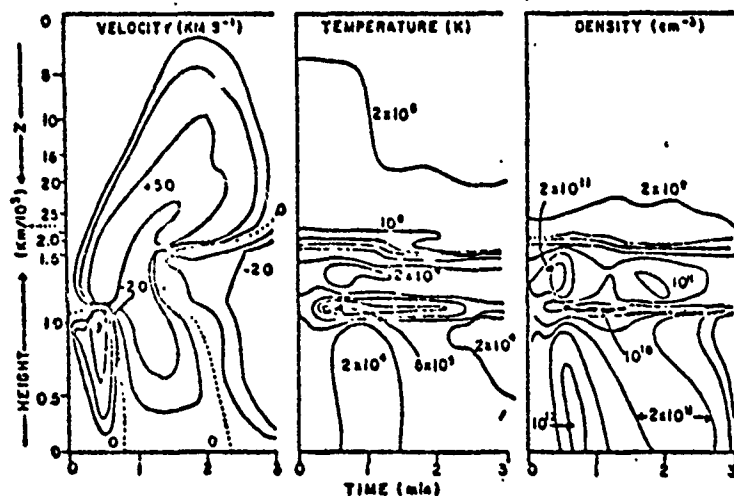


Fig. 2. Velocity (positive upwards), temperature and density as a function of column mass and time in a model surge. Note cool dense core of surge material above 1000 km, the initial energy release height. See Figure 1 caption regarding non-linear vertical axis.

of chromospheric material into the corona occurs. The Lagrangian vertical axis in Figure 2 does not explicitly show the motion, but integration of the velocity over time shows that this small surge reaches a height of only 5000 km. The most interesting feature of the calculation is the lack of heating of the surge material by the energy release; in fact the material is compressed as it is driven upwards and cools rapidly through the enhanced radiative loss rate. Thus we have a possible explanation for the appearance of cool, dense surges in the corona.

While investigating the dynamic formation of an atmosphere with a corona-transition-zone-chromosphere structure from an initially uniform plasma, Craig and McClymont (1979) found that incorrect results were obtained for high conductive fluxes through the transition region. It is now clear that only fluxes for which the scale height of temperature variation is greater than the finite difference grid spacing can be reproduced accurately. That is, the flux F is limited to $p\kappa(T)/(k \Delta N)$, where p is pressure, $\kappa(T)$ is the conductivity, k is Boltzmann's constant and ΔN is the Lagrangian grid spacing. With the grid spacing typically used in numerical modelling of this type (e.g. Kostyuk and Pikel'ner, 1975; Kostyuk, 1976; Somov et al., 1978; Craig and McClymont, 1979) this criterion is marginally satisfied in the quiet solar atmosphere but grossly violated under flare conditions. Under dynamic flare conditions there is an "evaporative" conduction front moving through the plasma at a "velocity" u ($\text{cm}^{-2} \text{s}^{-1}$). In order to reproduce the temporal behavior of the atmosphere satisfactorily, conditions at a grid point must change slowly compared to the timestep Δt , i.e. we require $u \Delta T \ll L(T) = p\kappa/(2 kF)$, where $L(T)$ is the characteristic scale of T variation, $[(T)(dT/dN)]^{-1}$. Under flare conditions this is very severe restriction on the timestep; we must depart from conventional finite difference techniques to handle the transition region. We suggest the following methods, none of which have been investigated in detail:

- (1) Within the transition zone, formulate the equations for a set of grid points which convect through the plasma with the conduction front.
- (2) Introduce a "pseudo-conductivity" term in analogy with the pseudo-viscosity term, with suitable modification of the energy equation.
- (3) Approximate the transition region as a thin interface between an upper temperature T_1 in the corona and a lower temperature T_2 in the chromosphere.

Craig, I.J.D., and McClymont, A.N.: 1976, Solar Phys., 50, p. 133.
 Canfield, R.C., and Ricchiazzi, P.: 1979, submitted to Astrophys.J.
 Craig, I.J.D., and McClymont, A.N.: 1979, submitted to Solar Phys.
 Kostyuk, N.D., and Pikel'ner, S.R.: 1975, Sov.Astron., 18, p. 590.
 Kostyuk, N.D.: 1976, Sov.Astron., 19, p. 458.
 Somov, B.V., Spektor, A.R., and Syrovatskii, S.I.: 1978, Izv.Acad.Sci. USSR. Phys.Ser., 41, p. 273.

iii) The Dynamic Formation of Quasi-Static Active Region Loops

This paper describes further development of the numerical techniques, beyond the work described above. It is the first paper to discuss the full dynamics of chromospheric evaporation, on which our observational results have focused. From a computational point of view, it demonstrates the importance of proper spatial resolution in numerical simulations. As a result, our subsequent theoretical studies used a much more sophisticated numerical technique, i.e. adaptive regridding.

al speeds are of the same
r. From the bright knots
of attraction lying along
aming material as well as

THE DYNAMIC FORMATION OF QUASI-STATIC ACTIVE REGION LOOPS

I. J. D. CRAIG*

Department of Mathematics, University of Waikato, Private Bag, Hamilton, New Zealand

and

A. N. McCLYMONT

Department of Physics, University of California, La Jolla, Calif. U.S.A..

(Received 3 September, 1979; in revised form 19 June, 1980)

Abstract. A hydrodynamic model is used to analyse the formation of an active region coronal loop. After an impulse of energy that 'lifts' part of a cool uniform plasma into the domain of radiative instability ($T > 10^5$ K) the atmosphere is allowed to relax dynamically to a new quasi-steady equilibrium. Although the radiative-hydrodynamic coupling leads to quite complex physical phenomena, the final state of the plasma shows excellent agreement with previous quasi-static loop calculation.

The bearing of this analysis on the evolution of flare plasmas is then discussed. In particular, it is shown that the energy flux emanating from an excited coronal source leads to the 'dynamic evaporation' of cool transition-zone and chromospheric material. The analysis indicates, however, that an accurate description of the transition zone in solar flares requires considerably more sophistication than has hitherto been employed.

Finally, a discussion is given of the uniqueness and stability of the quasi-static loop. It is concluded that, despite thermal instability, a quasi-static model should adequately describe the gross features of quiescent coronal loops.

1. Introduction

High resolution X-ray and EUV observations indicate that active region plasmas are organized by the solar magnetic field into filamentary loop structures. The loops are generally quiescent; they undergo little change in either brightness or structure throughout the greater part of their lifetime. In consequence an individual loop may satisfy a simple quasi-static equilibrium in which local energy losses by conduction and radiation are balanced by a stationary heating mechanism.

Quasi-static loop models (Landini and Fossi, 1975; Craig *et al.*, 1978; Rosner *et al.*, 1978) seem in reasonable accord with the observations: they explain, in a fairly natural way, the fact that small hot loops are several orders of magnitude denser than larger, cooler structures. On the theoretical side, however, there has been speculation that certain loop configuration may be thermally unstable. Antiochos (1979) and Hood and Priest (1979) have already argued on the basis of linearized normal mode analyses, that the loop models of Rosner *et al.* (1978) lack stability. This view is not shared by Habbel and Rosner (1979) who contend that virtually all plausible heating mechanisms give rise to stable or metastable thermal structures.

Which of these views is nearer the truth is best established by a full dynamic treatment of the loop evolution. But, thermal stability aside, the real beauty of the

* Formerly at Department of Astronomy, The University, Glasgow G12 8QQ, Scotland.

dynamic approach is that the transition between successive loop configurations can be followed in detail. Hence the influence of mass flow and chromospheric evaporation on the loop structure can be more readily understood.

In this paper therefore, we analyze the dynamic formation of a quasi-state loop. The analysis is similar in philosophy to the dynamical 'quiet' coronal model proposed by Brown and Bessey (1973). Our emphasis however, is on the closed loop topology of the active region plasma rather than on the freely expanding 'open' geometry of Brown and Bessey. In fact our treatment gives rise to far more complex and interesting physical phenomena - for instance, radiative condensations generated by the hydrodynamic response of the loop - which are of direct relevance to both quiescent active region and dynamic flare problems.

In Section 2 we briefly summarize the essential features and limitations of quasi-static loop modelling. The complete system of hydrodynamic equations is introduced in Section 3 and assumptions underlying the boundary and initial conditions of the problem are fully discussed. In Section 4 we present a detailed interpretation of the numerical results. Finally, in Section 5, we discuss the importance of our conclusions to future active region and flare modelling.

2. Background - The Quasi-Static Loop

As already mentioned, many quasi-static models of quiescent active region plasmas have been developed, with the central assumption that dynamic effects can be neglected in the energy balance. Accordingly the energy equation is simply

$$\frac{\partial}{\partial z} \left(K \frac{\partial T}{\partial z} \right) = n^2 f(T) - \epsilon(z), \quad (2.1)$$

where T is the plasma temperature, n is the electron number density, K is the classical coefficient of heat conduction,

$$K = K_0 T^{5/2}, \quad (2.2)$$

with $K_0 \approx 10^{-6}$ cgs units, $f(T)$ is the radiative loss function for an optically-thin plasma (e.g. Cox and Tucker, 1969; Tucker and Koren, 1971), and $\epsilon(z)$ is the stationary heating term. The space coordinate z is measured along the axis of the loop from its apex; the loop is assumed to be of constant area and symmetric about this point. In addition most analytic models assume uniform pressure, viz.

$$P = 2nkT = \text{constant}, \quad (2.3)$$

since the gravitational scale height in the corona and transition region is much greater than the vertical extent of the region under study (c.f. the numerical modelling of Vesecky *et al.*, 1979).

The analytic model of Landini and Fossi (1975) and Rosner *et al.* (1978), is based on two further assumptions, namely uniform energy deposition and vanishing conductive flux deep in the chromosphere. However, as emphasized by Craig *et al.*

(1978), since both the energy deposition and mass flow are rather possible. Thus, following of temperature rather than physically realistic heating half of the loop.

Defining the half length

$$l(T_1) = \int_{T_1}^{T_0} \left| \frac{dz}{dT} \right| dT$$

where T_1 is a reference temperature, then it is possible to derive a density, T_0 and n_0 . In particular

$$n_0 = 3.8 \times 10^{14} \text{ cm}^{-3}$$

where $\mathfrak{F}(T_1)$ is the condensation flux, $2 \times 10^{-11} n_0 T_0^{3/4} \text{ erg cm}^{-2} \text{ s}^{-1}$ accounting for the 'shape' of the loop.

$$\int_{T_1}^{T_0} \epsilon(T) dT = \mathfrak{F}(T_1)$$

Equation (2.5) already appears in Rosner *et al.*: For uniform energy deposition and heat flux $\mathfrak{F}(T_1)/\mathfrak{F}_0 \approx 0.1$ the choice of power law $(10^5 \text{ K} < T < 10^7 \text{ K})$ so that various authors have noted (Rosner *et al.*, 1978). In approximation to the gl variable cross-section area

Perhaps we should emphasize that the *function* is implicitly included in the determination of the peak temperature or better $\epsilon_0 \approx K_0 T_0^{7/2} / l^2$ maintains that most authors that relationship (2.5) can be combined with the heating function profile and l , can be combined with $\mathfrak{F}(T_1)$. More detailed information by differentiating the differential equation

top configurations can
chromospheric evapora-

of a quasi-state loop.
ronal model proposed
a closed loop topology
ng 'open' geometry of
r more complex and
nsations generated by
ect relevance to both

es and limitations of
dynamic equations is
boundary and initial
we present a detailed
n 5, we discuss the
e modelling.

active region plasmas
ra. effects can be
tion is simply

(2.1)

er density, K is the

(2.2)

for an optically-thin
71), and $\varepsilon(z)$ is the
along the axis of the
and symmetric about
ressure, viz.

(2.3)

egion is much greater
nerical modelling of

al. (1978), is based
ition and vanishing
sized by Craig *et al.*

(1978), since both the chromospheric energy balance and the form of the energy deposition are rather poorly understood, it is wise to avoid these assumptions if possible. Thus, following Craig *et al.* (1978), we regard the energy input as a function of temperature rather than of position. This is generally plausible, because, for physically realistic heating functions, T is always a monotonic function of z in each half of the loop.

Defining the half length of the loop by

$$l(T_1) = \int_{T_1}^{T_0} \left| \frac{dT}{dz} \right|^{-1} dT, \quad (2.4)$$

where T_1 is a reference temperature at the base of the atmosphere ($T_1 \approx 10^5$ K) it is then possible to derive a relationship between l and the central temperature and density, T_0 and n_0 . In particular we obtain

$$n_0 = 3.8 \times 10^4 \beta^{1/2} [1 + (\mathfrak{Z}(T_1)/\mathfrak{Z}_0)^2]^{-1/2} T_0^{9/4}/l, \quad (2.5)$$

where $\mathfrak{Z}(T_1)$ is the conductive flux entering the lower atmosphere ($T < T_1$), $\mathfrak{Z}_0 = 2 \times 10^{-11} n_0 T_0^{5/4}$ erg cm⁻² s⁻¹ is a reference coronal flux and β is a number of 0(1) accounting for the 'shape' of the heating function:

$$\int_{T_1}^{T_0} \varepsilon(T) T^{5/2} dT = \beta \varepsilon(T_0) \int_{T_1}^{T_0} T^{5/2} dT. \quad (2.6)$$

Equation (2.5) already incorporates the expressions derived by Landini and Fossi, and Rosner *et al.*: For uniform deposition $\beta = 1$, while for negligible chromospheric heat flux $\mathfrak{Z}(T_1)/\mathfrak{Z}_0 \approx 0$. Note that the exponent of T_0 in Equation (2.5) depends on the choice of power law approximation to the coronal radiative loss function (10^5 K $< T < 10^7$ K) so that the slight differences in the power of T_0 obtained by various authors have no inherent physical significance (e.g. Landini and Fossi, 1975; Rosner *et al.*, 1978). Note also that Equation (2.5) generally provides a good approximation to the global loop structure, even when effects due to gravity and variable cross-section are taken into account (see Vesecky *et al.*, 1979).

Perhaps we should emphasise at this point that the *amplitude of the coronal heating function* is implicitly incorporated in Equation (2.5); the magnitude of the heating determines the peak temperature of the loop (in fact, to an accuracy of typically 20% or better $\varepsilon_0 \approx K_0 T_0^{7/2}/l^2$), a point evidently not appreciated by Jordan (1980) who maintains that most authors neglect the influence of the heating strength. It follows that relationship (2.5) can be used to provide a two-parameter (ε_0, β) description of the heating function provided that measurement of the coronal parameters n_0 , T_0 , and l , can be combined with a plausible estimate of the chromospheric heat flux $\mathfrak{Z}(T_1)$. More detailed information on the heating can be derived, at least in principle, by *differentiating* the differential emission measure function, $\xi(T)$, but this approach

will remain unsound unless the typically crude, two or three parameter, representation of ξ can be considerably improved upon (cf. Jordan, 1980).

The possibility that certain loop configurations may be thermally unstable can be anticipated from Field's (1965) criterion for stability of a homogeneous, isothermal, plasma of length l :

$$n < 2.2 \times 10^5 T^{9/4} / l. \quad (2.7)$$

Although not directly applicable to the inhomogeneous loop plasma, this result suggests that if the coronal density becomes too high, or the coronal scale length too great, then conduction can no longer control perturbations in the thermally unstable plasma. Moreover, comparison of this condition with Equation (2.5) suggests that instability is less likely to occur for low β values and high conductive fluxes through the base.

Antiochos (1979) has recently performed a global perturbation analysis for static, closed loop structures. He finds that loop models which assume vanishing conductive flux at the base (e.g. Rosner *et al.*, 1978) are always thermally unstable (see also Hood and Priest, 1979). The instability, however, vanishes when the base conductive flux is increased to approximately 15% of its peak coronal value. Antiochos then speculates that regions of low conductive flux in the lower transition zone may develop oscillatory (period of ~ 1 s) behaviour as material heats, expands and then cools and condenses. However, only a detailed dynamic calculation is capable of supporting this assertion.

Finally we remark that Rosner *et al.* (1978) have asserted, *incorrectly*, that the temperature at the apex of the quasi-static loop must be maximal in order to maintain the thermal stability of the plasma; they fail to take account of the fact that conduction can stabilise the instability provided the coronal length scale is not too large (see also Vesecky *et al.*, 1979).

3. Equations and Boundary Conditions

The hydrodynamic equations for a fully ionized coronal plasma may be written in the following form (Craig and McClymont, 1976):

$$\frac{D\rho}{Dt} = -\rho \frac{\partial v}{\partial z}, \quad (3.1)$$

$$\rho \frac{Dv}{Dt} = -\frac{\partial P}{\partial z}, \quad (3.2)$$

$$\frac{3}{2}\rho \frac{D}{Dt}(P/\rho) = \frac{\partial}{\partial z} \left(K \frac{\partial T}{\partial z} \right) - P \frac{\partial v}{\partial z} - n^2 f(T) + \epsilon, \quad (3.3)$$

where $\rho = m_H n$ is the mass density, m_H is the mass of the hydrogen atom and v is the fluid velocity. Note that we neglect gravitational acceleration and viscosity and

model the chromosphere, however, are in conclusion.

As usual we set

$$\frac{dT}{dz}.$$

At the base of the loop, the temperature must vanish (cf. Kopp's theoretical view of the solar wind). This is the only point where we are assuming that the temperature is essentially uniform.

Other possible boundary conditions, for example, fixed temperature at the base, are not considered here. In the absence of a detailed model to determine the temperature distribution, we assume an insulating boundary at the base because it represents the most realistic situation.

Also, while the temperature is optically thin, the temperature is introduced into the energy equation. Various forms of the temperature distribution have been considered (Canfield 1979) and this is equivalent to assuming a constant temperature.

In the present model, the main requirements are realistic coronal loop relaxation times and the global-magnetohydrodynamic conditions:

$$T_i$$

$$n_i$$

The radiative constant per unit volume is

$$\epsilon_0$$

ree parameter, represen-
n, 1980).

thermally unstable can be
homogeneous, isothermal,

(2.7)

loop plasma, this result
coronal scale length too
in the thermally unstable
uation (2.5) suggests that
conductive fluxes through

urbation analysis for static,
ume vanishing conductive
ermally unstable (see also
when the base conductive
nal value. Antiochos then
ower transition zone may
al heats, expands and then
c ation is capable of

erted, *incorrectly*, that the
ximal in order to maintain
account of the fact that
onal length scale is not too

tions

lasma may be written in the

(3.1)

(3.2)

(3.3)

hydrogen atom and ν is the
eleration and viscosity and

model the chromospheric radiation only crudely (see below). These simplifications however, are mainly for ease of exposition and in no way affect our central conclusions.

As usual we suppose that the loop evolution is symmetrical about the apex, so that

$$\frac{dT}{dz} = \frac{dn}{dz} = \frac{dv}{dz} = 0 \quad \text{at } z = 0. \quad (3.4)$$

At the base of the model the temperature gradient and the fluid velocity are taken to vanish (cf. Kostyuk and Pikel'ner, 1975). This condition is very convenient from the theoretical viewpoint since it means that the hydrodynamic system is isolated from its surroundings in that there is no mass or energy flux through the footpoints. Radiation is the only process by which the loop can lose energy. In essence, therefore, we are assuming that there is some region, immediately below the base of the loop, which is essentially unaffected by events in the overlying plasma.

Other possibilities for the lower boundary condition have also been considered. In particular, we have experimented with the idea of keeping the base temperature fixed, so that the lower chromosphere can act, in effect, as an infinite source or sink of heat. In the absence of a self-consistent model chromosphere however, it is difficult to determine whether this condition is much superior to the assumption of a rigid insulating barrier. For the present we adopt the thermally isolated atmosphere, not because it provides, necessarily, the most physically realistic model, but because it represents the simplest, non-trivial approximation to the chromospheric response.

Also, while radiation from the corona and transition zone can be treated in the optically-thin approximation, it is clear that some form of opacity correction must be introduced in the chromosphere to keep the radiative losses down to a realistic level. Various forms of semi-empirical opacity have been investigated by McClymont and Canfield (1979; unpublished results). We adopt here only a zeroth order correction; this is equivalent to setting $f(T) = 10^{-36} T^3$ (cgs units) in the region below $\sim 10^5$ K.

In the present application the initial atmosphere is, to a large extent, arbitrary. The main requirement is that the loop contains sufficient mass and energy to form a realistic coronal-transition region structure. Since we are interested in the *dynamic loop relaxation* rather than in the details of the *initial static atmosphere*, it is sufficient to select the simplest static loop consistent with the boundary conditions and the global-mass-energy requirements. Accordingly we chose uniform initial conditions:

$$\left. \begin{aligned} T_i &= 6 \times 10^4 \text{ K} \\ n_i &= 10^9 \text{ cm}^{-3} \end{aligned} \right\} \quad (3.5)$$

The radiative losses are supported by a quiescent energy input which is assumed to be constant per unit mass:

$$\epsilon_q = n n_i f(T_i). \quad (3.6)$$

A transient energy pulse, ε , of gaussian half-width σ – short compared to the half length l of the loop – is then used to perturb the static atmosphere:

$$\left. \begin{aligned} \sigma &= 5 \times 10^8 \text{ cm} \\ l &= 3.3 \times 10^9 \text{ cm} \end{aligned} \right\} \quad (3.7)$$

Consequently ε has two components,

$$\varepsilon = \varepsilon_q + \varepsilon_t, \quad (3.8)$$

ε_t being sinusoidal in time reaching a maximum amplitude of 10^{-2} ergs $\text{cm}^{-2} \text{s}^{-1}$ after 100 s. Note that this amplitude must be sufficient to 'lift' enough of the plasma into the domain of the radiative instability ($T \geq 10^5$ K). When the pulse is switched off ($\varepsilon_t = 0$ for $t > 200$ s) the atmosphere is allowed to relax dynamically to a new quasi-steady state.

In obtaining a numerical solution the hydrodynamic equations were written in terms of the Lagrangian variable

$$\zeta(z) = \int_0^z \rho(z') dz'. \quad (3.8)$$

Results were then derived from a second order, implicit finite difference scheme, incorporating self-adjustable time step (0.1 to 1.0 s) and pseudo-viscosity in the momentum equation (e.g. Richtmyer and Morton, 1967).

4. Results and Interpretation

4.1. THE DYNAMIC CORONA

Figures 1–12 show the detailed evolution of the loop.

We observe that during the first minute or so of transient energy deposition the plasma is heated at approximately constant density. As soon as the central temperature exceeds 10^5 K the local radiative losses diminish; the plasma near the top of the loop, driven partly by the instability, heats rapidly until conduction counter balances the instability at approximately 2×10^6 . However, the enhanced thermal energy in the newly developed corona drives a pressure wave into the cooler material. By 200 s sufficient mass has been driven into this region to form a cool, dense radiative condensation ($T \approx 2 \times 10^4$ K; $n \approx 10^{11} \text{ cm}^{-3}$). Figures 1, 2, and 3 show the gradual development of the condensation into a chromosphere as the pressure wave advances. Material which is first compressionally heated by the wavefront rapidly cools by radiation due to the density enhancement. Note also, in Figure 7, how a velocity reversal at the origin results from a temporary reduction in the local coronal pressure.

After 500 s (Figure 4) the loop structure is virtually fully developed: coronal and chromospheric regions are separated by a narrow transition layer ($\sim 10^7$ cm thick).

DYNAMIC

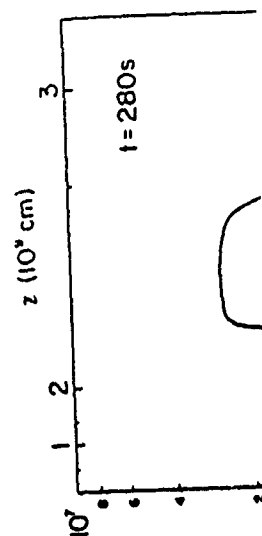
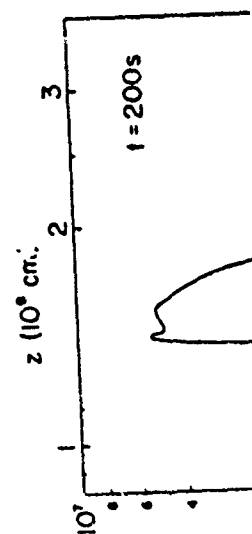


Fig. 1. Distribution of temperature, density and pressure in the loop at the end of transient heating ($t = 200$ s). Temperature is in units of degrees K, density in units of 10^6 cm^{-3} and pressure in units of $10^{-6} \text{ dyne cm}^{-2}$. Note the non-linear scale across the top of the figure. Compressionally heated material is seen at $z \approx 3.3 \times 10^{-6} \text{ cm}$; behind it a



mpared to the half
ere:

(3.7)

(3.8)

$2 \text{ ergs cm}^{-2} \text{ s}^{-1}$ after
of the plasma into
ulse is switched off
amically to a new

ns were written in

(3.8)

difference scheme,
do-...osity in the

ergy deposition the
ne central tempera-
near the top of the
on counter balances
thermal energy in
r material. By 200 s
ol, dense radiative
3 show the gradual
the pressure wave
wavefront rapidly
in Figure 7, how a
in the local coronal

veloped: coronal and
er ($\sim 10^7 \text{ cm}$ thick).

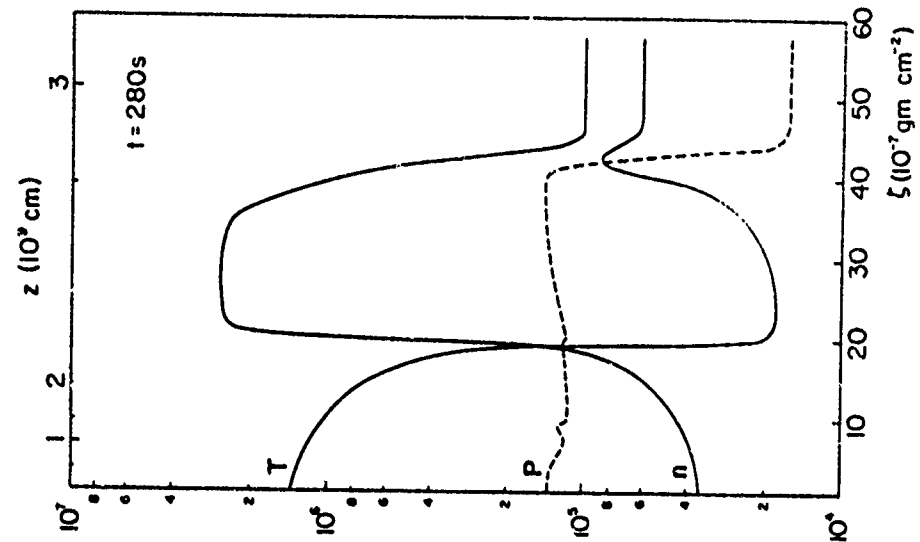


Fig. 1. Distribution of temperature, density and pressure in the loop at the end of transient heating ($t = 200 \text{ s}$). Temperature is in units of degrees K, density in units of 10^{-6} cm^{-3} and pressure in units of $10^{-6} \text{ dyne cm}^{-2}$. Note the non-linear z scale across the top of the figure. Compressional heating is seen at $\zeta \approx 3.3 \times 10^{-6} \text{ gm cm}^{-2}$; behind it a radiative condensation is forming ($1.8 \times 10^{-6} \text{ gm cm}^{-2} < \zeta < 3.3 \times 10^{-6} \text{ gm cm}^{-2}$).

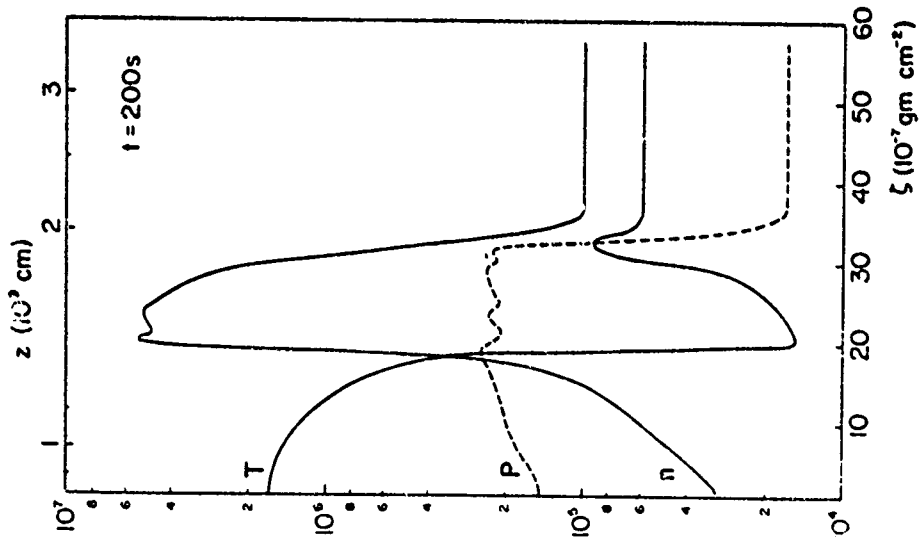


Fig. 2. Units as in Figure 1. After 280 s, the radiative condensation is still widening.

Fig. 1

Fig. 2

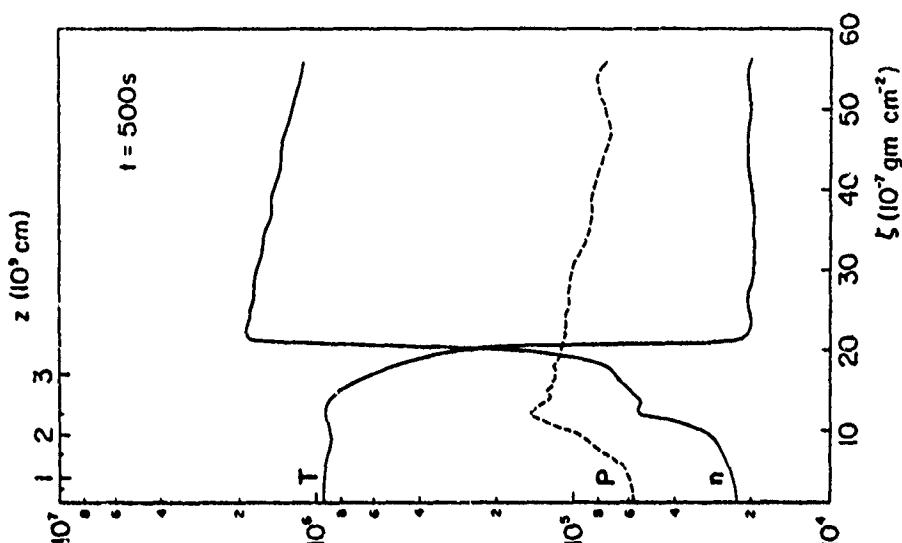


Fig. 3. Units as in Figure 1. At $t = 400$ s, the pressure wave has reached the footpoints of the loop, leaving behind it the nascent chromosphere.

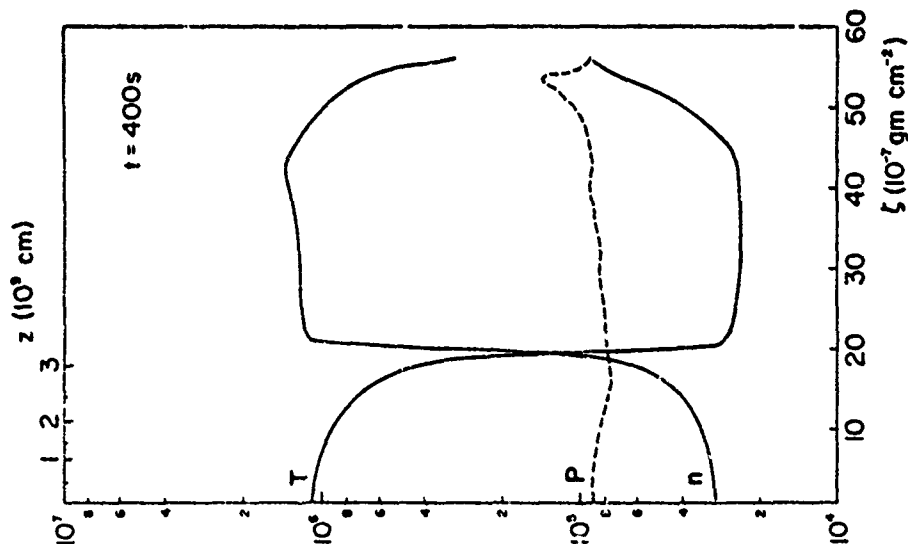


Fig. 4. Units as in Figure 1. The corona-transition region-chromosphere structure is now fully developed. The corona accounts for only $\sim \frac{1}{3}$ of the mass in the loop but 90% of the volume. The pressure wave, after reflecting at the footpoint, is now moving back up towards the loop apex.

Fig. 3

Fig. 4

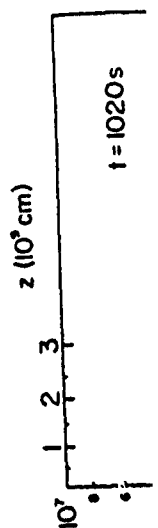
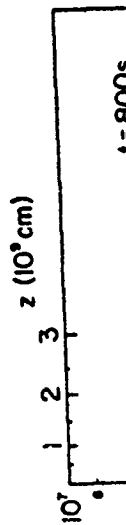


Fig. 5. After 800 s the pressure gradients are falling as mass motions die out. The major change from Figure 4 ($t = 500$ s) is the higher temperature and lower density in the



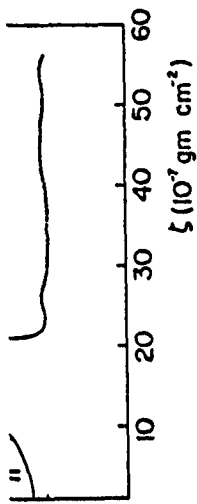


Fig. 3

corona-transition region-chromosphere structure is now fully developed. The corona accounts for only $\sim \frac{1}{3}$ of the mass in the loop but 90% of the volume. The pressure print, after reflecting at the foot, is now moving back up towards the loop apex.

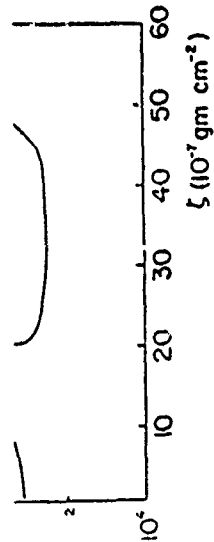


Fig. 4

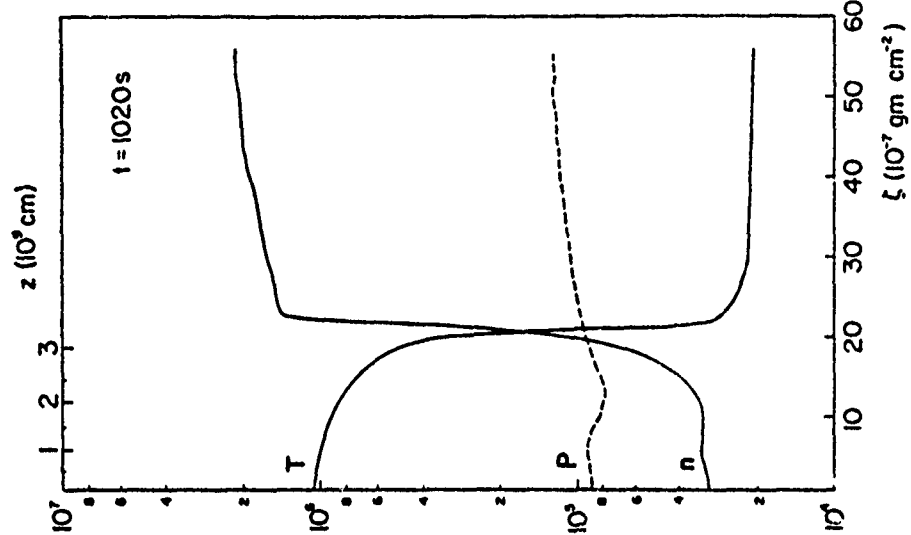


Fig. 5

Fig. 5. After 800s the pressure gradients are falling as mass motions die out. The major change from Figure 4 ($t = 500$ s) is the higher temperature and lower density in the chromosphere.

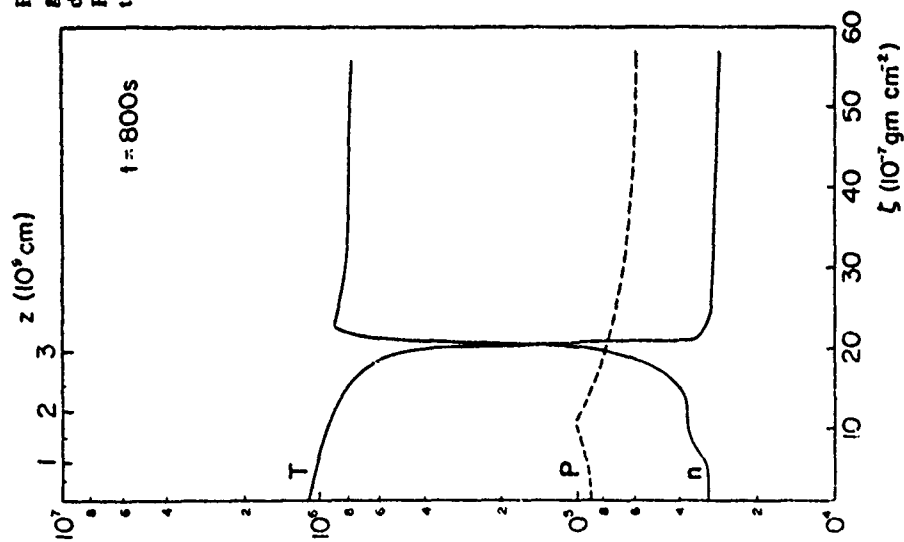


Fig. 6

Fig. 6. At $t = 1020$ s it is evident that the chromospheric temperature and density are still oscillating in anti-phase (cf. Figure 5).

Chromospheric material is now flowing up through the transition zone enhancing the coronal density and pressure. Although the pressure gradient has once again reversed after 800 s the loop is now able to relax through fairly minor adjustments in the thermal profile (Figures 5 and 6).

Figures 7, 8, and 9 illustrate the velocity profiles in the loop, while an overview of the evolution is provided by Figures 10, 11, and 12. Figures 10 and 11 illustrate the evolution of the coronal temperature, density and pressure at the top of the loop. Quasi-static equilibrium is attained after ~ 1800 s (30 min), since by this time oscillations of the coronal plasma are almost absent: indeed the final coronal parameters show excellent agreement with the T_0 , n_0 , and l scaling law of Equation (2.5).

A global picture of the hydrodynamic evolution of the loop is illustrated in Figure 12. It is clear that the quasi-static state is established once the ratio of global kinetic to thermal energy of the plasma has decreased from $\sim 10^{-1}$ to $\sim 10^{-4}$, while the complex transient behaviour at earlier times is replaced by a simple oscillation with period corresponding to the acoustic propagation time along the loop (~ 300 s).

4.2. THE EFFECT OF FLARE ENERGIZATION

In this section we consider two effects of relevance to hydrodynamic flare modelling. The first effect is entirely physical in origin and results from the dynamic response of the chromosphere and low transition zone to enhanced coronal energy flux; the second is a spurious numerical effect that arises through inadequate resolution in the (model) flare transition zone.

We begin by investigating the response of the fully-formed quasi-static atmosphere to a transient injection of energy at 1600 s. (The dynamic heating ϵ , remains the same as before). The dotted lines in Figures 10 and 11 indicate the evolution of the coronal loop. It is clear that a substantial fraction of the energy flux emerging from the coronal source is 'reflected back' off the denser material in the transition zone and chromosphere. The net effect is a dynamic evaporation of cool material. Thus the coronal density which is initially diminished by motions down the pressure gradient, becomes rapidly enhanced by the initial backflow of relatively dense material through the transition zone. Likewise, the pressure achieves its maximum value after the transient heating has ceased, almost concurrent with the density maximum. In contrast the coronal temperature declines steadily throughout the initial relaxation. The analysis shows very clearly how the hydrodynamic oscillation of the loop is superposed on the slower variation of density and temperature.

As already implied, we believe that dynamic evaporation is a general manifestation of the flare phenomenon. The effect moreover, is not strongly dependent on the evolution of the lower boundary temperature; thus when the base temperature is held fixed, rather than allowed to float as in the present calculation (see Section 3), the dynamic evaporation is not appreciably diminished. It would appear therefore, that a rising coronal density (or emission measure) can be associated quite naturally

zone enhancing the
ent has once again
minor adjustments in

while an overview of
and 11 illustrate the
the top of the loop.
since by this time
the final coronal
ing law of Equation

illustrated in Figure
tio of global kinetic
 $\sim 10^{-4}$, while the
ple oscillation with
a loop (~ 300 s).

nic flare modelling.
ynamic response of
al energy flux; the
ite lution in the

quasi-static atmos-
heating ϵ , remains
te the evolution of
ergy flux emerging
al in the transition
n of cool material.
down the pressure
of relatively dense
sure achieves its
t concurrent with
declines steadily
ly how the hydro-
ariation of density

s a general mani-
ngly dependent on
ase temperature is
on (see Section 3),
appear therefore,
ted quite naturally

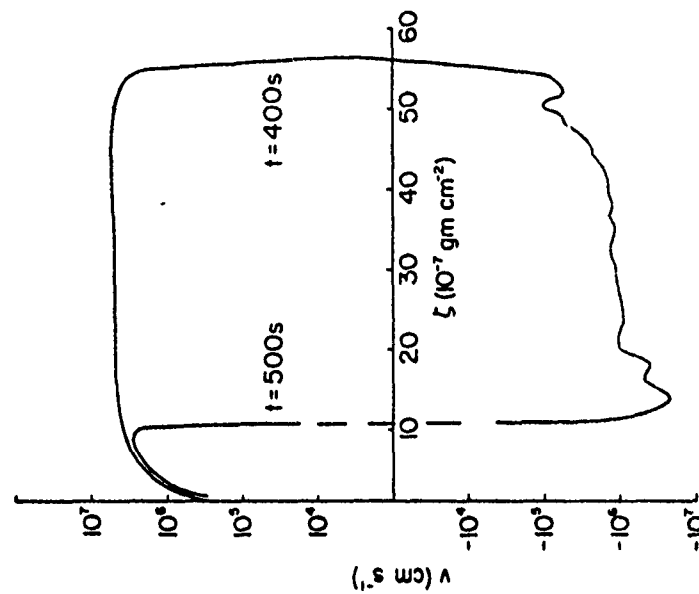


Fig. 8. Velocity profiles after 400 and 500 s.

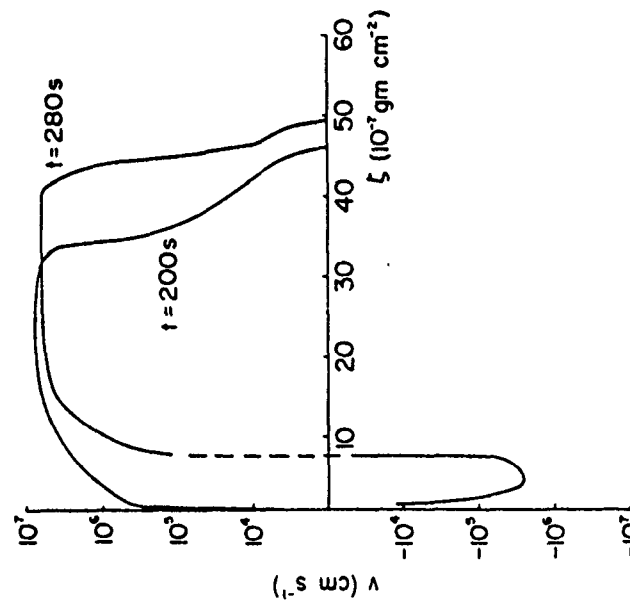


Fig. 7. Velocity profiles in the loop at 200 and 280 s. Positive velocities are directed away from the apex, negative velocities towards the top of the loop.

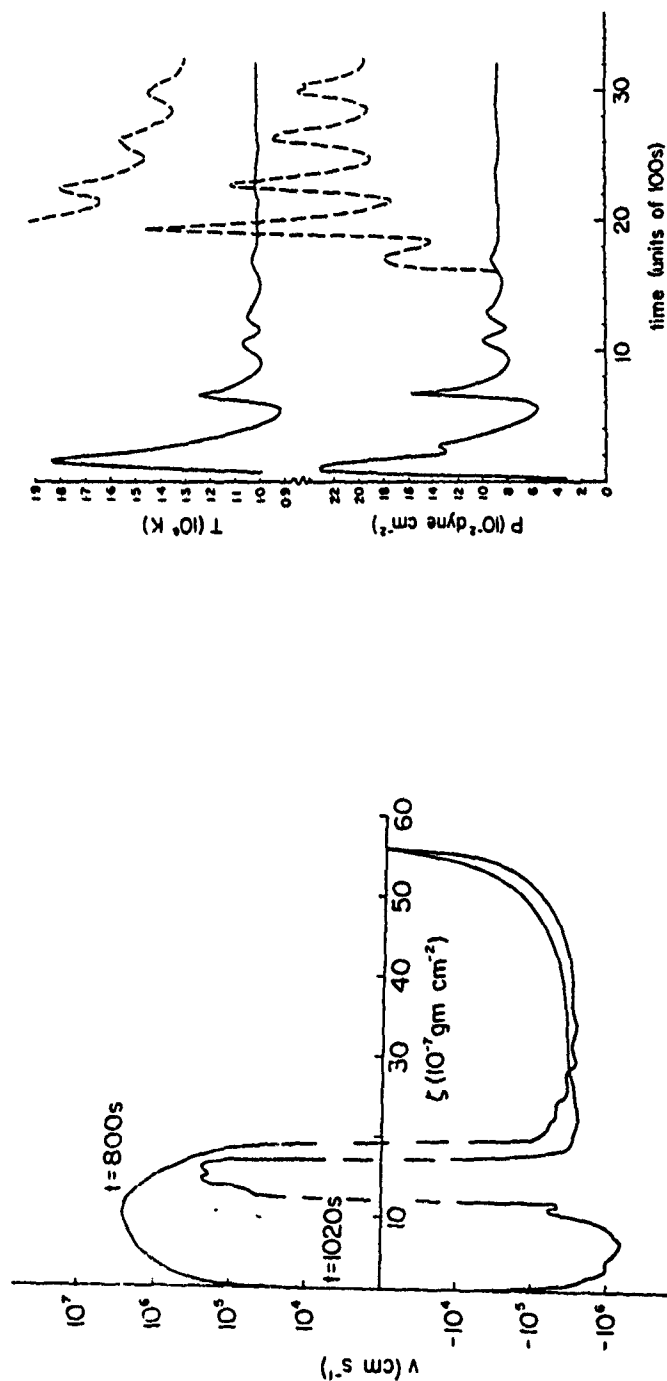
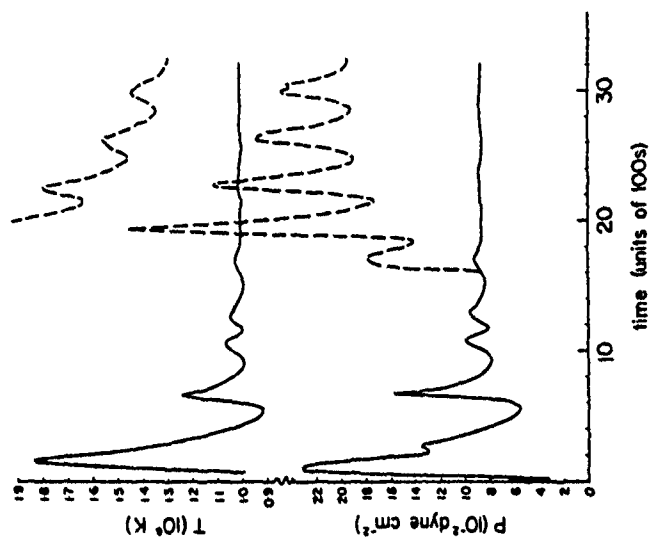


Fig. 9. Velocity profiles after 800 and 1020 s.

Fig. 10. Temperature and pressure at the top of the loop as a function of time. The broken lines show the response to a second transient energy injection at $t = 1600$ s.

time (units of 100s)

Fig. 10. Temperature and pressure at the top of the loop as a function of time. The broken lines show the response to a second transient energy injection at $t \approx 1600$ s.

-10^7
 -10^8

Fig. 9. Velocity profiles after 800 and 1020 s.

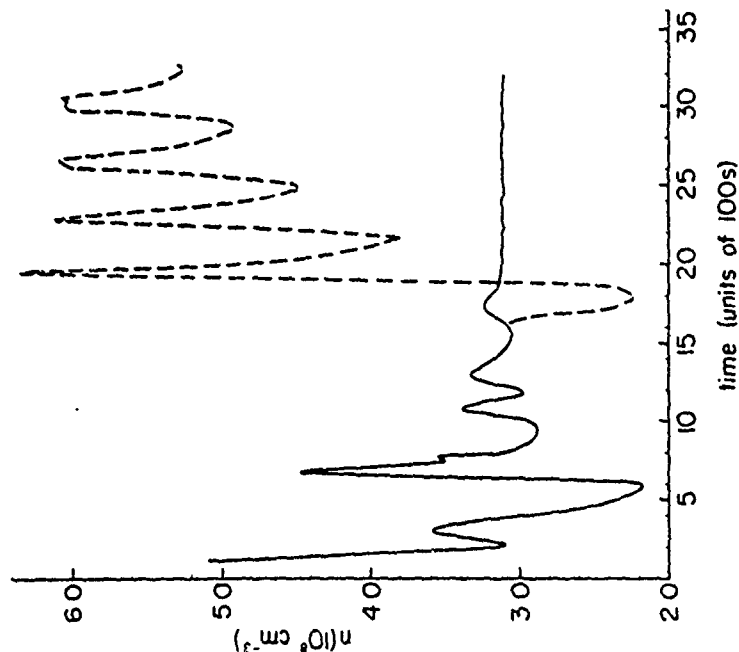


Fig. 11. Density at the top of the loop as a function of time. The broken line shows the response to a second transient energy injection at $t \approx 1600$ s.

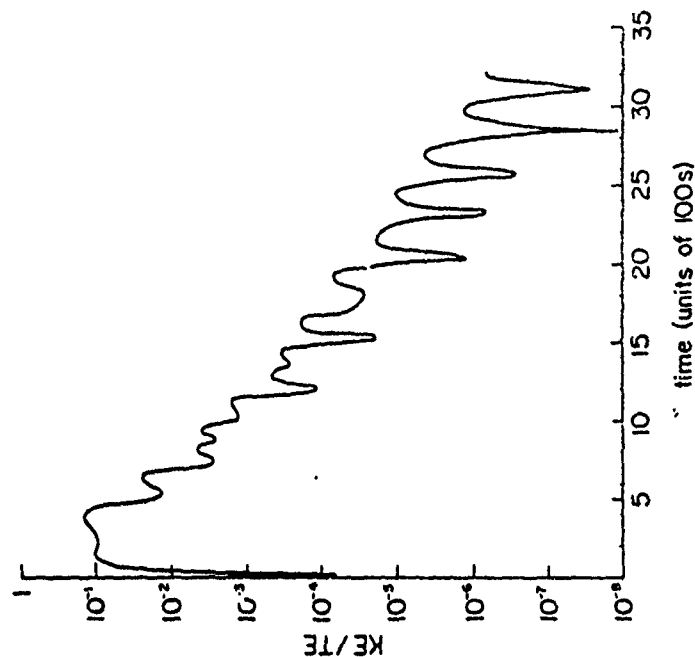


Fig. 12. Ratio of total kinetic energy in the loop to total thermal energy. The decay timescale is ~ 250 s. The transient initial behaviour gives way to a steady damped oscillation after ~ 1800 s.

with a falling coronal temperature during the initial phases of the flare (cf. Švestka, 1976).

There is one respect however, in which our 'flare-analysis' may not be sufficiently accurate; the trend of the temperature, density and particularly the pressure profile suggest that the atmosphere will not relax back to its previous quasi-steady state; rather it appears to relax to a new, higher energy equilibrium. This implies that an infinite family of solutions is possible, all with the same stationary heating but differing in thermal energy content. On the other hand, it appears (see Section 4.3 below) that the quasi-state equations introduced in Section 2 admit only two solutions, the original isothermal state and one 'corona-chromosphere' state. (A second isothermal state where the stationary heating is balanced by the bremsstrahlung losses at $T \approx 10^{10}$ K is also possible in principle.) This discrepancy probably indicates that our numerical finite difference scheme lacks accuracy in the transition region at high conductive fluxes. There the relatively poor spatial resolution may prevent the temperature gradient from steepening as much as it should, effectively bottling up the coronal conductive flux. Thus when equilibrium is reached in the numerical simulation the corona may be too hot and the chromosphere too cool.

That this problem is particularly severe for flare plasmas can be seen by the following simplified argument: The criterion that the grid spacing in the loop should not exceed the temperature scale height readily yields a restriction on the local heat flux:

$$\mathfrak{F}(T) \leq \frac{K_0 T^{7/2}}{\Delta z}. \quad (4.1)$$

For a Lagrangian scheme employing approximately one hundred grid points the grid spacing, Δz , in the chromosphere and lower transitions zone is of order 10^6 cm. It follows from (4.1) that the maximum heat flux that can be transmitted into the region below say $T = 10^5$ K, is approximately $10^{3.7}$ erg cm $^{-2}$ s $^{-1}$. This restriction appears not to be critical in the earlier 'dynamic corona' calculation since the already weak coronal flux ($\sim 3 \times 10^3$ erg cm $^{-2}$ s $^{-1}$) is strongly depleted by radiation in the region from 10^5 – 10^6 K. However, during the second energy injection at 1600 s the *maximum* coronal temperature corresponds to a *minimum* coronal density implying that the bulk of the enhanced conductive flux ($\sim 10^7$ erg cm $^{-2}$ s $^{-1}$) should be transferred into the lower transition zone ($T < 10^5$ K). In this case condition (4.1) is likely to be violated.

Although the above argument neglects the dependence of the grid spacing on the varying density distribution, it does bring home the difficulty of modelling a high conductive flux through the transition zone. In fact, the problem seems to afflict most gas dynamic flare analysis: The calculations of Kostyuk and Pikel'ner (1975), Kostyuk (1976), Somov *et al.* (1977), and Nagai (1980) all contain a transition zone that carries a similar or greater heat flux, while employing a finite difference grid spacing which in the transition zone is almost identical to our own. The problem is recognised by Antiochos and Krall (1978) who use an analytic approximation to the

transition r
way, it app
extent to w
treated.

4.3. UNIQ

The preser
quiescent l
imposed on
problem of
Although it
return to its
it remains t
static soluti
tion; for the

Consider
energy equ
heating str
and bottom
determined
atmosphe
point (T''
parameters
specified, tl
Integration
vanishing te
It follows th
quadrature:

By this cons
definiteness
defined inv
predetermin
constraints
isolate a uni
Despite t
amenable to

the flare (cf. Švestka, 1976). It may not be sufficiently accurate to use the pressure profile as a boundary condition for the quasi-steady state; this implies that an adiabatic heating but not a cooling (see Section 4.3) is admitted only two 'atmosphere' states. (A discrepancy probably due to the lack of spatial resolution may be that it should, effectively, be reached in the atmosphere too cool. This can be seen by the fact that the heating in the loop should be balanced on the local heat

(4.1)

distributed grid points the size of order 10^6 cm. is transmitted into the atmosphere. This restriction is imposed since the already existing heating by radiation in the transition at 1600 s the column density implying 10^{21} cm $^{-2}$ should be transmitted (4.1) is likely

the grid spacing on the order of modelling a high temperature seems to afflict most of the models (cf. Pikel'ner (1975), 1976). A transition zone of finite difference grid points is required. The problem is that the approximation to the

transition region structure as the boundary condition at the end of their loop. Either way, it appears that only a more sophisticated numerical treatment can determine the extent to which physical processes in the flare transition zone are being realistically treated.

4.3. UNIQUENESS OF THE QUASI-STATIC LOOP

The present analysis raises an interesting question as to the *uniqueness* of the quiescent loop with respect to the boundary conditions and global constraints imposed on the problem. This question of uniqueness has direct bearing on the problem of loop-stability but so far has received scant attention in the literature. Although it seems reasonable on physical grounds that a cooling 'flare' loop should return to its original quiescent state (the dynamic heating having been switched-off), it remains to be seen what class of boundary condition is sufficient to yield a unique static solution. We postpone a detailed discussion of this topic to a future investigation; for the moment we indicate the plausibility of uniqueness in the present study.

Consider the problem of generating a static loop structure by integrating the energy equation (2.1) from the chromospheric base upwards. We assume that the heating strength is specified and that the temperature gradient vanishes at the top and bottom of the loop. Now observe that the chromospheric energy balance is determined by four parameters, the temperature and density at the base of the atmosphere (T_∞ and n_∞ respectively), the concavity of the temperature profile at this point (T'' at $T = T_\infty$) and the strength of the chromospheric heating. Yet only three parameters can be chosen independently and with the heating source already specified, the loop is determined by two parameters from the set $(T_\infty, n_\infty, T_\infty'')$. Integration of the energy equation from the base upwards yields a second point of vanishing temperature gradient which defines the apex temperature, T_0 , of the loop. It follows that the column mass and the half-length of the loop may be determined by quadrature:

$$\zeta = \int_{T_\infty}^{T_0} \rho \left(\frac{dT}{dz} \right)^{-1} dT,$$

$$l = \int_{T_\infty}^{T_0} \left(\frac{dT}{dz} \right)^{-1} dT.$$

By this construction we see that ζ and l are functions of two base parameters, for definiteness say n_∞ and T_∞ . Alternatively it follows, under the assumption of well defined inverse functions, that unique base parameters can be associated with predetermined values of loop-length and column mass – these constitute the global constraints on the analysis. In this case the boundary conditions will be sufficient to isolate a unique static solution.

Despite this general argument, since the thermal structure of the loop is not amenable to closed analytic expression, a numerical investigation is required to

establish uniqueness in any particular case. Independent numerical studies by the present authors, and by Wragg (1980), indicate that uniqueness is generally achieved for plausible values of column mass and loop-length but such studies are not yet exhaustive enough to be definitive.

If uniqueness is assumed we must account for the fact that the cooling flare loop fails to return to its original quiescent state. However, it is readily established by a direct static calculation (as outlined above) that the peak coronal temperature is a rather sensitive function of the concavity of the thermal profile at the chromospheric base. A poorly resolved transition zone implies that the temperature profile and in particular its *second derivative* cannot be accurately modelled, in which case the peak coronal temperature may be subject to gross errors. The net effect in practice, is an underestimation of the thermal coupling between the transition zone and chromosphere, which gives rise to a spurious enhancement of the coronal temperature.

Finally, we ask to what extent the dynamically-generated atmosphere (of Section 4.1) approximates a truly static coronal structure. To this end we have constructed a sequence of static solutions which have the same length scale and column mass as the dynamic loop. We find that it is possible to approximate the dynamic solution (after some 5000 s evolution) to better than 10% in the coronal and chromospheric temperature and density. This suggests that we may claim a global accuracy of around ten percent in the dynamic corona calculation.

5. Conclusions

Our numerical modelling has illustrated several points of physical interest. In the first place, a dynamic loop of fixed mass which, apart from radiative losses, is energetically isolated from its surroundings, will relax on the conductive and radiative time-scales to a quasi-steady equilibrium. Natural hydrodynamic oscillations of the loop are superposed on the relaxation. The oscillation period (first symmetric mode) is approximately

$$\tau \approx 2l/c \approx 10^{-4} l/T^{1/2}, \quad (5.1)$$

where l is the loop half-length, c is the coronal sound speed, and T the coronal temperature. We would expect therefore, for both active region and flare plasmas, variations in coronal emission of approximately this period. Of course, if an assemblage of coronal flux tubes is being observed, these oscillatory effects may be smeared out and rendered indiscernable in the data. Contrary to the speculation of Antiochos (1979), we see no evidence of high frequency oscillations ($\tau \sim 1$ s) in the lower transition zone due to effects of radiative instability. However, we agree with Antiochos in that, despite thermal instability, quasi-static models should describe the gross features of quiescent coronal loops.

In connection mainly with solar flares, we have seen that the transition zone and chromosphere respond dynamically to enhanced coronal energy flux by driving mass into the upper atmosphere. But our analysis suggests that the details of this process

have not yet
($\geq 10^9$ erg cm $^{-2}$ s $^{-1}$)
that numerical re
(1975) should be c
flare transition zc

We would like to
Craig has benefit
would like to ack

Antiochos, S. K.: 197
Antiochos, S. K. and
Browne, S. L. and Be
Cox, D. P. and Tucke
Craig, I. J. D. and M
Craig, I. J. D., McCly
Field, G. B.: 1965, A
Habbel, S. R. and Re
Hood, A. W. and Pri
Jordan, C.: 1980, As
Kostyuk, N. ' 976
Kostyuk, N. ' J P
Landini, M. and Fossi
Richtmyer, R. D. and
Rosner, R., Tucker, '
Somov, B. V., Spekt
Švestka, Z.: 1976, So
Tucker, W. H. and K
Vesecky, J. F., Antio
Wragg, M.: 1980, Ph

tical studies by the
generally achieved
studies are not yet

e cooling flare loop
ily established by a
al temperature is a
the chromospheric
ature profile and in
which case the peak
ct in practice, is an
zone and chromo-
ial temperature.

osphere (of Section
have constructed a
column mass as the
amic solution (after
ind chromospheric
global accuracy of

interest. In the first
ses, is energetically
diative time-scales
ns of the loop are
mmetric mode) is

(5.1)

and T the coronal
and flare plasmas,

Of course, if an
tory effects may be
the speculation of
ions ($\tau \sim 1$ s) in the
ever, we agree with
should describe the

transition zone and
lux by driving mass
tails of this process

have not yet been adequately simulated for the high energy fluxes ($\geq 10^9$ erg cm $^{-2}$ s $^{-1}$) that characterize the solar flare. In consequence we recommend that numerical results obtained by previous authors (e.g. Kostyuk and Pikel'ner, 1975) should be closely re-examined to determine the extent to which they model the flare transition zone in a realistic manner.

Acknowledgements

We would like to thank Dick Canfield and John Brown for helpful discussions. Ian Craig has benefitted from participation in the Skylab Active Region Workshop, and would like to acknowledge the financial support of the Science Research Council.

References

- Antiochos, S. K.: 1979, *Astrophys. J.* **232**, L125.
Antiochos, S. K. and Krall, K. R.: 1978, SUIPR Report No. 751 (Skylab/ATM Preprint).
Browne, S. L. and Bessey, R. J.: 1973, *Solar Phys.* **31**, 351.
Cox, D. P. and Tucker, W. H.: 1969, *Astrophys. J.* **157**, 1157.
Craig, I. J. D. and McClymont, A. N.: 1976, *Solar Phys.* **50**, 133.
Craig, I. J. D., McClymont, A. N., and Underwood, J. H.: 1978, *Astron. Astrophys.* **70**, 1.
Field, G. B.: 1965, *Astrophys. J.* **142**, 531.
Habbel, S. R. and Rosner, R.: 1979, *Astrophys. J.* **234**, 1113.
Hood, A. W. and Priest, E. R.: 1979, *Astron. Astrophys.* **77**, 223.
Jordan, C.: 1980, *Astron. Astrophys.*, in press.
Kostyuk, N. D.: 1976, *Soviet Astron.* **19**, 458.
Kostyuk, N. D. and Pikel'ner, S. B.: 1975, *Soviet Astron.* **18**, 590.
Landini, M. and Fossi, B. C.: 1975, *Astron. Astrophys.* **42**, 213.
Richtmyer, R. D. and Morton, K. W.: 1967, *Difference Methods for Initial-Value Problems*, Interscience.
Rosner, R., Tucker, W. H., and Vaiana, G. S.: 1978, *Astrophys. J.* **220**, 643.
Somov, B. V., Spektor, A. R., and Surovatskii, S. I.: 1977, *Bull. Acad. Sci. USSR, Physical Series* **41**, 32.
Švestka, Z.: 1976, *Solar Flares*, D. Reidel Publ. Co., Dordrecht, Holland.
Tucker, W. H. and Koren, M.: 1971, *Astrophys. Publ. Co. J.* **168**, 283 (170, 621).
Vesecky, J. F., Antiochos, S. K., and Underwood, J. H.: 1978, SUIP Report No. 741.
Wragg, M.: 1980, Ph.D thesis, St. Andrews University.

iv) A Probabilistic Approach to Radiative Energy Loss Calculations
for Optically Thick Atmospheres: Hydrogen Lines and Continua

This was the first step in improving the treatment of radiative cooling of optically thick atmospheres, which was necessary to use the chromospheric observations to infer the physical processes taking place in flare chromospheres. The method described was developed in order to improve on the theoretical treatment of flare energy balance. It turned out that an even better method was later developed, and first applied to quasars. The new technique is described in the quasar theory section below. Because superior methods were developed, some of the techniques described here were never applied.

The main value of this paper was to develop expressions for computation of the probability of escape of continuum photons, i.e. radiation in features like the Balmer and Lyman continua of hydrogen. This is a key element of the theoretical treatment of flare radiative cooling.

A PROBABILISTIC APPROACH TO RADIATIVE ENERGY LOSS CALCULATIONS FOR OPTICALLY THICK ATMOSPHERES: HYDROGEN LINES AND CONTINUA

RICHARD C. CANFIELD

Center for Astrophysics and Space Science, University of California, San Diego

AND

PAUL J. RICCHIAZZI

Department of Physics, University of California, San Diego

Received 1979 May 14; accepted 1980 February 4

ABSTRACT

We simultaneously solve an approximate probabilistic radiative transfer equation and the statistical equilibrium equations for a model hydrogen atom consisting of three bound levels and ionization continuum. We explicitly solve the transfer equation for $L\gamma$, $L\beta$, $H\gamma$, and the Lyman continuum, assuming complete redistribution. We have tested the accuracy of this approach by comparing source functions and radiative loss rates to values obtained with a method that solves the exact transfer equation. Two recent model solar-flare chromospheres are used for this test. We show that for the test atmospheres the probabilistic method gives values of the radiative loss rate that are characteristically good to a factor of 2. The advantage of this probabilistic approach is that it retains a description of the dominant physical processes of radiative transfer in the complete redistribution case, yet it achieves a major reduction in computational requirements.

Subject headings: line formation — radiative transfer — Sun: chromosphere

I. INTRODUCTION

To calculate the rate at which a stellar atmosphere is cooled or heated by radiative processes in cases where the line-forming regions of the atmospheres become effectively thick, it is necessary to solve the radiative transfer equation. Many methods exist for this purpose. In this paper we utilize a probabilistic approach that is based on the approximation that the transfer of radiation in the atmosphere is a consequence only of the local variation of the photon escape probability. The advantage of this approximation is that the simplified transfer equation is a first-order ordinary differential equation, and can be solved very rapidly in numerical applications. The radiative transfer equation that results from this approximation was first derived by Athay (1972a) by a heuristic argument, assuming a two-level atom and noncoherent scattering. Subsequent work was done by Delache (1974) and Athay (1976). A more rigorous physical and mathematical basis has been provided by Frisch and Frisch (1975).

The first application of this method to the problem of hydrogenic radiative loss from plane-parallel atmospheres was made by Canfield (1974, hereafter Paper I) within a very restricted framework. The radiative transfer equation was solved only in Lyman α ($L\alpha$) and Balmer α ($H\alpha$), and only in an independent, two-level sense—no interlocking effects were incorporated; ionization was assumed to occur only in optically thin continua from the second and third levels; $L\alpha$ and $H\alpha$ were assumed to represent the only sources of radiative loss. Applications of the methods of Paper I have been made to heating of the solar-flare chromosphere by Brown, Canfield, and Robertson (1978) and Labonte (1978).

The methods described in the present paper represent a considerable improvement over those of Paper I. First, we treat the radiative transfer in a fully consistent multilevel framework, accounting for the effects of all interlocking transitions. Second, we extend the method to solve the approximate transfer equation in bound-free continua, which are of course treated as both interlocking transitions and a source of radiative loss. As shown numerically in this paper by a comparison of the present probabilistic method to a more physically complete matrix-inversion method, for a specific model atmosphere, the accuracies of the two approaches are comparable, while the probabilistic method is very much faster.

II. MULTILEVEL FORMULATION

The form of the approximate transfer equation for a multilevel model atom in the case of noncoherent scattering follows in a straightforward manner from the two-level form first formulated by Athay (1972a)

$$2 \frac{dJ}{dN} - \frac{J}{N} = \frac{c}{1 + \epsilon} (J - B), \quad (1)$$

where $J = \int J_\nu \Phi_\nu d\nu$, J_ν is the usual monochromatic mean intensity, Φ_ν is the normalized line absorption coefficient profile, N is the mean number of scatterings required for escape from the atmosphere, which is the reciprocal of the probability that a photon will escape from the atmosphere after a scattering event at line-center optical depth τ_0 , ϵ is the ratio of coefficients of collisional to radiative de-excitation, and B is the Planck function. The generalization to multilevel form can be seen particularly clearly by an argument parallel to Delache's (1974) derivation of equation (1). The usual radiative transfer equation for a two-level atom and noncoherent scattering can be written

$$-\frac{\Phi_0}{4\pi} \frac{d}{d\tau_0} F_\nu = (J_\nu - S) \Phi_\nu. \quad (2)$$

Here F_ν is the monochromatic radiative flux at frequency ν , and S is the line source function, independent of frequency for noncoherent scattering. In the probabilistic approximation, Delache (1974) shows that the left-hand side of equation (2) can be written as

$$-\frac{\Phi_0}{4\pi} \frac{d}{d\tau_0} F_\nu = \left(2 \frac{dJ_\nu}{dN} - \frac{J_\nu}{N} \right) \Phi_\nu. \quad (3)$$

In this equation it is clear how the flux divergence at an optical depth τ_0 depends on the local escape probability. It is important from the point of view of generalization to the multilevel case that no assumptions have been made regarding the nature of local photon sources and sinks. Combining equations (2) and (3) and integrating over frequency, we obtain

$$2 \frac{dJ}{dN} - \frac{J}{N} = J - S. \quad (4)$$

In a two-level atom, statistical equilibrium implies that

$$S = \frac{J + \epsilon B}{1 + \epsilon} = \left(1 - \frac{\epsilon}{1 + \epsilon} \right) J + \frac{\epsilon}{1 + \epsilon} B, \quad (5)$$

from which it is easy to see that the right-hand sides of equations (1) and (4) are equivalent, as Delache (1974) showed. It is clear that the generalization to a multilevel atom is accomplished through an appropriate expression of S through the statistical equilibrium equations, which can be written in the form (see, e.g., Athay 1972b, chap. 2)

$$S = \frac{J + \epsilon^* B}{1 + \epsilon^\dagger}. \quad (6)$$

The parameters ϵ^* and ϵ^\dagger are in general not equal to ϵ because of interlocking effects. Actual expressions for ϵ^* and ϵ^\dagger depend on the model of the atom used and the specific level considered; this point is discussed in detail by Athay (1972b). It follows from equations (4) and (5) that the multilevel generalization of equation (1) is

$$2 \frac{dJ}{dN} - \frac{J}{N} = \frac{\epsilon^\dagger}{1 + \epsilon^\dagger} \left(J - \frac{\epsilon^*}{\epsilon^\dagger} B \right). \quad (7)$$

The right-hand sides of both equations (1) and (7) express the net amount of line radiation destroyed per scattering, but equation (1) includes only direct collisional processes, whereas equation (7) also includes sources and sinks of line radiation which are introduced through interlocking.

III. FREE-BOUND CONTINUA

For a variety of physical conditions in stellar chromospheres there exist free-bound continua that are not effectively thin—for example, the Lyman continuum in solar-flare chromospheric models. In order to be able to treat such problems, it is necessary for us to formulate and solve the approximate free-bound radiative transfer equation and calculate escape probabilities.

a) Transfer Equation

To cast the free-bound transfer equation in the same form as equation (7), we follow an argument very similar to that of Athay (1972b, pp 35 *et seq.*). Calling attention to the free-bound transition $c \rightarrow i$, we write the statistical equilibrium equation for level c in a multilevel atom as follows:

$$W_i (C_{ci} + A_{ci}) = b_i W_i (C_{ic} + R_{ic}) + \sum_{m \neq i, c} (b_m P_{mc} - P_{cm}). \quad (8)$$

Here W_i and W_c are the product of the statistical weight and the Boltzmann factor for levels i and c , respectively, C_{ci}

and C_{ic} are the collisional transition coefficients, R_{ic} and A_{ci} are the radiative transition coefficients, b_j is the usual non-LTE departure coefficient for level j ($b_c \equiv 1$), and P_{ij} is used to represent the product of W_i and the radiative and collisional transition coefficients given above.

If we define ϵ as above and θ by

$$\theta = \frac{1}{W_c A_{ci} \sum_{m \neq l, c} P_{cm}},$$

then equation (8) becomes

$$\frac{1}{b_i} = \left(\frac{W_i R_{ic}}{W_c A_{ci}} + \epsilon + \frac{1}{W_c A_{ci} \sum_{m \neq l, c} F_{mc} b_m / b_i} \right) / (1 + \epsilon + \theta). \quad (9)$$

By introducing the usual escape coefficient ρ_{ci} in order to write equation (8) in terms of net radiative rate coefficients between levels c and i , it is straightforward to show that equation (8) implies that

$$\epsilon + \rho + \theta = b_i \left(\epsilon + \frac{1}{W_c A_{ci} \sum_{m \neq l, c} P_{mc} b_m / b_i} \right). \quad (10)$$

If we define ϵ^* and ϵ^\dagger as

$$\epsilon^* = (\epsilon + \rho + \theta) / b_i, \quad (11)$$

$$\epsilon^\dagger = \epsilon + \theta, \quad (12)$$

then equation (9) becomes

$$\frac{1}{b_i} = \left(\frac{W_i R_{ic}}{W_c A_{ci}} + \epsilon^* \right) / (1 + \epsilon^\dagger). \quad (13)$$

The total upward and downward radiative coefficients R_{ic} and A_{ci} can be written (assuming hydrogenic absorption-coefficient profiles and neglecting stimulated emissions) in terms of frequency-averaged intensity \bar{J} and Planck function \bar{B} as

$$R_{ic} = 4\pi \frac{\alpha_0 v_i^3}{h} \int_{v_i}^{\infty} \frac{J_v}{v^4} dv \equiv 4\pi \frac{\alpha_0}{h} \bar{J}, \quad (14)$$

$$A_{ci} = \frac{W_i}{W_c} 4\pi \frac{\alpha_0 v_i^3}{h} \frac{2h}{c^2} \int_{v_i}^{\infty} \frac{\exp(-hv/kT)}{v} dv \equiv \frac{W_i}{W_c} 4\pi \frac{\alpha_0}{h} \bar{B}. \quad (15)$$

Then equation (13) becomes

$$\frac{1}{b_i} = \frac{\bar{J}/\bar{B} + \epsilon^*}{1 + \epsilon^\dagger}. \quad (16)$$

Thus

$$\bar{S} = \frac{\bar{B}}{b_i} = \frac{\bar{J} + \epsilon^* \bar{B}}{1 + \epsilon^\dagger}. \quad (17)$$

We then follow the procedure of § II; for a hydrogenic absorption-coefficient profile.

$$\Phi_v = \frac{2v_0^2}{v^3} \quad \text{for } v \geq v_0. \quad (18)$$

Then from equation (3),

$$(J_v - S) \frac{2v_i^2}{v^3} = -\frac{1}{4\pi} \frac{d}{d\tau_0} F_v = \left(2 \frac{dJ_v}{dN} - \frac{J_v}{N} \right) \frac{2v_i^2}{v^3} \quad \text{for } v > v_i, \quad (19)$$

which after some algebra, integration, and use of equation (10) reduces to the desired form

$$2 \frac{d\bar{J}}{dN} - \frac{\bar{J}}{N} = \frac{\epsilon^\dagger}{1 + \epsilon^\dagger} \left(\bar{J} - \frac{\epsilon^*}{\epsilon^\dagger} \bar{B} \right) \quad (20)$$

Before we can solve equations (7) and (20) we must calculate the escape probability, and thus the mean number of scatterings, as a function of optical depth.

b) Escape Probability

The escape probability, $P_e(\tau_0)$, in a plane-parallel atmosphere is given by

$$P_e(\tau_0) = \frac{1}{2} \int_{-\infty}^{\infty} \int_0^1 \Psi_\nu \exp(-\tau_\nu/\mu) d\mu d\nu \quad (21)$$

(Athay 1972a), where Ψ_ν is the emission profile normalized to unit area and μ is the direction cosine. When dealing with bound-bound transitions we make the assumption that $\Psi_\nu = \Phi_\nu$. Approximate formulae for P_e under these conditions have been presented by many authors. In this paper we have used the one given by Athay (1972a).

In the free-bound case, when stimulated recombinations are ignored, the normalized emission profile is given by

$$\Psi_\nu = \frac{\exp(-h\nu/kT_e)}{\nu E_1(h\nu_0/kT_e)} \quad \text{for } \nu \geq \nu_0 \quad (22)$$

(see Jefferies 1968, § 6.6.3). The frequency-dependent optical depth τ_ν is equal to $\tau_0(\nu_0/\nu)^3$. Inserting these expressions into (21), performing the μ integration, and letting $x = \nu/\nu_0$, we obtain

$$P_e(\tau_0) = \frac{1}{2E_1(\alpha)} \int_1^\infty \frac{dx}{x} e^{-\alpha x} E_2(\tau_0 x^{-3}),$$

where

$$\alpha = \frac{h\nu_0}{kT_e}.$$

We have evaluated this integral numerically at several values of the electron temperature assuming the Lyman continuum value of ν_0 . The results of these calculations are presented in Figure 1. In this plot it is evident that the probability of escape at any particular optical depth decreases with decreasing temperature. This can be understood in the following way: A photon produced by photorecombination has an energy equal to the threshold energy $h\nu_0$ plus the original kinetic energy of the free electron. At lower temperatures the mean kinetic energy of the electrons is smaller. Hence most of the created photons have energies closer to the threshold energy, thus having a greater probability of photoionizing another hydrogen atom before being able to escape the atmosphere.

The other distinctive feature of the free-bound escape probability is its very abrupt attenuation as the optical depth varies between $\tau_0 = 1$ and $\tau_0 = 100$. Whereas the bound-bound escape probability varies as $[\tau_0(\ln \tau_0)^{1/2}]^{-1}$ for large τ_0 , P_e in the bound-free case varies roughly as $\exp[-\tau_0(\nu_0/\nu_1)^3]$, where ν_1 is the mean frequency of photons which manage to escape. These characteristics are, of course, the basis of the so-called "on-the-spot" approximation of nebular physics (see Osterbrock 1974).

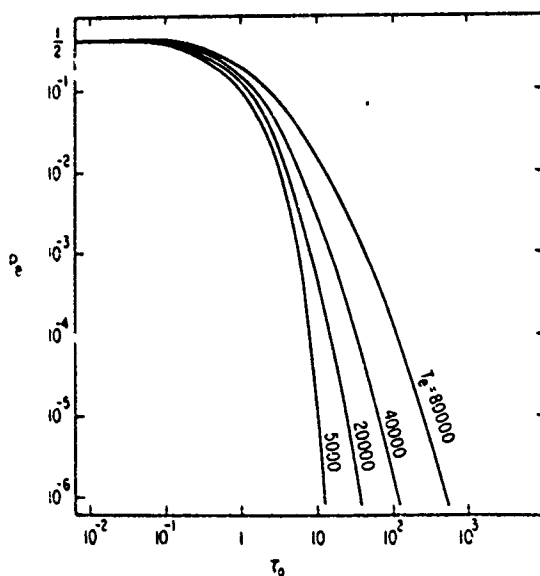


FIG. 1 — Photon escape probabilities for the Lyman continuum, as a function of the optical depth at the edge, τ_0 , for four values of electron temperature T_e .

Unfortunately to obtain the exact value of P_e given by (23) at each grid point in the atmosphere over many iterations would significantly increase the run time of our radiative transfer code. Therefore, since computational simplicity is one of our main objectives in this research, we have used in our radiative-loss calculations a crude but simple approximation to (23) which has the form

$$P_e = \frac{1}{2} \exp [-\tau_0/x_0^3 - \alpha(x_0 - 1)]/x_0, \quad (24)$$

where $x_0 = \max [(3\tau_0/\alpha)^{1/4}, 1]$. Even though this formula will yield escape probabilities which are in error by as much as a factor of 3 for $\tau_{c1} \gg 1$, we have verified that this produces a very small effect in the computed total hydrogenic radiative loss.

c) Limiting Form for the Escape Coefficient

In general the escape coefficient ρ can be found only after evaluating equation (7) or (20) for the transition in question. However, in regions of the atmosphere for which the probability of escape is much smaller than the probability of destroying the upper-level state without producing the line photon, a simple formula for ρ_{ji} can be derived. One can then use these values of ρ_{ji} in the radiative loss formulae (as in § IV) and in place of the radiative rates in the statistical equilibrium equations (see Athay 1972b, eq. [II-16]), thereby avoiding the integration of (7) or (20).

Starting with equation (7) we make the assumption that the probability of destruction, $P_d = \epsilon^+/(1 + \epsilon^+)$, and the thermal source term, $(\epsilon^*/\epsilon^+)B$, are constants. By applying the proper boundary conditions for a semi-infinite atmosphere Athay (1972a) shows that (7) can be integrated to yield

$$J = \left(\frac{1}{2} \frac{P_d}{P_e}\right)^{1/2} \exp\left(\frac{1}{2} \frac{P_d}{P_e}\right) \frac{\epsilon^*}{\epsilon^+} B \sqrt{\pi} \operatorname{erfc}\left[\left(\frac{1}{2} \frac{P_d}{P_e}\right)^{1/2}\right]. \quad (25)$$

For $P_d \gg P_e$ the first two terms of the asymptotic expansion of equation (25) are

$$J = \frac{\epsilon^*}{\epsilon^+} B \left(1 - \frac{P_e}{P_d}\right). \quad (26)$$

From equation (6) or (17) we get

$$S = \frac{\epsilon^*}{\epsilon^+} B \left(1 + P_e - \frac{P_e}{P_d}\right). \quad (27)$$

Thus we find ρ given by

$$\rho = 1 - \frac{J}{S} = 1 - \frac{1 - (P_d/P_d)}{1 + P_e - (P_e/P_d)} = \frac{P_e}{1 + P_e - (P_e/P_d)} \approx P_e. \quad (28)$$

A transition for which this result is most readily applied is the Lyman continuum. For the radiation fields typical of a solar-type atmosphere it is easy to see that the probability of destruction for Lyman continuum (LC) photons is in fact on the order of 1/2. That is, about half of the processes by which free electrons recombine into the first bound level do not produce LC photons. Therefore we should be able to avoid integrating (20) (one must still integrate [7] for the bound-bound transitions) by merely replacing ρ_{c1} by P_e everywhere.

We have made one run using this simplification, obtaining radiative losses which are smaller, but within 15% of those from the usual method. The benefit of using this technique is that it produces a converged solution in 12% less computer time.

IV. RADIATIVE ENERGY LOSS

a) Method

The radiative energy loss rate per unit volume in a certain transition Q is obtained directly from J for that transition (see Paper I) as follows:

$$Q = h\nu A_{ul}\rho, \quad (29)$$

where

$$\rho = 1 - \frac{J}{S}. \quad (30)$$

and S is related to J by (6). A self-consistent set of values of J , ϵ^* , and ϵ^+ is obtained iteratively as in Paper I, by alternatively resolving the radiative-transfer equation in each transition and the steady-state equation until

convergence is obtained in J at all points in the atmosphere to within some tolerance, usually an upper limit to the change in S of 1% in all transitions.

One must also decide which transitions to include within the model atom. Here, the observations are clearly the best guide, but lacking these, one should include only those transitions which make a large contribution to the radiative loss somewhere in the atmosphere. The following discussion applies to radiative-loss calculation in a pure hydrogen atmosphere.

In regions where $L\alpha$ is effectively thin (escape probability greater than destruction probability), it will be a large contributor to the radiation loss, owing to its large Einstein A and relatively large upper-level population. Since collisional de-excitation from the second level is not a very efficient means of destroying a $L\alpha$ photon, the probability of destruction is small and the region where $L\alpha$ is effectively thin is quite extensive.

In the region of optical depth greater than 1, other Lyman lines will not be important, because they tend to degrade into combinations of α lines of higher series; their destruction probabilities are large (approaching 1). This, combined with large opacity in the Lyman lines, implies very low loss from the non- α Lyman transitions over all but the most superficial regions of the atmosphere. In the optically thin regions $L\alpha$ will also dominate the Lyman series loss, which will be proportional to $n_u v_{u1} A_{u1}$. The variation of A_{u1} dominates the variation of this quantity, and A_{u1} decreases rapidly (e.g., $A_{31} \sim 10^{-2} A_{21}$) with upper-level quantum number u . The decrease of n_u with increasing u works in the same direction, and more than offsets the $v_{u1}(u)$ dependence.

Other subordinate lines also suffer from large destruction probabilities, but smaller lower-level populations keep their opacity small, making them good effective radiators. These lines should be included as long as the energy of the transition involved is not much smaller than the average thermal energy of electrons in the atmosphere. This is equivalent to choosing only those lines that yield photons with energies near and above the peak of $B_e(T_e)$. This criterion would imply that the entire Balmer series should be included. This conclusion is supported by the observations of the spectrum of the radiative output of the 1973 September 5 (Canfield *et al.* 1980) solar flare. Since it is our purpose only to compare the probabilistic code to the flux divergence code we chose to neglect radiative loss from all of the Balmer series lines except for $H\alpha$, even though there is no physical basis for doing so. A calculation of the radiative loss accurate to better than a factor of 2 would require that at least seven bound levels be included explicitly in the hydrogen model atom, in order to find the loss of the Balmer lines up to $H\epsilon$. One could then make the assumption that all bound levels above the seventh were in equilibrium with the continuum finding the loss rate from the formula

$$Q_{u2} = h\nu A_{u2} p_e(\tau) n_u^*,$$

where n_u^* is found through the Saha equation. Above some even higher level, typically level 20, Stark broadening causes the levels to merge together fully, in which case treatment of individual lines is unnecessary.

The large bandwidth and low opacity in the Balmer and higher continua make them effective radiators. To determine how important these transitions are we examine their radiative loss function:

$$Q_c = 7.8 \times 10^9 \frac{W_1}{W_c} k T n_e / l^5.$$

Ignoring factors common to all the continua we have

$$Q_c \propto l^{-3},$$

which implies that anything past the Balmer and Paschen continua need not be included in the cooling rate calculation.

b) Calculations

To demonstrate the utility of the approach discussed above, we have made a comparison of radiative-loss rates Q obtained using solutions of the probabilistic transfer equations (7) and (20) to those using solutions of the usual transfer equation in integral (flux-divergence) form. In all other respects, the probabilistic and flux-divergence results are based on the same methods. We obtain the source functions for $L\alpha$, $L\beta$, $H\alpha$, and LC by solving the radiative transfer equation. The Balmer and Paschen continua are assumed to be optically thin.

The model atmosphere for which we have made our comparison is Lites and Cook's (1979) one-dimensional semi-empirical model of the solar chromosphere during the flare of 1973 August 9. The model is based on spectral synthesis of observed UV spectra of lines and continua of C I–C IV and the wings of $L\alpha$, which determines the model in the temperature range between 5500 and 10^5 K. Below 5500 K, the facular model of Shine and Linsky (1974) was used.

In Figure 2 we show source functions and Planck functions for $L\alpha$ (2–1 transition) and $H\gamma$ (3–2 transition). Of course, $L\beta$ source functions can also be inferred from these results. Solid curves show Planck functions. The long-dashed curves are source functions from the exact transfer equation, the short-dashed curves from the probabilistic equation. Heights of unit optical depths in the exact calculation are indicated. S_{21} saturates to B_{21} in the upper

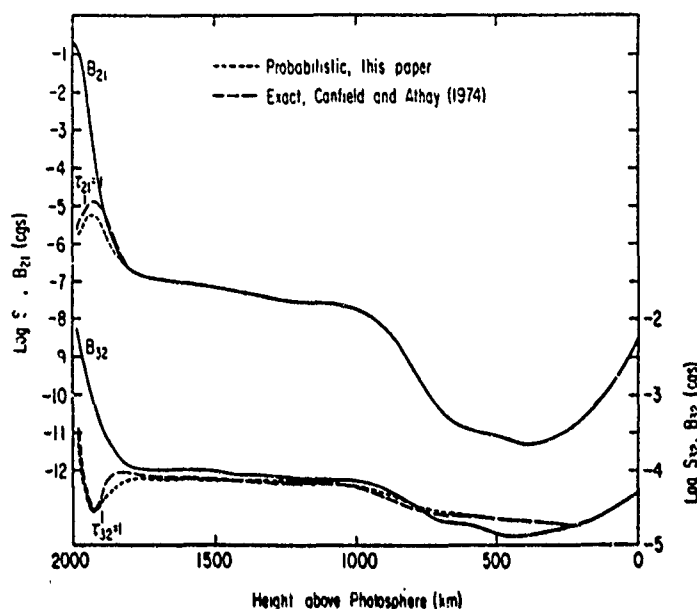


FIG. 2.—Comparison of probabilistic and exact line source functions for $L\alpha$ (2–1 transition, upper part of figure, left-hand ordinate) and $B\alpha$ (3–2 transition, lower part of figure, right-hand ordinate). Broken lines show source functions, solid lines show Planck functions.

chromosphere; S_{32} saturates in the upper photosphere. For this model the probabilistic source functions are within a factor of 2 of the exact source function everywhere in the test atmosphere. Maximum departures are reached in just those regions where downward transfer of radiation is most important. This is not unexpected, since such transfer is ignored in the probabilistic method. We have carried out numerical experiments to look at the effect of variation in Doppler width, and find that the variations present in the Lites and Cook (1979) model are too small to be important. Hence if one wishes to compute complete-redistribution line profiles to within the accuracy of the probabilistic method, the method described here gives an economical means of doing so.

In Figure 3 we compare four different methods for estimating the energy-loss rate as a function of height in the atmosphere of Lites and Cook (1979). The probabilistic and flux-divergence methods are those described above.

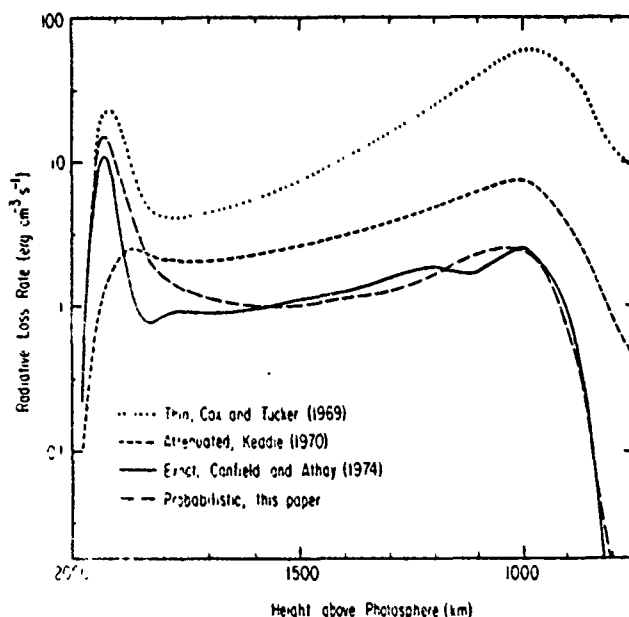


FIG. 3—Comparison of total hydrogen radiative-loss rates, computed by various methods, for the solar flare model of Lites and Cook (1979).

The losses plotted are the sums of losses in all lines incorporated in the model, i.e., $L\alpha$, $L\beta$, $H\alpha$, and the Lyman, Balmer, and Paschen continua, which we call Q , below. The curve labeled Cox and Tucker has been computed by a power-law extrapolation to lower temperatures of the curves of Cox and Tucker (1969) for hydrogen. The ionization equilibrium has been obtained in the approximation that $L\alpha$ is in detailed balance and all hydrogen ionization takes place in the optically thin Balmer continuum, due to the undisturbed quiet-Sun radiation field. This curve includes radiative losses by all hydrogen lines and continua, all in an optically thin "coronal" approximation. Hence part of the difference between the Cox and Tucker curve and the above two curves is due to inclusion of radiation from other lines and continua, and part is due to the neglect of radiative transfer. The fourth curve is that of Keddie (1970), which has been used by various authors, including Brown (1973), Kostyuk and Pikel'ner (1975), and Kostyuk (1976) for solar flare models. The ionization equilibrium was obtained as in the optically thin Cox and Tucker calculation.

The assumption that the chromosphere is optically thin breaks down, as one should expect, in the upper chromosphere, where $L\alpha$ begins to saturate. The thin assumption gives radiative-loss rates that are characteristically an order of magnitude high through most of the chromosphere in this model.

The method of Keddie (1970) neglects lines. It assumes that Balmer and higher continua are effectively thin (a valid approximation), but attenuates the Lyman continuum in proportion to $\exp(-\tau_c)$ —a rough approximation at best. For the test atmosphere, as can be seen, the Keddie approximation underestimates the radiative-loss rate above about 1900 km height, and overestimates the loss rate below. This is due to the fact that $L\alpha$ is the cause of the peak.

Clearly the probabilistic code does the best job of duplicating the results of the exact calculation. The probabilistic code also agrees with the exact solution in identifying which transitions are the dominant contributors to the radiative loss at a given height. Both methods indicate that radiative losses by $L\alpha$ dominate above 1850 km (for the Lites and Cook model atmosphere) while the Balmer continuum is dominant below 1750 km. Comparisons of the cooling rate for some of the individual lines reveal some large discrepancies, however. For example there are some regions in the Lites and Cook atmosphere where the $L\beta$ (and sometimes $H\alpha$) flux divergence differs in sign between the two codes. But in all regions where this occurs the $L\beta$ contribution to the total radiative loss rate is small and the total cooling rate seems to be duplicated rather well.

This reflects the fact that most of the cooling in this particular atmosphere is dominated by either $L\alpha$ in the upper chromosphere or the Balmer continuum in the middle chromosphere. By getting the correct cooling rate for $L\alpha$, which is not a heavily interlocked transition, we are guaranteed good agreement near the surface. In the middle chromosphere it is only necessary to find accurate values for the degree of ionization to calculate the optically thin loss from the Balmer continuum. Our simplified method accomplishes this by obtaining relatively accurate bound level populations, an inherently easier problem than the calculation of accurate ρ values when ρ is near zero. Given accurate bound level ratios, agreement in the ionized fraction is guaranteed since identical radiation temperatures for the Balmer and Paschen continua have been assumed in both codes.

Of the four methods mentioned above, the one which should be used for any given problem depends not only on the desired accuracy but also on the amount of computer time available. The Keddie and the Cox and Tucker schemes are computationally very simple and quick but suffer in accuracy comparisons with the flux-divergence method. If order of magnitude errors in the radiative-loss rate are acceptable in a particular problem, then some combination of these two methods could be used. When more accuracy is required the probabilistic method has two important advantages: it is more accurate than either the Keddie or Cox and Tucker methods and it is much faster to calculate than the exact method. We have found that the amount of processing time needed to complete one full iteration (as described above) on a CDC 7600 computer is 16,000 ms for the exact method and only 40 ms for the probabilistic code. Both techniques require about 15 iterations to arrive at a solution converged to 1% in source functions at all heights. Thus, whereas the exact and probabilistic methods are comparable in accuracy, the probabilistic method is about 400 times faster, an obvious advantage in problems involving the repeated solution of the radiative transfer equations (e.g., for many bound levels or at each time step of a dynamic problem).

We wish to thank R. Puetter for many helpful discussions. This work has been supported by the Air Force Office of Scientific Research, Air Force Systems Command, USAF, under grant AFOSR 76-3071, and by the National Aeronautics and Space Administration under grant NSG-7406. Computing support was provided by the National Center for Atmospheric Research, which is supported by the National Science Foundation.

REFERENCES

- Athay, R. G. 1972a, *Ap. J.*, 176, 659.
 ——— 1972b, *Radiation Transport in Spectral Lines* (Dordrecht: Reidel).
 ——— 1976, *Ap. J.*, 204, 160.
 Brown, J. C. 1973, *Solar Phys.*, 31, 143.
 Brown, J. C., Canfield, R. C., and Robertson, M. N. 1978, *Solar Phys.*, 57, 399.
 Canfield, R. C. 1976, *Ap. J.*, 194, 483 (Paper 1).
 Canfield, R. C., Cheng, C.-C., Dere, K. D., Dulk, G. A., McLean, D. J., Robinson, R. D., Jr., Schmelzer, E. J., and Schoolman, S. A. 1980, in *Solar Flares*, ed. P. A. Sturrock (Boulder: University of Colorado Press).
 Cox, D. P., and Tucker, W. H. 1969, *Ap. J.*, 157, 1157.
 Delache, P. 1974, *Ap. J.*, 192, 475.

- Frisch, U., and Frisch, H. 1975, *M.N.R.A.S.*, 173, 167.
Jefferies, J. T. 1968, *Spectral Line Formation* (Waltham: Blaisdel).
Keddie, A. W. C. 1970, Ph.D. thesis, University of Glasgow.
Kostyuk, N. D. 1976a, *Soviet Astr.*, 19, 458.
Kostyuk, N. D., and Pikel'ner, S. R. 1975, *Soviet Astr.*, 18, 590.
Labonte, B. J. 1978, preprint.
Lites, B. W., and Cook, J. W. 1979, *Ap. J.*, 228, 598.
Osterbrock, D. E. 1974, *Astrophysics of Gaseous Nebulae* (San Francisco: W. H. Freeman).
Shine, R. A., and Linsky, J. L. 1974, *Solar Phys.*, 37, 145.

RICHARD C. CANFIELD and PAUL J. RICCHIAZZI: Center for Astrophysics and Space Science, Mail Code C-011, University of California, San Diego, La Jolla, CA 92093

v) Flare Loop Radiative Hydrodynamics. I. Basic Methods

This paper describes in detail the techniques for theoretical simulation of flare hydrodynamic processes developed during this grant. The methods are the culmination of the theoretical part of our program. The computer codes based on these methods have been debugged fully, and will be applied to a variety of problems in the future. Their first application is described in the paper following this one.

The unique property of these methods is that they permit the inclusion of the effects of radiative opacity on the energy and momentum balance of the flare plasma in a manner that is both computationally efficient and physically sound. This is critical in treating the chromospheric flare, since cruder approximations that were used in the past gave rise to order of magnitude errors in the radiative cooling rate. The methods used for these radiative transfer aspects are described in Section iii of the quasar theory section below. The methods used in this paper are also an improvement over previous flare simulations in that they use adaptive computational gridding, in order to ensure that the grid of cells that is used to simulate the plasma is sufficiently fine that the simulation is physically meaningful. This circumvents the problems discussed in the previous paper.

The development of these methods will certainly be one of the major contributions of this grant.

FLARE LOOP RADIATIVE HYDRODYNAMICS

I. BASIC METHODS

A.N. McClymont^{*} and Richard C. Canfield

Center for Astrophysics and Space Sciences
University of California, San Diego

Submitted: _____

Running Title: Flare Loop Radiative Hydrodynamics

^{*} Now at Department of Mathematics, University of Waikato,
New Zealand

ABSTRACT

Many flare phenomena involve both the coronal and chromospheric regimes of flare loops. The exchange of matter, energy and momentum between these regimes couples them strongly. The major non-local effect in coronal regions is thermal conduction; in chromospheric regions, it is radiative transfer. In order to study the role of these processes, as well as to use concurrent flare emissions as a diagnostic of flare energization processes, we have developed a numerical method for simultaneously solving the continuity, momentum, and energy equations, the time-dependent atomic ionization and excitation rate equations, and the radiative transfer equations. In this preliminary study, we assume that all components of the plasma move together at the same velocity, and have the same kinetic temperature. They are constrained to move in one dimension, parallel to a loop of variable cross-section, which is defined by a sufficiently strong magnetic field. We account for non-hydrogenic and negative hydrogen radiative losses in an optically thin approximation, and confine our study of radiative transfer effects to a model hydrogen atom with two bound levels and the ionized state. The radiative transfer is treated probabilistically; this has a substantial computational

advantage, but involves assumptions that must be checked ex post facto. The one-dimensional equations are solved in implicit finite-difference form on an adaptive non-uniform Lagrangian grid, to second order accuracy. The equations are solved simultaneously by linearization and iteration; a fully implicit method is used for the atomic rate equations. Using these methods, we are able to study a wide variety of problems concerning the radiative hydrodynamic interaction of the chromosphere and the corona.

I. INTRODUCTION

(a) Motivation

It has become increasingly clear in recent years, particularly in the wake of Skylab and Solar Maximum Year, an era of extensive cooperation between observational groups and careful synchronization of a wide variety of experiments, that the detailed analysis of an isolated observation is often unfruitful. Solar flares may most readily be understood through the correlation of many diverse observations, yielding information on processes taking place in different temperature regimes of the flare. Through theoretical interpretation of carefully synchronized observations of the temporal evolution of flares we can hope to arrive at an understanding of the nature and location of the primary energy release and of the mechanisms that transport this energy throughout the flare volume.

Although it is generally believed that flare energy release takes place in the corona, a considerable fraction of the energy radiated by flares comes from the chromosphere (Canfield et al. 1980). Therefore it is important to understand the processes responsible for energy transport throughout the flare volume. Furthermore, the fact that chromospheric emission in the visible waveband is much more accessible to observation than is X-ray and

EUV radiation from the corona emphasizes the importance of making the best possible use of the wealth of the available optical data.

Because of the strong coupling between the high temperature ($T > 10^5$ K) and low temperature ($T < 10^5$ K) regions of the flare and the highly non-linear, non-local nature of radiative transfer in the chromosphere, the use of numerical simulation is essential to the theoretical interpretation of flare observations. This is not to say that flares cannot be understood in simple terms, but rather that the theoretical tools required to arrive at the understanding are as sophisticated as the experimental tools required to obtain data on flares.

In order to study the correlation between the high and low temperature regions of flares and their concurrent evolutions, we must adopt a global model capable of following the evolution of the whole atmosphere, from photosphere to corona. Of the three fundamental processes in the active solar atmosphere - mass motions, magnetic field effects and radiative transfer - we have chosen to ignore the magnetic field. We are primarily interested in obtaining a self consistent picture of the interaction between the corona and chromosphere through thermal conduction, hydrodynamics and radiative transfer. Therefore we model a

compact flare loop, assuming that the magnetic field is sufficiently strong to define a time-independent, one dimensional, geometry.

Subject to this restriction, we can, for any postulated form of flare heating, derive parameters for comparison with observations. Among the diagnostics computed from theoretical models which we believe will help understand the mechanisms of flares are the relationship between the distributions of high-temperature and low-temperature emission (e.g. soft X-rays and $H\alpha$), and the relationship between flow velocities observed in such emissions, as a function of time. We should, moreover, be able to pick out other useful interpretative and predictive aids not yet apparent in the data.

(b) Comparison with Previous Work

Considerable effort has been expended in recent years on the hydrodynamic modeling of flares, at the expense of magnetohydrodynamic and radiative transfer treatments, both intrinsically more difficult problems. Our desire to examine the interactions of the high temperature and low temperature parts of the flare leads us to a combined treatment of hydrodynamics and radiative transfer.

To date hydrodynamic studies have either ignored the optically-thick chromosphere entirely (Craig and McClymont 1976; Antiochos and Sturrock 1976, 1978) or treated its chromospheric radiation by ad hoc modification of the optically thin radiative losses (Kostyuk and Pikel'ner 1975; Kostyuk 1976; Somov et al. 1977; Henoux and Nakagawa 1978; McClymont and Canfield 1980; Nagai 1980; Craig and McClymont 1981; Craig et al. 1981). In addition to the limitations imposed on these models by their crude treatment of chromospheric radiative losses, all but the last two are subject to the criticisms of McClymont and Canfield (1980), Craig and McClymont (1981) and Craig et al. (1981) regarding their lack of resolution of the transition region, with the result that they do not properly represent conductive energy transfer to the chromosphere.

In addition to coupling hydrodynamics and radiative transfer in flare modeling, our study is unique in another respect, in that we treat radiative transfer using a probabilistic approximation. To date, radiative hydrodynamic computations (none of which have been applied to solar flares) have used frequency dependent radiative transfer (e.g. Klein, Stein, and Kalkofen 1976, 1978; Kneer and Nakagawa 1976). This approach has the advantage of considerable generality; for instance, it treats exactly overlapping lines and continua. The price of generality

is complexity: of order 25 equations per atomic line transition and at least 5 per continuum are required to define the photon spectrum over frequency. Since there is no reason to expect the primary hydrodynamic mechanisms of the chromosphere to involve overlapping lines and continua, the probabilistic approach can be quite useful.

The probabilistic method (Frisch and Frisch 1975; Canfield, Puetter, and Ricchiazzi 1981), on the other hand, represents radiative transfer in each spectral feature (line or continuum) by a single equation for the total photon flux in that feature. Thus the probabilistic method can be orders of magnitude faster computationally, an important consideration in a time dependent calculation where the complete set of hydrodynamic and radiative transfer equations must be solved at each time step. The advantage of the probabilistic method in this respect is enhanced by the fact that we wish to do routine, "production run" simulations, not merely to demonstrate this or that effect of radiative transfer.

The remainder of this paper is devoted to a description of our formulation of the problem and discussion of the numerical methods used to obtain a solution. Results of physical relevance to solar flare loops are presented in McClymont and Canfield

(1981, Paper II) and subsequent papers. In Section II we discuss the physics represented in our simulation and present the relevant equations. Numerical techniques for the solution of the equations are described in Section III; and in Section IV we compare our approach to that adopted in previous solar and stellar studies of coupled hydrodynamics and radiative transfer. A summary of the major points is given in Section V.

II. PHYSICS OF THE MODEL

(a) Assumptions and Approximations

Here we justify our approach and point out approximations made in three areas - the structure of the magnetic field in the flare region, the treatment of hydrodynamics and the treatment of radiative transfer.

We shall refer to Table 1, which shows quantities of interest for microscopic and macroscopic plasma processes under a variety of conditions in the solar atmosphere. Shown are the temperature, density, pressure and ionization representative of the temperature minimum, lower chromosphere, upper chromosphere and corona of the quiet Sun, and of the flaring corona, both in the initial stage of a flare (before the coronal density

increases significantly (indicated by I), and later in the gradual phase, (indicated by II). Also shown are the time scales for momentum exchange and for energy exchange between electrons, protons and hydrogen atoms and the magnetic field strength required for the magnetic pressure to equal the gas pressure.

(1) Structure and Magnetic Field Geometry

It is well known observationally that many flares occur in loops without seriously disrupting the preflare magnetic field geometry. From Table 1 we find that the minimum magnetic field required for containment of the hot coronal plasma is ~ 100 gauss, which is reasonable for small, compact flares. We do not intend to model "eruptive" flares in which the preflare field is significantly altered; there, magnetic effects are clearly important.

In addition to assuming a time independent geometry, we neglect the effect of any helicity of the magnetic field and assume that the loop is symmetric about the loop apex. While flare phenomena are sometimes observed first at one footpoint of a loop, other flares seem to develop symmetrically with nearly simultaneous H α brightenings at both footpoints. The boundary conditions presented here are appropriate to the symmetric case, in which only one half of the loop need be modelled. The computer

code may easily be amended to model the more general case, for instance, of energy release at one footpoint.

We can model an arbitrary variation of loop cross-sectional area along the loop, and present an appropriate formulation. In the first few of the following papers, we will initially assume a constant cross-section.

An important assumption we make is that the state of the plasma at a given position along the loop is independent of radius perpendicular to the loop axis. Since transport by diffusion across the magnetic field is slow and since radiation in the corona, being optically thin, cannot homogenize material across a loop cross-section, we are postulating that flare energy release takes place uniformly across the loop.

(ii) Hydrodynamics

Our assumptions with respect to the hydrodynamic variables are concerned with the equilibrium of the different species of particle in the plasma - electrons, protons, hydrogen atoms and other atoms and ions.

From Table 1 we see that all collision times for momentum exchange τ_M , are very much shorter than the hydrodynamic time scale, $\tau_{HD} \sim 10^1 - 10^2$ s. (The time scales for other species are

comparable to those for hydrogen.) Therefore all species move together with the same flow velocity v and we may discuss the motion of a fictitious particle of mass $m = 1.56 m_p$. (Most of the mass in excess of hydrogen is due to helium.) In the corona chromosphere all particles are strongly tied to the magnetic field lines; near the temperature minimum some cross-field flow of neutral atoms is possible. We neglect this effect.

Turning to the energy equation we find from Table 1 that the time scales for energy exchange between particles (τ_E) are short, except in the corona, where the electron-proton temperature equilibration time is comparable to (or greater than) the hydrodynamic and radiative ($\tau_{RAD} \approx 10$ s) time scales. Thus species-dependent heating or cooling terms in the energy equation can result in temperature differences between the species. Such effects have been explored by several authors. Thermal conduction and radiative losses affect the electron temperature while viscous heating is restricted to protons. In the absence of detailed information concerning the nature of the flare heating mechanism, the most obvious sources of temperature differences are the radiative cooling of electrons and the viscous heating of protons in shock fronts. During the passage of a shock, plasma kinetic energy (carried mainly by the protons) is transformed to heat, which is not immediately communicated to the electrons

(Zel'dovich and Raizer 1967). For our initial studies we have chosen not to introduce separate energy equations for the electrons and protons, although this can easily be done at a later stage. We are chiefly interested in the interaction between hydrodynamic and radiative transfer effects; to deal with species-dependent heating and cooling terms (important only in the corona) only introduces unnecessary complications. We are not yet ready to study the consequences of the temperature, density and species dependence of the flare heating mechanism.

To this end we make the simplest possible assumptions concerning both the ambient steady state heating term and the flare energy input. We assume that the ambient heating is constant per unit mass; it may vary in space (specifically, it is a function of column density), but is independent of the state of the plasma. The flare heating mechanism is taken to energize all species equally.

(iii) Radiative Transfer and Atomic Physics

Our major approximation in this area is our neglect of radiative transfer effects for all elements but hydrogen. The contribution of other elements to the radiative loss rate is approximated by the Cox and Tucker (1969) optically thin

radiative loss function with the hydrogen contribution removed (more recent publications do not permit separation of hydrogen from other elements). Hydrogen itself is treated as an n-bound level plus continuum atom, with $n = 2$ or 3 initially; probabilistic radiative transfer is applied to the resulting transitions. The radiation due to H^- (important only deep in the chromosphere and photosphere) is presently assumed to be optically thin. Since we do not explicitly treat the atomic physics of elements other than hydrogen, a constant contribution of free electrons, amounting to an ionization $x_e = 8 \times 10^5$, is assumed from the heavy metals.

In the corona all transport processes are constrained by the magnetic field to operate along the loop except for radiation, which being optically thin, can escape freely in all directions. This, however, does not alter the one-dimensional nature of the present problem. In the chromosphere, also, energy transport by radiative transfer is unaffected by the magnetic field. However, for all the smallest observationally resolvable features, vertical radiative transfer dominates over horizontal.

Finally, we assume that the gradients of velocity, density and temperature are not large enough to invalidate the probabilistic method of radiative transfer (see Canfield, Puetter

and Ricchiazzi 1981). Gradients in density and temperature in empirical equilibrium models do not impose severe restrictions; source function gradients in the flare chromosphere of Lites and Cook (1979) or the models of Vernazza, Avrett and Loeser (1981) are orders of magnitude smaller than those which violate the assumptions. On the other hand, large velocity, density, and temperature gradients, which invalidate escape probabilities calculated on a static assumption, may be encountered in shock fronts. Failing such extremes, quite large velocity gradients may nevertheless be treated through static escape probabilities (cf. Mihalas 1979; Hummer and Rybicki 1981). Of course, the validity of these assumptions can and must be checked ex post facto. Development of probabilistic methods for treatment of density, temperature and velocity jumps in shocks is beyond the scope of this paper.

(b) The Equations and Boundary Conditions

In this section we present the equations governing hydrodynamics, atomic excitation and ionization, and radiative transfer. We then give the boundary conditions to be imposed and define the functions appearing in the equations, in terms of the basic variables, which are temperature, density, atomic level populations and the mean intensity and optical depth in each

transition. The symbols used are defined in Table 2.

(i) The Equations

We have written the equations in Lagrangian form, that is, the independent variables are time t and column density N . Thus the spatial coordinate identifies a unique element of the plasma. The column density is defined by

$$N = \int_0^z A n dz', \quad (1)$$

where $v(z=0) = 0$. Note that N measures the total number of particles in the loop, not the number per unit cross sectional area. We should also emphasize that the density n is the density of "equivalent hydrogen atoms", $n = n_p + n_H$. The total particle density is given by $(1 + \gamma + x)n$. However, we will use the term "particle" to mean "equivalent hydrogen atom".

Conservation of mass is expressed by

$$n = \left(A \frac{dz}{dN} \right)^{-1} ; \quad \frac{\partial z}{\partial t} = v, \quad (2)$$

from which the conventional form of the continuity equation is obtained easily. The momentum equation is

$$m \frac{\partial v}{\partial t} = - A \frac{\partial P^*}{\partial N} + m g_{||} , \quad (3)$$

where the right hand side represents acceleration due to the pressure gradient and to gravity. The energy equation is

$$\frac{\partial \epsilon}{\partial t} = Q - R + \frac{\partial}{\partial N} \left(A^2 n \kappa \frac{\partial T}{\partial N} \right) - P^* \frac{\partial A v}{\partial N} , \quad (4)$$

which states that changes in thermal energy are due to external energy input, radiative losses, thermal conduction, and work done by pressure. The stress P^* comprises hydrostatic pressure and viscous stress

$$P^* = P - \frac{4}{3} A^{3/2} n n \frac{\partial (A^{-1/2} v)}{\partial N} . \quad (5)$$

The energy input term (4) consists of ambient heating Q_A , which is constant, and a term Q_p which is time dependent.

The quantum states of hydrogen are denoted by ϕ_i .

$$R_{ji} \phi_j - R_{ij} \phi_i \quad (6a)$$

Through conservation of particles, we use the number of hydrogen ($i = 1, \dots, N_B$) and the continuum population ϕ_c^* by the equation

$$\sum_{i=1}^{N_B} \phi_i + \phi_c^* = N_B \quad (6b)$$

by the equation (Canfield, Puetter

$$-2\sqrt{p_{u2}} \frac{d}{d\tau_{u2}} (\sqrt{p_{u2}} S_{u2}) \quad (7)$$

for the equations than for the text. The characters ϕ and θ are quite different.

where the optical depth is given by

$$\frac{d\tau_{ul}}{dN} = \sigma_{ul} . \quad (8)$$

Note that (7) is the steady state radiative transfer equation, which neglects the flight time of photons.

(ii) Boundary Conditions

The boundary conditions imposed at the top of the loop express our assumption of symmetry and the fact that the corona is optically thin. We take the loop apex to be the origin ($N = 0$, $Z = 0$) where the velocity and optical depths vanish. All other quantities are symmetric about this point, so their gradients vanish. The footpoints of the loop (taken to lie beneath the photosphere) are assumed to remain unperturbed by events in the overlying atmosphere, therefore the footpoint values of all variables are fixed at their initial values. We assume that LTE holds at the footpoints, so that the mean intensities there are given by the Planck function.

(iii) Definition of Functions in the Hydrodynamic Equations

Here we define the pressure, thermal energy, conductivity, viscosity and radiative loss rate which appear in (2) - (5). Numerical constants are in c.g.s. units. The plasma pressure is

$$P = (1 + y + x)nkT, \quad (9)$$

and thermal (translational plus internal) energy per particle is

$$\epsilon = \frac{3}{2} (1 + y + x)kT + \sum_l \epsilon_l \phi_l. \quad (10)$$

Thermal conductivity is given by (Spitzer 1962; Shmeleva and Syrovatskii 1973; Moore and Pung 1972).

$$\kappa = \Gamma \kappa_e + \kappa_H, \quad (11)$$

where the electron conductivity is

$$\kappa_e = \frac{1.79 \times 10^{-5} T_e^{5/2}}{\Lambda_{ee}} \quad (12)$$

where Λ_{ee} is the electron Coulomb logarithm

$$\Lambda_{ee} = 9.25 + \frac{1}{2} \left[\ln(T_e^3/n) - \max(0, \ln T_e / 4.2 \times 10^5 \text{ K}) \right]. \quad (13)$$

For completeness we give here the reduction factor for incomplete ionization

$$\Gamma = \frac{1 + 4.49r + 3.37r^2 + 0.59r^3}{(1 + 3.86r + 0.94r^2)^2}, \quad (14)$$

where

$$r = \tau_{ee}/\tau_{eH} = 3.60 \times 10^{-10} \frac{n_H}{n_e} \frac{T_e^2}{\Lambda_{ee}}, \quad (15)$$

and the neutral hydrogen conductivity

$$\kappa_H = \frac{29.6 T_H}{1 + n_p/n_H (T_H/7.6 \times 10^5 K)^{1/2}}. \quad (16)$$

However, we find that neither of these effects are important. The reduction factor Γ only differs significantly from unity for $T \approx 1.5 \times 10^4$ K, in which regime conduction is predominantly by neutral hydrogen; this process is itself completely overwhelmed by radiative transfer.

The viscosity η consists of two terms, the physical viscosity (Spitzer 1973), important only for $T_p \geq 2 \times 10^7$ K

$$\eta_0 = \frac{2.21 \times 10^{-15} T_p^{5/2}}{\Lambda_{pp}}, \quad (17)$$

where the Coulomb logarithm for protons is

$$\Lambda_{pp} = 8.94 + 1/2 \ln(T_p^3/n_p), \quad (18)$$

and pseudo-viscosity, which we use to control the thickness of shock fronts on the numerical grid (Richtmyer and Morton 1967)

$$\eta_1 = \begin{cases} (\alpha \Delta N)^2 \left| \frac{\partial v}{\partial N} \right| & \frac{\partial v}{\partial N} < 0 \\ 0 & \frac{\partial v}{\partial N} > 0 \end{cases} \quad (19)$$

The latter term is negligible outside of shock fronts.

The radiative loss rate per particle is

$$R = n_e \left[f(T) + 2.21 \times 10^{-30} \frac{n_H}{n} T \right] + \sum_{U>L} h\nu_{UL} (R_{UL} \phi_U - R_{LU} \phi_L), \quad (20)$$

where the first two terms represent emissions treated as optically thin (X-ray/EUV and H^- radiation respectively) and the summation is over the lines and continua of hydrogen. For continua we use

the mean photon energy in (20),

$$h\nu_{ul} = kT e^{-\alpha} / E_1(\alpha), \quad (21)$$

where α is defined in (22).

(iv) Definitions of Functions in the Radiative Equations

In the following, ν_{ul} is the line center frequency in the case of lines and the continuum edge frequency for continua. We define the ratio of photon energy to thermal energy

$$\alpha_{ul} = h\nu_{ul} / kT_e \quad (22)$$

and the mean thermal velocity of hydrogen atoms

$$v_{th} = \sqrt{2k T_H / m_H}. \quad (23)$$

The atomic transition rates R_{ji} , which each comprise collisional and radiative contributions, are well known (see, for example, Johnson 1972, and Mihalas 1978).

We also have used the source function

$$S_{ul} = \frac{2h\nu_{ul}^3}{c^2} \left(\frac{g_u}{g_l} \frac{\phi_l}{\phi_n} - 1 \right)^{-1} \quad (24)$$

and the opacities per particle (cross-sections), both for lines at

their center

$$\sigma_{u\ell} = \frac{2.97 \times 10^{-18} f_{\ell u}}{v_{th} h\nu_{u\ell}} \left(\phi_{\ell} - \frac{g_{\ell}}{g_u} \phi_u \right), \quad (25)$$

and for continua at the ionization limit

$$\sigma_{u\ell} = 7.91 \times 10^{-18} \ell \left(\phi_{\ell} - \frac{g_{\ell}}{g_u} \phi_u \right). \quad (26)$$

For line transitions we give, for example, only the $L\alpha$ escape probability

$$p_{21} = \frac{1}{2} [1 + 3.545 \sqrt{\ln(e + \tau_{21})} \tau_{21}]^{-1}. \quad (27)$$

A more extensive discussion of escape probabilities appropriate to other lines is given by Canfield and Puetter (1981) and Puetter (1981). For continua, the escape probabilities are (see Canfield and Picchiazzi 1970)

$$p_{u\ell} = \begin{cases} \frac{1}{2} e^{-\tau_{u\ell}} & \psi \leq 1 \\ \frac{1}{2} \psi^{-1} e^{-\alpha_{u\ell} (\frac{4}{3} \psi - 1)} & \psi > 1, \end{cases} \quad (28)$$

where

$$\psi = (3 \tau_{ul} / \alpha_{ul})^{1/4}. \quad (29)$$

III. NUMERICAL SOLUTIONS OF THE EQUATIONS

To integrate equations (2) - (8) we must discretize the equations, replacing physically continuous functions by a finite set of discrete variables. We have used the conventional point-approximation scheme in which the variable y_i^j represents the value of the function $y(N,t)$ at the discrete space-time point (N_i, t^j) , $i = 0, 1, \dots, M$; $j = 0, 1, \dots$. The derivative of a function with respect to space or time is replaced by a finite difference between adjacent (in space or time) point approximations to the function. As far as possible, we have maintained second order accuracy in the integration by proper centering of the finite difference approximations.

As illustrated in Figure 1, we regard the loop as being composed of a number of cells of plasma; associated with each cell are the variables n , T , ρ , and J_{ul} . The values of these variables are defined at the cell center, at column depth $N_{i+1/2}$, and denumerated by half-integral values $i+1/2$. The cells are compressible, moving with the fluid and changing their volumes in response to movements of the cell edges, which are denumerated by integral values of i , and at which point the spatial coordinates

N , z , τ_{ul} and the velocity v are defined.

The variables defined at cell centers are local "thermodynamic" properties of the plasma while those defined at cell boundaries can be regarded as fluxes or global coordinates. These two sets of variables are, to a large extent, complementary. Thus, for example, the rate of change of density in a cell is determined by the velocity difference between its edges while the change in optical depth across a cell is determined by the atomic populations within the cell. On a uniform grid, then, most of the finite differences approximating derivatives with a second order error can be represented as a difference between adjacent grid points. This quasi-conservative approach avoids the "leapfrog" nature of centered finite differences otherwise required for second order error, which can give rise to spurious oscillations in the solution.

(b) Non-Uniformity of the Grid

Unfortunately, due to the extremely non-uniform structure of the atmosphere, we cannot use a uniform grid. The width (ΔN) of a cell is determined by the condition that finite differences across it reasonably approximate the continuous derivatives of the original problem. In the corona, with length scales of $\sim 10^3$ km and

densities of $\sim 10^9 \text{ cm}^{-3}$ we have $\Delta N \approx 10^{16} \text{ cm}^{-2}$, while in the chromosphere and photosphere $\Delta N \approx 10^{16} - 10^{23} \text{ cm}^{-2}$. In the transition region, grid spacings as small as $\Delta N \approx 10^{15} \text{ cm}^{-2}$ are required to resolve the temperature structure, even in a quiescent atmosphere.

Moreover, since we follow the dynamic evolution of the atmosphere, the grid must be adaptive, increasing the density of grid points where required to accurately resolve the current state of the atmosphere.

Two principal methods are available to handle these problems. The approach we follow here is to use a non-uniform grid in N-space, constructing finite differences with second order error using divided difference formulae. The grid is modified dynamically by inserting and deleting cell boundaries (equivalently, splitting and merging cells) to maintain the necessary resolution.

The second method (not used here) is to transform to a new independent space variable s , the transformation being chosen so that a uniform s -grid produces the necessary density distribution of grid points in N-space. This method has been applied to the solar atmosphere by McClymont and Canfield (1980), Craig and

McClymont (1981), and Craig et al. (1981) using a fixed (non-adaptive) transformation chosen a priori (see Craig et al. (1981) for details). In these studies the transformation could be chosen a priori since the position and range of movement of the transition zone (the region requiring most careful treatment) were known from preliminary studies.

In general, where the required distribution of grid points is more complex, the best approach is to use an adaptive s-grid whose grid points move so as to "follow" features requiring a higher density of grid points (e.g. Tscharnuter and Winckler 1979; Gelinas et al. 1981). The fact that the grid points tend to move with features of the atmosphere (e.g. the transition region, shock fronts) overcomes a major disadvantage of static grids pointed out by McClymont and Canfield (1980) and in Section (c) below. The main disadvantage of the moving grid is that it may amplify any tendency towards numerical instability (Tscharnuter and Winckler 1979).

(c) Movement of Features Relative to the Grid

By choosing to formulate the problem in a Lagrangian reference frame rather than an Eulerian frame, we have eliminated a major cause of time variation of quantities at a grid point,

i.e., advection of fluid properties at the fluid velocity. However, transport relative to the Lagrangian frame still occurs, for instance by thermal conduction. The presence of fast moving, steep gradients in the plasma can cause severe restrictions on the time step.

The most obvious example of such behavior is the propagation of shocks, in which a property of the plasma, say temperature, changes at a rate

$$\frac{1}{T} \frac{\partial T}{\partial t} \sim Mc/\lambda$$

during the passage of a shock front of Mach number M and thickness λ , where c is the sound speed. The Lagrangian frame is not a great improvement over the Eulerian frame in this case, as the rate of change at a grid point is reduced only by the ratio of the mean density in the shock front to the ambient density ahead of the shock. If, in the interests of accuracy, we restrict the change in fluid properties at a grid point to say 10% per time step, we need $\sim 10 \ln(T_1/T_0)$ time steps to resolve the passage of the shock front, where T_1 and T_0 are respectively the temperatures behind and ahead of the shock. Since the sound speed is approximately the ion thermal velocity and the shock thickness is of the order of the ion mean free path, the time of passage of the shock front is of the order of the ion self-collision time, $\sim 1s$ in

the corona. Thus $\Delta t \leq 0.15$. In the chromosphere the collision time is, of course, very much shorter. However, we omit discussion of chromospheric shocks as the additional complications of steep gradients in the radiative transfer treatment enter the picture, and are beyond the scope of the method, as presently developed.

The same problem arises, to a lesser extent, in the transition region. To produce the observed rate of increase in soft X-ray emission measure during large flares, the transition region must propagate into the chromosphere at close to the chromospheric sound speed, implying a rapid change of temperature and density at grid points within the transition region. However, the major problem of the transition region may not be its numerical treatment but its physics. The thermal flux required to drive the transition region at such high speeds must be near the flux saturation limit, which suggests that collisionless energy transport plays a role (e.g. Brown and Smith 1980) and that the resulting non-thermal structure modifies the conventional physics of radiative losses based on a Maxwellian distribution (Shoub 1981). In view of these uncertainties we have restricted our attention to events where we may assume that the transition region is described sufficiently well by the fluid equations and where the use of a static (but adaptive) grid does not seriously affect

the time step.

For treatment of the hydrodynamic variables across shock fronts, we follow the usual approach of invoking artificial viscosity (equation (19); Richtmyer and Morton 1967). Artificial viscosity is negligible outside shock fronts, but dominates within a shock front, to the extent of spreading the front over a macroscopic distance. Since the shock thickness is determined mainly by viscosity while the overall shock structure (e.g. Mach number, pressure jump) is almost independent of this quantity, satisfactory results may be obtained providing no physically significant processes depend critically on the amount of plasma in the intermediate temperature and density range within the shock front (see also Klein, Stein, and Kalkofen 1978, henceforth KSK, and Kneer and Nakagawa 1976, henceforth KN).

(d) Finite Differences in Time

Discretization in time is much simpler to handle than discretization in space. We use the single-step Crank-Nicholson finite difference scheme, transforming the set of equations (2) - (8), which we represent symbolically as

$$\dot{y} = f(x, t, y, y', y'') , \quad (30)$$

where y represents the set of variables $(n, v, T, z, J_{ul}, \rho_l, \tau_{ul})$ and x represents the spatial coordinate N , to the finite difference form

$$\frac{y^{j+1} - y^j}{\Delta t} = (1 - \theta) f^j + \theta f^{j+1} \quad 0 \leq \theta \leq 1. \quad (31)$$

For $\theta \neq 0$ the above set of equations is implicit, since the right hand side involves complicated functions of the unknown vector y^{j+1} . The equations must therefore be solved by iteration. The use of an explicit method ($\theta = 0$), although conceptually and computationally simpler, would imply a very strong limitation on the time step. For instance, in the case of the thermal conduction term, to maintain numerical stability we require that the time step be less than about the conductive time scale across a finite difference cell,

$$\frac{3kT}{\Delta t} > \frac{\kappa_0 n T^{7/2}}{\Delta N^2}.$$

For $T = 10^5 K$, $n = 10^{10} \text{ cm}^{-3}$ and $\Delta N = 10^{15} \text{ cm}^{-3}$ this requires $\Delta t < 10^{-2} \text{ s}$. The situation is dramatically worsened in the case of the rate equations, where use of an explicit method would restrict the time step to atomic time scales ($\sim 10^{-8} \text{ s}$). For all equations except the atomic rate equations we set $\theta = 1/2$. Then the system is numerically stable for all time steps and the finite difference

approximation to the time derivative is centered at time $t^{j+1/2}$ and so has second order error.

Since almost all atomic time scales are much shorter than the microscopic time scales of interest, it is almost possible to treat the rate equations in the steady state approximation. However, the recombination time scale in the upper chromosphere can be long ($\geq 10^2$ s). Since this fact could have important consequences during a flare, we retain the time derivative (see also KN). The atomic rate equations, although numerically stable for $\theta = 1/2$ in the sense that the error term does not grow with time, exhibit strong, weakly damped oscillations which are completely unphysical (see KSK). To see this, consider the simple rate equation

$$\dot{u} = -u/\tau, \quad (32)$$

with solution

$$u(t) = u_0 e^{-t/\tau}, \quad (33)$$

and apply the Crank-Nicholson formula

$$\frac{u^{j+1} - u^j}{\Delta t} = -\frac{1}{\tau} [(1 - \theta) u^j + \theta u^{j+1}] \quad (34)$$

which, although implicit, can be solved immediately by virtue of its linearity to give

$$u^{j+1} = \frac{1 - (1-\theta) \Delta t/\tau}{1 + \theta \Delta t/\tau} u^j . \quad (35)$$

Unless we are prepared to integrate on the atomic time scale, we are forced to take $\Delta t \gg \tau$. Clearly (35) gives a monotonically decaying solution only in the limit $\theta \rightarrow 1$. (With $\theta = 1$, (35) is the Euler one step backward difference formula which is L-stable (or stiffly A-stable); with $\theta = 1/2$ the formula is merely A-stable - see Lambert 1977). This first order method is accurate for $\Delta t \ll \tau$ and $\Delta t \gg \tau$. Only for $\Delta t \approx \tau$ is the error noticeable.

(e) Finite Differences on a Non-Uniform Grid

To discretize equations (2) - (8) with second order error on the non-uniform grid, we use divided differences based on the Lagrange interpolation polynomial (e.g. Conte and de Boor 1972)

$$p_n(x) = \sum_{i=0}^n f(x_i) \prod_{\substack{j=0 \\ j \neq i}}^n \frac{x - x_j}{x_i - x_j} , \quad (36)$$

which interpolates $f(x)$ at x_0, x_1, \dots, x_n . Writing f_i for $f(x_i)$ and defining

$$\Delta_i = x - x_i, \quad (37)$$

we find

$$f(x) \approx p_n(x) = \sum_i f_i l_i(x), \quad (38)$$

$$f'(x) \approx \frac{dp_n(x)}{dx} = \sum_i f_i l'_i(x), \quad (39)$$

$$f''(x) \approx \frac{d^2 p_n(x)}{dx^2} = \sum_i f_i l''_i(x), \quad (40)$$

where

$$l_i(x) = \prod_{j \neq i} \frac{\Delta_j}{\Delta_j - \Delta_i}, \quad (41)$$

$$l'_i(x) = l_i(x) \sum_{j \neq i} \frac{1}{\Delta_j} \quad (42)$$

and

$$l''_i(x) = l_i(x) \sum_{j \neq i} \sum_{\substack{k \neq i \\ k \neq j}} \frac{1}{\Delta_j \Delta_k}, \quad (43)$$

and all sums and products are understood to range over $0 - n$. When

evaluated at a point on a uniform grid with $n = 2$, (39) and (40) reduce to the usual finite difference formulae for the first and second derivatives. We use (38) to interpolate cell center values of variables defined at cell boundaries and vice versa, while (39) and (40) enable us to find derivatives at cell centers or edges of variables defined at either centers or edges. To achieve second order error we require in general three grid points ($n = 2$) in (38) and (39) and four points ($n = 3$) in (40); however, interpolation and first order differentiation at a cell center using edge values requires only 2 points (the edges of the cell in question), by symmetry. That is, $f_{i+1/2} = (f_{i+1} + f_i)/2$, and $f'_{i+1/2} = (f_{i+1} - f_i)/\Delta x_{i+1}$. In cases where the interpolation points cannot be symmetrically arranged around the point at which the result is required, the extra point may lie to the left or the right; the closer one is chosen.

Using the symbolic notation (30) in the finite difference form (31), our set of equations (2) - (8) becomes

$$\begin{aligned} \frac{y_i^{j+1} - y_i^j}{\Delta t} &= (1-\theta)f_i^j + \theta f(x_i, t^{j+1}), \sum_k y_{i+k}^{j+1} z_{i+k}(x_i), \\ &\sum_k y_{i+k}^{j+1} z'_{i+k}(x_i), \sum_k y_{i+k}^{j+1} z''_{i+k}(x_i) \quad (44) \end{aligned}$$

In this equation f_i^j is regarded as a known constant that has been evaluated in the manner made explicit for f_i^{j+1} . The summations over k are understood to include the grid points surrounding the point i , relevant to the particular interpolation or differentiation, including the degenerate case ($k = 0$ only; $f_i(x_i) = 1$) of "interpolation" at the point i itself. Note that some of the components of the vector y_i are actually defined at cell centers, for instance, $T_{i+1/2}$. The offset is to be understood in these cases.

Lack of symmetry on the non-linear grid partially destroys the advantages of stability and conservation obtained by the use of a staggered grid on which certain variables are defined at cell centers and others at cell edges. The radiative transfer equation (7) is the most notable example of this effect. Initially, we centered the equation on the grid in the way immediately suggested by (7), at the cell edges. However, the rapid change in the escape probability near the $\tau_{ul} = 1$ point induced oscillations in J_{ul} when the 3-point approximation to the derivative of J_{ul} at a cell edge was used. We found it necessary to center the equation midway between cell centers instead, so that the finite difference approximation to the derivative (by symmetry) involved only two adjacent values of J_{ul} .

(f) Solution by Linearization and Iteration

To advance the solution of equations (2) - (8) by a time step using the Crank-Nicholson formula, we must solve the large set of strongly coupled, non-linear implicit equations (44). This can only be achieved through iteration. To guide our search for the solution x^* of the equations, which we represent symbolically as $g(x) = 0$ where $x = (y_i^{j+1}; i = 0, \dots, M)$ we use Newton-Ralphson iteration, that is we write, for $x = x^*$

$$g(x) + \frac{\partial g(x)}{\partial x} \cdot (x^* - x) = 0, \quad (45)$$

so that

$$x^{(n+1)} = x^{(n)} - \left[\frac{\partial g(x^{(n)})}{\partial x} \right]^{-1} \cdot g(x^{(n)}) \quad (46)$$

is hopefully a better approximation to x^* than was $x^{(n)}$. The Newton-Ralphson procedure is not guaranteed to converge; however, our experience to date has been that in fact it converges rapidly, providing the linearization is accurate and consistent (see below) and the initial estimate of the solution vector is not too far from the true solution x^* . During time dependent calculations we use the solution at the previous time step as the initial estimate and achieve convergence in, on average, 3 iterations. Difficulty

in convergence can usually be cured by halving the time step.

Linearizing the finite difference equation (44) to obtain the Newton-Ralphson formula (45) we find

$$\sum_k \left[\left(\frac{\partial f}{\partial y} \right)_i^{j+1} \delta_{i,i+k} + \left(\frac{\partial f}{\partial y'} \right)_i^{j+1} \delta'_{i+k} + \left(\frac{\partial f}{\partial y''} \right)_i^{j+1} \delta''_{i,i+k} - \frac{\delta_{i,i+k}}{\phi \Delta t} I \right] \times \delta y_{i+k} = \frac{y_i^{j+1} - y_i^j}{\theta \Delta t} - (f_i^{j+1} + \frac{1-\theta}{\theta} f_i^j), \quad (47)$$

where δy_i is the iterative correction to be added y_i^{j+1} . In the above equation $\delta_{i,j}$ is the Kronecker delta and we have written $\delta_{i,j}$ for $\delta_j(x_i)$.

An important point concerning the evaluation of the linearization derivatives must be made. The dependence of an equation on a variable is sometimes determined by the difference between two terms almost identical in value. The most dramatic example of this is the radiative transfer equation in conditions close to LTE, where the term $J_{ul} - S_{ul}$ varies very slowly with change of J_{ul} , if the induced changes in the population are accounted for. Thus an accurate, self-consistent evaluation of the derivative is required. Our first attempt at calculating

$$\frac{(J_{ul} - S_{ul})}{J_{ul}} = 1 - \left(\frac{\partial S_{ul}}{\partial \phi_l} \frac{\partial \phi_l}{\partial J_{ul}} + \frac{\partial S_{ul}}{\partial \phi_u} \frac{\partial \phi_u}{\partial J_{ul}} + \delta_u^c \frac{\partial S_{ul}}{\partial x} \frac{\partial x}{\partial J_{ul}} \right) \quad (48)$$

involved analytical differentiation of S_{ul} with respect to ρ and a numerical evaluation (be re-evaluating the populations with a perturbed J_{ul}) of $\partial\rho/\partial J$. This gave completely spurious results. Differentiation of the entire term numerically using a perturbed J_{ul} gave a more meaningful result, but this was still not sufficiently accurate to ensure convergence of the iteration. Reliable values were obtained only when the complete derivative was evaluated analytically, using populations (which have to be obtained by iteration on the rate equations) consistent with the radiation field to about one part in 10^6 .

(g) Reduction of the Order of the Matrix Equation

We now consider a method for reducing the number of equations to be solved simultaneously in (47). The coefficient matrix in (47) is a band matrix whose bandwidth N_w is the product of the number of variables N_v per cell $(4 + (N_b + 1)^2)$, where N_b is the number of bound levels in the hydrogen atom) and the maximum number of gridpoints used in any interpolating polynomials (five, if we allow the fourth point of $l''(x)$ to be chosen on either the left or the right). The total number of equations N_e is just the number of variables per cell times the number of cells.

The computing time required to solve the band matrix

equation (47) is proportional to $N_w^2 N_e$, i.e. to N_v^3 (on a parallel-processing machine these become $N_w N_e$, N_v^2). If we can split the problem into N separate parts, each involving N_v/N variables, the computation would be speeded up by a factor of N^2 (N on a vector machine). We cannot actually solve explicitly for a subset of the variables, but we can achieve the same effect by substituting for a subset of the variables in terms of the remaining variables (cf. Mihalas 1979). A variable can be eliminated if its spatial derivative is not involved in its definition as a function of the remaining variables. Thus, making use of the continuity equation (2), we can express density as a function of position and substitute in (47)

$$\left(\frac{\partial f}{\partial n}\right)_i^{j+1} \delta n_i = \left(\frac{\partial f}{\partial n}\right)_i^{j+1} \sum_k \left(\frac{\partial n_i}{\partial z_{i+k}}\right)^{j+1} \delta z_{i+k}, \quad (49)$$

where the derivative of n with respect to z is obtained from the finite difference form of (2). The position z can in turn, be eliminated, since

$$\frac{z_i^{j+1} - z_i^j}{\Delta t} = \frac{1}{2} (v_i^{j+1} + v_i^j), \quad (50)$$

and we substitute

$$\delta z_i = \frac{1}{2} \Delta t \delta v_i . \quad (51)$$

Finally, the atomic populations ρ can be expressed in terms of other variables. Since the rate equations do not involve spatial derivatives we can extract them from (47), linearize and invert the resulting matrix equation at each grid point independently, thus expressing perturbations to the populations in terms of perturbations to other variables.

Solution of the band matrix (47) then gives corrections to be applied to the variables v , T , J and τ at each grid point. We could then find the linearized corrections to n , z and ρ using (49), (51) and the linearized rate equations. Instead we re-solve the original equations for these quantities, rather than their linearized forms. Since the equation (50) for z is linear, this has no effect on z ; solving (2) for n rather than using (49) ensures consistency and conserves mass. Solution of the rate equations (6), using the new values of n , T and J , is essential to the convergence of the iteration. If relatively large corrections to the radiation field (δJ) are generated, the resulting linearized corrections to the populations may carry a level population outside the physical range $0 < \rho_i < 1$. We find that convergence is improved if we also make the optical depths consistent with the populations at each iteration. To do this we reject the linearized

corrections δr and instead integrate (8) using the new values of all variables.

(h) Error Control

There are four sources of error to be considered; incomplete convergence of the iterative solution of the rate equations (6), incomplete convergence of the iterative solution of the other equations (47), truncation error due to finite differencing in time and truncation error due to finite differences in space.

Since we find that a high order of consistency between the populations and radiation field is required, we use a strict convergence criterion for the rate equation iteration, $|\delta\phi_2|/\phi_2 < 10^{-6}$.

In order to obtain a "reasonable" criterion for the convergence of the outer iteration, we assume that the truncation errors are randomly distributed, so that after N steps, each with error ϵ , the error will be $\epsilon\sqrt{N}$. The error ϵ_F required at the end of the simulation, at time t_F , is specified; then we impose the convergence criterion

$$|\delta y/y| < \epsilon_F \sqrt{\Delta t/t_F} \quad (52)$$

for all monitored variables y at all grid points. Currently, for

typical time steps $0.1s < \Delta t < 10s$ this criterion allows discrepancies of $\leq 1\%$. Note that for sufficiently small errors (less than a few percent) the Newton-Raphson iteration converges quadratically; convergence to one part in 10^4 can be achieved with just one further iteration. The monitored variables are n , T , J_{ul} and ρ_l . It is unnecessary to check on the remaining variables, since changes in velocity and position are closely tied to changes in density, while the optical depth is directly related to the populations.

Our algorithm for time step control is very simple; if all monitored variables at all grid points change by less than 15%, we double the time step; if any monitored variable at any point changes by more than 40%, or if the iteration is reluctant to converge, we halve the step. Rather than iterating to convergence before checking whether the time step should be halved, we check after the first iteration. Usually the changes computed at this point are within a factor of two of the final result.

A similar scheme is used to control the spatial distribution of grid points. If any variable changes by more than some factor (presently 1.6) between adjacent points, the cell is divided into two smaller cells; if all variables change by less than some other amount (presently 20%) then two adjacent cells are merged.

However, the density of cells is not allowed to fall below a preset minimum; undesirable effects arise whenever any cell occupies more than a few percent of the total length of the loop, either in N or z .

(i) Computational Procedure

Our procedure is first to obtain an atmosphere that satisfies all the basic equations in the steady state, and then to calculate its development in response to a perturbation. Thus, the calculation separates into an initialization procedure, which obtains a steady state solution, followed by the time dependent calculation. The purpose of the initialization procedure is to obtain a steady-state, non-LTE, hydrostatic equilibrium atmosphere consistent with a specified temperature distribution $T(N)$.

(j) Initialization

1. Choose a $T(N)$ for the initial steady-state atmosphere.
2. Solve for radiative transfer variables consistent with the adopted $T(N)$ by iteration.
 - (a) Get starting values by guessing $n(N)$ and assuming LTE, which defines $J(N)$, $\tau(N)$, $z(N)$ and $\rho(N)$.
 - (b) Calculate the coefficients of the linearized radiative

transfer, optical depth and steady state atomic rate equations.

- (c) Solve for corrections to J .
 - (d) Update J and recalculate consistent ρ from the rate equations and τ from the optical depth equations.
 - (e) Iterate steps (b) - (d) until converged.
3. Solve for radiative transfer variables and density consistent with the adopted $T(N)$ by iteration.
- (a) Get starting values from results of step 2.
 - (b) Calculate coefficients of linearized radiative transfer, optical depth, steady state atomic rate equations, and steady state momentum equation.
 - (c) Solve for corrections to J and z .
 - (d) Update J , z and recalculate consistent ρ , τ and n .
 - (e) Iterate steps (b) - (d) until converged.
4. Calculate the required ambient energy input Q_A at each grid point from the steady state energy equation.

(ii) Time Dependent Calculation

- 1. Scan the grid, inserting and deleting cells as necessary to resolve the structure of the atmosphere.
- 2. Calculate the amplitude of flare heating during the time step.
- 3. Solve the full set of time-dependent equations.

- (a) Calculate coefficients appearing in the linearized equations of radiative transfer, optical depth, atomic rates, momentum and energy.
 - (b) Solve for the corrections to v , T and J .
 - (c) Update v , T and J then recalculate consistent n , z , ρ and τ .
 - (d) If this is the first iteration, decide whether the changes in the monitored variables warrant a change in the time step. If so, change the time step and go to step 2.
 - (e) Repeat from (a) until converged; if convergence is not achieved in N_{\max} iterations, halve the time step and repeat from step 1.
4. Move on to the next time step; go to step 1.

IV. DISCUSSION AND COMPARISON WITH PREVIOUS RADIATIVE HYDRODYNAMIC CALCULATIONS

As indicated in Section I, the present treatment of flare hydrodynamics is unique in that we explicitly solve the radiative transfer equation. It is instructive to compare our methods with previous studies which, although they did not treat the flare problem, combined radiative transfer with hydrodynamics. The most relevant examples are KN, who studied the effects of a thermal

pulse introduced at the bottom of the solar chromosphere, and KSK, who modelled the propagation of a piston driven shock in a stellar chromosphere.

Although the basic physics of these studies is similar to our own, there are important differences both in the formulation of the problem and in the numerical methods used to obtain a solution. The three treatments are compared in Table III.

The most important difference is that KN and KSK use a frequency-dependent Eddington form of the radiative transfer equation, as opposed to our probabilistic formulation. The computational advantage of the probabilistic method, in which a frequency integration has been performed analytically, has already been pointed out. In Section III (g) we noted that the CPU time required to solve the equations is proportional to the number of variables cubed (squared, on a parallel processing machine) and in Section I (b) we pointed out that at least 25 variables per line and 5 per continuum are required to define even crudely the photon spectrum J_ν in a frequency dependent calculation, while only 2 variables (J_{ul} and τ_{ul}) per spectral feature are required in the probabilistic method. (The τ_ν need not be calculated in a frequency dependent method as there is no explicit dependence on optical depth, such as arises through the escape probabilities in

the probabilistic calculation.) In our present computations involving only two bound levels and the continuum of hydrogen, the solution of the band matrix accounts for nearly 40% of the total run time (another 40% of the CPU time is used in calculating atomic rates, source functions etc., and scales roughly as the number of transitions). With the introduction of further bound states of hydrogen or the treatment of radiative transfer in more elements, the run time will quickly become dominated by the band matrix solution. The computational advantage of the frequency integrated approach is clear; with presently available computing power the probabilistic method is the only feasible means of performing routine multi-element, multi-transition, time-dependent simulations.

V. SUMMARY

We reiterate the following major points:

The probabilistic method for radiative transfer enables time-dependent, multi-transition radiative hydrodynamic simulations to be carried out on a routine basis. By applying this method to the solar flare problem we can treat the whole atmosphere, from photosphere to corona, and learn how to interpret the simultaneously observed evolutions of the coronal and

chromospheric flares in terms of energy transport mechanisms. The major potential limitations of the present method arise from the inability of the probabilistic radiative transfer to treat overlapping lines and continua and its breakdown in the vicinity of extreme velocity gradients in optically thick (but effectively thin) parts of the chromosphere.

A major theoretical problem in flare studies is the formulation of a consistent description of the physics of the transition region, particularly proper representation of thermal conduction there. It is essential to use an adaptive, non-uniform finite difference grid in order to properly resolve features of the flaring atmosphere, especially the transition region. The moving adaptive grid is probably ultimately the best method with which to accomplish this goal, but because of the relatively unknown properties and possible drawbacks of the method, we have initially used a static adaptive grid.

We have carried out several studies using the framework outlined in this paper. In Paper II (McClymont and Canfield 1981) we carry out linear stability studies of empirical models of loops that extend throughout the visible solar atmosphere, from the photosphere to the corona. In Paper III (An, Canfield and McClymont 1981) we study the non-linear evolution of the models.

We are grateful to Chang-Hyuk An and George Fisher for help with a wide variety of problems during the later stages of this research. This work has been supported by the National Aeronautics and Space Administration through grant NSG-7406 and the National Science Foundation through grant ATM-8112866. The numerical methods have been developed using the Cray 1 at the National Center for Atmospheric Research, which is sponsored by the National Science Foundation.

REFERENCES

- An, C.-H., Canfield, R.C. and McClymont, A.N. 1981, in preparation (Paper III).
- Antiochos, S.K. and Sturrock, P.A. 1976, Solar Phys. 49, 359.
- Antiochos, S.K. and Sturrock, P.A. 1978, Ap.J. 220, 1137.
- Brown, J.C. and Smith, D.F. 1980, Rep.Prog.Phys. 43, 125.
- Canfield, R.C., Cheng, C.-C., Dere, K.P., Dulk, G.A., McLean, D.J., Robinson, R.D., Schmahl, E.J. and Schoolman, S.A. 1980, Solar Flares, A Monograph from Skylab Solar Workshop II, P.A. Sturrock ed. (Boulder, University of Colorado Press).
- Canfield, R.C. and Puetter, R.C. 1981, Ap.J. 243, 381.
- Canfield, R.C. and Ricchiazzi, P.J. 1980, Ap.J. 239, 1036.
- Canfield, R.C., Puetter, R.C. and Ricchiazzi, P.J. 1981, Ap.J. 248, 82.
- Conte, S.D. and de Boor, C. 1972, Elementary Numerical Analysis: an Algorithmic Approach (2nd ed.) (McGraw-Hill).
- Cox, D.P. and Tucker, W.H. 1969, Ap.J. 157, 1157.
- Craig, I.J.D. and McClymont, A.N. 1976, Solar Phys. 50, 133.
- Craig, I.J.D. and McClymont, A.N. 1981, Solar Phys. 70, 97.
- Craig, I.J.D., Robb, T.D. and Rollo, M.D. 1981, Solar Phys.

in press.

- Frisch, U. and Frisch, H. 1975, M.N.R.A.S. 173, 167.
- Gelinas, R.J., Doss, S.K. and Miller, K 1981, J.Comp.Phys. 40, 202.
- Henoux, J.C. and Nakagawa, Y. 1978, Astr.Ap. 66, 385.
- Hummer, D.G. and Rybicki, G.B. 1981, B.A.A.S. 12, 798.
- Johnson, L.C. 1972, Ap.J. 174, 227.
- Klein, R.J., Stein, R.F. and Kalkofen, W. 1978, Ap.J. 220, 1024.
- Kneer, F. and Nakagawa, Y 1976, Astr.Ap. 47, 65.
- Kostyuk, N.D. and Pikel'ner, S.B. 1975, Sov.Astr. 18, 590.
- Kostyuk, N.D. 1976, Sov.Astr. 20, 206.
- Lambert, J.D. 1977, The State of the Art in Numerical Analysis, p451, D.A.H. Jacobs ed. (Academic Press).
- Lites, B.W. and Cook, J.W. 1979, Ap.J. 228, 598.
- McClymont, A.N. and Canfield, R.C. 1981, Solar and Interplanetary Dynamics, p313, eds. M. Dryer and E. Tandberg-Hanssen.
- McClymont, A.N. and Canfield, R.C. 1981, Ap.J., submitted (Paper II).
- Mihalas, D. 1978, Stellar Atmospheres, 2nd ed (W.H. Freeman and Co., San Francisco).
- Mihalas, D. 1979, M.N.R.A.S. 189, 671.
- Moore, R.L. and Fung, P.C.W. 1972, Solar Phys. 23, 78.
- Nagai, F 1980, Solar Phys. 68, 351.

Puetter, R.C. 1981, Ap.J., in press.

Richtmyer, R.D. and Morton, K.W. 1967, Difference Methods for Initial Value Problems, 2nd ed. (Interscience).

Schmeleva, O.P. and Syrovatskiik S.I. 1977, Solar Phys. **33**, 341.

Shoub, E. 1981, Ap.J., in press.

Somov, B.V., Spektor, A.R. and Syrovatskii, S.I. 1977, Izv.Acad.Sci. USSR, Phys.Ser. **41**, 273

Spitzer, L. 1962, Physics of Fully Ionized Gases, (Interscience).

Tscharnuter, W.M. and Winckler, K.-H. 1979, Computer Phys.Comm. **18**
171.

Vernazza, J.E., Avrett, E.H. and Loeser, R. 1981, Ap.J.Suppl. **45**,
635.

Zel'dovich, Ya. B. and Raizer, Yu. P. 1967, Physics of Shock Waves and High Temperature Hydrodynamic Phenomena, Vol. II
(Chapter VII) (Academic Press).

TABLE 1

COLLISION TIMES IN THE SOLAR ATMOSPHERE *

Quantity (cgs)	Temperature Minimum	Lower Chromo- sphere	Upper Chromo- sphere	Quiet Corona	Flaring Corona (I)†	Flaring Corona (II)†
T	3.6	3.7	3.9	6.3	7.5	7.0
n	15.3	14.3	11.3	9.0	9.0	10.7
P	3.1	2.1	-0.3	-0.3	0.9	2.1
x	-4.0	-3.0	-0.0			

Momentum Exchange Time Scales (s)

e-p	-7.3	-7.2	-7.0	-1.4	+0.3	-2.0
e-H	-4.3	-4.3	-3.2			
p-H	-3.3	-3.3	-3.2			

Energy Exchange Time Scales (s)

e-p	-4.1	-4.0	-4.1	+1.9	+3.7	+1.3
e-H	-1.1	-1.1	-0.2			
p-H	-3.3	-3.3	-3.2			

B(gauss)	2.2	1.8	0.6	0.6	1.2	1.8
----------	-----	-----	-----	-----	-----	-----

* All entries are \log_{10} of the relevant quantity.

† I: Before significant coronal density increase; II: After.

TABLE 2

Symbol and Constant Definitions^{*}

SUBSCRIPTS:

i	Denumerates spatial grid points (occasionally denotes atomic level).
j	Occasionally denotes atomic level.
l	Denotes atomic level (principal quantum number); when l appears with u then l denotes lower level.
u	Denotes upper atomic level.
c	Denotes continuum atomic level.
e,p,H	Denote electron, proton and hydrogen atom.

SUPERSCRIPT:

j	Denumerates temporal grid points.
---	-----------------------------------

SYMBOLS:

a	Artificial viscosity parameter = 2.0.
c	Speed of light.
f_{lu}	Line absorption oscillator strength.
g_l	Statistical weight of atomic level l.
g_i	Component of gravitational acceleration parallel to the loop axis.
h	Planck's constant.
k	Boltzmann's constant.
m	Mean mass per particle = $1.56 m_H$
n	Number density of particles.
P_{ul}	Escape probability for a photon in transition u-l.
t	Time

v	Bulk velocity.
v_{th}	Ion thermal velocity.
x	Ionized fraction $= \rho_c + x_H$
x_H	Ionization due to non-hydrogen atoms $= 8 \times 10^{-5}$
y	Number of non-hydrogen atoms per particle $= 0.15$.
z	Position measured along the loop from the apex.
A	Loop cross-sectional area
J_{ul}	Mean intensity in transition $u-l$ per unit frequency interval, at line center or at the continuum edge.
J	The set of J_{ul} for all transitions at a point in the atmosphere.
N	Column density of particles in the loop.
P	Plasma pressure
P^*	Total stress (plasma pressure plus viscous stress).
Q	Total energy input rate per particle.
R	Total radiative loss rate per particle.
R_{ij}	Total transition rate from state i to state j .
S_{ul}	Source function (at line center or continuum edge).
T	Temperature
ϵ	Mean thermal (translational plus internal) energy per particle.
ϵ_l	Binding energy for atomic level l (negative).
η	Viscosity
κ	Thermal conductivity
ν_{ul}	Line center or continuum edge frequency for transition $u-l$.
σ_{ul}	Opacity per particle (cross-section) at line center or continuum edge in transition $u-l$.
τ_{ul}	Optical depth (line center or continuum edge)

in transition $u-l$.

τ The set of τ_{ul} for all transitions at a point in the atmosphere.

ρ_l Fractional population of atomic level l .

ρ The set of ρ_l for all levels at a point in the atmosphere.

* "Particle" means "equivalent hydrogen atom," i.e. the number of particles is the number of neutral hydrogen atoms plus the number of protons.

TABLE 3

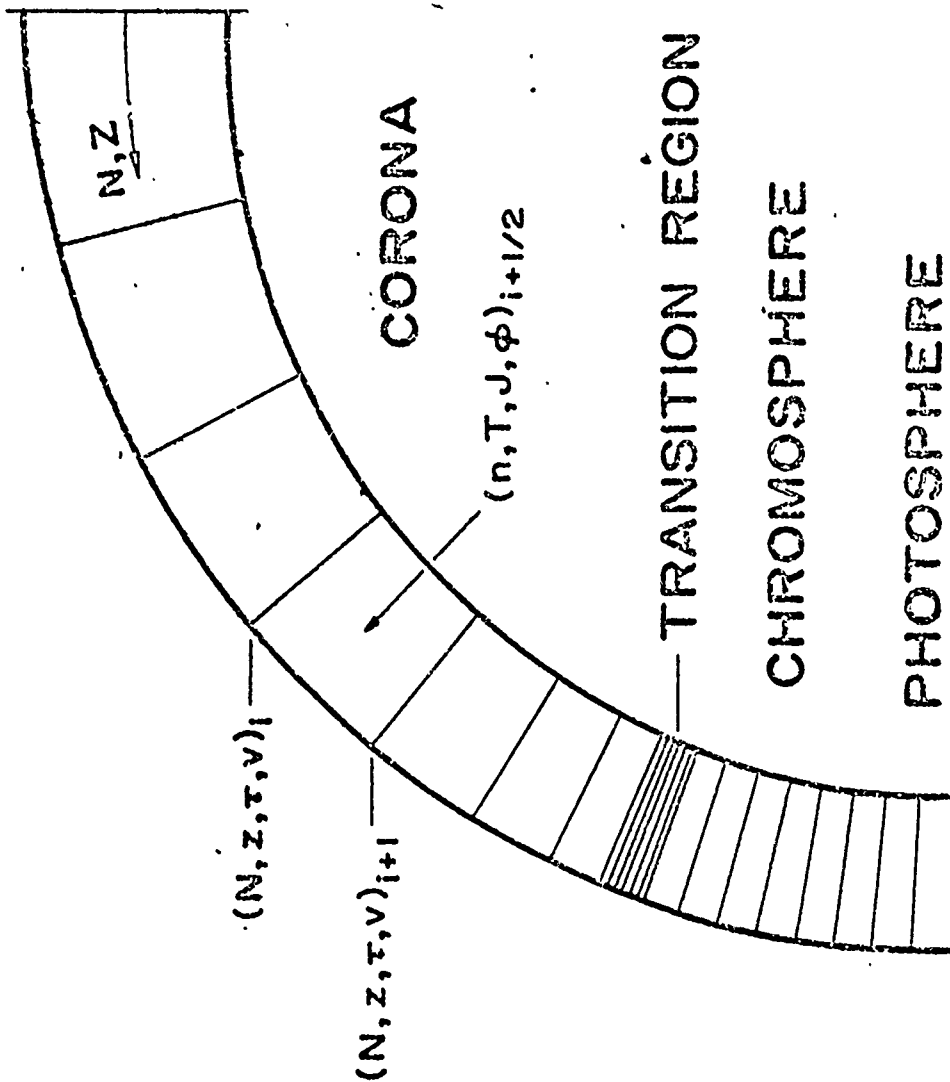
Comparison of Radiative Hydrodynamic Calculations

	Kneer & Nakagawa (KN)	Klein, Stein & Kalkofen (KSK)	Present Paper
Model atmosphere	Plane parallel solar chromo- sphere	Plane parallel stellar chromo- sphere	Loop geometry, solar chromo- sphere and corona
Discretization	Uniform Eulerian mesh	Lagrangian mesh uniform in ln N	Adaptive Lagrangian mesh
R.T. Method	Frequency dependent Eddington approximation	Frequency dependent with variable Eddington factors	Probabilistic (frequency integrated)
Model H atom	2b+c	2b+c (plus levels 3-10 in LTE)	2b+c
Transitions treated by R.T.	L α , Lc	Lc, Bc (includes free- free and bound- free opacities for levels 3-10)	L α , Lc, Bc
Approximate treatment of other transitions	H $^{-}$ (gray, optically thin), H α collisional approx- imation)		EUV, X-rays (optically thin), H (LTE, optically thin)
Atomic rate equations	Time dependent	Steady state	Time dependent

FIGURE CAPTION

Figure 1. Representation of physical and mathematical variables and boundary conditions in the finite-cell representation of a loop.

APEX: $i = 0$
 $N = 0$
 $z = 0$
 $\tau = 0$
 $v = 0$
 $T' = 0$
 $n' = 0$



Richard C. Canfield
Center for Astrophysics and Space Sciences, C-011.
University of California, San Diego
La Jolla, CA 92093

Alexander N. McClymont
Department of Mathematics
University of Waikato
New Zealand

vi) Flare Loop Radiative Hydrodynamics.

II. Radiative Stability of Empirical Models

This paper reports the development of techniques capable of predicting the linear hydrodynamic stability of the plasma contained in the flare loops. Only under certain circumstances can plasma in such a flux tube be hydrodynamically stable, even in the presence of thermal conduction. The contribution of this paper was to treat, for the first time, the effect of radiative transfer on radiative hydrodynamic stability. The significant finding is that radiative transfer has an important stabilizing effect in the chromosphere. We showed in this paper that if this stabilizing influence is neglected, and the plasma is treated as if it was optically thin, then the stabilizing influence of the chromosphere will be missed completely. The models built in the past, neglecting the stabilizing influence of the chromosphere, reached incorrect conclusions because these effects were not taken into account. Having developed these techniques, we will be able to avoid this mistake ourselves, in the future.

FLARE LOOP RADIATIVE HYDRODYNAMICS.

II. RADIATIVE STABILITY OF EMPIRICAL MODELS

A. N. McClymont^{*} and Richard C. Canfield

Center for Astrophysics and Space Sciences

University of California, San Diego

Submitted _____

Running Title: Radiative Stability of Empirical Loop Models

^{*} Now at Department of Mathematics, University of Waikato,
Hamilton, New Zealand

PRECEDING PAGE BLANK-NOT FILMED

ABSTRACT

The importance of loop structures in the corona, both for flares and the quiet sun, has stimulated considerable attention to questions of their radiative stability. Previous studies have focused their attention on the coronal part of the loop. In this paper we examine loop stability by treating the entire observable loop, from its photospheric footpoints to its coronal apex. This approach allows the chromosphere and corona to interact naturally, thus avoiding possibly artificial boundary conditions imposed at transition-region footpoints.

We develop a numerical eigenfunction method for the study of stability, which is based on the methods discussed in the preceeding paper. For exemplary purposes, we have applied these methods to several loop models based on semi-empirical model chromospheres, under the assumption that the rate of ambient energy input per unit mass of plasma depends only on column density. Our principal study is of a loop model based on the semi-empirical Model F of Vernazza, Avrett, and Loeser (1981).

We find that this loop model has one unstable eigenmode, with a growth time of two minutes. This mode appears in the transition region, centered around the peak of the optically thin radiative loss function at $T \approx 10^5$ K. However, we provide evidence that

suggests that this instability is not a feature of real loops. More importantly, we find that (1) this atmosphere is stable to the hydrogen-induced radiative instability of optically thin gases at temperatures around $10^{4.3}$ K; (2) if it were not for radiative transfer effects, this atmosphere would be dramatically unstable, with growth times in the range $1 \leq \tau \leq 18$ s; (3) the stability when radiative transfer is taken into account can be understood primarily as the result of the reduction of the hydrogen peak at $10^{4.3}$ K that would exist if the chromosphere were optically thin. This reduction is due to the significant optical depth, and consequent low escape probability, of radiation of the dominant coolant ($L\alpha$) at upper chromospheric temperatures.

I. INTRODUCTION

The instability of astrophysical plasmas whose temperature is such that radiative energy losses decrease with increasing temperature has been of interest for many years. The most important contribution to this study came from Field (1965), who gave the stability criterion for an isothermal plasma of finite extent, in the presence and absence of thermal conduction. Extension of this analysis to thermally conducting plasmas with temperature gradients, or to optically thick plasmas, is not easy. The stability of a conducting plasma in the presence of temperature gradients, specifically the corona and transition region of magnetic loop structures, has been discussed by Antiochos (1979), Habbal and Rosner (1979), and Hood and Priest (1980). These authors define the footpoints of the loop to be in the transition region, in order to avoid dealing with the optically thick chromosphere. Their boundary conditions fix either the conductive flux or the temperature. The majority opinion is that a loop with small or zero conductive flux through its transition-region footpoints is unstable, while a larger flux may render the loop stable. Our concern with the imposition of boundary conditions at the transition region has motivated the present study; physically, it seems more appropriate to apply

these boundary conditions lower in the atmosphere, say in the photosphere.

Craig and McClymont (1981a) and Craig, Robb, and Rollo (1981) have carried out a more complete treatment of the problem. They solved numerically the full one-dimensional hydrodynamic equations governing the evolution of plasma in a loop, including the lower transition region and the chromosphere, which were omitted in previous treatments. Their treatment is approximate in that they reduce the optically thin radiative loss function in the chromosphere by an empirical opacity factor (but see Section V). These results show that loops can be stable, even against finite amplitude perturbations. Instability is encountered only if the chromosphere is hot ($T \approx 10^5$ K) or if its mass is small compared to the coronal mass; theoretical analysis of this numerical result is given by Craig and McClymont (1981b) and McClymont and Craig (1981).

In this paper we take a further step toward realism by incorporating chromospheric radiative transfer. We couple the equations of one-dimensional hydrodynamics with a probabilistic treatment of radiative transfer in a two-level plus continuum hydrogen atom (Canfield, Puetter, and Ricchiazzi 1981). In Section II the equations used and the assumptions of the model are described only to the minimum extent necessary for this paper. For

fuller details of the equations and the numerical methods, the reader is referred to McClymont and Canfield (1981), hereafter referred to as Paper I. In Section III the linearized eigenmode equations are formulated, and in Section IV the stability of semi-empirical loop models is examined. The results are discussed in Section V, and the conclusions are stated in Section VI.

II. EQUATIONS AND ASSUMPTIONS

The hydrodynamic and radiative transfer equations describing the model loop are set out below in Lagrangian form for a loop of uniform cross-sectional area, using the methods and notation of Paper I. We assume that the ambient energy input heats electrons and ions equally and that the growth time of the instability will be greater than the coronal electron-proton temperature equilibration time scale, which can be as long as 1 minute in a long, cool loop. We are then justified in assuming a common electron and proton temperature. In the present investigation the ambient energy input Q is assumed to be constant per unit mass. The role of the functional form of Q in determining stability is discussed in Section V.

Along with the hydrodynamic equations, we solve the atomic rate equations for a two-level plus continuum hydrogen atom and

the probabilistic radiative transfer equations for the radiation field in the resulting transitions. The total radiative energy loss rate consists of the losses from these transitions plus losses from other elements (assumed optically thin), which we obtain from the radiative loss function computed by Cox and Tucker (1969) with the hydrogen contribution removed. To these losses is added an LTE approximation to H^- radiation, relevant in the lower chromosphere.

The geometry of the coronal loop, of semi-toroidal form, is defined by a rigid magnetic field (we assume a low β plasma). The footpoints of the loop are embedded in the photosphere, where the temperature remains fixed. We set the velocity to zero there, and there assume that the radiation field and atomic populations /are determined by LTE. For simplicity we take the loop to be symmetric about its apex; thus our second boundary condition defines the velocity and the gradients of temperature and density to be zero here. Lastly, optical depths are set to zero at the apex.

The acceleration of a fluid element is caused by gas pressure, gravity and viscosity as described by the momentum equation:

$$\bar{m} \frac{\partial v}{\partial t} = - \frac{\partial P}{\partial N} + \bar{m} g_{\parallel} + \frac{\partial}{\partial N} (n \eta \frac{\partial v}{\partial N}) \quad (1)$$

where N is the column density of atoms and ions. Rate of change of internal energy through ambient heating, radiative energy loss, thermal conduction, work done by pressure and viscosity is governed by the energy equation:

$$\frac{\partial \varepsilon}{\partial t} = Q - R + \frac{\partial}{\partial N} (n\kappa \frac{\partial T}{\partial N}) - P \frac{\partial v}{\partial N} + n\eta \left(\frac{\partial v}{\partial N}\right)^2. \quad (2)$$

The continuity equation

$$\frac{\partial n}{\partial t} = - n^2 \frac{\partial v}{\partial N} \quad (3)$$

is replaced, for computational purposes, by the equivalent equations defining velocity and density in terms of the spatial position of fluid elements;

$$n = \left(\frac{\partial z}{\partial N}\right)^{-1}; \quad \frac{\partial z}{\partial t} = v. \quad (4)$$

The population of an atomic level of hydrogen changes in response to transitions to and from the level according to the rate equation

$$\frac{\partial \phi_i}{\partial t} = \sum_{j \neq i} (R_{ji} \phi_j - R_{ij} \phi_i) \quad i=1,2,c. \quad (5)$$

In the probabilistic formulation the change in mean intensity in transition $u-l$ with optical depth, due to escape of photons and to a changing source function is

$$\frac{d}{d\tau_{ul}} (J_{ul} - S_{ul}) = -2\sqrt{p_{ul}} \frac{d(\sqrt{p_{ul}} S_{ul})}{d\tau_{ul}} \quad \begin{matrix} l=1, \dots, u-1 \\ u=2, c \end{matrix} \quad (6)$$

Finally, we relate optical depth (in the transition $u-l$) to column density through the opacity cross-section

$$\frac{d\tau_{ul}}{dN} = \sigma_{ul} \quad (7)$$

We also use the definitions of pressure

$$P = (1+y+x)nkT, \quad (8)$$

where x is the ionization, and thermal energy

$$\epsilon = \frac{3}{2} (1+y+x)kT + \sum_i \epsilon_i \phi_i, \quad (9)$$

together with expressions for η , R , κ , R_{ij} , S_{ul} , P_{ul} and σ_{ul} that are given in Paper I, along with a discussion of the numerical finite difference methods that are used to solve the equations.

III. FORMULATION AND SOLUTION OF THE LINEARIZED EQUATIONS

In this analysis we seek only isobaric modes of instability. It is easily shown that, provided radiative losses increase with increasing density, these modes are the most unstable. In fact, the modes should strictly be called quasi-isobaric, because we allow the pressure to change to maintain hydrostatic equilibrium as the gas moves infinitesimally in the gravitational field of the sun. We will use the term isobaric in this sense in this paper. The isobaric mode is obtained in the usual way by neglecting the inertial mass of the plasma, thus treating the momentum equation as steady state (see Antiochos 1979, Field 1965). The validity of the isobaric assumption can be checked a posteriori by comparing the growth time of an instability to the sound travel time across the region disturbed by the eigenmode. We have also used the steady state approximation to the rate equations, assuming that all atomic rates are much faster than the instability growth rate. This approximation is valid for all transitions except perhaps for recombination near the base of the transition region.

Introducing the eigenvalue (growth rate) ν we expand all quantities to first order, writing, for example,

$$T(N,t) = T_0(N) + T_1(N)e^{\nu t} . \quad (10)$$

Then equations (1) - (3) become, in the isobaric approximation,

$$v n_1 = - n_0^2 v_1' \quad (11)$$

$$0 = - p_1' + \bar{m} \frac{dg_{||}}{dz} z_1 \quad (12)$$

$$v \epsilon_1 = - R_1 + C_1 - p_0 v_1' \quad (13)$$

where (') denotes differentiation with respect to N , C_1 (a function of n_0 , T_0 , x_0 , n_1 , T_1 , x_1 and their derivatives) denotes the first order contribution of the conduction term, and R_1 is the linearized perturbation on the radiative loss rate.

With the approximation of steady state in the rate equations, equations (5) - (7) can be regarded simply as relationships which yield the atomic populations, intensities and optical depths at all points in the atmosphere, given the temperature and density distributions. Hence, for any given distributions of T_1 and n_1 , we can calculate immediately the corresponding distributions of pressure, radiative loss rate and conductivity.

We next eliminate v_1' by combining (11) and (13) to obtain

$$v \left(\epsilon_1 - \frac{P_0}{2} \frac{n_1}{n_0} \right) = C_1 - R_1 \quad (14)$$

and then note that n_1 and T_1 are related by the steady state equation

$$\left(P_1' / \frac{dg_{||}}{dz} \Big|_0 \right)' + \bar{m} n_1 / n_0^2 = 0 \quad (15)$$

which is obtained from the continuity equation (11) and the isobaric momentum equation (12). Since P_1 depends on n_1 , T_1 , and x_1 , and x_1 is known as a function of T_1 and n_1 , from equations (5) - (7) we can, in principle, find n_1 given T_1 . In the limit of vanishing gravity (an approximation used in previous loop stability studies), (15) is replaced by

$$P_1' = 0$$

or

$$n_1 / n_0 + T_1 / T_0 + x_1 / (1 + y + x_0) = P_1 / P_0 = \text{constant} \quad (16)$$

where, since the equations are linear, the constant is arbitrary.

Finally, v_1 may be expressed as a functional of T_1 using the continuity equation (11)

$$v_1 = -v \int_0^N \frac{n_1}{n_0^2} dN' \quad (17)$$

which, if gravity is non-zero, may be expressed using (15) as

$$v_1 = \frac{v}{m} p_1' / \left. \frac{dg_{||}}{dz} \right|_0 . \quad (18)$$

We have shown that all perturbed quantities may be expressed as functionals of the temperature perturbation T_1 , which we now choose as the principal variable. The other variables are determined self-consistently by the remaining (steady state) equations. We seek eigenfunctions $T_1(N)$ and eigenvalues v satisfying (11), (12), (14), (5), (6), and (7).

We now move directly to the discretized form of the equations in which spatial derivatives are replaced by finite differences. Then we can find the effect of a perturbation at one grid point on conditions at another, bypassing the usual linearization of the equations with respect to all variables and derivatives followed by substitution of finite difference operators for the differential operators. Thus we write (14) as

$$v \left[\epsilon_{1i} - \left(\frac{p_0}{n_0^2} \right)_i n_{1i} \right] = C_{1i} - R_{1i} \quad i=1, \dots, M \quad (19)$$

where the suffix i denotes grid point number. Then, recognizing that physical quantities at grid point i are affected, through the

coupling of radiative transfer and (for nearby points) through the spatial derivatives, by a perturbation on temperature at any other point, we write

$$\epsilon_{1i} = \sum_{j=1}^M \frac{d\epsilon_{0i}}{dT_j} T_{1j} \quad (20)$$

with similar expressions for n_1 , C_1 , and R_1 . Note that the derivative is a total derivative, incorporating changes induced through all possible pathways. Thus, assuming for illustration that pressure and ionization are constant ($P_1 = 0$; $x_1 = 0$), we have

$$\frac{dn_{1i}}{dT_{1j}} = - \left(\frac{n_0}{T_0} \right)_i \delta_{ij} \quad (21)$$

where δ_{ij} is the Kronecker delta function. But when ionization is not held fixed, this is not true (even with $P_1 = 0$);

$$\frac{dn_{1i}}{dT_{1j}} \neq 0 \quad (22)$$

because, for instance, a change in the temperature at a point deep in the atmosphere changes the radiation field at all points above; this in turn changes the ionization and so upsets the pressure

balance, demanding a change in density. Thus (19) becomes

$$\sum_j v \left[\frac{d\epsilon_i}{dT_j} - \left(\frac{p}{n^2} \right)_i \frac{dn_i}{dT_j} \right]_0 T_{1j} = \sum_j \frac{d}{dT_j} (C_i - R_i) \Big|_0 T_{1j} . \quad (23)$$

We write

$$X_i = (T_1/T_0)_i \quad (24)$$

and define

$$A_{ij} = \frac{d\epsilon_i}{d \ln T_j} \Big|_0 - \left(\frac{p_0}{n_0^2} \right)_i \frac{dn_i}{d \ln T_j} \Big|_0 \quad (25)$$

$$B_{ij} = \frac{d}{d \ln T_j} (C_i - R_i) \Big|_0 . \quad (26)$$

Then (23) can be written in standard eigenmatrix form as

$$[\underline{A}^{-1} \underline{B}] \underline{X} = v \underline{X} . \quad (27)$$

We evaluate the matrices of derivatives \underline{A} and \underline{B} numerically by perturbing the temperature at each grid point j in turn. At each perturbation, we re-solve the equations of radiative transfer and hydrostatic equilibrium, that is, we solve iteratively the set of equations (1) and (4) - (7) with velocity dependent terms and time derivatives set to zero (see Paper I for the solution procedure). The energy equation (2) is omitted, since the

temperature is predefined. Density (and hence, through (4), spatial position) is related to pressure, ionization and the known temperature through (9). At each grid point i we then evaluate ϵ_i , n_i and the right hand side of the energy equation and hence construct numerical approximations to the derivative matrices A and B. When the matrices are completely filled we solve (27) using a standard eigenvalue solver.

In comparing our analysis with that of Antiochos (1979) two facts should be kept in mind. First, when evaluating the derivative matrices by re-solving the equations with a perturbed temperature, we retain the same boundary conditions at the loop apex. Since these specify symmetry about the apex, we find only symmetric eigenmodes, whereas Antiochos pays most attention to anti-symmetric modes. Secondly, we note that the perturbations n_1 and T_1 in density and temperature are different from those in the Eulerian system used by Antiochos. Working in a Lagrangian system, the quantity n_1 represents the difference between the time dependent density and the original density at the same column depth. In Antiochos' Eulerian formulation, the original density is taken at the same spatial position. These definitions differ by a convective term;

$$n_{1L} = n_{1E} + n_0 \frac{\partial v_1}{\partial z} \quad (28)$$

where the subscripts L and E refer to Lagrangian and Eulerian coordinates. The same is true of the temperature perturbation T_1 .

IV. RESULTS

We have applied the stability analysis developed in Section III to several loop models based on semi-empirical atmospheres; the HSRA model of the average quiet sun (Gingerich et al., 1971); the plage model (P) of Basri et al. (1979); the bright network element model (F) of Vernazza, Avrett, and Loeser (1981). This last model (called VAL/F below) is one of a series of the most complete semi-empirical models of the solar chromosphere and photosphere presently available, being derived from observations in a wide variety of lines and continua. We will concentrate on our results for this model, and mention the others only as corroboratory evidence.

Despite the relative completeness of the VAL/F model, it does not permit us to study a loop defined in its entirety by observations; we must add a corona. In extending the atmosphere to higher temperatures, we assume that the conductive flux and its divergence vary in a physically plausible manner across the

transition region. We are then forced to discard the uppermost two tabulated points of the VAL/F model, as (together with the third point) they imply a huge flux divergence; this divergence is so large that it requires a large, negative ambient heating rate in this region. To further smooth the spatial distribution of heating, we found it necessary to increase the temperature gradient at $T \approx 4.5 \times 10^4$ K by reducing the spacing between grid points (4) and (5) of the VAL/F atmosphere from 6 km to 3 km.

Our final VAL/F loop model has a plausible combination of loop length, apex temperature and ambient heating rate. It was constructed by integrating the steady state equations (1), (2) and (4) for a fully ionized, optically thin plasma, into the corona, with a lower boundary condition specifying a conductive flux of $3 \times 10^4 \text{ erg cm}^{-2} \text{ s}^{-1}$ at $T = 5 \times 10^4$ K. In order to produce a reasonably high coronal temperature at the apex we had to assume that the heating function Q decreases toward the loop apex. The assumed variation of $Q(N)$ leads to an apex temperature of 1.1×10^6 K with a loop half-length of 2.9×10^9 cm.

The variation of temperature, pressure, conductive flux, and ambient heating rate throughout our entire VAL/F loop model are shown in Figure 1 (upper panel), against cell number on the numerical grid. The junction of the VAL/F chromosphere and our coronal extension occurs near cell number 30. We call attention to

the highly nonlinear relationship between cell number and column density; of the 82 cells into which our loop is partitioned, over 20 are assigned to the transition region. This avoids the pitfalls of under-resolution of the steep temperature gradients (previously discussed by Antiochos and Krall, 1978, McClymont and Canfield, 1980, Craig and McClymont, 1981, and Craig, Robb, and Kollo, 1981) which, in the analysis presented here, can give rise to spurious instabilities. In the lower chromosphere ($N \approx 10^{19.5} \text{ cm}^{-2}$) the ambient heating rate Q is balanced by H^- radiative losses, while in the upper chromosphere ($n \approx 10^{18.5} \text{ cm}^{-2}$), optically thick atomic hydrogen emission predominates. Above this level, radiation from elements heavier than hydrogen (assumed optically thin) is balanced by both conduction and ambient heating. Despite the precautions taken to realize a physically plausible loop structure, we anticipate that this loop may be unstable, since the heating function Q differs from the radiative loss rate R by at most a factor of two throughout the atmosphere (see Craig, McClymont, and Underwood, 1978, and McClymont and Craig, 1981).

In order to illustrate the importance of optically thick radiative transfer, we have performed two stability analyses of the VAL/F loop model. In both cases we use the full set of equations including radiative transfer in our model hydrogen atom. In the first case we compute the optically thick radiative loss

rate for hydrogen (treating the other elements as optically thin); in the second case we treat all emission as optically thin and use the total radiative loss function computed by Cox and Tucker (1969). Thus the role of radiative transfer in determining ionization equilibrium is maintained in both cases; only the radiative loss rates are different.

In case I, when we compute the optically thick loss rate for hydrogen, we find only one unstable mode, with a relatively slow growth rate of $7.2 \times 10^{-3} \text{ s}^{-1}$ (growth time $\approx 140 \text{ s}$). The form of this mode is given by the computed eigenfunction shown by a heavy curve in the lower panel of Figure 1. Comparison with the temperature structure of the atmosphere shows that the instability is sharply peaked in the transition region (cf. Antiochos 1979). The eigenfunction is clearly well resolved from a numerical point of view, but is physically very narrow—only about 60 km wide at half-maximum. It is sufficiently narrow that it is consistent with the isobaric assumption, since the sound travel time across the feature is only a few seconds. Since the electron-proton equilibration time in the transition region is only 0.1 s (see Spitzer, 1962), our one-temperature representation is also justified.

Very different results are obtained if we assume that all elements, including hydrogen, radiate as if their emission was

optically thin--Case II above. Whereas in Case I, there was only one growing mode, there are now ten! These are shown in the lower panel of Figure 1, as light curves. Of these, nine are entirely new, but the tenth is clearly the same mode found in Case I. Its shape is very similar, as is its growth rate ($6.7 \times 10^{-3} \text{ s}^{-1}$). The other nine unstable modes, which have growth rates ranging from 9.7×10^{-1} to $5.7 \times 10^{-2} \text{ s}^{-1}$, are all sharply peaked in the vicinity of the upper chromospheric temperature plateau, cells 40 through 48. Clearly radiative energy transport is a strong stabilizing mechanism in this region.

A further result worthy of note was established in the preliminary stability analysis of the VAL/F atmosphere, in which we did not modify its uppermost (transition region) structure in order to obtain a positive definite heating rate Q . We then found the full loop model to be completely stable. The same result, unconditional stability, was found for the HSRA atmosphere which, with our coronal extension to it, also has a region of large, negative Q in the upper transition region. On the other hand, the Basri et al. atmosphere, which has a positive peak in Q in the upper transition region much more pronounced than that in the VAL/F loop model, was found to have several unstable modes with much faster growth rates than the sole unstable mode of the VAL/F loop.

The behavior of the MSRA and Basri et al. model atmospheres with regard to the effect of opacity in the hydrogen transitions is entirely consistent with the effects observed in the VAL/F model. In all cases many unstable modes were found in the temperature regime $T \approx 2 \times 10^4$ K when hydrogen emission was treated as optically thin; these were suppressed by the inclusion of the effects of hydrogen opacity in the radiative loss function.

V. DISCUSSION OF RESULTS

It is of considerable interest that when hydrogen radiative transfer is taken into account, no chromospheric instability is found. The reason for stability becomes clear when one examines the effect of opacity on the radiative loss process. The region that is unstable in the optically thin case, Case II, is the upper chromospheric temperature plateau, which extends from cell 40 to cell 48. Consider, for instance, the middle of this range, where the temperature is about 2.5×10^4 K. The optical depth of the most effective radiator in this range, $L\alpha$, is about 25, corresponding to an escape probability of only about 10^{-2} . Hence, newly created $L\alpha$ photons scatter approximately 10^2 times before ultimately escaping. (Since this optical depth is much smaller than the degradation depth, virtually all photons created here escape). This large number of scatterings makes both the radiation

field and the atomic populations highly nonlocal. This means that no local treatment (such as an optically thin, or even effectively thin, approximation) can be fully satisfactory in its representation of radiative hydrodynamic phenomena.

In the optically thin or effectively thin case, $L\alpha$ is largely responsible for the bump near $\tau \approx 2.5 \times 10^4 \text{ K}$ in the isobaric radiative loss function shown in Figure 2. This is the usual function $f(T)$ shown by Cox and Tucker (1969), McWhirter et al. (1975) and others, divided by T . The function $f(T)/T$ is of interest because in the absence of thermal conduction, the gas is unstable to isobaric perturbations whenever the slope of the function is negative (i.e. for $10^{4.2} < T < 10^{4.5} \text{ K}$ and $T > 10^{4.9} \text{ K}$). In the solar atmosphere, opacity effects may be important in the former range. The long-dashed curve in Figure 2 is from Cox and Tucker (1969); the dot-dashed curve is from McWhirter et al. (1975). There are at most factor-of-two differences between the two different authors' results where the contribution of hydrogen is dominant, at $T < 10^{4.5} \text{ K}$. The short-dashed curve is from Cox and Tucker (1969), with the hydrogen contribution subtracted off. This is the function we use to represent optically thin losses.

Although the question of radiative stability in an optically thick medium is complicated by highly nonlinear interactions and nonlocal effects, we can demonstrate very clearly the effect of

opacity by computing the effective isobaric radiative loss function for the optically thick case. This is given by the solid curve in Figure 2, which shows the run of the computed values of $R/(n_e T)$ as a function of temperature through the upper chromosphere and lower transition region of the VAL/F loop model. Clearly the effect of opacity is to greatly reduce the importance of hydrogen emission in comparison with the other elements. Note that the effective loss function is not quite strictly increasing at all temperatures below 10^5 K. This shows that either (a) even at $T \approx 2 \times 10^4$ K energy transport by thermal conduction is sufficient to stabilize the residual instability and/or (b) energy transport by radiative transfer (not accounted for in the first approximation by the effective loss rate) fulfills the same role. We will return to this question in a later study.

We would expect that even in the absence of an efficient stabilizing mechanism, instability over a narrow range of temperature would not pose a threat to the overall stability of solar loops. The atmosphere will merely arrange itself so that the regions of instability are spanned by mini-transition regions, so that virtually no unstable material is present.

We now turn to a discussion of the unstable transition region mode, which has a growth time of 140 s, and peaks at $T \approx 10^5$ K. The fundamental reason for the existence of this instability is

probably the fact that radiative losses are balanced very nearly (within a factor of two) by ambient heating, throughout the VAL/F loop model. Thus, conductive stabilization is ineffective (Craig, McClymont, and Underwood, 1978). In our model based on the Basri *et al.* chromosphere, in which an even closer balance between radiative losses and ambient heating exists, we find much faster growing instabilities in the transition region ($T \approx 10^5$ K). On the other hand, the large negative heating rates in the upper transition region that appeared in our HSRA and preliminary VAL/F loop models, force a greater conductive dominance than is expected in nature. We found these atmospheres to be completely stable.

As no physical mechanism is known that would preferentially heat or cool a narrow region of rapidly varying temperature, it is generally believed that the structure of the real transition zone is determined by a balance between conduction and radiation (e.g. Moore and Fung, 1972, Craig, McClymont, and Underwood, 1978). Although Antiochos (1979) and Hood and Priest (1979) have contended that coronal loops are dramatically unstable, even with a spatially uniform ambient heating function (which allows a close balance between conduction and radiation in the transition region), Craig and McClymont (1981b) and McClymont and Craig (1981) have recently demonstrated that this result is due to the fact that these authors truncated the loop in the transition zone,

thus neglecting the influence of the chromosphere.

The influence of the chromosphere may be argued as follows. Consider an atmosphere with given coronal and chromospheric temperatures. If the ambient heating peaks in the corona and is small at transition region temperatures, a steep transition region is called for to carry the required conductive flux. In this situation the corona and chromosphere are strongly coupled, and the radiatively stable chromosphere and lower transition region are able to act as a heat sink for the corona, and so is a stabilizing influence. On the other hand, a transition region carrying relatively little flux is produced by relatively pronounced heating in the transition region. In this case the radiatively unstable corona is effectively decoupled from the lower atmosphere; it cannot get rid of the excess energy that results from a (positive) temperature perturbation.

It should be noted that not only is the spatial variation of heating important in determining stability, but any dependence of the heating rate on depth and temperature is just as important as the dependence of the radiative loss rate on these parameters. Hence the observational evidence for loop stability may lead us to constraints on the coronal heating mechanism. A first step in this direction was taken by Rosner, Tucker and Vaiana (1978), and the analysis has been elaborated by McClymont and Craig (1981).

Finally, we note that the dynamic simulations and stability analyses performed in the optically thin approximation by Craig, McClymont, and Underwood (1978), Craig and McClymont (1981a,b), Craig, Robb, and Rollo (1981), and McClymont and Craig (1981) have used the empirical radiative loss function $f(T)/T = 10^{-26} \times (T/10^5 \text{ K})^{\pm 2} \text{ erg s}^{-1} \text{ cm}^3 \text{ K}^{-1}$ (positive exponent for $T < 10^5 \text{ K}$), which is a convenient fit to the major features of the effective loss function shown in Figure 2. We therefore suggest that future work in the optically thin approximation should omit the hydrogen peak in the all-species curves of Figure 2.

VI. CONCLUSIONS

Our primary conclusions are as follows:

1. Although the complete loop model that we have developed based on the Vernazza, Avrett, and Loeser Model F (VAL/F) is globally unstable with a growth time of 140 s, according to our isobaric linear stability analysis, this instability is driven by radiative instability in the transition region in the familiar manner (see, e.g., Antiochos 1979). Since we have been obliged to build the complete loop model by attaching two separate models based on completely different techniques, this instability may not be physically significant. We believe that the peak in the heating rate in the transition region is unrealistic, and may be

the major cause of the instability (see Craig, McClymont, and Underwood, 1978). The requirement that some loops be long-lived, as observed, may enable constraints to be placed on the form of the coronal heating mechanism (see McClymont and Craig, 1981). We do not consider this instability further, except to note that the sole unstable eigenmode for this atmosphere is strongly localised in the transition region, and has no significant chromospheric extension.

2. No radiative instability is indicated in the chromosphere defined by the VAL/F model. This is very significant, for three reasons. First, we show that were it not for radiative transfer in the upper chromosphere of the VAL/F model, it would be highly unstable. We find that in the absence of radiative transfer, many eigenmodes would exist, sharply confined to the upper chromospheric temperature plateau, with growth times in the range 1 - 20 s. Second, although the only hydrogenic transitions considered are $L\alpha$, the Lyman continuum, and the Balmer continuum, these include the dominant contributors to the optically thin radiative loss function for all elements. Third, the VAL/F is the most realistic and definitive semi-empirical model of the brightest structures of the chromospheric network.

3. The reason for the stability of the VAL/F model is seen to be the high optical depth in $L\alpha$, the dominant coolant at the level

of the upper chromospheric plateau. The high optical depth means that the probability of direct escape of newly created photons is small, and makes them likely to scatter many times before escaping. This makes the radiative loss process very nonlocal. The effect is to smooth the hydrogen peak at temperatures around $10^{4.3}$ K in the effective radiative loss function for all elements.

We speculate that the stabilizing effect of opacity is a general feature of the sun's chromosphere (and by implication, many other kinds of stars); if this is so, it means that the stability of coronal loops can be studied without concern for the destabilizing effects of the hydrogen peak in the radiative loss function (cf. Craig and McClymont, 1981a,b, Craig, Robb, and Rollo, 1981, and McClymont and Craig, 1981). If the stabilizing effect of opacity is not a general feature under all chromospheric conditions, then the structure of the atmosphere should be determined to some extent by the stability requirement; the atmosphere will arrange itself in a series of plateaus connected by mini-transition regions, each transition region spanning an interval of instability. We suggest that the testing of semi-empirical models for stability might enable a closer constraint to be placed on the derived structure.

With reference to future work, we see the necessity of constructing an atmosphere, from photosphere to corona, that is

consistent with the physics in the theoretical model, rather than relying on observationally derived atmospheres that may exhibit features not described within the physical framework of the model. Such atmospheres would be interesting, even for simplified models of the radiative processes such as we have used here. Of course, models based on a treatment of a more complete set of elements than just a two-level plus continuum hydrogen atom would be more relevant to comparison with semi-empirical models and real observations. Our stability analysis should be complemented by a non-linear dynamic calculation, which will be the subject of the next paper of this series (An, Canfield and McClymont, 1982, Paper III). Our stability analysis should also be extended to the study of antisymmetric linear modes (Antiochos, 1979). Finally, Vernazza, Avrett, and Loeser (1981) have also derived models of other features of the solar atmosphere; it would be interesting to see if they, too, are stable to the hydrogen-induced radiative instability.

We wish to thank George Fisher for his help in generating the VAL/F loop model discussed in this paper. This research was sponsored by NASA grant NSG-7406 and AFOSR grant 76-3071. The computations were carried out at the National Center for Atmospheric Research, which is sponsored by the National Science Foundation.

REFERENCES

- An, C.-H., Canfield, R.C., and McClymont, A.N. 1982, in preparation.
- Antiochos, S.K. 1979, Ap.J. 232, L125.
- Antiochos, S.K., and Krall, K.R. 1979, Ap.J. 229, 788.
- Basri, G.S., Linsky, J.L., Bartoe, J.-D.F., Brueckner, G.E., and Van Hoosier, M.E. 1979, Ap.J. 230, 924.
- Cox, D.P., and Tucker, W.H. 1969, Ap.J. 157, 1157.
- Craig, I.J.D., and McClymont, A.N. 1981a, Solar Phys. 70, 97.
- Craig, I.J.D., and McClymont, A.N. 1981b, Solar Phys. (submitted).
- Craig, I.J.D., McClymont, A.N., and Underwood, J.H. 1978, Astron.Astrophys. 70, 1.
- Craig, I.J.D., Robb, T.D., and Rollo, M.D. 1981, Solar Phys. (submitted).
- Field, G.W. 1965, Ap.J. 142, 531.
- Gingerich, O., Noyes, R.W., Kalkofen, W., and Cuny, Y. 1971, Solar Phys. 18, 347.
- Habbal, S.R., and Rosner, R. 1979, Ap.J. 234, 1113.
- Hood, A.W., and Priest, E.R. 1980, Astron.Astrophys. 87, 126.
- McClymont, A.N., and Canfield, R.C. 1980, in M. Dryer and E. Tandberg-Hanssen (eds.), Solar and Interplanetary Dynamics, D. Reidel Publ.Co., Dordrecht.
- McClymont, A.N., and Canfield, R.C. 1981, Ap.J. (submitted), Paper I.

McClymont, A.N., and Craig, I.J.D. 1981, Nature (submitted).

McWhirter, R.W.P., Thonemann, P.C., and Wilson, R. 1975, Astr.Ap.
40, 63.

Moore, R.L., and Fung, P.C.W. 1972, Solar Phys. 23, 78.

Rosner, R., Tucker, W.H., and Vaiana, G.S. 1978, Ap.J. 220, 643.

Spitzer, L. 1962, Physics of Fully Ionized Gases, Interscience,
New York.

Vernazza, J.E., Avrett, E.H., and Loeser, R. 1981, Ap.J.Suppl. 45,
319.

FIGURE CAPTIONS

Fig. 1. (Top) The run of temperature (T), pressure (P), ambient heating per particle (Q), and conductive flux (F) in the VAL/F loop model, as a function of cell index and the logarithm of the column density (N). (Bottom) Unstable eigenfunctions, in both thick and thin cases, on the same abscissa as above.

Fig. 2. Isobaric radiative loss functions $f(T)/T$, as a function of temperature (T). The Cox and Tucker (1969) "no hydrogen" curve is their "all species" curve, with their hydrogen contribution removed.

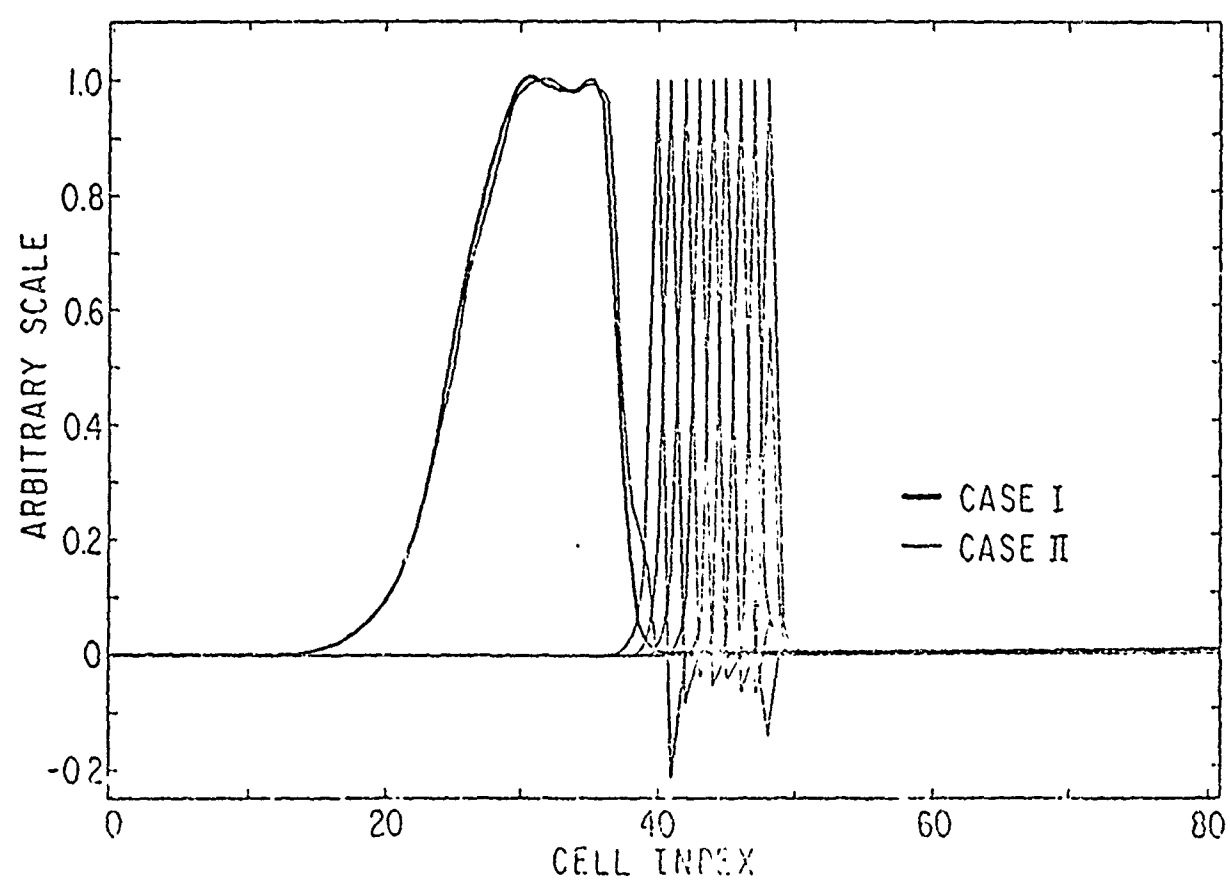
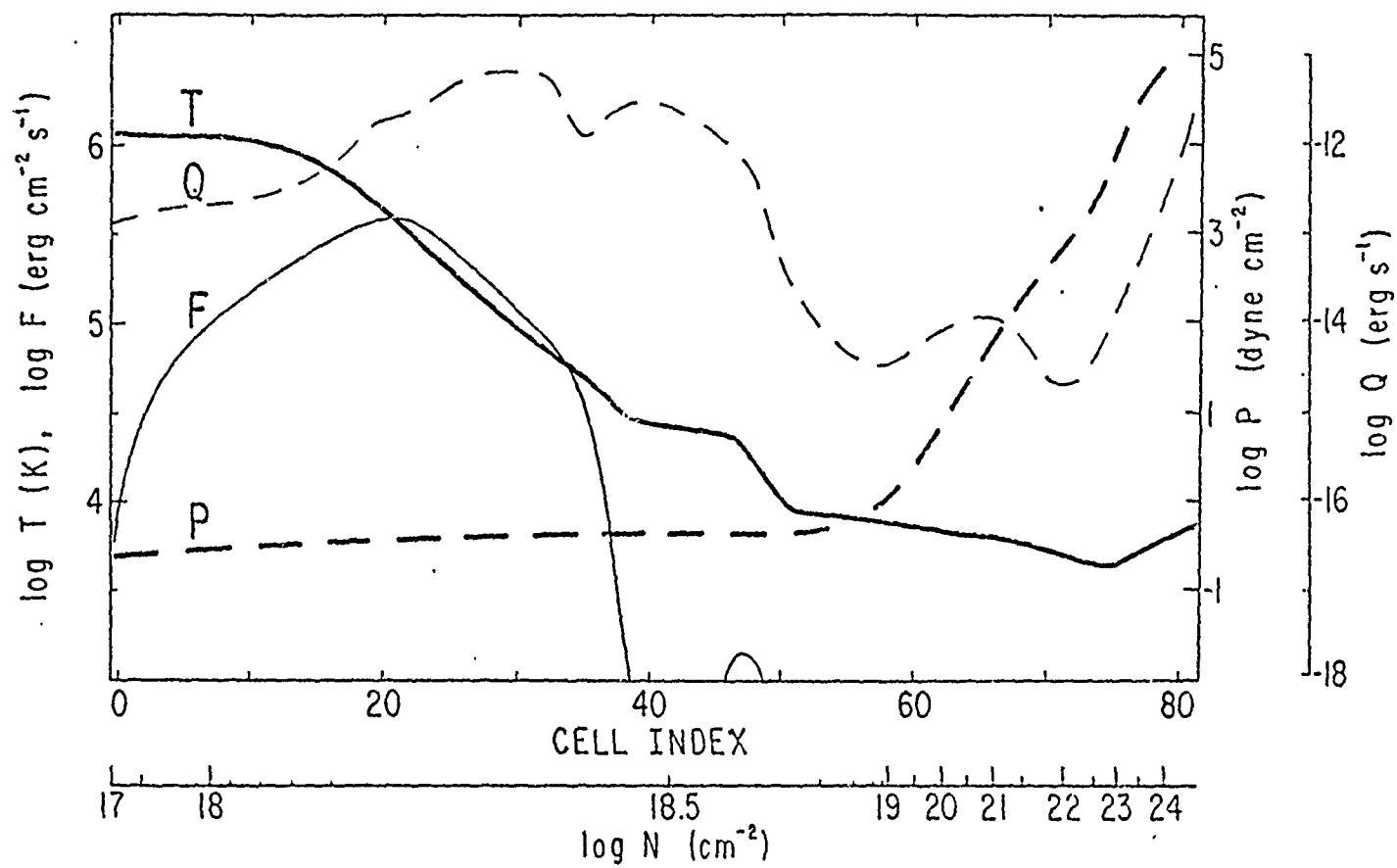


Figure 1.

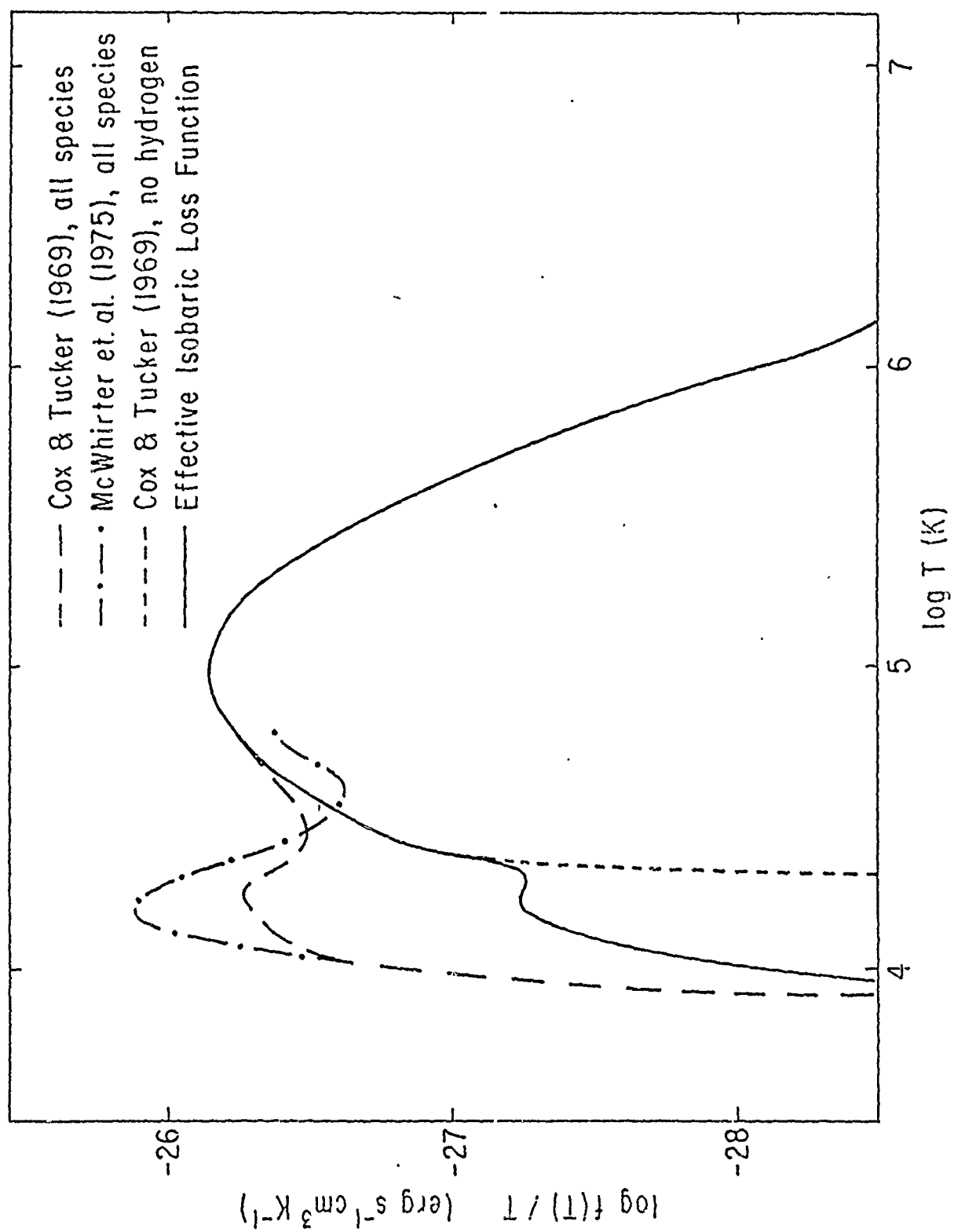


Figure 2.

AUTHORS' ADDRESSES

Richard C. Canfield

Center for Astrophysics and Space Sciences

Code C-011

University of California, San Diego

La Jolla, CA 92093

Alexander N. McClymont

Department of Mathematics

University of Waikato

Hamilton, New Zealand

vii) The Effects on the MHD Stability of Field Line Tying
to the End Faces of a Cylindrical Magnetic Loop

One of the important new directions that we believe we should be taking is to merge the concepts of radiative hydrodynamics, described in Section vi, and magnetohydrodynamics. Hence we have begun to do some work in the MHD area; this paper represents such work, accomplished during the grant. It bears no direct relationship to the other work done to date, but is indirectly related in that our radiative hydrodynamic work assumes that the plasma is confined by a sufficiently strong magnetic field, so that the motion of the plasma is confined to follow the field, which is rigid. In this paper we studied the influence of the fact that the field lines are tied motionless in the solar photosphere. We found that this magnetic field line tying effect is negligible, for loops which are long and narrow. This is relevant, because observed loops have this property.

THE EFFECTS ON THE MHD STABILITY OF FIELD LINE TYING TO THE END FACES OF A CYLINDRICAL MAGNETIC LOOP

CHANG-HYUK AN

Center for Astrophysics and Space Sciences, University of California,
San Diego, La Jolla, Calif. 92093, U.S.A

(Received 10 April, 1980; in final form 5 March, 1981)

Abstract. We examine the magnetohydrodynamic (MHD) stability of a magnetic loop, taking into account field line tying at its foot points. We use the ideal MHD energy equation to derive a stability equation for a specific class of perturbations.

We found that for a loop with large aspect ratio (≥ 10) the field line tying effect is negligible to the $m = 1$ kink mode but important to the localized modes. The stability criterion for high m localized modes is derived and compared with the Suydam criterion. The result shows that for the perturbation of the class studied, there are two effects of field line tying, one is a field line bending effect which is always stabilizing and the other is a shear effect which is stabilizing or destabilizing depending on the sign of the gradient of potential magnetic field. The net effect of field line tying is determined by the sum of these two effects.

The result of this work is contrary to the result of Hood and Priest, in which they found that the field line tying effect is significant to the $m = 1$ mode. We believe that the contradiction comes from their incomplete minimization of the energy equation.

1. Introduction

Numerous Skylab observations have shown that solar flares occur in magnetically confined loops. The geometry of these loops and the critical role of MHD instability on the flare mechanisms have been discussed in several observational papers (Foukal *et al.*, 1975; Vorpahl *et al.*, 1975; Gibson, 1977; Cheng, 1977). There is an obvious similarity of the geometry and equilibrium magnetic field configuration of solar loops and tokamaks used in magnetic fusion research. This has lead several authors (Chiuderi *et al.*, 1977; Giachetti *et al.*, 1977; Van Hoven, 1977) to apply the ideal MHD stability theory developed in fusion research to study the magnetic field configuration that might explain the apparent stability of solar loops. This similarity also promoted a solar flare model (Spicer, 1977) based on resistive MHD instability theory.

However, there are several differences between solar loops and tokamaks, which might significantly alter the results of MHD stability as derived for tokamaks. The thermal effects (i.e., heat conduction, radiation, mechanical heating, etc.) are much more important in solar loops (Foukal, 1975, 1976; Rosner *et al.*, 1978) than in tokamaks. Solar loops have approximately semitoroidal geometry with the magnetic field frozen at the foot points of the loop (Foukal, 1975) and with non-uniform equilibrium profiles (i.e., density, temperature, magnetic field, etc.) along the loop direction (Somov *et al.*, 1976), while tokamaks are closed toroidal loops with

axisymmetric equilibrium profiles. Furthermore, because solar loops are not confined by rigid boundaries, various external effects may play important roles on determining the stability of the magnetic loop. For better theoretical understanding of the solar flare mechanism, it is very important to consider more realistic flare models and to apply the well established MHD stability theory from the magnetic fusion research. Full, realistic consideration of solar flares, however, is impossible to handle. Under the complex conditions of solar flares one must take a step by step approach to realistic modeling.

Among the differences between tokamaks and flare loops, the most visible is that flare loops are not toroidal, but have foot points fixed in the photosphere. In this paper, we choose the effect of field line tying at the foot points of the loop as a step toward a more realistic flare loop model. This study does not depart much from the MHD stability theory for tokamaks and is the simplest problem solvable within the framework of the MHD theory. This study is aimed at clarifying how much the field line tying affects the MHD stability and how the effect alters stabilizing mechanisms in flare loops. This work will also give a good indication of the importance of field line tying for further study of more realistic and more complicated flare loop conditions.

The model adopted is a semi-toroidal loop in which it is assumed that the equilibrium magnetic field and plasma pressure are axisymmetric and the cross section of the loop is uniform along the loop direction. Furthermore, the solar loops we want to model are observed to be thin in proportion to their length, i.e., they have large aspect ratio (the ratio of the loop radius to the radius of the loop cross section). In this case, a semi-toroidal geometry can be approximated by a circular cylinder. We use the ideal MHD energy equation to derive the stability condition of the loop.

There are several papers that treat the field line tying effect in a cylindrical plasma loop. Raadu (1972) studied the kink instability of a cylindrical loop considering field line tying by neglecting the plasma pressure terms in the energy equation. Solov'ev (1971) also treated the same problem by assuming that plasma is divergency free i.e., he neglected the term $\gamma P_0 |\nabla \cdot \xi|^2$ in the energy equation [see Equation (1)]. They impose boundary conditions in which the plasma displacement is zero while the magnetic field is not frozen at the foot points of the loop. Their results show the field line tying enhances the stability of the loop plasma. A more complete treatment of the field line tying problem was done by Hood and Priest (1979). They included the finite pressure as well as the compressibility of the plasma, both of which were neglected by Raadu (1972) and Solov'ev (1971). They minimized the energy equation and applied Newcomb's theorem (Newcomb, 1960) to study the effect of field line tying on the global stability of a circular cylindrical loop. When minimizing the energy equation, for simplicity, they assume that the component of the perturbed displacement parallel to the field is zero. With the assumptions they made, the energy equation is not completely minimized, as they mention in their paper. As a consequence, their results show higher stability. The perturbed displacement ξ with field line tying becomes identical to ξ without field line tying as we let $h = 0$ in the expression of Hood and Priest (1979). Therefore, their minimized energy equation in

the case with
without field
equation with
assumption
departs more
zero. The co
Shafranov li

This paper
a special clas
field complet
pressure. Thi
equation is r
Fourth, we st
the stability c

The analys
be very large
line tying effe
is defined as
that of an in
field line tyi
becomes mor
surface. We
and compare
field line tyin
two condition
compressibili
stabilizing for
additional sta
field gradient
criterion deri
for various lo
magnitude of
gradient of p
and extremel
of the field g
data.

This paper
the perturbed
end faces of a
studied near
localized mod
Section 4. In S
the results for

solar loops are not play important roles on theoretical understanding of more realistic flare activity from the magnetic field. However, is impossible to just take a step by step

the most visible is that the photosphere. In this case, the foot points of the loop as a step to depart much from the ideal case, which is solvable within the framework of the MHD. Regarding how much the field line tying affects the stabilizing mechanisms, the importance of field line tying under ideal flare loop conditions, it is assumed that the magnetic field is symmetric and the cross section is circular. Furthermore, the solar loops are considered to be incompressible, i.e., they have the same cross section as a circular cylinder. We consider the condition of the loop in a cylindrical plasma loop considering field line tying. Solov'ev (1979) is a divergency free i.e., $\nabla \cdot \mathbf{v} = 0$. Equation (1)] They mention that the current is zero while the results show the field line tying. A complete treatment of the field line tying (1979). They included the field line tying, both of which were minimized the energy equation to study the effect of field line tying on the loop. When minimizing the component of the perturbed magnetic field, they made, the energy equation is minimized in their paper. As a perturbed displacement ξ with field line tying as we let $h = 0$ in the minimized energy equation in

the case with field line tying should be identical to the minimized energy equation without field line tying (Newcomb, 1960). However, one cannot derive the energy equation without field line tying by letting $h = 0$ in their energy equation due to the assumption that ξ_{\parallel} is zero. As a result, they found that the critical twist for stability departs more from the Kruskal-Shafranov limit (Kadomtsev, 1966) as h decreases to zero. The correct result should show that the critical twist should be the Kruskal-Shafranov limit for $h \rightarrow 0$.

This paper departs from the above papers in the following points. First, we choose a special class of perturbed displacements ξ , which makes the perturbed magnetic field completely frozen at the foot points. Second, we do not neglect the plasma pressure. Third, we do not assume the parallel component of ξ to be zero. The energy equation is rigorously minimized for three independent components of ξ , ξ_r , ξ_{θ} , ξ_z . Fourth, we study the field line tying effect on both local and global modes. We derive the stability criterion for localized modes for the case with field line tying.

The analysis is characterized by assuming the aspect ratio of the cylindrical loop to be very large. The problem is reduced to a boundary layer problem in which the field line tying effect is important only near a mode rational surface [mode rational surface is defined as a magnetic surface on which the field lines have the same topology as that of an instability being considered (Bateman, 1978)]. This study indicates that field line tying is unimportant to the large scale internal MHD instability, but becomes more important as a perturbation is more localized near a mode rational surface. We derive a stability criterion in the limit of high poloidal mode number m and compare it with the Suydam stability criterion (Suydam, 1958). The effects of field line tying on the stability are not as obvious as we might expect because of the two conditions, completely freezing of field lines at the foot points of the loop and the compressibility of the plasma ($\nabla \cdot \mathbf{v} \neq 0$). The freezing of field lines produces a stabilizing force in addition to the shear stabilization and the compressibility gives an additional stabilizing or destabilizing force depending on the sign of the potential field gradient. Detailed comparisons between the Suydam criterion and the stability criterion derived in this work are made in order to evaluate the field line tying effects for various loop conditions. We find that field line tying enhances the stability if the magnitude of the potential B field is much larger than non-potential B field and the gradient of potential B field is negative. If the gradient of potential B field is positive and extremely large, the field line tying might reduce the stability. The importance of the field gradient to flare is mentioned in connection with the observational data.

This paper is organized as follows. In Section 2, energy equation is minimized by the perturbed displacement which makes the perturbed magnetic field zero at the end faces of a cylinder. In Section 3, the effect of field line tying on the stability is studied near and far from the mode rational surface, and a stability criterion for a localized mode is derived. The physical meaning of the result is presented in Section 4. In Section 5, the results of the study are summarized and the implication of the results for the flare loops is discussed.

2. Energy Equation and its Minimization

In order to study the effects of field-line tying on the stability of flare loop, several assumptions are made for simplification of the problem. A semi-toroidal flare loop with large aspect ration is approximated by a circular cylindrical loop with uniform cross section along the loop direction. Equilibrium quantities are assumed to be functions only of r , the radical coordinate. Since the time scales of conduction, radiative cooling and mechanical heating are much larger than the MHD times scale under most flare loop conditions, adiabatic energy equation is adopted. After neglecting the resistivity for simplification, we can use the ideal MHD equations. The effect of field line tying on the resistive instability will be briefly considered later. The most convenient way to study the stability of ideal MHD is to use the energy equation (Bernstein *et al.*, 1958). In the study of loop stability our attention is confined only to internal MHD modes in which the plasma loop is surrounded by a rigid conducting wall rather than coronal atmosphere.

The energy equation for the internal modes (Newcomb, 1960) is

$$2\delta W = \int [\gamma P_0 |\nabla \cdot \xi|^2 + (\xi \cdot \nabla P_0)(\nabla \cdot \xi^*) + |B_1|^2 + (\nabla \times B_0) \cdot \xi^* \times B_1] d^3x, \quad (1)$$

where P_0 , B_0 are equilibrium pressure and magnetic field and ξ , B_1 are perturbed displacement and perturbed magnetic field respectively. We use ξ^* , the complex conjugate of ξ , to make δW real and self adjoint for complex perturbations such as Equation (7). The perturbed magnetic field B_1 is defined as

$$B_1 = \nabla \times (\xi \times B_0). \quad (2)$$

The equilibrium equation for a circular cylinder is

$$\frac{dP_0}{dr} + B_z \frac{dB_z}{dr} + \frac{B_\theta}{r} \frac{d}{dr}(rB_\theta) = 0. \quad (3)$$

Here P_0 is normalized with a typical magnetic field B_0^2 , B_z and B_θ with B_0 , and a length is normalized with a , radius of the loop cross-section. The geometry and the coordinate system is given in Figure 1.

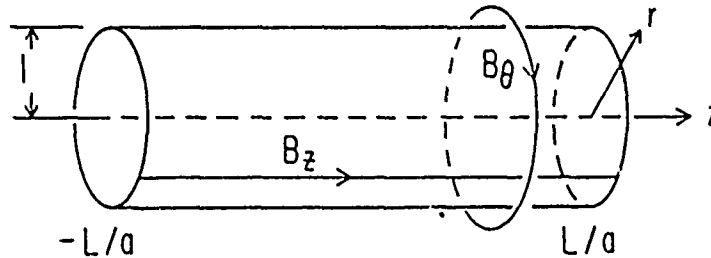


Fig. 1. Coordinate system of a circular cylinder with poloidal and toroidal B field, B_θ and B_z respectively.

The field-line

B_1

The boundary condition on ξ

$\xi =$

$\frac{\partial \xi}{\partial z}$

There have been many studies relating to the field-line tying to the force-free field. Hood and Priest (1979) choose a perturbation

$\xi(r)$

Here, $n \geq 2$ and it is noted that (7) results obtained are the least stable perturbed displacement in the rest of the spectrum (including $n = 1$ coefficient in (7)).

For a loop, Equation (7) is used.

By using Equation

$2\delta W$

Here dS is an area element and quantities are eliminated to obtain

$2\delta W$

By changing the variables

$\eta =$

$\xi =$

* In this paper we

tion

lity of flare loop, several semi-toroidal flare loop and toroidal loop with uniform properties are assumed to be on the scales of conduction, than the MHD times scale equation is adopted. After ideal MHD equations. The energy equation is considered later. The case the energy equation is confined only to a rigid conducting

(1960) is

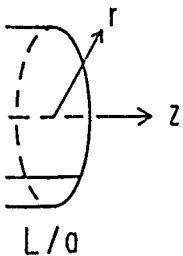
$$\nabla \times \mathbf{B}_0 \cdot \xi^* \times \mathbf{B}_1] d^3r, \quad (1)$$

and ξ , \mathbf{B}_1 are perturbed. We consider ξ^* , the complex conjugate perturbations such as

(2)

(3)

B_z and B_θ with B_0 , and a constant. The geometry and the



toroidal B field, B_θ and B_z

The field-line tying at $z = \pm L/a$ is expressed as

$$\mathbf{B}_1 = \nabla \times (\xi \times \mathbf{B}_0) = 0 \quad \text{at} \quad z = \pm L/a. \quad (4)$$

The boundary condition (Equation (4)) can be satisfied if we impose as boundary condition on ξ

$$\xi = 0, \quad (5)$$

$$\frac{\partial \xi}{\partial z} = 0. \quad (6)$$

There have been controversies about the boundary condition describing the field line tying to the foot points.[†] However, we note that the boundary condition of ξ used by Hood and Priest (1979) ($\xi = 0$ at $z = \pm L/a$) does not alter our results at all. We choose a perturbation which satisfies the conditions (5) and (6):

$$\xi(r, \theta, z) = \xi(r) \cos^n \alpha z e^{i(m\theta + \kappa z)}, \quad (7)$$

$$\xi(r) = (\xi_r(r), \xi_\theta(r), \xi_z(r)).$$

Here, $n \geq 2$ and $\alpha = [(J + 1/2)\pi a]/L$ in order to satisfy the Equation (5). It should be noted that (7) is just a trial function and not the most general displacement. Thus the results obtained are only necessary for stability. When $J = 0$ and so $\alpha = (\pi/2)(a/L)$, the least stable case occurs because the magnetic field lines are least disturbed by the perturbed displacement. Since we are interested in the least stable case we let $J = 0$ in the rest of this study. We also let $n = 2$ in Equation (7). The different choice of n (including $n = 1$) in Equation (7) does not alter the result much but only change the coefficient in Equation (9) below.

For a loop with large aspect ratio ($\equiv L/a$) 10, α will be about 0.1. If $\alpha = 0$ the Equation (7) becomes the usual ideal MHD stability displacement equation.

By using Equations (2), (3), and (7), the energy Equation (1) becomes:

$$2\delta W = \int \{A \cos^4 \alpha z + B \sin^2 2\alpha z + C \cos^2 \alpha z \sin^2 \alpha z\} dz dS. \quad (8)$$

Here dS is an infinitesimal element of the loop cross-section. Since the equilibrium quantities are independent of z , integration with respect to z is performed to eliminate the z dependence in δW without any difficulty. The result is:

$$2\delta W = \left(\frac{3\pi}{8\alpha}\right) \int \{A + \frac{1}{3}\alpha^2 B\} dS. \quad (9)$$

By changing the independent variables ξ_θ, ξ_z to η, ζ (Newcomb, 1960) such as

$$\eta = \frac{im}{r} \xi_\theta + ik \xi_z, \quad (10)$$

$$\xi = i\xi_\theta B_z - i\xi_z B_\theta,$$

[†] In this paper we will use the term 'field line tying' for the boundary conditions (5) and (6)

A and B can be expressed as

$$\begin{aligned}
 A = & \gamma P_0 \left\{ \frac{1}{r} (r\xi_r)' + \eta \right\}^2 + \xi_r^2 (k \cdot B)^2 + (\zeta k - (\xi_r B_\theta)')^2 + \\
 & + \left(\frac{1}{r} (r\xi_r B_z)' + \frac{m}{r} \zeta \right)^2 - \frac{B_z m}{r^2} \xi_r \zeta + \frac{2k}{r} (rB_\theta)' \xi_r \zeta - \\
 & - \frac{1}{r} (rB_\theta)' (\xi_r B_\theta)' \xi_r + P_0' \frac{\xi_r}{r} (r\xi_r)' - \frac{B_z' m}{r} \xi_r \zeta - \frac{\xi_r}{r} (rB_z \xi_r)' B_z', \\
 B = & \gamma P_0 \left(\frac{m\zeta - rB_z \eta}{krB_z + mB_\theta} \right)^2 + \xi_r^2 B_z + \zeta^2.
 \end{aligned} \quad (11)$$

Here prime indicates a derivative with respect to r . Note that ξ_θ and ξ_z as functions η and ζ seem to diverge at $krB_z + mB_\theta = 0$, but do not diverge as functions of the minimizing modes of η and ζ in Equation (14).

Equation (9) is rewritten in a different form for the systematic minimization of δW :

$$2\delta W = \left(\frac{3\pi}{8\alpha} \right) \int dS \left\{ C_1 \left(\eta + \frac{C_2}{2C_1} \right)^2 + D_1 \left(\zeta + \frac{D_2}{2D_1} \right)^2 + \left(D_3 - \frac{D_2^2}{4D_1} \right) \right\}. \quad (12)$$

Here

$$\begin{aligned}
 C_1 = & \gamma P_0 \left\{ 1 + \frac{\frac{4}{3}\alpha^2 r^2 B_z^2}{(krB_z + mB_\theta)^2} \right\}, \\
 C_2 = & \frac{2}{r} (r\xi_r)' \gamma P_0 - \gamma P_0 \frac{\frac{8}{3}\alpha^2 m r B_z}{(krB_z + mB_\theta)^2} \zeta, \\
 D_1 = & k^2 + \frac{m^2}{r^2} + \frac{4}{3}\alpha^2 + \frac{\alpha^2 \frac{4}{3}\gamma P_0 m^2}{(krB_z + mB_\theta)^2 + \frac{4}{3}\alpha^2 r^2 B_z^2}, \\
 D_2 = & \frac{2\xi_r}{r^2} (krB_\theta + mB_z) - \frac{2\xi_r'}{r} (krB_\theta - mB_z) + \\
 & + \frac{\frac{8}{3}\alpha^2 m r B_z \left(\frac{\xi_r}{r} + \xi_r' \right) \gamma P_0}{(krB_z + mB_\theta)^2 + \frac{4}{3}\alpha^2 r^2 B_z^2}.
 \end{aligned} \quad (13)$$

The last parenthesis of Equation (12) will be expressed explicitly later. δW can easily be minimized by letting

$$\eta = -\frac{C_2}{2C_1} \quad \text{and} \quad \zeta = -\frac{D_2}{2D_1}. \quad (14)$$

The minimization conditions for η and ζ of Equation (14) are major departure from the work by Hood and Priest (1979). They determine the relation between ξ_θ and ξ_z from the assumption that the component of ξ parallel to the magnetic field (ξ_\parallel)

is zero. How energy equal

For the c determining field-line tyi compressibil will be explai ξ_n is

Here

A more co (15) by parts

Here

is zero. However, ξ_θ and ξ_z with which ξ_j is zero do not completely minimize the energy equation.

For the case without field-line tying, the energy equation is minimized by determining η such that η satisfies $\nabla \cdot \xi = 0$ (Newcomb, 1960). Because of the field-line tying effect, however, η in Equation (14) does not satisfy $\nabla \cdot \xi = 0$. The compressibility of plasma, $\nabla \cdot \xi \neq 0$, gives a subtle effect on the stability whose effect will be explained later. The minimized δW , which has only one independent variable ξ_r , is

$$\begin{aligned} & \eta^2 + \\ & \xi - \\ & \frac{\xi_r}{r} (rB_z \xi_r)' B_z', \end{aligned} \quad (11)$$

at ξ_θ and ξ_z as functions η verge as functions of the

stematic minimization of

$$\left(\frac{1}{r} \right)^2 + \left(D_3 - \frac{D_2^2}{4D_1} \right) \}. \quad (12)$$

(13)

I explicitly later. δW can

(14)

(14) are major departure
e the relation between ξ_θ
d to the magnetic field (ξ_j)

Here

$$\begin{aligned} 2\delta W &= \frac{3\pi}{8\alpha} \int dS \left\{ D_3 - \frac{D_2^2}{4D_1} \right\} \\ &= \left(\frac{3\pi}{8\alpha} \right) 2\pi \int [Q_1 \xi_r^2 + Q_2 \xi_r'^2 + Q_3 \xi_r \xi_r'] dr. \end{aligned} \quad (15)$$

$$\begin{aligned} Q_1 &= r(k^2 B_z^2 - \frac{2B_\theta(rB_\theta)'}{r} + \frac{4}{3}\alpha^2 B_z^2(1+S)r + \\ &\quad + \frac{(krB_z - mB_\theta)^2 + \alpha^2 T_1 + \alpha^4 T_3}{r\{k^2 r^2 + m^2 + \alpha^2 T_2\}}, \end{aligned} \quad (16)$$

$$Q_2 = \frac{r(mB_\theta + krB_z)^2 + \alpha^2 r^3 T_4 + \alpha^4 T_3 r}{k^2 r^2 + m^2 + \alpha^2 T_2} + \alpha^4 \frac{3}{4} r^3 B_z^2 S, \quad (17)$$

$$Q_3 = \frac{2\{k^2 r^2 B_z^2 - m^2 B_\theta + 2\alpha^2 T_3 r^3 + \alpha^4 T_3\}}{k^2 r^2 + m^2 + \alpha^2 T_2} + \alpha^4 \frac{28}{3} r^2 B_z^2 S, \quad (18)$$

$$S = \frac{\gamma P_0}{(krB_z + mB_\theta)^2 + \frac{4}{3}\alpha^2 r^2 B_z^2}, \quad (19)$$

$$T_1 = \frac{4}{3} r^2 (B_z^2 + B_\theta^2) + \frac{4}{3} r^2 S \{m^2 (B_\theta^2 - B_z^2) - 2mkrB_z B_\theta\}, \quad (20)$$

$$T_2 = \frac{4}{3} r^2 (1 + m^2 S), \quad (21)$$

$$T_3 = -(\frac{4}{3} m r^2 B_z)^2 S^2, \quad (22)$$

$$T_4 = \frac{4}{3} (B_\theta^2 + B_z^2) + \frac{4}{3} S \{ (B_\theta^2 - B_z^2) m^2 + 2krmB_\theta B_z \}, \quad (23)$$

$$T_5 = \frac{4}{3} \frac{B_z^2 - B_\theta^2}{r} - \frac{4}{3} S \left(\frac{B_\theta^2 + B_z^2}{r} \right) m^2. \quad (24)$$

A more convenient form of energy equation is obtained by integrating Equation (15) by parts to eliminate the term $\xi_r \xi_r'$:

$$\delta W = \left(\frac{3\pi}{8\alpha} \right) \int [Q_2 (\xi_r')^2 + g \xi_r^2] dr. \quad (25)$$

Here

$$g(r) = Q_1 - \frac{1}{2} Q_3. \quad (26)$$

Further minimization of δW , Equation (25), gives a second order ordinary differential equation for ξ , and the MHD stability can extensively be studied by solving the differential equation (Newcomb, 1960). However, we can study how the field line tying affects the stability without solving the differential equation by investigating Equations (16)–(24). Noticing that the terms with α^2 and α^4 in Equations (16)–(18) are due to the field line tying effect we will consider the mathematical behavior of the terms, especially near a mode rational surface, where $krB_z + mB_\theta = 0$ is satisfied.

3. The Effect of Field-Line Tying on the Stability

The effect of field line tying can be studied without further use of Equation (25) by scrutinizing Equations (16)–(26). If we let $\alpha = 0$, the perturbed displacement Equation (7) and Equations (16)–(26) become equations without field line tying that appear in Newcomb (1960) and Shafranov (1970). In this case, Equation (26) has singular points r_s 's, which satisfy $Q_2(r_s) = 0$ or

$$kr_s B_z(r_s) + mB_\theta(r_s) = 0. \quad (27)$$

The singular surface r_s is usually called a mode rational surface (Bateman, 1978), which has a profound implication to the MHD stability. A perturbation can grow at the mode rational surface without disturbing the field lines on the surface. On the other hand, if we let $\alpha \neq 0$, there is no singular surface r which satisfies $Q_2(r) = 0$. No singular surface means that no perturbation can grow without disturbing the field lines, even at a surface r_s which satisfies Equation (27). The perturbation of a field line at the surface r_s produces a stabilizing force due to field line tension, which does not appear at r_s if there is no field line tying (i.e., $\alpha = 0$). The effect of field line tying can be understood by carefully considering the terms that contain α . Since α defined as $\pi/(2L/a)$ is a very small quantity for a loop of large aspect ratio ($\alpha^2 = 0.01$ for $L/a = 10$), the correction terms of field line tying in Equations (16)–(24) can be negligible. However, this is not true near a mode rational surface r_s which satisfies the Equation (27). To see the behavior of the Equations (16)–(18) or Equations (26) near the mode rational surface r_s , let us take a term $\alpha^2 S$ appearing in any Equations (16)–(24) as an example. From Equation (19) for S , we can find, that, $\alpha^2 S$ is negligible at flux surfaces far from the mode rational surface r_s . Near the mode rational surface r_s where $(krB_z + mB_\theta)^2$ is near zero, however, $\alpha^2 S$ is not negligible anymore but becomes

$$\frac{\gamma P_0}{3r^2 B_z^2}$$

as r closes to r_s . That means that the effect of field line tying is negligible at flux surfaces far from the mode rational surface r_s but important near the mode rational surface. The mathematical behavior of the field line tying effect near a mode rational surface is not found by Hood and Priest (1979), probably because they minimize the

energy equation by tying effect near the in the next section derive a stability cr

4. De

Before deriving an general stability the $Q_2(r)$ in Equation determines the stability for the given Shafranov (1970) d mode numbers m f

$$\Delta(nq) \approx$$

and

$$\Delta(nq) \approx$$

$$\Delta(nq) \approx$$

Here $\Delta(nq)$ is an int field line twisting, d

$$nq(r) =$$

n is the number of right-hand side of E deriving Equations

For a plasma current with r . In this case (28) shows that the n on the cross section narrower than for $m = nq(r)$ mode rational

For a circular cylindrical poloidal mode number and r_s are mode rational

a second order ordinary equation can be extensively studied by numerical methods. However, we can study how the effect of the differential equation by terms with α^2 and α^4 in the perturbation equation. In effect we will consider the mode rational surface, where

Stability

For the use of Equation (25) by the perturbed displacement Equation (26) without field line tying that is the case, Equation (26) has

(27)

at the surface (Bateman, 1978). A perturbation can grow at the surface. On the other hand, it satisfies $Q_2(r) = 0$. No perturbation without disturbing the field line tension, which is $g(r) = 0$. The effect of field line tension that contains α . Since α is a large aspect ratio ($\alpha^2 = 0.01$) Equations (16)–(24) can be used at the surface r_s which satisfies the condition (18) or Equations (26) near the surface. In any Equations (26) we can find, that, $\alpha^2 S$ is not negligible near the mode rational surface. Near the mode rational surface, $\alpha^2 S$ is not negligible

the tying is negligible at flux surfaces near the mode rational surface. The effect near a mode rational surface is negligible because they minimize the

energy equation by assuming $\xi_1 = 0$. Understanding the behavior of the field line tying effect near the mode rational surface makes it easy to derive a stability criterion. In the next section we will discuss the stabilities of the $m = 1$ and $m \gg 1$ modes and derive a stability criterion for the $m \gg 1$ modes.

4. Derivation and Interpretation of the Stability Criterion for a Localized Mode

Before deriving an equation for the stability criterion we will review briefly the general stability theory for the case of no field line tying. For $\alpha = 0$ in Equation (7), $Q_2(r)$ in Equation (26) is always positive and the sign of $g(r)$ in Equation (26) determines the stability (Shafranov, 1970), i.e., $g(r) > 0$ at all flux surfaces means stability for the given displacement while $g(r) < 0$ at any flux surface can be unstable. Shafranov (1970) derived the width in r of the unstable region for various poloidal mode numbers m from the condition $g(r) < 0$:

$$\Delta(nq) = \frac{4 \left(1 - \frac{3}{2} \frac{\gamma P'_0}{B_\theta^2} \right)}{3} \quad \text{for } m = 1, \quad (28)$$

and

$$\left. \begin{aligned} \Delta(nq) &= \frac{4k^2 r^2}{m(m^2 - 1)} & (P' = 0) \\ \Delta(nq) &= 2kr \sqrt{\frac{r |P'|}{B_\theta^2} \frac{2}{m^2 - 1}} & (P' \neq 0), \end{aligned} \right\} \quad \text{for } m \geq 2. \quad (29)$$

Here $\Delta(nq)$ is an interval in $q(r)$ where $g(r) < 0$, $q(r)$ is a safety factor, a measure of field line twisting, defined as

$$nq(r) = \frac{-krB_z(r)}{B_\theta(r)}, \quad (30)$$

n is the number of wavelength in the cylinder length $2L$, and the minus sign on the right-hand side of Equation (30) is due to the definition of ξ in Equation (7). When deriving Equations (28) and (29), $kr/m \ll 1$ (valid for $B_z \gg B_\theta$) is assumed.

For a plasma current density which decreases with r , $q(r)$ increases monotonically with r . In this case $\Delta[nq(r)]$ represents the width of instability region in r . Equation (28) shows that the $m = 1$ mode is a large scale instability which is globally distributed on the cross section of a cylinder. However, for $m \geq 2$ the unstable region is much narrower than for $m = 1$ and the mode with $m \gg 1$ is extremely localized near $m = nq(r)$ mode rational surface.

For a circular cylindrical plasma, the typical behavior of ξ , with r for different poloidal mode number m are shown in Figure 2 (Bateman and An, 1977). Here, r_1 and r_s are mode rational surfaces for $m = 1$ and $m \geq 2$ modes respectively. It shows

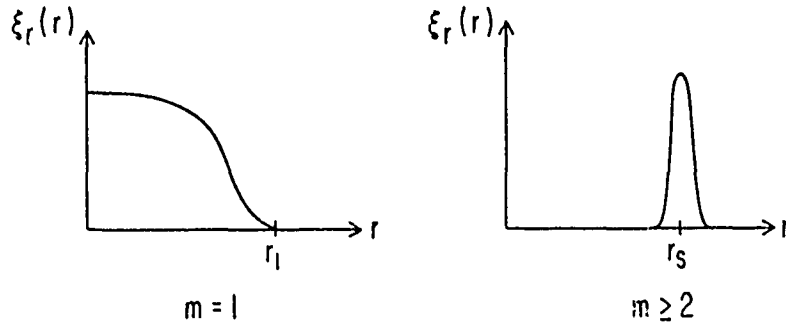


Fig. 2. Variations of the radial component of the perturbed displacement ξ_r with r for the $m = 1$ and $m \geq 2$ modes. The perturbed displacement shown in this figure are solutions of equation of motion for $m = 1$ and $m \geq 2$.

that the $m = 1$ mode is strikingly different from the $m \geq 2$ modes. The $m = 1$ mode is finite at $r < r_1$ where the field line tying effect is negligible and is zero at $r = r_1$ where field line tying effect is important. Therefore, the contribution of the field line tying effect to the $m = 1$ mode is negligibly small. The result is entirely contradictory to the result by Hood and Priest (1979). Their results show that the field line tying effect on the $m = 1$ mode is significant. Furthermore, the critical safety factor (q_c) over which the $m = 1$ mode is stable is much smaller than 1 (the Kruskal-Shafranov limit). Their resulting bound on stability is that q_c decreases as the aspect ratio increases. For example q_c approximately equals 0.6 and 0.3 for aspect ratio 10 and 50 respectively. If we notice that the terms in Equations (16)–(18) due to field line tying become negligible as the ratio increases [as is also true for the equations of Hood and Priest (1979)], we can easily understand that q_c should approach to 1, the Kruskal-Shafranov limit, as the aspect ratio increases.

On the other hand, the $m \geq 2$ mode is localized near a singular surface r_s where the field line tying effect is important. Since the localization of perturbation increases with m , the field line tying effect becomes more important as m increases. From the argument mentioned above, it is obvious that we need to study the field line tying effect in detail for only a high m mode. The stability criterion for a localized mode ($m \gg 1$) with no field line tying is derived by Suydam (1958). By taking the limit $m \rightarrow \infty$ keeping the safety factor $q(r_s)$ fixed we will derive a Suydam like stability criterion and will give an interpretation of the result.

The quantity $g(r)$ in Equation (26) is evaluated at r_s where $kr_s B_z(r_s) + mB_\theta(r_s) = 0$ is satisfied, and the limit $m \rightarrow \infty$ is taken keeping $q(r_s)$ of Equation (30) finite, resulting in

$$g(r_s) = g_0(r_s) + \alpha^2 g_2(r_s), \quad (31)$$

where

$$g_0(r_s) \equiv 2P'_0(r) \left(\frac{B_\theta^2}{\gamma P_0 + B_\theta^2} \right) - 2B_z B'_z \frac{\gamma P_0 (B_\theta^2 / B_z^2)}{\gamma P_0 + B_\theta^2}, \quad (32)$$

$$g_2(r_s) \equiv$$

and

$$B_0^2 \equiv B_\theta^2$$

For the evaluation resulting in

$$(mB_\theta + k$$

while letting $kr_s B_z + Q_2(r)$ near r_s become

$$Q_2(r_s) =$$

$$r$$

$$f(r_s) = -$$

By using the integra

$$\int \chi^2 \left(\frac{d\xi}{d\chi} \right)$$

for the first te get

$$\frac{1}{4} f(r_s) + k$$

Using Equation (31

$$\frac{r^2}{4} \left(\frac{q'}{q} \right)^2$$

This is a Suydam-like loop. The effect of field line tying on the Suydam criterion for

$$\frac{r^2}{4} \left(\frac{q'}{q} \right)^2 +$$

The comparison between the two terms in Equation (31) shows that the term $(\nabla \cdot \xi \neq 0)$. The last term in Equation (38) is destabilizing for $\alpha > 0$. It is not obvious whether field line tying will be given later. It may alter the stability for

$$g_2(r_s) \equiv \frac{4}{3} r B_z^2. \quad (33)$$

and

$$B_0^2 \equiv B_\theta^2 + B_z^2.$$

For the evaluation $Q_2(r)$ of Equation (26) we expand $(mB_\theta + krB_z)^2$ near $r = r_s$, resulting in

$$(mB_\theta + krB_z)^2 = 2B_\theta^2 m^2 \left(\frac{q'}{q} \right)^2 (r - r_s)^2 \quad (34)$$

while letting $krB_z + mB_\theta = 0$ in T_2 , T_3 and T_4 of $Q_2(r)$. By taking the limit $m \rightarrow \infty$, $Q_2(r)$ near r_s becomes

$$Q_2(r_s) = f(r_s)(r - r_s)^2, \quad (35)$$

$$f(r_s) = \frac{r B_\theta^2 \left(\frac{q'}{q} \right)^2 B_z^2}{B_0^2 + \gamma P_0}.$$

By using the integral inequality (Shafranov, 1970)

$$\int \chi^2 \left(\frac{d\xi}{d\chi} \right)^2 d\chi \geq \frac{1}{4} \int \xi^2 d\chi \quad (36)$$

for the first term of Equation (25), and from the condition for stability, $\delta W > 0$, we get

$$\frac{1}{4} f(r_s) + g(r_s) \geq 0. \quad (37)$$

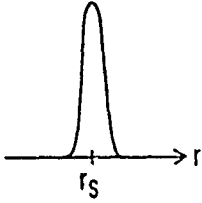
Using Equation (31)–(35), Equation (37) is explicitly expressed as

$$\frac{r^2}{4} \left(\frac{q'}{q} \right)^2 + \frac{2P_0' r}{B_z^2} - \frac{2B_z B_z'}{B_z^2} r \left(\frac{\gamma P_0}{B_z^2} \right) + \frac{4}{3} \alpha^2 r^2 \frac{\gamma P_0 + B_0^2}{B_\theta^2} \geq 0. \quad (38)$$

This is a Suydam-like criterion in the case of field line tying at the foot points of the loop. The effect of field line tying can be studied by comparing Equation (38) with the Suydam criterion for no field line tying,

$$\frac{r^2}{4} \left(\frac{q'}{q} \right)^2 + \frac{2\gamma P_0'}{B_z^2} \geq 0. \quad (39)$$

The comparison between Equation (38) and Equation (39) shows that the last two terms in Equation (38) are due to the field line tying and compressibility of plasma ($\nabla \cdot \xi \neq 0$). The last term of Equation (38) is a stabilizing term due to field line bending and the term increases with the potential magnetic field. The third term of Equation (38) is destabilizing for $B_z' > 0$, but stabilizing for $B_z' < 0$. Because of this term it is not obvious whether field line tying improves the stability. The interpretation of this term will be given later. Next, we will study how and how much the field line tying effect alter the stability for several specific cases.



$m \geq 2$

at ξ_s with r for the $m = 1$ and
ans of equation of motion for

ides. The $m = 1$ mode is
id is zero at $r = r_1$ where
on of the field line tying
rely contradictory to the
field line tying effect on
y factor (q_c) over which
-S' nov limit). Their
ect ratio increases. For
10 and 50 respectively.
field line tying become
ions of Hood and Priest
ch to 1, the Kruskal-

star surface r_s where the
perturbation increases
; m increases. From the
study the field line tying
on for a localized mode
(8). By taking the limit
a Suydam like stability

$\cdot kr_s B_z(r_s) + mB_\theta(r_s) = 0$
f Equation (30) finite,

(31)

(32)

First, we assume the plasma current density and B_z are uniform over the cross section. In this case, $q'(r) = 0$ and Equation (38) becomes

$$\frac{2P_0' r}{B_z^2} + \frac{4}{3} \alpha^2 r^2 \frac{\gamma P_0 + B_0^2}{B_0^2} \geq 0. \quad (40)$$

The assumption $B_z' = 0$ makes it easy to estimate the stability without solving the equilibrium equation, because plasma pressure is confined only by B_θ and so we can make the approximations $P(r) \approx B_\theta^2/2$ and $rP_0'(r) \approx -P_0(r)$ for $P_0'(r) < 0$. Using this approximation we get the minimum ratio of nonpotential to potential B field for a localized instability to set in. The result is

$$\frac{B_\theta^2}{B_z^2} \leq \frac{1}{2} \left(\frac{4}{3} \alpha^2 r^2 \left(\frac{\gamma}{2} + 1 \right) + \left\{ \left[\frac{4}{3} \alpha^2 r^2 \left(\frac{\gamma}{2} + 1 \right) \right]^2 + \frac{16 \alpha^2 r^2}{3} \right\}^{1/2} \right). \quad (41)$$

For a solar loop with aspect ratio 10, the loop will be unstable for the localized mode if $B_\theta/B_z \geq 0.3$. The $m = 1$ mode, on the other hand, is unstable if $q = rB_z/RB_\theta$ is smaller than 1 or $B_\theta/B_z > 0.1$ for a loop with aspect ratio 10. Therefore, we can say that the higher field line twist is needed for the $m \gg 1$ modes to be unstable than for the $m = 1$ mode when $q'(r) = 0$ and $B_z' = 0$. If field lines are not tied at the foot points of a loop and $P'(r) < 0$, $q'(r) = 0$, Equation (29) shows no stability for the $m \gg 1$ mode even when the $m = 1$ mode is stable.

Next, we consider a case with uniform plasma current density and $B_z'(r) \neq 0$. In this case, Equation (38) becomes

$$\frac{r^2}{4} \left(\frac{q'}{q} \right)^2 - \frac{2rq'}{q} \frac{\gamma F_0}{B_z^2} + \frac{2P_0' r}{B_z^2} + \frac{4}{3} \alpha^2 r^2 \frac{\gamma P_0 + B_0^2}{B_0^2} \geq 0. \quad (42)$$

The second term of Equation (42) shows that the field line tying reduces the shear stabilizing effect if $q'(r) > 0$. The influence of field line tying on the stabilizing effect of shear can be explained using (Figure 3). The exaggerated drawings of (A) and (B) in Figure 3 show how field lines move by perturbation without and with field line frozen at the end faces for $q'(r) > 0$ respectively. Line (1) is a field line on an outer flux surface and is assumed not to move. Line (2) is an another field line on an inner flux surface and moves to the outer flux surface by a perturbation, which becomes the field line (3) which crosses the line (1). This is how shearing of field lines makes a stabilizing effect (Kadomstev, 1966; An and Bateman, 1980).

Let us consider a field line parallel to field line (1) that intersects field line (3) at the point where field line (3) touches the outer cylinder. The angle between these field line is less in (B) than in (A), because the field line in (B) is frozen at the end faces. Therefore, the effective shearing of field lines decreases for a loop with field line tying if $q'(r) > 0$. If $B_z' = 0$, the reduction of the effective shear disappears because of the relative motion of the field line (1) to the line (3). The reduction of the effective shear for $B_z' > 0$ and uniform plasma current density is the one effect of the B_z' term in Equation (38). In general, the effect of the B_z' term on the stability is interpreted as a combination of the effects of the field line tying and the compressibility of plasma.

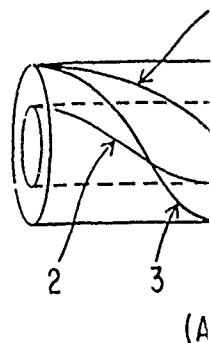


Fig 3. The motion of the end faces. Line (1)

Even though the overall effect of B_z' is positive or negative, the effect of B_z' is positive or negative on the stability for a localized mode. Equation (38), for a numerical calculation.

We have studied the semi-toroidal loop ideal MHD energy line tying effect from the mode rational surface studies of the resistive mode is strongly studied two ways. First, it produces a resistive mode is associated with shear stabilizing potential field in when $B_z'(r) = 0$; with all the flux.

However, the resistive diffusion (1973a, b) or a resistive diffusion

uniform over the cross

(40)

ility without solving the
only by B_θ and so we can
for $P'_0(r) < 0$. Using this
o potential B field for a

$$\left. \frac{2}{r^2} \right)^{1/2}. \quad (41)$$

nstable for the localized
unstable if $q = rB_z/RB_\theta$
0. Therefore, we can say
s to be unstable than for
not tied at the foot points
bility for the $m \gg 1$ mode

sit, $B'_z(r) \neq 0$. In this

(42)

e tying reduces the shear
on the stabilizing effect of
drawings of (A) and (B) in
and with field line frozen
eld line on an outer flux
eld line on an inner flux
tion, which becomes the
ing of field lines makes a
(80).

tersects field line (3) at the
angle between these field
is frozen at the end faces.
a loop with field line tying
disappears because of the
ction of the effective shear
e effect of the B'_z term in
stability is interpreted as a
compressibility of plasma.

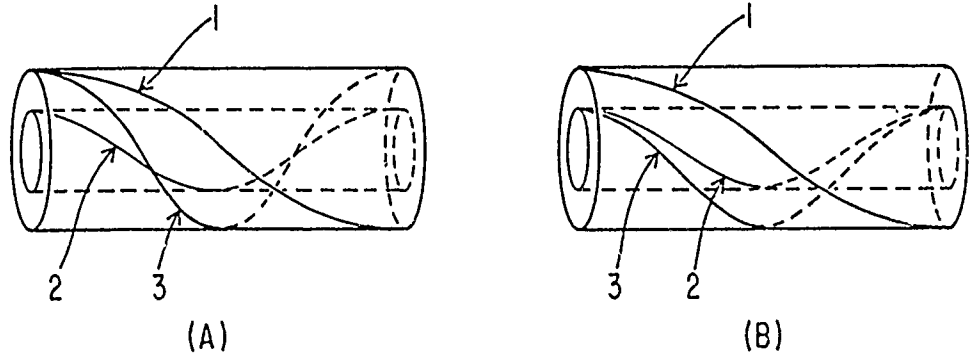


Fig 3. The motion of a field line on a flux surface for the cases without (A) and with (B) field line tying to the end faces. Line (1) is a field line on an outer flux surface, line (2) is on an inner flux surface, and line (3) is moving to the outer flux surface by a perturbation.

Even though the second term of Equation (42) reduces the stability for $q'(r) > 0$, the overall effect of the field line tying is stabilizing if $B_\theta \ll B_z$ and rB'_z/B_z is small. When B_z is positive and extremely large, however, the field line tying might reduce the stability for a localized mode. The detailed estimation of the stability criterion, Equation (38), for equilibrium other than the simple cases discussed above, requires a numerical calculation, which is not intended in this study.

5. Summary and Discussion

We have studied the effects of field line tying on the MHD stability of a solar loop. A semi-toroidal loop with large aspect ratio is approximated by a circular cylinder. The ideal MHD energy equation is used to get a necessary stability condition. The field line tying effect is important only near a mode rational surface and is negligible far from the mode rational surface. The importance of field line tying near a mode rational surface is similar to the importance of the resistivity only near the surface in studies of the resistive instability (Furth *et al.*, 1963). The effect of field line tying has been studied extensively for a high m localized mode, because only this localized mode is strongly affected by the field line tying. The field line tying effects appear in two ways. First it gives an additional stretching and bending of field lines which in turn produce a restoring force to a perturbation. Second, the effect of field line tying is associated with the compressibility of the plasma ($\nabla \cdot \xi \neq 0$), which reduces the shear stabilizing effect for $B'_z(r) > 0$. It appears from this study that as the non-potential field increases the $m = 1$ mode becomes unstable before the localized mode when $B'_z(r) = 0$ and $q'(r) = 0$. This result can be generalized for equilibria compatible with all the flare loop condition except the case when $B'_z(r)$ is positive and large.

However, theoretical calculations show that a magnetic field can evolve through resistive diffusion to a very steep gradient magnetic field configuration (Low, 1973a, b) or a reverse field configuration (Taylor, 1974) depending on the initial

twisting of the field line. If the field gradient is positive after resistive diffusion the third term of Equation (38) becomes an important destabilizing term. In this case, the field line tying can reduce the stability of certain modes. A toroidal z pinch experiment in magnetic fusion (Robinson *et al.*, 1969) shows that the toroidal magnetic field can have negative gradient with a reverse field near the plasma edge after the resistive diffusion. If the initial twisting of the loop field line is similar to that of a z pinch, however, there will be a high negative gradient of the magnetic field. In this case, field line tying much enhances the stability. The theoretical studies and the experimental results imply that the third term of Equation (38) plays an important role to determine the stability of a localized mode. In this study we have considered the field line tying effects on the circular cylindrical plasma. We expect that the field gradient, B'_z , will play a more important role to determine the stability of semi-toroidal loop. In the toroidal geometry the eigenfunction $\xi(r)$ should be summation of all poloidal harmonic modes because there is no symmetry along the θ direction any more. Let us consider the pressure-driven interchange mode in a toroidal geometry, as considered to derive Equation (38). The toroidal interchange mode will be the summation of every localized mode near its mode rational surface. Under this situation, the field gradient [c.f. the third term of Equation (38)] affects the stability of all the field lines and then the effect of the field gradient, B'_z , will be bigger for the semi-toroidal loop than for the circular cylindrical loop. Observational studies indicate that the field gradient is an important factor in triggering the flare (Rust, 1973; Švestka, 1976). We do not intend to relate directly the observational results to our result for the effect of the field gradient at this moment. We, rather, suggest that for the special class of perturbations studied the field gradient of the loop is an important factor to determine the stability, and the importance will increase for the semi-toroidal loop with foot points fixed at the photosphere. Further studies should be done using more general class of perturbations for cylindrical and semi-toroidal loops to verify the argument mentioned above.

We neglect the resistivity in this study to simplify the problem. It is believed that the resistivity effect is very important to the solar flare mechanisms. However, the detailed calculation of the resistive instability of the loop with field line tying is certainly out of the scope of this paper. As we mentioned in Section 3, the importance of field line tying only near a mode rational surface is similar to that of resistivity. Because of this similarity we can expect that field line tying will affect the resistive instability. The field line tying effect on the resistive instability can be estimated roughly by considering the equations for the width of a resistive boundary layer and the growth rate of the instability. The width of the resistive boundary layer ϵ is

$$\epsilon \sim \left(\frac{q'}{q} \right)^{-5/2}$$

and the growth rate Ω is

$$\Omega \sim \left(\frac{q'}{q} \right)^{2/5}$$

for the $m \geq 2$ field line tying $B'_z > 0$, therefore growth rate Ω of mode. On the other hand, and reduces the stability in this case.

Even though we expect that the field line tying will have any more effect on the stability.

In conclusion, the field line tying is an important but important discrepancy between the theoretical and observational results is probably due to the field line tying on it, and so does.

The author thanks the referee for the comments during the course of the work.

This work was supported by the Air Force Command, USAF, NSG-7406.

- An, C. H. and Bates, G. R.: 1978, *Phys. Rev. Lett.* **41**, 1000.
 Bateman, G. and Bernstein, I. B.: 1977, *Phys. Rev. Lett.* **38**, 1000.
 Cheng, C. C.: 1977, *Phys. Rev. Lett.* **38**, 1000.
 Chuderi, C., Giacchetti, R. Van H. and Gibson, E. G.: 1977, *Phys. Rev. Lett.* **38**, 1000.
 Foukal, P. V.: 1975, *Phys. Rev. Lett.* **35**, 1000.
 Foukal, P. V.: 1976, *Phys. Rev. Lett.* **36**, 1000.
 Furth, H. P., Killeen, J., Giacchetti, R. Van H. and Gibson, E. G.: 1977, *Phys. Rev. Lett.* **38**, 1000.
 Hood, A. W. and Priest, E. R.: 1979, *Phys. Rev. Lett.* **42**, 1000.
 Kadomtsev, B. B.: 1977, *Phys. Rev. Lett.* **38**, 1000.
 Bureau, N. Y.: 1977, *Phys. Rev. Lett.* **38**, 1000.
 Low, B. C.: 1973a, *Phys. Rev. Lett.* **31**, 1000.
 Low, B. C.: 1973b, *Phys. Rev. Lett.* **31**, 1000.
 Newcomb, W. A.: 1972, *Phys. Rev. Lett.* **29**, 1000.
 Raadu, M. A.: 1972, *Phys. Rev. Lett.* **29**, 1000.
 Robinson, D. C. and Tucker, R.: 1969, *Phys. Rev. Lett.* **23**, 1000.

after resistive diffusion the stabilizing term. In this case, the modes. A toroidal z pinch (1) shows that the toroidal field near the plasma edge up field line is similar to that of the magnetic field. In theoretical studies and the on (38) plays an important study we have considered ia. We expect that the field nine the stability of semi- $\xi(r)$ should be summation rety along the θ direction range mode in a toroidal idal interchange mode will ational surface. Under this m (38)] affects the stability t, B'_z , will be bigger for the op. Observational studies triggering the flare (Rust, he sional results to it. We, rather, suggest that gradient of the loop is an tance will increase for the re. Further studies should indrical and semi-toroidal

problem. It is believed that mechanisms. However, the op with field line tying is Section 3, the importance nilar to that of resistivity. ng will affect the resistive stability can be estimated istive boundary layer and ve boundary layer ϵ is

for the $m \geq 2$ resistive tearing mode (Bateman, 1978). In Section 4, we find that field line tying reduces (increases) the effective shear if B'_z is positive (negative). For $B'_z > 0$, therefore, the width of the resistive boundary layer increases while the growth rate Ω decreases. In this case field line tying is a stabilizing effect to the tearing mode. On the other hand, for $B'_z < 0$, the field line tying increases the growth rate and reduces the width of the boundary layer. Field line tying is a destabilizing effect in this case.

Even though field line tying has some effects on the resistive mode, we do not expect that the effect is significant because plasma is not frozen to the magnetic field line any more due to the finite resistivity.

In conclusion, the field line tying effect is not important for the $m = 1$ global mode but important for the $m \gg 1$ localized mode when the aspect ratio is large. The discrepancy between the results of this paper and of Hood and Priest (1979) is probably due to the fact that they choose different trial displacement and constraints on it, and so derive different bounds on the stability.

Acknowledgments

The author thanks Dr R. C. Canfield for his valuable discussions and comments during the course of this work. The author also thanks Dr A. W. Hood for his comments on this work.

This work is supported by the Air Force of Scientific Research, Air Force Systems Command, USAF, under Grant No. AFOSR-76-3071, and by NASA under Grant NSG-7406.

References

- An, C. H. and Bateman, G.: 1980, Oak Ridge National Laboratory Rep. ORNL/TM-7074.
- Bateman, G.: 1978, *MHD Instabilities*, M.I.T. Press, Cambridge, Mass.
- Bateman, G. and An, C. H.: 1977, not published.
- Bernstein, I. B., Frieman, E. A., Kruskal, M. D., and Kulsrud, R. M.: 1958, *Proc. Roy. Soc. A* **244**, 17.
- Cheng, C. C.: 1977, *Astrophys. J.* **213**, 558.
- Chuderi, C., Giachetti, R., and Van Hoven, G.: 1977, *Solar Phys.* **54**, 107.
- Foukal, P. V.: 1975, *Solar Phys.* **43**, 327.
- Foukal, P. V.: 1976, *Astrophys. J.* **210**, 575.
- Furth, H. P., Killeen, J., and Rosenbluth, M. N.: 1963, *Phys. Fluids* **6**, 459.
- Giachetti, R., Van Hoven, G., and Chuderi, C.: 1977, *Solar Phys.* **55**, 371.
- Gibson, E. G.: 1977, *Solar Phys.* **53**, 123.
- Hood, A. W. and Priest, E. R.: 1979, *Solar Phys.* **64**, 303.
- Kadomtsev, B. B.: 1966, in M. A. Leontovich (ed.), *Review of Plasma Physics* **2**, 153, Consultants Bureau, N.Y.
- Low, B. C.: 1973a, *Astrophys. J.* **181**, 917.
- Low, B. C.: 1973b, *Astrophys. J.* **184**, 917.
- Newcomb, W. A.: 1960, *Ann. Phys.* **10**, 232.
- Raadu, M. A.: 1972, *Solar Phys.* **22**, 425.
- Robinson, D. C. and King, R. E.: 1969 *Proc. 3rd Int. Conf. Plasma Physics and Controlled Nuclear Fusion Research*, Novosibirsk, USSR 1968, IAEA, Vienna, Austria.
- Rosner, R., Tucker, W. H., and Variana, G. S.: 1978, *Astrophys. J.* **220**, 643.

- Rust, D. M.: 1973, Sacramento Peak Obs. Contr. No. 209.
 Shafranov, V. D.: 1970, *Sov. Phys. - Tech. Phys.* **15**, 175.
 Solov'ev, L. S.: 1971, *Soviet Atomic Energy* **30**, 14.
 Somov, B. V. and Syrovatskii, S. I.: 1976, *Sov. Phys. Usp.* **19**, No. 10, 813.
 Spicer, D. S.: 1977, *Solar Phys.* **53**, 305.
 Suydam B. R.: 1958, *Proc. Second Internat. Conf. Peaceful Uses of Atomic Energy*, (Geneva: United Nation) **31**, 157.
 Švestka, Z.: 1976, *Solar Flares*, D. Reidel Publ. Co., Dordrecht, Holland, p. 28.
 Taylor, J. B.: 1974, in *Proceedings of the Fifth International Conference on Plasma Physics and Controlled Nuclear Fusion Research*, Tokyo, Japan, (International Atomic Energy Agency, Vienna, 1975), Vol. I, p. 161.
 Van Hoven, G., Chiuderi, C., and Giachetti, R.: 1977, *Astrophys. J.* **213**, 869.
 Vorpahl, J. A., Gibson, E. G., Landecker, P. B., McKenzie, D. L., and Underwood, J. H.: 1975, *Solar Phys.* **45**, 199.

AL

High Altitude C

Abstract. The no
 The flux tubes an
 waves are time-d
 investigated by se
 waves into motio
 artificially suppre
 chromosphere. T
 (2) As the fast sho
 transverse to B_0
 seconds. Such fea
 (3) Alfvén waves
 Spicules, and the
 magnetic heating
 chromosphere in
 depositing heat in

The propagatio
 considered in p
 I and II, respec
 the propagatio
 importance of
 corona. Paper
 the radiative,
 corona. It doe
 suggests that t
 nonlinear dissi
 waves exert on
 mass motions;
 these forces.

The purpose
 of Alfvén waves

* Present Address
 Durham, NH 0382

** Present Address
 Garching bei Munc

Solar Physics **75**
 Copyright © 198.

d) Quiet Sun Studies

These quiet sun studies were largely unrelated to the basic objective of this grant; they are "odds and ends" left over from previous work by the principal investigator, primarily before the grant began. They were published because they were of merit in themselves.

i) Spatial Structure in Lines in the 3398-3526 Å Region

at the Extreme Limb: Observation, Identification and Interpretation

The observation obtained and explained in this paper was that some spectral lines of the quiet sun showed spatial variability, while others did not. The difference was explained in terms of radiative transfer effects, and is of little direct relevance here.

SPATIAL STRUCTURE IN LINES IN THE 3398-3526 Å REGION AT THE EXTREME LIMB: OBSERVATION, IDENTIFICATION AND INTERPRETATION

RICHARD C. CANFIELD

Department of Physics, C-011, University of California, San Diego, La Jolla, Calif. 92093, U.S.A.

JAY M. PASACHOFF*

Hopkins Observatory, Williams College, Williamstown, Mass. 01267, U.S.A.

ROBERT E. STENCEL

SC-23, NASA/Johnson Space Center, Houston, Tex. 77058, U.S.A.

and

JACQUES M. BECKERS

*Sacramento Peak Observatory,** Sunspot, NM 88349, U.S.A.*

(Received 21 March, 1978)

Abstract. We have obtained spectrograms of high spatial and spectral resolution of the extreme solar limb, using the vacuum tower telescope of Sacramento Peak Observatory. We have identified emission lines in the range 3398-3526 Å, and classified them according to intensity, spatial structure (intensity variation), and profile. Some lines show spatial intensity variation, others do not. We show that this effect is related to the abundance of the element responsible for the line and the mean lower-level excitation potential of interlocked lines. We explain the effect in terms of radiative interlocking with other lines, as well as the characteristic size of the volume contributing to the mean intensity.

1. Introduction

Lines observed at the extreme solar limb vary considerably in the extent to which they show fine-scale spatial structure. Pasachoff *et al.* (1968) found that while Ca II H, K and the IR triplet, H I H ϵ and He I D₃ showed spicular structure, various weak lines did not. Pierce's (1968) comprehensive atlas of the chromospheric spectrum from 3040-9266 Å includes comments on the diffuseness of lines. Unfortunately his tables cannot be used to infer the presence or absence of spatial structure, since lines can be sharp, not diffuse, yet show no structure. Livingston and White (1974) compared four different classes of lines - rare earths, metals (mainly Fe I), Na I D₂ and He I D₃ - all observed simultaneously on a single high-quality spectrogram. They found that the weaker metal lines showed spatial structure that was distinctly different from that shown by strong metal lines, D₂ and D₃. They also identified a rare earth line that completely lacked spatial structure. They attributed these effects to differences of line opacity and line formation mechanism.

* Also Five College Astronomy Department, Amherst, Mass. 01003, U.S.A.

** Operated by the Association of Universities for Research in Astronomy Inc. under contract with the National Science Foundation.

The paper is organized as follows: In Section 2 we present our observations of several hundred lines and our classification of their spatial structure characteristics, etc. In Section 3 we show that interesting relationships exist between spatial structure and atomic parameters. In Section 4 we explain these relationships in terms of the mechanism of formation of the lines.

2. Observations

Our observations represent the first attempt that we know of to systematically classify all the lines in a spectral region according to spatial structure. The spectra that form the observational basis of this work have been described by Pasachoff *et al.* (1974); a print of one spectrogram can be found in their paper. Not all of these data were of sufficient quality for spatial structure studies. Although adequately high spatial resolution was present over a wide spectral range, only in the region 3398–3526 Å (covered in the present work) was the slit located at the limb position that optimized the study of emission-line structure. The spectra were obtained at the vacuum tower telescope of Sacramento Peak Observatory, using a 300 line mm⁻¹ grating in the 17th order on 70 mm Eastman Kodak film 5375. The spatial scale along the slit is 270 μ/arc sec. The spatial resolution is approximately 1", as the result of seeing effects and limited telescopic resolution.

For all identifiable emission features in the range 3398–3526 Å we determined wavelengths, line strengths, spatial variation and atomic identification. Wavelengths for emission features were measured on contact prints, to which a scale based on photospheric reference lines was attached. Visual estimates, on a subjective scale, were made of line strengths and the presence or absence of spatial structure. Line identifications were accomplished in the usual manner, by wavelength coincidence and multiplet checking, using the standard references (Moore, 1959; Moore *et al.*, 1966; Pierce, 1968; Meggers *et al.*, 1975).

Table I lists the observed emission features and their characteristics. Each row of the Table corresponds to an individual emission peak. Hence a spectral line that is centrally reversed, i.e. shows two emission peaks separated by an absorption feature, appears as two rows in Table I. In such cases the two rows are printed unseparated by vertical spacing (e.g. 3399.03, 3399.11). Single emission features appear on isolated rows in Table I, separated by a blank space from adjacent features (e.g. 3398.867). An asterisk (*) in any column except column 1 indicates uncertainty in the entry in that column. An asterisk in column 1 indicates uncertainty of all parameters in the row.

The following information and notation appear in Table I:

Col. 1: Measured wavelength (in Å).

Col. 2: Profile information: BBA = bordered on blue by absorption, BRA = bordered on red by absorption, BBRA = bordered on both blue and red by absorptions, W = wide.

Col. 3: Intensity of feature: F = faint, M = moderate, S = strong.

Col. 4: Spatial intensity variation: Y = yes, N = no.

Col. 5: Atomic identification: element, ionization stage, multiplet number.

Col. 6: Comments on centrally reversed lines:

BB = blue emission peak brighter.

E = enhanced: blended with emission line.

M = masked: blended with absorption line.

RB = red emission peak brighter.

RU = reality of reversal uncertain.

SV = reversal shows spatial variation.

SY = symmetric: emission peaks of equal strength.

3. Analysis

We now consider the relationship between spatial variation and identification of the lines in Table I. We use only the lines with the most secure identifications, which leaves 165 lines. We divide them according to characteristics of spatial intensity variation and spectral line classification in Table II. We list the numbers of the multiplets of these lines, as well as the number of lines observed in each multiplet. For each species we have computed $\langle\chi_l\rangle$, the average value of the lower-level excitation potential, excluding the lowest and highest χ_l values for smoothness. In the final column we list the appropriate value of $\log N_E$, the logarithm of the elemental abundance by number, from Allen (1973).

For rare-earth lines the relationship is clear. An obvious feature of Table II is that there are no rare-earth lines among the group that exhibits spatial intensity variations on an arc-second scale. This effect has already been commented on by Pasachoff *et al.* (1968), Pierce (1968), Livingston and White (1974) and Canfield and Stencel (1976); the characteristics at this variation-free class of lines were first pointed out by Menzel (1931).

The situation with metal lines is not as simple. Some metal lines show variations; others do not. There is a tendency for the lines that show variation to have lower values of $\langle\chi_l\rangle$. Lines that show no spatial variation tend to originate on levels ranging from those of lower excitation in less-abundant metals to those of higher excitation in more-abundant metals.

To see how spatial structure is related to $\log N_E$ and $\langle\chi_l\rangle$ for our data as a whole, we have plotted the data of Table II in Figure 1. The crosses represent lines with spatial intensity variation; the circles, those without. Dy II cannot be plotted, since the energy level structure is unknown. With the exception of a few high-excitation lines of V II that show structure (possibly due to chance coincidence of a V II line with a strong chromospheric line), there is a strong tendency for the lines with spatial variation to appear in the upper-left region of Figure 1, and for lines without structure to appear elsewhere.

One can see that the diagonal line plotted in Figure 1 separates the regions with and without structure reasonably well. This line is given by $N_0 \exp(-\langle\chi_l\rangle/kT)$,

TABLE I
Emission features in the solar limb spectrum, 3398–3526 Å

λ (Å)	Prof.	I	SI	ID	Com.	λ (Å)	Prof.	I	SI	ID	Com.
3398.67	BBA	F	N			3413.33*	BBRA	F	N*	Gd II 91	BB, M
3398.867	BBA	M	N	Co I 157*		3413.41*		F	*	Zr II 60*	
3398.99		F	N	Ho II		3413.79		M	N	Dy II	
3399.03		F	N	Re I*	RU	3414.67		M	N	Zr II 73*	
3399.11*		F	N			3414.85		F	Y	Zr I 17	BB, E
3399.81*		F	Y*	NH*, Hf*	RU					Ni I 19	
3399.90*		F	Y*			3415.53*		F	N	Co I 5	
3400.000		M	N	Gd II 22		3415.99		F	Y		BB*
3400.41	W	F	N*	V I 46*		3416.07		F	Y	Fe II 16	RU
3400.85		F	N*			3416.12*		F	Y*		
3401.66	BRA	F	N*	Co I 44*		3416.915		F	N	Gd II 22	
3401.80		F	N	W II 9*	RB	3417.01		F	N	Fe II 53	RB
3401.90		M	N	Co I 157*		3417.45		F	N	Ce II 100	
3402.05		M	N			3417.70		F	N*	Co I 122*	
3402.12		F	N	Gd II 91, 149	BB	3418.73		S	N	Gd II 7	
3402.341		F	Y*	Fe II 53						NH*	
3402.16		M	Y*	V I*	SV	3420.18		F	N	V II 159*	
3402.68*		F	N*	V I*						Fe I*	
3402.85		F	N	Zr II 91*		3420.35*		F	N	NH*	
3403.19		M	Y*	Gd II 73*		3420.32*		F	N	Co I 42*	
3403.25*		F	Y*	Cr II 21*	RU	3421.13		S	Y		
				Fe I 377, 304*		3421.26		S	Y	Cr II 3	RB
3403.33	BBRA	M	N	Cr II 3		3422.59		F	Y	Fe I 444*	
3403.60	W	F	Y	Cr I 254*		3422.66	BBRA	S	Y	Gd II 2*	RB, E
3403.68	W	F	Y	Zr II 59	RB	3422.77		S	Y	Fe I 85*	RB
3404.06*		F	N*	Ce II*						Cr II 3	
3404.54		M	Y			3423.65		F	Y		
3404.59		M	Y	Pd I 2	RB	3423.80		F	Y	Ni I 20	BB
3404.812		M	N			3423.939		M	N	Gd II 7	
3404.85		M	N	Zr II 11	SY*	3424.61		M	N	Gd II 22	
3407.15		F	Y			3425.09	BBA	M	N	Fe II 7	
3407.27		F	Y	Fe II 1	RB*	3425.55*		F	N*	Fe II 5*	
3407.51		F	*			3425.63		F	N	Gd II 91*	RB
3407.60		F	N*	Gd II 91	RU	3426.217		M	N	Ce II 14	
3407.81		S	N	Dy II		3426.46*	BBA	F	N*	Eu II*	
3408.087		S	N	Zr II 72*		3427.88		F	N*		
3408.71		S	Y			3428.06		F	N*	Fe I p 616*	
3408.86		S	Y	Cr II 3	RB*	3428.26		F	*		
3409.77		F	Y	Fe II 1	RB	3428.332		M	N	Zr I 17	RB, M
3409.90		F	Y			3430.13		M	Y*		
3410.25	BBRA	M	N	Zr II 11	RB, M	3430.56		M	Y*	Zr II 11	RB
3410.287		M	N			3432.418	BBA	M	N	Zr II 58	
				Fe III 61*		3433.24		S	Y		
3410.74	W	F	N	Fe III 62*		3433.36		S	Y	Cr II 3	RB
				Dy II*		3433.49		F	Y	Ni I 19	
3411.04*		F	N*	Cr I*		3433.63		F	Y	Cr I 52*	SY*
				Gd I*		3433.92		M	N	Zr II 58	
3411.22		F	N*	Dy II*		3434.39		M	N*	Dy II	
3412.18*		F	N*								
3412.941		M	N	Nb II 3*		3434.900		S	N	Rh I 2	
						3435.62*	BBRA	F	N	Ho II*	

Table I (continued)

$\lambda(\text{\AA})$	Prof.	I	δI	ID	Com.	$\lambda(\text{\AA})$	Prof.	I	δI	ID	Com.
3436.744		S	N	Ru I 4		3452.43		M	Y		
3437.69*	BBA	F	N	Co I 162*		3457.52		M	Y	Ti II 99	SV
3438.190		S	N	Zr II 1		3452.81		F	Y		
3438.29*	BBRA	F	N*	Hf II 77	BB,M	3452.977*	BBRA	F	*	Ni I 17	RB,M
3438.91		M	Y	Mn II 1		3453.09*	BBRA	F	*	V II 132*	
3439.02*	BBRA	F	Y	Fe I 299*	BB,M	3453.17	BBA	M	N	La II 46*	
3439.10*		F	Y		RU	3453.68	BRA	M	N	Tm II 7	
3439.22		S	N	Gd II 23		3454.33	BBA	S	N	Dy II	
3439.56*		F	N	NH*		3454.917		M	N	Gd II 7	
3439.79		M	N	Gd II 22		3455.00*		F	Y	Cr II 136*	
3439.998		M	N	Gd II 7		3455.56*		F	N*		
3440.35*		F	*	Pb II*		3455.68		F	N*	Cr I 51*	RB*
3440.51		F	Y			3455.95	W	S	N		
3440.73		F	Y	Fe I 6	SY	3456.08	W	S	N	Fe II 4	RU
3440.91		F	Y			3456.34		M	Y		
3441.11		F	Y	Fe I 6	SY	3456.45		M	Y	Ti II 99	SV
3441.14*		F	*	Cr I 52*		3456.572		M	N	Dy II	
3441.22*		F	*	Cr II 8*	RU	3456.75*		F	N	Ce II*	
				Cr II 45*		3456.78*		F	N	Ce II*	
3441.41		F	N*			3457.00*	BBA	F	N*	Co I 5*	
3441.52		F	N*	Cr I 52*	RB					Fe II 76*	
3441.906		S	Y			3457.16*	BBA	F	N*	V II 147*	
3442.11		S	Y	W II 3	BB	3458.10		F	Y		
3442.87*	BRA	F	N	Co I 6*		3458.16		F	Y	Fe II 10*	SY
3443.21		M	N	Co I*		3458.376*	BBRA	F	*		
3443.36		F	Y*			3458.57		F	Y	Ni I 19	BB*
3443.43		F	Y*	Ti II 99	RB	3458.95		S	N	Zr II 58	
3443.57		F	N*	Zr II 73*		3460.01		F	Y	Mn II 1	
3443.74		F	N*	Co I 22*	RB,E*	3460.10		M	Y*	Dy II*	RB*
3443.78		F	Y	Fe II 16		3460.250		S	Y	Mn II 3	
3443.99		F	Y	Fe I 6	SY*	3460.41		S	Y		RB
3444.220		S	Y			3460.75*	BBA	F	N	Gd II 73*	
3444.41		S	Y	Ti II 6	SV					Pd I 2*	
3444.58*	BBA	F	N	Tb II*		3460.97		S	N	Dy II	
3445.33*		F	N	Pb II*						Y II 40*	
3445.56		M	N	Fe II 76*		3461.42		S	Y		
				Dy II*		3461.58*	BBRA	F	*	Ti II 6	BB,M
3446.16		F	Y			3461.75		F	Y	Ni I 17	RU
3446.362		F	Y	Ni I 20	SV	3462.05*		F	N	Rh I 3	
3447.12		F	N	Cr I 52*		3462.203		S	N	Tm II*	
				Mo*		3463.00		S	N	Gd II 3*	
				Co I 161*		3463.04		S	N	Zr II 90*	
3447.36	BBA	F	N	Zr I 16*		3463.76*		F	N	Ce II*	
				Cr I 52*		3463.94		F	Y	Fe II 4	
3447.63*		F	N			3464.008		M	Y*	Gd II 40*	RB
3447.96*	BBA	F	N	Er II*		3464.21*	BBA	F	N*	Ce II*	
3448.350		F	N	Co I 163		3464.43*		F	N		
3449.09*		F	N			3464.55		F	N	Fe II 114	RB
3449.25*		F	N	Co I 22	RB	3464.66*		F	N		
3449.62		M	N	Gd II 7		3464.76*		F	N		RB*
3449.899		F	N	Dy II*							
3450.40	BBA	F	N	Gd II 22							
3451.243		S	N	Gd II 22							

Table I (continued)

$\lambda(\text{\AA})$	Prof.	I	δI	ID	Com.	$\lambda(\text{\AA})$	Prof.	I	δI	ID	Com.
3465.520		F	Y	Ti II 99	BB*	3477.11		S	Y	Ti II 6	SY*
3465.59		F	Y*			3477.27		S	Y		
3465.62		M	N*	Zr I 17	SY*	3478.496		S	N	Zr II 84	
3465.68		M	N*			3478.57*	BRA	F	Y*	Fe II 16 Co I 120*	
3465.71		F	Y*	Co I 5*	SY*	3478.68*	BBA	F	Y*	N IV 1* Nb I*	
3465.98		F	Y	Fe I 6		3478.85*	BBA	F	Y*	Yb II*	
3466.97	BBA	F	N	Gd II 23		3479.00		S	Y*	Hf II	
3467.283		S	N	Gd II 22		3479.04		S	Y	Zr II 20*	
3467.44		F	Y	Ni I 3*	BB*	3479.15		S	Y		
3467.59		F	Y			3479.43		S	Y	Zr II 46	RB
3468.03		F	N	Gd II*	SY	3479.62*	BRA	F	N*	Fe I 443,812*	
3468.12		F	N			3479.76*	W	F	N*	Fe I 443,812*	
3468.14	BRA	F	N	Dy II		3479.89		M	Y		
3468.64		F	Y	Fe II 114	SY*	3479.96		M	Y	Fe II 4	SY*
3468.72		F	Y			3480.403	BBA	S	N	Zr II 58	
3469.342	W,BRA	M	N			3480.55*	BBA	F	N*	Gd II 23	
3469.91*	BBA	F	N	Th II* Zr II 59		3480.85		F	Y		
3470.18*	BRA	F	N*	Y II 40*		3480.94		F	Y	Ti II 22*	RU*
3470.67		F	N	Rh I 3		3481.13		S	Y	Zr II 46	RU*
3470.86		F	N	Nd II*		3481.20		S	Y	Pd I 2	
3471.12		S	N	Dy II	BB,M	3481.28	BRA	F	N*	Gd II 22	
3471.20		M	N	Zr II 114 Zr I 15		3481.46		F	N	Zr II 59	
3471.41	BBRA	M	N	Co I 161*	RB,M	3481.81		M	N	Gd II 22	
3471.53	W	M	N	Dy II		3482.35		F	N*	Ce II*	
3471.72		S	N	Er II* Tb II*		3482.50*	BBA	F	N*	U II*	
3472.191		F	N	Co I 161*		3482.61		F	N*	Gd II 40*	
3472.47		F	Y			3482.84		S	Y		
3472.64		F	Y	Ni I 20	SY	3482.969		M	Y	Mn II 3	BB,M
3472.71*	BBRA	F	N	Co I 160*		3483.15	BBA	F	N*	Co I* Ru I*	
3473.23*	BRA	F	N	Gd II 7		3483.57		M	Y*	Zr II 33	
3473.90	BRA	M	Y	Co I 4		3483.64*		F	Y*	Zr II 103	
3474.01*	BBRA	F	*	Mn II		3483.71		F	Y	Co I 5	BB*
3474.10*	BBRA	F	*	Mn II 3		3483.87		F	Y	Ni I 6 Ti II 125	
3474.21	BBA	S	Y	Mn II 3		3484.12		F	Y		
3475.101	BBRA	M	Y	Cr II 2	BB,M	3484.20		F	Y	Cr II 2	BB
3475.17	BBRA	M	Y			3484.69		F	N	Dy II	
3475.26	BBRA	M	Y	Fe II 4	BB,M	3484.82*		F	N	Fe I 185 Ho II	
3475.37	BBRA	M	Y	Cr I 141*	SY	3484.92	BBA	S	N	N IV 1*	
3475.56		F	Y	Fe I 6		3485.057		S	N	Ce II 44	
3475.60		F	Y	Fe I 78*	RU	3485.29		F	Y	Fe I 37	BB*
3475.73		S	Y	Fe II 4	SY*	3485.42		F	Y	Co I 162	
3475.79		S	Y			3485.78*		F	Y*	Yb II*	
3476.25		F	N	Y II 58		3485.83		F	Y	Ni I 17	RB*
3476.40*	BBA	F	N	Co I 161*		3485.97		F	Y	Y II 6	
3476.61	BBRA	M	Y	Fe I 6	BB,M	3486.28*		F	N		
3476.81	BBRA	M	Y								
3476.922	BBRA	M	Y	Ti II 6	RU						
3477.08	BBRA	M	Y								

Table I (continued)

λ (Å)	Prof.	I	Sl	ID	Com.	λ (Å)	Prof.	I	Sl	ID	Com.
3486.834		F	N	Er II*		3498.70*	BRA	F	N*	Dy II	
3487.40		F	N	Sm II*		3498.939		S	N	Dy II Ru I 4	
3487.96		M	Y			3499.10		S	Y*	Ti I 84*	
3488.04		M	Y	Fe II 4	SV					Er II*	
3488.57		M	Y			3499.54*		F	N*		
3488.612		S	Y	Ce II 187*		3499.60		F	N*	Zr II 9	RB
3489.09*		F	N*	Cr II 135*		3499.80*		F	N*		
				Nb II*		3499.91*		F	N*	V II 5	RU
3489.35		F	Y			3500.28		M	Y		
3489.48		F	Y	Co I 36	SY*	3500.40		M	Y	Ti II 6	RB
3489.71	BBRA	F	Y*			3500.77		F	Y		
3489.81		M	Y	Ti II 6	RB,M	3500.94		F	Y	Ni I 6	SY*
3490.22*	W	F	N*								
3490.48		M	Y			3501.15*		F	Y*	Ba I*	
3490.69		M	Y	Fe I 6	BB,M					Os I*	
3490.982		S	Y			3501.454		M	N	Ce II 67	
3491.13		S	Y	Ti II 6	RB	3501.65*		F	Y	Ca II 2*	
3491.26		F	Y*			3501.78*		F	Y*	Fe III 48*	RB,E*
3491.40*		F	Y*	Co I 6*	BB	3502.53	BBRA	M	N*	Rh I 2	
3491.99		F	N*	Co I 159*		3502.98		F	N*	Fe II 3*	
				Tb II*						Co I 135*	
3492.372		F	N	Ti II 125*		3503.10		F	N*	Fe II 3*	
3492.87		F	Y			3503.19		F	N	Dy II	
3493.07		F	Y	Ni I 18	SY*	3503.44		M	Y		
3493.13		F	*	V II 6	RB,E	3503.517		M	Y	Fe II 4	SV
3493.23		F	N			3503.97*	BBRA	F	N*	Fe III 48*	
3493.44		F	Y			3504.18*		F	N*		
3493.54	BBRA	F	Y	Fe II 114	SY*	3504.25*		F	N*		RB
3494.41		S	N	Gd II 7		3504.39	W	M	Y	V II 6	
3494.50		S	N	Dy II		3504.51		M	N*	Dv II	RB,E
3494.57*		F	N*	Cr II 2*	RU	3504.63	BRA	F	Y	Os I*	
3494.635		M	Y			3504.73	BBRA	M	Y*	Co I 115	
3494.72		M	Y	Fe II 16	BB,M	3504.81		S	Y		
3494.90*	BRA	F	N*	Cr I 109*		3504.96		S	Y	Ti II 88	RB
3495.01*		F	N*	Ce II		3505.23	BRA	M	N	Hf II 7	
3495.23		F	Y								
3495.35	BBRA	F	*	Fe I 238	RU	3505.52		S	Y*	Zr II 90*	
3495.43		M	N	Cr II 2	RU					Gd II 22	
3495.60		F	Y	Co I 22		3505.626		M	Y	Fe II 3*	
3495.77	BBRA	M	*	Ti I 84*	RU	3505.71		M	Y	Zr II 1	RB,M*
3495.95		F	Y	Hf II 30*		3505.85*		F	Y*		
3496.01		F	Y*	Ti I 22*	RU	3505.94*		F	Y*	Ti II 88	RB
3496.05		M	Y			3506.04		S	N	Zr II 84	
3496.12		M	Y*	Y II 3	RU	3506.82		F	N*	Dy II	
3496.16		S	Y			3507.325		M	N	Rh I 2	
3496.26		S	Y	Zr II 1	SY*						
3496.756		M	Y			3507.38		F	Y	Fe II 16	
3496.87	BBRA	M	Y	Mn II 3	RB,M	3507.44		F	Y	Fe I 500	SV
										Lu II*	
3497.47		S	Y			3507.49		F	N		
3497.59		S	Y	Mn II 3	SY*	3507.55*		F	N*	V II 159	RB
3497.75		F	Y	Fe I 6		3507.96*	BBRA	F	N*	Ce II 51	
3497.93	BBRA	F	*	Zr II 58	BB,M	3508.17		M	Y	Fe II 4	SV
						3508.25		M	Y		

Table I (continued)

λ (Å)	Prof.	I	SI	ID	Com.	λ (Å)	Prof.	I	SI	ID	Com.
3508.85*	BRA	F	N*	Eu II 13*		3517.53		F	N*	V II 57	
3509.184	BBA	M	N	V II 47*		3518.04		F	N	Ce II 92*	
3509.33		M	N	Zr I 15		3518.17		F	N	Er II*	
3509.68*		F	Y*			3518.28		F	Y		
3509.78*	BBRA	F	*	Pr II 88	RU	3518.43*		F	Y*	Co I 36	BB
						3519.08		F	N*	Ce II 92	
3510.25*		F	Y*	Ni I 18		3519.614		S	N	Zr I 13*	
3510.51*		F	*	Zr II 20*	RB	3519.69		F	Y		
				Co I 6*		3519.86*		F	Y*	Ni I 5*	BB
3510.79		S	Y	Pr II 88	BB,E	3519.97		F	Y*		
3510.913		S	Y			3520.04*	BBRA	F	*	V II 5	BB,M
3511.23*	W	F	N*	Sm II 12							
3511.37*	W	F	N*			3520.21		S	Y		
3511.58*		F	Y*			3520.30		S	Y	Pr II 98	SV
3511.68		F	*	Pr I 22	RB						
3511.80		F	Y*			3520.52		F	N*	Ce II 55	
3511.88	BBRA	F	Y	Cr II 2	SV					V II 57	
						3520.64		F	N		
3512.50*		F	Y*	Gd II 89*		3520.79		F	N		
3512.56	BRA	F	Y	He I 38*	RB	3520.91		F	N	Zr II 19,59	SY*
				Dy II*							
3512.91		F	Y*			3521.18		F	Y	Fe I 24	
3513.01*	BBRA	F	*	Pr II 6*	RU	3521.37		F	Y	Zr II 58	SV
3513.41		F	Y			3521.48		F	Y	Co I 20	
3513.56		F	N*	Co I 5	RU	3521.575	BBRA	M	Y*	Fe II 10*	RB,E*
3513.64		F	N	Ir I 2		3522.68		F	N*		
						3522.77		F	N*	Fe I p 53R	RB
3513.71		F	Y	Ce II*		3523.987		S	N	Dy II*	
3513.89	BBRA	F	*	Fe I 24	RU	3524.14		F	Y*	Fe I 238,239	RU
3513.98		F	Y*	V II 117		3524.18		F	Y*		
				Ni I 17		3524.31		F	Y*	Fe I 130*	RB
3514.41		F	N*								
3514.50		F	N*	V II 57	RU	3524.43		F	Y		
3514.57*		F	Y*			3524.65		F	Y	Ni I 18	SY*
3514.69	W	F	N*	Zr II 114	RB,E*	3524.69		F	Y		
3514.96		F	Y			3524.75		F	Y	V II 5	SV
3515.14		F	Y	Ni I 19	RB	3524.91*		F	Y*	Er II*	
3515.47	BRA	F	N			3525.26	BRA	F	N*		
3516.952		S	N	Pd I 1*		3525.774		F	N*	Dy II*	
				DY II						Pb II*	
3517.24		M	Y	V II 6		3525.95*	BBRA	F	Y		
3517.37		S	N*	Ce II 230*	RB,E	3526.10*		F	*	Fe I 6	BB,M
				He I 37*							

where $\log N_0 = 3$ and $T = 4200$ K. The latter temperature was chosen to mimic (within a few hundred degrees) a typical ionization/excitation temperature of a line seen at the extreme limb, and the intercept was chosen to best separate the two regions, given the slope appropriate to 4200 K. The fact that a line computed from the Boltzmann law separates the two regimes well is not surprising, if the presence of spatial structure is related to the average lower-level population $\langle n_l \rangle$, where $\langle n_l \rangle = N_0 \exp(-\chi_l/kT)$. This seems to be quantitative support for the conclusion of Livingston and White (1974) that the spatial structure is related to an opacity effect, since the opacity is directly proportional to n_l . However, another test must be made to show whether this is true (see below).

TABLE II
Lines sorted according to spatial intensity variation and species

	Species	Multiplets	No. lines	$\langle\lambda I\rangle$, eV	$\log N_E$
Spatial variation	Metals:				
	Fe I	6, 24, 78	9, 1, 1	0.2	7.6
	Fe II	4, 16, 114	6, 3, 2	1.2	7.6
	Cr II	2, 3	3, 4	2.4	5.9
	Ti II	1, 6, 22, 88, 98, 99	2, 8, 1, 2, 1, 2	0.7	5.1
	Ni I	6, 17, 18, 19, 20	2, 3, 2, 3, 3	0.1	6.3
	Mn II	1, 3	2, 7	1.8	5.4
	Co I	4, 5, 6, 20, 36	1, 1, 1, 1, 2	0.4	5.1
	Zr II	1, 11, 46	2, 1, 2	0.4	2.5
	V II	5, 6	1, 3	1.1	4.4
	Rare earths: none				
No spatial variation	Metals:				
	Fe I	238, 239, 443, 538, 812	1, 1, 1, 1, 1	3.0	7.6
	Fe II	114	1	4.1	7.6
	Cr II	2, 3	1, 1	2.4	5.9
	Ti II	53, 99	1, 1	1.6	5.1
	Co I	5, 135, 159	1, 1, 1	2.6	5.1
	Zr I	15, 17	1, 1	0.1	2.5
	Zr II	11, 19, 58, 59, 84	2, 1, 4, 3, 2	0.9	2.5
	V II	57, 117, 159	1, 1, 1	2.5	4.4
	Rh I	2, 3	3, 2	0.3	1.2
	Rare earths:				
	Ce II	44, 67, 92, 100	2, 1, 1, 1	0.3	1.8
	Gd II	7, 22, 23, 91, 149	8, 9, 3, 2, 1	0.7	1.1
	Tm II	7	2	0.0	0.3
	Dy II	-	17	-	1.1

We next ask whether there is a significant correlation for individual lines between observed line strength and observed spatial structure, which would imply that opacity differences alone might fully explain the observations, since many of the lines in our data are weak enough to be optically thin, and should therefore have intensities directly proportional to the atmospheric optical thickness τ . First, it might be that if a line were weak it would show less spatial variation because the geometric length of the line of sight in the solar atmosphere over which the line is formed is greater than for a strong line. If this explanation were valid, one would expect a direct correlation between line strength and spatial variation. Secondly, if a line were weak, it would tend to be formed lower in the atmosphere, where the geometric size of known structures is somewhat smaller than in the upper atmosphere. In this case, again, one would expect a direct correlation between line strength and spatial variation. The best way to check for such a correlation is to ask

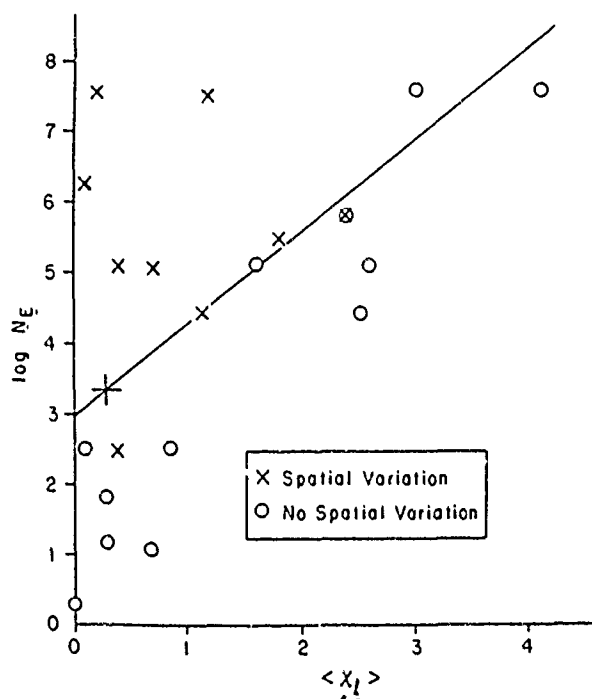


Fig. 1 The dependence of observed spatial intensity variation on $\log N_E$, the log of the solar abundance of element E by number ($\log N_H = 12$), and $\langle x_l \rangle$, the averaged lower-level excitation potential. The meaning of the line and the + symbol are discussed in the text.

whether the lines that show structure have an intensity distribution function that is significantly more skewed toward higher intensities than lines that show no structure. These distribution functions are shown in histogram form in Figure 2, which applies this test to only *metal* lines, some of which show structure and some of which do not. We cannot apply this test to our entire data set, since obviously $\langle n_l \rangle$ and τ for an individual line are reasonably independent only with a narrow range of $\log N_E$. Figure 2 shows that weak lines predominate in both structured and non-structured classes. We take \sqrt{N} , where N is the number of samples in each intensity category, to be a measure of the uncertainty. For all categories, the error bands of the two classes abut or overlap, which indicates that there is no statistically significant evidence that the intensity distributions differ. There is therefore no significant correlation between line strength and spatial variation.

In summary, we find evidence for two relationships, which seem at first to be contradictory, but can be understood as an effect of interlocking as discussed below. First, within observational uncertainty, structure seems to be present only above a critical value of $\langle n_l \rangle$, which represents in an approximate way a certain average lower-level population, where the average is taken over lines of the same structure classification in the same species. Secondly, within a narrow range of elements -

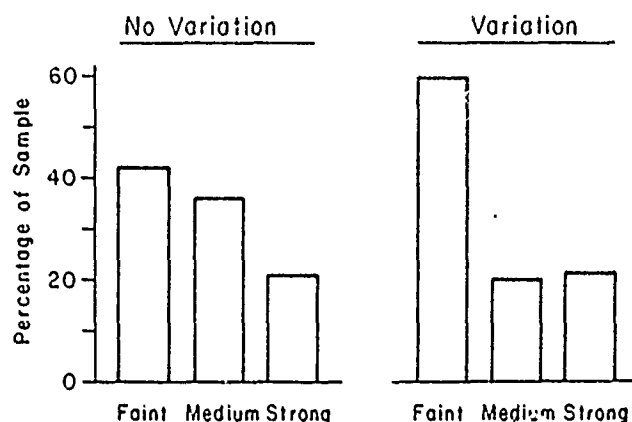


Fig. 2. Histogram presentation of line-strength distributions for the 33 securely-identified metal lines that show no spatial intensity variation and the 99 that do.

only the metals - there is no significant tendency for the lines that show structure to be dominated more by strong lines than the lines that do not show structure.

4. Interpretation

4.1. INTERLOCKING

To interpret the observed phenomena, it is necessary to consider possible mechanisms of *indirect* transitions between atomic states. Such interlocking is discussed in various monographs, cf. Jefferies (1968) or Athay (1972).

We assume complete frequency redistribution of scattered photons. This is a reasonable assumption for weak and medium-strength lines formed at and below the temperature minimum, and is applicable to almost all the lines of Table I. Following Jefferies (1968), we write the line source function S_L for a line formed between upper and lower levels u and l respectively as

$$S_L = \frac{\int J_\nu \phi_\nu d\nu + \epsilon B(T_e) + \eta B(T^*)}{1 + \epsilon + \eta}, \quad (1)$$

where, neglecting stimulated emissions:

$$\epsilon = \frac{C_{ul}}{A_{ul}}, \quad (2)$$

$$\eta = \frac{\sum_u}{A_{ul}}, \quad (3)$$

$$B(T^*) = \frac{2h\nu^3}{c^2} \frac{g_l \sum_l}{g_u \sum_u} = \frac{2h\nu^3}{c^2} e^{-x_{ul}/kT^*}, \quad (4)$$

$$\Sigma_u = \sum_{j \neq l} P_{uj} q_{jl, u}, \quad (5)$$

$$\Sigma_l = \sum_{j \neq u} P_{lj} q_{ju, l}. \quad (6)$$

Here P_{ij} is the total (radiative plus collisional) transition rate from level i to level j and $q_{ij, k}$ is the probability that a transition from level i arrives at level j before level k . The techniques for calculation of the values of $q_{ij, k}$ are discussed by Jefferies (1968) and Canfield (1971a). For the present discussion the relevant quantities are Σ_u and Σ_l . Σ_u is the rate of indirect transitions from u to l by way of all intermediate states. The analogous rate from l to u is Σ_l .

Efforts to study the effects of interlocking in the above framework have been made for two rather restricted cases by Thomas (1957) and Canfield (1971a). Thomas discussed the influence of adding a third (continuum) level to a two-level atom, i.e. the case in which the interlocking occurs only through the continuum. Canfield extended the discussion to atoms of many bound levels and continuum whose spectra consisted solely of weak lines.

4.2. INTERLOCKING THROUGH THE CONTINUUM

We can easily check the influence of continuum interlocking following the example of Thomas (1957), given in convenient form by Jefferies (1968). The influence of continuum interlocking on S_l when there are only two bound levels is measured by the ratio of the direct de-excitation term $\epsilon B(T_e)$ to the interlocking term $\eta B(T_e)$,

$$\frac{\epsilon B(T_e)}{\eta B(T_e)} \sim 10^{-6} e^{v_{ul}/kT_e}, \quad (7)$$

where T_e is the radiation temperature for ionizing radiation. We adopt typical temperatures in the vicinity of the solar temperature minimum, viz. $T_e = 4200$ K, $T_e = 5000$ K. Using Equation (7) we have computed $\epsilon B(T_e)/\eta B(T_e)$ for four representative multiplets: Fe I multiplets 6 and 443, low- and high-excitation neutral metals respectively; Ca II H and K, a low-excitation ionized metal; and Ce II multiplet 44, a low-excitation ionized rare earth.

Our calculations of the influence of the continuum are shown in Table III. The values of $\epsilon B(T_e)/\eta B(T_e)$ in Table III imply that continuum interlocking will play an important role for neutral metals, since $\epsilon B/\eta B(T_e) \ll 1$. In contrast, the ionized metal and rare earth lines are collisionally controlled, since $\epsilon B(T_e)/\eta B(T_e) \gg 1$. These characteristics bear no relationship to the observed dependence of spatial structure on species, however. Both low-excitation ionized rare earths and high-excitation neutral metals tend not to show spatial variation, whereas they have entirely different $\epsilon B(T_e)/\eta B(T_e)$ values. We conclude that interlocking with the continuum does not satisfactorily explain the observations.

4.3. INTERLOCKING THROUGH BOUND LEVELS

We now consider the effects of interlocking through bound levels following

TABLE III
Calculations of $\epsilon B(T_e)/\eta B(T_e)$ for various lines

Line	X_{kl}	X_{ul}	$\frac{\epsilon B(T_e)}{\eta B(T_e)}$
Neutral metal, low excitation	7.9	3.5	6×10^{-3}
Neutral metal, high excitation	5.0	3.5	7×10^{-6}
Ionized metal, low excitation	11.9	3.2	1×10^2
Ionized rare earth, low excitation	10.9	3.5	6×10^0

Canfield (1971a). He studied complex model atoms and found that $\epsilon B(T_e)/\eta B(T_e)$ was much less than unity. The quantities Σ_u and Σ_l (Equations (5) and (6)) are dominated by indirect *radiative* interactions with bound levels, so that T_e is nearly equal to the radiation temperature for excitations. Because interlocking is dominated by radiative processes, not collisional ones, control of S_L is potentially very non-local. The weaker the interlocked transitions are, the more non-local the value of S_L will be, since decreasing the opacity increases the spatial volume that contributes to the mean intensity. This effect explains the present observations also, since we have seen that the spatial intensity variation is directly related to the average value of the lower-level population for all lines of the species that show the same spatial-variation properties, but not to the strength of the individual line.

Our interpretation of the observed phenomenon is that the line source functions of most of the lines in the present data sample, weak and medium-strength lines of neutral and ionized metals and ionized rare earths, are dominated by interlocking via radiative excitation. Because of the non-local nature of radiative excitation, in contrast to collisional excitation, the extent to which the line source function is sensitive to local variations depends on the relative values of the characteristic geometric and optical depth scales of variations of temperature and density. If the interlocked lines are weak, the geometric length corresponding to unit optical length will be large relative to the characteristic size of structures. The value of S_L will be insensitive to local variations, hence the line will tend to show less spatial variation than lines whose interlocking is dominated by stronger lines.

4.4. QUANTITATIVE INTERPRETATION

One can easily demonstrate that the interlocking hypothesis is quantitatively consistent with the observations, using previous work. Canfield (1971b) found that for a typical observed low-excitation line of the singly-ionized rare earth Ce II, $\lambda 4364.663$, the ratio of continuum to line-center opacity τ_0 near the temperature minimum is well represented by

$$\tau_0 \equiv \frac{\kappa_c}{\kappa_0} = 4\tau_c^{0.3}, \quad (8)$$

where τ_c is the usual continuum optical depth, measured radially. If we assume formation at $\tau_c = 10^{-3}$, as justified above, Equation (8) yields $r_0 \sim 0.5$. At $\tau_c = 10^{-3}$ in the Harvard-Smithsonian Reference Atmosphere, Gingerich *et al.* (1971) give $\kappa_c \sim 1.4 \times 10^{-2} \text{ gm}^{-1} \text{ cm}^{-1}$ and density $\rho \sim 1.2 \times 10^{-8} \text{ g cm}^{-3}$. If we define a characteristic geometric length scale L_r that corresponds to unit line-center optical depth in a uniform atmosphere, then L_r is given by

$$\kappa_0 \rho L_r = \frac{\kappa_c}{r_0} \rho L_r = 1. \quad (9)$$

Adopting the values of κ_c , r_0 and ρ given above, we find that $L_r \sim 3 \times 10^4 \text{ km}$ for this line. This implies that for $L_r \sim 10^4 \text{ km}$, which is the order of magnitude of the characteristic horizontal scale of temperature and density fluctuations in the upper photosphere, an abundance approximately 30 times greater than that of cerium is required. Since for cerium $\log N_E \approx 1.8$ in the notation of Figure 1, this means that a point on the dividing line between spatial variation and no spatial variation should occur at approximately $\log N_E = 1.8 + \log 30$ and $\langle \chi_I \rangle = 0.3$, which is the $\langle \chi_I \rangle$ value for Ce in our data sample. This point appears as a + symbol in Figure 1, and falls on the dividing line justified above on a strictly empirical basis. We therefore conclude that the interpretation proposed above provides both a qualitatively and quantitatively satisfactory explanation of the observations.

5. Summary

We have used our observations of the extreme limb spectrum in the wavelength range 3398–3526 Å to identify lines and classify them according to whether or not they show small-scale spatial intensity variation (structure). We have shown that such structure is present only above a certain average lower-level number density, but is not related in detail to the strength of individual lines within a specific group of elements, the metals. We find that this can be explained as the result of interlocking by radiative excitation, but not by radiative ionization. We use previous work to show that one can understand quantitatively the critical level of elemental abundance above which spatial variation should appear, as a consequence of the mechanism of line formation and the characteristic size of spatial variations in the upper photosphere.

Acknowledgements

We gratefully acknowledge the assistance of Frederick S. Harris and Stanley N. Fri at Williams College in the measurement of wavelengths and the identification and classification of lines. Jay M. Pasachoff has been supported in part by a grant from the Research Corporation. R. C. Canfield has been supported by the Air Force Office of Scientific Research, Air Force Systems Command, USAF, under Grant No. AFOSR-76-3071.

References

- Allen, C. W.: 1973, *Astrophysical Quantities*, Athlone Press, London, 3rd ed.
- Athay, R. G.: 1972, *Radiation Transport in Spectral Lines*, D. Reidel Publ. Co., Dordrecht.
- Canfield, R. C.: 1971a, *Astron. Astrophys.* **10**, 54.
- Canfield, R. C.: 1971b, *Astron. Astrophys.* **10**, 64.
- Canfield, R. C. and Stencel, R. E.: 1976, *Astrophys. J.* **209**, 618.
- Gingerich, O., Noyes, R. W., Kalkofen, W., and Cuny, Y.: 1971, *Solar Phys.* **18**, 347.
- Jefferies, J. T.: 1968, *Spectral Line Formation*, Blaisdell Publ. Co., Waltham.
- Livingston, W. C. and White, O. R.: 1974, *Solar Phys.* **39**, 289.
- Meggers, W. F., Corliss, C. H., and Scribner, B. F.: 1975, NBS Monog. No. 145, *Tables of Spectral-Line Intensities*, U.S. Govt. Printing Office, Washington, 2nd ed.
- Moore, C. E.: 1959, NBS Tech. Note 36, *A Multiplet Table of Astrophysical Interest*, U.S. Dept. of Commerce, Washington, Rev. ed.
- Moore, C. E., Minnaert, M. G. J., and Houtgast, J.: 1966, NBS Monog. No. 61, *The Solar Spectrum 2935 Å to 8770 Å*, U.S. Govt. Printing Office, Washington.
- Pasachoff, J. M., Noyes, R. W., and Beckers, J. M.: 1968, *Solar Phys.* **5**, 131.
- Pasachoff, J. M., Harris, F. S., and Beckers, J. M.: 1974, in R. Grant Athay (ed.), 'Chromospheric Fine Structure', *IAU Symp.* **56**, 31.
- Pierce, A. K.: 1968, *Astrophys. J. Suppl. Ser.* **17**, 1.
- Thomas, R. N.: 1957, *Astrophys. J.* **125**, 260.

ii) The Height Variation of Velocity and Temperature Fluctuations
in the Solar Photosphere

This paper applies a radiative transfer technique to a study of motions in the solar atmosphere. Again, it is of little direct relevance to this grant, but was a positive step forward in understanding photospheric velocity fields at the time it was published.

The Height Variation of Velocity and Temperature Fluctuations in the Solar Photosphere

Stephen L. Keil¹, Richard C. Canfield²

¹Department of Applied Mathematics, The University of Sydney, Australia*

²Department of Physics, The University of California, San Diego, USA

Received October 19, 1977

Summary. The Vacuum Tower Telescope of Sacramento Peak Observatory is used to observe intensity and velocity fluctuations in several Fe I lines as functions of heliocentric angle. We derive the vertical and horizontal components of the velocity fluctuations, using the technique developed by Canfield (1976) to separate granular and oscillatory velocities. We also find a set of height-dependent temperature perturbations which are capable of reproducing the observed intensity fluctuations. The horizontal component of the granular velocity is found to be between one and two km s^{-1} greater than the vertical component (depending on height in the atmosphere). A temperature perturbation (constant with height) of 175 ± 10 K in the upper layers of the atmosphere ($\tau_{5000} \lesssim 0.1$) is sufficient to reproduce the intensity fluctuations in the strong lines. In deeper layers the temperature perturbations must increase rapidly with depth to reproduce the observed intensity fluctuations in the continuum and weak lines.

Key words: solar atmosphere — solar velocity fluctuations — solar temperature structure

Introduction

The computation of a dynamic multi-dimensional model of the solar photosphere will either predict or use as observational input the spatial distribution of velocity and temperature fluctuations in the photosphere. The height variation of the vertical component of the combined granular and oscillatory velocities has been derived by Canfield and Mehltretter (1973). Canfield (1976, called

Paper I below) separated this velocity distribution into oscillatory and granular components using Canfield and Musman's (1973) observations of the vertical velocity amplitude of the five-minute oscillation. The presence of horizontal motions inside granular-sized elements (spatial dimensions < 2000 km) and the nature of the flow pattern has been established by Beckers and Morrison (1970). They derive the variation of velocity across a mean granule by superimposing velocity measurements across many granules. Based on their estimate that the observed velocities originate at a height $h \approx 125$ km above the $\tau = \cos(\theta)$ level, their measurements refer to a mean height range between 130–150 km above $\tau_{5000} \lambda = 1$. Dravins (1975) has observed the height variation of the horizontal component of the rms velocity in the range 120–200 km above $\tau_{5000} = 1.0$, however, his resolution was not sufficient to deduce the granular component.

Presently (to our knowledge) there is no set of data giving the height variation of the horizontal component of the granular rms velocity throughout the height range of the photosphere. This has motivated us in this paper to apply the methods given in Paper I to a new set of velocity measurements made in the same spectral region as those of Paper I (10 Fe I lines near the Mg b lines). In addition to measurements at disk center we have a complete set of measurements at heliocentric angle $\theta = 37^\circ$ (where $\mu = \cos \theta = 0.8$), as well as measurements in several of the lines at $\theta = 53^\circ$ and 66° ($\mu = 0.6$ and 0.4). Hence we are able to derive both the horizontal and vertical components of the rms velocity. In addition, we give the observed rms intensity fluctuations in each line and deduce a model for the height variation of temperature fluctuations.

2. The Data

2.1. Observations

The data were obtained from four high spatial resolution spectrograms selected from a large set of spectrograms

*Offprint requests to: Stephen L. Keil

Currently, NAS/NRC Resident Research Associate, Air Force Astrophysics Laboratory, Sacramento Peak Observatory, Sunspot, NM 88349, USA

Sacramento Peak Observatory is operated by the Association of Universities for Research in Astronomy, Inc. under contract with the National Science Foundation

Table 1. Observed rms intensity fluctuations, rms velocity fluctuations and computed restoration factors β . Velocity restoration factors are computed for cases in which (a) only granular and oscillatory contributions are considered and (b) height-independent large-scale horizontal fluctuations are also included

λ (Å)	λ_v (km)	λ_h (km)	Intensity			Velocity			β	β
			RMS		β	RMS		β		
			Signal	Noise		Signal	Noise			
$\mu=1.0$										
cont.	0	0	.050	.007	.49	-	-	-	-	-
5178	149	40	.060	.016	.43	.195	.119	.48	.48	.48
5184	170	87	.064	.010	.67	.157	.071	.51	.51	.51
5187	183	96	.067	.009	.68	.155	.066	.52	.52	.52
5187	203	114	.071	.008	.51	.145	.034	.48	.48	.48
5188	219	137	.079	.008	.56	.137	.041	.50	.50	.50
5185	415	270	.078	.008	.61	.108	.024	.42	.42	.42
5191	465	430	.119	.012	.74	.426	.030	.76	.76	.76
5192	353	471	.125	.012	.79	.453	.013	.78	.78	.78
5191	470	447	.148	.015	.92	.534	.016	.90	.90	.90
5187	508	511	.164	.016	.87	.636	.016	.94	.94	.94
$\mu=0.8$										
cont.	-	0	.046	.006	.61	-	-	-	-	-
5178	154	49	.050	.014	.45	.138	.121	.45	.45	.45
5184	165	96	.067	.017	.49	.143	.119	.46	.46	.46
5187	185	104	.069	.009	.50	.136	.093	.46	.46	.46
5187	212	166	.078	.010	.55	.163	.065	.47	.47	.47
5184	252	204	.081	.009	.78	.152	.073	.49	.49	.49
5185	371	245	.084	.010	.64	.137	.044	.52	.52	.52
5191	447	438	.129	.012	.74	.462	.030	.75	.75	.75
5192	461	490	.125	.012	.92	.489	.038	.71	.71	.71
5191	478	460	.143	.014	.87	.567	.013	.71	.71	.71
5187	525	405	.149	.015	.93	.553	.019	.86	.86	.86
$\mu=0.6$										
cont.	-	23	.030	.007	.34	-	-	-	-	-
5178	167	63	.045	.013	.39	.444	.108	.37	.37	.37
5187	223	164	.057	.011	.47	.195	.095	.33	.33	.33
5191	474	456	.048	.011	.74	.565	.010	.77	.77	.77
5192	465	500	.070	.012	.74	.642	.010	.69	.69	.69
$\mu=0.4$										
cont.	-	46	.023	.007	.30	-	-	-	-	-
5178	167	1.2	.043	.013	.39	.422	.113	.31	.31	.31
5187	213	133	.033	.011	.46	.170	.098	.34	.34	.34
5191	473	461	.036	.013	.74	.572	.013	.71	.71	.71
5192	467	435	.036	.013	.74	.568	.016	.71	.71	.71

made over a four-month period in the late summer and fall of 1976, with the echelle spectrograph of the Vacuum Tower Telescope of Sacramento Peak Observatory. Spectrograms were made at $\mu = 1.0, 0.8, 0.6$ and 0.4 . The spectrograph slit was 140 microns wide, 155 mm long, curved to match the solar limb and oriented parallel to the limb. Other relevant data are: image scale, 0.304 mm/arc-sec parallel to the slit, 0.279 mm/arc-sec perpendicular to it; wavelength region $5150 \text{ \AA} - 5200 \text{ \AA}$; exposure 2 s at disk center on Kodak Linagraph Shellburst; the exposure was adjusted to maintain the same light level at other disk positions; dispersion varies from 10.05 mm/Å at 5200 \AA to 9.80 mm/Å at 5150 \AA . The PDS densitometer at KPNO was used to record the lines shown in Table 1 and a continuum window at 5189 \AA . Scans were made perpendicular to the dispersion with slit dimensions 100×100 microns ($240 \text{ km} \times 10 \text{ m\AA}$) and the lines were sampled every 50 microns in both spatial and wavelength coordinates ($120 \text{ km} \times 5 \text{ m\AA}$). Densitometer readings were converted to relative intensities using calibration spectra made by positioning a step wedge directly in front of the slit.

Line center position and intensity were determined as follows. Dispersion scans were constructed from the spatial scans and smoothed to give an effective spectral resolution half-width of 4 data points (20 \AA). The data points in the core of the line were fitted with a parabolic

function, and the magnitude and position of its minimum was located. Line-centershifts (hereinafter referred to as velocities, see Section 3) were measured relative to second-order polynomial which was fitted, using least squares, to the line center positions. This has the effect of removing line curvature and the velocity component due to solar rotation as well as the slow variation along the slit resulting from differential rotation. A second-order polynomial is also subtracted from the intensity record to remove the effects of line curvature, slowly-varying slit width and vignetting effects across the film.

Each set of data consists of

$$\frac{I_c(x) - \bar{I}_c(x)}{\bar{I}_c(x)}, \quad \frac{I_0(x) - \bar{I}_0(x)}{\bar{I}_0(x)}, \quad \text{and} \quad V_0(x) - \bar{V}_0(x)$$

where x is horizontal position along the slit and $\bar{I}_c(x)$ and $\bar{V}_0(x)$ are the fitted polynomials. After removal of bad data near the edge of the film, each data set corresponded to $341''$ on the sun. The rms variation and power spectrum of each data set and cross-correlation functions between sets were then computed.

2.2. Corrections and Restoration

High frequency spatial noise, introduced through film granularity, instrumental electronics, and positioning errors, was suppressed by computing the one-dimensional spatial power spectrum of each data set and, using least squares, fitting the high frequency tail with a straight line. A filter was constructed to suppress this level of noise and applied to the data in the Fourier domain. Noise levels computed in this manner are shown in Table 1, along with rms from which the noise has been removed. The only correction for low frequency noise was the removal of the second-order polynomials described above.

After suppressing the noise, the coefficient required to restore each set of data for the effects of finite spatial resolution was estimated as follows. The observed two-dimensional power per unit wavenumber $P_0(k)$ is computed from

$$P_0(k) = -\frac{d}{dk} \int_0^\infty G_0[k_x] d(k_x^2 - k^2)^{1/2},$$

where $G_0[k_x]$ is the observed, noise-filtered, one-dimensional spectrum, and $k_x = k \cos(\phi)$, where ϕ is azimuthal angle in the plane of the solar surface. This relationship is valid if $P_0(k)$ is azimuthally symmetric, which Torgler (1974) has shown to be a good assumption for sufficiently long data strings. The corrected two-dimensional power is computed from $P_c(k) = P_0(k)/M^2(k)$ where $M(k)$ is the transform of the combined instrumental and atmospheric smearing functions. Instrumental effects include smearing due to finite aperture of telescope and scanning of scattered light, and film resolution. Unfortunately we do not have a direct measurement of $M(k)$. Rather than

entirely on theoretical functions for instrumental effects, we adopted the procedure used by Keil (1977) to estimate $M(k)$ for continuum intensity fluctuations. The two-dimensional power spectrum of the continuum intensity fluctuations at disk center is restored to correspond to the shape of the spectrum found by Deubner and Mattig (1975), and to yield a similar value for the continuum rms intensity (δI_c). The restoration coefficient (β) to be applied to the rms measurement is given by

$$\beta = \left[\frac{\int_0^\infty P_o(k) dk}{\int_0^\infty P_c(k) dk} \right]^{1/2} \quad (1)$$

At the other disk positions the continuum power spectra are restored to match the observed shape of the two-dimensional spectra given by Keil (1977). This produces a center-to-limb variation (CLV) of δI_c similar to that found by Pravdjuk et al. (1974) from observations made with the Soviet Stratospheric Solar Observatory (SSSO). We determine possible restoration coefficients for the SSSO data by computing the effect of a 50 cm telescope aperture (Krat, 1971) and a 66 km square scanning slit (Pravdjuk et al., 1974) on a two-dimensional sinusoidal pattern with a spatial wavelength of 1160 km (Altrock, 1976). The resultant values of β are 0.76, 0.73, 0.67 and 0.54 at $\mu = 1.0, 0.8, 0.6$ and 0.4 respectively. Observed and restored distributions are shown in Figure 5.

Having obtained $M(k)$ for the continuum fluctuations at each disk position, we initially assumed that line-center intensity and velocity fluctuations would suffer the same spatial smearing and thus have the same restoration as do the continuum fluctuations. However, it appeared that the restoration function $M(k)$ giving the most probable restoration for the continuum, over restored high frequency power in the lines, especially in the intensity power spectra of the stronger lines. Furthermore, because intensity and velocity fluctuations have contribution functions of different forms, they need not have identical restoration functions. A detailed discussion of this problem is given by Mehlretter (1973).

These problems led us to incorporate the restoration into our computations of the fluctuating quantities by smearing our theoretically computed rms values. This is done by assuming two-dimensional sinusoidal patterns to represent the intensity and velocity fluctuations (cf. Altrock, 1976). Using the theoretical smearing functions for finite telescope and scanning apertures given by Altrock and Keil (1977), and assuming a Gaussian spread function for atmospheric smearing of the form $[1/\sqrt{\pi}\sigma] \exp -(x^2/\sigma^2)$ in the spatial domain, we can write

$$\delta I^o = \delta I \cdot M(k_L). \quad (2)$$

In Equation (2) $k_L^2 = (1/\mu L)^2 + (1/L)^2$, L is the spatial wavelength of the two-dimensional pattern and δI^o is the value of δI we would observe through the system defined

by $M(k)$. A similar equation holds for the velocity fluctuations.

From Equations (1) and (2) we have $\beta = M(k_L)$. Since β has already been determined for the continuum fluctuations of each frame we have only to specify a mean wavelength L in order to determine the "seeing parameter" σ for each frame. Using plots of the data and computations of mean spatial frequencies we estimate $L \approx 1200$ km as being most representative of the continuum fluctuations. Finally, to obtain values of β for the lines we have only to specify values of L for the oscillations and the relative contribution of granular and oscillatory elements to the observed rms signal. This is done in the following sections in which the computations are described. The resultant values of β are shown in Table 1.

3. Velocities

3.1. Velocity Weighting Functions

The rms velocities given in Table 1 do not represent the actual rms velocities in the solar atmosphere. The problems of interpreting line shifts as line-of-sight Doppler velocities have been discussed by several authors (cf. Mein, 1971; Beckers and Milkey, 1975) and a review of the problems is given by Beckers and Canfield (1975). Among the problems are horizontal and temporal smearing and line-of-sight averaging. The first and, to some extent, the second problem are dealt with through the restoration coefficients given in Table 1.

The third problem, line-of-sight averaging, is treated through the use of velocity weighting functions as described in Paper I. Thus observed line-of-sight velocity fluctuations $\delta v_o(h)$ are related to the actual height-dependent line-of-sight velocity fluctuations $\delta v(h)$ through the equation

$$\delta v_o(h_o) = \int_{-\infty}^{\infty} W(h, \mu) \delta v(h) dh, \quad (3)$$

where $W(h, \mu)$ is the velocity weighting function, h is the height above $\tau_{5000} = 1$, and for convenience we define a mean height

$$\bar{h}_v = \frac{\int_{-\infty}^{\infty} W(h, \mu) h dh}{\int_{-\infty}^{\infty} W(h, \mu) dh}. \quad (4)$$

$W(h, \mu)$ is determined from [see Equation (13), Paper I]

$$W(h, \mu) = \frac{C \kappa_L(h)}{\Delta \lambda_D(h)} \left[S(h) e^{-u(h)\mu} - \int_{-\infty}^h S(h') \kappa(h') e^{-u(h')\mu} dh' / \mu \right], \quad (5)$$

where C is a normalization constant given by

$$C = \int_{-\infty}^{\infty} W(h, \mu) dh,$$

and κ_l is the line opacity, $\kappa = \kappa_l + \kappa_c$ the total opacity, κ_c the continuum opacity, $\tau(h) = \int_{-\infty}^h \kappa(h)dh$ and $S(h)$ the total source function.

To compute $W(h, \mu)$ for a given line we need the variation with depth of κ_l , κ_c , S and $\Delta\lambda_D$. These parameters are determined by fitting computed line profiles to observed spatially-averaged profiles as described in Paper I, using the calculations of excitation and ionization equilibrium for Fe I and the non-thermal velocities given by Lites (1972). The model for which he makes calculations is very similar to the HSRA (Gingerich et al., 1972). The problems with, and reasons for, using Lites' non-thermal velocities were discussed in Paper I. Here we simply note that their use could be a source of systematic error. Observed line parameters for the spatially-averaged profiles were taken from the Preliminary Edition of the Kitt Peak Solar Atlas (Brault and Testerman, 1972) and from Moore et al. (1966). The population of the lower-level, n_l , and the line source function, S_l , were obtained from Lites' results. For some lines Lites explicitly solves for the population of the required state, for others he may provide the departure coefficient b_l/b_c . A complete discussion of how Lites' results are used is given in Paper I. In Table 2 we give the lower level and line from which respectively n_l and S_l/B were determined using Lites' results.

3.2. The Model

Having determined velocity weighting functions we proceed by specifying a model for $\delta v(h)$. The rms velocity fluctuations are then computed from Equation (3) and,

Table 2. Sources of Level-Population and Source Function Information and Central Intensities at $\mu = 1.0$ and 0.2

λ	I_o/I_c	n_l or b_l/b_c	S_l/B
5178.801	.71 (.74)*	$z^3G_3^0$	LTE
5164.552	.52 (.61)	$z^3G_3^0$	LTE
5180.069	.49 (.60)	$z^3G_3^0$	LTE
5187.917	.41 (.54)	$\gamma^5F_5^0$	LTE
5184.273	.31 (.47)	$\gamma^5F_5^0$	LTE
5165.415	.25 (.40)	$\gamma^5F_5^0$	LTF
5191.465	.14 (.21)	$z^3P_2^0$	55232
5192.353	.13 (.19)	$z^3P_2^0$	55232
5171.610	.14 (.20)	a^3F_4	44602
5167.500	.11 (.16)	a^3F_4	44602

* Value at $\mu = 0.2$

taking into account the appropriate smearing function compared to observation. Assuming the various velocity fluctuations contributing to the observed velocity are normally distributed and obey gaussian statistics we may write

$$\delta v^2(h) = [\delta v_{gran}^2(h) + \delta v_{osc}^2(h) + \delta v_{LS}^2(h)]^{1/2} \quad (6)$$

where all of the velocity fluctuations refer to the line-of-sight component (the μ dependence being understood). $\delta v_{gran}(h)$ and $\delta v_{osc}(h)$ are the rms granular and oscillatory velocity fluctuations respectively. $\delta v_{LS}(h)$ refers to possible contributions from other large-scale velocity fluctuation (such as supergranules) which are predominantly horizontal.

That the oscillatory velocities obey gaussian statistics was demonstrated by Cha and White (1973). From Figure 1 we see that, aside from small variations due to the finite sample size, none of the plotted velocity distribution differ greatly from gaussian. Thus the assumptions giving Equation (6) are probably justified.

In Paper I it was shown that the most probable form for $\delta v_{gran}(h)$ and $\delta v_{osc}(h)$ are respectively decreasing and

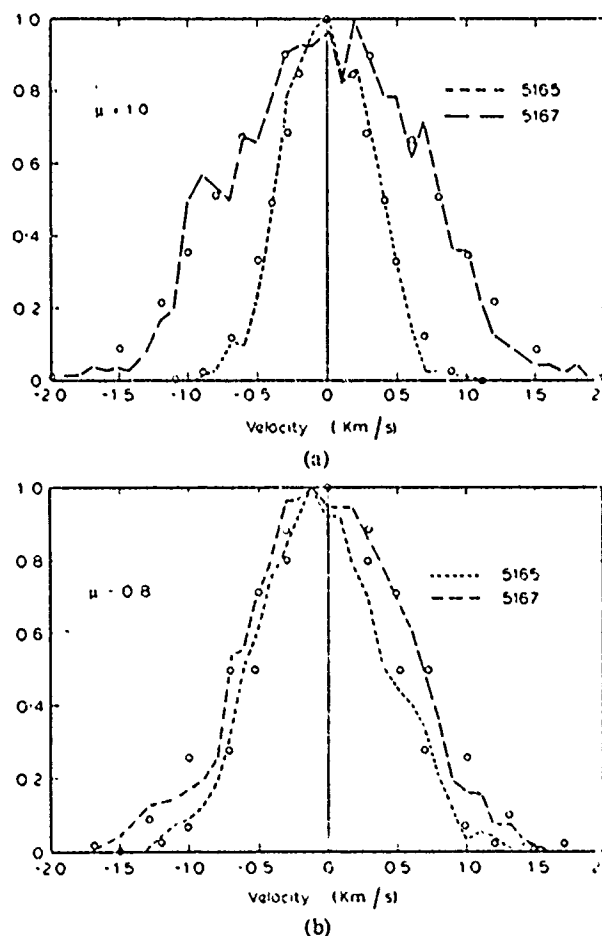


Fig. 1a and b. Normalized velocity distribution for 5167 (dashed) and 5165 (dotted). Gaussian distributions having approximately the same FWHM (circles)

increasing exponential functions of height. We shall assume $\delta v_{LS}(h)$ represents purely horizontal fluctuations. Attempts to discover the height dependence of v_{LS} by spatial filtering of the $\mu = 0.8, 0.6$ and 0.4 observations were inconclusive. For simplicity we assume v_{LS} is constant with height over the observed height range. Consequences of this assumption are discussed below. We may write our model for the line-of-sight velocity fluctuations as:

$$\begin{aligned}\delta v_{gran}(h) &= v_{gran}^0 e^{-h/H_0} \\ \delta v_{osc}(h) &= v_{osc}^0 e^{-h/H_0} \\ \delta v_{LS}(h) &= (1 - \mu^2)^{1/2} v_{LS}(h)\end{aligned}\quad (7)$$

where H_0 is negative, v^0 refers to the velocity at height $h = 0$ ($\tau_{5000} = 1$), and v_{LS} is strictly horizontal.

3.3. Smearing Factors

To compare computed values of $\delta v_0(h)$ with observed values we must compute the smearing factors $\beta = M(k_L)$ of Equation (2). Thus a representative wavelength, L , must be specified as a function of height. We assume that the spatial scale associated with v_{LS} is sufficiently large to ignore spatial smearing. The assumption of sinusoidal patterns then allows the observed value of L to be related to the granular and oscillatory values through the expression

$$\frac{1}{L} = \left(\frac{\delta v_{gran}(h)}{\delta v(h)} \right)^2 \frac{1}{L_{gran}} + \left(\frac{\delta v_{osc}(h)}{\delta v(h)} \right)^2 \frac{1}{L_{osc}} \quad (8)$$

For the values of the parameters in Equation (7) which lead to reasonable fits of the data, taking $L_{gran} = 1200$ km (Section 2.2) and $L_{osc} = 5000$ km yields good agreement between L computed from Equation (8) and L estimated from the velocity fluctuation power spectra.

3.4. Vertical and Horizontal Components

Observations at disk center give a direct measurement of the vertical component, δv_z , of the rms velocity fluctuations. The horizontal component, δv_x , in the plane defined by the spectrograph slit and the line-of-sight is found from the expression

$$\delta v^2(h) = \mu^2 \delta v_z^2(h) + (1 - \mu^2) \delta v_x^2(h) + 2\mu(1 - \mu^2)^{1/2} \langle v_x * v_z \rangle \quad (9)$$

where $\langle v_x * v_z \rangle$ is the cross-correlation between the vertical and horizontal components of the velocity at zero lag averaged over the slit. We assume that the velocities are randomly distributed so that the cross-correlation can be ignored. We do not observe, δv_y , the component of the horizontal velocity perpendicular to the slit. If azimuthal symmetry exists and v_x and v_y are statistically independent, the horizontal velocity fluctuations are given by $\sqrt{2} \delta v_x$. In the following we shall use "horizontal component" to refer solely to the v_x component.

Table 3. Coefficients giving the best fit between computed and observed velocity fluctuations. Values above the dashed line are obtained when $v_{LS} = 0$, those below the line are found when v_{LS} has the value shown and we assume the oscillatory velocities have no horizontal component

μ	H_g (km)	v_{gran}^0 (km/sec)	H_o (km)	v_{osc}^0 (km/sec)	v_{LS} (m/sec)	slit (km ²)
1.0	140 \pm 15	1.45 \pm .10	-1100 \pm 150	.37 \pm .03	20	360 \times 264
1.0*	150	1.27	-1130	.34	22	
0.8	250 \pm 10	2.30 \pm .10	-1550 \pm 200	.40 \pm .04	18	450 \times 264
0.6	220 \pm 20	2.20 \pm .25	-1300 \pm 225	.32 \pm .05	4	600 \times 264
0.4	230 \pm 25	2.70 \pm .20	-2000 \pm 250	.30 \pm .05	5	900 \times 264

					v_{LS} (km/sec)	
0.8	210 \pm 10	2.25 \pm .10	-1100 \pm 200	0.37 \pm .03	18	0.48
0.6	200 \pm 15	2.00 \pm .15	-1100 \pm 150	0.22 \pm .04	2	0.39
0.4	180 \pm 10	2.80 \pm .20	-1100 \pm 200	0.15 \pm .04	7	0.26

* Canfield (1976)

3.5. Results

Results for the velocity fluctuations are presented in Table 3 and Figures 2, 3, and 4. Two cases are investigated. Initially all of the observed fluctuations are attributed to granular and oscillatory components, thus we set $v_{LS} = 0$. The upper portion of Table 3 gives the resultant values for the coefficients of Equation (7) which minimize the standard deviation, σ_v , between computed and observed velocities. The corresponding restoration coefficients β are given in column (a) of Table 1. The

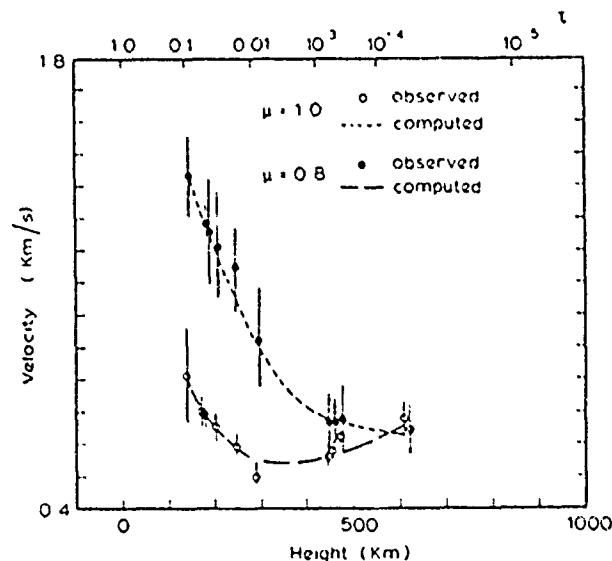


Fig. 2. Observed and computed rms velocity fluctuations at $\mu = 1.0$ and 0.8 . Observed velocities have been restored by the factors β in Column (a) of Table 1. The height at which each velocity is plotted is h_i given in Table 1. The error bars represent the internal uncertainty determined by dividing each data string into 5 segments and computing the rms velocity fluctuation separately for each segment

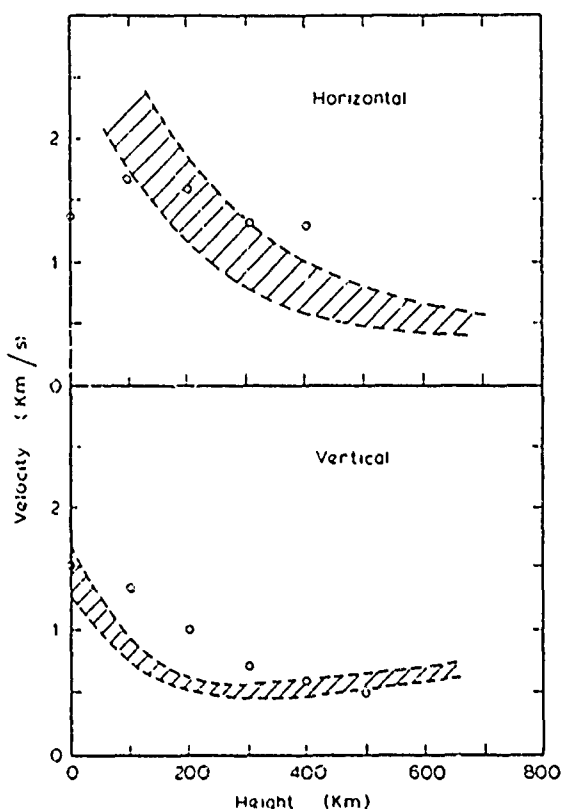


Fig. 3. Total (granular + oscillatory) rms velocity fluctuations as a function of height separated into horizontal and vertical components. Open circles represent values found by Canfield and Beckers (1975)

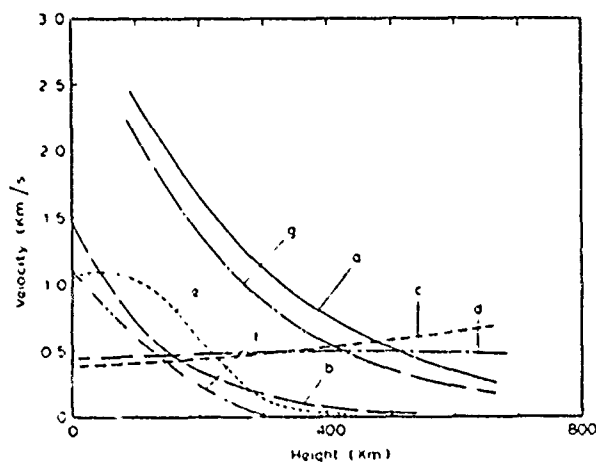


Fig. 4. (a) Horizontal and (b) vertical components of the granular rms velocity fluctuations, and (c) vertical and (d) horizontal components of the oscillatory fluctuations found when only granular and oscillatory fluctuations are considered (i.e. $v_{LS} = 0$) (e) Horizontal and (f) vertical components of the granular rms velocity fluctuations computed by Nelson and Musman (1977) (g) Horizontal component of the granular fluctuations found when large-scale height independent velocity fluctuations are included

uncertainties shown in Table 3 are determined by finding the range over which the parameters could vary without changing σ_v by more than ± 0.5 m/s. We obtain results at $\mu = 0.6$ and 0.4 even though only four lines were observed at each position. These results are used to estimate the uncertainty in the $\mu = 0.8$ results. The difference between the granular component of the vertical velocity found here and in Paper I results from the greater degree of continuum restoration in this study and the difference between the two studies reflects the uncertainty in measurements of the rms granular contrast. The values we find for r_{osc}^0 and H_0 are in good agreement with the observations of Canfield and Musman (1973).

In Figure 2 the computed and observed velocities at $\mu = 1.0$ and 0.8 are plotted. The observed velocities were divided by the restoration coefficients of Table 1 Column (a). The horizontal and vertical components of the total (i.e. granular + oscillatory) velocity fluctuations are plotted in Figure 3. The range of values given for the vertical component represents the internal uncertainty at $\mu = 1.0$. The range for the horizontal component was determined by computing a weighted mean from the horizontal velocities found at $\mu = 0.8, 0.6$ and 0.4 , and determining the standard deviation about the mean. The weights were proportional to the number of lines observed at each μ . For comparison a set of "macro" (i.e. resolved) velocity fluctuations obtained from the summary of Canfield and Beckers (1975) are also plotted. The latter velocity fluctuations were deduced by fitting mean line profiles, while our observations represent a more direct measurement of the fluctuations.

In Figure 4 the horizontal and vertical components of the granular and oscillatory velocity fluctuations deduced from the $\mu = 1.0$ and 0.8 measurements are plotted separately. The horizontal component, δv_{LS} , (Curve a) of the granular velocity fluctuations exceeds the vertical component (Curve b) throughout the observed height range. The predicted horizontal component of the oscillations (Curve d) remains constant with height at approximately 0.5 km s^{-1} . Since we have taken $v_{LS} = 1$ Curves (a) and (d) represent upper limits on the possible magnitude of the granular and oscillatory contributions. Evidence indicates that oscillatory velocities are predominantly vertical (cf. Stix and Wöhl, 1974). Thus it is likely that at least part if not all of Curve (d) results from taking $v_{LS} = 0$.

The above results led us to investigate a second case in which we assume the oscillations are strictly vertical. For $\mu \neq 1.0$ we can then write

$$\delta v_{osc}(h, \mu) = \mu \delta v_{osc}(h, \mu = 1) \quad (10)$$

and r_{osc}^0 , H_0 and v_{LS} are the only free parameters in Equation (7). With our assumption that v_{LS} is constant the values of v_{LS} giving the best fit of computed to observed velocities when Equation (10) is valid are $0.48, 0.30$ and

0.26 km s⁻¹ at $\mu = 0.8, 0.6$ and 0.4 respectively. The other parameters of Equation (7) and the standard deviations of the fits are given in the lower portion of Table 3. The corresponding restoration factors are shown in Column (b) of Table 1. Weighting each value of v_{LS} by the number of lines observed gives a mean value of 0.39 km s⁻¹ with an rms deviation of ± 0.11 km s⁻¹. This value lies within the range of 0.3 to 0.5 km s⁻¹ usually found for supergranular velocities (cf. Gibson, 1973, p. 164).

Curves (e) and (f) of Figure 4 are respectively the horizontal and vertical fluctuations computed by Nelson and Musman (1977) from a dynamic two-dimensional model of the photosphere. Curve (g) is the horizontal component of the granular fluctuations deduced from our measurements at $\mu = 1.0$ and 0.8 when $v_{LS} = 0.48$ km s⁻¹. At a height of 150 km above $\tau_{5000} = 1.0$ the velocity fluctuations we derive are greater by a factor of ~ 2.5 when $v_{LS} = 0$ or ~ 2 when $v_{LS} = 0.48$ km s⁻¹ than those predicted by Nelson and Musman. The fact that our method of separating the various contributions to the velocity fluctuations would attribute any resolved fluctuations which decrease rapidly with height to the granulation may account for part of the difference. Deubner (1971) has shown that horizontal supergranular velocities do decrease slightly with height, however not enough to account for the difference between our findings and those of Nelson and Musman. The difference between Curves (a) and (g) gives some idea of the uncertainty resulting from the unknown magnitude of the contribution from large scale fluctuations.

Whether or not the granular velocities continue to increase with depth or whether they reach some maximum and then remain constant or decrease with increasing depth cannot be determined from the lines observed. However, we can place a lower limit on the value they must attain, given our assumption on the exponential shape of the granular velocity distribution. This is done by placing an upper limit on the value $v_{gran}(h)$ can take in Equation (7). At $\mu = 1.0$ we find this limit must be greater than or equal to 1.55 km s⁻¹, otherwise the agreement between computed and observed rms values deteriorates. At $\mu = 0.8$ this limit is 2.4 km s⁻¹. Putting these limits into Equation (10) places a lower limit of ~ 3.4 km s⁻¹ on the value the horizontal component of v_{gran} must attain. We point out that results for vertical velocities below ~ 100 km and horizontal velocities below ~ 150 km involve considerable extrapolation and should be interpreted with care.

4. Temperature Fluctuations

4.1. Model

An estimate of the magnitude of the horizontal temperature fluctuations required to produce the observed rms

intensity fluctuations is made by considering sinusoidal perturbations to the mean atmosphere, for which we again use the HSRA. The integral solution to the transfer equation at the solar surface involves a two-dimensional cross-section along the line-of-sight of the three-dimensional solar atmosphere. Therefore, we consider fluctuations only along one horizontal co-ordinate; however, when computing the rms values, we still assume the fluctuations are represented by two-dimensional sinusoidal patterns, and thus obtain a factor of two between the magnitude of the fluctuations and the computed rms values. Horizontal fluctuations in the velocity will also affect the emergent radiation and must be considered. Thus, using primed quantities to refer to the perturbed atmosphere we write

$$T'(x, h) = \bar{T}(h) + \Delta T(h) \cos \frac{2\pi x}{L_T} \quad (11)$$

for the perturbed temperature distribution and

$$v'(x, h) = \sqrt{2}\delta v_{gran}(h) \cos \left(\frac{2\pi x}{L_{gran}} \right) + \sqrt{2}\delta v_{osc}(h) \cos \left(\frac{2\pi x}{L_{osc}} + \psi \right) \quad (12)$$

for the line-of-sight velocity, where $\delta v_{gran}(h)$ and $\delta v_{osc}(h)$ are computed from Equation (7) using the coefficients of Table 3, L_T and L_{gran} and L_{osc} are mean spatial wavelengths referring to temperature and velocity fluctuations, and ψ represents a phase difference between the fluctuations. In Table 4 we give the uncorrected cross-correlation coefficients for the various data strings. The rapid drop in the correlation between continuum intensity and line center velocity fluctuations occurring between 5165 and 5191 suggests we take $L_T = L_{gran}$ below approximately 350 km and equal to L_{osc} above this height. L_{gran} and L_{osc} are chosen to correspond to our choice in Section 3.3. ψ is taken to be 180° .

Assuming horizontal pressure equilibrium with the HSRA, we have $P'_0 \equiv P_0(h)$. At continuum optical depths, LTE is assumed and thus from $T'(x, h)$, $P_0(h)$, and the abundances given for the HSRA we can compute $\rho'(x, h)$, $P'_E(x, h)$ and thus $\kappa'_c(x, h)$, where H, H⁻, electron scattering and Rayleigh scattering are explicitly considered as sources of continuum opacity. In the lines, the total opacity is given by

$$\kappa'_l(x, h) = n'_l(x, h)\sigma'_0(x, h)\phi'_l(x, h) + \kappa'_c(x, h) \quad (13)$$

where n'_l is the population of the lower state, $\sigma'_0(x, h)$ the line center opacity and $\phi'_l(x, h)$ the absorption profile. The velocity distribution will affect the opacities by differentially shifting the absorption profiles along the line of sight.

To compute $n'_l(x, h)$ we assume the perturbations will not affect the departure coefficients and thus variations

Table 4. Correlation coefficients

$\lambda(\text{\AA})$	$u = 1.0$			$u = 0.8$			$u = 0.6$			$u = 0.4$		
	(a)	(b)	(c)	(a)	(b)	(c)	(a)	(b)	(c)	(a)	(b)	(c)
5178.801	0.22	0.51	0.59	0.39	0.40	0.57	0.10	0.17	0.70	0.06	0.07	0.68
5164.552	0.27	0.49	0.41	0.27	0.39	0.37	-	-	-	-	-	-
5180.069	0.32	0.53	0.32	0.33	0.45	0.36	-	-	-	-	-	-
5187.917	0.21	0.51	0.21	0.28	0.44	0.25	0.13	0.21	0.52	0.08	0.10	0.60
5184.273	0.01	0.43	0.21	0.15	0.43	0.27	-	-	-	-	-	-
5165.415	-0.11	0.38	0.11	0.12	0.42	0.21	-	-	-	-	-	-
5171.465	-0.13	0.11	0.04	-0.11	0.15	0.15	0.17	0.31	0.32	-0.15	0.16	0.40
5172.353	-0.12	0.08	0.07	-0.12	0.10	0.14	0.13	0.32	0.29	-0.12	0.14	0.38
5171.610	0.14	0.10	-0.03	0.01	0.13	0.08	-	-	-	-	-	-
5157.508	0.11	-0.05	-0.05	0.05	0.12	0.07	-	-	-	-	-	-

(a) line center intensity and velocity (b) continuum intensity and velocity (c) line center intensity and continuum intensity

in n_i will be directly proportional to those variations that would have occurred in LTE. Thus we may write

$$\frac{n'_i}{n_i} = \frac{n'_0}{n_0} \frac{U_0(T)}{U_0(T')} \exp \left[-\frac{h\nu}{kT} \left(\frac{T}{T'} - 1 \right) \right] \quad (14)$$

where n_0 is the number of Fe I atoms and $U_0(T)$ is the partition function which is computed by considering the first thirteen energy levels of Fe I.

In the continuum and the weaker lines for which Lites (1972) has shown LTE to hold for the source functions (labelled 'LTE' in Table 2), we take $S'_i(x, h) = B'_i(T'_i(x, h))$. For the stronger lines we write

$$S'_i(x, h) = (S/B)_0 B'_i(x, h) \quad (15)$$

where $(S/B)_0$ is the ratio computed by Lites for the unperturbed atmosphere. Use of Equation (15) may overestimate the fluctuations in S , since photon channeling effects due to opacity variations (cf. Athay, 1972, p. 65) and velocity variations (cf. Canon and Rees, 1971; Cannon, 1971) tend to reduce horizontal fluctuations in the source function. The use of $(S/B)_0$ is consistent with our assumption that perturbations will not alter departures from LTE.

The emergent intensity is computed from

$$I_i(x_0, \mu) = \int_{h_0}^{\infty} S'_i(x, h) \times \exp \left(\int_{h_0}^h \kappa'_i(x'', h'') dh'' / \mu \right) \kappa'_i(x, h) dh / \mu$$

with the condition $x - x_0 = (h_0 - h) \tan \theta$, where h_0 is the value of h at the solar surface. We associate a mean height of formation with the line-center intensity using the contribution function $C_i(h, \mu)$

$$\bar{h}_i = \frac{\int_{h_0}^{\infty} h C_i(h, \mu) dh}{\int_{h_0}^{\infty} C_i(h, \mu) dh} \quad (16)$$

where

$$C_i(h, u) = S'_i(x, h) \times \exp \left(-\int_{h_0}^h \kappa'_i(x'', h'') dh'' / \mu \right) \kappa'_i(x, h) / \mu,$$

with x and h related as above. Note that \bar{h}_i is not necessarily equal to \bar{h}_i , computed from Equation 4. Finally, the relative rms intensity is computed from

$$\delta I_i(\mu) = \frac{\left[\frac{1}{L} \int_0^L I_i(x_0, \mu) - \bar{I}_i(\mu)^2 dx_0 \right]^{1/2}}{\bar{I}_i(\mu)}$$

where $\bar{I}_i(\mu)$ is the mean intensity and then compared with observation, taking into consideration the appropriate smearing functions, which for our choices of spatial wavelengths are shown in Table 1. The only parameter which must still be specified is $\Delta T(h)$.

4.2. Results

The contribution of velocity fluctuations to δI_i is estimated by setting $\Delta T(h) = 0$ at all h . The resultant values of δI_i vary from approximately 0.9% in the weakest lines to less than 0.1% in the strongest. Thus in the height range under observation we would be justified in ignoring the effect of velocity fluctuations when computing rms intensity fluctuations.

Because the intensity contribution functions have a finite width (the FWHM varies from ~80 km for 5178 to 250 km for 5171), a unique model for $\Delta T(h)$ cannot be deduced from the observations. Thus, for simplicity, we adopt the procedure used by Altrock (1976) in which intersecting straight lines are used to represent $\Delta T(h)$. Letting $\gamma = dT/dh = \text{constant}$, we set $\Delta T(i) = T_0 - h\gamma$ up to a height $h_m = (\Delta T_0 - \Delta T_{\min})/\gamma$ at which $\Delta T(h)$

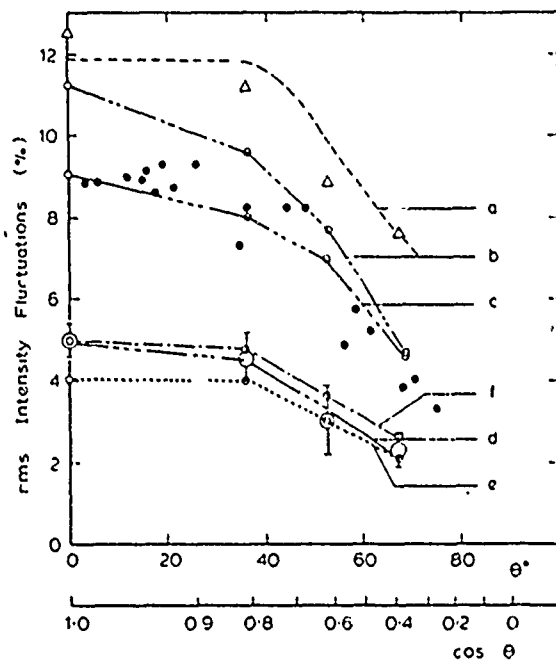


Fig. 5. Continuum intensity fluctuations as a function of heliocentric angle, observed (large circles with error bars), restored (triangles). The filled-in circles are the observed values of Pravdjuk et al. Curve (a) is obtained by averaging the Pravdjuk et al. data at $\mu = 1.0, 0.8, 0.6$ and 0.4 and applying the restoration factors given in Section 2.2. The other curves are: computations of intensity fluctuations at 4600 \AA with $\Delta T_{\min} = 175 \text{ K}$, $\Delta T_0 = 700 \text{ K}$ and (b) $\gamma = 25 \text{ K/km}$, (c) $\gamma = 20 \text{ K/km}$; and computed fluctuations at 5190 \AA with $\Delta T_{\min} = 175 \text{ K}$ and (d) $\Delta T_0 = 700 \text{ K}$, $\gamma = 25 \text{ K/km}$, (e) $\Delta T_0 = 700 \text{ K}$, $\gamma = 20 \text{ K/km}$ and (f) $\Delta T_0 = 900 \text{ K}$, $\gamma = 20 \text{ K/km}$.

reaches the minimum value ΔT_{\min} . Above h_m we set $\Delta T(h) = \Delta T_{\min}$. The calculations proceed by varying ΔT_0 , γ , and ΔT_{\min} until computed values of δI_c , reduced by the restoration factors β given in Table 1, agree with the observed values to within the observational uncertainty.

The observed values of δI_c in the continuum [$\delta I_c(\mu)$] and their internal uncertainty are plotted in Figure 5. The internal uncertainty is estimated by dividing the data strings into five 50 000 km segments and computing δI for each segment. Also shown are restored values of $\delta I_c(\mu)$ using the coefficients β from Table 1. For comparison we plot the values of $\delta I_c(\mu)$ found from the Soviet Stratospheric Solar Observatory (SSSO) data by Pravdjuk et al. (1974) as well as the theoretical restoration of the SSSO data discussed in Section 2.2. In Figure 6 we plot values of $\delta I_c(h)$ observed at $\mu = 1.0$. The height associated with each line is h_i computed from Equation (16) and listed in Table 1.

Using our assumed spatial wavelengths of 1200 km for L_{gran} and 5000 km for L_{osc} , the best fit solutions for $\delta I_c(\mu)$ (Figure 5, Curve d) and $\delta I_c(h)$ (Figure 6) are

obtained with $\Delta T_0 = 700 \pm 50 \text{ K}$, $\gamma = 25 \pm 2 \text{ K/km}$, and $\Delta T_{\min} = 175 \pm 25 \text{ K}$. The uncertainties given for ΔT_0 and γ represent the range over which these parameters can vary without changing the standard deviation of the continuum fit by more than 1%. Although keeping ΔT_{\min} constant does not yield a perfect fit to observations, Figure 6 indicates that any change in ΔT_{\min} with height must be small ($\pm 25 \text{ K}$). Computed values of $\delta I_c(\mu)$ are affected very little by changes in ΔT_{\min} of this magnitude. Placing an upper limit on the value $\Delta T(h)$ can reach deep within the atmosphere we find that this limit must be greater than or equal to 2500 K, otherwise the quality of the fit deteriorates rapidly. Thus $\Delta T(h)$ must continue to increase to a depth of approximately 70 km below $\tau_{5000} = 1$, below this depth temperature fluctuations have little effect on the emergent intensity.

The values we find for ΔT_0 , γ , and to a lesser extent ΔT_{\min} are sensitive to the assumed spatial wavelengths. If for example: the granular wavelength is reduced to 800 km, ΔT_0 must increase to 900 K and γ decrease to 20 K/km, in order to retain a reasonable fit to the data (Fig. 5, Curve f). The value we find for ΔT_{\min} ($175 \pm 25 \text{ K}$) is in good agreement with the value of 200 K found by Altrock and Keil (1977) from fluctuations in the Mg 4571 line. The source function for 4571 is controlled by local variables and thus LTE is a good assumption (Altrock and Canfield, 1974). The agreement between the two results suggests that the assumptions leading to Equations (14) and (15) are reasonable.

Some idea of the uncertainty introduced through restoration can be obtained by comparing our results

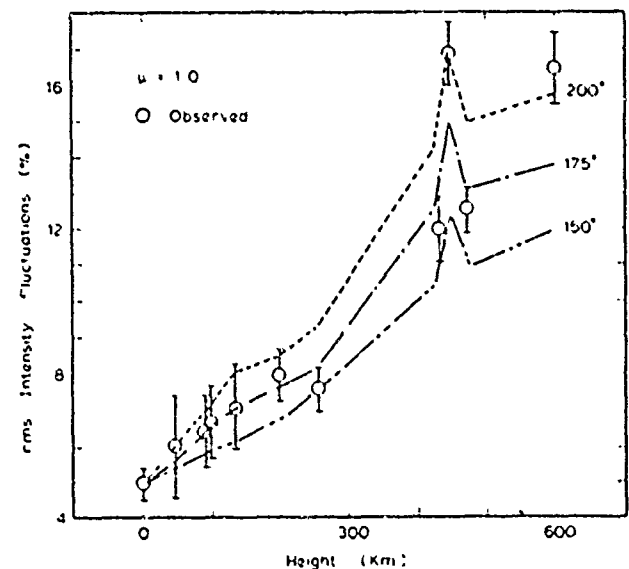


Fig. 6. Intensity fluctuations in the lines as a function of height. The observed values (large circles with error bars) are plotted at height h_i given in Table 1. The curves are all computed with $\Delta T_0 = 700 \text{ K}$, $\gamma = 25 \text{ K/km}$ and ΔT_{\min} as shown in the figure.

with those of Altröck (1976). Altröck fits the SSSO data of Pravdjuk et al. (1974) for which atmospheric smearing is not important (Section 2.2). Altröck obtains his "best fit" solution with $\Delta T_0 = 690$ K, $\gamma = 20$ K/km, and $\Delta T_{min} = 0$. If we try to match the SSSO data with our best fit solution, $\Delta T_0 = 700$ K, $\gamma = 25$ K/km, and $\Delta T_{min} = 175$ K, using β computed for the SSSO data in Section 2.2, our computed rms intensities are too large (Fig. 5, Curve *b*). To obtain a reasonable fit γ must be reduced to 20 K/km (Fig. 5, Curve *c*), in agreement with Altröck's results. If we attempt to match our observations with this value of γ (Fig. 5, Curve *e*) the computed rms intensities are too small. Thus our observations and their subsequent restoration require larger temperature fluctuations below $\tau_{5000} = 1.0$ and smaller fluctuations above $\tau_{5000} = 1.0$ than do the SSSO observations.

In Figure 7 the rms temperature distribution ($\delta T(h) = \Delta T(h)/2$) we obtain is compared with the distributions found by Altröck (1976) and computed by Nelson and Musman (1977). The two latter distributions refer solely to convective (granular) fluctuations, while our distribution is obtained for the combined effects of convection and oscillations. A negative value for δT implies that the fluctuations (ΔT) change sign. The problem, mentioned above, concerning the widths of the contribution functions, and the fact that the contribution functions for the intermediate strength lines (5165 and 5185) overlap regions dominated by both convection and oscillations make it difficult to determine whether the fluctuations change sign near 120 km as predicted by Nelson and Musman (1977). The rapid decrease in the correlation (Table 4) between continuum and line center intensity fluctuations ($\delta I_c \cdot \delta I_0$) with height may suggest this, however, we do not observe a change in the sign of the correlation until reaching the height at which 5171 is formed (~ 450 km above $\tau_{5000} = 1.0$).

5. Discussion and Summary

We have attempted a direct measurement of the height-dependence of the horizontal and vertical components of the granular velocity. For this purpose we obtained high resolution spectrograms of compatible quality, as judged by their rms intensity fluctuations in the continuum, at $\mu = 1.0$ and 0.8. To separate granular from oscillatory velocities the assumptions leading to Equation (7) are made. The most probable values for the parameters of Equation (7) are shown in Table 3. We find that the horizontal component of the granular velocity exceeds the vertical over the entire depth range observed. The information content for velocity fluctuations, in the lines observed, falls off rapidly below ~ 150 km above $\tau_{5000} = 1.0$, thus we are unable to determine whether the velocities

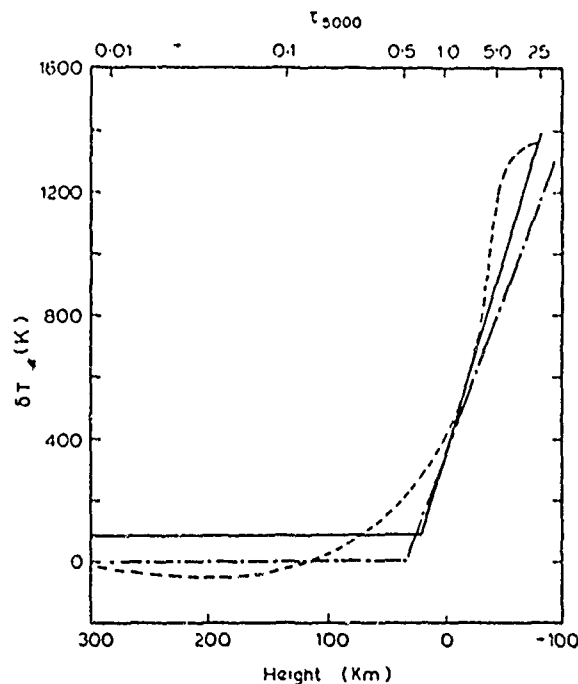


Fig. 7. "Best fit" solution for the rms temperature fluctuations as a function of height (solid line). Altröck (dot-dash), Nelson and Musman (dashed)

continue to increase with depth, or whether they reach some maximum value and then decrease, as found, for example, by Gurtor'enko (1975a,b) and as predicted by Nelson and Musman (1977).

Our observations, along with those of Pravdjuk et al. (1974), Keil (1977), and Altröck and Musman (1976) are compatible with temperature fluctuations which increase monotonically with depth in the lower photosphere. This disagrees with the earlier work of Wilson (1969) based on observations of Edmonds (1962). To reproduce Edmonds' observations Wilson found $\Delta T(h)$ must reach a maximum near $\tau_{5000} = 0.7$ and then decrease sharply with depth, with a possible second peak in deeper layers. He attributed the peak(s) to the release of thermal energy in these layers. Such a peaked distribution for $\Delta T(h)$ is not compatible with our data unless the peak occurs below the layers which contribute significantly to the emergent intensity.

Finally our observations lead to several conclusions concerning the transport of energy in the photosphere. Using our results for $\delta I_c(h)$ and $\delta T(h)$ the convective flux can be estimated from $c_p \rho \delta \Gamma \delta \tau$, where c_p is the heat capacity at constant pressure and ρ the density (cf. Cox and Giuli, 1969, p. 297). We find convection carries 15%, 4%, and 0.2% of the total energy flux at $\tau_{5000} = 5, 1$ and 0.1 respectively. The magnitude of temperature fluctuations due solely to convective transport can be estimated from the expression $\Delta T_{conv} = t_R (dT/dz)$ where t_R is the radiative relaxation time and dT/dz the temperature

gradient, which is superadiabatic below $\tau_{5000} \approx 0.8$. At $\tau_{5000} = 1.0$ we have $v_z = 1.45 \text{ km s}^{-1}$, $dT/dz \approx 24 \text{ K/km}$ and $t_R \approx 2 - 3 \text{ s}$ (cf. Alrock and Musman, 1976; Levy, 1974), which gives ΔT_{conv} between 70 K and 100 K. Thus radiative transport must account for most of the observed temperature fluctuations. The large value we find for ΔT at $\tau_{5000} = 1.0$ (700 K) and the rapid increase in ΔT below this level (25 K/km) are in agreement with the argument of Alrock and Musman (1976) that temperature fluctuations in the deeper layers of the photosphere are controlled largely by radiative heating from below.

Acknowledgements. We wish to thank H. Mauter, R. Mann and H. DeMastus for help in obtaining the observations and S. Musman for useful comments on the manuscript. R. Canfield has been supported by the Air Force Office of Scientific Research, Air Force Systems Command, USAF, under Grant No. AF OSR 76-3071. The observations were obtained while one of us (SLK) held a Joint Institute for Laboratory Astrophysics Postdoctoral Appointment at Sacramento Peak Observatory. This work has been supported in part by the Australian Research Grants Committee.

References

- Alrock, R. C.: 1976, *Solar Phys.* 47, 517
 Alrock, R. C., Canfield, R. C.: 1974, *Astrophys. J.* 194, 733
 Alrock, R. C., Keil, S. L.: 1977, *Astron. Astrophys.* 57, 159
 Alrock, R. C., Musman, S.: 1976, *Astrophys. J.* 203, 533
 Athay, R. G.: 1972, *Radiation Transport in Spectral Lines*, D. Reidel Pub. Co.
 Beckers, J. M., Canfield, R. C.: 1975, in *Physique des mouvements dans les atmosphères stellaires*, R. Cayrel and M. Steinberg (eds.) CNRS Colloq. 250, 207
 Beckers, J. M., Milkey, R. W.: 1975, *Solar Phys.* 43, 289
 Beckers, J. M., Morrison, R. A.: 1970, *Solar Phys.* 14, 280
 Brault, J., Testerman, I.: 1972, *Kitt Peak Solar Atlas*, Prelim. Ed.
 Canfield, R. C.: 1976, *Solar Phys.* 50, 239 (Paper I)
 Canfield, R. C., Beckers, J. M.: 1975, in *Physique des mouvements dans les atmosphères stellaires*, R. Cayrel and M. Steinberg (eds.), CNRS Colloq. 250, 291
 Canfield, R. C., Mehltretter, J. P.: 1973, *Solar Phys.* 33, 33
 Canfield, R. C., Musman, S.: 1973, *Astrophys. J. Letters* 184, L131
 Cannon, C. J.: 1971, *Solar Phys.* 21, 82
 Cannon, C. J., Rees, D. E.: 1971, *Astrophys. J.* 169, 157
 Cha, M. Y., White, O. R.: 1973, *Solar Phys.* 31, 55
 Cox, J. P., Giuli, R. T.: 1969, *Principles of Stellar Structure*, Vol. 1, Gordon and Breach Pub.
 Deubner, F. L.: 1971, *Solar Phys.* 17, 6
 Deubner, F. L., Mattig, W.: 1975, *Astron. Astrophys.* 45, 167
 Dravins, D.: 1975, *Solar Phys.* 40, 53
 Edmunds, F. N.: 1962, *Astrophys. J. Suppl.* 6, 357
 Gibson, F. G.: 1973, *The Quiet Sun* (NASA SP-303)
 Gingerich, O., Noyes, R. W., Kalkofen, W., Cuny, Y.: 1972, *Solar Phys.* 18, 347
 Gurtovenko, E. A.: 1975a, *Astrometrija Astrofiz.* 27
 Gurtovenko, E. A.: 1975b, *Solar Phys.* 45, 25
 Keil, S. L.: 1977, *Solar Phys.* 53, 359
 Krat, V. A.: 1971, *Trans. I.A.U. XIVB*, 112
 Levy, M.: 1974, *Astron. Astrophys.* 31, 451
 Lites, B. W.: 1972, NCAR Cooperative Thesis No. 28 (unpublished)
 Mehltretter, J. P.: 1973, *Solar Phys.* 30, 19
 Mein, P.: 1971, *Solar Phys.* 20, 3
 Moore, C. E., Minnaert, M. G. J., Houtgast, J.: 1966, *NBS Monograph* 61
 Nelson, G. D., Musman, S.: 1977, *Astrophys. J.* 214, 912
 Pravdjuk, I. M., Karpinskij, N. N., Andrejko, A. V.: 1974, *Solnechnye Dannye*, No. 2, 70
 Stix, M., Wöhl, H.: 1974, *Solar Phys.* 37, 63
 Teske, R. G.: 1974, *Solar Phys.* 39, 363
 Wilson, P. R.: 1969, *Solar Phys.* 6, 364

e) Quasar Theory

The papers in this section concern themselves with the development of theoretical methods for radiative transfer, as well as their application to quasars. Although this work might seem quite unrelated to the main thrust of the grant, upon closer inspection it is seen to be of direct benefit to the main objective. Most notably, the third paper of this section deals with the derivation of the form of the radiative transfer equation that is used in the theoretical studies of solar flares. It is also worth pointing out that because we applied these techniques to quasars, one of the outstanding major problems of quasar emission lines was solved. Hence, the application to quasars was worthwhile, in itself, in addition to the significance of the theory in the solar flare work that is the primary objective.

i) The Implications of Hydrogen Emission Line Ratios in Quasi-Stellar Objects

This was a brief summary paper, which contained the main results from the astronomical point of view, but with little explanation of the methods used. These results are explained more completely in the following papers.

THE IMPLICATIONS OF HYDROGEN EMISSION LINE RATIOS IN QUASI-STELLAR OBJECTS

RICHARD C. CANFIELD AND R. C. PUETTER

Center for Astrophysics and Space Science, University of California, San Diego

Received 1979 June 25; accepted 1979 November 6

ABSTRACT

We summarize the results of multilevel, depth-dependent, fully interlocked radiative transfer calculations for hydrogen emission line strengths in a single QSO emission line cloud (ELC). We find that hydrogen line intensity ratios in the range of observed values ($L\alpha/H\alpha/H\beta/P\alpha \sim 1/1/0.25/0.2$) arise naturally from our theoretical models, for physical conditions in the ranges $7 \times 10^3 \leq T_e \leq 2 \times 10^4$ K, $10^7 \leq N_H \leq 10^{11}$ cm $^{-3}$, and radiation fields less than about 10^{-6} ergs cm $^{-2}$ s $^{-1}$ Hz $^{-1}$ at 1 rydberg, without recourse to dust internal or external to the ELC. The hydrogen-line forming region of the ELC is quite thick ($10^3 \leq \tau_{el} \leq 10^5$), which we show to be reasonable and consistent with heating of a pure hydrogen cloud by photoionization.

Our results indicate that three factors seriously compromised the validity and success of past models. First, the volume-averaged escape probability approach introduces large errors by assuming, in effect, that a single point in the ELC is representative of the emergent radiation. Second, it is imperative that one explicitly recognize the influence of frequency redistribution on the photon escape probability in resonance and subordinate lines. Third, full consistency between excitation and ionization processes must be maintained. In our calculations $L\alpha$ continuum interlocking results in an extremely extended H II region. There is thus an urgent need for self-consistent multielement ELC energy balance calculations that consistently incorporate the effects of radiative transfer in the dominant cooling lines.

Subject headings: line formation — quasars — radiative transfer

1. INTRODUCTION

The large amount of energy available in the ultraviolet continuum of QSOs strongly suggests that photoionization is the primary energy source for the line emitting region. As a consequence many authors have produced photoionization models of QSOs (see, e.g., Davidson 1972, 1973; MacAlpine 1972; Shields 1973; Scargle, Caroff, and Tarter 1974; Chan 1974). However, several recent investigations have suggested that simple photoionization/recombination models are unable to explain the observed line ratios in QSOs. Composite QSO spectra (Baldwin 1977) and combined optical-IR measurements of $L\alpha/H\beta$ by Puetter, Smith, and Willner (1979), Soifer *et al.* (1979), and Hyland, Becklin, and Neugebauer (1978) and combined UV-optical measurements of $L\alpha/H\beta$ by Davidsen, Hartig, and Fastie (1977) and Baldwin *et al.* (1978) show $L\alpha/H\beta \approx 3$ to within a factor of ~ 2 and a steep Balmer decrement. Many authors have attempted to explain this departure from the simple recombination ratios as being due to the effects of dust (Baldwin and Netzer 1978; Shuder and MacAlpine 1979; Hyland, Becklin, and Neugebauer 1978). Other authors have proposed that radiative transfer effects with or without dust might produce the observed line ratios (Netzer 1975; Krolik and McKee 1978; Shuder and MacAlpine 1979; Puetter, Smith, and Willner 1979; Puetter *et al.* 1978). The observation of both $P\alpha$ and the Balmer lines in the same QSO (Grasdalen 1976; Puetter *et al.* 1978) has demonstrated that simple recombination line strengths

reddened by dust are unable to account for the observed line ratios. Recent theoretical work by Terland and Netzer (1979) has suggested that internal dust alone also may not be able to explain the anomalous $L\alpha/H\beta/P\alpha$ ratio. These considerations all seem to suggest that radiative transfer effects may be extremely important in the ELCs.

In this Letter we describe a different approach to modeling quasar ELCs from any that has been taken in the past. In § II we briefly describe the theoretical framework for the calculation. In § III we first show that this framework is successful in describing the observed hydrogen line ratios. We then examine the important differences between our calculation and past calculations. Finally, we indicate improvements to the present theoretical framework necessary to construct models that can more meaningfully be compared to observations.

II. MULTILEVEL, FULLY INTERLOCKED MODEL ELC

Our concern over the neglect of potentially important depth-dependent interlocking through radiative and collisional excitation and ionization in previous ELC models prompted us to attempt a more rigorous optical-depth-dependent calculation of the sources and sinks of photons. We modeled the hydrogen atoms in the ELC as having six fully interlocked levels, five bound levels, and the ionized state; numerical experiments showed higher bound levels to be unimportant to the transitions we consider here. We modeled an individual ELC as a plane-parallel atmosphere of uniform electron

temperature and hydrogen density of considerable optical thickness. This ELC is thought to be one of many clouds irradiated by a power-law external radiation field. We expect that the dependence of the emergent hydrogen line ratios upon ELC geometry will be small. We have used a scaling-law approximation to the solution of the radiative transfer equation (cf. Athay 1972; Ivanov 1973). We used depth-dependent escape probabilities appropriate to the various lines. For the Lyman lines we used the partial redistribution result of Ferland and Netzer (1979, eq. [6]). For the other lines it is appropriate to use an escape probability based on complete redistribution in a radiatively damped Voigt profile (cf. Ivanov 1973, eq. [2-7.29]). The probability of escape for continuum photons was calculated by averaging the escape over the spontaneous emission profile (see Canfield and Ricchiazzi 1980). These escape probabilities were used in calculating frequency-integrated radiation fields in boundary regions of the ELC, and subsequently the values of ρ , the usual "escape coefficient" or "net radiative bracket" (Athay 1972), and line center source functions S_0 . The net radiative rates in both lines and continua, along with collisional rates (Krolik and McKee 1978) and radiative rates due to the external ionizing flux, were iterated to solve the atomic steady-state equations consistent with the scaling-law solutions to the radiative transfer equation. From these solutions we then calculate emergent fluxes by integrating the flux divergence ρS_0 over optical depth. Full details of the calculation will be given elsewhere (Canfield and Puetter 1980).

III. RESULTS

a) The Emission Line Ratios

In Figure 1 we present our results and compare them to observations. The parameters of our standard model are $T_e \equiv T_e/10^4 \text{ K} = 1$, $N_H \equiv N_H/10^9 \text{ cm}^{-3} = 1$ and $I/I_0 = 1$, where T_e is the electron temperature, N_H is the hydrogen density, and $I_0 = 10^{-3} \text{ ergs cm}^{-2} \text{ s}^{-1} \text{ Hz}^{-1}$ at 1 rydberg. All calculations in this Letter assume $I/I_0 \propto \nu^{-1}$. We have calculated line ratios for our standard model and variations in T_e , I/I_0 , and N_H . Results are shown in Figure 1a, b, and c, respectively. The predictions of our standard model are shown in all three panels. The line ratios all depend on the thickness of the ELC, which we measure by τ_{cl} , the Lyman-limit optical depth. Each curve in Figure 1 shows how the line ratios depend on τ_{cl} for a specific T_e , I , and N_H . Symbols along the curves are separated by one decade in τ_{cl} , and some τ_{cl} values are given as space permits. The rectangle shows the range of $H\beta/H\alpha$ and $L\alpha/H\alpha$ values that we believe are compatible with the observations. For $P\alpha/H\alpha$ we plot a solid curve when the $P\alpha/H\alpha$ ratio agrees satisfactorily with the observations, dashed otherwise. In Figure 1a we see that our standard model (open triangles) can explain the observations for $\tau_{cl} \sim 3 \times 10^3$. The enhanced-temperature model ($N_H = 1$, $I/I_0 = 1$, $T_e = 2$) never simultaneously achieves the observed $H\beta/H\alpha$ and $L\alpha/H\alpha$ ratios at any value of τ_{cl} ; the same is true of the reduced-temperature model. Figure 1b shows the effects of varying I/I_0 , and in

Figure 1c varying N_H . In Figure 1b, the $I/I_0 = 0$ curve is added to illustrate the line ratios that would emerge from a $T_e = 10^4$ cloud that has no radiation field incident upon it. From the results shown in Figure 1 it is clear that our models can explain the observations for physical conditions in the approximate ranges $7 \times 10^3 \leq T_e \leq 2 \times 10^4 \text{ K}$, $10^7 \leq N_H \leq 10^{11} \text{ cm}^{-3}$, and $I \leq 10^{-6} \text{ ergs cm}^{-2} \text{ s}^{-1} \text{ Hz}^{-1}$ at 1 rydberg, for clouds that are quite thick at the head of the Lyman continuum ($10^3 \leq \tau_{cl} \leq 10^5$).

It is instructive to compare our results with case B. From Figure 1 one readily sees that our $L\alpha/H\alpha$ and $H\alpha/H\beta$ ratios for $\tau_{cl} \leq 1$ agree well with case B values. In our standard model, the observed line ratios emerge from a cloud for which the region of $T_e \sim 1$ extends to $\tau_{cl} \sim 10^3$. The absolute intensity of $H\alpha$ in this case is about $5 \times 10^6 \text{ ergs s}^{-1} \text{ cm}^{-2}$. In comparison, the (optically thin) $H\alpha$ from a model with case B population ratios and $\tau_{cl} \sim 10^3$ is about $1.3 \times 10^7 \text{ ergs s}^{-1} \text{ cm}^{-2}$. The close resemblance of these two numbers is coincidental; in our models the emissivity at these depths is much higher than in case B, but the probability of escape is much lower. The optical depth at which the standard model achieves the observed line ratios is $\tau_{cl} = 3 \times 10^3$ (see Fig. 1). The n_2 population at this point is $\sim 3 \times 10^3$ as opposed to $\sim 4 \times 10^3$ for case B. The optical depth in $H\alpha$ at this point is $\sim 4 \times 10^5$ and the probability of photon escape is $\sim 8 \times 10^{-5}$. Thus while both models produce similar line fluxes, the physical conditions in the ELC are vastly different.

b) Comparison with Past ELC Models

Several things immediately become apparent from the results of our calculations. First, a depth-dependent treatment is essential to a full understanding of the line ratios in realistic ELC models. Second, the form of the escape probability is of paramount importance. Third, inclusion of ionization processes from upper-bound levels combined with consistent radiative transfer solutions makes the ionization structure of our models dramatically different from past models.

Our results confirm the suspicions of previous authors that neglect of depth-dependent effects might lead to serious errors. In Figure 2 we plot the flux divergence per decade in line-center optical depth ($\rho S_0 / \log_{10} \nu$), which measures the depth of origin of the emergent energy versus optical depth at the Lyman limit, for $L\alpha$, $H\alpha$, $P\alpha$ for three different forms of the escape probability. In Figure 2c we plot the flux divergence for a form of the escape probability, p_c , that assumes complete redistribution over a Doppler profile (Ivanov 1973, eq. [2-7.12]). This form of p_c has been the most widely used form in past ELC model calculations. Note the very different depths of origin of the energy that emerges as radiation in $L\alpha$ and $H\alpha$ under these assumptions. Clearly in this case no single point in the ELC can possibly be characteristic of all the lines. Figures 2a and 2b show the flux divergence for more realistic forms of the escape probability (Fig. 2a is the more realistic case). Note in these two cases that while $L\alpha$ and $H\alpha$ are not formed in completely distinct regions, the

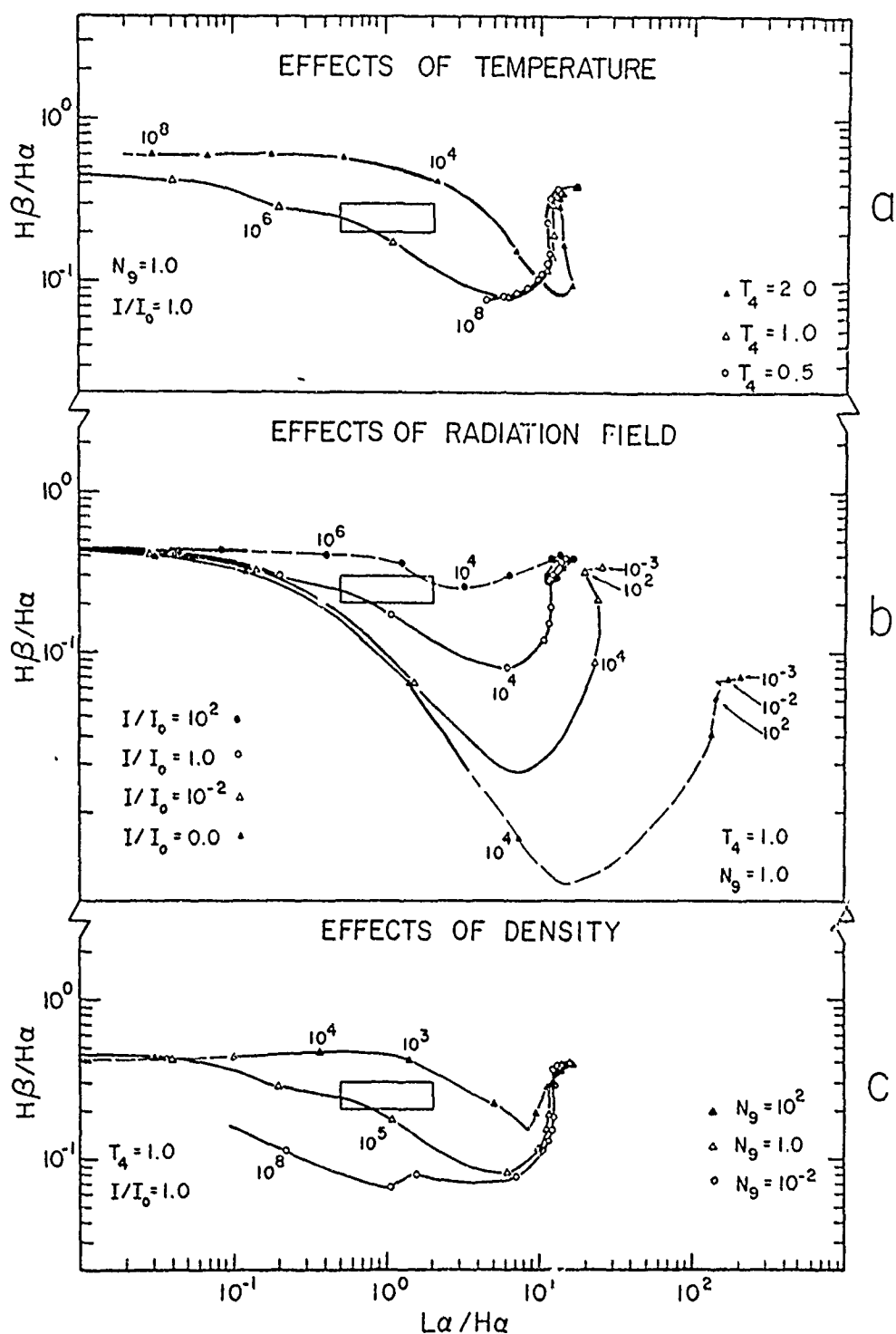


FIG. 1.—Calculated value of $L\alpha/H\alpha$ ($H\beta/P\alpha$) for different ELC parameters as a function of the Lyman limit optical depth ($\tau_{L\alpha}$). The ELC parameters explored are T_4 , N_9 , and I/I_0 . In all models we assumed an ionizing flux that varied as $\nu^{-1.0}$, where $I_0 = 10^{-4}$ ergs cm^{-2} s^{-1} Hz^{-1} at 1 rydberg. The portions of the curves that are drawn as solid lines indicate where the calculated $P\alpha/H\alpha$ ratio achieves the range of observed values. The rectangle shows the typical range of observed $L\alpha/H\alpha$ and $H\beta/H\alpha$ ratios. The symbols on each curve indicate 1 decade intervals in optical depth at the Lyman limit. (a) Here we explore the effects of temperature. Note that the lower label 10^5 belongs to the $T_4 = 0.5$ curve (circles), while the 10^6 label belongs to the $T_4 = 1.0$ curve (triangles). (b) Here the effects of different ionizing flux intensities are shown. (c) Here we show the effects of different total hydrogen densities. The standard model ($I/I_0 = 1.0$, $N_9 = 1.0$, $I/I_0 = 1.0$) is displayed in each panel.

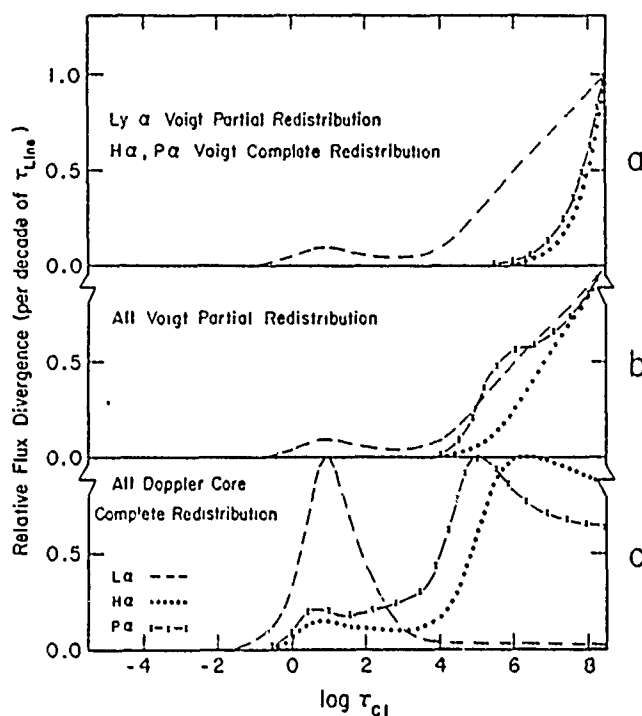


FIG. 2—Flux divergence per decade of $\tau_{L\alpha}$ ($\rho S/r \log_{10} e$) arbitrarily scaled to unity at its maximum value for $L\alpha$, $H\alpha$, and $P\alpha$, versus $\log \tau_{c1}$ for the standard model (i.e., $I_1 = 1.0$, $N_H = 1.0$, $I_{H\alpha} = 1.0$) under different assumptions of the physics of photon redistribution. (a) The most realistic approximation. We assume here that the Lyman line escape probability is given by the partial redistribution calculation of Ferland and Netzer (1979) and that the escape probability in the subordinate lines may be calculated by assuming complete redistribution over a radiatively damped Voigt profile. (b) We assume here that the Ferland and Netzer result applies to all lines. (c) Here we assume complete redistribution over the Doppler core only.

region of appreciable emission is nevertheless extremely extended. The escape probability varies by a large factor over this region (roughly three orders of magnitude for $L\alpha$ between Lyman limit optical depth $\tau_{c1} = 10^6$ and 10^9 in Fig. 2a) and thus cannot adequately be represented by a single characteristic p_e value.

A realistic form of the escape probability is essential to the construction of physically meaningful ELC models. By comparison of frames a, b, and c of Figure 2 one can appreciate the extreme sensitivity of the depth dependence of the relative flux divergence on the form of the escape probability. This is a consequence of the fact that the different forms of p_e give very different values for the same optical depth. As an example we cite the values of p_e for Doppler core complete redistribution, the Ferland and Netzer partial redistribution result, and complete redistribution in a radiatively damped Voigt profile for an optical depth of $\tau = 3 \times 10^9$. This τ corresponds to the depth in $L\alpha$ at which our standard model produces the observed line ratios. The values one obtains are 1.0×10^{-11} , 1.0×10^{-9} , and 8.6×10^{-7} , respectively. Hence it is apparent that errors of several orders of magnitude can arise from the use of unrealistic forms of the escape probability in ELC calculations.

Finally, it is important to incorporate self-consistently all ionization and excitation processes and the solutions to the radiative equations, as can be seen by

comparing our results with those of Ferland and Netzer (1979). Although the Ferland and Netzer calculation is based on a more realistic treatment of the radiative transfer in $L\alpha$ than our own, their work is limited by the fact that it is only a two-level plus continuum calculation for $L\alpha$ with the added restriction that the ionization balance is not required to be consistent with the $L\alpha$ line transfer (the ionization structure was previously calculated and was assumed to be fixed). For the range of physical parameters discussed in this Letter this leads to serious errors deep in the ELC. The strong diffuse $L\alpha$ radiation field present in this region provides a very rapid rate from the ground level to the first excited state from which the atom can easily be ionized by electron collision or continuum photoionization (photoionization by the higher diffuse continua being the dominant effect). This rapid rate from $n = 1$ to $n = 2$ (and higher bound levels) to the continuum is what maintains the high ionization state deep into the ELC. While our calculations show excellent agreement with the Ferland and Netzer result at low optical depths, we find that if the electron temperature is greater than about 7×10^3 K, the neutral fraction deep into the cloud ($\tau_{c1} \geq 10^9$) is very small (the hydrogen is highly ionized!)—i.e., is approaching the LTE value at these temperatures. In fact, in our standard model the ionized fraction of H is essentially unity throughout the entire cloud. We ascribe the lack of this

effect in the Ferland and Netzer calculation to the previously mentioned failure to require the ionization balance to be consistent with the line transfer calculation. Thus our $L\alpha$ source function does not drop dramatically as in the Ferland and Netzer calculation due to a drop in the electron density, but eventually settles (either increasing or decreasing) to the LTE value, provided there is sufficient line optical depth.

As an aside, it is appropriate to comment that there seems to be some confusion over the role of thermalization in quasar ELCs. Thermalization can either increase or decrease a source function. The effect is always to move the source function toward the Planck value. Thus thermalization of $L\alpha$ is not to be equated with collisional destruction of $L\alpha$. For many reasonable QSO models (i.e., those having commonly accepted temperature, density, and ionizing flux), the effects of thermalization are to increase the $L\alpha$ source function. The major effects of thermalization, on the other hand, do not involve $L\alpha$ at all! It is much more difficult to obtain superthermal Balmer source functions than Lyman source functions by recombination at 10^4 K. Thermalization almost always tends to increase Balmer line source functions, which in turn leads to enhanced Balmer line emission. Our models thus confirm the previous suggestions (e.g., Baldwin 1977) that it is enhanced Balmer line emission and not depressed $L\alpha$ emission that helps explain the low $L\alpha/H\alpha$ ratio in quasar ELCs.

c) Directions for Future Work

In our opinion, the area that most urgently needs attention at the present time is modeling of energy balance in steady-state ELCs, which would give us justification for dropping the assumptions of constant temperature and density. These models must incorporate (1) a depth-dependent treatment of the radiative transfer in all lines and continua; (2) photon escape processes appropriate to the atomic physics of the various lines and continua; (3) self-consistency of ionization and excitation, i.e., simultaneous solution of atomic equilibrium equations and the radiative transfer

equation in both lines and continua (direct and diffuse). From optical observations of QSOs, the hydrogen lines are the strongest emission features present that are likely to form deep within the ELCs (with the possible exception of Mg II). Thus, unless there are important IR cooling lines, hydrogen will dominate the cooling deep within the ELC. It is unlikely that far-IR lines are important because at 10^4 K the Planck function at their wavelengths is small. If the hydrogen lines are the dominant coolants (as seems likely) and the Lyman continuum is the dominant heat source, then temperatures deep in the ELC of near 10^4 K are not unreasonable. For our standard model ($T_1 = 1.0$, $N_2 = 1.0$, $I/I_0 = 1.0$) at an optical depth of 3×10^3 in the Lyman continuum (the depth at which the model produces the observed $L\alpha/H\alpha$ H β /Pa ratio) the Lyman continuum heating is 6.1×10^4 ergs s^{-1} cm^{-2} per unit τ_{cl} (here we have neglected, of course, the effects of opacities due to heavy elements which will reduce this heating rate). The cooling from our three different temperature models is 8.9×10^{-1} , 1.1×10^2 , and 7.7×10^4 ergs s^{-1} cm^{-2} per unit τ_{cl} at $T_1 = 0.5$, 1.0, and 2.0 respectively, summed over the 15 hydrogenic transitions that we considered. Thus while we assumed 10^4 K in this region, it seems more likely that the temperature is slightly lower, say 9000 K. In addition, for an increase of 10 in τ_{cl} , similar considerations indicate that the electron temperature must fall well below 10^4 K. This suggests that the optical depth of the 10^4 K region naturally arises from energy balance considerations. In any case, it is obvious that the effects of radiative transfer need to be incorporated in any realistic attempt to calculate the cooling function deep within quasar ELCs.

We wish to thank Paul Ricchiazzi for many helpful discussions. This research has been supported by the Air Force Office of Scientific Research, Air Force Systems Command, USAF, under grant AFOSR-76-3071, by NASA under grant NGR-05-005-055, and by the National Science Foundation under grant AST 76-82890.

REFERENCES

- Athay, R. G. 1972, *Radiation Transport in Spectral Lines* (Dordrecht: Reidel).
 Baldwin, J. A. 1977, *M.N.R.A.S.*, 178, 67P.
 Baldwin, J. A., and Netzer, H. 1978, *Ap. J.*, 226, 1.
 Baldwin, J. A., Rees, M. J., Longair, M. S., and Perryman, M.A.C. 1978, *Ap. J. (Letters)*, 226, L57.
 Canfield, R. C., and Puetter, R. C. 1980, in preparation.
 Canfield, R. C., and Ricchiazzi, P. J. 1980, *Ap. J.*, submitted.
 Chan, Y. T. 1974, Ph.D. thesis, University of California at San Diego.
 Davidson, A., Hartig, G., and Fastie, W. 1977, *Nature*, 269, 203.
 Davidson, K. 1972, *Ap. J.*, 171, 213.
 ———. 1973, *Ap. J.*, 181, 1; 186, 399.
 Ferland, G., and Netzer, H. 1979, *Ap. J.*, 229, 274.
 Grasdalén, G. L. 1976, *Ap. J. (Letters)*, 208, L11.
 Hyland, A., Becklin, E. E., and Neugebauer, G. 1978, *Ap. J. (Letters)*, 220, L75.
 Ivanov, V. V. 1973, *Transfer of Radiation in Spectral Lines*, N.B.S. Spec. Pub. 385, U.S. Government Printing Office, Washington.
 Krollik, J., and McKee, C. 1978, *Ap. J. Suppl.*, 37, 459.
 MacAlpine, G. M. 1972, *Ap. J.*, 175, 11.
 Netzer, H. 1975, *M.N.R.A.S.*, 171, 395.
 Puetter, R. C., Smith, H. E., Soifer, B. T., Willner, S. P., and Pipher, J. L. 1978, *Ap. J. (Letters)*, 226, L53.
 Puetter, R. C., Smith, H. E., and Willner, S. P. 1979, *Ap. J. (Letters)*, 227, L5.
 Scargle, J. D., Caroff, L. J., and Tarter, C. B. 1974, *Ap. J.*, 189, 181.
 Shields, G. A. 1973, Ph.D. thesis, California Institute of Technology.
 ———. 1974, *Ap. J.*, 191, 309.
 Shuder, J. M., and MacAlpine, G. M. 1979, *Ap. J.*, 230, 348.
 Soifer, B. T., Oke, J. B., Matthews, K., and Neugebauer, G. 1979, *Ap. J. (Letters)*, 227, L1.

RICHARD C. CANFIELD and R. C. PUETTER: Center for Astrophysics and Space Science, C-011, University of California, San Diego, La Jolla, CA 92093

ii) Theoretical Quasar Emission Line Ratios.

I. Transfer and Escape of Radiation

This paper lays out a simplified approach to solving steady state radiative transfer problems that, while unsophisticated, was pedagogically valuable. Without it, the solar flare radiative hydrodynamics work would not have been possible. Simplified solutions to the radiative transfer problem were used here, but were subsequently replaced by more rigorous methods, laid out in Section iii.

THEORETICAL QUASAR EMISSION LINE RATIOS. I. TRANSFER AND ESCAPE OF RADIATION

RICHARD C. CANFIELD AND R. C. PUETTER

Center for Astrophysics and Space Science, University of California, San Diego

Received 1980 April 4; accepted 1980 August 6

ABSTRACT

We describe a formalism for the solution of the frequency-integrated radiative transfer equation and the atomic steady state equation appropriate to an externally irradiated, semi-infinite medium. The source functions are cast into equivalent two-level forms, and the equations linking the emergent flux, the line center source function, the flux divergence coefficient ρ , and the atomic steady state equations are given. Asymptotic forms for scaling law solutions to the radiative transfer equation are developed. Escape probabilities appropriate to the above scaling law solutions are discussed for subordinate lines, strongly interlocked resonance lines, weakly interlocked resonance lines, and the bound-free continuum.

Subject headings: line formation — quasars — radiative transfer

I. INTRODUCTION

The extreme breadth and "anomalous" line ratios of the permitted line emission from QSOs have generated a great deal of interest. There is now a rather large data base on the broad-line emission from QSOs at many wavelengths. This data base makes it reasonable to explore what conditions might be considered "typical" of the broad emission line clouds (ELCs). Perhaps the most striking feature of the emission lines is the unexpectedly low ratio of Lyman- α ($L\alpha$) to the Balmer lines. Baldwin (1977) first suggested that the $L\alpha/H\beta$ ratio was about 3 on the basis of a composite QSO spectrum. This value has since been confirmed to within a factor of about 2 (see Davidson, Hartig, and Fastie 1977; Baldwin *et al.* 1978; Hyland, Becklin, and Neugebauer 1978; Soifer *et al.* 1979, Puetter *et al.* 1979, 1981). This low ratio along with the apparent lack of significant reddening of the Balmer lines and $P\alpha$ (Puetter, Smith, and Willner 1978; Puetter *et al.* 1980) seems to require an explanation of the hydrogen line ratios in terms of radiative transfer effects (with or without dust). The methods we describe below outline an approach appropriate to modeling the radiative transfer in quasar ELCs. The preliminary results of such calculations have been summarized briefly in a previous paper (Canfield and Puetter 1980) and are described in detail in another paper (Canfield and Puetter 1981a).

II. GEOMETRY

The picture of the broad line region that we adopt is that of many high-density ($n_H \geq 10^9 \text{ cm}^{-3}$), optically thick condensations surrounding a powerful central ionizing source with power law spectral form [$\mathcal{F}_\nu =$

$\mathcal{F}_1(\nu/\nu_1)^{-\alpha}$]. We attribute the breadth of the line emission to rapid motion of the individual clouds relative to one another. The symmetry of the lines in the majority of QSOs and the observed continuum variability then indicate that there are a large number of small emitting clouds that neither completely obscure the central source nor one another. The particular geometry of individual ELCs will affect the amount of emission by factors on the order of 2 or less, and the line ratios by an even smaller amount. Although the emission line region contains many ELCs, in the present calculation we model only one. If the physical conditions among ELCs vary widely and affect the line ratios, an ensemble average will have to be taken to predict the overall QSO emission. Because of the insensitivity of the line ratios to individual ELC geometry, we have modeled an ELC as a plane-parallel atmosphere with escape of photons from the front side only (i.e., the side facing the ionizing source). It is necessary to consider the variation of all parameters of the radiative transfer problem with line center optical depth. This is because significant emission in any given line can arise from the many decades in optical depth. Moreover, different lines may originate in distinctly different regions of the ELC. In short, no one point in the ELC can be considered as a representative or average point.

III. RADIATIVE TRANSFER

Proper treatment of the radiative transfer in optically thick quasar ELC models is probably the most critical aspect of such calculations. It is essential to incorporate self-consistently both depth dependence and interlocking of lines and continua. It is quite adequate for the purposes of this paper to solve the radiative transfer

equation (RTE) in a frequency-integrated form (cf. Athay 1972a):

$$\frac{dH}{d\tau} = M^{-1} \left(J - \int d\nu S_\nu \Phi_\nu \right), \quad (1a)$$

$$S_\nu = \frac{J + \bar{\epsilon} \bar{B}}{1 + \bar{\epsilon}} \frac{\psi_\nu}{\bar{\Phi}_\nu} = S_0 \frac{\psi_\nu}{\bar{\Phi}_\nu}, \quad (1b)$$

$$J = \int d\nu J_\nu \Phi_\nu, \quad (1c)$$

$$M^{-1} = \int d\nu \phi_\nu, \quad (1d)$$

$$H = \frac{1}{2} \int d\nu \int d\mu \mu I_\nu(\mu). \quad (1e)$$

In equation (1), S_ν is the line source function, ψ_ν is the normalized (i.e., $\int d\nu \psi_\nu = 1$) emission coefficient profile and Φ_ν is the normalized absorption coefficient profile. We have implicitly assumed that the stimulated emission profile is the same as the absorption profile. Throughout this paper, the optical depth τ will be understood to mean the line-center optical depth for lines and the optical depth at the ionization edge for continua. J_ν is the mean intensity at frequency ν , and ϕ_ν is the absorption profile scaled to one at line center (or for continua, at the head of the continuum). H is the flux integrated over the line, μ is the direction cosine from the normal to the plane-parallel atmosphere, and I_ν is the specific intensity. The specific forms of destruction coefficient $\bar{\epsilon}$ and effective Planck function, \bar{B} , that we use for each transition, ul , are those of Jefferies (1968), given by

$$\bar{\epsilon} = \epsilon + \eta, \quad (2a)$$

$$\bar{B} = \frac{\epsilon B + \eta B^*}{\epsilon + \eta}, \quad (2b)$$

$$\epsilon = \frac{C_{ul}}{A_{ul}} \{ 1 - \exp(-\chi_{ul}/kT) \}, \quad (2c)$$

$$\eta = \frac{\Sigma_{ul}}{A_{ul}} \left\{ 1 - \frac{g_l}{g_u} \frac{\Sigma_{lu}}{\Sigma_{ul}} \right\}, \quad (2d)$$

$$B^* = \frac{2h\nu^3}{c^2} \left\{ \frac{g_u}{g_l} \frac{\Sigma_{ul}}{\Sigma_{lu}} - 1 \right\}^{-1}, \quad (2d)$$

$$\Sigma_{ij} = \sum_{k \neq i, j} R_{ik} q_{kj, i}, \quad (2f)$$

B is the Planck function at the transition of interest, for electron temperature T . C_{ul} is the coefficient for the

direct collisional rate from the upper state, u , to the lower state l . A_{ul} is the Einstein coefficient for spontaneous radiative decay. The quantity χ_{ul} is the energy difference between levels u and l . R_{ij} is the coefficient for the total rate from level i to j and $q_{ij, k}$ is the probability of going from i to j without passing through level k . We evaluate $q_{ij, k}$ following Jefferies (1968) and Canfield (1971). The quantities g_l and g_u are respectively the statistical weights for the lower and upper states.

Equation (1) divides S_0 into two distinct parts: a scattering term proportional to J , and a source term proportional to $\bar{\epsilon} \bar{B}$. The value of J is potentially a very "nonlocal" quantity (Thomas 1965). The value of J can be affected by distant regions of the ELC if the scattering albedo $(1 + \bar{\epsilon})^{-1}$ is near unity. The values of $\bar{\epsilon}$ and \bar{B} are explicitly local. However, there is a "hidden" nonlocal nature to both $\bar{\epsilon}$ and \bar{B} ; they both depend on the value of J in other transitions, which may be highly nonlocal quantities.

The coefficients Σ_{ul} and Σ_{lu} are extremely useful quantities in their own right. They are the rate coefficients for indirect transitions from the upper to the lower and the lower to the upper states, respectively (i.e., indirect rates of destruction and creation of ul photons). Thus, Σ_{ul} and Σ_{lu} measure the *interlocking* between the transition in question (the ul transition) and all other transitions. The largest terms in these sums identify those transitions with which the ul transition most intimately exchanges energy. However, since they are not formulated in terms of net rates, they do not identify those indirect paths that most affect the u to l population ratio.

The value of $\bar{\epsilon}$ is directly related to the destruction probability per scattering, p_d :

$$p_d = \frac{\bar{\epsilon}}{1 + \bar{\epsilon}}. \quad (3)$$

Both direct collisional de-excitation and conversion of the energy of the ul photon to other transitions contribute to the destruction process. In the evaluation of the probability of destruction it is extremely important to use the so-called "full set" definition of $\bar{\epsilon}$ and \bar{B} given in equation (2) rather than the "upper level" or "lower level" definitions (Athay 1972a). The latter definitions have the advantage of expressing $\bar{\epsilon}$ only in terms of quantities related to the transition in question; however, they treat some photon creation processes as negative destruction processes and some destructions as negative creations. This does not matter, of course, in the calculation of source functions, but it does not allow one to estimate the average number of scatterings a photon will undergo before being destroyed.

The radiative transfer equation must be solved consistently with the atomic steady state equation (SSE)

for the number density n_i of level i :

$$n_i \sum_{j \neq i} R_{ij} = \sum_{j \neq i} n_j R_{ji}, \quad (4a)$$

$$\begin{aligned} R_{ij} &= C_{ij} + A_{ij} \rho_{ij}, & i > j, \\ &= C_{ij}, & i < j, \end{aligned} \quad (4b)$$

$$\rho_{ij} = 1 - \frac{B_{ij} n_i - B_{ji} n_j}{A_{ij} n_j} \int d\nu J_\nu \Phi_\nu, \quad (4c)$$

where for lines, A_{ij} and B_{ij} are the Einstein rate coefficients. For the continua A_{ij} is the spontaneous recombination rate (see, for example, Jefferies 1968, eq. [6.63]). The use of this formalism in the continuum is equivalent to assuming that all recombinations occur at the ionization edge in computing the stimulated recombination rate. This is an excellent approximation for the n th bound-free continuum when the ionization energy from level n is much greater than kT . For the higher levels, the exact value of ρ_{en} has little effect on the calculation of level populations and thus is unimportant in determining line fluxes, etc.; however, the above approximation is inadequate for calculating radiative loss in the high bound-free continua. The quantity $A_{ij} \rho_{ij}$ is the coefficient for the net radiative rate between levels i and j ; for this reason ρ_{ij} has been referred to as the net radiative bracket (Thomas and Athay 1961). It is well known (cf. Athay 1972a) that the coefficient ρ_{ij} can be written as

$$\rho_{ij} = 1 - J/S_0. \quad (5)$$

For convenience we drop the ij subscript from ρ , realizing that it relates J and S_0 in one specific transition, that between i and j . The quantity ρ is very useful since it directly links the SSE with the RTE:

$$\frac{dH}{d\tau} = M^{-1} \rho S_0 \quad (6)$$

(see Athay 1972a). From equation (6) one can see that an appropriate name for ρ would be the flux divergence coefficient.

While the flux divergence is directly proportional to ρ , it is important to distinguish ρ from a photon escape probability (see Canfield, Puetter, and Ricchiazzi 1981). In general, the value of ρ is not equal to p_e , although it approaches p_e for large values of τ if $\bar{\epsilon}$ and \bar{B} do not vary strongly (see § IV). The quantity ρ expresses the mismatch of photon creations and destructions in a given transition and volume element; it is equal to p_e if the mismatch between creations and destructions is due only to escape of photons to the atmosphere boundary and not due, for example, to escape of photons to other regions of the atmosphere. The value of ρ must be calculated for optical depths less than the saturation

depth τ_{sat} [where τ_{sat} is defined by $\rho_{ei}(\tau_{\text{sat}}) = \bar{\epsilon}$] because at these depths, local destructions cannot be evaluated in terms of local quantities but are a function of J , which is controlled nonlocally by all depths $\tau < \tau_{\text{sat}}$. At larger optical depth, the values of J and S_0 saturate to \bar{B} , provided there are no rapid variations in $\bar{\epsilon}$ or \bar{B} . This can be demonstrated by combining equations (1b) and (5):

$$S_0 = \frac{\bar{\epsilon}}{\bar{\epsilon} + \rho} \bar{B}. \quad (7)$$

For $\tau > \tau_{\text{sat}}$ (in the absence of variations of $\bar{\epsilon}$ and \bar{B}) the value of ρ is less than $\bar{\epsilon}$ and approaches p_e , which is a monotonically decreasing function of τ . Thus, the deviation of S_0 from \bar{B} becomes smaller and smaller. In addition, the value of J also approaches \bar{B} :

$$J = (1 - \rho) S_0 = \frac{\bar{\epsilon}(1 - \rho)}{\bar{\epsilon} + \rho} \bar{B}. \quad (8)$$

The scaling law approach discussed in § IV employs escape probabilities to calculate the values of J and ρ . Thus, it is crucial to understand exactly which photon escape processes apply to the various lines and how these affect the escape probabilities, as discussed in § V. Once the escape probabilities have been determined, it is possible to obtain a solution to the radiative transfer in the diffuse radiation field. From the value of the mean intensity of the diffuse radiation field J^d and the external radiation field J^e the value of ρ for the diffuse radiation field can be calculated:

$$\rho(\tau) = \frac{F + \bar{\epsilon}(1 - f)}{F + \bar{\epsilon} + f}. \quad (9a)$$

$$f = J^d / \bar{B} \quad (9b)$$

$$F = J^e / \bar{B}. \quad (9c)$$

F usually can be neglected for lines, but may be non-negligible for the continua due to their large frequency bandwidth. For power-law ionizing sources $\mathcal{F}_\nu \propto \nu^{-\alpha}$, and attenuation by a hydrogenic absorption coefficient [$\phi_\nu = (\nu/\nu_i)^{-\beta}$], J^e is given by

$$J^e(\tau) = \frac{1}{4\pi} \mathcal{F}_\nu \tau_i^{-\theta} \gamma(\theta, \tau_i), \quad (10)$$

where ν_i is the frequency at the head of the i th continuum, τ_i the optical depth at this frequency, \mathcal{F}_ν is the flux per hertz at ν_i , $\theta = (3 + \alpha)/3$, and $\gamma(\theta, \tau)$ is the incomplete gamma function [i.e., $\gamma(\theta, \tau \rightarrow \infty) = \Gamma(\theta)$]. Here, we have assumed that the external continuum photons enter the ELC perpendicular to the face of the ELC. For treating the rates due to the radiation field given by equation (10), we found it most convenient to

add the total rate coefficients based on J^* directly to the net rate coefficients for the diffuse field.

Once the rate coefficients have been determined, the SSE can be solved consistently with the radiative transfer solution. We have used an iterative approach. One scheme (which we used to produce the models described in Canfield and Puetter 1981a, b) is the following. An initial guess is made as to the level populations and values of ρ ; normally $\rho=0$ (i.e., LTE) is chosen. This determines optical depth scales and the values of all transition rates. These rates allow the evaluation of $\bar{\epsilon}$ and \bar{B} while the τ scales allow evaluation of $p_e(\tau)$ in all transitions. These quantities are then used to solve the radiative transfer equation (i.e., calculate f) which yield new values for ρ . This constitutes the zeroth order step. The new ρ values are used to resolve the SSE for new level populations and hence new τ scales. Next new values of $\bar{\epsilon}$ and \bar{B} need to be calculated. This naturally brings up the question of "balance" between the SSE and the RTE. If the SSE is used only to establish the τ scales through the level populations, then the SSE has been given a low weight in the calculation relative to the RTE. The convergence of the iterative scheme will reflect this fact. The source functions as calculated from the SSE (S_{SSE}) through the level populations will agree poorly with the source functions calculated from the RTE (S_{RTE}) from J , $\bar{\epsilon}$, and \bar{B} . One method of introducing the SSE in a more equal partnership with the RTE is through the rates in the calculations of $\bar{\epsilon}$ and \bar{B} . We use $J=(1-\rho)S_{SSE}$ for the value of the radiation field in each transition. This is a compromise mix of the RTE and the SSE value for J and gives relatively rapid convergence. We found that normally 10 iterations establish a better than 1% convergence in all the line ratios (although the level populations had not settled down to this level). The self-consistency of the calculation can be easily checked by a comparison of the values of the source functions S_{SSE} and S_{RTE} . After 10 iterations we find the agreement to be excellent (~5%). The independent variable we chose was the optical depth in the Lyman continuum (τ_{cl}). We found two grid points per decade in τ_{cl} were quite adequate from comparisons with calculations having three and four points per decade.

The radiative flux emerging from the ELC in a particular transition can be calculated by integrating the flux divergence, ρS_0 , over the atmosphere. The emergent flux is (cf. eq. (6)):

$$H = M^{-1} \int d\tau \rho(\tau) S_0(\tau). \quad (11)$$

For Voigt profiles in which $a \ll 1$ (or for any profile in which the line wings are weak compared to the Doppler core) we can write to sufficient accuracy:

$$M^{-1} = \pi^{1/2} \Delta \nu_D, \quad (12)$$

where $\Delta \nu_D$ is the Doppler width.

We might rewrite (11) in another form:

$$H = M^{-1} \int d\tau \frac{\bar{\epsilon} \rho}{\bar{\epsilon} + \rho} \bar{B}. \quad (11')$$

Equation (11') shows the direct interplay between scattered photons (i.e., ρ , which depends on J) and the sources of local photon creation and destruction (which enter into $\bar{\epsilon}$ and \bar{B}) in determining the emergent flux. For example, if $\rho \approx 1$ (i.e., there is a negligible number of scattered photons), then the escaping flux is simply the local creation rate $\bar{B}\bar{\epsilon}/(1+\bar{\epsilon})$ integrated over the atmosphere. On the other hand, if $\rho \approx 0$, then local creations and destructions are in balance (so $S_0 = \bar{B}$) and the radiative loss from the atmosphere is directly proportional to ρ . Notice also that equation (11') implies that for transitions in which the local destruction probability is very nearly unity (i.e., $\bar{\epsilon} \gg 1$) the emergent flux is again directly proportional to ρ and $S_0 \approx \bar{B}$ (this is the situation for forbidden lines in the high-density limit, for example).

The line profile from a single ELC can be calculated readily by using the monochromatic transfer equation

$$\mu \frac{dI_\nu}{d\tau} = \phi_\nu (I_\nu - S_0). \quad (13)$$

In equation (13) we have made the assumption $\phi_\nu \approx \Phi_\nu$. This is quite accurate for all lines other than $L\alpha$ (see § V). It must be noted that for intrinsically narrow features such as lines, profiles as calculated using (13) cannot be related directly to observation of QSOs; the velocity distribution of the ELCs must also be taken into account.

IV. SCALING LAW SOLUTIONS TO THE RADIATIVE TRANSFER EQUATION

Section III has shown that in order to calculate the emergent radiation we must determine the value of ρ (see eq. (11)). To do this, we simply need to calculate the value of f (see eq. (9)). This amounts to a solution of the radiative transfer equation. The radiative transfer equation, as posed in equation (1), is expressed in terms of an equivalent two level atom source function. The frequency independent two level atom source function has been studied extensively (e.g., Avrett 1965; Avrett and Hummer 1965; Hummer 1968). The cases in which $\bar{\epsilon}$ and \bar{B} are assumed to be constant and in which $\bar{\epsilon} \ll 1$ show characteristic solutions for S_0/\bar{B} at small optical depths that vary as $\bar{\epsilon}^{1/2}(\tau+1)^{1/2}$. This is equivalent to setting $S_0/\bar{B} = \bar{\epsilon}^{1/2} p_e^{-1/2}(\tau)$. In other words, this "scaling law" solution depends only on the means of photon escape at small optical depths. These scaling laws are computationally expedient compared with solving the full frequency-dependent transfer equation.

The saturation depth τ_{sat} (as defined in § III) divides the atmosphere into two regimes. For optical depths greater than τ_{sat} if $\bar{\epsilon}$ and \bar{B} do not vary too rapidly (see § III), we expect $S_0 \approx \bar{B}$. In this limit we can obtain an asymptotic expression for all the radiative transfer quantities such as ρ , f , etc. For optical depths less than τ_{sat} , the value of S_0 falls below \bar{B} due to significant photon loss (i.e., escape processes significantly upset the balance between local creation and destruction rates). One way we can obtain quantitative values of the radiative transfer quantities is to formulate the radiative transfer in a probabilistic way (see Athay 1972b; Delache 1974; Frisch and Frisch 1975; Canfield and Ricchiazzi 1980). Athay (1972b) first derived the equation:

$$\frac{dJ}{dN} = \frac{1}{2} \left[\frac{J}{N} - \frac{\bar{\epsilon}}{1+\bar{\epsilon}} (J - \bar{B}) \right], \quad (14)$$

where N is the mean number of scatterings undergone by an escaping photon. Later work by Delache (1974) and Athay (1976) provided a more rigorous physical basis for this equation. Note that in (14), N is the mean number of scatterings of a photon that will ultimately escape. Such a photon is not necessarily a typical photon.

The solution to equation (14) for a semi-infinite slab is given by Athay (1972b):

$$J(N) = \frac{1}{2} N^{1/2} \exp \left[\frac{1}{2} \bar{P}_d(N) \right] \int_N^\infty d\tau p_d \bar{B} \exp \left[-\frac{1}{2} \bar{P}_d(\tau) \right], \quad (15)$$

where

$$\bar{P}_d(N) = \int_0^N d\tau p_d(\tau) \text{ and } p_d = \bar{\epsilon}/(1+\bar{\epsilon}).$$

Note that J has the limiting value of B as N goes to infinity (since there $B = \bar{B}$). Also, note that if p_d and \bar{B} are constant, we have

$$f = J^d / \bar{B} = \pi^{1/2} \left(\frac{p_d N}{2} \right)^{1/2} \exp \left(-\frac{p_d N}{2} \right) \text{erfc} \left[\left(\frac{p_d N}{2} \right)^{1/2} \right], \quad (16)$$

where $\text{erfc}(x)$ is the complementary error function. As $p_d N/2$ becomes large, the asymptotic expression for f is

$$f \approx \left(1 - \frac{1}{p_d N} \right). \quad (17)$$

In the absence of strong external radiation fields (i.e.,

$F \approx 0$) as p_e goes to zero, equations (17) and (9) give

$$\rho \approx \frac{\bar{\epsilon}(1-f)}{\bar{\epsilon}+f} \approx p_e. \quad (18)$$

Also, note that the onset of this asymptotic form occurs roughly at $\tau = \tau_{\text{sat}}$.

In atmospheres in which the local creation rate $p_d \bar{B}$ is not effectively constant, the above scaling laws will give a much better estimate for f than for ρ (cf. eqs. [17] and [18]). If ρ is small, however, the value of S_0 will still be quite accurate. In this case one can get a good estimate of the emergent radiative flux in a particular transition with the following expression:

$$H = M^{-1} \int d\tau p_e(\tau) S_0(\tau). \quad (19)$$

For optical depths smaller than τ_{sat} we still need an expression for f . Equation (15) shows that the contribution to J from regions deeper than the saturation depth is very small [it drops off like $\exp(-p_d/p_e)$]. The value of J is thus determined by the region of largest $p_d \bar{B}$ (i.e., creation rate per scattering) with $\tau < \tau_{\text{sat}}$. If this quantity varies slowly on the scale of τ_{sat} we have

$$\frac{J}{\bar{B}(\tau_{\text{sat}})} \equiv f \frac{\bar{B}(\tau)}{\bar{B}(\tau_{\text{sat}})} \approx (p_d N)^{1/2}, \quad (20)$$

which justifies the scaling laws for constant $\bar{\epsilon}$ and \bar{B} . This approximation must be checked on a case-to-case basis. It turns out to be sufficient for the hydrogen line emission calculations in quasar ELCs (Canfield and Puetter 1980, 1981a), for two reasons. First, \bar{B} and p_d do not vary too strongly in this region if one uses the "full set" definitions of p_d and \bar{B} as described in § III. Second, the boundary region produces negligible line radiation in comparison to the region for which $\tau > \tau_{\text{sat}}$, for cloud depths that match the observed line ratios (Canfield and Puetter 1980, 1981a).

We have shown how f can be calculated in terms of the variation of N with optical depth. The mean number of scatterings, N , undergone by an escaping photon is related to the probability of escape per scattering of these photons by $N = p_e^{-1}$. We now discuss p_e for the various transitions.

V. ESCAPE PROBABILITIES

A critically important factor in calculation of the probability of photon escape from optically thick media is the emission coefficient profile. This profile is determined by the physical processes that populate the upper level. (We are ignoring stimulated emission, for the time being.) For permitted transitions, total rates will be dominated by radiative processes. Two very

different radiative processes populate the upper level. The first is absorption from the lower level of the transition in question; the second is interlocking. The role played by each of these processes is discussed below.

There is an extensive literature on some aspects of frequency redistribution of scattered radiation and photon escape (see, for example, Mihalas 1978); however, most of this work is too highly idealized for our present study. In addition, some of the observed hydrogen lines in QSOs present problems that have not been worked out in detail. Specifically, those lines that involve subordinate transitions (i.e., nonresonance transitions like $H\alpha$) or resonance-series lines that are strongly interlocked with subordinate transitions (like $L\beta$) have not been treated thoroughly. In this section we in turn discuss escape probabilities for subordinate lines, strongly interlocked resonance lines, weakly interlocked resonance lines, and the bound-free continua.

Published studies of redistribution upon scattering in subordinate lines (which have both upper and lower levels broadened by radiative damping) are restricted to the rest frame of the atom. Nonetheless, these studies establish a physical understanding that is adequate for our present purposes. The expression for the atom's frame redistribution function was derived by Weisskopf (1933) and Woolley (1938), and is discussed by Woolley and Stubbs (1953) and Mihalas (1978). From this expression it is straightforward to show that if the widths of the upper and lower levels are approximately the same, then first, almost all scattered line-center photons will be redistributed into a Lorentz profile in the atom's frame, and second, scattered wing photons are approximately equally likely to appear at line center, or to scatter coherently in the atom's frame. This strong redistribution of scattered radiation over the absorption coefficient profile in the atom's frame will result in a strong tendency for scattered photons to assume an emission profile equal to the absorption profile. In addition, we need to consider photons created through interlocking. This process in subordinate lines has not been treated in the literature. For the present, we will assume that wing photon creation is dominated by the scattering term. In other words, in these transitions p_e is the single flight escape probability:

$$p_e(\tau) = \frac{1}{2} \int_0^\infty d\nu \int_0^1 d\mu \psi_e \exp(-\tau_0 \phi_e / \mu), \quad (21)$$

with ψ_e and ϕ_e being the Voigt profile with the Voigt parameter being determined by the natural width of the upper and lower levels, and where the expression above assumes we are dealing with a semi-infinite atmosphere. This function has been analyzed meticulously by Ivanov (1973) (for the case $\psi_e = \phi_e$), who gives

asymptotic expansions of this function [$\frac{1}{2} K_2(\tau)$ in his notation] for Doppler, Voigt, and Lorentz line profiles.

One can easily see that the contribution to p_e due to escape by multiple, nearly coherent scatterings is small by noting the large destruction probability per scattering indicated by the value of $\bar{\epsilon}$ given in equation (2). The value of p_e is always close to unity for lines other than $L\alpha$, because the radiative branching ratios are close to unity. For example, decays from level 3 are roughly equally likely to produce $H\alpha$ or $L\beta$ photons. Thus, the destruction probability for both these lines should never be less than about one-half.

The problem of resonance-series lines strongly interlocked with subordinate lines or continua (such as $L\beta$, which is strongly interlocked with $H\alpha$) also has not yet been treated accurately in the literature. However, simple physical arguments based on the above considerations can be applied in order to understand photon escape in these lines. The frequency dependence of S_e depends on whether direct scattering or interlocking dominates the line source function. The scattering in resonance-series lines is characterized by strong frequency coherence in the line wings. For $L\alpha$, since interlocking is unimportant, the $\bar{\epsilon}\bar{B}$ term of S_e is small and the scattering term dominates. On the other hand, for $L\beta$ and the higher Lyman lines, the large values of $\bar{\epsilon}$ indicate that, after absorption of a line photon, conversion of the photon's energy to other line photons has an equal or greater probability than reemission of the original Lyman photon. In practice, this also indicates that it is highly likely that many of the atoms in the upper level arrive there by means other than direct radiative transitions from the lower level. As a result, one should not expect the higher Lyman lines to have the same relationship between the emission and absorption coefficient profiles as $L\alpha$, i.e., the same form of p_e . This problem, that of the extent of redistribution in a multilevel hydrogen atom, has not been treated in the literature. For the present, since the well-observed lines and continua of hydrogen (see Canfield and Puetter 1981a) are very insensitive to the higher Lyman lines, we have assumed that the role of interlocking is to create new photons in the higher Lyman lines distributed in proportion to their absorption coefficient profile. Thus a single flight escape probability in which we take ψ_e and ϕ_e to be the Voigt profile will be assumed to calculate p_e deep into the atmosphere.

To calculate the escape probability for the subordinate lines and higher Lyman lines when the emission profile is very nearly equal to the absorption profile, we must have the appropriate absorption profile. For densities thought typical of quasar E1Cs (i.e., $n_H \approx 10^9 \text{ cm}^{-3}$), the wings of the line absorption profiles will be determined by radiative damping alone. The value of the Voigt damping parameter can be calculated from the spontaneous downward rate coefficient

cients:

$$a_{ul} = \frac{\Gamma_{ul}}{1\pi\Delta\nu_D}, \quad (22a)$$

$$\Gamma_{ul} = \sum_k (A_{uk} + A_{lk}), \quad (22b)$$

where $\Delta\nu_D$ is the Doppler width. Equation (22b) breaks down when absorptions and stimulated emission processes significantly alter the lifetime of the states u and l . If this is the case, then (22b) must be replaced by:

$$\Gamma_{ul} = \sum_k (R_{uk} + R_{lk}), \quad (22b')$$

where R_{ij} is the total rate coefficient from i to j . With the above definition of a , the escape probabilities in the subordinate and higher Lyman lines can be approximated by:

$$p_e(\tau) = p_e^D(\tau) + p_e^V(\tau), \quad (23a)$$

$$p_e^D(\tau) \approx \frac{1}{2 + 4\pi^{1/2}\tau(\ln(\tau+1))^{1/2}}, \quad (23b)$$

$$p_e^V(\tau) \approx \frac{a^{1/2}}{3\pi^{1/4}\tau^{1/2}}, \quad (23c)$$

where (23b) and (23c) are asymptotic expressions for escape from the Doppler core and Voigt wings, respectively, given by Ivanov (1969) with (23b) altered to have the correct limiting form at $\tau=0$. Knowledge of the probability of escape is most important for calculating line ratios in clouds of large optical depths in the region in which the flux divergence is directly proportional to ρ (see the discussion of eq. [11'] at the end of § III). This is usually the region of major emission, at least in models with large optical depths and constant electron temperature. For this region (23c) gives a good approximation to the actual value of $p_e(\tau)$ as given by equation (21).

For electron densities of order 10^{11} cm^{-3} or greater, Stark broadening cannot be ignored. As the density increases, the lines with the smallest radiatively damped wings will show the effects of Stark broadening first. These lines are typically the higher lines of each series. Escape probabilities in the limit of domination by Stark broadening are discussed by Drake and Ulrich (1979) and Weisheit (1979); a more complete treatment dealing with the case in which Stark broadening does not completely dominate the line absorption coefficient profile will appear in a subsequent paper in this series (Canfield and Puetter 1981b).

Next, we turn to $L\alpha$, for which much detailed work has been done. The results of previous work that as-

sume that the $L\alpha$ source function is determined by coherent scattering can be applied whenever the population of level 2 is determined by resonant scattering of $L\alpha$ photons. It is well known that $L\alpha$ wing scattering is predominantly coherent when the wing absorption coefficient is dominated by radiative damping. This will, of course, not be the case for large electron densities. At large densities Stark broadening produces non-coherent wings just outside the Doppler core. For large enough optical depths, however, escape becomes dominated by photons with frequencies far enough from line center that the major opacity is again given by the radiatively damped wings. In this regime the most efficient escape process is redistribution to optically thin frequencies over the Stark portion of the total line absorption profile (see Canfield and Puetter 1981b).

Assuming that radiative damping is the only important contribution to the line wings, we can follow the development of Adams (1972). Adams points out that for radiatively damped resonance lines the sharp lower level of the transition causes the wing scattering to be coherent. This in turn severely reduces the efficiency of photon escape. Scattered photons are no longer able to change their frequency to frequencies of small optical depth, as can subordinate lines. Adams shows that his solutions to the frequency-dependent transfer equation can be understood by supposing that escape is dominated by diffusion in space at frequencies greater than x_* . The quantity x_* is a displacement from the line center in units of Doppler widths: $x_* = \Delta\nu_D^{-1}|\nu_* - \nu_0|$. The frequency ν_* is that frequency at which the photon random walks out of the atmosphere before it scatters back to line center. The value of x_* is

$$x_* = \left(\frac{a\tau}{\sqrt{\pi}} \right)^{1/3}, \quad (24)$$

and the escape probability for a radiatively damped resonance line in the absence of destruction processes in a uniform, semi-infinite plane-parallel atmosphere is:

$$p_e^A(\tau) = \frac{1}{2} \int_x^\infty dx \frac{\Phi(x)}{N(x)} = \frac{1}{3\pi^{1/2}\tau} \quad (25)$$

for depths at which wing escape predominates (Adams 1972). In (25), $N(x) \sim x^2$ is the mean number of scatterings undergone by a photon at frequency x before returning to the line core. The fact that the escape probability asymptotically varies as τ^{-1} has also been demonstrated by Harrington (1973) and by extensive numerical calculations of Hummer and Kunasz (1980). The latter authors also give the departures of p_e from $p_e^A \sim \tau^{-1}$ at smaller optical depths.

As is evident, the Adams escape probability is not a single-flight escape probability; it does not describe the local confinement of photons in the same way. Hence,

it is not suitable for determination of the value of J or S_0 at $\tau < \tau_{\text{sat}}$. However, if these quantities are known (as, for example, for $\tau > \tau_{\text{sat}}$), then the Adams escape probability is suitable for calculation of the emergent flux.

The value of $\bar{\epsilon}$ as given in equation (2) gives a means of directly assessing the importance of photon destruction. For regions of the ELC that have large radiation fields in the transitions interlocked with $L\alpha$ (e.g., line fluxes in $H\alpha$ approaching thermal values at $T = 10^4$ K), destruction can begin to affect the efficiency of diffusion in space at the frequency x_* . The mean number of scatterings before escape at x_* is quite large; $N \sim x_*^2$ and slightly smaller for $x > x_*$. If the value of $\bar{\epsilon}$ is large enough, the probability of destruction before x_*^2 scatterings may be very high. Thus, equation (25) must be altered.

If destruction of photons prevents escape at frequency x_* , then escape becomes dominated by frequencies less affected by destruction. In other words, escape is dominated by photons at frequencies which scatter less often before escaping (i.e., photons at frequencies greater than x_*). If $\bar{\epsilon}$ is large, the frequency, x' , at which only a fraction of the photons are destroyed before they diffuse out of the atmosphere, then becomes the relevant frequency of escape. The value of this frequency can be calculated by the following considerations. In units of line-center optical depth, τ , the mean free path traveled per scattering at frequency x is given by $\phi^{-1}(x)$. Thus, the number of scatterings needed to escape the atmosphere, $N(x)$, can be calculated by setting $N^{1/2}(x)\phi^{-1}(x) = \tau$, or in other words,

$$N(x) = \tau^2 \phi^2(x) = \frac{a^2 \tau^2}{\pi x^4}, \quad (26)$$

assuming we are in the wings. Thus, if $p_d = \bar{\epsilon}/(1 + \bar{\epsilon})$ is the destruction probability per scattering, then x' may be calculated from

$$\frac{1}{\alpha} = (1 - p_d)^{N(x')}, \quad (27)$$

where we shall select an appropriate value for α below. In other words,

$$x'(\alpha) = \left(\frac{a\tau}{\sqrt{\pi}} \right)^{1/2} \left[\frac{\ln(1 + \bar{\epsilon})}{\ln \alpha} \right]^{1/4}. \quad (28)$$

If the destruction probability for $L\alpha$ photons is almost unity, it is clear that we must recover the complete redistribution (CRD) result for $p_e(\tau)$ given by (21). In other words,

$$p_e(\tau) = \frac{1}{2} \int_0^\infty dx \Phi(x) E_2(\tau \phi(x)) = \frac{a^{1/2}}{3\pi^{1/4} \tau^{1/2}}. \quad (29)$$

The expression in (29) has often been approximated as

$$p_e(\tau) = \frac{1}{2} \int_0^\infty dx \Phi(x) E_2(\tau \phi(x)) \approx \frac{1}{2} \int_{x_*}^\infty dx \Phi(x), \quad (30)$$

where x_* is considered the "frequency of escape" (cf. Osterbrook 1962). Using the expression given in (30) we find that, if destruction processes dominate photon escape in $L\alpha$,

$$p_e(\tau) \approx \int_{x_*}^\infty dx \Phi(x) = \frac{a^{1/2}}{\pi^{1/4} \tau^{1/2}} \left[\frac{\ln(1 + \bar{\epsilon})}{\ln \alpha} \right]^{3/4}. \quad (31)$$

In practice, we may choose to set the value of $p_e(\tau)$ to the CRD value of equation (29) whenever $\bar{\epsilon} \geq 1$ (i.e., $p_d \geq 0.5$). This indicates an appropriate choice for the value of α in equation (31), i.e., $\ln \alpha = 3^{4/3} \ln 2$.

Thus a complete formula for $p_e(\tau)$ must reflect the fact that when $\bar{\epsilon} \ll 1$, $p_e(\tau)$ must behave as indicated by Adams's escape probability as given by equation (25). However, when $\bar{\epsilon} \gtrsim 1$, $p_e(\tau)$ must go over to the CRD result of equation (29). Thus to approximate $p_e(\tau)$ we find we may write

$$p_e(\tau) \approx \frac{a}{3\pi \bar{x}^3} + \begin{cases} \frac{a^{1/2}}{3\pi^{1/4} \tau^{1/2}} \left[\frac{\ln(1 + \bar{\epsilon})}{\ln 2} \right]^{3/4}, & \bar{\epsilon} \leq 1 \\ \frac{a^{1/2}}{3\pi^{1/4} \tau^{1/2}}, & \bar{\epsilon} > 1, \end{cases} \quad (32)$$

where $\bar{x} = \max\{x_*, x'(\alpha=2)\}$. Equation (32) accounts for both multiple scattering escapes in the wings and escape by photons created at optically thin frequencies by interlocked processes. The choice of \bar{x} in (32) rather than x_* allows for the fact that destruction processes may interfere with multiple scattering escape at frequency x_* .

Finally, we turn to the bound-free continua. In the high ionization limit (i.e., n_e and n_p constitute essentially the entire particle density) primary electrons reach a Maxwellian distribution before recombining. Following Canfield and Ricchiazzi (1980), equation (21) leads to

$$p_e(\tau) = \frac{1}{2E_1(\alpha)} \int_1^\infty \frac{dx}{x} e^{-\alpha x} E_2(\tau x^{-3}), \quad (33a)$$

where

$$\alpha = h\nu_0/kT, \quad E_n(t) = \int_1^\infty x^{-n} e^{-tx} dx. \quad (33b)$$

In equation (34) we have assumed a ν^{-3} dependence of the absorption profile, and stimulated emission has been ignored. An approximation to $p_e(\tau)$ in equation (34) that is accurate enough for our purposes is

$$p_e(\tau) \approx \frac{1}{2\beta} \exp[-\tau\beta^{-3} - \alpha(\beta-1)] \quad (34)$$

where $\beta = \max\{(3\tau\alpha^{-1})^{1/4}, 1\}$ (cf. Canfield and Ricchiazzi 1980).

VI. CONCLUSIONS

We have described a general procedure for calculating the flux of radiation emerging from a plane-parallel atmosphere irradiated by an external source. This procedure is applicable to a wide variety of problems including quasar emission-line clouds, solar flare chromospheres, and X-ray binaries. To proceed, one needs to know the dependence of the probability of photon escape, $p_e(\tau)$, in the important transitions as a function of some reference optical depth. These escape probabilities depend sensitively on atomic physics and the physical conditions in the medium. Knowledge of $p_e(\tau)$ permits the solution of the probabilistic, frequency-integrated radiative transfer equation. Although in this paper we have chosen to do this through scaling laws, in many cases other methods may be more suitable. Through an iterative procedure, a

simultaneous solution of the radiative transfer equation and the steady-state atomic equilibrium equations is obtained. This solution determines the values of the flux divergence coefficient ρ and the line-center source function S_0 . The values of these two parameters lead directly to local rates of radiative heating and cooling. In addition to allowing a straightforward calculation of the emergent line and bound-free fluxes, knowledge of these parameters are essential for construction of energy-balance models.

In future papers, we plan to improve various aspects of the procedure described above. These include replacement of the scaling laws by a depth-dependent probabilistic scheme, development of a single-flight escape probability for weakly interlocked resonance lines like $L\alpha$, and modifications to the form of $p_e(\tau)$ due to linear Stark broadening and interlocking.

We wish to thank Paul Ricchiazzi for many useful discussions, and Lawrence Cram for helpful comments on the manuscript. We wish to thank the referee for his suggestions regarding the form of the $L\alpha$ escape probability in the regime where destructions become important. This research has been supported by the Air Force Office of Scientific Research, Air Force Systems Command, USAF, under grant AFOSR-76-3071, by NASA under grant NGR-05-005-0055, and by the National Science Foundation under grant AST76-82890.

REFERENCES

- Adams, T. F. 1972, *Ap. J.*, 174, 439.
 Athay, R. G. 1972a, *Radiation Transport in Spectral Lines* (Dordrecht: Reidel), chap. 6.
 ———. 1972b, *Ap. J.*, 176, 659.
 ———. 1976, *Ap. J.*, 204, 160.
 Athay, R. G., and Johnson, H. R. 1960, *Ap. J.*, 131, 413.
 Avrett, E. H. 1965, *SAO Spec. Rept.*, No. 174.
 Avrett, E. H., and Hummer, D. C. 1965, *M.N.R.A.S.*, 130, 295.
 Baldwin, J. A. 1977, *M.N.R.A.S.*, 178, 67P.
 Baldwin, J. A., Rees, M. J., Longair, M. S., and Perryman, M. A. C. 1978, *Ap. J. (Letters)*, 226, L57.
 Canfield, R. C. 1971, *Astr. Ap.*, 10, 54.
 Canfield, R. C., and Puetter, R. C. 1980, *Ap. J. (Letters)*, 236, L7.
 ———. 1981a, *Ap. J.*, 243, 390.
 ———. 1981b, in preparation.
 Canfield, R. C., Puetter, R. C., and Ricchiazzi, P. J. 1981, in preparation.
 Canfield, R. C., and Ricchiazzi, P. J. 1980, *Ap. J.*, 239, 1036.
 Davidson, A., Hartig, G., and Fastie, W. 1977, *Nature*, 269, 203.
 Delache, P. 1974, *Ap. J.*, 192, 475.
 Drake, S. A., and Ulrich, R. K. 1979, *Ap. J.*, 235, 680.
 Frisch, U., and Frisch, H. 1975, *M.N.R.A.S.*, 173, 167.
 Harrington, J. P. 1973, *M.N.R.A.S.*, 162, 43.
 Hummer, D. G. 1964, *Ap. J.*, 140, 276.
 ———. 1968, *M.N.R.A.S.*, 138, 73.
 Hummer, D. G., and Kunasz, P. B. 1980, *Ap. J.*, 236, 609.
 Hyland, A., Becklin, E. E., and Neugebauer, G. 1978, *Ap. J. (Letters)*, 220, L73.
 Ivanov, V. V. 1973, NBS Spec. Pub., No. 385.
 Jefferies, J. T. 1968, *Spectral Line Formation* (Waltham: Blaisdell).
 Mihalas, D. 1978, *Stellar Atmospheres* (San Francisco: Freeman).
 Osterbrock, D. E. 1962, *Ap. J.*, 135, 195.
 Puetter, R. C., Smith, H. E., Soifer, B. T., Willner, S. P., and Pipher, J. L. 1979, *Ap. J. (Letters)*, 225, L53.
 Puetter, R. C., Smith, H. E., and Willner, S. P. 1978, *Ap. J. (Letters)*, 227, L5.
 Puetter, R. C., Smith, H. E., Willner, S. P., and Pipher, J. L. 1981, *Ap. J.*, 243, 345.
 Soifer, B. T., Oke, J. B., Matthews, K., and Neugebauer, G. 1979, *Ap. J. (Letters)*, 227, L1.
 Thomas, R. N. 1960, *Ap. J.*, 131, 429.
 ———. 1965, *Some Aspects of Non-Equilibrium Thermodynamics in the Presence of a Radiation Field* (Boulder: University of Colorado Press).
 Thomas, R. N., and Athay, R. G. 1961, *Physics of the Solar Chromosphere* (New York: Interscience).
 Weisskopf, V. 1933, *Observatory*, 56, 291.
 Weisheit, J. C. 1979, *J. Quant. Spectrosc. Rad. Transf.*, 22, 585.
 Woolley, R. 1938, *M.N.R.A.S.*, 98, 624.
 Woolley, R., and Stubbs, D. 1953, *The Outer Layers of a Star* (Oxford: Clarendon Press).

RICHARD C. CANFIELD and RICHARD C. PUETTER: Center for Astrophysics and Space Sciences, Code C-011, University of California, San Diego, La Jolla, CA 92093

iii) Theoretical Quasar Emission Line Ratios.

II. Hydrogen $L\alpha$, Balmer, and Paschen Lines, and the Balmer Continuum

This paper describes an application of the methods of the previous paper to the problem of quasar emission line ratios. There is much in common between this problem and that of solar flares. In both cases, the irradiation of the emitting plasma by a strong source of radiation plays a significant role in determining the nature of the emergent radiation. In the case of a quasar, it is thought that the emission comes from clouds illuminated by a central power-law continuum source. In solar flares, the analogous situation is the illumination of the chromosphere and photosphere by radiation from the hot overlying X-ray emitting flare plasma.

THEORETICAL QUASAR EMISSION LINE RATIOS. II. HYDROGEN $L\alpha$, BALMER, AND PASCHEN LINES, AND THE BALMER CONTINUUM

RICHARD C. CANFIELD AND R. C. PUETTER

Center for Astrophysics and Space Science, University of California, San Diego

Received 1980 April 4; accepted 1980 August 6

ABSTRACT

We explore the formation of the hydrogen $L\alpha$, Balmer, and Paschen lines and the Balmer continuum in highly idealized QSO broad emission line clouds (ELCs) of constant temperature and density irradiated by an external source of power-law spectral form. We simultaneously solve the equations governing excitation, ionization, and transfer of both external and diffuse radiation fields. Our calculations show that the typical observed broad emission line ratios of $L\alpha/H\alpha$, $H\beta/H\alpha$, $P\alpha/H\alpha$, and Balmer continuum/ $H\alpha$ can be understood for ELC conditions in the temperature range $7 \times 10^3 \lesssim T_e \lesssim 2 \times 10^4$ K, hydrogen density range $10^8 \lesssim n_H \lesssim 10^{12}$ cm $^{-3}$, and for external fluxes $\mathcal{F} \lesssim 10^{-6}$ ergs cm $^{-2}$ s $^{-1}$ Hz $^{-1}$ at the Lyman continuum limit.

Important results are:

1. The $L\alpha/H\alpha$ ratio is very sensitive to the optical thickness of the cloud at the optical thickness that we think are appropriate for QSOs.
2. It is not necessary to postulate dust either internal or external to the ELC.
3. The ELCs are very optically thick; the Balmer lines and $P\alpha$ originate in a region for which the Lyman-limit optical depth $\tau_{\ell} \gtrsim 10^2$.
4. A very extended ionized zone results from ionization from excited states.
5. The radiation from various transitions arises from very extended and sometimes quite different regions of the cloud. This renders a mean escape probability approach inappropriate.
6. Predicted line ratios and cooling rates depend critically on the functional form of the photon escape probability.
7. Acceptable values of the area covering factor and static energy balance require temperatures somewhat in excess of 10^4 K.

Subject headings: line formation — quasars — radiative transfer

I. INTRODUCTION

The observed hydrogen emission lines in QSOs have received increased interest since Baldwin (1977) first suggested that the intrinsic $L\alpha/H\beta$ line intensity ratio is depressed by a factor of about 10 from the typical recombination value. This result has since been observationally confirmed by numerous authors (see Davidsen (1980) for a brief review of the observational situation). In the present paper we review the results of a fully interlocked depth-dependent radiative transfer calculation for hydrogen using the technique outlined in the first paper of this series (Canfield and Puetter 1981, hereafter Paper I). A previous paper (Canfield and Puetter 1980) briefly outlined these results. Here we discuss the results of the calculation in considerably more detail and make minor improvements.

II. FRAMEWORK OF THE MODEL

There are two basic aspects to modeling quasar emission lines. First, one must decide on what the physical conditions of the emission line region are:

second, one must decide how adequately to describe the emitters of the observed radiation (i.e., how to model the atomic physics of the problem). We discuss these two points in the subsections below.

a) The Conditions in Quasar Emission Line Clouds

Our basic assumptions concerning the geometry and physical conditions in the broad emission line region have been outlined in Paper I. We envision the emission line region to contain a large number of emission line clouds (ELCs) each having considerable optical thickness. Each ELC is illuminated by a powerful central ionizing source of power law form. We specify the ionizing flux in our models by the parameter $\mathcal{F}/\mathcal{F}_0$, where \mathcal{F} is the ionizing flux at 1 Rydberg and $\mathcal{F}_0 = 10^{-6}$ ergs cm $^{-2}$ s $^{-1}$ Hz $^{-1}$. In all the models described below we have assumed a power law spectral index, α , of 1 (i.e., $\mathcal{F}/\mathcal{F}_0 \propto \nu^{-\alpha}$, with $\alpha = 1.0$). Simple arguments based on the absence of broad forbidden lines suggest that the total hydrogen density, n_H , in the ELC is considerably larger than in galactic H II regions or planetary

nebulae. Typical values used in modeling quasar ELCs are around $n_{\text{H}} = 10^9 \text{ cm}^{-3}$. We parametrize the density in our models by $n_9 (\equiv n_{\text{H}}/10^9 \text{ cm}^{-3})$. In addition we make the assumption that n_9 is a constant throughout the ELC. Typical temperatures of ELCs are expected to be about 10^4 K . We specify our model electron temperatures by $T_4 (\equiv T/10^4 \text{ K})$. Again we make the artificial assumption of constant T_4 . While the emission line region probably contains very many ELCs, in the present paper we model only one ELC. If the emission in the different ELCs varies widely, an ensemble average will need to be taken. This was deemed unwarranted in the present study. We expect the variation of line ratios due to various ELC geometries to be very small and so have modeled our ELC as a plane-parallel atmosphere with emission from only one side (i.e., the side facing the central source).

In this paper, we have not attempted to calculate a self-consistent thermal balance model of quasar ELCs. Such a problem is considerably more difficult than calculating line ratios given a particular atmosphere. The calculation of the local heating and cooling rate is of paramount importance in such a calculation. This requires a more sophisticated solution to the equation of transfer than our scaling law technique (see Paper I) provides. The lack of a self-consistent atmosphere is one of the major deficiencies in our present models, and makes this work more an exploration of radiative transfer effects than a physically realistic model of quasar ELCs. However, if the major emission from the ELCs arises in a roughly constant temperature region or from regions in which the electron temperature does not affect the source function strongly (such as for small optical depths), then we expect our models to reflect actual QSO emission regions.

Even though our models suffer significantly from our artificial assumptions of constant density and temperature, we have made a significant advance over past quasar ELC models by incorporating an improved treatment of radiative processes. It is encouraging that we are able to reproduce the observed quasar emission-line spectrum from such idealized models. We fully expect, however, that the relationship between line ratios, absolute line intensities, etc., and temperature and density will change when thermal balance models which incorporate the effects we have explored become available.

b) The Atomic Model

We chose to model our hydrogen atom as five bound levels and the ionized state. We include only six levels because numerical experiments with the number of levels indicated that line strengths are determined to roughly 1% when one level above the upper level of the transition in question is included. Our primary interest at the present time is in the lines $\text{L}\alpha$, $\text{L}\beta$, $\text{H}\alpha$, and $\text{P}\alpha$.

These lines should change by only about 1% upon including higher levels in the calculation. The uncertainties introduced by other effects are, of course, greater than this. We also chose not to resolve angular momentum substructure of the atomic levels. At the densities we consider, collisional / mixing is very rapid. Relatively few scatterings are needed before collisional mixing occurs. This means that even if there is a departure of the source functions of the individual angular momentum substates, they scale together with some typical lag in optical depth which is small in comparison with the total optical depth. Thus, as the individual source functions saturate, the disagreement between the individual source functions can only persist over negligible portions of the atmosphere. Another way of viewing this effect is to note that as the optical depths become large, the net radiative rates are severely reduced. This reduction in the net radiative rates implies that the source functions of all the substates begin to become collisionally interlocked. Thus the substates tend to have thermal populations deep into quasar emission line clouds.

The atomic rates we have adopted were obtained from the following sources. Collisional excitation and ionization rate coefficients were taken from the work of Johnson (1972). The photoionization cross sections were taken from the approximate formulae given in Jefferies (1968) calculated with Gaunt factors at the absorption edges taken from Allen (1973). The spontaneous radiative emission coefficients for the hydrogen lines were taken from Weise, Smith, and Glennon (1966). All the inverse rates were calculated on the basis of detailed balance.

Other aspects of the atomic physics are the processes of line broadening and photon frequency redistribution. The probability of photon escape is of utmost importance. Questions of absorption coefficient profiles, line broadening, and frequency redistribution are extremely pertinent. We have dealt with these questions in considerable detail in Paper I.

III. LINE RATIOS AS A FUNCTION OF PHYSICAL CONDITIONS

The exact physical conditions in the broad line region are not well determined. Therefore it is appropriate to explore the effects on line ratios of varying physical conditions, as this might rule out certain physical conditions as unrealistic. A general picture of what might be considered "reasonable" conditions has, however, grown out of past models. Thus we explore only a moderate variation of parameters about what we shall term our standard model. In Figures 1 and 2 we display the variation of the $\text{L}\alpha/\text{H}\alpha$, $\text{H}\beta/\text{H}\alpha$, $\text{P}\alpha/\text{H}\alpha$, and $\text{B}\gamma/\text{H}\alpha$ ratios as a function of optical depth at the Lyman continuum edge, τ_{L} , the electron temperature,

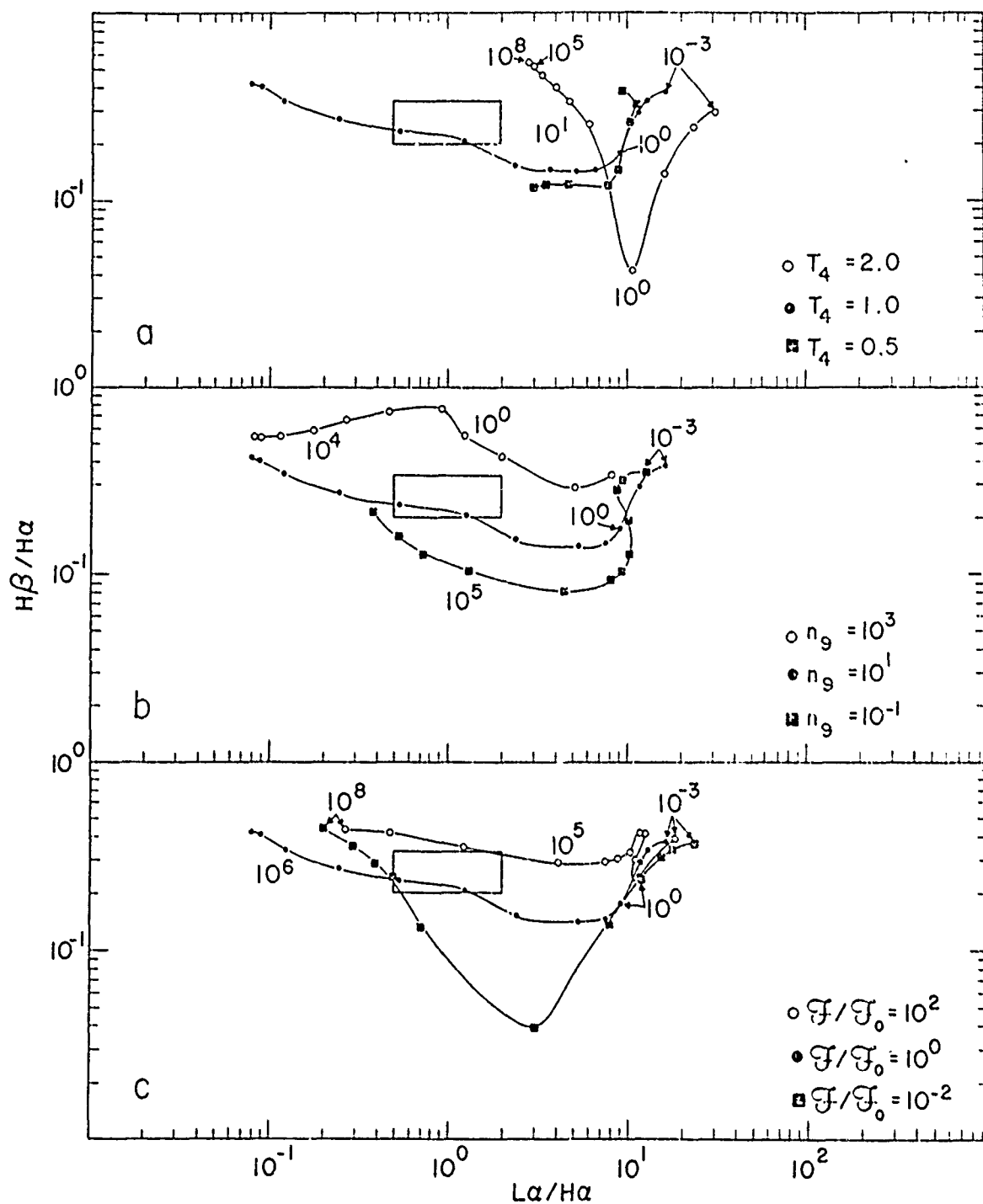


FIG. 1.—The calculated values of the line flux ratios of $H\beta/H\alpha$ and $Ly\alpha/H\alpha$ for different ELC parameters as a function of Lyman limit optical depth. The ELC parameters explored are (a) electron temperature T_4 , (b) total hydrogen density n_9 , and (c) ionizing flux Γ/Γ_0 where $\Gamma_0 = 10^{-4} \text{ ergs cm}^{-2} \text{ Hz}^{-1}$ at 1 Rydberg. In all models we assume that the ionizing flux varies as ν^{-10} . The symbols on each curve indicate one decade intervals in optical depth at the Lyman limit unless specifically noted otherwise. The standard model ($T_4 = 1.0$, $n_9 = 10.0$, and $\Gamma/\Gamma_0 = 1.0$) is shown in all three panels. The rectangle indicates typical observed ranges of the ratios.

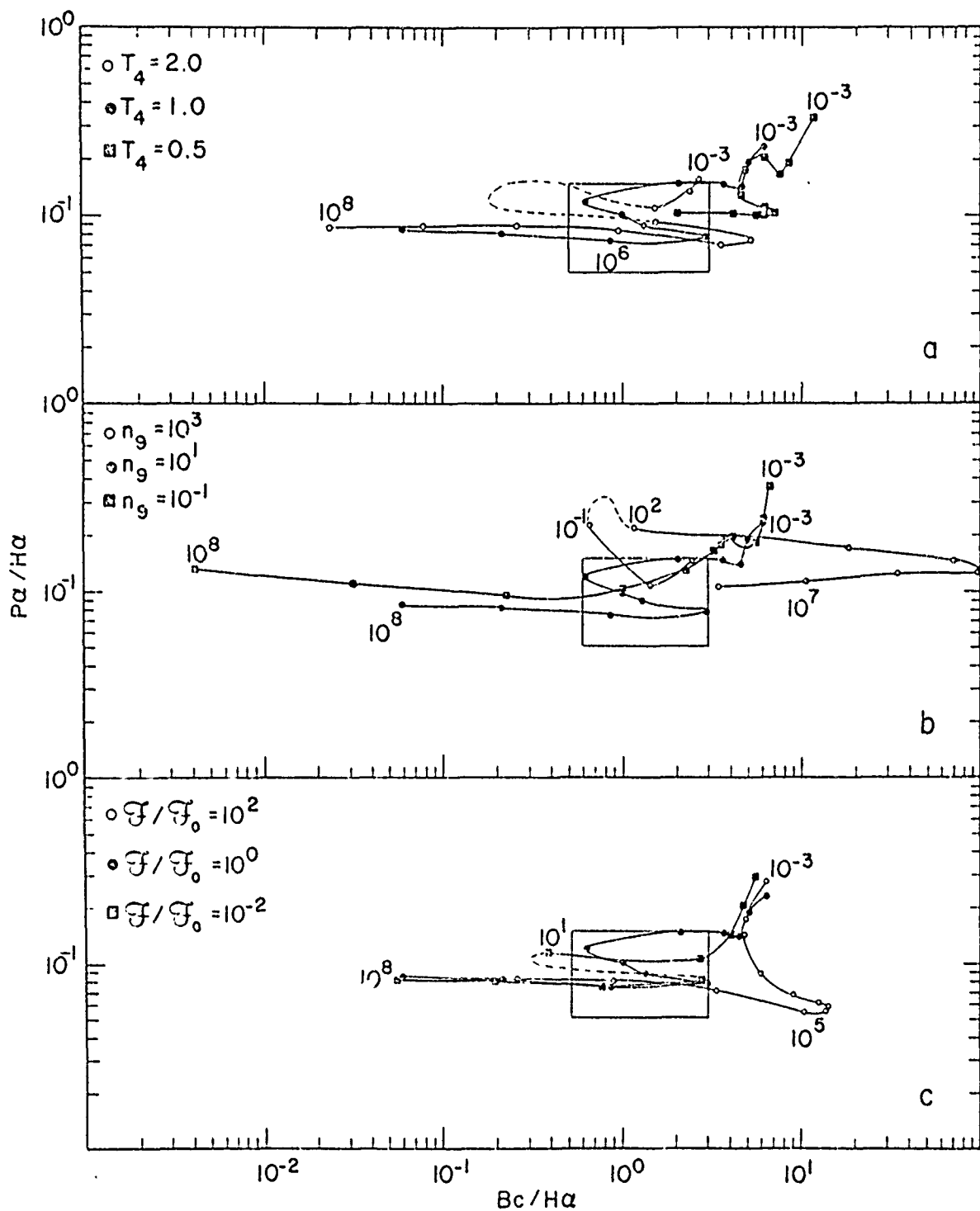


FIG. 2.— The calculated values of the flux ratios of $P\alpha/H\alpha$ and $Bc/H\alpha$ (Bc =Balmer continuum) for different ELC parameters as a function of Lyman limit optical depth. The ELC parameters explored are. (a) T_4 , (b) n_9 , and (c) F/F_0 . The symbols on each curve indicate one decade intervals in τ_L . The rectangle indicates typical observed ranges of the ratios. Regions of uncertainty, indicated by dashed lines, are discussed in § III.

the total hydrogen density, and the ionizing flux at 1 Rydberg, \bar{F} . The standard model ($T_4 = 1.0$, $n_9 = 10.0$, $\bar{F}/\bar{F}_0 = 1.0$ where $\bar{F}_0 = 10^{-8}$ ergs cm^{-2} Hz^{-1}) is shown in each panel of Figures 1 and 2. The marks along each curve indicate one decade intervals in τ_{c1} and some labels are given as space permits. The box shown in each panel represents the observed range of $L\alpha/H\alpha$ and $H\beta/H\alpha$ in Figure 1 and of $P\alpha/H\alpha$ and $B\epsilon/H\alpha$ in Figure 2. Any model that hopes to explain the observed line ratios must pass through the boxes in both figures. In Figures 1a and 2a we illustrate the effects of varying the electron temperature, while in Figures 1b, 2b and 1c, 2c we illustrate the effects of variations in \bar{F}/\bar{F}_0 and n_9 , respectively. We now turn to a more detailed description of Figure 1.

Figure 1a shows the effects of varying the electron temperature of the ELC. Notice, first, the values of $L\alpha/H\alpha/H\beta$ obtained for low values of τ_{c1} . The low density limit case A values of this ratio are 12.6/1.00/0.37, 11.4/1.00/0.35, and 10.5/1.00/0.32 for $T_4 = 0.5$, 1.0, and 2.0, respectively. Our calculations agree fairly well with the case A values for $T_4 = 0.5$ and 1.0. For $T_4 = 2.0$, however, we obtain a different result. At $T_4 = 2.0$ and the densities we consider, collisional effects are extremely important compared to recombination. In fact, the collisional creation rate of $L\alpha$ from level 1 is roughly 2.5 times larger than the direct recombination rate to level 2. Thus it is not surprising to find the actual $L\alpha/H\alpha$ ratio roughly three times the predicted low density case A value.

As the optical depth increases, the $L\alpha/H\alpha$ and $H\beta/H\alpha$ ratios fall. The former ratio decreases because $L\alpha$ has a rapidly decreasing escape probability due to the ever increasing $L\alpha$ optical depth, while $H\alpha$ remains optically thin. The latter ratio decreases as the conversion efficiency of $L\beta$ photons to $H\alpha$ photons increases as $L\beta$ becomes optically thick. Still deeper into the ELC, the Balmer lines become optically thick, and the $H\beta/H\alpha$ ratio begins to increase as the line source functions begin to grow. The $L\alpha/H\alpha/H\beta$ at large optical depth is determined by the relative photon escape probabilities since the source functions have all reached LTE values. The low $L\alpha/\text{Balmer}$ line ratio is due to the very inefficient escape of $L\alpha$ as compared to other lines. This confirms the suggestion of Baldwin (1977) that the low $L\alpha/H\alpha$ ratio is due to the relative enhancement of $H\alpha$, and not to destruction of $L\alpha$. The limiting $L\alpha/H\alpha$ ratio at large τ depends upon the escape probability in both $L\alpha$ and $H\alpha$. The escape probability for $L\alpha$ in turn depends upon the creation rate of photons at optically thin frequencies by interlocked transitions (primarily $H\alpha$). The escape probability of $H\alpha$ depends upon the size of the radiatively damped wings. Thus at the densities we consider here, the limiting $L\alpha/H\alpha$ ratio for $\tau \rightarrow \infty$ is solely a function of T_e . The final $H\alpha/H\beta$ ratio is determined by the relative size of the Voigt damping parameter in $H\alpha$ and

$H\beta$ and, of course, the electron temperature (see Paper I).

Figures 1b and 1c also both show the same general trends in the $L\alpha/H\alpha/H\beta$ ratio as in Figure 1a. There are a few minor differences, however. The high density case in Figure 1b has a "wobble" in it between $\tau_{c1} = 10^{-2}$ and 10^1 . The upturn in the $H\beta/H\alpha$ ratio at $\tau_{c1} \sim 10^{-2}$ corresponds to the point at which $H\alpha$ becomes optically thick, while the sudden break in the rise in $H\beta/H\alpha$ corresponds to the point at which $H\beta$ becomes optically thick. This effect is most pronounced in the high density case because this has the largest recombination rate and produces the largest emitted optically thin fluxes of any model. In the high density model, it was necessary to include the effects of Stark broadening in order to model accurately the photon escape probability (see Canfield and Puetter 1981b for a detailed description of Stark broadening as applied to photon escape). In Figure 1c we indicate the effects of different ionizing radiation intensities. The low intensity and standard model $L\alpha/H\alpha/H\beta$ ratios are similar at low optical depth. The low intensity ratios depart from the standard model values as the optical depth increases because the higher electron density of the standard model causes the source functions to thermalize at lower optical depth values.

In Figure 2 we explore the effect of the model parameters on the integrated Balmer continuum ($B\epsilon$) emission and the $P\alpha$ line emission. The rectangle corresponds to the observed range of $P\alpha/H\alpha$ and $B\epsilon/H\alpha$ (Puetter et al. 1981). At low optical depths the $P\alpha/B\epsilon/H\alpha$ ratios do not agree particularly well with the case B values. The case B values for $P\alpha/B\epsilon/H\alpha$ are 0.13/1.1/1.0, 0.12/1.4/1.0, and 0.11/0.95/1.0 for $T_4 = 0.5$, 1.0, and 2.0, respectively (see, for example, Osterbrock 1974, where we assume $n_e = 10^4$). The reason for the departure of the $P\alpha/H\alpha$ ratio from the case B value at $\tau_{c1} = 10^{-3}$ is easily understood. Case B calculations assume that all the Lyman lines are extremely optically thick. At $\tau_{c1} = 10^{-3}$, lines connecting levels 3 and 4 with level 1 are not extremely thick. The optical depth in $L\gamma$ is roughly 1 at this point and $L\delta$ is still thin. As the cloud becomes thicker, the $P\alpha/H\alpha$ ratio approaches the case B value but continues to decrease because of the larger radiatively damped wings of $H\alpha$. The enhanced $B\epsilon/H\alpha$ ratio relative to case B at small optical depth is due to the overestimation of the level 3 population in the case B approximation which results in producing too high an $H\alpha$ flux at this optical depth.

The decrease in the $B\epsilon/H\alpha$ ratio toward the case B value is due to the increase in the optical depth of the Lyman lines. The general "zigzag" nature of the $P\alpha/B\epsilon/H\alpha$ curve can be understood in terms of the following effects. When the $L\alpha$ source function reaches its maximum value, the decrease in the $B\epsilon/H\alpha$ ratio stops (see discussion of Fig. 5 in § IV). Instead,

the Bc emission now increases relative to $\text{H}\alpha$ (which is optically thick) as the Bc source function starts to increase toward its LTE value. This increase in $\text{Bc}/\text{H}\alpha$ stops when the Balmer continuum becomes optically thick and the higher escape efficiency of $\text{H}\alpha$ photons causes this ratio to decrease toward large optical depths. The unusual appearance of the high density case in Figure 2 is due to the onset of the importance of linear Stark broadening.

In Figure 2, there are several portions of the curves that are given as dashed lines. The dashed portions of the curves indicate regions in which our results are uncertain. Our model calculation assumes that the ELC is a semi-infinite atmosphere. In order to obtain results for clouds of smaller total optical depths, we truncate our semi-infinite results at the appropriate optical depth. Generally this turns out to be a good approximation. This procedure, however, gives poor results when the source functions and effective Planck functions at optical depths less than the truncation depth τ are materially affected by the radiation fields from greater optical depths. Clearly, in this case the physical conditions for optical depths less than τ , in a cloud of total optical depth τ , differ markedly from the conditions for $\tau < \tau$, in a semi-infinite atmosphere even under otherwise identical conditions. Realistic results in the above cases could be obtained, of course, by solving the radiative transfer for a slab rather than a semi-infinite atmosphere as we have done. Such a calculation employing an improved treatment of the radiative transfer is currently in progress.

IV. DETAILS OF THE STANDARD MODEL

Having now discussed the different physical conditions that can produce the observed line ratios, we shall find it instructive to examine one particular model in more detail. Several aspects of the standard model and their impact on our understanding of the physics of the ELCs and their implications for the conditions in the ELC region are quite interesting. Among these are the run of the various level populations, source functions, and effective Planck functions, \bar{B} (see Paper I), through the ELC. These quantities aid in understanding the local emission rates and the way in which this emission arises. Another important quantity is the value of the emergent flux per unit optical depth $M^{-1} p_e S_0$ in each transition. Finally, the absolute intensities are of interest as they give information on the amount of emitting area required to produce the observed emission. This, in turn, has implications for area covering factors and the total emitting mass in the broad line region. These various points are discussed in the subsections below.

a) Level Populations, Source Functions, and Effective Planck Functions

In Figure 3, we display the level populations relative to the LTE values for our standard model. In Figures 4 and 5 we display the normalized effective Planck function, $\bar{B}/B(T_e)$ (see Paper I), and the normalized source function, $S_0/B(T_e)$, for several different lines and bound-free continua. Along the bottom of each figure

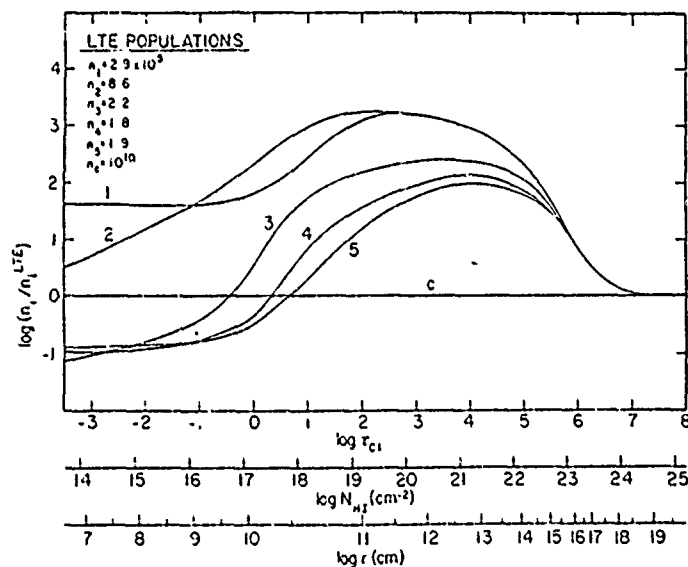


FIG. 3.—Level populations for the standard model ($T_e = 1.0$, $n_9 = 10.0$, $\mathcal{F}/\mathcal{F}_0 = 1.0$) relative to their LTE values, as a function of position in the cloud. In addition to the τ_{c1} scale, we also show the neutral column density and distance into the cloud from the edge facing the ionizing source.

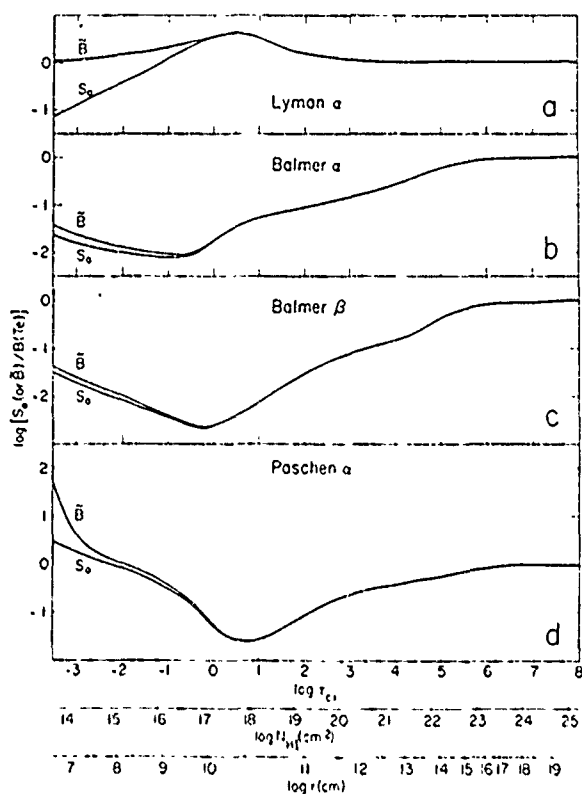


FIG. 4.—Standard model source functions and effective Planck functions \tilde{B} , relative to the Planck function $B(T_e)$ for various lines, as a function of depth into the cloud. In addition to the τ_{01} scale, the neutral column density and distance into the ELC from the side facing the ionizing source are given (a) La , (b) Ha , (c) $\text{H}\beta$, and (d) Pa .

in addition to the Lyman edge optical depth we give the total neutral column density and the distance into the ELC in centimeters. Inspection of these figures reveals several interesting features which we discuss below.

Figure 3 shows that the electron density is essentially constant and equal to the LTE value throughout the entire ELC. This high state of ionization results from the rapid photoionization rates out of the higher bound levels. The large line fluxes tie the higher bound levels tightly to level 1. Thus there is a rapid path from level 1 (which constitutes the majority of all neutrals) through the upper bound levels to the continuum. At the depth at which the standard model achieves the observed line ratio, the photoionizations are due to the external radiation field since the ELC is still optically thin in the higher bound-free continua. Deep into the ELC, however, the external radiation field drops, but the diffuse bound-free continuum fluxes grow. The growth of the diffuse continua maintains the high ionization rate. In fact, the ionization rate per bound level deep into the ELC due to the diffuse continua is several orders of

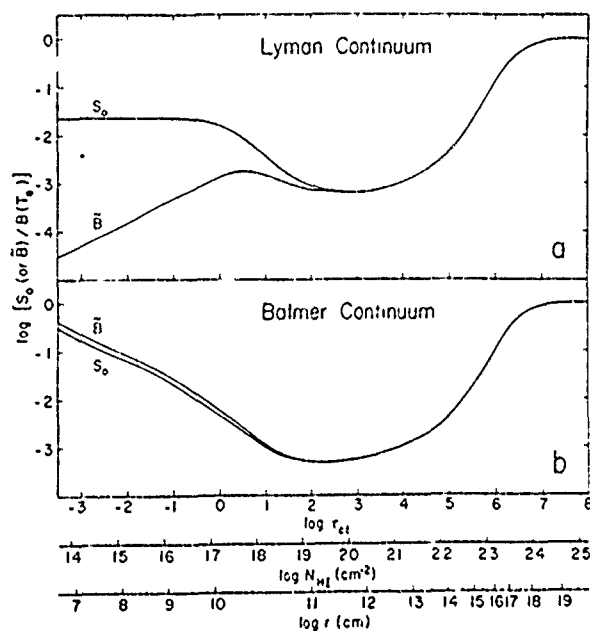


FIG. 5.—Source functions and effective Planck functions \tilde{B} , relative to the Planck function $B(T_e)$ for (a) the Lyman continuum and (b) the Balmer continuum as a function of depth into the ELC. In addition to the τ_{01} scale, the neutral column density and distance into the ELC are given.

magnitude greater than the rate due to the external field at small optical depths.

Figure 3 also shows the behavior of the bound-bound source functions. Consider first the populations of levels 1 and 2 which give direct information on the Lyman alpha source function, S_{21} . Note that for small optical depths the relative level 2 population is smaller than the relative level 1 population. This means that the value of S_{21} is subthermal, as is confirmed by Figure 4. Past $\tau_{01} = 10^{-1}$, however, the relative level 2 population exceeds that of level 1, i.e., S_{21} is superthermal. At $\tau_{01} \sim 3 \times 10^2$, n_2/n_1^{LTE} joins with n_1/n_1^{LTE} . This means that S_{21} has thermalized (also see Fig. 4). Note that Figures 3 and 4 both show the rest of the line source functions thermalizing at $\tau_{01} \sim 10^6$. And Figures 3 and 5 show the bound-free source functions thermalizing at $\tau_{01} \sim 10^7$. Note also that for $\tau_{01} \lesssim 10$ the values of S_{c3} , S_{c4} , and S_{c5} are all superthermal.

The relative behavior of the level populations can be understood in the following manner. At the top of the ELC atmosphere, the external radiation field is very high. This results in a highly ionized gas. Since the radiation fields in the lines and continua are very much lower than the LTE values, the spontaneous radiative downward rates result in a large superthermal population of level 1 and small subthermal populations in the other bound levels. Since the La radiation field is relatively strong, however, even at the top of the atmo-

sphere, the population of level 2 also manages to be superthermal. As we proceed deeper into the ELC, the continually growing $L\alpha$ radiation field (which is "feeding" off the strong nonthermal Lyman continuum) causes the relative population of level 2 to exceed the relative population of level 1. In addition, the growing radiation fields in the other transitions cause the higher bound level populations to grow. At $\tau_{c1} \sim 10^2$, the Lyman continuum source function ceases to be dominated by the nonthermal external radiation field (see Fig. 5) because of the large Lyman limit opacity. The absence of this nonthermal component from the Lyman continuum interlocking term in the $L\alpha$ effective Planck function causes S_{21} to thermalize. The $L\alpha$ source function, having thermalized causes the relative n_1 and n_2 populations to be equal and "track" together. As the other line source functions begin to thermalize near $\tau_{c1} \sim 10^6$ all the bound level populations begin to drop towards their LTE values; however, they are able to obtain their thermal values only when the continuum source functions thermalize at $\tau_{c1} \sim 10^7$.

In Figure 4 we plot the effective Planck functions and the source functions for several different transitions. The effective Planck functions give us information on what is driving the source functions to a particular value, and the source functions tell us the emission per unit optical depth in each transition. At the top of the ELC atmosphere we see that, with the exception of $L\alpha$, the effective Planck functions for all the lines shown here decrease toward large τ . There are two reasons for the increase in the effective Planck function for $L\alpha$. First, the destruction rates of Lyman line photons remain constant because the optical depths of the interlocked transitions (i.e., the lines of higher series) are still less than unity. Second, the creation rates in the Lyman lines increase due to the rising populations of the higher bound levels, which cause the photoionization rates and hence recombination rates to increase. The effective Planck functions for the lines of higher series decrease for the following reasons. First, indirect destructions increase; the rates at which electrons from the upper level u arrive in the lower level l by indirect paths increase. For example, one indirect destruction path for $H\alpha$ is $3 \rightarrow 1 \rightarrow 2$ (i.e., emission of $L\beta$ followed by absorption of $L\alpha$). The efficiency of this path is increased into the ELC because the $L\alpha$ radiation field increases faster than the $L\beta$ radiation field. The remainder of the decrease in the effective Planck functions of the lines other than the Lyman lines is due to the decreasing effectiveness of indirect creations. To create a ul photon indirectly, one must take an electron from l to u by an indirect path. The most productive indirect paths for small optical depths involve spontaneous radiative decays. The transition $l \rightarrow 1$ is among these transitions. The effectiveness of any path containing the step $l \rightarrow 1$ de-

creases as the radiation field in that transition increases. Thus the increasing Lyman line radiation fields directly cause the reduction in \bar{B} in the other transitions by decreasing the indirect creation rates.

The turnover in the value of \bar{B} in $L\alpha$ at about $\tau_{c1} \sim 3$ is due to the onset of effective destruction of $L\alpha$ photons. This point corresponds to the place in the atmosphere at which the probability of escape is equal to the probability of destruction (destruction here includes all means, direct and indirect, radiative and collisional, of destroying ul photons, see Paper I). At this depth the energy stored in the $L\alpha$ transition starts to "flow" back into the other lines, the value of \bar{B} in $L\alpha$ drops, and the values of \bar{B} in the other transitions increase. By $\tau_{c1} \sim 3 \times 10^2$, $L\alpha$ has come into the thermodynamic equilibrium with the electrons. The source functions in the other transitions slowly rise past $\tau_{c1} \sim 10^1$ in response to the continuing increase of collisional effects as the net radiative rates decrease.

In Figure 5 we consider the Lyman and Balmer continua. At small optical depths the source function, S_{c1} , is dominated by the strong external radiation field. At $\tau_{c1} \sim 1$ the external radiation field begins to drop and so does S_{c1} . The general rise in \bar{B}_{c1} at small optical depths is due to the increase in the total ionization rate from the upper levels. For small optical depths the other bound-free continua are also thin, and the increasing bound level populations cause a net increase in the total rate to the continuum—i.e., the Lyman continuum is "feeding" off the external radiation fields in the other continua. The $L\alpha$ source function reaches its largest value at $\tau_{c1} \sim 3$. As a result, \bar{B}_{c1} turns over at this point and decreases as S_{21} thermalizes. The decrease in \bar{B}_{c2} for small optical depths is due to the decreasing effectiveness of the indirect creation path $2 \rightarrow 1 \rightarrow c$. The increasing $L\alpha$ radiation field competes strongly with the $1 \rightarrow c$ step. An ever increasing number of electrons that decay from level 2 to level 1 find themselves returning to level 2 via a $L\alpha$ absorption rather than finding their way to the continuum. This causes \bar{B}_{c2} to decrease. As S_{21} thermalizes, \bar{B}_{c1} and \bar{B}_{c2} stabilize and eventually grow to thermal values as the net radiative rates become unimportant in comparison to the collisional rates.

b) The Depths of Line Formation

In Figure 6 we give the values of $p_e S_0 \tau$ arbitrarily normalized to unity at the point of maximum value versus $\log \tau_{c1}$ for several different transitions, for a semi-infinite atmosphere. In addition to the τ_{c1} scale we also include the τ scales for each transition plotted. The function $p_e S_0 \tau$ measures the flux that emerges from optical depth τ per unit $\ln \tau$. The relative maximum in the $L\alpha$ emission per unit logarithmic optical depth at $\tau_{c1} \sim 10^1$ is due to the superthermal nature of S_{21} at this point. The value of $p_e S_0 \tau$ for $L\alpha$ begins to decrease

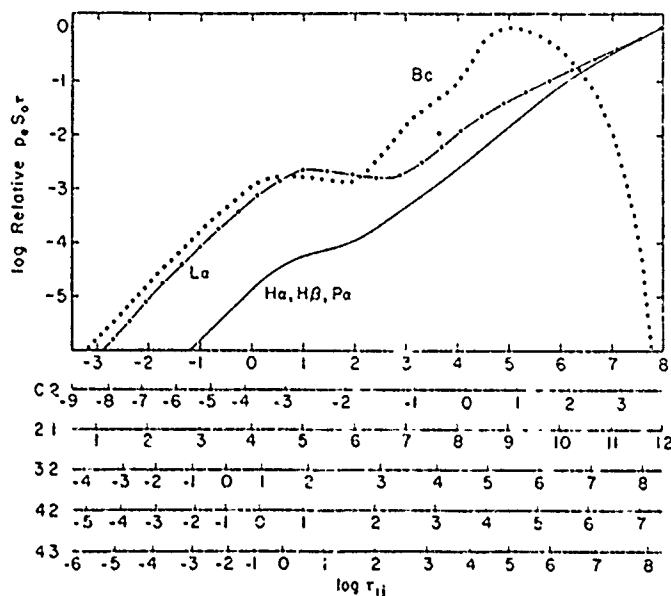


FIG. 6.—The relative value of $p_e S_0 \tau$, the flux emergent from depth τ , per unit $\ln \tau$, for the standard model. In addition to the standard τ_{e1} depth scale, we give optical depth scales for all the transitions plotted. The dot-dashed line gives the relative value of $p_e S_0 \tau$ for $L\alpha$, scaled to unity at its point of maximum value; the dotted line gives the Balmer continuum, and the solid line gives $H\alpha$, $H\beta$, and $P\alpha$, which are essentially identical.

until about $\tau_{e1} \sim 3 \times 10^2$ because S_{21} is thermalizing. From this point deeper into the ELC the value of $p_e S_0 \tau$ for $L\alpha$ would be roughly constant since S_0 is constant and $p_e \sim \tau^{-1}$, due to diffusion in space (see Paper I) were it not for the effect of interlocked transitions. Destruction of $L\alpha$ by interlocking quickly causes the diffusion in space by multiple scattering to become very inefficient. Hence the probability of photon escape by diffusion in space decreases faster than τ^{-1} past $\tau_{e1} \sim 3 \times 10^3$. Compensating for this effect, however, is creation of $L\alpha$ photons at optically thin frequencies by interlocking. Thus $p_e(\tau)$ takes on a $\tau^{-1/2}$ dependence. Consequently, past $\tau_{e1} \sim 3 \times 10^3$, $p_e S_0 \tau$ increases as $\tau^{1/2}$. In contrast to $L\alpha$, the Balmer and higher lines are subthermal far deeper than where $L\alpha$ thermalizes. Thus initially $p_e S_0 \tau$ in these lines will grow faster than $L\alpha$ in the region with $S_0(L\alpha) = B$. After these lines thermalize at $\tau_{e1} \sim 10^6$ the values of $p_e S_0 \tau$ in these transitions increase as $\tau^{1/2}$ because $p_e \propto \tau^{-1/2}$ due to complete frequency redistribution over the radiatively damped Voigt profile. Thus past $\tau_{e1} \sim 10^6$, $p_e S_0 \tau \propto \tau^{1/2}$ for $H\alpha$, $H\beta$, and $P\alpha$. Hence at large τ the $L\alpha/H\alpha/H\beta/P\alpha$ ratio locks to a constant value as long as T_e is constant.

Figure 6 also displays the value of $p_e S_0 \tau$ for the Balmer continuum. As can be seen from the figure, the largest contribution to the Bc emission would come from the region $\tau_{e2} \sim 10^1$ if the ELC were thick enough. The peak in $p_e S_0 \tau$ in the Balmer continuum occurs at $\tau_{e2} \sim 10^1$ because of the sharp drop in $p_e(\tau_{e2})$ for τ_{e2}

exceeding 1 (see Paper I) and the steady rise of S_0 throughout this range. Thus the total Balmer emission increases rapidly until the total ELC optical depth exceeds $\tau_{e1} \sim 10^5$ after which point it only slowly increases and remains roughly constant for clouds exceeding $\tau_{e1} \sim 10^7$. For the standard model, however, the Balmer lines grow much more rapidly with increasing column density than does the Bc emission. Thus the Bc/Balmer line ratios peak at about $\tau_{e1} \sim 10^3$ where the Balmer continuum is still thin. Thus observationally, one should expect the objects which show the largest Balmer continuum emission relative to the Balmer lines to exhibit an optically thin Balmer continuum profile. This conclusion seems to be confirmed by the observations of Puetter *et al.* (1981).

The above considerations indicate that the low $L\alpha$ /Balmer line ratio may imply a lower limit to the column density of emitting gas. Using Figure 1 as a guide, we see that apparently no models with $\tau_{e1} \lesssim 10^2$ are able to produce a low enough $L\alpha$ /Balmer line ratio. In addition, the fact that the $L\alpha$ /Balmer ratio is not observed to be extremely small ($L\alpha/H\alpha \lesssim 0.1$, say) seems to require that the total emitting column density is in some way self-limiting. Perhaps the gas becomes too cold to support a high state of ionization past a certain point and the line source functions drop off sharply. The resolution of this problem will have to wait until energy balance models that incorporate adequate radiative transfer are available for quasar ELCs.

c) *Total Line Intensities and Area Covering Factors*

As can be seen from Figure 2, our model ELC populations vary by several orders of magnitude over the range of optical depths considered. This dramatically demonstrates that the assumption of constant populations, as, for example, in case B type models of quasar ELCs, may produce grave errors. Nonetheless, it is instructive to compare our results with those of case B since the large majority of past ELC models have made use of such assumptions.

The calculation of case B level populations or line intensities assumes that the lines other than the Lyman lines are optically thin. In addition, it has become customary to also include collisional effects (see, for example, Osterbrock 1974). The effects of collisions, however, are always small at $T_e \sim 10^4$ K unless the optical depths are large (i.e., the net radiative rates are small) or the densities are considerably larger than thought typical of quasar ELCs. Therefore the case B lines intensities are dominated by the downward spontaneous radiative rates and are straightforward to calculate. Under case B assumptions, the line intensities are directly proportional to the volume emissivities, which are in turn proportional to the population of the upper level of the transition. Since the net radiative rates in our ELC at the top of the atmosphere are similar in all transitions but $L\alpha$ to the optically thin rates assumed in case B, it is not surprising that the level populations we calculate for levels 1, 3, 4, 5, and c compare favorably with the case B values (of course, our values depart significantly from case B as we move deeper into the ELC). Our n_2 population is in nearly exact agreement with case B while our n_1 population is within 25% of case B. In addition, the populations we calculate for levels 3, 4, and 5 are all within a factor of 2 of the case B values. The case B value for level 2, on the other hand, is not very well founded. Case B calculations by nature do not include in detail the effects of radiative transfer in $L\alpha$ or the other Lyman lines. If we assume, however, that every recombination produces a $L\alpha$ photon that escapes unimpeded, the level 2 population one obtains is $\sim 5.5 \times 10^{-2} \text{ cm}^{-3}$ at 10^4 K. Our level 2 population at small τ ($\tau_{c1} = 10^{-3}$) is $2.7 \times 10^1 \text{ cm}^{-3}$, which is in poor agreement with the above value. We can improve the agreement with the "case B" level 2 population by assuming only $p_e(\cdot)$ of the created $L\alpha$ photons escape and thus in some way account for the "pile-up" of $L\alpha$ photons. If we do this the new "case B" value for the population in level 2 is still only 8.8×10^{-1} or a factor of roughly 30 too small. Thus it seems that there is no simple extrapolation of the case B assumptions that is able to reproduce the correct population of the second level.

The total emitted intensities from our standard model are considerably smaller than those of case B (a factor

of 18 for $H\beta$ for $\tau_{c1} \sim 10^3$ for the same column densities. However, this is not unexpected. With large optical depths the escape of photons from deep in the ELC becomes increasingly unlikely. To compensate for this effect and maintain an ELC that has a high efficiency for converting the ionizing energy into line flux, the production of photons deep into the ELC must increase. Parenthetically we note that one can, of course, always produce an arbitrarily large amount of radiation in any line with $p_e \tau$ a monotonically increasing function by increasing the column density until the wings become sufficiently thick to provide the radiation. This, however, may (and probably will) upset the constraint of the observed line ratios.

The intrinsic line fluxes, $\mathcal{F}_L^{\text{int}}$, along with the assumed intrinsic ionizing flux per hertz at 1 Rydberg, \mathcal{F}^{int} , and the observed values of the line flux and continuum flux unambiguously determine the area covering factor:

$$\epsilon_A = \frac{\mathcal{F}_L^{\text{obs}}}{\mathcal{F}_L^{\text{int}}} \frac{\mathcal{F}^{\text{int}}}{\mathcal{F}^{\text{obs}}}, \quad (1)$$

where we have assumed that ϵ_A is small enough that the correction to $\mathcal{F}_L^{\text{obs}}$ due to obscuration by the emission line clouds is negligible. The value of $\mathcal{F}_{H\beta}^{\text{obs}}/\mathcal{F}^{\text{obs}}$ as calculated from the data of Baldwin (1975) is about 10^{14} Hz . We have not included 3C 273 or the two extreme spectral index objects in this sample in calculating this value since they seem atypical. Thus our standard model produces a value of ϵ_A of roughly 2. This demonstrates that the standard model is unphysical. The problem is that the standard model is a bit too inefficient in producing line radiation per unit ionizing flux. However, for this very same reason, the standard model is too inefficient at cooling itself and must heat up past 10^4 K. The $T_4 = 2.0$ model, on the other hand, is much more efficient at producing line radiation. The value of the covering factor for this model for the optical depth that most nearly achieves the observed ratios (see Fig. 1) is $\epsilon_A \approx 0.03$. In addition, the models with enhanced density and less intense ionizing radiation field also produce covering factors of less than unity at 10^4 K and would produce covering factors considerably less at higher temperatures. At this time, in view of the fact that the present ELC models are not energy balance models, it seems unwarranted to worry about the exact covering factor or absolute line intensities. Suffice it to say that the covering factors produced by the present models fall within the range of values commonly accepted for the broad emission line region.

V. DISCUSSION

a) *Previous Calculations*

In the recent past, several papers have appeared that address the question of hydrogen line ratios in QSOs—

most importantly the $H\alpha$ (or $H\beta$)/ $L\alpha$ ratio. The emphasis of these calculations is much different from ours, and it seems worthwhile to make an intercomparison in order to highlight the important issues.

The models of Krolik and McKee (1978) include some processes that we do not. First, unlike our models, they treat the angular momentum substates of each principal quantum state individually. For clouds of densities and optical depths consistent with the observations (see § III), however, our assumption of angular momentum mixing leads to errors in the $L\alpha/H\alpha$ ratio of probably no more than 10%. Second, Krolik and McKee base their radiative transfer calculation on a mean photon escape probability assuming complete redistribution over a Doppler absorption coefficient profile. We include the effects of partial and complete redistribution over the radiatively damped line wings. In addition, our calculation is depth-dependent. Krolik and McKee include many more bound levels in their model atom than we do. We included only those bound levels that our numerical experiments showed were necessary to obtain $L\alpha/H\alpha/H\beta$ ratios accurate to a few percent.

Another calculation addressing the hydrogen line emission from QSOs is that of Shuder and MacAlpine (1979). Their calculation is again based on the same mean escape probability approach as in Krolik and McKee (1978). Apart from this difficulty, their calculation is more sophisticated than ours. The most important difference is that they attempt to treat the complex problem of energy balance of a multi-element cloud in equilibrium with the ionizing external radiation field. We ignore this complexity by assuming constant density and temperature. They also consider the effects of charge-exchange reactions and of dust both internal and external to the ELC, neither of which we consider. The models of Shuder and MacAlpine are able to produce some of the observed hydrogen line ratios by adjusting the amounts of both internal and external dust, while our models do not require dust to reproduce the observed line ratios.

Our models represent a conceptual advance with respect to the radiative transfer over the so-called mean escape probability calculations. We have shown elsewhere (Canfield and Puetter 1980) that large (order of magnitude) errors arise due to the breakdown of the assumptions in this approach because no single point in the ELC can be identified as the depth of origin of the emergent radiation (also see § IVb). In addition, past calculations have used an escape probability based on complete redistribution within a pure Doppler absorption coefficient profile. The order-of-magnitude error in the $L\alpha/H\alpha/H\beta$ ratios due to this assumption is discussed in § Vb.

Ferland and Netzer (1979) also have carried out calculations aimed at understanding the $L\alpha$ /Balmer

line ratio. However, they treat the radiative transfer in $L\alpha$ only and do not take into account the strong interlocking between $L\alpha$ and the other lines and continua. Their calculation, like ours, is more a study of radiative transfer effects under possible ELC conditions than a physically realistic model. Their ionization structure, for example, has not been calculated in a way which is consistent with their $L\alpha$ line transfer solution just as we made no attempt to make our temperature structure consistent with our line transfer solution. We will return to this point in § Vc. Other differences are that while we treat the radiative transfer in all transitions of an atom with five bound levels and a continuum state, they treat $L\alpha$ only; while we use scaling law radiative transfer solutions, they use a more realistic Monte Carlo method.

Recently, Kwan and Krolik (1979) have completed a study of ELC emission that includes heavy elements and attempts to perform a thermal balance calculation. Their model hydrogen atom is very similar to ours: they assume six bound levels plus the continuum while we assume five levels plus the continuum. The real advantage of their calculation is that it is a thermal balance calculation that includes heavy elements. However, they use photon escape probabilities that assume complete redistribution in a Doppler absorption coefficient profile in all transitions. In Paper I we have shown this to be inaccurate since it ignores important line wing redistribution processes. In fact it can lead to errors of several orders of magnitude in the escape probabilities at optical depths of interest (see § IVb, d). In addition, they have not considered the radiative transfer in the diffuse higher bound level hydrogen continuum (§ IVc discusses these important effects).

b) The Effects of the Form of p_e on Line Ratios

As discussed in Paper I, the scaling law solutions of the radiative transfer equation (RTE) require knowledge of the mean number of scatterings, $N[\equiv 1/p_e(\tau)]$ or thus equivalently $p_e(\tau)$, of the average line or continuum photon. For large optical depths, the radiative loss from an isothermal atmosphere turns out to be directly proportional to the probability of escape, p_e . For this reason, the exact form of p_e is extremely important. Canfield and Puetter (1980) briefly discussed the variation of the depth of formation (i.e., the flux divergence per unit τ_{line}) of line photons as a function of the form of p_e . In Figure 7 we display the variation in the line ratios $L\alpha/H\alpha$ and $H\beta/H\alpha$ as a function of optical depth at the head of the Lyman continuum, τ_{c1} , for four different assumptions concerning photon escape. All four curves assume $n_0 = 1.0$, $\mathcal{S}/\mathcal{S}_0 = 1.0$, and $T_e = 1.0$. All curves are labeled by marks separated by one decade in τ_{c1} . Curve 7a assumes that escape in all lines is governed by a single flight escape probability with complete redistribution

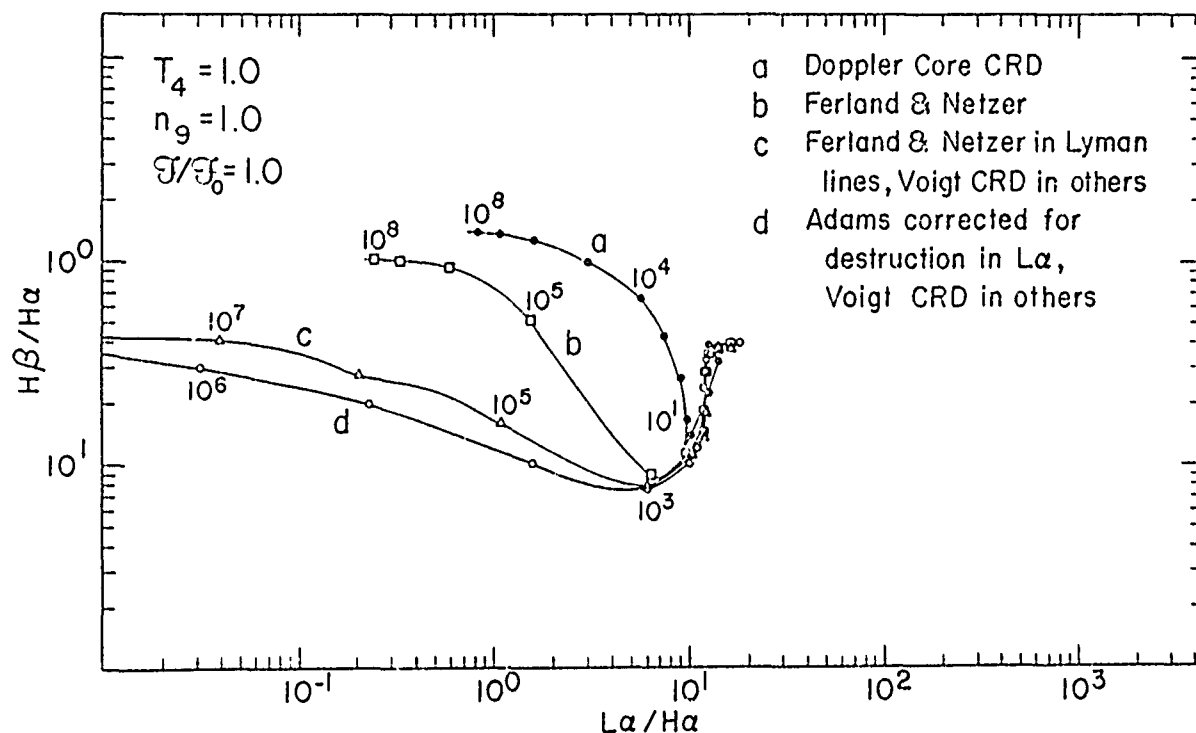


FIG. 7.— The effects of four different escape probabilities on the emergent $H\beta/H\alpha$ and $L\alpha/H\alpha$ line ratios, for $T_4 = 1.0$, $n_9 = 1.0$, $\bar{\nu}/\bar{\nu}_0 = 1.0$. (a) Complete redistribution (CRD) over a pure Doppler core. (b) Partial redistribution (PRD) result of Ferland and Netzer (1979). (c) Ferland and Netzer p_e for the Lyman lines and CRD over a Voigt profile for the other lines. (d) The most realistic form for p_e in all transitions, Adams's (1972) PRD and CRD over a Voigt profile for the other lines (see Paper I). Tick marks indicate 1 decade intervals in τ_{01} .

(CRD) over a Doppler core. Curve 7b assumes the Ferland and Netzer partial redistribution (PRD) escape probability for all lines. Curve 7c assumes that p_e for the Lyman lines is given by the Ferland and Netzer partial redistribution result while for the subordinate lines p_e is given by a single-flight escape probability assuming complete redistribution over a radiatively damped Voigt profile (Achay 1972). Finally, curve 7d assumes the PRD result of Adams (1972) for $L\alpha$ and the single-flight CRD value of p_e for a radiatively damped Voigt profile for the other lines.

Note that the order-of-magnitude discrepancies in the line ratios for the same value of τ_{01} are typical for different forms of p_e at large optical depths. In view of these results it is quite obvious that one must make every effort to model accurately the true physics of photon escape in the various lines.

Curve 7a employs the most widely used form of the escape probability. The assumption of CRD over the Doppler core is excellent for small optical depths whenever some portion of the Doppler core is thin. However, once the entire core becomes thick, wing processes start to dominate photon escape. The onset of this regime is at about $\tau_{01} \sim 1$ for $n_9 = 1.0$, $T_4 = 1.0$, and $\bar{\nu}/\bar{\nu}_0 = 1.0$ as can be seen from Figure 7. It is

interesting to note that not only do the various escape probabilities give different line ratios in detail, but they also give different asymptotic limits. At large optical depths the source functions for the various lines "saturate" to the Planck function. Thus for a given T_e , the emergent flux depends only on the form of p_e . The escape probabilities for curves 7a and 7b depend only on the optical depths which in turn depend only on the electron temperature deep into the cloud. Thus the line ratios in curves 7a and 7b are converging toward a constant (but different) value that depends only on the electron temperature. The situation is quite different for curves 7c and 7d. In curves 7c and 7d the escape probability depends on both the optical depth and the Voigt parameter a . Thus the line ratios in 7c and 7d are functions of the atomic physics as well as the electron temperature.

Figure 7 shows several interesting trends. All the curves give roughly the same results for small optical depths. This is because in this regime Doppler core CRD determines the value of p_e . For these depths, all the curves essentially reproduce the "standard" case B line ratios. For large optical depths, curves 7a and 7b go to constant limiting values as described above. Curves 7c and 7d have extremely small $L\alpha/H\alpha$ ratios

when compared to case B values. The continuing decrease in $L\alpha/H\alpha$ in curves 7c and 7d is due to the very inefficient PRD escape in $L\alpha$ due to coherent wing scattering. Finally, a comparison of the large τ $L\alpha/H\alpha$ ratio in curves 7c and 7d to the asymptotic value shown in Figure 1 shows that inclusion of the interlocking increases the $L\alpha$ escape probability by creating some $L\alpha$ photons at optically thin wavelengths.

The high density limit presents a regime which we have not adequately treated in Paper I. In this limit, other line broadening processes become important to photon escape. Linear Stark broadening starts to alter the absorption coefficient profile for those lines with small radiatively damped wings and intrinsically large Stark wings. Of the lines we consider in our model atom, $L\delta$ and $B\alpha$ are strongly affected even at an electron density of 10^{10} cm^{-3} . At a density of 10^{12} cm^{-3} there are no lines that are not strongly affected. For the high density model presented in Figures 1 and 2, we have used escape probabilities that incorporate Stark broadening. The details of the derivation of p_e when linear Stark broadening is important are given by Weisheit (1979) and Canfield and Puetter (1981b).

At extreme optical depths, an effect we have neglected becomes important. For the largest optical depth we present, the effects of electron opacity are nonnegligible. Once the optical depth to electron scattering approaches unity, the continuous emission begins to dominate the observed spectra. This does not, however, compromise the results for the optical depths that produce the observed line ratios. At these depths, the electron scattering optical depth is still considerably less than unity.

c) The Importance of Consistency of Ionization and Excitation

It is imperative to incorporate self-consistently all ionization and excitation processes and the solutions to the radiative transfer equation. It is a serious mistake to calculate an ionization structure for quasar ELC without regard to the line transfer solution. For the range of physical parameters discussed in this paper, the strong diffuse $L\alpha$ radiation field present deep in the ELC provides a very rapid rate from the ground level to the first excited state. From the second level, a significant number of atoms can be ionized by electron collision or continuum photoionization (photoionization by the higher diffuse continua is the dominant effect at large τ). This rapid rate from level 1 to level 2 (and higher bound levels) to the continuum maintains a high ionization state deep into the ELC. While our calculations show excellent agreement with previous models at low optical depths, we find that if the electron temperature is greater than about $7 \times 10^3 \text{ K}$, the neutral fraction deep into the cloud ($\tau_{e1} \gtrsim 10^3$) is very small. Thus our $L\alpha$ source function does not drop

dramatically as in previous models due to a drop in the electron density, but eventually settles to the LTE value, provided there is sufficient line optical depth.

d) Energy Balance Considerations

The hydrogen lines are the strongest emission features present that are likely to form deep within the ELCs (with the possible exception of Mg II). Thus, unless there are important IR cooling lines, hydrogen will dominate the cooling deep within the ELC. It is unlikely that far-IR lines are important, because at 10^4 K the Planck function at their wavelengths is small. If the hydrogen lines are the dominant coolants (as seems likely) and the Lyman continuum is the dominant heat source, then temperatures deep in the ELC of near 10^4 K are not unreasonable. For our standard model ($T_4 = 1.0$, $n_9 = 10.0$, $\bar{v}/\bar{v}_0 = 1.0$) at an optical depth of 10^3 in the Lyman continuum (the depth at which the model produces the observed $L\alpha/H\alpha/P\alpha$ ratio) the Lyman continuum heating is $1.1 \times 10^4 \text{ ergs cm}^{-2} \text{ per unit } \tau_{e1}$ (here we have neglected, of course, the effects of opacities due to heavy elements which will reduce this heating rate). The cooling from our three different temperature models is 7.5×10^2 , 1.8×10^3 , and $2.3 \times 10^6 \text{ ergs cm}^{-2} \text{ per unit } \tau_{e1}$ at $T_4 = 0.5$, 1.0, and 2.0, respectively, summed over the 15 hydrogenic transitions that we considered. Thus while we assumed 10^4 K in this region, it seems likely that the temperature be higher than this. (This conclusion differs from that of Canfield and Puetter 1980 because of slightly modified escape probabilities.)

It is essential to note that in the construction of energy balance models, it is essential that a physically realistic form of $p_e(\tau)$ be used. The cooling rate at considerable depths is very sensitive to $p_e(\tau)$. For example, $L\alpha$ is the thermalized at $\tau_{e1} = 10^3$, the point at which the standard model achieves the observed line ratios; at this depth, $\tau_{21} = 1.1 \times 10^7$. This means that the $L\alpha$ cooling rate is directly proportional to $p_e(\tau_{21})$. The values of $p_e(\tau_{21})$ at this depth that one might adopt without full consideration of the physics of photon frequency redistribution range over more than three orders of magnitude. The Voigt form (Paper I, eq. [23c]) gives $p_e(\tau_{21}) = 1.3 \times 10^{-6}$; the Ferland and Netzer (1979, eq. [6]) form gives 1.1×10^{-7} ; the Adams (1972) form (Paper I, eq. [25]) gives 1.7×10^{-8} ; the pure Doppler form (Paper I, eq. [23b]) gives 3.2×10^{-9} . The strong need for care in the choice of the form to be used for $p_e(\tau)$ is obvious.

VI. SUMMARY AND CONCLUSIONS

In this paper we have investigated the formation of the well-observed lines of the hydrogen spectrum in QSOs, under the hypothesis that this spectrum is due to the illumination of broad emission line clouds (ELCs)

by a power-law external radiation field. The models are highly idealized, and are not intended to be definitive thermodynamic models of quasar ELCs. In particular, we artificially assume that density and temperature are constant throughout the ELC. Furthermore, we use a simplified model hydrogen atom.

We have taken into account radiative and collisional excitations and ionizations. Our results on the relationship of model parameters and emergent line ratios show that the $L\alpha/H\alpha$ ratio is very sensitive to the optical depth of the cloud. On the other hand, the other ratios are much more complicated functions of temperature, density, ionizing flux, and ELC optical depth. Our models show that the typical observed broad emission line ratios of $L\alpha/H\alpha$, $H\beta/H\alpha$, $P\alpha/H\alpha$ and $B\gamma/H\alpha$ of QSOs can be understood as originating in an ELC for which $7 \times 10^3 \lesssim T_e \lesssim 2 \times 10^4$ K, $10^8 \lesssim n_H \lesssim 10^{12}$ cm⁻³, and $\mathcal{F} \lesssim 10^{-6}$ ergs cm⁻² s⁻¹ Hz⁻¹ at the Lyman continuum limit. It is not necessary to postulate dust either external or internal to the ELC in order to understand the observed ratios. Our results suggest that the ELCs must have considerable optical thickness: $\tau_{cl} \gtrsim 10^2$ at the head of the Lyman continuum.

We discuss at some length our standard model which is capable of producing all the observed line ratios given above (this model, however, is not the only model that will satisfy the observations). An important new result is that the ELC is highly ionized at large optical depths due to ionizations from levels two and above. Another important realization is that the various spectral features of hydrogen emerge from very extended and in some cases different regions of the ELC. It is this effect that most compellingly demonstrates the failure of mean escape probability approximations.

We find that the emitted intensities of our standard model are much less than those of case B, for the same column densities. This relative inefficiency of photon production is shown to be equivalent to requiring too large an area covering factor, or in other terms, assum-

ing an unrealistically low temperature from the point of view of energy balance considerations. Our exploration of the effects of temperature shows that a somewhat greater temperature would not only produce a physically acceptable area covering factor, but is compatible with the observed line ratios and energy balance.

We discuss recent theoretical calculations that address the question of the hydrogen line ratios, especially $L\alpha/H\alpha$ (or $H\beta$). The major respects in which our treatment represents an advance are: (1) depth-dependent radiative transfer; (2) photon escape probabilities based on physically plausible frequency redistribution; (3) self-consistent (interlocked) treatment of ionization and excitation. We show how important it is to use the proper escape probability, since in particular the $L\alpha/H\alpha$ line ratio is extremely sensitive to the form of p_e . In addition, the adopted form of p_e in the various transitions has a major impact on energy balance calculations since the cooling rate for different forms of p_e can differ by several orders of magnitude at large optical depths. We also show that neglect of self-consistency of ionization and excitation can lead to the wrong ionization structure of the ELC, and that ionization from excited levels can dominate over that from the ground level. Finally, though our calculation is not intended to be an energy balance calculation, we show that our results imply that the actual temperature of the cloud with the density and incident ionizing flux of the standard model must be somewhat higher than 10^4 K at the depth implied by agreement of the predicted and observed line ratios.

We wish to thank H. E. Smith for many useful comments on the manuscript. This research has been supported by the Air Force Office of Scientific Research, Air Force Systems Command, USAF, under grant AFOSR-76-3071, by NASA under grant NGR-05-005-055, and by the National Science Foundation under grant AST 76-82890.

REFERENCES

- Adams, T. F. 1972, *Ap. J.*, 174, 439.
 Allen, C. W. 1973, *Astrophysical Quantities* (London: Athlone Press).
 Athay, R. G. 1972, *Radiation Transport in Spectral Lines* (Dordrecht: Reidel).
 Baldwin, J. A. 1977, *M.N.R.A.S.*, 178, 67p.
 Canfield, R. C., and Puetter, R. C. 1980, *Ap. J. (Letters)*, submitted.
 ———. 1981a, *Ap. J.*, 243, 381 (Paper I).
 ———. 1981b, in preparation.
 Davidson, A. F. 1980, in *IAU Symposium 92, Objects of High Redshift*, G. Abell and J. Peebles (Dordrecht: Reidel), (in press).
 Ferland, G., and Netzer, H. 1979, *Ap. J.*, 229, 274.
 Jefferies, J. T. 1968, *Spectral Line Formation* (Waltham: Blaisdell).
 Johnson, L. C. 1972, *Ap. J.*, 174, 227.
 Krolik, J., and McKee, C. 1978, *Ap. J. Suppl.*, 37, 459.
 Kwan, J., and Krolik, J. H. 1979, *Ap. J. (Letters)*, 233, L91.
 Osterbrock, D. E. 1974, *Astrophysics of Gaseous Nebulae* (San Francisco: Freeman).
 Puetter, R. C., Smith, H. E., Willner, S. P., and Pipher, J. L. 1981, *Ap. J.*, 243 in press.
 Shuder, J. M., and MacAlpine, G. M. 1979, *Ap. J.*, 230, 348.
 Weise, W. L., Smith, M. W., and Glennon, B. M. 1966, *Atomic Transitions Probabilities: Volume 1, Hydrogen through Neon* (NBS/NSRDS).
 Weisheit, J. C. 1979, *J. Quant. Spectrosc. Rad. Transf.*, 22, 585.

RICHARD C. CANFIELD and RICHARD C. PUETTER: Center for Astrophysics and Space Sciences, Code C-011, University of California, San Diego, La Jolla, CA 92093

iv) Theoretical Quasar Emission Line Ratios.

III. Flux Divergence and Photon Escape

This is the paper in which the basic radiative transfer methods used for the radiative hydrodynamics of solar flares were developed. The same radiative transfer equation that was derived here for the quasar problem was also used in the solar flare work. Even the mathematical techniques were very similar. The transfer of radiation in atomic lines can be handled with the same theoretical techniques, regardless of the distance between the source and the earth! Because of the fundamental role of the radiative transfer equation derived in this paper, this is one of the most important research papers of this grant.

THEORETICAL QUASAR EMISSION-LINE RATIOS. III. FLUX DIVERGENCE AND PHOTON ESCAPE

RICHARD C. CANFIELD, R. C. PUETTER, AND PAUL J. RICCHIAZZI¹

Center for Astrophysics and Space Sciences, University of California, San Diego

Received 1981 February 23; accepted 1981 March 3

ABSTRACT

In this paper we develop a computationally useful version of the probabilistic first-order differential radiative transfer equation of Frisch and Frisch. This approximate radiative transfer equation is especially appropriate for the evaluation of radiative transfer effects in multilevel atomic systems due to its extreme computational efficiency and reasonably accurate description of the physics of radiation transfer. In particular, it recognizes the distinction between the flux divergence coefficient, ρ , and the photon escape probability, p_e . We show that this distinction is crucial for calculations that attempt to construct self-consistent energy balance models since substitution of p_e for ρ in such models leads to large errors (of sign as well as magnitude) in the local cooling rate.

Subject headings: line formation — quasars — radiation mechanisms — radiative transfer

1. INTRODUCTION

Recently, a great deal of effort has been directed toward understanding physical conditions in the broad emission-line regions of quasars. Initial attempts to explain "anomalous" line ratios (e.g., $\text{Ly}\alpha/\text{H}\alpha \approx 1$ —a factor of roughly 10 below the expected case B recombination value) invoked simple recombination plus reddening by dust either internal or external to the emission-line clouds. More recent models (e.g. Netzer 1975; Krolik and McKee 1978; Shuder and MacAlpine 1979; Kwan and Krolik 1979; Matthews, Blumenthal, and Grandi 1980; and Canfield and Puetter 1980, 1981a, b) recognized the failure of dust to explain completely the observed spectrum and explored the effects of large optical depths upon the structure and emergent spectrum of QSO emission-line clouds. Not surprisingly, the effects of large optical depths were found to be quite substantial.

It is clear from observational evidence that the cooling of the emission-line region is dominated by the strong permitted transitions. Since these lines are apparently quite optically thick, it is imperative that an accurate physical study of the effects of radiative transfer on the cooling rate be made. On the other hand, there is also the need to explore a wide range of physical conditions, the effects of various elements, etc. Thus it is advantageous to make the numerical techniques used for this study very efficient from a computational point of view. The recent models listed above used photon escape probabilities or scaling laws based on photon escape

probabilities to calculate the physical conditions in the emission-line regions. These techniques are very computationally economical; however, in many cases they are too inaccurate. Many of these models assumed that the local cooling rate is directly proportional to photon escape probability. Strictly speaking, these models are, of course, not radiative transfer calculations. They make no attempt to solve explicitly the radiative transfer equation. They assume, in effect, that the net rate of loss of radiation from a volume element is always directly due to loss through the boundary of the atmosphere. This neglects the often dominant effect of radiative exchange with adjacent volume elements. This treatment is accurate only when restricted to cases in which the source functions change only very slowly, as is the case at extremely large optical depths in isothermal clouds. Because p_e is always positive, this approximation can never reproduce net heating of a volume element by radiation from nearby brighter volume elements, i.e., the effects of a sharp rise or drop in the source function. This effect is particularly important in the study of transition regions, in which the sharp drop in the source function produces an effective boundary to the emission region which may be much closer than the physical boundary of the medium. In this case, escape of radiation to the transition region boundary dominates photon loss.

Realizing that it is necessary both to account adequately for changes in the source function in calculating local cooling rates and to employ a computationally economical scheme for calculating these effects, we turned to probabilistic radiative transfer techniques. These methods have been demonstrated in the past (see Athay 1972; Delache 1974; Frisch and Frisch 1975;

¹Also Department of Physics, University of California, San Diego

Canfield and Ricchiazzi 1980) to be relatively accurate and computationally expedient. This technique uses photon escape probabilities in an approximate radiative transfer equation to calculate the mean intensity in the gas. In § I of this paper we derive a form of the equation of Frisch and Frisch (1975) that is particularly useful in solving the radiative transfer in multilevel atomic systems. In § III we discuss the local cooling rate predicted by this equation and contrast it with the rate predicted on the assumption that the local cooling rate is directly proportional to escape probability.

II. A PROBABILISTIC RADIATIVE TRANSFER EQUATION

We wish to derive a first-order differential equation that relates the changes in the mean intensity with depth into the cloud to changes in the source function (i.e., upper and lower atomic level populations) and in the probability of photon escape.

The mean intensity of radiation integrated over the absorption coefficient profile J is related to frequency-independent source function S by the equation (cf. Ivanov 1973)

$$J(\tau) = \int_0^\infty K_1(t-\tau)S(t)dt, \quad (1a)$$

where

$$J \equiv \int J_\nu \Phi_\nu d\nu \quad (1b)$$

and

$$K_1(\tau) = \int_0^\infty d\nu \Phi_\nu \phi_\nu E_1(\tau\phi_\nu). \quad (1c)$$

The absorption coefficient profile Φ_ν is normalized, i.e.,

$$\int \Phi_\nu d\nu = 1, \quad (1d)$$

and

$$S = \frac{2h\nu^3}{c^2} \left(\frac{g_u n_l}{g_l n_u} - 1 \right)^{-1}. \quad (1e)$$

Here τ is a reference optical depth, n_i and g_i are the population and statistical weight of level i respectively, and we have assumed the atmosphere to be semi-infinite. From this equation, we will derive a first-order differential equation relating the changes in the mean intensity to changes in the source function and probability of photon escape. A mathematical lemma important to the present discussion was developed by Frisch and Frisch (1975):

LEMMA: If $K_1(t)$ is a positive, even function of the variable t with

$$\int_{-\infty}^{\infty} dt K_1(t) = A < \infty,$$

and with

$$\lim_{\tau \rightarrow \infty} S(\tau) = S_\infty,$$

then

$$\int_0^\infty d\tau S(\tau) \frac{\partial}{\partial \tau} \int_0^\infty dt K_1(\tau-t)S(t) = \frac{1}{2} AS_\infty^2.$$

In the following paragraphs we use this lemma in much the same way as Frisch and Frisch (1975) did in the development of their equation.

Following Frisch and Frisch (1975), we apply the operator $\int_0^\infty d\tau S(\tau)(\partial/\partial \tau)$ to both sides of equation (1) to obtain

$$\begin{aligned} \int_0^\infty d\tau \frac{\partial J}{\partial \tau} S(\tau) &= \int_0^\infty d\tau S(\tau) \frac{\partial}{\partial \tau} \int_0^\infty dt K_1(\tau-t)S(t) \\ &+ \int_0^\infty d\tau S(\tau) \frac{\partial}{\partial \tau} \int_0^\infty dt K_1(\tau-t)S(t). \end{aligned} \quad (2)$$

Now using equation (2) and the lemma, we obtain

$$\begin{aligned} \int_0^\infty d\tau \frac{\partial J}{\partial \tau} S(\tau) &= \int_0^\infty d\tau S(\tau) \frac{\partial}{\partial \tau} \int_0^\infty dt K_1(\tau-t)S(t) + \frac{1}{2} S_\infty^2. \end{aligned} \quad (3)$$

If the scale of variation of $K_1(t)$ is smaller than that of $S(t)$, we can approximate equation (3) by

$$\int_0^\infty d\tau \frac{\partial J}{\partial \tau} S(\tau) = S_\infty^2 \int_0^\infty d\tau \frac{\partial}{\partial \tau} \int_0^\infty dt K_1(\tau-t) + \frac{1}{2} S_\infty^2 \quad (4a)$$

$$= -S_\infty^2 \int_0^\infty dt K_1(\tau-t) + \frac{1}{2} S_\infty^2. \quad (4b)$$

We can now evaluate the integral in equation (4) in terms of $K_2(\tau)$, the probability of escape of outwardly directed photons. Note that

$$p_e(t) = \frac{1}{2} K_2(t), \quad (5a)$$

where

$$K_2(t) = \int_{-\infty}^{\infty} dt K_1(t), \quad (5b)$$

where $p_e(\tau)$ is the single-flight photon escape probability in a semi-infinite atmosphere. That is, by the definitions of K_1 and K_2 we have (cf. Ivanov 1973)

$$\int_0^\sigma dt K_1(\sigma-t) = \int_0^\sigma dt K_1(t) = \frac{1}{2} [1 - K_2(\sigma)]. \quad (6)$$

Equation (4) can now be written

$$\int_0^\infty d\tau \frac{\partial J}{\partial \tau} S(\tau) = -\frac{1}{2} S_\infty^2 [1 - K_2(\sigma)] + \frac{1}{2} S_\infty^2 \quad (7a)$$

$$= \frac{1}{2} (S_\infty^2 - S_\sigma^2) + S_\sigma^2 p_e(\sigma). \quad (7b)$$

Applying the operator $(1/S_\sigma)(\partial/\partial\sigma)$ to both sides of (7) and renaming σ by τ , we obtain

$$-\frac{\partial J}{\partial \tau} = -\frac{\partial S}{\partial \tau} + \frac{\partial p_e}{\partial \tau} S + 2p_e \frac{\partial S}{\partial \tau}, \quad (8a)$$

$$\frac{\partial(J-S)}{\partial \tau} = -2p_e^{1/2} \frac{\partial}{\partial \tau} (p_e^{1/2} S), \quad (8b)$$

or

$$\frac{\partial \rho}{\partial \tau} = \frac{\partial p_e}{\partial \tau} + (2p_e - \rho) \frac{\partial \ln S}{\partial \tau}, \quad (8c)$$

where ρ is the flux divergence coefficient (see Canfield and Puetter 1981a) or the net radiative bracket (see Athay 1972)

Integration of equation (8) with semi-infinite boundary conditions, $J_\infty = S_\infty$, gives an explicit formula for J :

$$J(\tau) = S(\tau) + 2 \int_\tau^\infty dt p_e^{1/2}(t) \frac{\partial}{\partial t} [p_e^{1/2}(t) S(t)]. \quad (9)$$

It should also be noted that equation (9) gives an accurate expression for $J(t)$ at small optical depths even if the scale of variation of S is much smaller than that of K_1 . Equation (9) remains accurate at small τ any time the locally created photons in the optically thin region of the atmosphere are dominated by photons created in other volume elements regardless of the scale of variation in S . This is generally the case in thick atmospheres unless the source function rises dramatically at small optical depths.

Equation (9) is of a form that is much easier to implement in a numerical treatment than equation (1), for two reasons. First, unlike equation (1), the presence of a difference kernel in equation (1) forces a time-consuming evaluation of the entire integral at each optical depth. Second, a direct numerical evaluation of equation (1) requires very high accuracy at large optical depth since duplication of the correct asymptotic behavior of $J-S$ (which is built into equation [9]) is essential in the calculation of the radiative loss.

These attractive qualities are also shared by Frisch and Frisch's (1975) equation 6.10. We can, of course, use their equation directly to calculate the values of J and S . However, to use their equation we would first have to evaluate the values of $\bar{\epsilon}$ and \bar{B} (see Canfield and Puetter 1981a). The quantities $\bar{\epsilon}$ and \bar{B} are the effective values of ϵ and B when the multilevel source function is cast into equivalent two-level form. They are directly related to the local photon destruction probability,

$$p_d = \bar{\epsilon}/(1 + \bar{\epsilon}), \quad (10)$$

and the local photon creation probability per scattering, $p_d \bar{B}$. The calculation of p_d and \bar{B} is very complicated and time-consuming in a multilevel atomic system. Evaluation of J directly from S through equation (8) is much more efficient.

In practice, we find both equations (8) and (9) are useful. Equation (8), in differential form, is suitable for a linearization approach (e.g., Mihalas 1978) in which both the atomic level equations and the radiative transfer equations are solved simultaneously by a Newton-Raphson type approach. In this regard, equation (8) is a major improvement over the equation of Frisch and Frisch (1975) since performing a Newton-Raphson calculation with their equation requires extremely complicated and time-consuming evaluations of derivatives of the effective Planck function with respect to radiation fields and level populations. Equation (9), the integral form, can be used in an iterative scheme (Athay 1972) in which the atomic level equations are solved alternatively with the radiative transfer equation until convergence is achieved.

One must remember, however, that equation (8) is only an approximate equation. Its accuracy depends upon the variation of $S(t)$ being slower than that of $K_1(\tau-t)$ in equation (3). The extent of the inaccuracy of equation (9) has been shown by Frisch and Frisch (1975), in their Figures 3 and 4. These figures give a comparison of the source functions calculated exactly and through the use of Frisch and Frisch's equation (6.10) for several different optical depth variations of the thermal source in a two-level system. To find the error in J , we note that $\Delta J/J = \Delta S/(S - p_d B)$. Since the value of $p_d B \approx S$ in the Frisch and Frisch calculation, $\Delta J/J = \Delta S/S$. As can be seen from the figures, the largest errors occur where the source function is most poorly approximated by a constant. Note that whenever the local value of the source function overestimates the average value of S within the characteristic scale of variation of $K_1(\tau)$, the approximate scheme overestimates the value of J and vice versa.

These calculations show that, in general, accuracy to better than a factor of 2 can be obtained except in the most extreme cases, such as purely exponential source distributions. We need not concern ourselves with these extreme cases here. In our models (see Canfield and

Puetter 1981*a, b*), heating occurs by radiative processes that vary only gradually, subject to scaling laws like $S \propto p_e^{-1/2}(\tau)$. In such cases, Frisch and Frisch (1975) have shown that one can expect to reproduce the exact result to within a few tens of percent.

III. COOLING RATES IN QUASARS

Equation (8c) illustrates most clearly how departures of ρ from p_e can occur if the line source function is not constant. Note particularly that ρ can take negative values, i.e., the radiation in the transition can heat as well as cool the volume element, whereas p_e is always positive. Since, in every atmosphere (even isothermal ones), the value S varies by orders of magnitude, there is reason for concern whenever the $\rho = p_e$ approximation is applied. We illustrate this point in Figures 1 and 2 where we plot the ratio of p_e/ρ for H β and the Balmer continuum (Bc) for an isothermal atmosphere. In this calculation, we have assumed that the hydrogen atom could be approximated by five bound levels plus the ionized state. The electron temperature is 10^4 K, the total hydrogen density is 10^{10} cm^{-3} , and there is an ionizing flux density at the top of the atmosphere of $F_0 = F_0(\nu/\nu_0)^{-1}$, where $F_0 = 10^{-8} \text{ ergs cm}^{-2} \text{ s}^{-1} \text{ Hz}$ and

ν_0 is the frequency at 1 rydberg. In all aspects, this calculation is identical to the standard model of Canfield and Puetter (1981*b*) except that the explicit radiative transfer equation (9) was used instead of assuming scaling law solutions. In all of the 15 hydrogenic transitions of this calculation, the scale of the variation of S was larger than that of K , except perhaps at extremely small optical depths. In none of these cases was the validity of our approach compromised, since the contribution from small τ to $J(\tau)$ was negligible. The variation of S at small τ under these circumstances was due to interlocking effects with optically thick transitions.

These figures show that errors of sign as well as large errors of magnitude would be made from the substitution of p_e for ρ . In particular, in the region from $\tau_{H\beta} \approx 10^{-6} - 10^0$ and from $\tau_{Bc} \approx 10^{-7} - 10^{-1}$, the H β and Bc transitions respectively heat the atmosphere rather than cool it. Note too, that for $\tau_{H\beta} \geq 1$ and for $\tau_{Bc} \geq 10$, ρ is given approximately by p_e in the respective transitions since the source functions have thermalized. In these regions, the $p_e = \rho$ substitution would be excellent; however, when $\rho_{Bc} = p_e(\text{Bc})$, the cooling rate due to the Bc is insignificant and can be ignored altogether, while the importance of H β cooling varies significantly

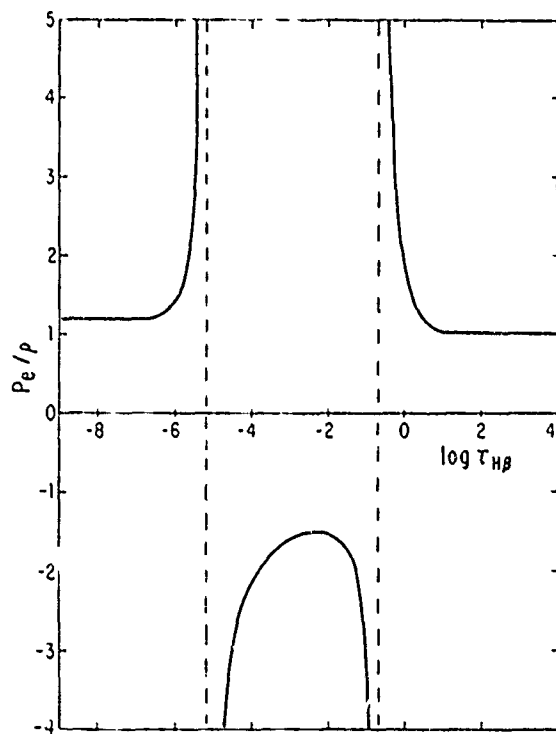


FIG. 1 — The ratio of the photon escape probability p_e to the flux divergence coefficient for H β in an isothermal, constant density atmosphere, as a function of the optical depth at the center of H β .

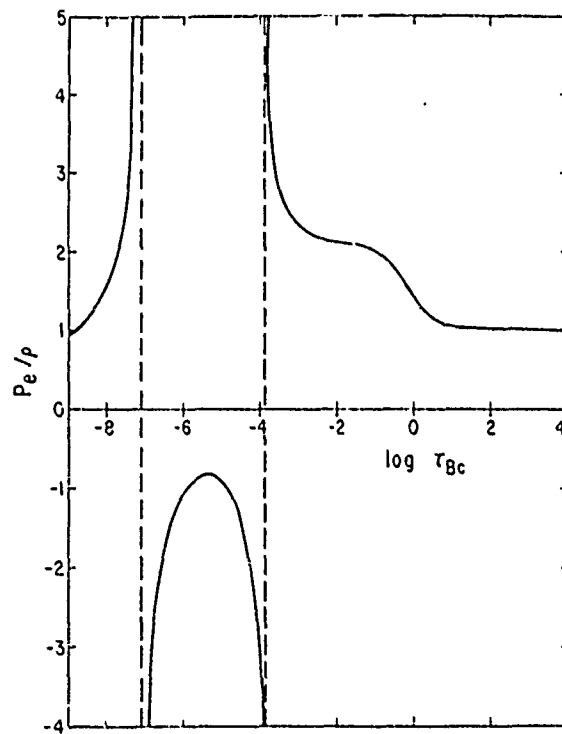


FIG. 2.— The ratio of the photon escape probability p_e to the flux divergence coefficient for the Balmer continuum in an isothermal, constant density atmosphere, as a function of the optical depth at the head of the Balmer continuum.

in the $\rho_{H\beta} = p_e(H\beta)$ region. Initially, the $H\beta$ cooling is totally dominated by $B\gamma$ cooling for which $\rho \neq p_e$. The variations of p_e/ρ in both of these transitions are similar. This, however, is somewhat fortuitous. Not all transitions (even with $n = 2$ being the lower level) show this behavior. The region in which $\rho < 0$ in these transitions, in fact, are not the same. The beginning of the $\rho_{B\gamma} < 0$ region occurs considerably deeper in the atmosphere than the beginning of the $\rho_{H\beta} < 0$ region. These transitions were chosen as examples because they dramatically illustrate the errors that can arise from a $\rho = p_e$ substitution. In addition, they illustrate the effect in an easily observable line and bound-free continua. On the other hand, that is not to say this type of behavior is unusual.

Of the 15 transitions that we model, 10 transitions show similar behavior (five lines and all five bound-free continua). In less ideal atmospheres where T_e is not constant, we expect even more serious difficulties with a $\rho = p_e$ approximation. Obviously, great care should be taken in evaluating the radiative cooling rates in such atmospheres.

This research has been supported by grants from the U.S. Air Force Office of Scientific research (AFOSR-76-3071), the National Aeronautics and Space Administration (NSG-7406 NAGW-30) and the National Science Foundation (AST-79-19842).

REFERENCES

- Athay, R. G. 1972, *Radiation Transport in Spectral Lines* (Dordrecht: Reidel).
 Canfield, R. C., and Puetter, R. C. 1980, *Ap. J. (Letters)*, 236, L7.
 ———. 1981a, *Ap. J.*, 243, 381.
 ———. 1981b, *Ap. J.*, 243, 390.
 Canfield, R. C., and Ricchiazzi, P. J. 1980, *Ap. J.*, 239, 1036.
 Delache, P. 1974, *Ap. J.*, 192, 475.
 Frisch, U., and Frisch, H. 1975, *M.N.R.A.S.*, 173, 167.
 Ivanov, V. V. 1973, *Transfer of Radiation in Spectral Lines*, N.B.S. Spec. Publ. 385 (Washington, D.C.: GPO).
 Krolik, J. H., and McKee, C. 1978, *Ap. J. Suppl.*, 37, 459.
 Kwan, J., and Krolik, J. H. 1979, *Ap. J. (Letters)*, 233, L91.
 Matthews, W. G., Blumenthal, G. R., and Grandi, S. A. 1980, *Ap. J.*, 235, 971.
 Mihalas, D. 1978, *Stellar Atmospheres* (San Francisco: Freeman).
 Netzer, H. 1975, *M.N.R.A.S.*, 171, 395.
 Shuder, J. M., and MacAlpine, G. M. 1979, *Ap. J.*, 230, 348.

RICHARD C. CANFIELD, RICHARD C. PUETTER, and PAUL J. RICCHIAZZI: Center for Astrophysics and Space Sciences, University of California, San Diego, La Jolla, CA 92093.

v) The Lyman- α /H α Ratio in Solar Flares and Quasars

We wrote this paper primarily as a response to other work that had dealt with both solar flares and quasars. It uses as part of the observational data base the measurements of Lyman α and H α for solar flares that were made during the Skylab Solar Flare Workshop. Our primary conclusion was that just because there are many similarities between quasar and solar flare spectral line ratios, one should not generalize that there are profound similarities in all details among these two diverse astrophysical phenomena.

PRECEDING PAGE BLANK-NOT FILME

THE LYMAN- α /H α RATIO IN SOLAR FLARES AND QUASARS

RICHARD C. CANFIELD, R. C. PUETTER, AND PAUL J. RICCHIAZZI

Center for Astrophysics and Space Sciences, University of California, San Diego

Received 1980 August 29, accepted 1981 April 7

ABSTRACT

Recent observations of the Ly α /H α ratio in both solar flares and quasars confirm Zirin's conclusion that this ratio is near unity in both these phenomena. However, typical values of the Ly α and H α brightness temperature in solar flares are not about 17,000 K. Instead, $T_b \sim 10,000$ K for Ly α and $\sim 7,000$ K for H α , in medium sized (class 2) flares.

We have constructed constant temperature and density solar flare models based on the same theoretical framework as our previous quasar models. We find that acceptable values of the intensity ratios Ly α /H α and H β /H α correspond to temperatures in the range $9,000 \leq T_e \leq 13,000$ K and hydrogen density in the range $10^{11} \leq n_H \leq 10^{12} \text{ cm}^{-3}$. The H α and Ly α source functions are thermalized at depths consistent with those inferred from independent studies, but this does not mean that the observed Ly α /H α ratio implies an electron temperature appropriate to the Planck function ratio. We show that our model values of n_H and T_e reflect reasonable nonlinear averages of those parameters in the depth dependent solar flare chromosphere model of Lites and Cook and that the value of Ly α /H α depends on n_H , T_e , and the optical depth of the emitting chromospheric layer. The existence of temperature plateaus is not required in quasar emission line clouds.

Subject headings: quasars — Sun: flares

1. INTRODUCTION

The hydrogen Ly α /H α ratio, particularly in quasars and active galaxies, has recently received considerable attention from observers. Many authors have pointed out the fact that the observed ratios cannot be understood in terms of basic nebular photoionization and recombination theory. This has often been attributed to optical depth effects. In previous papers we have shown that indeed, optical depth effects alone can account for the Ly α /H α ratio, as well as many other hydrogen line and continuum ratios in QSOs.

Several interesting suggestions were made in a paper by Zirin (1978), who first pointed out that the Ly α /H α ratio is approximately unity in solar flares, quasars, and the quiet solar chromosphere. He gave two explanations for this: (1) For quasars and flares, the unit value of the Ly α /H α ratio is a consequence of great optical depth and a thermal stabilization mechanism that leads to Planckian emission of Ly α and H α in plateaus of temperature 15,000–20,000 K; and (2) for the quiet chromosphere, the unit value of the Ly α /H α ratio is a consequence of some ratio stabilization mechanism independent of temperature and density, as long as the Ly α optical depth exceeds 10^4 .

Canfield and Puetter (1980, 1981a, b) have discussed the formation of several lines and continua of hydrogen, including Ly α and H α , in quasars. In this paper we extend their methods and apply them to solar flares. We do not discuss the solar chromosphere because our methods of estimating the output of a cloud through a semi-infinite calculation breakdown due to the importance of the nonlocal Balmer continuum from the photosphere. The

results from our models compare favorably with those based on more detailed methods. We find Zirin's explanations of the Ly α /H α ratios are too simplistic since line ratios depend upon both photon creation and photon escape, not simply electron temperature. In addition, our models require considerably lower temperatures than those suggested by Zirin. We provide an alternative explanation of the Ly α /H α ratio.

In § II we summarize the most recent observational data on the Ly α /H α ratio in solar flares and quasars. In § III we calculate solar flare models comparable to our previous quasar emission line cloud models. In § IV we discuss what the Ly α /H α ratio implies. Our conclusions are summarized in § V.

II. OBSERVATIONS

In the two years that have elapsed since Zirin's (1978) paper, a much more complete data base on both the solar flare and quasar Ly α and H α lines has become available.

a) Line Ratios

For solar flares, there is still very little Ly α /H α data available. Canfield and Van Hoosier (1980) have reported the first calibrated observations of the profile of Ly α before, during, and after maximum of two flares. H α data are not available for these flares, however, so they are only able to conclude on the basis of Svestka's (1976) "typical" H α profiles that the Ly α /H α ratio was about unity, to within a factor of 2. A more compelling result came from Canfield *et al.* (1980b), who reported estimates of the radiative output at the maximum of a single flare. For the

first time, their data give values of $\text{Ly}\alpha/\text{H}\alpha$ based on measurements of both $\text{Ly}\alpha$ and $\text{H}\alpha$ during an individual flare, in contrast to comparisons based on "typical" values. This is particularly important. It is hard to give a typical value of $\text{H}\alpha$, since the $\text{H}\alpha$ output of flares varies by orders of magnitude from flare to flare. Canfield *et al.* (1980b) find $\text{Ly}\alpha/\text{H}\alpha = 0.5$, with an uncertainty of a factor of 2.

For quasars and active galaxies, the observational situation is much better. Values of the $\text{Ly}\alpha/\text{H}\alpha$ ratio for 10 quasars and active galaxies are given in Table 1. We give both observed values (col. [2]) and values corrected for reddening in our Galaxy (col. [4]). We have used the correlation found by Burstein and Heiles (1978) between $E(B-V)$, 21 cm hydrogen column density, and the galaxy counts of Shane and Wirtanen (1967) to calculate the galactic extinction in the direction of each object. We then dereddened the $\text{Ly}\alpha/\text{H}\alpha$ line ratios using Savage and Mathis's (1979) mean galactic extinction curve. Clearly this correction does not materially alter the conclusion that there is surprisingly little variation about the average values, which are $\langle \text{Ly}\alpha/\text{H}\alpha \rangle_{\text{obs}} = 1.3 \pm 0.7$ and $\langle \text{Ly}\alpha/\text{H}\alpha \rangle_{\text{corr}} = 1.5 \pm 0.8$, where the estimated errors reflect only the scatter of the $\text{Ly}\alpha/\text{H}\alpha$ values, and not their individual uncertainties.

Our improved set of data for flares, quasars, and active galaxies clearly supports Zirin's (1978) assertion that both flares and quasars show characteristic values of the $\text{Ly}\alpha/\text{H}\alpha$ ratio of about unity.

b) Brightness Temperature

The brightness temperature of $\text{Ly}\alpha$ and $\text{H}\alpha$ in quasars is, of course, not known. However, the situation in the case of solar flares is somewhat better. Data on $\text{Ly}\alpha$ in flares exist but are very limited. The only calibrated and even crudely spatially resolved line profiles are those of Canfield and Van Hoonier (1980), for two flares observed from Skylab. The first two entries in Table 2 refer to these

data, at flare maxima. The 1973 June 15 flare was of moderate size; $\text{H}\alpha$ classifications ranged from 1N to 2. The 1974 January 21 flare was very small. For both flares the profile appears to be self-reversed, so we give brightness temperatures T_b for both line center and the brighter peak. The latter figure is more physically meaningful. The line center is rendered less certain by the need to correct for geocoronal $\text{Ly}\alpha$ absorption, which has been done as well as possible in Table 2.

For $\text{H}\alpha$ more line profile data are available. In fact, Ellison (1952) has shown typical $\text{H}\alpha$ profiles for flares of various importance classifications. Class 2 flares are the largest for which he gives profiles. The line center and emission peak values of brightness temperature are given in the third entry in Table 2. The more extensive data set of Schoolman and Ganz (1980) is not suitable for our present purpose because of uncertainties in the calibration procedure. The only profile data on a larger flare is that of Tanaka (1977), given in Brown, Canfield, and Robertson (1978). Observations of the bright flare kernels were obtained by Zirin and Tanaka (1973). These profiles were obtained at the most energetic stage of a major flare.

Zirin (1978) made the assertion that the brightness temperature of $\text{Ly}\alpha$ and $\text{H}\alpha$ in flares is about 17,000 K. His statement is clearly not supported by the data of Table 1. Instead, the limited data for medium sized flares (class 2) seem to imply that for $\text{Ly}\alpha$, $T_b \sim 10,000$ K, and for $\text{H}\alpha$, $T_b \sim 7,000$ K. In addition, although there are only limited data available for $\text{H}\alpha$ in large flares, that of 1977 August 7 had a brightness temperature of $T_b \sim 8,000$ K in $\text{H}\alpha$. To guide our modeling, we will use the class 2 flare values.

III. FLARE MODELS

We have previously calculated (Canfield and Puetter 1981b, henceforth Paper II) hydrogen emission line ratios from models of quasar emission-line clouds (ELCs). These models make the simplifying assumptions of constant temperature and density. They are capable of explaining simultaneously the observed relative values of $\text{Ly}\alpha$, $\text{H}\alpha$, $\text{H}\beta$, $\text{P}\alpha$, and the Balmer continuum in quasars. Our purpose here is to make comparable models of solar flares, to see (1) if they are capable of explaining the observed solar flare $\text{Ly}\alpha/\text{H}\alpha$ ratios, (2) how the values of the model parameters compare with those derived independently by other methods, and (3) what physical mechanisms are important.

a) Method

The models are constructed as described by Canfield and Puetter (1981a, henceforth Paper I), except that here we obtain explicit numerical solutions of the radiative transfer equation of Canfield, Puetter, and Ricchiazzi (1981), rather than using scaling law solutions. We assume the radiating region to be plane parallel, composed of pure hydrogen with uniform temperature T_e , a uniform hydrogen density n_H (which includes both hydrogen ions and atoms), and in a steady state (see below). We use escape probabilities p_e that take into

TABLE 1
LY α /H α RATIOS FOR QUASARS AND ACTIVE GALAXIES

Object (1)	$\text{Ly}\alpha/\text{H}\alpha_{\text{obs}}$ (2)	$E(B-V)$ (3)	$\text{Ly}\alpha/\text{H}\alpha_{\text{corr}}$ (4)	References (5)
PG 0026+129	1.5 ± 0.5	0.036	1.8 ± 0.7	1
PHL 957	2.3 ± 0.8	0.030	2.7 ± 0.9	1
PKS 0237-233	1.7 ± 0.7	0.011	1.8 ± 0.7	2
3C 020	0.5 ± 0.4	0.147	1.4 ± 0.4	3
MK 79	0.5 ± 0.1	0.059	0.7 ± 0.2	3
Q 1101-264	1.5 ± 0.5	(0.03) ^a	2.2 ± 0.6	1
NGC 4151	0.7 ± 0.2	0.0004	0.7 ± 0.2	4
B2 1225-317	0.9 ± 0.3	(0.0003) ^a	0.9 ± 0.1	5, 6
3C 273	1.9 ± 0.7	0.010	2.0 ± 0.7	7
3C 390.3	0.4 ± 0.1	0.055	0.5 ± 0.1	8

^a Broad component.

^b From $\text{H}\alpha$ only—no galaxy counts.

^c $\text{H}\alpha$ uncertain.

REFERENCES.—(1) Puetter *et al.* 1980 (2) Hyland, Bevilacqua, and Neugebauer 1978 (3) Oke and Zinnerman 1979 (4) Davidson 1980. (5) Soffer *et al.* 1979 (6) Puetter, Smith, and Willner 1979 (7) Boggess *et al.* 1979 (8) Ferland *et al.* 1979.

TABLE 2
SOLAR FLARE BRIGHTNESS TEMPERATURES

Flare	Line	$\log I_\lambda$ ($\text{erg cm}^{-2} \text{s}^{-1} \text{\AA}^{-1}$)	T_e (K)	References
1973 June 15	Ly α center	6.31	9,600	1
	Ly α red peak	6.63	10,200	
1974 January 21	Ly α center	5.48	8,300	1
	Ly α red peak	6.24	9,500	
Class 2	H α center	6.57	6,600	2
	H α red peak	6.61	6,800	
1972 August 7	H α center	6.81	7,900	3

REFERENCES. —(1) Canfield and Van Hoosier 1980. (2) Ellison 1952. (3) Tanaka 1977

account escape by single flight (Voigt or Stark absorption coefficient profile, the latter following Puetter 1981), for both subordinate and resonance lines, and eventual escape through multiple coherent scattering and partial redistribution due to Stark or radiative broadening for Ly α . We model the hydrogen atom with five bound levels and the ionized state. By iteration the radiative transfer equations in the various transitions are solved simultaneously with the steady state ionization and excitation equations. For convergence we require that the populations change by only a few percent on the final iteration. Because soft X-ray irradiation of the flare chromosphere is thought to play only a secondary role (Canfield *et al.* 1980a), we set the intensity of the incident radiation field to zero for the solar flare models. The resulting run of values of the line center source function S_0 and the flux divergence coefficient ρ with line center optical depth τ is used to compute the emergent line ratios, as discussed in Paper I.

The assumption of a steady state in the treatment of the radiative transfer and atomic rate equations is suitable for calculation of a typical solar flare Ly α /H α ratio. There is no observational evidence for or against temporal variability of the Ly α /H α ratio over a flare. We thus adopt 100 s, which is short compared to the duration of most H α flares, as a conservative lower limit to the characteristic time on which this ratio changes. Excitation and de-excitation times are always much less than this time for permitted lines in flare chromospheres. Canfield and Athay (1974) show that the same statement applies to the ionization and recombination times, at the depths of interest in the formation of the Ly α /H α ratio. Hence as the temperature and density in flare chromospheric change, the excitation and ionization processes evolve through a series of effectively steady states.

b) Ly α /H α Calculations

We have computed several numerical models to explore the sensitivity of the Ly α /H α ratio to the values of the model parameters T_e and n_{H} in the solar flare case, much as we did in Paper II for quasar ELCs. Figure 1 shows the computed dependence of $\log \text{Ly}\alpha/\text{H}\alpha$ on $\log \tau_{\text{H}\alpha}$, the H α line center optical depth, for three models. The solid curve shows $T_e = 10,000$ K, $n_{\text{H}} = 10^{13} \text{ cm}^{-3}$. The dotted curve is for $T_e = 12,000$ K, $n_{\text{H}} = 10^{14} \text{ cm}^{-3}$.

The dashed curve is for $T_e = 12,000$ K, $n_{\text{H}} = 10^{13} \text{ cm}^{-3}$. The small rectangle indicates the range of Ly α /H α and $\tau_{\text{H}\alpha}$ values compatible with the observations. In the Ly α /H α coordinate, the observations discussed above imply Ly α /H α = 0.5, with an uncertainty of a factor of 2. In the $\tau_{\text{H}\alpha}$ coordinate Kulander's (1980) study of flare H α profiles gives $60 \leq \tau_{\text{H}\alpha} \leq 300$ as representative of several flares; this is the most extensive recent study of a wide variety of H α profiles. Before proceeding, we consider the results of other models and measurements that show that the values of T_e and n_{H} used in the figure are reasonable values for solar flares.

A value of T_e to represent the Ly α /H α ratio is somewhat uncertain. We know that Ly α and H α are formed at different temperatures in the quiet Sun (cf. Vernazza, Avrett, and Loeser, 1973, Fig. 1), and the same will be true

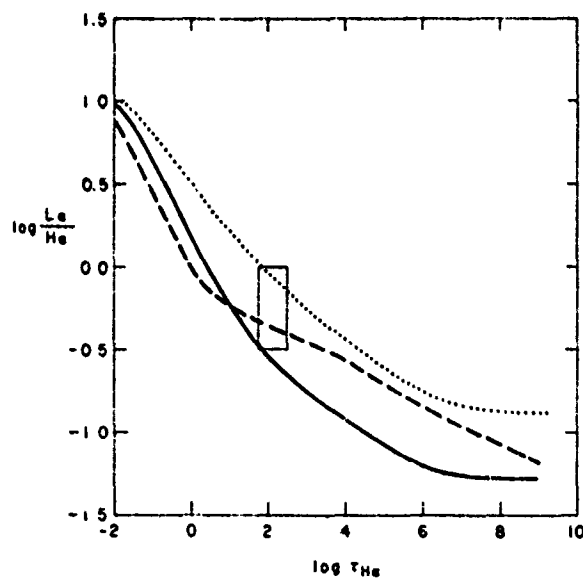


FIG. 1 — The dependence of the Ly α /H α ratio on H α optical depth at line center, for three different solar flare models. Solid curve: $T_e = 10,000$ K, $n_{\text{H}} = 10^{13} \text{ cm}^{-3}$; dotted curve: $T_e = 12,000$ K, $n_{\text{H}} = 10^{14} \text{ cm}^{-3}$; dashed curve: $T_e = 12,000$ K, $n_{\text{H}} = 10^{13} \text{ cm}^{-3}$. The small rectangle indicates the range of Ly α /H α and $\tau_{\text{H}\alpha}$ suggested by observations. The $T_e = 12,000$ K and $n_{\text{H}} = 10^{13} \text{ cm}^{-3}$ model is referred to as the standard flare model.

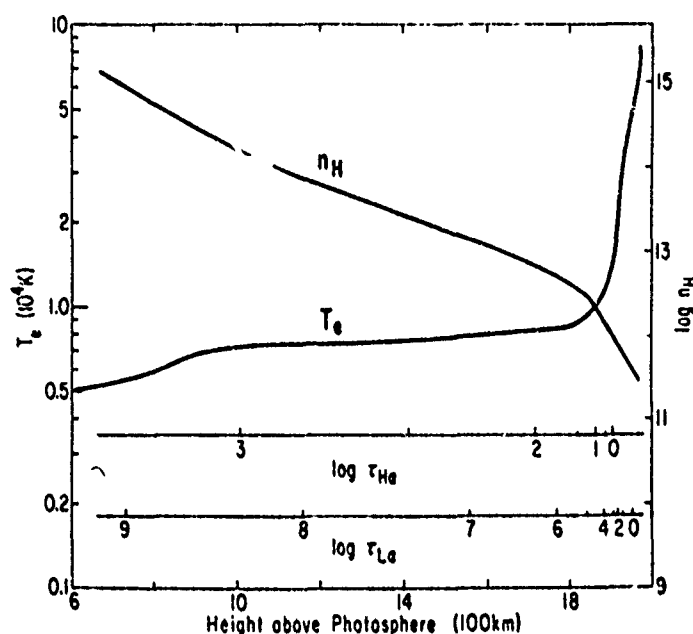


FIG. 2 - The depth dependent solar flare chromosphere model of Lites and Cook (1979) for comparison with our models (see § III) LEFT: the T_e scale; RIGHT: the n_H scale.

in flares. The most realistic model of a flare chromosphere presently available is that of Lites and Cook (1979). It was constructed to reproduce C I-C IV line profiles in a considerably smaller flare than the class 2 flares we are considering in this paper, but nonetheless it is illustrative of the run of T_e and n_H in a flare model. Figure 2 shows T_e , n_H , $\tau_{H\alpha}$, and $\tau_{Ly\alpha}$ as a function of height above the photosphere. The $\tau_{H\alpha}$ and $\tau_{Ly\alpha}$ scales were computed by Canfield and Ricchiazzi (1980). Most of the radiation will emerge from the Doppler cores of these lines, e.g., in the range $1 \leq \tau \leq e^9$, or $0 \leq \log \tau \leq 4$. In the range $0 \leq \log \tau_{Ly\alpha} \leq 4$, the Lites and Cook atmosphere has $11,000 \text{ K} \leq T_e \leq 50,000 \text{ K}$ and $11.6 \leq \log n_H \leq 12.2$. The maximum value of $\log \tau_{H\alpha}$ in this model is about 3 (note larger flares show lower $\tau_{H\alpha}$). In the range $0 \leq \log \tau_{Ly\alpha} \leq 3$, the Lites and Cook atmosphere has $7,000 \text{ K} \leq T_e \leq 14,000 \text{ K}$, and $12 \leq \log n_H \leq 14.2$. According to Svestka (1976, Table VII), typical values of T_e derived from the Balmer lines of hydrogen are in the range 7,000–10,000 K. One would expect the Ly α /H α ratio to require a higher value, since Ly α comes from a hotter region than H α . The typical brightness temperatures for Ly α and H α , from § II of this paper, are 10,000 K and 7,000 K respectively. The brightness temperature will be less than a typical value of T_e in the region of formation. Lites and Cook (1979), for example, found that where $\tau_{Ly\alpha} = 1$ in their model, $T_e = 9,700 \text{ K}$, while $T_b = 8,500 \text{ K}$. In summary, it is clear that $8,000 \text{ K} \leq T_e \leq 15,000 \text{ K}$ is a plausible range of temperatures to represent the spatial average of the regions of Ly α and H α formation.

There is a similar uncertainty in choosing a value of n_e that one would expect to represent, in an average sense, the Ly α and H α forming region. According to Svestka

(1976, Table VII), a typical value of n_e derived from the hydrogen Balmer series lines is $n_e \sim 2\text{--}3 \times 10^{13} \text{ cm}^{-3}$. Since Ly α is formed in a lower density region, we choose $n_H = 10^{13} \text{ cm}^{-3}$ as a value that one would expect to represent an average of the H α and Ly α forming regions, since one would expect n_H and n_e to be of the same order of magnitude.

Figure 1 shows that the model with $n_H = 10^{13} \text{ cm}^{-3}$ and $T_e = 12,000 \text{ K}$ does a satisfactory job of explaining the observations and independent estimates of $\tau_{H\alpha}$. One can also see that the Ly α /H α ratio is quite insensitive to $\tau_{H\alpha}$ and n_H , but fairly sensitive to T_e . The value of T_e that is best, $T_e = 12,000 \text{ K}$, is quite plausible in view of the arguments cited in the previous paragraph. For this reason, we refer to this model as the standard flare model below and discuss it in further detail in the following section. We could, of course, achieve an even better fit with $T \approx 11,000 \text{ K}$, but this is not the point of this paper. We could also make many calculations to determine the combinations of T_e and n_H that produce acceptable values of both Ly α /H α and $\tau_{H\alpha}$. This does not seem warranted. Based on the variations of the standard flare model only, we estimate that acceptable values of temperature will fall in the range $9,000 \text{ K} \leq T_e \leq 13,000 \text{ K}$, and density $10^{11} \leq n_H \leq 10^{15} \text{ cm}^{-3}$.

As an aside, we wish to point out that for the same single flare for which the Ly α /H α ratio has been measured, H β /H α values are also available. Canfield *et al.* (1980b) obtained $0.5 \leq \text{H}\beta/\text{H}\alpha \leq 0.8$. Since our model is based on a model hydrogen atom of five bound levels and the continuum, we can compute fairly reliable values for H β , the 4–2 transition, but not for H γ , the 5–2 transition. It is recognized that the highest bound level is

considerably affected by the neglect of higher levels (this point is discussed in more detail in Paper II). At $\tau_{H\alpha} = 160$, the depth at which the standard flare model achieves the observed Ly α /H α ratio, the H β /H α ratio is 0.7, in complete agreement with the observations. However, we assign little importance to this agreement. The H β /H α ratio is quite insensitive to $\tau_{H\alpha}$ in this range of $\tau_{H\alpha}$. For a specific value of $\tau_{Ly\alpha}$, which we use as an independent variable, H β /H α depends most sensitively on temperature.

c) The Standard Flare Model

The reasons for the optical depth dependence of the Ly α /H α ratio can easily be shown with the standard model. The essential features are shown in Figure 3. The flux divergence per unit natural logarithm of line center optical depth, $\rho S_0 \tau$, is an approximate measure of the depth of origin of the emergent radiation (if $\rho = p_e$, as is the case when S_0 is constant). Its slope depends on the depth dependence of both ρ and S_0 . Values of the depth at which S_0 saturates to the Planck function B are shown by asterisks in the figure. In the right side of the figure, for $\tau > \tau^*$ for both Ly α and H α , $S_0 = B$ and is therefore constant. There are two regimes of interest in Ly α . For $4 \leq \log \tau_{Ly\alpha} \leq 7$, partial redistribution within a Stark-broadened absorption coefficient profile dominates, so $p_e \propto \tau_{Ly\alpha}^{-3/4}$ (see Puetter 1981). For $\log \tau_{Ly\alpha} \geq 7$, photon collisional destructions so reduce the effectiveness of escape by multiple scatterings that single flight escape within a Stark-broadened profile applies, so $p_e \propto \tau_{Ly\alpha}^{-3/5}$. In H α , the latter process dominates

throughout the range of $\tau_{H\alpha}$ shown, so $p_e \propto \tau_{H\alpha}^{-3/5}$. The ratio between $\tau_{Ly\alpha}$ and $\tau_{H\alpha}$ is, of course, fixed where both source functions have saturated to the Planck function.

In the regions for which $\tau < \tau^*$, where the source functions are not saturated, both Ly α and H α show a different behavior. In H α , for $\log \tau_{H\alpha} < 0$, both ρ and S_0 become constant, and $\rho S_0 \tau$ is directly proportional to $\tau_{H\alpha}$. The transition between this regime and that for $\tau > \tau^*$ is affected by source function variations as S_0 approaches B . In Ly α , the region $\tau_{Ly\alpha} \leq 1$ is not shown. On the far left, where $\log \tau_{Ly\alpha} \leq 2$, p_e for Ly α makes a transition to the regime where p_e is dominated by eventual escape by multiple scattering (Adams 1972, cf. Paper I). Here $p_e \propto \tau^{-1}$, and since $\rho \approx p_e$, $\rho S_0 \tau$ is proportional to $\tau^{1/2}$, i.e., the same slope as $\rho S_0 \tau$ for H α in the region $\tau_{H\alpha} > \tau_{H\alpha}^*$. For Ly α , the transition at $\log \tau_{Ly\alpha} > 3$ is due to the saturation of S_0 to B and the loss of photons by multiple scattering plus Stark partial redistribution.

The behavior of the Ly α /H α ratio for the standard flare model shown in Figure 1 follows quite directly from the variation of $\rho S_0 \tau$ in Figure 3. The total emergent radiation that determines the line ratio tends to be dominated by the local flux divergence at the relevant value of τ .

IV. DISCUSSION

a) Implications for Quasar Models

What do we learn from the fact that the Ly α /H α ratio has a certain value? Strictly speaking, it gives a constraint on the relationship between n_H , T_e , τ , and the incident flux. Physically speaking, since the ratio is not overly sensitive to n_H or the incident flux, the ratio depends on the optical depth to which the atmosphere is heated to $T_e \sim 10^4$ K. We have shown above that when we have independent constraints like the estimates of $\tau_{H\alpha}$ and n_H for flares, a rather well defined value of T_e is implied by the Ly α /H α ratio. Furthermore, the implied value of T_e seems to be "representative," in the sense that it falls between the somewhat different values of temperature at which we might expect H α and Ly α to originate. To see this, we have gone back to the calculations made previously by Canfield and Ricchiazzi (1979), who solved the transfer equation for the full variable temperature Lites and Cook (1979) flare model. We have determined the value of temperature above which half of the emergent radiation originates. For H α , this temperature is about 9,000 K; for Ly α , it is about 22,000 K. Hence, the value of temperature implied by the constant temperature analysis is representative in the sense defined above, because the range of values of T_e found here for a constant temperature model (9,000–13,000 K) lies between the values of 9,000 K (H α) and 22,000 K (Ly α) appropriate to a variable temperature atmosphere.

On the other hand, what does it mean when with simple models (constant n_H and T_e), one can successfully reproduce the observed Ly α /H α value for flares? In flares, as we discussed above, Ly α and H α do not come from the same temperature (or density) regions. The answer to this question is that the observed Ly α /H α ratio by itself is only

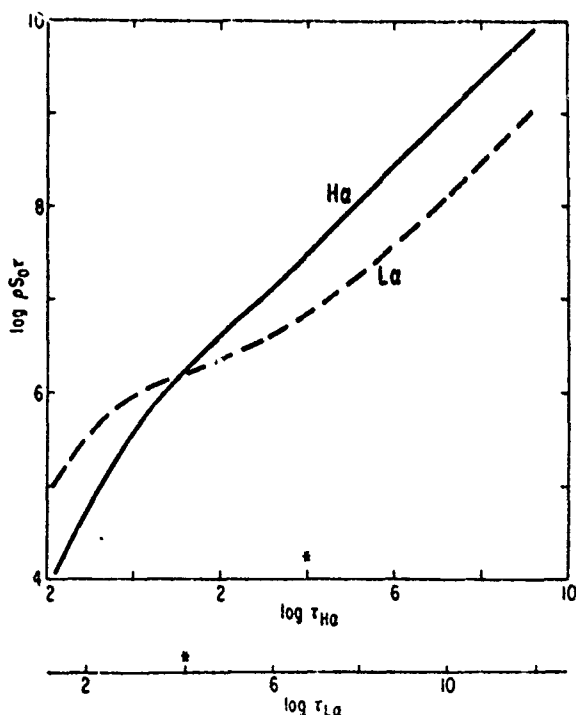


FIG. 3—The optical depth dependence of the flux divergence per unit in τ , $\rho S_0 \tau$, in the standard solar flare model

a single number and cannot be used to fix more than one free parameter of a model. Our results clearly show that it does not severely constrain the run of T_e and n_H , since a uniform model predicts the observed ratio for a plausible set of values of T_e , n_H , and $\tau_{H\alpha}$. Among other things, this shows that the ability of the uniform ELC model to predict the observed Ly α /H α ratios should not be used to infer that the regions of the ELC in which the radiation originates must be uniform (cf Paper II).

b) Inferences Drawn by Zirin (1978)

The models discussed can also be used to comment on some difficulties with the inferences drawn by Zirin (1978) on the significance of the Ly α /H α ratio itself, as well as the similarity of its values in quasars and solar flares. Zirin's inferences include:

1. *The Ly α and H α emission is Planckian.* In our models of solar flares, although the Ly α and H α source functions have essentially saturated to the Planck function by the time the full thickness of the line-forming region is reached, there still remains a dependence of the Ly α /H α ratio on optical depth. The Ly α /H α ratio, even in the thermalized region, is not determined by temperature alone.

2. *The temperature in the region of formation is 115,000 K $\leq T_e \leq$ 20,000 K.* Since the line ratio depends on more than just the temperature, one cannot immediately conclude that because the ratio of two emission lines corresponds to the ratio of their Planck functions at a certain temperature, the actual temperature in the region of line formation has that value. We see that although $B_{Ly\alpha}/B_{H\alpha} = 0.5$ for $T_e \approx 18,000$ K, the model temperature which best matches a variety of appropriate constraints, including most notably that of the radiative transfer equation, is $T_e \approx 11,000$ K. The observed Ly α /H α ratio cannot be reconciled with $15,000 \leq T_e \leq 20,000$ K for reasonable values of n_H and $\tau_{H\alpha}$, using our constant temperature and density models.

3. *Temperature plateaus exist.* Apart from the issue of the actual value of the temperature, the ability of the standard flare model to predict the observed Ly α /H α and H β /H α ratios for plausible values of T_e and n_H does not require the existence of temperature plateaus. Empirical flare chromosphere models that agree with the observed profiles of a wide variety of lines formed over a range of temperatures, such as the model of Lites and Cook (1979), certainly do not show plateaus that extend over the region of formation of Ly α and H α . It is only reasonable to expect that the T_e that one derives from the Ly α /H α ratio is some kind of nonlinear average of the values of T_e in the regions of Ly α and H α formation. The standard solar flare model is consistent with this statement.

4. *Some mechanism forces Ly α /H α to values ~ 1 for all $\tau_{Ly\alpha} > 10^4$.* The Ly α /H α ratio does indeed saturate to a fixed value for a certain regime at large τ , through this occurs at τ values much larger than 10^4 . In Figure 1 one clearly sees this regime for $7 \leq \log \tau_{Ly\alpha} \leq 9$. Physically, this regime is due to the fact that both Ly α and H α have the same functional form for $p_e(\tau)$, i.e., that appropriate to single flight escape from an absorption coefficient profile

dominated by Stark broadening. This form will obtain until still farther into the wings, where the Stark wings fall to the radiative damping wings.

We speculate that the typical value Ly α /H $\alpha \sim 1$ observed in quasars arises because the optical depth in Ly α (for example) and the temperature of the H α and Ly α emitting region is uniquely determined by the radiative nature of both the heating and cooling mechanisms. This can be demonstrated compellingly only through a physically realistic treatment of radiative transport in a multielement cloud, which has not been done up to the present time.

V. CONCLUSIONS

The conclusions we reach from the evidence presented in this paper, when combined with our previous work in quasars (Papers I and II), are both observational and theoretical.

a) Observations

1. We confirm the conclusion first reached by Zirin (1978) that the value of the hydrogen Ly α /H α ratio is of order unity in both quasars and solar flares.

2. The brightness temperature for moderately large (class 2) solar flares is about 7,000 K in H α and 10,000 K in Ly α , contrary to Zirin's assertion that $T_b \approx 17,000$ K in both Ly α and H α .

3. The value of Ly α /H α is poorly known for solar flares, having been measured for only a single flare, but it has now been measured for enough different quasars and broad line galaxies for the variations in the sample to be interesting.

b) Theoretical

1. We confirm the suggestion of many authors that Ly α /H $\alpha \sim 1$ means the optical depth in these lines must be large in both solar flares and quasar emission line regions.

2. For solar flares, in which $\tau_{H\alpha}$ is independently known, the observed value Ly α /H $\alpha \sim 0.5$ requires that $9,000 \leq T_e \leq 13,000$ K and $10^{11} \leq n_H \leq 10^{15}$ cm $^{-3}$.

3. While the temperature in the Ly α and H α emitting regions of solar flares and quasars are similar (not a very surprising conclusion), the densities in solar flares are probably about three orders of magnitude higher. The fact that Ly α /H $\alpha \sim 1$ in both solar flares and quasars does not require that they have the same physical conditions.

4. We can explain the observed solar flare Ly α /H α values in terms of values of n_H and T_e that are compatible with more sophisticated models. This lends confidence that the values inferred in quasars are indeed reasonable average values of these parameters over the region of hydrogen emission line formation.

5. The inferred model parameters are only representative values. Our success in explaining the observed hydrogen line ratios with models with certain (constant) values of temperature and density is not to be construed to mean that plateaus exist in which these values obtain.

6. For both solar flares and quasars, the Ly α /H α ratio is to some extent sensitive to all parameters of our models.

7. For solar flares, the Ly α /H α ratio is relatively much less sensitive to n_{H} than for quasars.

8. The fact that in solar flares the lines are formed in a region where the line source functions are very close to thermalization does not ensure that Ly α /H α is a function of T_e alone.

9. The approximate equality of the Ly α /H α ratio in solar flares and QSOs does not imply that their mechanisms need be the same. In this paper we explain the solar flare values in terms of models for which we set to zero the

incident nonthermal radiation field that proves very important in our quasar models.

This research has been supported by the Air Force Office of Scientific Research, AFSC, USAF, under grant AFOSR-76-3071, by National Aeronautics and Space Administration under grant NAGW-30, and by the National Science Foundation under grant AST79-19842. We wish to thank an anonymous referee for improvements to the manuscript.

REFERENCES

- Adams, T. F. 1972, *Ap. J.*, **174**, 439.
 Boggess, A. et al. 1979, *Ap. J. (Letters)*, **230**, L131.
 Brown, J. C., Canfield, R. C., and Robertson, M. H. 1978, *Solar Phys.*, **57**, 399.
 Burstein, D., and Heiles, C. 1978, *Ap. J.*, **225**, 40.
 Canfield, R. C., and Athay, R. G. 1974, *Solar Phys.*, **34**, 193.
 Canfield, R. C. et al. 1980a, in *Solar Flares, A Monograph from Skylab Solar Workshop, II*, ed. P. A. Sturrock (Boulder: University of Colorado Press), p. 231.
 Canfield, R. C., et al. 1980b, in *Solar Flares, A Monograph from Skylab Solar Workshop, II*, ed. P. A. Sturrock (Boulder: University of Colorado Press), p. 451.
 Canfield, R. C., and Puetter, R. C. 1980, *Ap. J. (Letters)*, **236**, L7.
 ———, 1981a, *Ap. J.*, **243**, 381 (Paper I).
 ———, 1981b, *Ap. J.*, **243**, 390 (Paper II).
 Canfield, R. C., Puetter, R. C., and Ricchiazzi, P. J. 1981, *Ap. J.*, in press.
 Canfield, R. C., and Ricchiazzi, P. J. 1980, *Ap. J.*, **239**, 1036.
 Canfield, R. C., and Van Hooser, M. E. 1980, *Solar Phys.*, **67**, 339.
 Davidsen, A. 1980, in *IAU Symposium 92, Objects of High Redshifts*, ed. G. Abell and J. Peebles (Dordrecht: Reidel).
 Ellison, M. A. 1952, *Proc. Roy. Soc. Edinburgh*, **1**, 75.
 Ferland, G. J., Ross, M. J., Longair, M. A., and Perryman, M. A. C. 1979, *M.N.R.A.S.*, **187**, 65p.
 Hyland, A., Becklin, E. E., and Neugebauer, G. 1978, *Ap. J. (Letters)*, **220**, L73.
 Kulander, J. L. 1980, *Solar Phys.*, submitted.
 Lites, B. W., and Cook, J. W. 1979, *Ap. J.*, **228**, 598.
 Oke, J. B., and Zimmerman, B. 1979, *Ap. J. (Letters)*, **231**, L13.
 Puetter, R. C. 1981, *Ap. J.*, in press.
 Puetter, R. C., Smith, H. E., and Willner, S. P. 1979, *Ap. J. (Letters)*, **227**, L5.
 Puetter, R. C., Smith, H. E., Willner, S. P., and Pipher, J. L. 1980, *Ap. J.*, **243**, 345.
 Savage, B. D., and Muthis, S. M. 1979, *Am. Rev. Astr. Ap.*, **17**, 73.
 Schoolman, S. A., and Fonz, E. D. 1981, *Solar Phys.*, **70**, 363.
 Shane, C. D., and Wirtanen, C. A. 1967, *Publ. Lick Obs.*, **22**, Part 1.
 Soifer, B. T., Oke, J. B., Matthews, K., and Neugebauer, G. 1978, *Ap. J. (Letters)*, **227**, L1.
 Svestka, Z. 1976, *Solar Flares* (Dordrecht: Reidel).
 Tanaka, K. 1977, personal communication.
 Vernazza, J. E., Avrett, E. H., and Loefer, R. 1973, *Ap. J.*, **184**, 605.
 Zirin, H. 1978, *Ap. J. (Letters)*, **222**, L105.
 Zirin, H., and Tanaka, K. 1973, *Solar Phys.*, **32**, 173.

RICHARD C. CANFIELD, RICHARD C. PULTER, PAUL J. RICCHIAZZI: Center for Astrophysics and Space Sciences, Code C-011, University of California - San Diego, La Jolla, CA 92093

vi) Theoretical Quasar Emission Line Ratios. VI. A Probabilistic
Radiative Transfer Equation for Finite Slab Atmospheres

This is another paper in which basic radiative transfer techniques are developed. The methods developed in Section iii are only suitable for semi-infinite media, such as the surface layers of the sun and stars. When the layers are more like thin slabs or cylinders, the techniques developed in this paper are appropriate. Although these methods were developed primarily for quasars, where the emission is thought to come from clouds that can be represented by finite slabs, the same methods will also be useful for solar phenomena like surges and prominences.

THEORETICAL QUASAR EMISSION LINE RATIOS VI.
A PROBABILISTIC RADIATIVE TRANSFER EQUATION
FOR FINITE SLAB ATMOSPHERES

R.C. Puetter, E.N. Hubbard,
Paul J. Ricchiazzi* and Richard C. Canfield

Center for Astrophysics and Space Sciences
University of California, San Diego

Received: _____

Subject Headings:

Line Formation

Radiative Transfer

Quasars

* Also Department of Physics, University of California, San Diego

PRECEDING PAGE BLANK-NOT FILMED

ABSTRACT

Previous papers in this series have been based on an approximation in which the line ratios were inferred from those computed for a semi-infinite cloud model. In this paper we present a superior method, which permits the treatment of the emission line clouds as slab atmospheres of finite thickness. In common with our previous semi-infinite approach, it is based on photon escape probabilities, yet recognizes the important distinction between the photon escape probability and the flux divergence. This distinction is neglected in all existing models of energy balance in QSO emission line clouds. This neglect can lead to order of magnitude errors in the cooling rates, casting doubt on the results of past models.

The present method reduces to the previous one in the semi-infinite case. It not only produces the correct source function S_{∞} at the surface of a semi-infinite atmosphere $S_{\infty}(\tau = 0) = \sqrt{\epsilon} B$ for a constant Planck function B and photon destruction probability ϵ , but it derives the empirical relationship $S_T(\tau = 0) = \sqrt{\epsilon} S_{\infty}(\tau = T)$ proposed by Avrett and Hummer (1965, MNRAS 130, 295) relating the source function at the surface of a finite slab of optical thickness T to the source function at $\tau = T$ in a semi-infinite slab. We show that the method provides a solution that departs from the exact solution by at most a few tens of percent in cases of physical interest, while retaining all the advantages of the previous method.

INTRODUCTION

Previous papers of this series have developed considerable formalism for handling radiative transfer effects in QSOs. We have stressed (Paper III, Canfield, Puetter and Ricchiazzi 1981) the importance of techniques that explicitly distinguish between the photon escape probability, p_e , and the flux divergence coefficient, ρ . Allowing the local cooling rate to be proportional to p_e can never account for the possibility that a volume element may be heated by a nearby, warmer element, since p_e is a positive definite quantity. There exist in the literature several probabilistic radiative transfer equations that recognize this difference (e.g. Athay 1972, Frisch and Frisch 1975, hereafter FF). However, in the past this approach has been developed only for the case of semi-infinite atmospheres. Since it seems unlikely that the emission line regions of quasars and Seyfert galaxies are well approximated by semi-infinite atmospheres and since in many cases the structure of slab atmospheres cannot be deduced from semi-infinite calculations (see Paper II, Canfield and Puetter 1981b, and Paper V, Puetter and LeVan 1981) it is important to develop a probabilistic radiative transfer technique for slabs. In the following section, we show how the probabilistic radiative transfer equation of Frisch and Frisch can be generalized to finite slabs; we then reform the expression for the source function into the more computationally useful expression for the mean intensity. In section III, we compare the probabilistic solutions to various

atmospheres with the analytical solutions of Avrett and Hummer (1965), and finally in section IV we summarize our results.

II. AN EQUATION FOR SLABS

As is well known, the mean intensity of radiation integrated over the photon absorption coefficient can be written

$$J(\tau) = \int_c^T dt S_0(t) K(\tau - t) + J^{\text{ext}}(\tau) \quad (1a)$$

$$K_1(t) = 1/2 \int dv \phi_v \psi_v E_1(t\phi_v) \quad (1b)$$

$$E_1(t) = \int_1^\infty dx \frac{\exp(-tx)}{x} \quad (1c)$$

and where for lines

$$J(\tau) = \int dv J_v \phi_v \quad (1d)$$

$$S_0 = \frac{2h\nu_0^3}{c^2} \left(\frac{g_u n_l}{g_l n_u} - 1 \right)^{-1} \quad (1e)$$

(see Paper I, Canfield and Puetter 1981a and Paper III) and for bound-free continua

$$J(\tau) = h\nu_0 \int d\nu \frac{J_\nu \phi_\nu}{h\nu} \quad (1f)$$

$$S_0 = \frac{2h\nu_0^3}{c^2} \left(\frac{g_u n_l}{g_l n_u} \right)^{-1} (s-1) e^\alpha E_{s-2}(\alpha) \quad (1g)$$

$$\alpha = h\nu_0/kT \quad (1h)$$

(see Paper V). In equation (1), J_ν is the mean intensity of radiation (i.e. $J_\nu = 1/4\pi \int d\Omega I_\nu$), T is the maximum optical depth of the slab, ψ_ν and ϕ_ν are the emission and absorption coefficients respectively normalized to unit integral over frequency, ϕ_ν is the absorption coefficient scaled to unity at ν_0 (i.e. $\phi_\nu = (\nu/\nu_0)^3$), and ν_0 is the frequency of the line or the head of the bound-free continuum. The quantities g_u and g_l are respectively the statistical weight of the upper and lower level and n_u and n_l are the population densities of those levels. $J^{\text{ext}}(\tau)$ is the contribution to $J(\tau)$ from external sources. Throughout equation (1) we have assumed a plane-parallel geometry.

In Paper III, we developed a first order differential equation for $J(\tau)$ from the definition in equation (1). This equation (which is essentially a recasting of the PF equation into a more useful form) is an equation which is well suited for rapid and accurate evaluation of multi-level radiative transfer quantities in semi-infinite atmospheres. In this paper we generalize this approach to include finite slabs. Following the lead of both Paper III and PF, we can write:

$$\begin{aligned}
\int_0^\sigma d\tau S(\tau) \partial/\partial\tau J(\tau) &= \int_0^\sigma d\tau S(\tau) \partial/\partial\tau \int_0^T dt S(t) K_1(t-\tau) \\
&= \int_0^\sigma d\tau S(\tau) \partial/\partial\tau \int_0^\sigma dt S(t) K_1(t-\tau) \\
&\quad + \int_0^\sigma d\tau S(\tau) \partial/\partial\tau \int_\sigma^T dt S(t) K_1(t-\tau).
\end{aligned}
\tag{2}$$

In this case, however, one can show that the first term of the right hand side of equation (2) is identically zero since $K_1(t - \tau) = K_1(\tau - t)$. Thus the fundamental lemma of Paper III and FF is unnecessary. The derivation may be completed exactly by analogy with FF and Paper III. Since $0 < \tau < 0 < t < T$, and the integrand vanishes for $\tau - t \gg 1$, we can write $S(\tau) = S(t) = S(\sigma)$. If S is slowly varying $1/S (dS/d\tau) \ll 1$,

$$\int_0^\sigma d\tau S(\tau) \partial/\partial\tau J(\tau) = S^2(\sigma) \int_0^\sigma d\tau \partial/\partial\tau \int_\sigma^T dt K_1(t-\tau) \tag{3}$$

$$\int_0^T dt K_1(t) = 1/2 - p_e(\tau) \tag{4}$$

but

$$\int_\sigma^T dt K_1(t-\tau) = p_e(\sigma-\tau) - p_e(T-\tau). \tag{5}$$

$$\begin{aligned}
\int_0^\sigma d\tau \partial/\partial\tau \int_\sigma^T dt K_1(t-\tau) \\
= p_e(0) - p_e(\sigma) - p_e(T-\sigma) + p_e(T)
\end{aligned}
\tag{6}$$

Replacing σ with τ we write ,

$$\begin{aligned} \partial/\partial\tau J(\tau) &= 2 [p_e(0) + p_e(T) - p_e(\tau) - p_e(T-\tau)] \partial S/\partial\tau \\ &- S(\tau) \partial/\partial\tau [p_e(\tau) + p_e(T-\tau)]. \end{aligned} \quad (7)$$

For the constant ϵ case, (here $\epsilon = \epsilon'/(1 + \epsilon') = p_d$ in Paper II)

$$\frac{\partial S}{\partial\tau} = \epsilon \frac{\partial B}{\partial\tau} + (1-\epsilon) \frac{\partial J}{\partial\tau} \quad (8)$$

Defining

$$P_T(\tau) = \epsilon + 2(1-\epsilon) [p_e(\tau) + p_e(T-\tau) - p_e(T)] , \quad (9)$$

it follows that

$$\sqrt{P_T(\tau)} \quad d/d\tau [S(\tau) \sqrt{P_T(\tau)}] = \epsilon \frac{\partial B}{\partial\sigma} \quad (10)$$

$$\frac{\partial S}{\partial\tau} = \epsilon \frac{\partial B}{\partial\tau} + [1-P_T(\tau)] \frac{\partial S}{\partial\tau} - \frac{S(\tau)}{2} \frac{\partial P_T}{\partial\tau} . \quad (11)$$

This result is identical to equation (6.9) in FF except for the redefinition of $P_T(\tau)$. A moment's inspection of equation (9) will show that as $T \rightarrow \infty$, the two definitions become identical.

Unfortunately, the selection of a boundary condition for equation (11) poses problems. Whereas FF chose the boundary condition $S(\infty) = B(\infty)$, our atmosphere is not defined at $\tau > T$ and we cannot expect that $S = B$ at any point. The formal solution of equation (11) is:

$$S_T(T^*) = \frac{S_T(\tau) \sqrt{P_T(\tau)}}{\sqrt{P_T(T^*)}} - \frac{\epsilon}{\sqrt{P_T(T^*)}} \int_{T^*}^{\tau} d\tau \frac{1}{\sqrt{P_T(\sigma)}} \frac{\partial B}{\partial \sigma} \quad (12)$$

where τ is an arbitrary point in the slab.

Instead of directly evaluating the value $S(T^*)$ which would be difficult, we will place limits on the quantity $S(\tau)$ through physical arguments. To do this, we will first consider the semi-infinite case where $B(\tau)$ goes abruptly to zero at depth T :

$$B(\tau) = \begin{cases} B_0(\tau) & ; \quad \tau < T \\ 0 & ; \quad \tau > T \end{cases} \quad (13)$$

A possible expression for this is:

$$B(\tau) = B_0(\tau) \int_{\tau}^{\infty} dt \delta(t-T) \quad (14)$$

The FF equation can be applied to this situation with the result:

$$S_{\infty}^T(\tau) = \begin{cases} \frac{\epsilon B_0(T)}{\sqrt{P_{\infty}(\tau) P_{\infty}(T)}} - \frac{\epsilon}{\sqrt{P_{\infty}(\tau)}} \int_{\tau}^T \frac{d\sigma}{\sqrt{P_{\infty}(\sigma)}} \frac{\partial B_0(\sigma)}{\partial \sigma} & \tau < T \\ 0 & ; \quad \tau > T \end{cases} \quad (15)$$

(In this and in the following equations the superscript on S indicates the thickness of the region in which B is non-zero and the subscript indicates the total optical depth of the

atmosphere.) We compare this to a finite slab version of this problem (i.e. no material in the $B = 0$ region) where our equation (12) yields:

$$S_T^T(T^*) = \frac{S(\tau) \sqrt{P_T(\tau)}}{\sqrt{P_T(T^*)}} - \frac{\epsilon}{\sqrt{P_T(T^*)}} \int_{T^*}^T \frac{d\sigma}{\sqrt{P_T(\sigma)}} \frac{\partial B_0}{\partial \sigma} \quad (16)$$

Physically, the finite slab solution differs from the semi-infinite case because in the latter case some radiation is scattered from the region $\tau > T$ back into the region $\tau < T$ instead of escaping completely as it would for a finite slab. In the absence of this backwarming, $S_T(\tau) < S_\infty(\tau)$ for any $\tau < T$. To get a lower bound on $S_T(\tau)$, we can consider the effectiveness of this backwarming.

The backwarming of the $\tau < T$ region by the $\tau > T$ region can be no more effective than placing a mirror at $\tau = T$ and reflecting all outgoing radiation back into the region $\tau < T$. Since the system with the mirror at $\tau = T$ is equivalent to a finite slab of thickness $2T$, $S_{2T}(\tau) > S_\infty^T(\tau)$ for $\tau < T$ if $B_0(\tau)$ is symmetric about the point T . If $B_0(\tau)$ is asymmetric about T , the relation will still hold if we define

$$\bar{B}_0(\tau) = \min(B_0(\tau), B_0(2T - \tau)) \quad (17)$$

and use $\bar{B}_0(\tau)$ to calculate $\bar{S}_\infty^T(\tau)$:

$$S_{2T}^{2T}(\tau) > \bar{S}_\infty^T(\tau) \quad (18)$$

Therefore, for any point $\tau < T/2$,

$$\bar{S}_{\infty}^{T/2}(\tau) < S_T^T(\tau) < S_{\infty}^T(\tau) \quad (19)$$

To evaluate these expressions for limits on $S_T(\tau)$ we will consider the expression at the point $T^* = 0$, $P_T(0) = P_{\infty}(0) = 1$. As always, $P_T(T) = 1$. The inequality for the high boundary condition is:

$$\begin{aligned} \frac{S_T(\tau) \sqrt{P_T(\tau)}}{\sqrt{P_T(T^*)}} &= \frac{\epsilon}{\sqrt{P_T(T^*)}} \int_{T^*}^{\tau} \frac{d\sigma}{\sqrt{P_T(\sigma)}} \frac{\partial B_0}{\partial \sigma} \\ &< \frac{\epsilon B(T)}{\sqrt{P_{\infty}(T) P_{\infty}(T^*)}} = \frac{\epsilon}{\sqrt{P_{\infty}(T^*)}} \int_{T^*}^T \frac{d\sigma}{\sqrt{P_{\infty}(\sigma)}} \frac{\partial B_0}{\partial \sigma} \end{aligned} \quad (20)$$

evaluating at $T^* = 0$, and solving for $S_T(\tau)$

$$S_T(\tau) < \frac{\epsilon \left[\frac{B(T)}{\sqrt{P_{\infty}(T)}} - \int_0^T \frac{d\sigma}{\sqrt{P_{\infty}(\sigma)}} \frac{\partial B_0}{\partial \sigma} + \int_0^{\tau} \frac{d\sigma}{\sqrt{P_T(\sigma)}} \frac{\partial B_0}{\partial \sigma} \right]}{\sqrt{P_T(\tau)}} \quad (21)$$

The corresponding inequality for the lower limit on the boundary condition is

$$\begin{aligned} \frac{S_T(\tau) \sqrt{P_T(\tau)}}{\sqrt{P_T(T^*)}} &= \frac{\epsilon}{\sqrt{P_T(T^*)}} \int_{T^*}^{\tau} \frac{d\sigma}{\sqrt{P_T(\sigma)}} \frac{\partial B_0}{\partial \sigma} \\ &> \frac{\epsilon \bar{B}_0(T/2)}{\sqrt{P_{\infty}(T^*) P_{\infty}(T/2)}} = \frac{\epsilon}{\sqrt{P_{\infty}(T^*)}} \int_{T^*}^{T/2} \frac{d\sigma}{\sqrt{P_{\infty}(\sigma)}} \frac{\partial \bar{B}_0}{\partial \sigma}, \end{aligned} \quad (22)$$

again evaluating at $T^* = 0$, and solving for $S_T(\tau)$

$$S_T(\tau) = \frac{\epsilon \left[\frac{\bar{B}_0(T/2)}{\sqrt{P_\infty(T/2)}} - \int_0^{T/2} \frac{d\sigma}{\sqrt{P_\infty(\sigma)}} \frac{\partial \bar{B}_0}{\partial \sigma} + \int_0^\tau \frac{d\sigma}{\sqrt{P_T(\sigma)}} \frac{\partial B_0}{\partial \sigma} \right]}{\sqrt{P_T(\tau)}} \quad (23)$$

An interesting limiting case of this expression is the case where B is constant throughout the slab. In this case, all of the integrals from equations (21) and (23) vanish and we are left with the expression:

$$\frac{\epsilon \bar{B}_0(T/2)}{\sqrt{P_T(\tau)} P_\infty(T/2)} < S_T(\tau) < \frac{B_0(T)}{\sqrt{P_T(\tau)} P_\infty(T)} \quad (24)$$

This result may be used as a derivation of the empirical observation by Avrett and Hummer (1965, eq. 4.9) that

$$0.75 < \frac{S_T(0)}{\sqrt{\epsilon S_\infty(T)}} < 1.0 \quad (25)$$

since

$$S_\infty(T) = \frac{\sqrt{\epsilon} B_0(T)}{\sqrt{P_\infty(T)}} \quad (26)$$

and in general, $0.75 < S(T/2)/S(T) < 1.0$ for a constant B slab.

While we have presented our results in terms of the source function $S(\tau)$ with the Planck function $B(\tau)$ defined, it is often

more useful computationally to be able to express the mean intensity $J(\tau)$ in terms of the source function (see Paper III). In this case we can define

$$p_e^*(\tau) = p_e(0) + p_e(T) - p_e(\tau) - p_e(T-\tau) \quad (27)$$

and combine it with equation (7) obtaining

$$\frac{\partial J}{\partial \tau} = 2p_e^* \frac{\partial S}{\partial \tau} + S(\tau) \frac{\partial p_e^*}{\partial \tau} \quad (28)$$

as a differential equation for $J(\tau)$. The definition of $J(\tau)$, equation (1a) can then be used to provide an explicit boundary condition for equation (28).

III. COMPARISON OF RESULTS

In Figure 1a we have plotted our approximation to the source function $S_T(\tau)$ for the constant B , $\epsilon = 10^{-4}$ case for various slab thicknesses T . For $T = \infty$, of course, our result is identical to that of PF. For $T = 10^2$ and $T = 10^4$ we have plotted our solution obtained with the logarithmic average of high and low boundary conditions:

$$\log [S_T(\tau)] = \frac{\log [S_T^{\text{high}}(\tau) + \log (S_T^{\text{low}}(\tau))]}{2} \quad (29)$$

The error bars near the $T = 10^2$ and the $T = 10^4$ lines represent the uncertainty in the boundary condition for that line. It is

important to realize that this uncertainty can only have the effect of shifting the entire curve up or down by the amount shown, it is not an uncertainty in the position of each individual point. The larger uncertainty in the $T = 10^2$ boundary condition is related to the difference between $S_{\infty}(T)$ and $S_{\infty}(T/2)$. For a slab which is either effectively optically thick ($T \approx 1/\epsilon$) or effectively optically thin ($T \ll 1/\epsilon$), $S_{\infty}(T)$ and $S_{\infty}(T/2)$ are not much different. However, in the intermediate case, $S_{\infty}(T)$ can differ from $S_{\infty}(T/2)$ by about 50%. In Figure 1b we present the ratio of the approximate solutions of Figure 1a to the analytical Avrett and Hummer results. For the $T = 10^4$ case, the approximation is excellent, as good as for the semi-infinite FF approximation. For the $T = 10^2$ case, the approximation is still good to about 30% at all points.

In Figure 2a, we present our results for a Planck function that is peaked in the center of the slab:

$$B(\tau) = 1 + \exp(-10) - \exp(\tau/10^3) - \exp[(T - \tau)/10^3] \quad (30)$$

In this case too, the results are quite acceptable. Once more, the error bar shows the uncertainty in the boundary condition for this case, and we have plotted the Planck function $B(\tau)$ as a reference. In Figure 2b, we show the ratio of our solution to the Avrett and Hummer solution to the same Planck function. Once again, our results are correct at a 10-20% level.

IV. CONCLUSIONS

We have presented an extension of previously published probabilistic approximations to the solution of the radiative transfer equation. Our solution recognizes the distinction between the photon escape probability p_e and the flux divergence coefficient ρ . This approximation gives results usually within 10-20 percent of the analytical solution presented by Avrett and Hummer (1965) in those cases tested, although it will certainly suffer the same inaccuracies as the Frisch and Frisch approximation in cases such as the exponential B function. When this solution is used as a formula for the source function $S(\tau)$, one of the greatest sources of error is the uncertainty in a boundary condition $S(0)$. We derive the empirical observation that

$$S_{\tau}(0) = \sqrt{\epsilon} S_{\infty}(T) \quad (31)$$

for constant B slabs. With this boundary condition, it is easy to see that the greatest uncertainty in the boundary condition will come where the function $S_{\infty}(T)$ is changing most rapidly. In the case of $\epsilon = 10^{-4}$, this seems to result in a maximum uncertainty in the boundary condition of about 50%. Our solution is valid for the case where the Planck function in the slab is asymmetric, as it almost certainly will be in any realistic case.

While generally providing an accuracy of about 10%, the major advantage of this method is that it is very fast. Canfield and Ricchiazzi (1980) present a calculation time comparison

between exact and probabilistic solutions of the radiative transfer equation for the semi-infinite case. In that comparison, the probabilistic approach had a factor of 400 advantage in computation time. This paper presents an extension of the probabilistic solution to situations where a semi-infinite slab is inappropriate.

REFERENCES

- Athay, R.G. 1972, Ap.J., 176, 659.
- Avrett, E.H., and Hummer, D.G. 1965, M.N.R.A.S., 130, 4.
- Canfield, R.C., and Puetter, R.C. 1981a, Ap.J., 243, 381 (Paper I).
- Canfield, R.C., and Puetter, R.C. 1981b, Ap.J., 243, 390 (Paper II).
- Canfield, R.C. Puetter, R.C., and Ricchiazzi, P.J. 1981, Ap.J., 248, 82 (Paper III).
- Canfield, R.C., and Ricchiazzi, P.J. 1980, Ap.J., 239, 1036.
- Frisch, U., and Frisch, H. 1975, M.N.R.A.S., 173, 167 (FF).
- Puetter, R.C., and LeVan, P.D. 1981, submitted to Ap.J. (Paper V).

This project has been supported by Air Force grant AFOSR-76-3071.

FIGURE CAPTIONS

Figure 1a. Probabilistic source functions:

$$B = \text{constant}, \epsilon = 10^{-4}.$$

Figure 1b. Ratios of probabilistic and exact source functions:

$$B = \text{constant}, \epsilon = 10^{-4}.$$

Figure 2a. Probabilistic source function:

$$B = 1 + \exp(-10) - \exp(\tau/10^3) - \exp((T-\tau)/10^3) \\ \epsilon = 10^{-4}, T = 10^4.$$

Figure 2b. Ratio of probabilistic and exact source function for

Figure 2a.

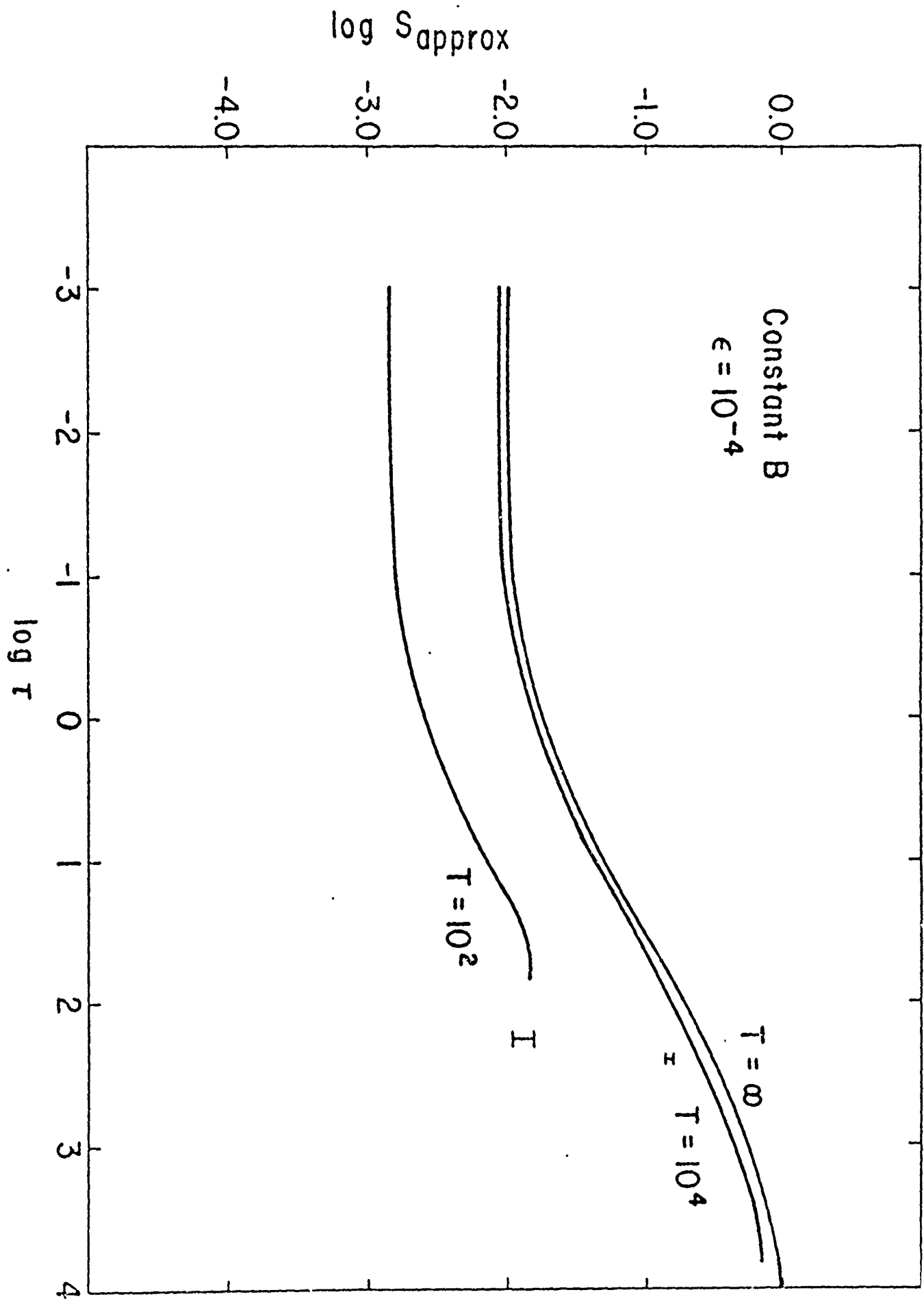


Figure 1a.

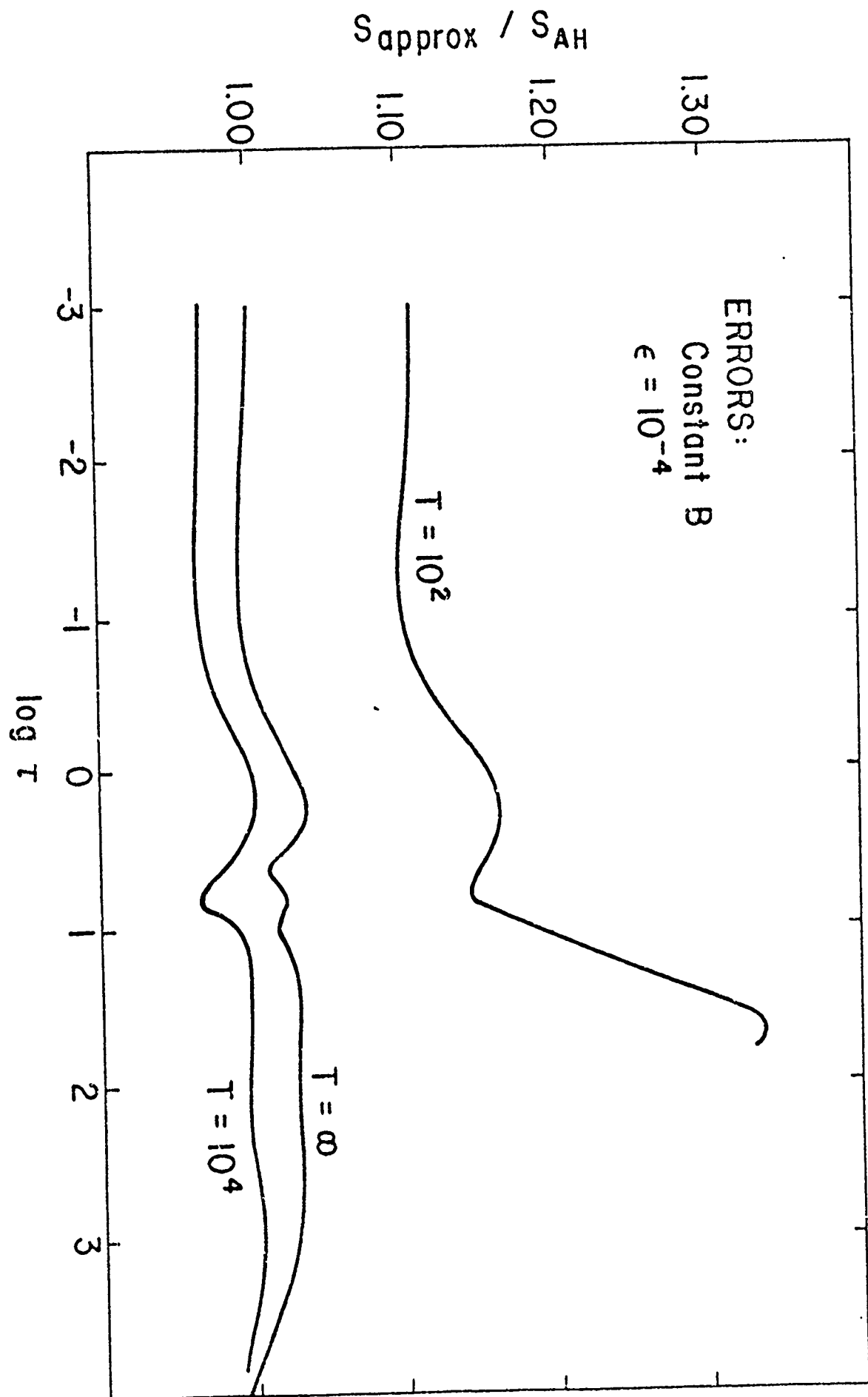


Figure 1b.

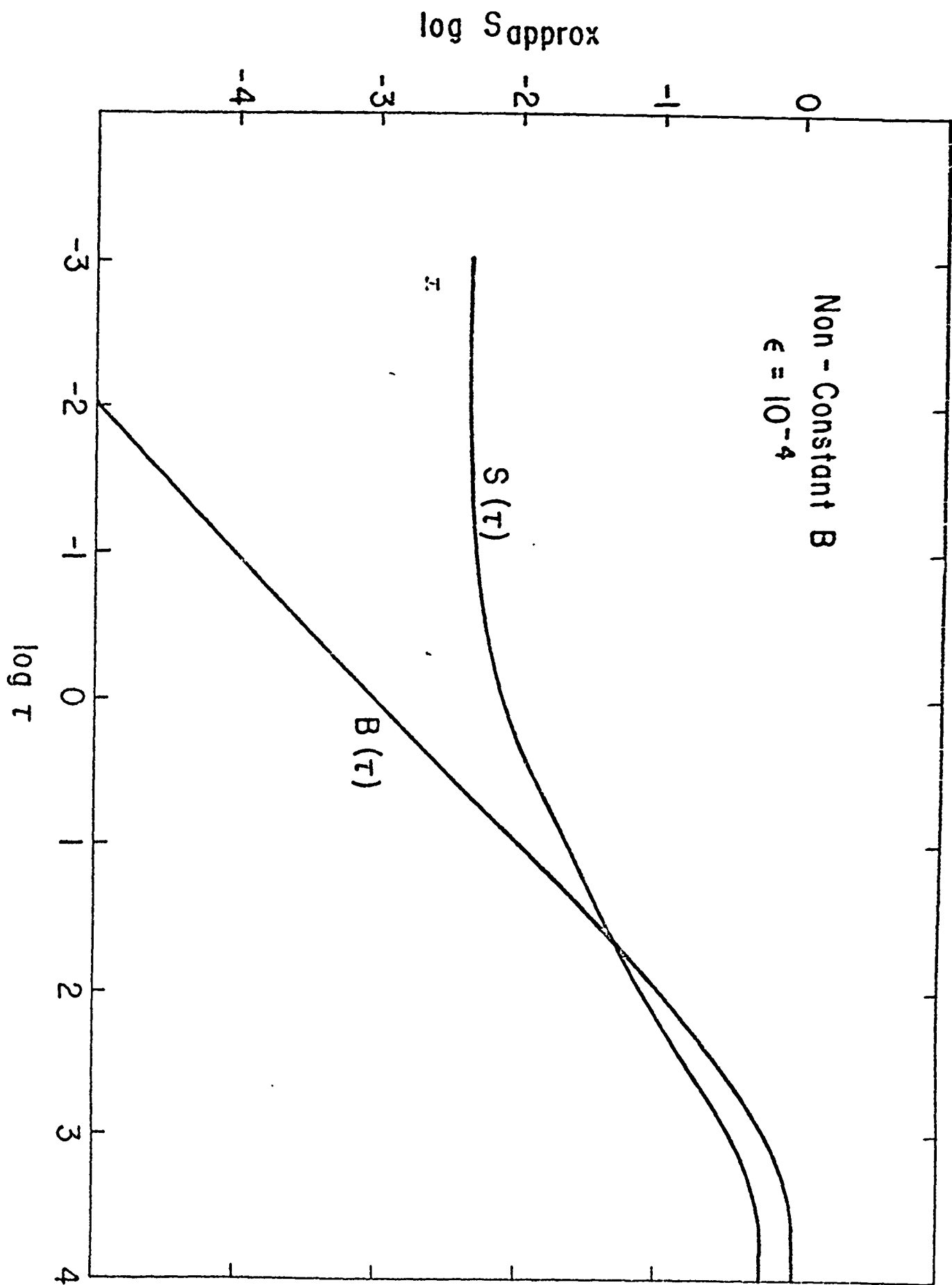


Figure 2a.

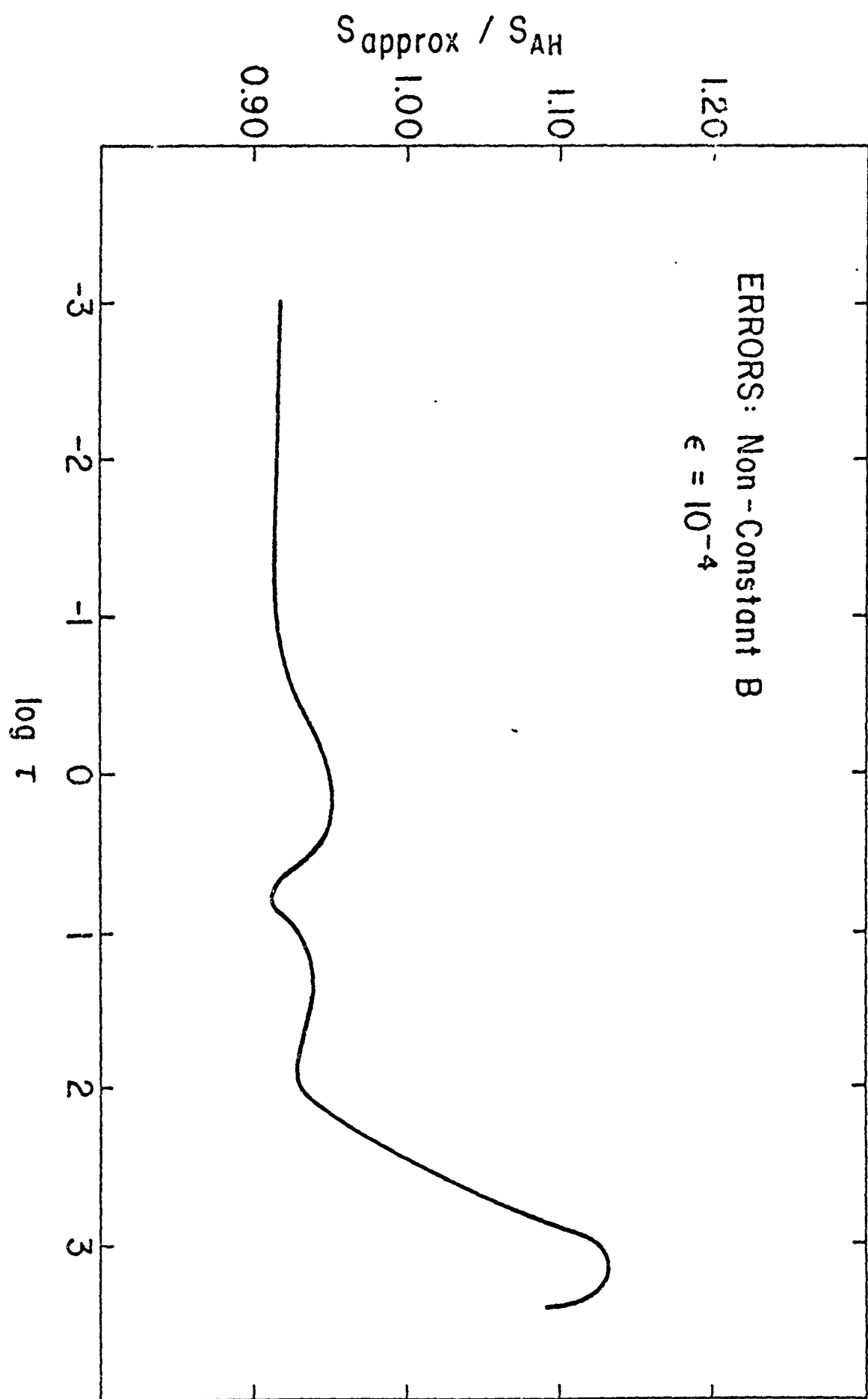


Figure 2b

R.C. Canfield

E.N. Hubbard

R.C. Puetter

Paul J. Ricchiazzi

Center for Astrophysics and Space Sciences, C-011

University of California, San Diego

La Jolla, CA 92093

R.C. Canfield

E.N. Hubbard

R.C. Puetter

Paul J. Ricchiazzi

Center for Astrophysics and Space Sciences, C-011

University of California, San Diego

La Jolla, CA 92093

f) Summary

The results of this grant can be summarized as follows:

Contributions to Skylab Solar Flare Workshop

(1) We participated actively in this two-year workshop, and served in a leadership role. This workshop was the most important international study effort in the field of solar flares during the several years preceeding the Solar Maximum Mission.

Interpretation of Existing Flare Observations

(1) We showed from Skylab observations that the solar flares observed accelerated protons much less effectively than electrons.

(2) We showed that the observations of one of the geophysically significant August 1972 solar flares implied that most of the flare energy goes into heat, not particle acceleration.

New Flare Observations

(1) We obtained the most complete data presently available on the profile of the most important chromospheric spectral line, the hydrogen Lyman- α line, before, during and after two solar flares.

(2) Our new Sacramento Peak Observatory observations of the spectrum of the H α line of hydrogen before, during and after a very interesting Solar Maximum Mission flare proved that the chromosphere was the source of the extremely hot plasma that emitted the flare X-rays.

New Theoretical Techniques

(1) We established the $H\alpha$ spectral signature of chromospheric evaporation.

(2) We established the $H\alpha$ spectral signature of accelerated electron beams.

(3) We developed a method of theoretical radiative transfer that is a major improvement in computational efficiency and physical understanding.

(4) We applied this method in the development of a powerful radiative hydrodynamics code capable of simulation of the chromospheric flare loop dynamics, for comparison with our observations.

(5) We began a program of theoretical magnetohydrodynamics of flare loops.

III. PROFESSIONAL PERSONNEL

Richard C. Canfield

Research Physicist

Principal Investigator

Alexander N. McClymont

Assistant Research Physicist

Chang-Hyuk An

Postgraduate Research Physicist

Richard C. Puetter

Postgraduate Research Physicist

Todd A. Gunkler

Research Assistant

Paul J. Ricchiazzi

Research Assistant

IV. PUBLICATIONS

Brown, J.C., Canfield, R.C., and Robertson, M.M. 1978; Solar Physics 57, 399, "H-alpha Profiles from Electron-Heated Solar Flares."

Keil, S.L., and Canfield, R.C. 1978; Astronomy and Astrophysics 70, 169, "The Height Variation of Velocity and Temperature Fluctuations in the Solar Photosphere."

Canfield, R.C., Pasachoff, J.M., Stencel, R.E., and Beckers, J.M. 1978; Solar Physics 58, "Spatial Structure in Lines in the 3398-3526 A Region at the Extreme Limb: Observation, Identification and Interpretation."

Canfield, R.C., and Cook, J.W. 1978; Astrophysical Journal 225, 650, "ATM Evidence for Low Non-Thermal Proton/Electron Energy Flux Ratio in Solar Flares."

Hudson, H.S., Canfield, R.C., and Kane, S.R. 1978; Solar Physics 60, 137, "Indirect Estimation of Energy Deposition by Non-Thermal Electrons in Solar Flares."

McClymont, A.N., and Canfield, R.C. 1979; in Solar and Interplanetary Dynamics, (ed. M. Dryer and E. Tandberg-Hanssen) p. 313, "Radiative Hydrodynamics of Flares: Preliminary Results and Numerical Treatment of the Transition Region."

Canfield, R.C., Brown, J.C., Brueckner, G.E., Cook, J.W., Craig, I.J.D., Dolschek, G.A., Emslie, A.G., Henoux, J.-C., Lites, B.W., Machado, M.E., and

Underwood, J.H. 1980; Solar Flares: A Monograph from Skylab Solar Workshop II (ed. P.A. Sturrock), "The Chromosphere and Transition Region."

Canfield, R.C., Cheng, C.C., Dere, K.P., Dulk, G.A., McLean, D.J., Robinson, R.D., Jr., Schmahl, E.J., and Schoolman, S.A. 1980; in Solar Flares: A Monograph from Skylab Solar Workshop II, (ed. P.A. Sturrock), "Radiative Energy Output of the 5 September Flare."

Canfield, R.C., and Ricchiazzi, P.J. 1980; Astrophysical Journal 239, 1036, "A Probabilistic Approach to Radiative Energy Loss Calculations for Optically Thick Atmospheres: Hydrogen Lines and Continua."

Canfield, R.C., and Puetter, R.C. 1980; Astrophysical Journal (Letters) 236, L7, "The Implications of Hydrogen Emission Line Ratios in Quasi-Stellar Objects."

Canfield, R.C., and Van Hoosier, M.E. 1980; Solar Physics 61, 339, "Observed Lyman- α Profiles for Two Solar Flares: 1412 UT, 15 June 1973 and 2316 UT, 21 January 1974."

An, C.-H. 1981; Solar Physics 75, p. 19, "The Effects on the MHD Stability of Field Line Tying to the End Faces of a Cylindrical Magnetic Loop."

Canfield, R.C., and Puetter, R.C. 1981; Astrophysical Journal 243, 381, "Theoretical Quasar Emission Line Ratios. I. Transfer and Escape of Radiation."

Canfield, R.C., and Puetter, R.C. 1981; Astrophysical Journal, 243, 390,

"Theoretical Quasar Emission Line Ratios. II. Hydrogen $L\alpha$, Balmer and Paschen Lines and the Balmer Continuum."

Canfield, R.C. 1982; Solar Physics **75**, 263, "A Qualitative Interpretation of 7 August 1972 Impulsive Phase Flare $H\alpha$ Line Profiles."

Canfield, R.C., Puetter, R.C., and Ricchiazzi, P.J. 1981; Astrophysical Journal **249**, 383, "The $L\alpha/H\alpha$ Ratio in Solar Flares and Quasars."

Canfield, R.C., Puetter, R.C., and Ricchiazzi, P.J. 1981; Astrophysical Journal **248**, 82, "Theoretical Quasar Emission Line Ratios III. Flux Divergence and Photon Escape."

McClymont, A.N., and Canfield, R.C. 1981; Astrophysical Journal (submitted), "Radiative Gas Dynamics of Flare Loops I. Basic Method."

McClymont, A.N., and Canfield, R.C. 1981; Astrophysical Journal (submitted), "Radiative Gas Dynamics of Flare Loops II. Stability of Empirical Models."

Acton, L.W., Canfield, R.C., Gunkler, T.A., Hudson, H.S., Kiplinger, A.L., and Lebacher, J.W. 1981; Astrophysical Journal (submitted), "Direct Evidence for Chromospheric Evaporation in a Well-Observed Compact Flare."

Puetter, R.C., Hubbard, E.N., Ricchiazzi, P.J., and Canfield, R.C. 1981; Astrophysical Journal (in press), "Theoretical Quasar Emission Line Ratios VI. A Probabilistic Radiative Transfer Equation for Finite Slab Atmospheres."

V. SPOKEN PAPERS

"ATM-Skylab Observations of Flare Lyman- α Line Profiles", R.C. Canfield and M.E. VanHoosier, Topical Conference on Solar and Interplanetary Physics, Tucson, 12 January 1977.

"ATM Evidence for a Low Nonthermal Proton/Electron Energy Flux Ratio in Solar Flares", R.C. Canfield and J.W. Cook, American Astronomical Society, Madison, 28 June 1978.

"Report of the Secondary Energy Release Team", R.C. Canfield, American Astronomical Society, Solar Physics Division, Ann Arbor, 15 November 1978.

"A Probabilistic Approach to Radiative Energy Loss Calculations for Optically Thick Atmospheres: Hydrogen Lines and Continua", R.C. Canfield Canfield and P.J. Ricchiazzi, American Astronomical Society, Mexico City, 9 January 1979.

"Theoretical Intensities of Lyman- α , Balmer- α and Paschen- α in QSO Clouds", R.C. Canfield and R.C. Puetter, American Astronomical Society, Mexico City, 9 January 1979.

"Radiative Hydrodynamics of Flares: Preliminary Results and Numerical Treatment of the Transition Region", A.N. McClymont and R.C. Canfield, IAU Symposium 91, Cambridge, MA, 28 August 1979.

"The Thermal vs. Non-Thermal Flare Controversy: More Fuel for the Fire", R.C.

Canfield, American Astronomical Society, San Francisco, CA, 14 January 1980.

"On the Formation of Lyman- α , the Balmer and Paschen Lines and the Balmer Continuum in Quasars", R.C. Canfield and R.C. Puetter, American Astronomical Society, San Francisco, CA, 15 January 1980.

"Solar Flares", R.C. Canfield, Solar Optical Telescope Symposium, Goddard Space Flight Center, 24 January 1980.

"Lyman- α /H α in Solar Flares and QSOs", R.C. Canfield and R.C. Puetter, American Astronomical Society, College Park, MD, 17 June 1980.

"Line and Continuum Cooling in QSO Emission Line Regions", R.C. Canfield and R.C. Puetter, American Astronomical Society, College Park, MD, 18 June 1980.

"A Method for Combined Hydrodynamics and Probabilistic Radiative Transfer", A.N. McClymont and R. C. Canfield, Solar Physics Division, American Astronomical Society, Taos, 9 January 1981.

"The Field Line Tying Effect on a MHD Stability of a Coronal Magnetic Loop", C.-H. An, American Astronomical Society, Albuquerque, 11 January 1981.

"A Sufficient Condition for Evaluation of the Stability of Solar Coronal Loops", C.-H. An, A.N. McClymont, and R.C. Canfield, Solar Physics Division, American Astronomical Society, Taos, 9 January 1981.

"CCD Observations of the Profile of H α Throughout the Flare of 1456 UT 07 May

1980", T.A. Gunkler and R.C. Canfield, Solar Physics Division, American Astronomical Society, Taos, 8 January 1981.

"A Probabilistic Radiative Transfer Equation for Finite Slab Models of QSO Emission Line Regions", P.J. Ricchiazzi, R.C. Puetter, E.N. Hubbard and R.C. Canfield, American Astronomical Society, Boulder, 11 January 1982.

"Models of Electron Heated Solar Flare Chromospheres", P.J. Ricchiazzi and R.C. Canfield, American Astronomical Society, Boulder, 11 January 1982.

"Non-Local Effects of Radiative Transfer on Radiative Hydrodynamic Stability", G.H. Fisher, R.C. Canfield, and A.N. McClymont, American Astronomical Society, Boulder, 11 January 1982.

"Non-Linear Development of the Radiative Hydrodynamic Instability in Empirical Solar Loop Models", C.-H. Im, R.C. Canfield, A.N. McClymont and G.H. Fisher, American Astronomical Society, Boulder, 12 January 1982

"Direct Evidence for Chromospheric Evaporation in a Well-Observed Compact Flare", R.C. Canfield, L.W. Acton, T.A. Gunkler, H.S. Hudson, A.L. Kiplinger, and J.W. Leibacher, American Astronomical Society, Boulder, 12 January 1982.

VI. CONSULTATIVE AND ADVISORY FUNCTIONS

Spacelab Proposal Review, National Aeronautics and Space Administration, Goddard Space Flight Center, Greenbelt, MD, 24-28 January 1977, R.C. Canfield

Committee on Space Physics, National Academy of Sciences, Washington DC, 27 February-1 March 1978, R.C. Canfield.

Committee on Space Physics, National Academy of Sciences, University of California, Los Angeles, CA, 25-26 May 1978, R.C. Canfield

Optical and Infrared Subcommittee, Astronomy Advisory Committee, National Science Foundation, Laramie, WY, 8 September 1978, R.C. Canfield

Committee on Space Physics, National Academy of Sciences, Marshall Space Flight Center, Huntsville, AL, 3-8 October 1978, R.C. Canfield.

Space Science Platform Study, Mid-Course Review, NASA Headquarters, Washington, DC, 22-23 January 1979, R.C. Canfield.

Spacelab Proposal Reviews. NASA Headquarters, Goddard Space Flight Center, Greenbelt, Md., 12-15 March 1979, R.C. Canfield.

Space Science Platform Study, Final Review, NASA Headquarters, Washington, DC, 23 March 1979, R.C. Canfield.

Astronomy Survey Committee, National Academy of Sciences, La Jolla, Calif.,

9 April 1979, R.C. Canfield.

Committee on Solar and Space Physics, National Academy of Sciences, Boulder, CO,
18-19 April 1979, R.C. Canfield.

Committee on Solar and Space Physics, National Academy of Sciences, Washington,
DC, 27-28 September 1979, R.C. Canfield.

Sacramento Peak Observatory Visiting Committee, Association of Universities for
Research in Astronomy, Sunspot, NM, 10-11 October 1979, R.C. Canfield.

Solar Terrestrial Observatory Science Study Group, NASA, Marshall Space Flight
Center, Huntsville, AL, 19-20 November 1979, R.C. Canfield.

Committee on Solar and Space Physics, National Academy of Sciences, La Jolla,
CA, 28-29 January 1980, R.C. Canfield.

Solar Terrestrial Theory Program Proposal Review, Goddard Space Flight Center,
MD, 4-6 February 1980, R.C. Canfield.

Solar Terrestrial Observatory Science Study Group, Boulder, CO, 20-22 February
1980, R.C. Canfield.

Science and Application Space Platform, Quarterly Review, Washington, DC,
27 March 1980, R.C. Canfield.

Solar Terrestrial Observatory Science Study Group, Pasadena, CA, 9-11 July

1980, R.C. Canfield.

Sacramento Peak Observatory Visiting Committee, Sunspot, NM, 6-8 August 1980,
R.C. Canfield.

Space Science Board, National Academy of Sciences, Washington, DC, 23-
25 October 1980, R.C. Canfield.

Committee on Solar and Space Physics, National Academy of Sciences, Washington,
DC, 3-4 November 1980, R.C. Canfield.

Solar Optical Telescope Proposal Review, National Aeronautics and Space
Administration, Goddard Space Flight Center, Greenbelt, MD 2-4 February 1981,
R.C. Canfield.

Space Science Board, National Academy of Sciences, Marshall Space Flight Center,
Huntsville, AL, 26-27 February 1981, R.C. Canfield.

Advisory Committee, Physics of the Sun Study, National Academy of Sciences,
Phoenix, AZ, 19-20 March 1981, R.C. Canfield.

Space Science Board, National Academy of Sciences, Washington, DC, 14-16 May
1981, R.C. Canfield.

Space Science Board, National Academy of Sciences, Washington, DC, 29-31 October
1981, R.C. Canfield.

Advisory Committee, Physics of the Sun Study, National Academy of Sciences,
Boulder, CO, 11 January 1982, R.C. Canfield.